Evgeniĭ Stanislavovich Borovik on the ninetieth anniversary of his birth

[DOI: 10.1063/1.1884421]

Almost 40 years have passed since the untimely death of Evgeniĭ Stanislavovich Borovik, and the feeling of shock at the unexpected passing of this energetic, robust, and charming man in the full flower of his talent still lingers in the community of physicists, especially those who knew him personally.

The multifaceted nature of Borovik's talent was impressive. He was an outstanding specialist in various fields of physics: low-temperature physics, magnetism, and plasma physics, and also in the techniques of cryogenics, high vacuum, and high magnetic fields.

After defending his Candidate's Dissertation entitled *The Heat Capacity of Liquids* in 1947, Borovik went to work on the problem of achieving ultrahigh vacuum. He developed a fundamentally new cryogenic method of obtaining ultrahigh vacuum, which significantly improved the productivity of a number of devices. This method became widely used both at home and abroad.

Borovik's fundamental contribution to solid-state physics was his research on galvanomagnetic phenomena. He obtained laws describing the behavior of metals at high magnetic fields which showed that the properties of the charge carriers in metals, the conduction electrons, are substantially different from those of free electrons. These interesting and important results could not be explained by the theoretical concepts of the existing electronic properties of metals. The series of papers on this subject was therefore of great value in stimulating the development of the modern electronic theory of metals. Thanks to Borovik's results, study of the galvanomagnetic properties of metals became the most efficient method for studying the electron energy spectrum of solids.

In 1958 Borovik showed that it was practical in principle for a thermonuclear reaction to occur in a high-density plasma at comparatively low temperatures and also pointed out the prospects for using high-pressure plasmas in other areas of science and engineering. In that same year the laboratory he created began the development of a new field of plasma physics—the study of the properties of discharge plasmas at high and ultrahigh pressures. His laboratory conducted wide-ranging research in the application of low-temperature technique to plasma physics, and one of the first achievements was the design and construction of multiple-ply solenoids of pure metals cooled to low temperatures.

Borovik and his co-workers were the authors of an adiabatic magnetic-mirror plasma trap project. This made extensive use of cryogenic technique: low-temperature solenoids for producing high pulsed and steady-state fields, condensation and helium pumps, which made it possible to study the process of penetration of fast protons into pure metal surfaces in deep vacuum (modeling the conditions at the walls of a thermonuclear reactor). Under Borovik's leadership

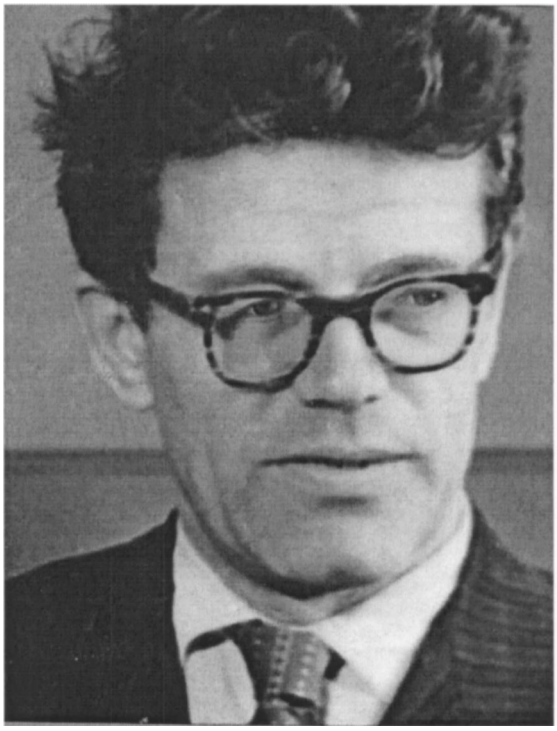

other original studies were done in connection with the use of cryogenic methods (betatron using cryogenic solenoids, the impulse strength of metals at low temperatures, etc.).

For many years Borovik taught a lecture course on ferromagnetism at Kharkov University, and under his leadership the Magnetism Group carried out wide-ranging research on magnetic materials. He trained quite a number of specialists in this field. Borovik's lecture course was the basis of an often reprinted textbook on magnetism. In the last years of his life, Borovik served simultaneously at the Ukrainian Physico-Technical Institute (UFTI) of the Academy of Sciences of the Ukrainian SSR and occupied the Chair of Ultrahigh Vacuum at the Kharkov State University.

In 1961 Borovik, who was the author of more than 120 scientific papers and patents, was elected Correspondent Member of the Academy of Sciences of the Ukrainian SSR. He was awarded the Medal of Distinction for his scientific activity.

Borovik was an outstanding physicist and a talented scientific organizer. Unselfishly devoted to science, he had an inexhaustible creativity and was a knowledgeable and talented investigator whose work had a significant influence on the development of research in a number of different fields of modern physics. Unfailingly charming and direct in manner and having an inexhaustible creative energy, Borovik stands as a model of the unselfish servant of science.

Many of Borovik's students and colleagues have contributed articles in his memory to this special issue honoring the

ninetieth anniversary of his birth. While the range of interests of Borovik and his students and others who have followed in his footsteps extends beyond the scope of the journal *Low Temperature Physics*, the Editorial Board has accepted papers consistent with the coverage of this journal: the electronic properties of metals, superconductivity, and low-temperature magnetism.

We thank the authors of those papers and all who cherish the memory of Evgeniĭ Stanislavovich Borovik.

V. V. Eremenko and V. S. Borovikov

Galvanomagnetic phenomena in layered organic conductors (Review)

M. V. Kartsovnĭk*

Walther-Meissner Institute, Walther-Meissner Str. 8, D-85748 Garching, Germany

V. G. Peschansky

B. Verkin Institute for Low Temperature Physics and Engineering, National Academy of Sciences of Ukraine, pr. Lenina 47, Kharkov 61103, Ukraine; V. N. Karazin Kharkov National University, pl. Svobody 4, Kharkov 61077, Ukraine

(Submitted October 8, 2004)
Fiz. Nizk. Temp. **31**, 249–271 (March–April 2005)

The experimental research on galvanomagnetic phenomena in layered organic conductors at high magnetic fields is discussed in terms of the theoretical ideas about charge transfer phenomena in conductors with a metallic type of conductivity and a quasi-two-dimensional electron energy spectrum of arbitrary form. Attention is devoted mainly to the problem of recovering the dispersion relation of the conduction electrons in layered organic charge-transfer complexes from experimental studies of their magnetoresistance and quantum oscillation phenomena at low temperatures. © *2005 American Institute of Physics.* [DOI: 10.1063/1.1884422]

1. INTRODUCTION

Interest in low-dimensional organic conductors rose sharply in the 1960s after Little's suggestion[1] that high-temperature superconductivity might be realized in one-dimensional polymer chains. Despite the fact that this idea has not found experimental confirmation, joint efforts of physicists and chemists have led to the creation of a new class of organic salts having metallic electrical conductivity.[2,3]

A characteristic feature of the electronic properties of the first organic metals was a pronounced anisotropy of a quasi-one-dimensional type due to their crystal structure. The main structural elements of these compounds are planar molecules having donor or acceptor properties. The best-known examples of such molecules are tetrathiafulvalene (TTF), tetramethyltetraselenafulvalene (TMTSF), tetraselenatetracene (TST), and tetracyanoquinodimethane (TCNQ), which are shown schematically in Fig. 1. The radical ions of these molecules form regular stacks along a preferred crystallographic direction. The interplane distance between molecules is often shortened as compared to the van der Waals separation. The mutual orientation of neighboring radical ions in the stack makes for significant overlap of the π molecular orbitals at minimal Coulomb repulsion. Fractional charge transfer from the radical ions to the counterions causes a partial occupation of the conduction bands thus formed. As a result, the conductivity σ along the stacks at room temperature in a number of compounds exceeds $\sim 10^3$ S/cm and grows with decreasing temperature. At the same time, the overlap of the molecular orbitals between stacks is much weaker, making for extremely low conductivity in the transverse direction, ~ 1 S/cm or less, at room temperature. Such high anisotropy of the electronic properties leads to Peierls instability of the metallic state, characteristic for quasi-one-dimensional conductors: as the temperature is lowered, the substance undergoes a transition to an insulating state with the formation of a charge- or spin-density wave.[4–6]

To suppress the insulator transition it is necessary to increase the dimensionality of the conducting system, i.e., to strengthen the coupling between stacks. On the one hand, this can be achieved by the application of high pressure. Indeed, a metallic state stable to the very lowest temperatures was first obtained at a pressure $P \approx 5$ kbar in the quasi-one-dimensional complex $(TST)_2Cl$.[7] Subsequently similar results were obtained on a number of other compounds.[8] The most exciting achievement was the discovery in 1980 of superconductivity under pressure ($P \sim 9$ kbar) in $(TMTSF)_2PF_6$ (Ref. 9) and then in the isostructural salts $(TMTSF)_2X$ with $X = AsF_6$, SbF_6, ClO_4, etc. (a detailed

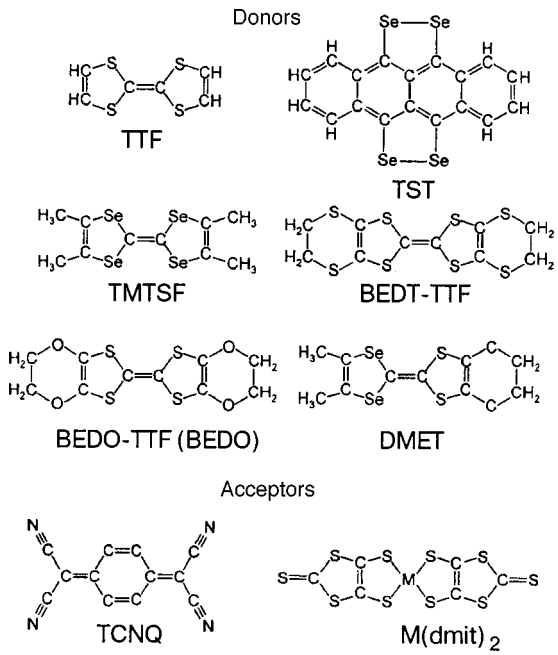

FIG. 1. Donor and acceptor molecules on which the best-known crystalline organic conductors are based (the full names of the molecules are given in the text).

review of the physical properties of these so-called Bechgaard salts can be found in Refs. 8 and 10). It must be noted, however, that the superconductivity in those compounds competes with instability of the Peierls type (in this case leading to a state with a spin-density wave), which limits the temperature of the superconducting transition to values in the 1 K region.

On the other hand, it has proved possible to synthesize conducting complexes in which the organic molecules do not form weakly coupled individual stacks but rather form integral layers with significant overlap of the π orbitals in two directions. For example, the first layered (quasi-two-dimensional) organic superconductor β-(BEDT-TTF)$_2$I$_3$ (BEDT-TTF denotes bis(ethylenedithio)tetrathiafulvalene; see Fig. 1) was synthesized in 1984.[11] The crystal structure of this compound is given in Fig. 2. The BEDT-TTF$^{0.5+}$ cation radicals form stacks arranged in layers alternating with the layers of I_3^- ions. The presence of a significant number of shortened contacts both inside the stacks and between them makes for an almost isotropic conductivity along the layers, $\sigma_\parallel \approx 30$ S/cm, at room temperature, while in the direction perpendicular to the layers the conductivity is almost three orders of magnitude lower.[12] Nevertheless the temperature dependence of the resistivity $\rho = 1/\sigma$ is of a metallic character independent of the direction of the current; the resistance falls off monotonically with cooling, and at $T = 2$ K it is more than two orders of magnitude lower than at room temperature. On further cooling the substance goes into the superconducting state ($T_c \approx 1.5$ K).[11] Interestingly, at a relatively low pressure (below 1 kbar) the superconducting transition temperature increases abruptly by a factor of five, jumping from 1.5 K to 7.5–8.0 K.[13,14]

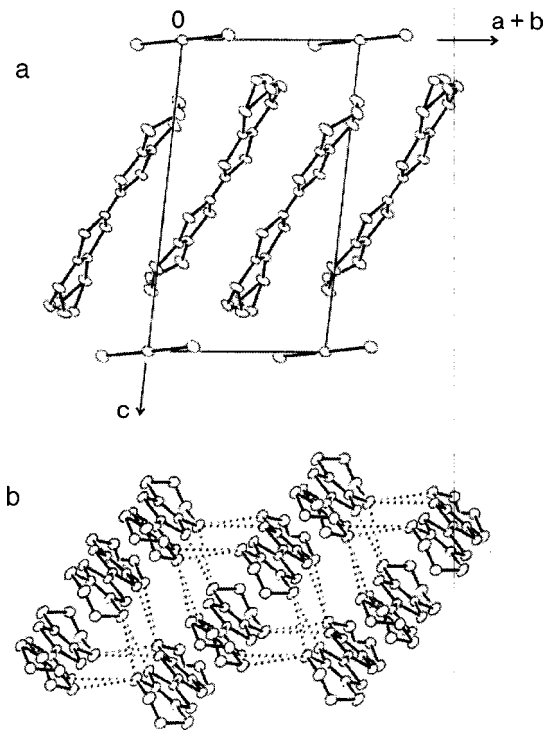

FIG. 2. Crystal structure of the quasi-two-dimensional organic superconductor β-(BEDT-TTF)$_2$I$_3$ according to the data of V. F. Kaminskiĭ, T. G. Prokhorova, R. P. Shibaeva, and É. B. Yagubskiĭ, JETP Lett. **39**, 17 (1984). The stacks of BEDT-TTF$^{0.5+}$ cation radicals, which lie in the crystallographic direction (**a**+**b**), form layers separated along the **c** axis by layers of I_3 anions (a); the arrangement of the molecules in the conducting layer; the dotted lines denote the shortened contacts responsible for the metallic conductivity between the sulfur atoms from neighboring molecules (b). The figure was kindly provided by S. S. Khasanov and R. P. Shibaeva.

Soon after the discovery of superconductivity in β-(BEDT-TTF)$_2$I$_3$ the isostructural superconducting salts of BEDT-TTF with the anions IBr_2^- and AuI_2^- were synthesized, with transition temperatures $T_c = 2.7$ K and 4.8 K, respectively,[15,16] significantly exceeding the highest transition temperature in quasi-one-dimensional superconductors. By now there are some dozens of layered organic superconductors known, most of which are BEDT-TTF salts.[10] Some of the other molecules for which superconducting compounds have been synthesized are shown in Fig. 1: bis(ethylenedioxy) tetrathiafulvalene (BEDO-TTF), dimethylethylenedithiodiselenadithiofulvalene (DMET), and metal complexes of bis-4,5-dimercapto-3-dithiol-2-thione (M(dmit)$_2$). The record values of T_c at present have been obtained in the layered compounds κ-(BEDT-TTF)$_2$[N(CN)$_2$]X with X = Br ($T_c \approx 11.6$ K, $P = 0$ kbar)[17] and X = Cl ($T_c \approx 12.8$ K, $P = 0.3$ kbar),[18] and β'-(BEDT-TTF)$_2$ICl$_2$ ($T_c \approx 14.2$ K, $P = 82$ kbar).[19]

To understand the nature of superconductivity and a number of other, no less interesting, phenomena observed in organic conductors (see the review in Ref. 10, for example), detailed knowledge of the electron band structure of these compounds is needed. In the case of ordinary metals high magnetic fields are a powerful tool for investigating the electronic spectrum. In particular, measurements of the anisotropy of the magnetoresistance permit one to investigate the topology of the Fermi surface of the metal,[20–24] and from the Shubnikov–de Haas oscillations one can determine the values of the extremal closed cross sections of the Fermi surface and some other important characteristics of the charge carriers.[23–25] These methods are widely used to study the electronic structure of ordinary three-dimensional metals.[25–27]

In 1988 Shubnikov-de Haas oscillations were observed in the layered superconductors β-(BEDT-TTF)$_2$IBr$_2$ (Refs. 28 and 29) and κ-(BEDT-TTF)$_2$Cu(NCS)$_2$ (Ref. 30) at magnetic fields ~ 10 T. These studies provided the first direct proof of the validity of the Fermi liquid description of the electronic properties of the given materials and stimulated intensive further research on organic conductors at high magnetic fields. By the mid-1990s extensive information had been accumulated on the subject, a detailed review of which was given by Wosnitza.[31] Some interesting results of the application of high fields for studying layered organic conductors are reviewed in Refs. 32 and 33.

By virtue of the extremely high anisotropy of the electronic properties of organic conductors, their behavior in a strong magnetic field differs substantially from that of ordinary three-dimensional materials. This is true of both the quantum oscillations of the magnetoresistance and its quasiclassical components, which demonstrate qualitatively new effects absent in moderately anisotropic three-dimensional metals and in purely two-dimensional conducting systems.

In this article we review the basic galvanomagnetic phenomena observed in layered organic conductors and their use

for quantitative study of the electronic spectrum of these materials. Attention is devoted mainly to the interlayer magnetoresistance features caused by the presence of a Fermi surface in the form of a cylinder with arbitrary cross section and with only a slight corrugation in the direction perpendicular to the highly conductive layers. A prominent example of a system having such a Fermi surface is the superconductor β-(BEDT-TTF)$_2$IBr$_2$ (Refs. 10, 31, and 32), which is isostructural to the complex β-(BEDT-TTF)$_2$I$_3$. In particular, the Shubnikov-de Haas oscillations with two close frequencies attest to a simply connected Fermi surface in the form of a slightly ($\sim$1%) corrugated cylinder occupying approximately half the volume of the Brillouin zone. Such simple topology of the Fermi surface and the high quality of single crystals of this compound make it an excellent model object for studying electronic phenomena in quasi-two-dimensional metals. Below we shall consider the quasiclassical magnetoresistance of β-(BEDT-TTF)$_2$IBr$_2$ and show that the effects observed, in particular, the peculiar dependence on the magnetic field direction, are due to the quasi-two-dimensional character of the electron spectrum and permit a quantitative description of the Fermi surface. Section 3 is devoted to Shubnikov-de Haas oscillations, the behavior of which in the substances considered is significantly different from the predictions of the standard three-dimensional theory based on the Lifshitz-Kosevich model. Although a quantitative description of the Shubnikov-de Haas effect for quasi-two-dimensional systems is far from complete, the existing models are capable of explaining a number of qualitative features observed experimentally. In the final Section we give a brief description of the Hall effect expected in a quasi-two-dimensional metal at high magnetic fields.

2. QUASICLASSICAL MAGNETORESISTANCE

The sharp anisotropy of the electrical conductivity of layered conductors is due to anisotropy of the velocities of the conduction electrons $\mathbf{v}=\partial\varepsilon/\partial\mathbf{p}$, and the energy of the charge carriers in such conductors,

$$\varepsilon(\mathbf{p})=\sum_{n=0}^{\infty}\varepsilon_n(p_x,p_y)\cos\left\{\frac{anp_z}{\hbar}+\alpha_n(p_x,p_y)\right\}; \qquad (1)$$

$$\varepsilon_n(-p_x,-p_y)=\varepsilon_n(p_x,p_y);$$

$$\alpha_n(p_x,p_y)=-\alpha_n(-p_x,-p_y)$$

depends weakly on the momentum projection $p_z=\mathbf{p}\cdot\mathbf{n}$ on the normal $\mathbf{n}$ to the layers (a is the distance between adjacent layers, and $\hbar$ is Planck's constant). It is natural to suppose that the functions $\varepsilon_n(p_x,p_y)$ with $n\geqslant 1$ are much less than the Fermi energy ε_F and fall off rapidly with increasing n, as occurs in the tight-binding approximation, for example.

The charge carrier velocity v_z along the normal to the layers is much less than the characteristic Fermi velocity v_F of the electrons along the layers, and the quasi-two-dimensionality parameter η of the charge-carrier energy spectrum can be determined as the ratio of the maximum value of v_z on the Fermi surface $\varepsilon(\mathbf{p})=\varepsilon_F$ to the value v_F, i.e.,

$$v_z=-\sum_{n=1}^{\infty}\frac{an}{\hbar}\varepsilon_n(p_x,p_y)\sin\left\{\frac{anp_z}{\hbar}+\alpha_n(p_x,p_y)\right\}\leqslant\eta v_F. \qquad (2)$$

Here the ratio of the transverse conductivity $\sigma_\perp$ to the conductivity σ_0 along the layers in the absence of magnetic field is equal in order of magnitude to the square of the quasi-two-dimensionality parameter, η^2.

In a magnetic field the components of the conductivity tensor, which relate the current density to the electric field $\mathbf{E}$,

$$j_i=\sigma_{ij}E_j, \qquad (3)$$

can be found using the Boltzmann transport equation in the τ approximation for the collision integral. Without any model assumptions about the electron energy spectrum, the quasiclassical expression for σ_{ij} in the case of periodic motion of a charge with period $T_B=2\pi/\omega_c$ in a magnetic field $\mathbf{B}$ has the form

$$\sigma_{ij}=-\frac{2e^3B}{c(2\pi\hbar)^3}\int d\varepsilon\frac{\partial f_0(\varepsilon)}{\partial\varepsilon}\int dp_B\int_0^{T_B}dt v_i(t)$$

$$\times\int_{-\infty}^{t}dt' v_j(t')\exp((t'-t)/\tau). \qquad (4)$$

Here t is the time of motion of a conduction electron in the magnetic field under the influence of the Lorentz force

$$d\mathbf{p}/dt=(e/c)[\mathbf{v}\times\mathbf{B}], \qquad (5)$$

e, τ, and $f_0(\varepsilon)$ are the charge, mean free time, and equilibrium Fermi distribution function of the conduction electrons, $\omega_c=eB/(m^*c)$ is the cyclotron frequency of an electron in a magnetic field $\mathbf{B}$, m^* is its cyclotron effective mass, p_B is the momentum projection in the magnetic field direction, and c is the speed of light.

The Fermi surface of layered conductors is weakly corrugated along the p_z axis; it can be multisheet and consist of topologically different elements in the form of slightly corrugated cylinders and slightly corrugated planes in momentum space. In the absence of marked anisotropy of the conductivity in the plane of the layers the most probable shape of the Fermi surface is that of a slightly corrugated cylinder; at least one sheet of the Fermi surface in such layered conductors is a cylinder with cross section located inside one unit cell of momentum space.

Let us consider galvanomagnetic phenomena in a conductor whose Fermi surface is in the form of just one cylinder which is slightly corrugated along the p_z axis, in a magnetic field $\mathbf{B}=(0,B\sin\theta,B\cos\theta)$. The sections of such a surface by the plane $p_B=p_z\cos\theta+p_y\sin\theta=$const at $(\pi/2-\theta)\gg\eta$ are almost the same for different values of the momentum projection p_B on the magnetic field direction, and the velocity components of the conduction electrons in the plane of the layers, $v_x(p_B,t)$ and $v_y(p_B,t)$, depend weakly on p_B. At the same time, the velocity along the normal to the layers is substantially different on different sections of the Fermi surface by the plane $p_B=$const. Hence it follows that the expansion of the components of the conductivity tensor (4) in power series in the quasi-two-dimensionality parameter η starts with the second or higher power terms, provided that at least one of the indices of σ_{ij} is z (Refs. 34 and 35).

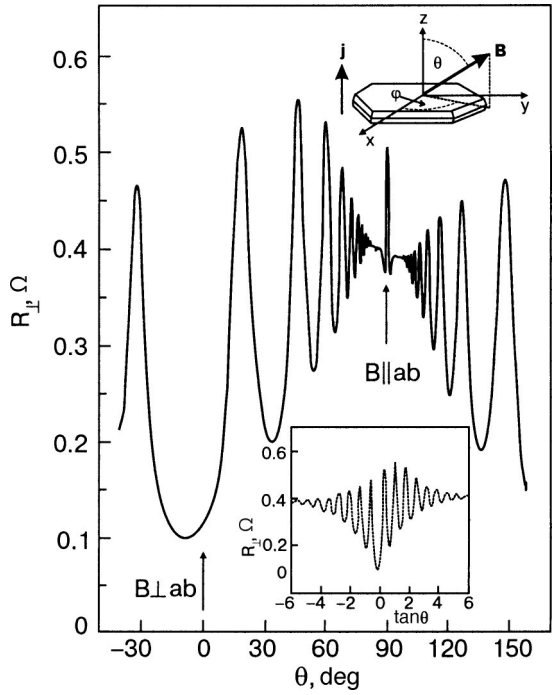

FIG. 3. Resistance of a β-(BEDT-TTF)$_2$IBr$_2$ single crystal measured in the direction perpendicular to the highly conductive plane ab, in a magnetic field $\mathbf{B}=15$ T, at $T=1.4$ K, versus the angle θ between the field direction and the normal to the ab plane. The geometry of the experiment is illustrated schematically in the upper inset. A characteristic feature of this dependence is the presence of strong oscillations that repeat periodically in the $\tan\theta$ scale, as is shown in the lower inset. In addition, a sharp peak of the magnetoresistance is observed in a narrow neighborhood of angles around $\theta=90°$ (see Sec. 2.2 and Fig. 7).

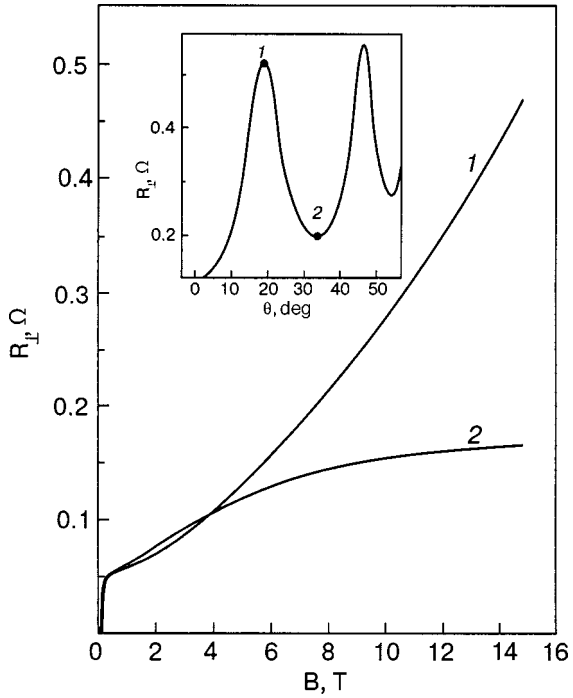

FIG. 4. Field dependence of the interlayer resistance $R_\perp$ of a β-(BEDT-TTF)$_2$IBr$_2$ single crystal at $T=1.4$ K for two different magnetic field directions. Curve *1* corresponds to a maximum and curve *2* to a minimum on the oscillatory angular dependence, as is shown in the inset.

The resistivity of such conductors along the layers is of the same order of magnitude as that of an uncompensated metal, i.e., at any orientation of the magnetic field the resistivity is essentially no different from that in the absence of field. In contrast, the resistivity ρ_{zz} along the ''hard'' direction of current flow, i.e., along the normal to the layers, is extremely sensitive to the orientation of a strong magnetic field.

Figure 3 shows an example of the angular dependence of the resistance $R_\perp$ measured in the direction perpendicular to the highly conductive plane ab of a β-(BEDT-TTF)$_2$IBr$_2$ single crystal as a magnetic field $\mathbf{B}=15$ T is rotated in a plane normal to the ab plane. The geometry of the experiment is shown schematically in the inset. The most remarkable feature of this dependence is obviously the strong oscillations of the magnetoresistance. The positions of the local maxima on the $R_\perp(\theta)$ curve are independent of the magnetic field strength and temperature,[36] and, as is seen in the figure, periodically repeat in the $\tan\theta$ scale over the entire range of angles except in a small neighborhood of $\theta=\pi/2$. The field dependence of the magnetoresistance varies sharply as the field direction is changed:[36,37] as is shown in Fig. 4, the resistance increases in approximate proportion to B^2 for the field direction corresponding to the maximum on the angular dependence (curve *1*), while at the minimum a tendency toward saturation in fields above 5 T is clearly seen.

Such behavior, which was first observed[29] in a high-quality sample of β-(BEDT-TTF)$_2$IBr$_2$, turns out to be a general property of quasi-two-dimensional metals and is manifested to some degree or other in practically all layered organic conductors (see, e.g., the review articles[31–33]) and in a number of other layered structures.[38–44] This orientation effect does not take place in ordinary metals and is observed only in layered conductors with a quasi-two-dimensional electron energy spectrum.

2.1. Angular oscillations of the magnetoresistance

When current is passed along the normal to the layers the electric field is almost parallel to the current, and ρ_{zz} is equal to $1/\sigma_{zz}$ to within corrections small in the parameter $\eta\ll 1$.

A significant first step in the explanation of the orientation effect was made by Yamaji,[45] who, for the case of a rather simple charge-carrier dispersion relation

$$\varepsilon=\frac{p_x^2+p_y^2}{2m}-2t_\perp\cos\left(\frac{ap_z}{\hbar}\right) \tag{6}$$

calculated, in the linear approximation in the small parameter $\eta\ll 1$, the dependence of the area of section of the isoenergy surface $S(\varepsilon,p_B)$ by a plane $p_B=\text{const}$ on the angle θ between the magnetic field vector and the normal to the layers:

$$S(\varepsilon_F,p_B)\cos\theta=\pi p_F^2 + 4\pi m t_\perp\cos\left(\frac{ap_B}{\hbar\cos\theta}\right)J_0\left(\frac{ap_F}{\hbar}\tan\theta\right), \tag{7}$$

where $p_F=(2m\varepsilon_F)^{1/2}$, and $J_0(u)$ is the zeroth-order Bessel function. It is clear from expression (7) that the areas of all the cyclotron orbits are practically equal at the periodically repeating zeroes of the Bessel function. Obviously this can

be achieved by an appropriate choice of the angle θ_c. At such an angle the drift velocity of the charge carriers,[46]

$$\overline{v_z}(p_B)=T_B^{-1}\int_0^{T_B}dtv_z(t,p_B)=\cos\theta\frac{\partial S/\partial p_B}{\partial S/\partial\varepsilon} \tag{8}$$

becomes negligibly small. This leads to a sharp decrease in the conductivity σ_{zz} and ultimately to a sharp peak of the magnetoresistivity ρ_{zz} at $\theta=\theta_c$.

Formulas (7) and (8) correctly reflect the qualitative nature of the angular oscillations of the magnetoresistance observed experimentally. In fact, the sharp decrease of the difference between the maximum area $S_{\max}$ and minimum area $S_{\min}$ of the cross section of the Fermi surface at the maxima of the angular dependence was evidenced back in the experiment of Ref. 29: at those orientations of the magnetic field for which the magnetoresistance took a maximum value the beats of the Shubnikov-de Haas oscillations, due to the difference $(S_{\max}-S_{\min})$, vanished.

The conductivity tensor component σ_{zz} at high magnetic field $(\omega_c\tau\gg1)$ in the case of the charge-carrier dispersion relation (6) with corrections taking into account small parameters η and $\gamma=1/\omega_c\tau$ has the form[34,47]

$$\sigma_{zz}=\frac{2ae^2m^*\tau\cos\theta}{\pi\hbar^4}t_\perp^2J_0^2\left(\frac{ap_F}{\hbar}\tan\theta\right)+\eta^2\sigma_0(\eta^2\Phi_1+\gamma^2\Phi_2), \tag{9}$$

where σ_0 is the conductivity along the layers in the absence of magnetic field, and Φ_1 and Φ_2 are functions of the tilt angle of the magnetic field to the layers and are of the order of unity.

For arbitrary field direction the Bessel function J_0 is generally nonzero, and the conductivity σ_{zz} is determined by the first term in expression (9). In that case the magnetoresistance is essentially the same as that observed in ordinary uncompensated metals: it is relatively low and goes to saturation at high magnetic field. For $\theta=\theta_c$, however, when $J_0=0$, the conductivity is proportional to γ^2, and the magnetoresistance to current transverse to the layers grows with magnetic field in proportion to B^2, reaching saturation only in the region of very high magnetic fields, i.e., for $\gamma\ll\eta$. Such a character of the field dependence is in good qualitative agreement with the experimental results presented in Fig. 4.

Naturally, a theoretical analysis of the transport phenomena with the use of a very simple model of the carrier dispersion relation in the form (6) cannot claim to give a quantitative description of the experimentally observed dependence of the magnetoresistance on the strength of the magnetic field and on its orientation with respect to the crystallographic axes; nevertheless, in many cases this model of the electron energy spectrum permits a correct comprehension of the nature of electronic phenomena in layered conductors.

In the case of an arbitrary dispersion relation of the charge carriers an asymptotic expression for $\sigma_{zz}(\eta,\gamma)$ at arbitrarily small γ and η has the form:[34,48]

$$\sigma_{zz}=\sum_{n=1}^{\infty}\int_0^{T_B}dt\int_{-\infty}^{t}dt'\left(\frac{an}{\hbar}\right)\varepsilon_n(t)\varepsilon_n(t')\frac{e^3B\cos\theta}{ac(2\pi\hbar)^2}\times\exp\left(\frac{t'-t}{\tau}\right)\cos\left\{\frac{an}{\hbar}[p_y(t)-p_y(t')]\right\}, \tag{10}$$

where all the functions in the integrand are functions of t and t' only. With corrections small in the parameters $\gamma\ll1$ and $\eta\ll1$ taken into account, the conductivity tensor component σ_{zz} takes the following form:[48,49]

$$\sigma_{zz}=\frac{ae^2m^*\tau\cos\theta}{2\pi\hbar^4}\sum n^2I_n^2(\theta)+\eta^2\sigma_0(\eta^2\varphi_1+\gamma^2\varphi_2); \tag{11}$$

where

$$I_n(\theta)=T_B^{-1}\int_0^{T_B}dt\varepsilon_n(t)\cos\{nap_y(t)\tan\theta/\hbar\}, \tag{12}$$

and the functions φ_1 and φ_2, which depend on the orientation of the magnetic field, are of the order of unity, as in the case of the carrier dispersion relation (6). The main contribution to the integral $I_n(\theta)$ for $\tan\theta\gg1$ comes from small neighborhoods of points of stationary phase, where $\partial p_y/\partial t=-(eH/c)v_x\cos\theta=0$. There are at least two such points on the closed electron orbit: these are the turning points where $v_x(t_{1,2})=0$. Here $\varepsilon_n(t_1)=\varepsilon_n(t_2)$ and, if there are no other points of stationary phase on the electron orbits, the asymptotic expression for $I_n(\theta)$ takes the form

$$I_n(\theta)=2\varepsilon_n(t_1)\frac{|2\pi\hbar|^{1/2}}{T_B|anp_y''(t_1)\tan\theta|^{1/2}}\times\cos\left\{\frac{nap_y(t_1)}{\hbar}\tan\theta-\frac{\pi}{4}\right\}, \tag{13}$$

where a prime denotes differentiation with respect to time. The functions $I_n(\theta)$ have a set of zeroes which for $\tan\theta\gg1$ repeat with a period[34,48]

$$\Delta(\tan\theta)=2\pi\hbar/aD_p, \tag{14}$$

where $D_p\equiv2p_y(t_1)$ is the extent of the cross section of the Fermi surface along the p_y axis. Thus for an arbitrary form of the quasi-two-dimensional electron energy spectrum for $\tan\theta\gg1$ the conductivity transverse to the layers, expressed by formula (11), and, hence, the interlayer resistance vary with period (14) on increasing $\tan\theta$.

From the periods of the angular oscillations of the magnetoresistance for different orientations of a strong magnetic field one can determine the shape of the cross section of the cylindrical Fermi surface. Such a procedure was first applied to β-(BEDT-TTF)$_2$IBr$_2$ in Ref. 46. The result is presented in Fig. 5. This effect is now widely used to study the Fermi surfaces of organic metals and other layered conductors (see, e.g., Refs. 31–33, 43, and 44).

Naturally, all the terms in the sum over n in formula (11) cannot vanish simultaneously. For example, at $\theta=\theta_1$, when $I_1(\theta)$ vanishes, all the functions $I_n(\theta)$ for which $(n-1)$ is not a multiple of four are substantially nonzero,[49] and the asymptotic behavior of σ_{zz} depends substantially on the character of the decay of the functions $\varepsilon_n(p_x,p_y)$ with in-

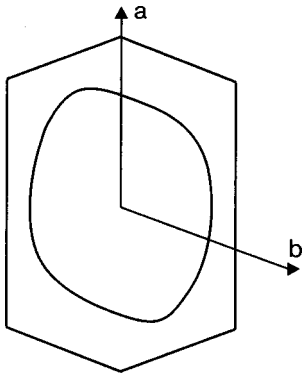

FIG. 5. Cross section of the Fermi surface of the layered organic superconductor β-(BEDT-TTF)$_2$IBr$_2$, determined from experiment on the angular oscillations of the magnetoresistance.[46] The Brillouin zone boundary and the directions of the crystallographic axes in the plane of the layers are shown.

creasing index n. Agreement with experiment can be achieved by keeping certain terms in the sum over n in the formula (11) for σ_{zz}.

A theoretical calculation of the resistance to current transverse to the layers with three terms retained in the sum over n in the formula (11) for σ_{zz} gives a result for the θ dependence of the magnetoresistance of the conductor β-(BEDT-TTF)$_2$IBr$_2$ that is closer to the experimentally observed dependence if $I_{n+1}/I_n=0.4$, while for the more anisotropic organic conductor (BEDT-TTF)$_2$DIA (DIA is diiodoacetylene) this is found for $I_{n+1}/I_n=0.2$ (Ref. 50). Figure 6 shows the results of a calculation of the angular dependence of the magnetoresistance of the organic conductor β-(BEDT-TTF)$_2$IBr$_2$ with several harmonics kept in the dispersion relation of the charge carriers for $I_{n+1}/I_n=0.04$ and $I_{n+1}/I_n=0.4$. The experimental angular dependence of the magnetoresistance was taken from Ref. 46.

The energy spectrum of the charge carriers in almost all organic compounds lacks symmetry with respect to the replacement of p_z by $-p_z$, and taking the phase of $\alpha_n(p_x,p_y)$ into account in formula (11) has a sensitive effect on the position of the sharp maxima of the magnetoresistance ver-

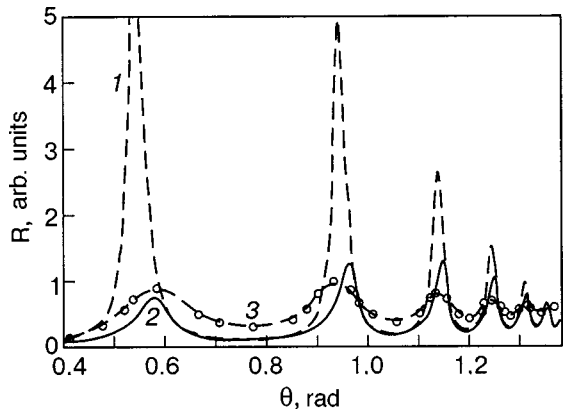

FIG. 6. Dependence of the magnetoresistance transverse to the layers for the organic conductor β-(BEDT-TTF)$_2$IBr$_2$ on the angle θ between the magnetic field vector and the normal to the layers, calculated theoretically with several Fourier components taken into account in the dispersion relation of the charge carriers: curve *1*—for $I_{n+1}/I_n=0.04$; curve *2*—for $I_{n+1}/I_n=0.4$. Curve *3*—experimental curve of the angular dependence of the resistance transverse to the layers.[46]

sus θ. In Ref. 46, by writing $\alpha_1(p_x,p_y)$ in the form of a linear combination of p_x and p_y, the results of the calculation were reconciled with the experimentally observed asymmetry in the angular dependence of the magnetoresistance.

2.2. Resistance in a magnetic field almost parallel to the layers

The contribution to the conductivity from the rapidly oscillating functions in the integrand in formula (12) for $\gamma \ll 1$ is smaller the larger the value of $\tan\theta$. Consequently, the monotonic part of the magnetoresistance increases with deviation of the magnetic field from the normal to the layers in proportion to $\tan\theta$, as long as $\eta\tan\theta \ll 1$.

When θ is quite close to $\pi/2$, specifically for $\eta\tan\theta \approx 1$, a necking of the electron orbit occurs along the p_x axis. In this region of angles θ a substantial rearrangement of the electron orbits occurs. When the neck width Δp goes to zero, a small orbit splits off from the highly elongated orbit; this small orbit is located completely inside one unit cell of momentum space. The nucleation of small electron orbits begins at a parabolic point of the Fermi surface, where the maximum value of the electron velocity along the magnetic field on the electron orbit occurs. In the case of charge-carrier dispersion relation (6) the small electron orbits arise when $\cos\theta=\eta$, and for an arbitrary shape of the Fermi surface in the form of a weakly corrugated cylinder, when $\cos\theta$ is of the order of η. With further growth of θ the number of small orbits increases, and at $\theta=\pi/2$ the relative fraction of charge carriers with small orbits in momentum space becomes of the order of $\eta^{3/2}$.

The character of the angular dependence of the magnetoresistance for $\eta\tan\theta \geqslant 1$ is easily ascertained for arbitrary dependence of the energy of the charge carriers on their momentum. In this region of magnetic-field tilt angles with respect to the layers the values of p_x, p_y, and v_x vary slowly with time, while p_z, to a sufficient degree of accuracy (to corrections small in η and $\cos\theta$) varies in time by a linear law almost everywhere on the slightly elongated orbits except in the vicinity of necks and turning points, where the velocity projection v_x is small.

To calculate the conductivity tensor component σ_{zz} for $\eta\tan\theta \approx 1$ we use the Fourier representation for the electron velocity along the z axis:

$$v_z(t)=\sum_{k=-\infty}^{\infty} v_z^{(k)}\exp(ik\omega_c t). \tag{15}$$

The contribution to the conductivity along the normal to the layers:

$$\sigma_{zz}=\frac{2e^2\tau}{(2\pi\hbar)^3} \times\int_0^{2\pi\hbar\cos\theta/a} 2\pi m^* dp_B\left\{\overline{v_z}^2+2\sum_{k=1}^{\infty}\frac{(v_z^{(k)})^2}{1+(k\omega_c\tau)^2}\right\} \tag{16}$$

from charge carriers executing motion along orbits with small necks is large, since they travel near the neck for a long time. Their period of gyration in a magnetic field diverges logarithmically as Δp goes to zero: $T_B\propto\ln(1/\Delta p)$, so

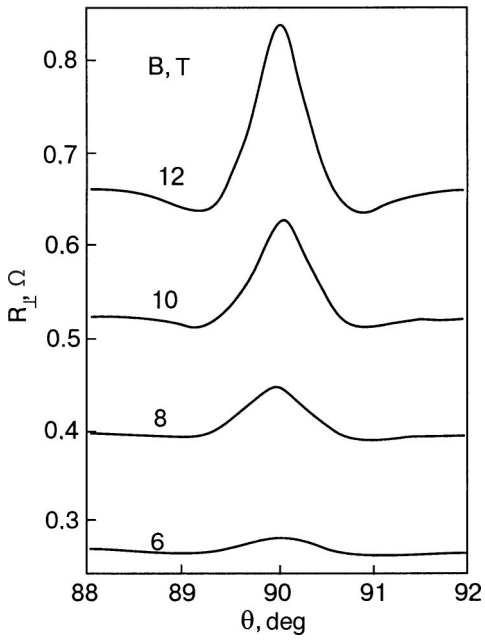

FIG. 7. Structure of the peak on the angular dependence of the magnetoresistance of β-(BEDT-TTF)$_2$I$_3$ in the vicinity of $\theta=90°$ for different values of the magnetic field. Plotted according to the data of Ref. 53.

that in a certain layer of electron orbits this period is much greater than the mean free time. The lower the cyclotron frequency ω_c, the more terms must be taken into account in the sum over k in formula (16), and for $\omega_c \to 0$ the contribution to σ_{zz} of such electrons is comparable to their contribution in the absence of magnetic field. Thus the appearance of self-intersecting electron orbits for $\eta \tan\theta \approx 1$ leads to improvement of the conductivity of the layered conductor.[51,52] As the angle θ approaches closer to $\pi/2$ the magnetoresistance begins to grow, since the term $\overline{v_z}$, which is independent of the magnetic field strength, goes to zero in proportion to $\cos^2\theta$ and the resistance to current transverse to the layers, after passing through a minimum in the region of angles where $\cos\theta$ is of the order of η, again increases, reaching its maximum at $\theta=\pi/2$.[51,52] In this case the resistance to current transverse to the layers increases without saturation with increasing magnetic field in the plane of the layers.

Formula (16) gives a good description of experiment. Indeed, the angular dependence of the magnetoresistance in Fig. 3 demonstrates a slight drop that is followed by a rapid rise at angles $\theta \to \pi/2$. A detailed study of the magnetoresistance peak in the vicinity of $\theta=\pi/2$ was carried out by Hanasaki *et al.*[53] for the layered conductor β-(BEDT-TTF)$_2$I$_3$, a close analog of the complex β-(BEDT-TTF)$_2$IBr$_2$. In particular, it was found experimentally that the width of the peak is practically unchanging with magnetic field strength. This is illustrated in Fig. 7, where the angular dependence of the magnetoresistance β-(BEDT-TTF)$_2$I$_3$ at various values of the field is shown for angles close to $\pi/2$. The constancy of the peak width permitted the authors of Ref. 53 to attribute its origins to the geometry of the Fermi surface, specifically, to the slight corrugation along the z axis, and thus to estimate the quasi-two-dimensionality parameter $\eta \cong 10^{-2}$.

Let us now consider the dependence of the resistance on the magnetic field strength for $\theta=\pi/2$. The main contribution to the conductivity tensor component σ_{zz} at $\theta=\pi/2$ is from the small fraction of conduction electrons with orbits near the self-intersecting cross section $p_B=p_c$ of the Fermi surface. These charge carriers move slowly along the z axis with a period $T(p_B)$ larger than or comparable to their mean free time τ for arbitrarily high values of the magnetic field. Since the velocity along the x axis for electrons on orbits $p_B=p_y$ close to p_c is small, which corresponds to a weak dependence of ε on p_x, in calculating the period $T(p_y)$ of the electron's motion one is justified in using an expansion of the energy in a power series for small p_x, dropping the higher-order harmonics in formula (1):

$$\varepsilon=\varepsilon_0(0,p_y)+p_x^2/2m_1+\varepsilon_1(0,p_y)\cos(ap_z/\hbar). \tag{17}$$

Using relation (17), one can easily calculate the period of the electron's motion along orbits close to self-intersecting,

$$T_B(p_y)=\eta^{-1/2}T_0\int_0^{\pi} d\alpha(\xi^2+\sin^2\alpha)^{-1/2}, \tag{18}$$

where $T_0=2\pi\hbar c/(aeBv_F)$ agrees in order of magnitude with the period of a conduction electron's motion in a magnetic field normal to the layers, and

$$\xi^2=[\varepsilon-\varepsilon_0(0,p_y)-\varepsilon_1(0,p_y)]/2\varepsilon_1(0,p_y). \tag{19}$$

As the self-intersecting orbit is approached, ξ becomes an arbitrarily small quantity, and the integral in formula (18) diverges logarithmically in proportion to $\ln(1/\xi)$.

Unlike ordinary metals, where the period of the carriers' motion is greater than or comparable to the mean free time only in an exponentially small region of the cross sections of the Fermi surface near the self-intersecting orbit,[54] in a quasi-two-dimensional conductor the condition $T_B > \tau$ is valid in a significantly wider region of electron orbits, since the period of the electrons' motion near the self-intersecting orbit, even for ξ of the order of unity, is inversely proportional to the small parameter $\eta^{1/2}$. Thus for $\eta^{1/2} \leqslant \gamma_0 \ll 1$, where $\gamma_0=T_0/\tau$, there are quite many charge carriers whose period of motion in the magnetic field are greater than or comparable to the mean free time. As a result of averaging over states of the conduction electrons the conductivity of a layered conductor falls off in proportion to $1/B$ with increasing magnetic field directed in or near the plane of the layers:[35]

$$\sigma_{zz}=\eta^2\sigma_0\gamma_0. \tag{20}$$

With increasing magnetic field the number of electrons whose periods of motion exceed the mean free time decreases, but in the limit of high magnetic field, when $\gamma_0 \ll \eta^{1/2} \ll 1$, the contribution of the small fraction of electrons with open trajectories in momentum space close to the self-intersecting cross section of the Fermi surface,

$$\sigma_{zz}=\eta^{3/2}\sigma_0\gamma_0^2, \tag{21}$$

nevertheless exceeds the contribution to σ_{zz} from all the other electrons. In this region of magnetic fields the linear growth of the resistance to current transverse to the layers gives way to a quadratic growth with magnetic field.[35,48]

In formulas (20) and (21) we have dropped numerical factors of order unity which depend on the concrete form of the electron energy spectrum.

An analogous dependence of σ_{zz} on magnetic field strength was obtained by Lebed and Bagmet[55] and by Schofield and Cooper[56] with the use of a model of the form (6) for the electron energy spectrum.

In the case of a carrier dispersion relation (6) the dependence of the momentum component p_z on time τ in a magnetic field parallel to the plane of the layers is described by the standard equation for a simple pendulum:

$$\frac{\partial^2 p_z}{\partial t^2}+\frac{2at_\perp e^2B^2}{mc^2\hbar}\sin\frac{ap_z}{\hbar}=0. \tag{22}$$

The solution of this equation enables one to write the dependence of the electron velocity v_z on time t explicitly with the aid of the Jacobi functions, which together with their Fourier transforms have been tabulated in sufficient detail, and Schofield and Cooper[56] had no difficulty in carrying out a numerical calculation of the dependence of the resistance to current transverse to the layers on the magnetic field strength over a wide range of magnetic field and parameter η. It follows from their calculation that in a quasi-two-dimensional conductor ($\eta\ll 1$) the contribution to σ_{zz} from electrons with small orbits for $\theta=\pi/2$ over a wide region of magnetic fields is significantly smaller than the contribution of the charge carriers with open trajectories in momentum space, which thus govern the behavior of the magnetoresistance at high magnetic fields, in accordance with what we have said above.

Concluding this Section, we note that the unrestricted growth of the magnetoresistance with in-plane field is due to the absence of drift of the charge carriers along the current direction, i.e., along the z axis,[20] whereas in a magnetic field tilted with respect to the layers the growth of the resistance to current transverse to the layers with increasing magnetic field, $\rho(B)=\rho_{zz}=1/\sigma_{zz}$, gives way to saturation at high fields:

$$\rho(\infty)=1/\langle\overline{v_z^2}\tau\rangle. \tag{23}$$

The angle brackets denote integration over the Fermi surface with weight factor $2e^3B/c(2\pi\hbar)^3$.

For any magnetic field orientation ρ_{zz} increases with magnetic field, since all the diagonal components of the conductivity tensor fall off monotonically with increasing magnetic field. One can readily see this by turning to formula (16), from which it follows that $\sigma_{zz}(0)\geqslant\sigma_{zz}(B)$, and

$$\frac{\partial\sigma_{zz}(B)}{\partial B}=-\frac{8e^2\tau}{(2\pi\hbar)^3B}\times\int_0^{2\pi\hbar\cos\theta/a}2\pi m^*dp_B\left\{\sum_{k=1}^{\infty}\frac{(v_z^k\omega_c\tau)^2}{[1+(k\omega_c\tau)^2]^2}\right\}\leqslant 0, \tag{24}$$

where the equals sign applies only in the case of the longitudinal conductivity of an isotropic conductor.

The rate of increase of the resistivity ρ_{zz} with magnetic field depends substantially on the saturation value (23) to which the resistivity tends in the limit of infinitely high magnetic field. At the maximum of the angular dependence of the resistivity the value of $\langle\overline{v_z}^2\tau\rangle$ is proportional to η^4, and the resistivity increases more strongly with magnetic field B than at the minima of $\rho(\theta)$. At those magnetic-field orientations for which $\rho(\theta)$ has a minimum it is significantly easier to achieve saturation with respect to magnetic field strength, as is indeed observed experimentally[36,37,57] (see Fig. 4).

3. SHUBNIKOV-DE HAAS EFFECT

With decreasing temperature the mean free path of the charge carriers increases, and the condition of high magnetic field ($\omega_c\tau\gg 1$), under which the dynamic properties of the conduction electrons are most clearly manifested, is realized in a wider range of magnetic fields. At very low temperatures, however, the quasiclassical treatment of the transport properties can turn out to be incorrect.

At Leiden in 1930 Shubnikov and de Haas observed a complicated magnetic-field dependence of the resistance at 20 K in a single-crystal bismuth sample of very high quality for that time.[58] Against the background of significant growth of the resistivity of bismuth with magnetic field a tendency toward oscillatory behavior of ρ versus B was seen, and an investigation at liquid helium temperature revealed a periodic dependence of magnetoresistance of bismuth on the inverse magnetic field.[59]

This effect, which came to be called the Shubnikov-de Haas effect, did not follow from a quasiclassical treatment of charge transport phenomena in solids and for a long time was regarded as another anomaly among the unusual properties of bismuth. It was only after 8 years that Landau showed[60] that oscillatory dependence of the magnetoresistance on $1/B$ and also the oscillations of the magnetic susceptibility of bismuth, which had been discovered by de Haas and van Alphen in 1930 as well,[61] are due to quantization of the energy of the charge carriers in a magnetic field and are inherent to all degenerate conductors. In a quantizing magnetic field the density of states of the electrons has a square-root singularity, which at the Fermi level repeats periodically with variation of $1/B$; this is what leads to the oscillatory dependence of the thermodynamic and kinetic characteristics of the conductor on the inverse magnetic field. Rather high magnetic fields are needed for observation of these oscillations, sufficient that the distance between the quantized Landau levels, $\Delta\varepsilon=\hbar\omega_c$, exceeds their width $\hbar/\tau$, and the temperature smearing of the Fermi distribution function k_BT (k_B is Boltzmann's constant) but nevertheless much less than the Fermi energy ε_F, i.e., the condition $k_BT\leqslant\hbar\omega_c\ll\varepsilon_F$ must be met. In metals the carriers responsible for these quantum oscillations comprise only a small fraction, of the order of $(\hbar\omega_c/\varepsilon_F)^{1/2}$, made up of those for which the area of section $S(\varepsilon,p_B)$ of the Fermi surface $\varepsilon(\mathbf{p})=\varepsilon_F$ by the plane $p_B=\text{const}$ is close to the extremal value S_{ext}.

From the period of the magnetization or magnetoresistance oscillations,

$$\Delta(1/B)=\frac{2\pi\hbar e}{cS_{\text{ext}}}, \tag{25}$$

one can determine the extremal area of plane sections of the Fermi surface. Thus a reliable spectroscopic method was developed[62–64] which is still being used successfully to reconstruct from experimental data the main characteristic of

the electron energy spectrum of degenerate conductors—the Fermi surface (see, for example, the monograph by Shoenberg[25]).

Oscillatory dependence of the magnetoresistance of a metal on $1/B$ due to quantization of the energy of the orbital motion of the charge carriers in a magnetic field was first calculated by Akhiezer[65] using Titeica's method.[66] The essence of Titeica's method is that by taking into account the oscillatory character of the motion of electrons in a magnetic field, one can represent the electric current as the drift of the centers of the electron orbits. Here the resistance to electrical current flowing in the direction orthogonal to a strong magnetic field arises because of scattering of the charge carriers. Akhiezer, following Titeica, assumed that the mechanism of dissipation in the system of conduction electrons was their scattering by phonons. Although Akhiezer's work contained a number of errors in the calculations of the amplitude of the magnetoresistance oscillations,[67] he nevertheless obtained the correct expression for the period of the oscillations and pointed out the significant growth of the quantum corrections to the magnetoresistance as the temperature approaches zero.

The quantum oscillation effects in the magnetoresistance of bismuth at extremely low temperatures, when the charge carriers are scattered mainly by impurity atoms, were considered by Davydov and Pomeranchuk.[68] Already in that paper it was shown that the probability of scattering of an electron will oscillate with variation of the magnetic field and that it is is extremely important to take such oscillations into account. Zil'berman[69] applied the Titeica's method in calculating the quantum oscillations of the magnetoresistance in the case of scattering of conduction electrons in a metal by heavy impurities and showed that the amplitude of the Shubnikov-de Haas oscillations for $\varepsilon_F/\hbar\omega_c \gg 1$ is determined mainly by the oscillatory dependence of the mean free time of the charge carriers on $1/B$. The magnetic fields available in the 1950s were not very high, and experimental research on electronic phenomena was restricted to fields of several tesla. Therefore Zil'berman's rather cumbersome and detailed calculations were confined to the use of formulas for the electron collision frequency and magnetoresistance valid for $k_BT \geqslant \hbar\omega_c$. The formula he obtained for the inverse mean free time of electrons in a quantizing magnetic field had the form

$$\frac{1}{\tau} = \frac{1}{\tau_0}\left\{1 + \frac{9\hbar\omega_c}{40\varepsilon_F} - \frac{5\sqrt{2}}{\sqrt{\varepsilon_F\hbar\omega_c}}\pi^2 k_B T \times \exp\left(-\frac{2\pi^2 k_B T}{\hbar\omega_c}\right)\cos\left(\frac{2\pi\varepsilon_F}{\hbar\omega_c} - \frac{\pi}{4}\right)\right\}. \quad (26)$$

Later Titeica's method was refined substantially by Kubo[70] and successfully used in a theoretical study of galvanomagnetic phenomena in metals in a quantizing magnetic field.[71]

In the theoretical papers mentioned above[65–69] the energy spectrum of the conduction electrons was assumed isotropic. Such a model of the carrier dispersion relation — the Drude-Lorentz-Sommerfeld model—was used in those years in many theoretical investigations of electronic phenomena in metals, even though the most probable open Fermi surfaces for electrons in metals with a face-centered cubic lattice had already been proposed in the monograph by Bethe and Sommerfeld (see Figs. 23–25 of Ref. 72). A quadratic isotropic energy spectrum of the charge carriers was also used later in the paper by Adams and Holstein,[73] which was devoted to the study of galvanomagnetic phenomena in conducting media.

In the case of an isotropic dispersion relation of the charge carriers there is only one extremal plane section of the Fermi surface—the central cross section, of area $S_{\max} = \pi p_F^2 = 2\pi\varepsilon_F m^*$.

Low-temperature experiments on the magnetic susceptibility of rather pure metals, carried out by Shoenberg and co-workers at Cambridge and by Verkin and Lazarev and co-workers at Kharkov (see Ref. 25 and the references cited therein), and also resonance and magnetoacoustic phenomena[23,24] have given evidence that even in ordinary quasi-isotropic metals, except for a small group of alkali metals, the electron energy spectrum is rather complex and is substantially different from the spectrum of free electrons.

To explain the experimental studies of quantum oscillation phenomena it was necessary to create a theory with the real electron energy spectrum taken into account. The success of Lifshitz and Kosevich's theory[64] of the de Haas-van Alphen effect under the most general assumptions about the form of the electron energy spectrum of metals with the use of only the area quantization rule

$$S(\varepsilon, p_B) = 2\pi\hbar(n + 1/2)eB/c, \quad (27)$$

where n is a nonnegative integer, stimulated investigation of the electronic properties of metals without the invocation of model assumptions about the charge carrier dispersion relation.

One of the first papers devoted to the theoretical study of galvanomagnetic effects in a quantizing magnetic field in conductors with an arbitrary carrier dispersion relation was that of Lifshitz.[74] In it the current density

$$\mathbf{j} = \mathrm{Tr}(e\hat{\mathbf{v}}\hat{f}) \quad (28)$$

was found by solution of the quantum kinetic equation for the single-particle statistical operator or density matrix $\hat{f}$, linearized with respect to a weak perturbation of the electronic system by a uniform external electric field. The theory of quantum phenomena in metals with an arbitrary carrier dispersion relation obtained its further development in the paper by Kosevich and Andreev,[75] who calculated in the Born approximation the correction oscillatory in $1/B$ to the collision integral in the case of electron scattering by impurity atoms with a short-range potential with the use of the Bogolyubov method.[76] Here the oscillatory (in $1/B$) dependence of the eigenvalues of the collision operator differed from that given in the paper by Zil'berman in the case of an isotropic spectrum of the charge carriers only by a relatively unimportant factor of order unity.

At sufficiently low temperatures that the charge carriers are scattered mainly by impurity atoms and their drift along, say, the z axis is nonzero, the asymptote of the conductivity tensor component σ_{zz} at high magnetic field has the form

$$\sigma_{zz} = -\frac{2e^3B}{(2\pi\hbar)^2 c}\sum_{n=0}^{\infty}\int_0^{2\pi\hbar\cos\theta/a} \times dp_B (v_z^{nn})^2 \tau(\varepsilon_n)^{\partial f_0(\varepsilon_n)/\partial\varepsilon_n}. \quad (29)$$

Following Landau,[60] we can easily write the terms in the expression for σ_{zz} which are oscillatory on variation of the magnetic field with the aid of Poisson's formula:

$$\sum_{n=0}^{\infty}\Phi_n = \sum_{k=-\infty}^{\infty}\int_{-1/2}^{\infty} dn\,\Phi(n)\exp(ikn). \quad (30)$$

Here the oscillatory part of the conductivity $\sigma_{zz}^{\rm osc}$ is determined mainly by the oscillatory dependence on $1/B$ of the mean free time of the charge carriers, which is due to the summation over states of the ''incoming'' electrons in the collision integral.

The problem of quantum oscillations of the conductivity of metals in a magnetic field has been the subject of many papers. The most transparent and lucid derivation of the oscillatory field dependence of the elastic scattering amplitude of charge carriers on impurity atoms in the Born approximation is given in Abrikosov's monograph.[24] For $\hbar\omega_c \ll \eta\varepsilon_F$ the frequency of electron scattering can be written in the form

$$\frac{1}{\tau(\varepsilon)} = \frac{1}{\tau_0}(1+\Delta_{\rm osc}), \quad (31)$$

where

$$\Delta_{\rm osc} = \left(\frac{e\hbar B}{m^* c\varepsilon}\right)^{1/2}\sum_e \left|\frac{\partial^2 S_e}{\partial p_B^2}\right|^{-1/2} g_e, \quad (32)$$

$$g_e = \sum_{k=1}^{\infty} a_k (-1)^k k^{-1/2}\cos\left(\frac{kcS_e}{e\hbar B}+\frac{\pi}{4}s\right)\cos\left(\frac{\pi k m^*}{m}\right). \quad (33)$$

Here the a_k are numerical factors that depend on the concrete form of the carrier dispersion relation, m is the mass of a free electron, $s = \mathrm{sgn}(\partial^2 S_e/\partial p_B^2)$, and S_e is the extremal value of the area of section of the isoenergy surface by a plane $p_B = \mathrm{const}$. In the case of several extremal sections S_e it is necessary to sum over all possible S_e in formula (32).

As a result, the conductivity, which is proportional to the relaxation time τ, acquires an oscillatory component $\sigma^{\rm osc} \sim \Delta_{\rm osc}\sigma_0$.

In formulas (32) and (33) the broadening of the quantized levels of the charge carrier energy due to scattering has not been taken into account. Dingle[77] proposed that to do this it is sufficient to introduce in the oscillatory (in $1/B$) correction to the kinetic coefficient and in $\Delta_{\rm osc}$ a factor

$$R_D = \exp(-1/\omega_c\tau), \quad (34)$$

which has come to be called the Dingle factor.

A rigorous analysis of the quantum oscillation effects, carried out by Bychkov[78] with the use of the diagram technique, showed that in many particular cases such a procedure is completely justified, although it can lead to the loss of interesting effects associated with magnetic-impurity-bound electronic states. The value calculated by Bychkov for the factor by which the amplitude of the quantum oscillations is lowered on account of scattering of conduction electrons differed from the Dingle factor only by a number factor of order unity in the argument of the exponential factor. In this regard the Kubo method has turned out to be more attractive for studying the Shubnikov-de Haas effect. In the Kubo formalism it is unnecessary to introduce a Dingle factor in the expression for the kinetic coefficients, since the broadening of the carrier energy levels due to scattering is automatically taken into account in the description of estimation of the linear response of the electron system to the perturbation with the aid of the retarded two-time Green's functions.[79–81]

Besides the weakening of the amplitude of the Shubnikov-de Haas oscillations $\sigma_{zz}^{\rm osc}$ due to scattering of charge carriers, there is a very significant decrease in amplitude with increasing temperature. While the part of the conductivity that changes monotonically with magnetic field, $\sigma_{zz}^{\rm mon}$, depends weakly on temperature, since the temperature smearing of the Fermi distribution function k_BT of the charge carriers is much less than the Fermi energy ε_F, the oscillatory component $\sigma_{zz}^{\rm osc}$ decreases rapidly when k_BT becomes of the order of or greater than the distance $\hbar\omega_c$ between Landau levels, even for $k_BT \ll \varepsilon_F$. The factor that decreases the amplitude of the oscillations has the form

$$R_T(u) = \frac{u}{\sinh(u)}, \quad \text{where} \quad u = \frac{2\pi^2 k_B T}{\hbar\omega_c}, \quad (35)$$

and for $u > 1$ it falls off exponentially with temperature [see formula (26)].

In the early 1950s the de Haas-van Alphen effect had already been observed in almost all metals, but for a long time the quantum oscillations of the magnetoresistance were hardly ever observed in metals for which the number of conduction electrons is of the order of one per atom. This is clearly due to the fact that the quantum correction to the classical expression for the conductivity is too small, being proportional to $(\hbar\omega_c/\varepsilon_F)^{1/2}$, while the amplitude of the quantum oscillations of the magnetic susceptibility is a factor of $(\varepsilon_F/\hbar\omega_c)^{3/2}$ larger than the Pauli paramagnetic susceptibility[82] and the Landau diamagnetic susceptibility.[83]

Layered organic conductors are an exceptionally convenient object for experimental study of the Shubnikov-de Haas effect, since a much larger number of charge carriers is involved in its formation than in the case of ordinary metals. In some compounds the amplitude of the resistance oscillations can reach giant values exceeding the minimum value of the resistance by one or two orders of magnitude.[32,84–87] Clearly the theory of quantum oscillation effects developed for materials with a relatively slight anisotropy is inapplicable in this case, especially under conditions such that the distance $\hbar\omega_c$ between adjacent Landau levels is considerably greater than the width $W_\perp$ of the conduction band in the direction perpendicular to the layers.

Pioneering research on the magnetic susceptibility of conductors with a markedly anisotropic quasi-two-dimensional electron energy spectrum was done in the years 1983–1985 by Wagner and co-workers[88,89] and by Shoenberg.[90] The thermodynamic theory of quantum oscillations has been under particularly intensive development in the last 10 years (see Refs. 91–102 and the references cited therein). There is now a consistent theory of the de Haas-van Alphen effect in layered systems which can in principle be used for quantitative analysis of the magnetization oscilla-

tions observed in organic conductors (see, for example, Refs. 91 and 103–105). A number of theoretical papers have been devoted to an examination of quantum oscillations of the magnetoresistance.[106–113] Unlike the case of the thermodynamic de Haas-van Alphen effect, the detailed description of quantum oscillations of the kinetic properties, which is complicated strongly by the necessity of taking the details of the scattering processes into account under conditions of extremely high anisotropy, is far from completed. Nevertheless, substantial progress in understanding some of the important features of the Shubnikov-de Haas effect in quasi-two-dimensional systems, at least on a qualitative level, has been made recently.

Let us consider in more detail the case of a comparatively strongly corrugated cylindrical Fermi surface, when the width of the conduction band in the direction perpendicular to the layers, $W_\perp$, is somewhat (but not very much) greater than the distance between adjacent Landau levels. This condition is realized in many layered organic conductors in fields of ~ 10 T. In this case the de Haas-van Alphen effect is still described well by the standard Lifshitz–Kosevich formula, which was obtained for moderately anisotropic metals.[64] At the same time, it turns out that the Shubnikov-de Haas effect manifests a number of specific features already at $W_\perp \geqslant \hbar\omega_c$. Among them are beats of the quantum oscillations of the magnetoresistance and an appreciable shift of their phase in relation to the beats of the oscillations of the magnetic susceptibility, which carries information about the spectrum of charge carriers.[109] The detection of slow quantum oscillations with a frequency proportional to the difference between the maximum and minimum areas of section of the Fermi surface has turned out to be very important.[110] These oscillations are observed at higher temperatures than the oscillations at the fundamental frequency, which is proportional to the extremal area of section of the Fermi surface.

Figure 8 shows a typical example of the field dependence of the interlayer resistance of β-(BEDT-TTF)$_2$IBr$_2$ in a magnetic field tilted at a small angle ($\theta = 15°$) from the normal to the conducting plane,[110] at temperatures of the order of 0.6 and 1.4 K. Two types of oscillations are clearly seen. The fast oscillations, which are particularly pronounced at 0.6 K, are the Shubnikov-de Haas effect on extremal orbits of the cylindrical Fermi surface.[29,32] By virtue of the slight corrugation of the cylinder the frequencies corresponding to the maximum and minimum cross sections of the Fermi surface are extremely close, as is reflected in the low-frequency modulation of the oscillation amplitude, which is proportional to $\cos(2\pi F_b/B+\varphi)$.

From the ratio of the beat frequency ($F_b \approx 20$ T) to the fundamental frequency ($F_0 \approx 3900$ T) one can estimate the relative value of the corrugation of the Fermi surface: $\Delta S/S = 2F_b/F_0 \approx 10^{-2}$. The ratio of the width of the conduction band in the direction perpendicular to the layers, $W_\perp \approx 4t_\perp$ [$t_\perp$ is the transverse transfer integral; see formula (6)], to the distance $\hbar\omega_c$ between Landau levels in a field of 10 T is equal to $2F_b/B \approx 4$. Consequently, taking the smallness of the oscillation amplitude into account ($\sim 1\%$ of the monotonic component of the resistance) and the practically total absence of higher harmonics of the fundamental

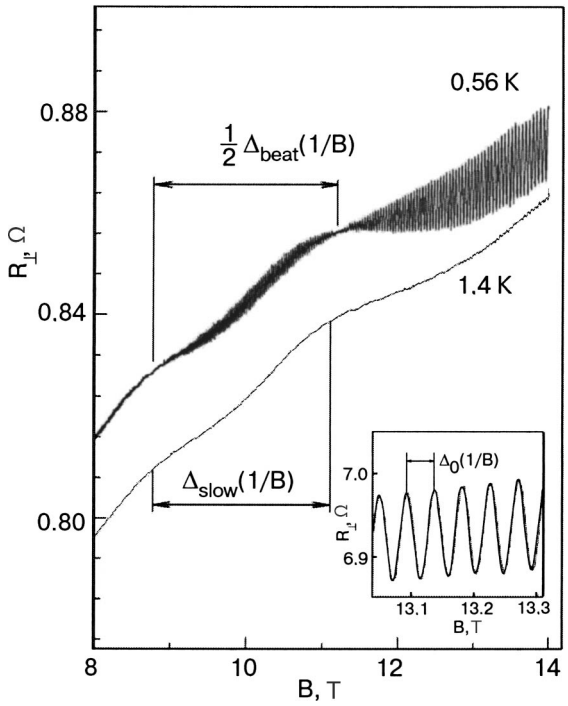

FIG. 8. Quantum oscillations of the interlayer magnetoresistance of β-(BEDT-TTF)$_2$IBr$_2$ in a magnetic field tilted at an angle $\theta \approx 15°$ from the normal to the layers, for different temperatures. The fundamental Shubnikov–de Haas oscillations, shown on an enlarged scale in the inset, have a frequency $F_0 = \Delta_0^{-1}(1/B) \approx 3900$ T and beat with a frequency $F_{beat} = \Delta_{beat}^{-1}(1/B) \approx 20$ T. In addition to the fundamental oscillations, which are rapidly damped with increasing temperature, slow oscillations which are periodic on a scale of $1/B$ but are practically independent of temperature are observed. Data of Ref. 110.

frequency,[109,110] it could be supposed that the standard ''three-dimensional'' model applies in the given situation. Indeed, the behavior of the magnetization oscillations in β-(BEDT-TTF)$_2$IBr$_2$ has been analyzed successfully by Wosnitza and co-workers[31,114] in the framework of the Lifshitz-Kosevich theory.[64] However, in the case of resistance oscillations new effects arise even under these conditions, due to the quasi-two-dimensional character of the charge carriers.

Perhaps the most obvious and important anomaly of the behavior presented in Fig. 8 is the presence of slow quantum oscillations of the interlayer resistance. These oscillations, which are periodic in the $1/B$ scale, were observed back in the first experiments on this compound,[28,29] but their nature has been understood only recently.[110,111] It has been established[110] that the dependence of the frequency of the slow oscillations on the orientation of the magnetic field, $F_{slow}(\theta)$, is strictly correlated with the angular oscillations of the quasiclassical part of the resistance $R_\perp(\theta)$, which were considered in Sec. 2.1. As is shown in Fig. 9, F_{slow} oscillates with variation of the field tilt angle θ, going to zero at angles corresponding to the maxima of $R_\perp(\theta)$. Such behavior attests to the direct link between the slow oscillations and the corrugation of the Fermi surface. Indeed, as was discussed above, the quasiclassical magnetoresistance takes on maximal values at those magnetic-field orientations for which the areas of all the cyclotron orbits become practically equal. This, in particular, means that the beat frequency F_b of the fundamental Shubnikov-de Haas oscillations goes to zero the

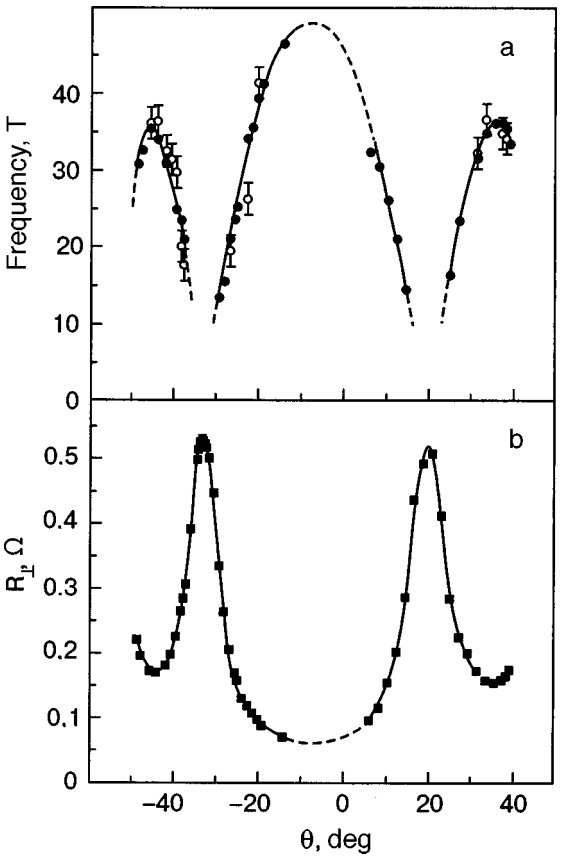

FIG. 9. Angular dependence of the frequency of slow oscillations F_{slow} (●) and twice the beat frequency $2F_{\text{beat}}$ (○) (a), and the corresponding angular dependence of the quasiclassical part of the interlayer magnetoresistance (b).[110]

the maxima of the angular oscillations of the magnetoresistance. Recent measurements have shown that the angular dependences $F_b(\theta)$ and $F_{\text{slow}}(\theta)$ actually coincide with each other to good accuracy over a wide range of angles, and the following relation holds:

$$F_{\text{slow}}(\theta)=2F_b(\theta). \tag{36}$$

Thus one can conclude that the slow oscillations, like the beats of the fundamental Shubnikov-de Haas oscillations, are not due to some independent small section but to the weak corrugation of the main cylinder of the Fermi surface.

To explain this effect we use the model dispersion relation (6), which under conditions of quantization of the orbital motion of the electrons takes the form

$$\varepsilon(n,p_z)=\left(n+\frac{1}{2}\right)\hbar\omega_c-2t_\perp\cos\left(\frac{ap_z}{\hbar}\right). \tag{37}$$

In a quantizing magnetic field **B** deviating substantially from the layers, i.e., when $(\pi/2-\theta)\gg\eta$, the resistance to the current transverse to the layers, as in the case when energy quantization is not taken into account, is determined mainly by the conductivity tensor component σ_{zz}.

Using the Poisson formula (30), applying it to expression (29) for σ_{zz}, we obtain a series of terms oscillatory in the inverse magnetic field:

$$\sigma_{zz}=-\frac{4t_\perp^2e^2a}{m\hbar(2\pi\hbar)^3}\int d\varepsilon\,\frac{\partial f_0(\varepsilon)}{\partial\varepsilon}\,\tau(\varepsilon)\times\left[1+\frac{\hbar\omega_c}{\pi t_\perp}\sum_{k=1}^{\infty}(-1)^k k^{-1}\cos\left(\frac{2\pi k\varepsilon}{\hbar\omega_c}\right)\times J_1\left(\frac{4\pi kt_\perp}{\hbar\omega_c}\right)R_D\right]. \tag{38}$$

The mean free time of the charge carriers also oscillates with variation of the magnetic field. In the Born approximation the oscillations are determined by oscillations of the density of states and, when the carrier dispersion relation (37) is taken into account, assume the form[115,94]

$$\tau(\varepsilon)\propto\left[1+2\sum_{k=1}^{\infty}(-1)^k\cos\left(\frac{2\pi k\varepsilon}{\hbar\omega_c}\right)J_0\left(\frac{4\pi kt_\perp}{\hbar\omega_c}\right)R_D\right]^{-1}, \tag{39}$$

where R_D is the usual Dingle factor, and $J_0(u)$ and $J_1(u)$ are Bessel functions. As is seen from expressions (38) and (39), the oscillations of the relaxation time and velocity of the electrons are modulated in amplitude by the Bessel functions of order zero and one, respectively, with an argument determined, as expected, by the ratio $t_\perp/(\hbar\omega_c)$. Obviously the product of two oscillatory functions in the expression for the conductivity will contain a slowly oscillating term.

At large arguments $u=4\pi t_\perp/(\hbar\omega_c)$ one can use the approximate expressions for the Bessel functions $J_0(u)\approx\sqrt{2/\pi u}\cos(u-\pi/4)$ and $J_1(u)\approx\sqrt{2/\pi u}\sin(u-\pi/4)$. Since in the experiment the amplitude of the oscillations is rather small, and all the harmonics except the first are substantially suppressed, we neglect the oscillations of the chemical potential and keep in the expansion for σ_{zz} only the terms of lowest order in the factors R_D and R_T, and after integration over ε we obtain[110]

$$\sigma_{zz}=\sigma_0\left(\frac{t_\perp}{\varepsilon_F}\right)^2\left\{1+2\sqrt{\frac{\hbar\omega_c(1+a^2)}{2\pi^2t_\perp}}\cos\left(\frac{2\pi\mu}{\hbar\omega_c}\right)\times\cos\left(\frac{4\pi t_\perp}{\hbar\omega_c}-\frac{\pi}{4}+\varphi\right)R_DR_T+\frac{\hbar\omega_c}{2\pi^2t_\perp}\times R_D^{*2}\sqrt{1+a^2}\cos\left(\frac{8\pi t_\perp}{\hbar\omega_c}-\frac{\pi}{2}+\varphi\right)\right\}, \tag{40}$$

where

$$a=\hbar\omega_c/(2\pi t_\perp),\quad \varphi=\arctan(a), \tag{41}$$

μ is the chemical potential of the charge carriers, and σ_0 is the monotonic part of the conductivity along the layers.

The second term in the sum (40) corresponds to the main oscillations with the fundamental frequency $F_0=\mu m^*c/\hbar e=cS/(2\pi\hbar e)$, modulated in amplitude at the frequency $F_{\text{slow}}=4t_\perp/\hbar\omega_c=2t_\perp m^*c/\hbar e$. The third term in (40) corresponds to slow oscillations with a frequency equal to twice the beat frequency, in complete agreement with experiment.

It must be noted that the amplitude of the slow oscillations does not contain a temperature factor, since these oscillations are independent of the electron energy (they are determined only by the value of $t_\perp$ in the dispersion relation). Indeed, as is seen in Fig. 8, the amplitude of the slow oscil-

lations remains almost unchanged when the temperature is increased from 0.6 to 1.4 K, while the fundamental harmonic of the Shubnikov oscillations is almost completely suppressed at 1.4 K. Strictly speaking, the slow oscillations are, of course, damped with temperature by virtue of the temperature-dependent scattering processes,[111] but this damping is considerably slower. In particular, in the compound β-(BEDT-TTF)$_2$IBr$_2$ the slow oscillations are observed all the way up to temperatures ~ 10 K, i.e., an order of magnitude higher than the fundamental Shubnikov oscillations.

Another consequence of the fact that the slow oscillations are independent of the carrier energy is the difference of the corresponding Dingle factor R_D^* from the standard one.[110,111] Usually the relaxation time that enters into the Dingle factor takes into account both point defects and other, macroscopic, imperfections of the crystal which influence the local value of the chemical potential: dislocations, mosaicity, local strains, etc. Since the chemical potential does not appear in the expression for the slow oscillations, the factor R_D^* is determined solely by the point defects. Indeed, experiment[110] has shown that in β-(BEDT-TTF)$_2$IBr$_2$ the relaxation time obtained from the Dingle factor of the slow oscillations is five times larger than the value determined from the fundamental Shubnikov-de Haas oscillations. Hence it can be concluded that the contribution of the macroscopic inhomogeneities to the suppression of the Shubnikov oscillations is dominant in this compound.

Thus the slow oscillations of the interlayer magnetoresistance are a general phenomenon observed in sufficiently pure layered metals by virtue of the superposition of the oscillations of the relaxation time and carrier velocity in the direction transverse to the layers, the amplitudes of which turn out to be comparable, when $W_\perp$ is of the order of $\hbar\omega_c$. Indeed, such oscillations have been observed not only in β-(BEDT-TTF)$_2$IBr$_2$ but also in a number of other layered organic conductors in fields ~ 10 T.[116–120]

It follows from relations (40) and (41) that the phase of the beats of the fundamental harmonic of the Shubnikov-de Haas oscillations contains an anomalous term φ which depends on the magnetic field. In fact, experiments on a number of organic metals[109,121–123] have revealed a significant phase shift of the beats of the magnetoresistance oscillations with respect to the beats of the magnetization oscillations in fields of the order of 10–20 T (recall that the latter are well described by the standard three-dimensional Lifshitz-Kosevich model[64]).

A detailed experimental study of the phase of the beats of the Shubnikov oscillations was carried out in Refs. 109 and 123, and it was shown that it is indeed substantially dependent on the ratio $\hbar\omega_c/W_\perp$. In particular, it was found that the phase shift φ increases strongly as the magnetic-field orientation approaches the direction corresponding to the peak in the angular oscillations of the classical part of the magnetoresistance. This result agrees with the fact that the effective interlayer transfer integral vanishes at the peak of the angular oscillations.[124] It should be noted, however, that the phase shift measured in Ref. 109 was approximately twice as large as the value predicted by formulas (40). This is illustrated in Fig. 10, where the symbols correspond to the

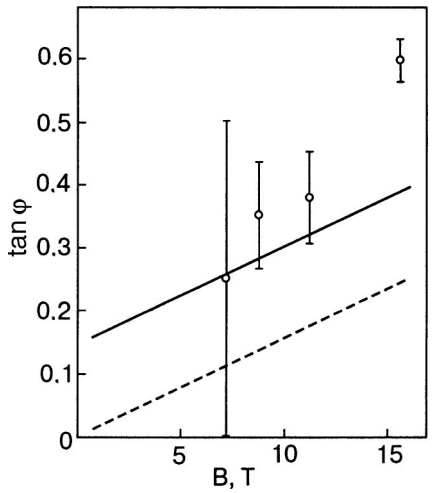

FIG. 10. Tangent of the phase shift of the beats of the Shubnikov oscillations in β-(BEDT-TTF)$_2$IBr$_2$ as a function of magnetic field according to the data of Ref. 109. The dashed line was constructed according to formulas (41), and the solid line is the result of a quantum-mechanical calculation.[111] The calculation was done using the values of the cyclotron mass $m_c = 3.9 \times 10^{-27}$ g and scattering time on point defects $\tau^* = 8 \times 10^{-12}$ s obtained from the Dingle factor of the slow oscillations.[110]

results of the measurements and the dashed line represents relation (41); here the ratio $\hbar\omega_c/t_\perp$ was taken from the beat frequency of the de Haas-van Alphen oscillations.

Subsequently a more rigorous theoretical analysis of the conductivity based on the Kubo formalism with the use of the self-consistent Born approximation[111] showed that a term $\approx \hbar/(2t_\perp\tau^*)$ must be added to the argument of the arctangent in formula (41), where τ^* is the scattering time on point defects (it can be determined from the Dingle factor for the slow oscillations, R_D^*). Then, as is shown in Fig. 10 (solid line), fair agreement with experiment[109] can be achieved for fields in the interval 7–12 T, which corresponds to values $\hbar\omega_c/t_\perp \approx 0.7-1.2$. However, upon further increase of the field the discrepancy between the theory[111] and experiment increases. Moreover, it has been observed[123] that for field orientations close to the direction corresponding to the peak in the angular oscillations of the magnetoresistance the phase shift φ is significantly greater than the limit $\pi/2$ predicted by the theory.[111]

Thus the results presented show that, unlike the thermodynamic quantum oscillations such as the de Haas-van Alphen effect, the quantum oscillations of the conductivity of layered metals display a number of anomalies even for $\hbar\omega_c/W_\perp < 1$. The existing theoretical models are able to describe the nature of these anomalies in a qualitative way. However, to achieve quantitative agreement between theory and experiment, especially under conditions when the ratio $\hbar\omega_c/W_\perp$ increases, approaching unity, further efforts will be necessary.

For $\hbar\omega_c \gg W_\perp$ the Boltzmann transport equation does not lead to a satisfactory result at high magnetic fields $(\omega_c\tau \gg 1)$. A detailed analysis of the conductivity σ_{zz} for the case $\hbar\omega_c \gg W_\perp$ in a field perpendicular to the layers $(\mathbf{B}\|\mathbf{z})$ was done by Champel and Mineev[112] and by Gvozdikov[113] on the basis of the Kubo formalism with the use of the self-consistent Born approximation. It was shown that with increasing field an ever greater contribution to the oscillations

of σ_{zz} is given by the purely quantum term, which does not have an analog in the semiclassical model. In particular, at integer occupation of the Landau levels this term almost completely compensates the semiclassical Boltzmann contribution, which gives rise to a ''pseudogap'' in the function $\sigma_{zz}(\varepsilon)$ and an activation temperature dependence $\sigma_{zz}(T)$ at integer $\mu/\hbar\omega_c$. Such a temperature dependence has indeed been observed[125] at fields greater than 20 T in the organic conductor β''-(BEDT-TTF)$_2$SF$_5$CH$_2$CF$_2$SO$_3$. Nevertheless, a detailed comparison of the Shubnikov–de Haas oscillations in this compound[125,126] with the results of the theoretical calculations reveals significant discrepancies. As was noted in Ref. 112, the cause of this may be the insufficiency of taking into account scattering only on point defects in the regime $\hbar\omega_c \gg W_\perp$. A more rigorous treatment of scattering processes in layered organic conductors is an extremely complex problem and has not been done at the present time.

4. HALL EFFECT

The Hall field at high magnetic fields, even in the presence of open sections of a Fermi surface in the form of a corrugated cylinder, i.e., for $\theta = \pi/2$, has the form[48]

$$\mathbf{E}_{\text{Hall}} = \frac{[\mathbf{j}\times\mathbf{B}]}{Nec}, \tag{42}$$

i.e., the same form as in the case of a magnetic field tilted with respect to the layers, when all the charge carriers in the collisionless limit ($\tau = \infty$) drift at a velocity

$$\mathbf{u} = c\frac{[\mathbf{E}\times\mathbf{B}]}{B^2}. \tag{43}$$

This is because the drift of the charge carriers along open orbits in a plane orthogonal to the magnetic field, with the velocity

$$v_x = \frac{2\pi\hbar c}{aeBT_B(p_B)}, \tag{44}$$

is naturally compensated in the expression for the current density

$$\mathbf{j} = Ne\mathbf{u}, \tag{45}$$

where $\mathbf{u}$, as in the case when θ is not equal to $\pi/2$, has the form (43). As a result, by measuring the value of the Hall field at a high magnetic field with any orientation, one can determine the charge carrier density N to the necessary accuracy.

At low temperatures such that it is important to take the quantization of the electron energy levels into account, for conductors with a single group of charge carriers the quantum corrections to the asymptote of the Hall field (42) for $\omega_c\tau \gg 1$ appear only in the higher terms of the expansion in a power series in the small parameter $\gamma = 1/\omega_c\tau$. Let us present Lifshitz' elegant proof of this assertion.[74]

We calculate the current density flowing in the direction orthogonal to the magnetic field with the aid of the solution of the quantum kinetic equation for the statistical operator $\hat{f} = \hat{f}_0 + \hat{f}_1$:

$$\{H\hat{f}\} = \hat{W}_{\text{coll}}(\hat{f}), \tag{46}$$

where $H = H_0(\mathbf{P} - e\mathbf{A}/c) - e\mathbf{E}\cdot\mathbf{r}$ is the Hamiltonian of a conduction electron in uniform electric and magnetic fields, $\mathbf{P}$ is the generalized momentum operator, $\mathbf{A}$ is the vector potential for the magnetic induction $\mathbf{B} = (0, B\sin\theta, B\cos\theta) = \text{curl}\mathbf{A}$, which in the Landau gauge has the form $\mathbf{A} = (0, xB\cos\theta, -xB\sin\theta)$, and in the absence of electric field the projections of the generalized momentum P_y and P_z are good quantum numbers.

The quantum analog of the collision integral $\hat{W}_{\text{coll}}(\hat{f})$ takes into account the scattering of electrons by the potential $\Sigma_i V(\mathbf{r} - \mathbf{r}_i)$ of impurity atoms located at coordinates $\mathbf{r}_i$. In the case when this potential is short-ranged and weak, the collision integral $\hat{W}_{\text{coll}}$ can lead to an integral operator acting on a single-particle statistical operator $\hat{f} = \hat{f}_0 + \hat{f}_1$. The operator $\hat{f}_0$ describes the unperturbed state of the system of conduction electrons, —its diagonal matrix elements are equal to the Fermi distribution function of the charge carriers, $f_0^{nn}(p_B) = f_0\{\varepsilon_n(p_B)\}$—and the operator $\hat{f}_1$ describes the perturbation of the charge carriers by the electric field.

In an approximation linear in the weak electric field the kinetic equation takes the form

$$\{H_0\hat{f}_1\} - \{e\mathbf{E}\cdot\mathbf{r}\hat{f}_0\} = \hat{W}_{\text{coll}}\{\hat{f}_1\}. \tag{47}$$

It is easy to see that the expression for the current density component orthogonal to the magnetic field,

$$[\mathbf{j}\times\mathbf{B}]/B = \text{Tr}(\text{e}[\hat{\mathbf{v}}\times\mathbf{B}]\hat{f}_1)/B, \tag{48}$$

where $\hat{\mathbf{v}}$ is the velocity operator of the conduction electrons, is proportional to the change of the momentum of the electron with time:

$$e[\hat{\mathbf{v}}\times\mathbf{B}] = c\frac{d}{dt}\hat{\mathbf{p}} = c\{H, \hat{\mathbf{p}}\}. \tag{49}$$

Using relation (49), we obtain

$$[\mathbf{j}\times\mathbf{B}]_y = (ic/h)\mathbf{Tr}(H\hat{f}_1\hat{p}_y - \hat{f}_1 H\hat{p}_y)$$
$$= -c\mathbf{Tr}(\{e\mathbf{E}\cdot\mathbf{r}\hat{f}_0\}\hat{p}_y) - c\mathbf{Tr}(\hat{W}_{\text{coll}}(\hat{f}_1)\hat{p}_y). \tag{50}$$

As a result, in the collisionless limit $\hat{W}_{\text{coll}}(\hat{f}_1) = 0$ we obtain

$$[\mathbf{j}\times\mathbf{B}]_y = ce\mathbf{Tr}(E_y\hat{f}) = \mathbf{Tr}(\hat{f}_0)ecE_y = NecE_y, \tag{51}$$

i.e., at arbitrary orientations of the current density and magnetic field the asymptote of the Hall field has the form (42). Taking the collision integral into account is extremely important for calculating the dissipative component of the current density.

Thus in layered conductors with a Fermi surface in the form of a slightly corrugated cylinder, the quantum oscillations of the off-diagonal components of the magnetoresistivity tensor, divided by the asymptote of the Hall field, are smaller than the quantum oscillations $\rho^{\text{osc}}/\rho^{\text{mon}}$ by at least a factor of $\omega_c\tau$.

However, in conductors with a multisheet Fermi surface the amplitude of the oscillations of the Hall field can be comparable to the the amplitude of the magnetoresistance oscillations.

Let us consider the case when the Fermi surface includes a pair of slightly corrugated planes in addition to the cylin-

drical part. Such a topology of the Fermi surface is quite common in organic metals.[31–33] In particular, it is characteristic for one of the best-known organic superconductors, κ-(BEDT-TTF)$_2$Cu(NCS)$_2$ (Ref. 30) and also for the normal metallic state of the compound α-(BEDT-TTF)$_2$MHg(SCN)$_4$, where M is a metal from the group K, Rb, Tl or NH_4 (Ref. 127). Open sections of such a Fermi surface by a plane p_B=const are encountered at practically any orientation of the magnetic field, and the magnetoresistance of such a conductor increases without saturation as the magnetic field is increased. The position of all the planes in p space can easily be determined from the anisotropy of the magnetoresistance in the plane of the layers.[20]

For $\eta \ll \cos\theta$ and $\gamma_0 \ll \cos\theta$ the magnetoresistance to a current flowing along the layers has the form[49,128]

$$\rho_{xx}=\frac{\sigma_1 \sin^2\varphi \cos^2\theta+\gamma_0^2\sigma_0}{\gamma_0^2\sigma_0(\sigma_0+\sigma_1)};$$

$$\rho_{yy}=\frac{\sigma_1 \cos^2\varphi \cos^2\theta+\gamma_0^2\sigma_0}{\gamma_0^2\sigma_0(\sigma_0+\sigma_1)}, \tag{52}$$

where σ_0 and σ_1 are equal in order of magnitude to the contribution from the charge carriers situated, respectively, on the cylindrical and planar parts of the Fermi surface to the conductivity along the layers in the absence of magnetic field and φ is the angle between the p_y axis and the corrugated plane of the Fermi surface.

The contribution of the charge carriers whose states belong to a sheet of the Fermi surface in the form of a slightly corrugated plane to the conductivity along the normal to the layers does not lead to a noticeable Hall effect provided that $\eta \ll \gamma_0$ and the resistivity along the z axis,

$$\rho_{zz}=\frac{1}{\sigma_{zz}}+\frac{\sigma_1 \cos^2\varphi \sin^2\theta}{\gamma_0^2\sigma_0(\sigma_0+\sigma_1)} \tag{53}$$

is determined mainly by the conductivity tensor component σ_{zz}.

In formula (52) and in the last term of formula (53) we have dropped unimportant factors of order unity which depend on the concrete form of the dispersion relation of the charge carriers, and the relationship between the mobilities of the conduction electrons of the two groups are assumed to be the same.

At rather high magnetic fields, when $\gamma_0 \leqslant \eta$, the Hall components of the resistivity tensor, in particular,

$$\rho_{xz}=\gamma_0^{-2}\frac{\sigma_1 \sin 2\varphi \sin 2\theta}{\sigma_0(\sigma_0+\sigma_1)}+\gamma_0^{-1}\frac{(\sigma_0+\sigma_1\sin^2\varphi)\sin\theta}{\sigma_0(\sigma_0+\sigma_1)} \tag{54}$$

are already comparable to ρ_{zz}.

The presence of an additional pocket of the Fermi surface in the form of weakly corrugated planes leads for $\gamma_0 \leqslant \eta$ to the unrestricted growth of the resistivity to a current transverse to the layers with magnetic field, and the Hall field, which is proportional to H^2, is now comparable to E_z.

The energy spectrum of the carriers whose states belong to the slightly corrugated planes in momentum space does not contain discrete levels, and therefore this group of conduction electrons does not take part in the formation of quantum oscillation effects, but its presence can have a substantial influence on the asymptote of the quantum oscillations of the Hall field. When the oscillatory dependence of the mean free time on $1/B$ at low temperatures for the conduction electrons with closed orbits on a sheet of the Fermi surface in the form of a corrugated cylinder is taken into account, the Hall field in a quantizing magnetic field takes the form[128]

$$E_x=j\frac{H\sin\theta}{2Nec} \times\left\{-\sin^2\varphi+\frac{H\sigma_0\sigma_1 \sin 2\varphi\cos\theta-Nec\sigma_0\cos^2\varphi}{Nec[\sigma_0+\sigma_1(1+\Delta_{\rm osc})]}\right\}, \tag{55}$$

$$E_y=j\frac{H\sin\theta}{Nec}\frac{H\sigma_0\sigma_1\cos\theta-Nec\sigma_1(1+\Delta_{\rm osc})\sin 2\varphi}{Nec[\sigma_0+\sigma_1(1+\Delta_{\rm osc})]}. \tag{56}$$

It is easy to see that the ratio of the oscillatory part $E_{\rm Hall}^{\rm osc}$ of the Hall field to the part that varies monotonically with magnetic field, $E_{\rm Hall}^{\rm mon}$, as follows from formulas (55) and (56),

$$E_{\rm Hall}^{\rm osc}/E_{\rm Hall}^{\rm mon}=-\Delta_{\rm osc}\frac{\sigma_1}{\sigma_0+\sigma_1} \tag{57}$$

is of the same order of magnitude as $\rho_{zz}^{\rm osc}/\rho_{zz}^{\rm mon}$.

Thus, by studying the dependence of the resistivity and Hall field on the value of a sufficiently strong magnetic field for different orientations of the field with respect to the layers, one can reconstruct completely the topological structure of the Fermi surface and determine the contribution of the individual groups of charge carriers to the total conductivity of the conductor.

5. CONCLUSION

At high magnetic fields the kinetic characteristics of low-dimensional conductors depend substantially on the concrete form of the energy spectrum of the charge carriers and contain detailed information about the dispersion relation of the conduction electrons. Intensive research on galvanomagnetic phenomena in organic layered conductors at low temperatures has revealed a number of peculiar effects specific to quasi-two-dimensional conductors. It turns out that the electronic phenomena in quasi-two-dimensional conductors are manifested in fundamentally different ways for different orientations of the quantizing magnetic field. Even in a moderately strong magnetic field orthogonal to the layers, when the discrete-continuous electron energy spectrum of the layered conductor contains a rather large number of quantized values of the momentum projection on the magnetic field direction at a fixed value of the energy, e.g., equal to the Fermi energy, at certain orientations of the magnetic field with respect to the layers only one or a few electron states with the Fermi energy are possible, i.e., the electron energy spectrum turns out to be quasi-discrete.

Thus, depending on the angle between the magnetic field vector and the normal to the layers, a layered conductor behaves as a three-dimensional conductor with highly anisotropic electron energy spectrum or as a two-dimensional conductor with a discrete spectrum of charge carriers. This orientation effect, which is specific to quasi-two-dimensional

conductors, is manifested in various kinetic phenomena. In particular, for certain orientations of the magnetic field a layered conductor is transparent to electromagnetic and acoustic waves,[129,130] and in such conductors the propagation of peculiar weakly damped electromagnetic and spin waves can occur,[131,132] carrying information about the electron energy spectrum and the relaxation properties of the charge carriers.

Layered conductors with a quasi-two-dimensional electron energy spectrum are extremely convenient objects for studying quantum oscillation effects, the formation of which involves a large number of charge carriers. The detection of low-frequency oscillations of the magnetoresistance of layered conductors at high temperatures such that the fundamental harmonics of the Shubnikov-de Haas oscillations are hardly observed, and the study of the phase relations of the oscillations of the magnetoresistance and magnetic susceptibility can yield detailed information about the dispersion relation of the conduction electrons.

Linear growth of the resistivity with magnetic field (the Kapitsa law) is very specific in quasi-two-dimensional conductors, being observed even in single-crystal samples. Linear growth of the resistivity of bismuth with magnetic field, which gave way to quadratic growth at higher fields, was observed by E. S. Borovik,[133] who devoted many years to studying the galvanomagnetic phenomena in metals. The magnetoresistance of a layered conductor in a magnetic field lying in the plane of the layers behaves in an analogous way. It is quite possible that the linear growth of the resistivity of bismuth with magnetic field is due to the marked anisotropy of the Fermi surface of that substance, the axes of the electron ellipsoid of the Fermi surface of bismuth differing by roughly a factor of 10.

The investigation of galvanomagnetic phenomena in layered conductors has been the subject of an enormous number of studies. We have not attempted to cover everything, and some interesting results of experimental and theoretical research on the classical and quantum galvanomagnetic effects may have been left out. The main goal of this paper was to demonstrate the effectiveness of galvanomagnetic measurements for investigating the electron energy spectrum.

We are grateful to the Editor-in-Chief of the journal *Low Temperature Physics* for inviting us to contribute to this special issue dedicated to the 90th anniversary of the birth of the outstanding physicist and fascinating man, Evgeniĭ Stanislavovich Borovik.

We are extremely grateful to W. Biberacher and P. D. Grigoriev for helpful discussions of the problems of charge transfer in organic conductors touched upon in this article, and to the INTAS foundation for support of this study (Grant 01.0791).

*E-mail: Mark.Kartsovnik@wmi.badw-muenchen.de

[1]W. A. Little, Phys. Rev. **134**, A1416 (1964).
[2]J. T. Devreese, R. P. Evrard, and V. E. van Doren (eds.), *Highly Conducting One-dimensional Solids*, Plenum Press, New York (1979).
[3]J. S. Miller (ed.), *Extended Linear Chain Compounds*, Plenum Press, New York (1982).
[4]R. E. Peierls, *Quantum Theory of Solids*, Oxford University Press, London (1955).
[5]J. C. Slater, Phys. Rev. **82**, 538 (1951).
[6]A. W. Overhauser, Phys. Rev. Lett. **4**, 462 (1960).
[7]V. N. Laukhin, A. I. Kotov, M. L. Khidekel', I. F. Shchegolev, and É. B. Yagubskiĭ, JETP Lett. **28**, 260, Erratum 464 (1978).
[8]D. Jérome and H. J. Schulz, Adv. Phys. **31**, 299 (1982); **51**, 293 (2002).
[9]D. Jerome, A. Mazaud, M. Ribault, and K. Bechgaard, J. Phys. (France) Lett. **41**, 95 (1980).
[10]T. Ishiguro, K. Yamaji, and G. Saito, *Organic Superconductors*, Springer Verlag, Berlin, Heidelberg (1998).
[11]É. B. Yagubskiĭ, I. F. Shchegolev, V. N. Laukhin, P. A. Kononovich, M. V. Kartsovnik, A. V. Zvarykina, and L. I. Buravov, JETP Lett. **39**, 12 (1984).
[12]L. I. Buravov, M. V. Kartsovnik, P. A. Kononovich, V. N. Laukhin, S. I. Pesotskiĭ, and I. F. Shchegolev, Zh. Éksp. Teor. Fiz. **91**, 2198 (1986) [Sov. Phys. JETP **64**, 1306 (1986)].
[13]V. N. Laukhin, E. É. Kostyuchenko, Yu. V. Sushko, I. F. Shchegolev, and É. B. Yagubskiĭ, JETP Lett. **41**, 81 (1985).
[14]V. B. Ginodman, A. V. Gudenko, P. A. Kononovich, V. N. Laukhin, and I. F. Shchegolev, JETP Lett. **44**, 673 (1986).
[15]J. M. Williams, T. J. Emge, H. H. Wang, M. A. Beno, P. T. Copps, L. N. Hall, K. D. Carlson, and G. W. Crabtree, Inorg. Chem. **23**, 3839 (1984).
[16]H. H. Wang, M. A. Beno, U. Geiser, M. A. Firestone, K. S. Webb, L. Núñez, G. W. Crabtree, K. D. Carlson, J. M. Williams, L. J. Azevedo, J. F. Kwak, and J. E. Schirber, Inorg. Chem. **24**, 2465 (1985).
[17]M. Kini, U. Geiser, H. H. Wang, K. D. Carlson, J. M. Williams, W. K. Kwok, K. G. Vandervoort, J. E. Thompson, D. L. Stupka, D. Jung, and M.-H. Whangbo, Inorg. Chem. **29**, 2555 (1990).
[18]J. M. Williams, A. M. Kini, H. H. Wang, K. D. Carlson, U. Geiser, L. K. Montgomery, G. J. Pyrka, D. M. Watkins, J. M. Kommers, S. J. Boryschuk, A. V. S. Crouch, W. K. Kwok, J. E. Schirber, D. L. Overmyer, D. Jung, and M.-H. Whangbo, Inorg. Chem. **29**, 3272 (1990).
[19]H. Taniguchi, M. Miyashita, K. Uchiyama, K. Satoh, N. Mori, H. Okamoto, K. Miyagawa, K. Kanoda, M. Hedo, and Y. Uwatoko, J. Phys. Soc. Jpn. **72**, 468 (2003).
[20]I. M. Lifshitz and V. G. Peschanskii, Zh. Éksp. Teor. Fiz. **35**, 1251 (1958) [Sov. Phys. JETP **8**, 875 (1959)].
[21]I. M. Lifshitz and V. G. Peschanskii, Zh. Éksp. Teor. Fiz. **38**, 188 (1960) [Sov. Phys. JETP **11**, 137 (1960)].
[22]S. P. Novikov and A. Ya. Mal'tsev, Usp. Fiz. Nauk **168**, 249 (1998).
[23]I. M. Lifshits, M. Ya. Azbel', and M. I. Kaganov, *Electron Theory of Metals*, Consultants Bureau, New York (1973), Nauka, Moscow (1971).
[24]A. A. Abrikosov, *Fundamentals of the Theory of Metals*, North-Holland, Amsterdam (1988), Nauka, Moscow (1987).
[25]D. Shoenberg, *Magnetic Oscillations in Metals*, Cambridge University Press, Cambridge (1984), Mir, Moscow (1986).
[26]B. Pippard, *Magnetoresistance in Metals*, Cambridge University Press, Cambridge (1989).
[27]P. Cracknell and K. C. Wong, *The Fermi Surface*, Oxford University Press, London (1973).
[28]M. V. Kartsovnik, V. N. Laukhin, V. I. Nizhankovskiĭ, and A. A. Ignat'ev, JETP Lett. **47**, 363 (1988).
[29]M. V. Kartsovnik, P. A. Kononovich, V. N. Laukhin, and I. F. Shchegolev, JETP Lett. **48**, 541 (1988).
[30]K. Oshima, T. Mori, H. Inokuchi, H. Urayama, H. Yamochi, and G. Saito, Phys. Rev. B **38**, 938 (1988).
[31]J. Wosnitza, *Fermi Surfaces of Low-dimensional Organic Metals and Superconductors*, Springer-Verlag, Berlin, Heidelberg (1996).
[32]M. V. Kartsovnik and V. N. Laukhin, J. Phys. I **6**, 1753 (1996).
[33]J. Singleton, Rep. Prog. Phys. **63**, 1111 (2000).
[34]V. G. Peschansky, J. A. Roldan Lopez, and Toji Gnado Yao, J. Phys. I **1**, 1469 (1991).
[35]V. G. Peschanskiĭ, Zh. Éksp. Teor. Fiz. **112**, 618 (1997) [JETP **85**, 337 (1997)].
[36]I. F. Schegolev, P. A. Kononovich, V. N. Laukhin, and M. V. Kartsovnik, Phys. Scr. **29**, 46 (1990).
[37]M. V. Kartsovnik, P. A. Kononovich, V. N. Laukhin, S. I. Pesotskiĭ, and I. F. Shchegolev, Zh. Éksp. Teor. Fiz. **97**, 1305 (1990) [Sov. Phys. JETP **70**, 735 (1990)].
[38]R. Yagi, Y. Iye, Y. Hashimoto, T. Odagiri, H. Noguchi, H. Sasaki, and T. Ikoma, J. Phys. Soc. Jpn. **60**, 3784 (1990).
[39]Y. Iye, M. Baxendale, and V. Z. Mordkovich, J. Phys. Soc. Jpn. **63**, 1643 (1994).
[40]M. Baxendale, V. Z. Mordkovich, and S. Yoshimura, Solid State Commun. **107**, 165 (1998).
[41]E. Ohmichi, H. Adachi, Y. Mori, Y. Maeno, T. Ishiguro, and T. Oguchi, Phys. Rev. B **59**, 7263 (1999).
[42]Y. Yoshida, A. Mukai, R. Settai, K. Miyake, Y. Inada, Y. Onuki,

K. Betsuyaki, H. Harima, T. D. Tatsuma, Y. Aoki, and H. Sato, J. Phys. Soc. Jpn. **68**, 3041 (1999).
[43]C. Bergemann, A. P. Mackenzie, S. R. Julian, D. Forsythe, and E. Ohmichi, Adv. Phys. **52**, 639 (2003).
[44]N. E. Hussey, M. Abdel-Jawad, A. Carrington, A. P. Mackenzie, and L. Balicas, Nature (London) **425**, 814 (2003).
[45]K. Yamaji, J. Phys. Soc. Jpn. **58**, 1520 (1989).
[46]M. V. Kartsovnik, V. N. Laukhin, S. I. Pesotskii, I. F. Shchegolev, and V. M. Yakovenko, J. Phys. I (France) **2**, 89 (1992).
[47]R. Yagi, Y. Iye, T. Osada, and S. Kagoshima, J. Phys. Soc. Jpn. **59**, 3069 (1990).
[48]V. G. Peschansky, Fiz. Nizk. Temp. **23**, 47 (1997) [Low Temp. Phys. **23**, 35 (1997)].
[49]V. G. Peschanskiĭ, Zh. Éksp. Teor. Fiz. **121**, 1204 (2002) [JETP **94**, 1035 (2002)].
[50]H. R. Atalla, Fiz. Nizk. Temp. **29**, 793 (2003) [Low Temp. Phys. **29**, 593 (2003)].
[51]V. G. Peschansky and M. V. Kartsovnik, Phys. Rev. B **60**, 11207 (1999).
[52]V. G. Peschansky and M. V. Kartsovnik, J. Low Temp. Phys. **117**, 1717 (1999).
[53]N. Hanasaki, S. Kagoshima, T. Hasegawa, T. Osada, and N. Miura, Phys. Rev. B **57**, 1336 (1998).
[54]V. G. Peschanskii and R. J. A. Lopez, Fiz. Nizk. Temp. **17**, 269 (1991) [Sov. J. Low Temp. Phys. **17**, 140 (1991)].
[55]A. G. Lebed and N. N. Bagmet, Phys. Rev. B **55**, R8654 (1997).
[56]A. J. Schofield and J. R. Cooper, Phys. Rev. B **62**, 10779 (2000).
[57]K. Kajita, Y. Nishio, T. Takahashi, W. Sasaki, R. Kato, H. Kobayashi, and Y. Iye, Solid State Commun. **70**, 1189 (1989).
[58]L. V. Schubnikov and W. J. de Haas, Leiden Commun. **19**, 207f (1930).
[59]W. J. de Haas, J. W. Blom, and L. V. Schubnikov, Physica **2**, 907 (1930).
[60]L. D. Landau, Proc. R. Soc. London, Ser. A **170**, 341 (1939).
[61]W. J. de Haas and P. M. van Alphen, Leiden Commun. **19**, 208d (1930).
[62]L. Onsager, Philos. Mag. **43**, 1006 (1952).
[63]I. M. Lifshitz and A. V. Pogorelov, Dokl. Akad. Nauk BSSR **96**, 1143 (1954).
[64]I. M. Lifshitz and A. M. Kosevich, Zh. Éksp. Teor. Fiz. **29**, 730 (1955) [Sov. Phys. JETP **2**, 636 (1956)].
[65]A. I. Akhiezer, Zh. Éksp. Teor. Fiz. **9**, 426 (1939).
[66]S. Titeica, Ann. Phys. **22**, 124 (1935).
[67]Yu. B. Rumer, Zh. Éksp. Teor. Fiz. **22**, 214 (1952).
[68]B. Davydov and I. Pomeranchuk, J. Phys. USSR **2**, 147 (1940).
[69]G. E. Zil'berman, Zh. Éksp. Teor. Fiz. **29**, 762 (1955) [Sov. Phys. JETP **2**, 650 (1956)].
[70]R. Kubo, J. Phys. Soc. Jpn. **12**, 570 (1957).
[71]R. Kubo, H. Hasegava, and N. Hashitsume, J. Phys. Soc. Jpn. **14**, 56 (1959).
[72]A. Sommerfeld and H. Bethe, *Elektronentheorie der Metalle*, Springer, Berlin (1933).
[73]E. W. Adams and T. D. Holstein, J. Phys. Chem. Solids **10**, 254 (1959).
[74]I. M. Lifshitz, Zh. Éksp. Teor. Fiz. **32**, 1509 (1957) [Sov. Phys. JETP **5**, 1227 (1957)].
[75]A. M. Kosevich and V. V. Andreev, Zh. Éksp. Teor. Fiz. **38**, 882 (1960) [Sov. Phys. JETP **11**, 637 (1960)].
[76]N. N. Bogolyubov, *Dynamical Problems in Statistical Physics* [in Russian], Gostekhizdat, Moscow (1946); N. N. Bogolyubov and K. P. Gurov, [Zh. Éksp. Teor. Fiz. **17**, 614 (1947)].
[77]R. B. Dingle, Proc. R. Soc. London, Ser. A **211**, 517 (1952).
[78]Yu. A. Bychkov, Zh. Éksp. Teor. Fiz. **39**, 1401 (1960) [Sov. Phys. JETP **12**, 977 (1961)].
[79]A. A. Abrikosov, L. P. Gor'kov, and I. E. Dzyaloshinskiĭ, *Methods of Quantum Field Theory in Statistical Physics*, Prentice-Hall, Englewood Cliffs, New Jersey (1963), Nauka, Moscow (1962).
[80]D. N. Zubarev, *Nonequilibrium Statistical Thermodynamics*, Consultants Bureau, New York (1974), Nauka, Moscow (1971).
[81]S. Doniach and E. H. Sondheimer, *Green's Functions for Solid State Physicists*, Imperial College Press, London (1998).
[82]W. Pauli, Z. Phys. **41**, 81 (1927).
[83]L. D. Landau, Z. Phys. **64**, 629 (1930).
[84]W. Kang, G. Montambaux, J. R. Cooper, D. Jerome, P. Batail, and C. Lenoir, Phys. Rev. Lett. **62**, 2559 (1989).
[85]V. N. Laukhin, A. Audouard, H. Rakoto, J. M. Broto, F. Goze, G. Coffe, L. Brossard, J. P. Redoules, M. V. Kartsovnik, N. D. Kushch, L. I. Buravov, A. G. Khomenko, E. B. Yagubskii, S. Askenazy, and P. Pari, Physica B **211**, 282 (1995).
[86]J. Wosnitza, S. Wanka, J. Hagel, H. v. Lohneysen, J. S. Qualls, J. S. Brooks, E. Balthes, J. A. Schlueter, U. Geiser, J. Mohtasham, R. W. Winter, and G. L. Gard, Phys. Rev. Lett. **86**, 508 (2001).
[87]M.-S. Nam, A. Ardavan, J. A. Symington, J. Singleton, N. Harrison, C. H. Mielke, J. A. Schlueter, R. W. Winter, and G. L. Gard, Phys. Rev. Lett. **87**, 117001 (2001).
[88]I. D. Vagner, T. Maniv, and E. Ehrenfreund, Phys. Rev. Lett. **51**, 1700 (1983).
[89]I. D. Vagner and T. Maniv, Phys. Rev. B **32**, 8398 (1985).
[90]D. Shoenberg, J. Low Temp. Phys. **56**, 417 (1984).
[91]N. Harrison, R. Bogaerts, P. H. P. Reinders, J. Singleton, S. J. Blundell, and F. Herlach, Phys. Rev. B **54**, 9977 (1996).
[92]P. D. Grigoriev and I. D. Vagner, JETP **69**, 156 (1999).
[93]M. A. Itskovsky and T. Maniv, Phys. Rev. B **64**, 174421 (2001).
[94]T. Champel and V. P. Mineev, Philos. Mag. **81**, 55 (2001).
[95]P. D. Grigoriev, Zh. Éksp. Teor. Fiz. **119**, 1257 (2001) [JETP **92**, 1090 (2001)].
[96]V. M. Gvozdikov, A. G. M. Jansen, D. A. Pesin, I. D. Vagner, and P. Wyder, Phys. Rev. B **68**, 155107 (2003).
[97]G. W. Martin, D. L. Maslov, and M. Yu. Reizer, Phys. Rev. B **68**, 241309(R) (2003).
[98]S. Alexandrov and A. M. Bratkovsky, Phys. Lett. A **234**, 53 (1997).
[99]J.-Y. Fortin and T. Ziman, Phys. Rev. Lett. **80**, 3117 (1998).
[100]T. Champel, Phys. Rev. B **65**, 153403 (2002).
[101]K. Kishigi and Y. Hasegawa, Phys. Rev. B **65**, 205405 (2002).
[102]J.-Y. Fortin, E. Perez, and A. Audouard, Physica B **346–347**, 373.
[103]N. Harrison, C. H. Mielke, D. G. Rickel, J. Wosnitza, J. S. Qualls, J. S. Brooks, E. Balthes, D. Schweitzer, I. Heinen, and W. Strunz, Phys. Rev. B **58**, 10248 (1998).
[104]M. A. Itskovsky, S. Askenazy, T. Maniv, I. D. Vagner, E. Balthes, and D. Schweitzer, Phys. Rev. B **58**, R13347 (1998).
[105]J. Wosnitza, S. Wanka, J. Hagel, E. Balthes, N. Harrison, J. A. Schlueter, A. M. Kini, U. Geiser, J. Mohtasham, R. W. Winter, and G. L. Gard, Phys. Rev. B **61**, 7383 (2000).
[106]E. Datars and J. E. Sipe, Phys. Rev. B **51**, 4312 (1995).
[107]V. M. Gvozdikov, Fiz. Nizk. Temp. **27**, 956 (2001) [Low Temp. Phys. **27**, 704 (2001)].
[108]N. S. Averkiev, L. E. Golub, S. A. Tarasenko, and M. Willander, J. Phys.: Condens. Matter, **13**, 2517 (2001).
[109]P. D. Grigoriev, M. V. Kartsovnik, W. Biberacher, N. D. Kushch, and P. Wyder, Phys. Rev. B **65**, 060403(R) (2002).
[110]M. V. Kartsovnik, P. D. Grigoriev, W. Biberacher, N. D. Kushch, and P. Wyder, Phys. Rev. Lett. **89**, 126802 (2002).
[111]P. D. Grigoriev, Phys. Rev. B **67**, 144401 (2003).
[112]T. Champel and V. P. Mineev, Phys. Rev. **66**, 195111 (2002); Physica B **346–347**, 392 (2004).
[113]V. M. Gvozdikov, Phys. Rev. B **70**, 085113 (2004).
[114]J. Wosnitza, G. Goll, D. Beckmann, S. Wanka, D. Schweitzer, and W. Strunz, J. Phys. I **6**, 1597 (1996).
[115]V. M. Gvozdikov, Fiz. Tverd. Tela (Leningrad) **26**, 950 (1984) [Sov. Phys. Solid State **26**, 1560 (1984)].
[116]M. V. Kartsovnik, P. A. Kononovich, V. N. Laukhin, S. I. Pesotskiĭ, and I. F. Shchegolev, JETP **49**, 519 (1989).
[117]E. Ohmichi, H. Ito, T. Ishiguro, G. Saito, and T. Komatsu, Phys. Rev. B **57**, 7481 (1998).
[118]T. G. Togonidze, M. V. Kartsovnik, J. A. A. J. Perenboom, N. D. Kushch, and H. Kobayashi, Physica B **294–295**, 435 (2001).
[119]L. Balicas, J. S. Brooks, K. Storr, D. Graf, S. Uji, H. Shinagawa, E. Ojima, H. Fujiwara, H. Kobayashi, A. Kobayashi, and M. Tokumoto, Solid State Commun. **116**, 557 (2000).
[120]S. Uji, H. Shinagawa, Y. Terai, T. Yakabe, C. Terakura, T. Terashima, L. Balicas, J. S. Brooks, E. Ojima, H. Fujiwara, H. Kobayashi, A. Kobayashi, and M. Tokumoto, Physica B **298**, 557 (2001).
[121]H. Weiss, M. V. Kartsovnik, W. Biberacher, E. Balthes, A. G. M. Jansen, and N. D. Kushch, Phys. Rev. B **89**, R16259 (1999).
[122]M. Schiller, W. Schmidt, D. Schweitzer, H.-J. Koo, M. H. Whangbo, I. Heinen, T. Klausa, P. Kircher, and W. Strunz, Europhys. Lett. **51**, 82 (2000).
[123]M. Kartsovnik, P. Grigoriev, W. Biberacher, A. Groeger, D. Andres, S. Pesotskii, and N. Kushch, Synth. Metals **133-134**, 111 (2003).
[124]Y. Kurihara, J. Phys. Soc. Jpn. **61**, 975 (1992).
[125]M.-S. Nam, A Ardavan, J. A. Symington, J. Singleton, N. Harrison, C. H. Mielke, J. A. Schlueter, R. W. Winter, and G. L. Grand, Phys. Rev. Lett. **87**, 117001 (2001).
[126]J. Woznitza, S. Wanka, J. Nagel, H. v. Löhneysen, J. S. Qualls, J. S. Brooks, E. Balthes, J. A. Schlueter, U. Geiser, J. Mohtasham, R. W. Winter, and G. L. Gard, Phys. Rev. B **86**, 508 (2001).

[127]R. Rousseau, M.-L. Doublet, E. Canadell, R. P. Shibaeva, S. S. Khasanov, L. P. Rozenberg, N. D. Kushch, and E. B. Yagubskii, J. Phys. I (France) **6**, 1527 (1996).
[128]V. G. Peschanskiĭ and Khasan Raid Atalla, Fiz. Met. Metalloved. **94**, 14 (2002).
[129]V. G. Peschansky, Phys. Rep. **288**, 305 (1997).
[130]O. V. Kirichenko and V. G. Peschansky, Fiz. Nizk. Temp. **25**, 1119 (1999) [Low Temp. Phys. **25**, 837 (1999)].
[131]V. G. Peschansky and D. I. Stepanenko, JETP Lett. **78**, 322 (2003).
[132]O. V. Kirichenko, V. G. Peschanskii, and D. I. Stepanenko, Zh. Éksp. Teor. Fiz. **126**, 1435 (2004) [JETP **99**, 1253 (2004)].
[133]E. S. Borovik, Fiz. Met. Metalloved. **2**, 33 (1956).

Translated by Steve Torstveit

Spin gap in low-dimensional magnets (Review)

A. N. Vasil'ev,* M. M. Markina, and E. A. Popova

M. V. Lomonosov Moscow State University, Moscow 119992, Russia
(Submitted October 18, 2004)
Fiz. Nizk. Temp. **31**, 272–299 (March–April 2005)

The main mechanisms of formation of a spin gap in low-dimensional metaloxide compounds are reviewed. Among the objects in which a singlet ground state is formed are dimers, alternating chains with half-integer spin, uniform chains with integer spin, spin ladders, and two-dimensional ensembles of exchange-coupled spins. In some of these systems the spin gap in the spectrum of magnetic excitations is present from the start, while in others it is formed as a result of magnetoelastic interaction, charge ordering, or orbital ordering. [DOI: 10.1063/1.1884423]

INTRODUCTION

Magnetism, together with superfluidity, superconductivity, and charge-density waves, is among the quantum cooperative phenomena observed in condensed media at low temperatures. Each of these phenomena is of fundamental interest and can present new aspects with each new object of study. An important place in the list of such objects is held by low-dimensional magnets. The dimensionality and topology of the magnetic subsystem and also its interactions with the other subsystems of the magnet—elastic, charge, orbital—have a decisive influence on the formation of the ground state of the substance.

It is difficult to speak of the dimensionality of a system solely on the basis of the arrangement of magnetic ions in the crystal. For example, a transition-metal ion with a magnetic moment in a crystal can be treated at high temperatures as a 0-dimensional system. As the temperature is lowered, when the exchange interaction parameters become comparable with the temperature, these ions can form a three-dimensional antiferromagnetic or ferromagnetic state. If the transition-metal ions, in conformity with the motifs of the crystal lattice, form chains or planes distant from each other, then magnetic ordering may not set in at all. Intermediate states in the realm of low-dimensional magnetism belong to clusters of several closely spaced ions and spin ladders, which consist of two or three magnetic chains lying close together.

The simplest magnetic cluster is the dimer, a unified pair of magnetic ions. In the case when the ions in the dimer are coupled by an antiferromagnetic interaction, a spin singlet state is formed in it at low temperatures. The spin singlet is a configuration of spins in which the projection of their total magnetic moment on any direction is equal to zero. The singlet state is separated from the excited triplet states by a spin gap, and the formation of a spin gap in concentrated magnetic systems is manifested in their behavior as nonmagnetic substances at low temperatures.

A spin gap is also formed in isolated alternating chains in which different exchange interaction parameters (J and αJ) alternate along them. For $\alpha \to 0$ such a chain can be represented as a set of noninteracting dimers. However, there are classes of compounds containing isolated chains of integer spins (Haldane chains) or spin ladders in which a singlet ground state is reached without breaking the translational invariance. Such a state of the system is called a spin liquid. In Haldane chains and in ladders with an even number of ''legs'' the excited states are separated from the magnetic ground state by a spin gap, whereas in isolated uniform chains ($\alpha = 1$) of half-integer spins and in ladders with an odd number of legs the spectrum of magnetic excitations is gapless.

Various metaloxide compounds with the singlet ground state have been observed in recent years. Representatives of this class of substances are systems containing dimers of $BaCuSi_2O_6$ and $CaCuGe_2O_6$, plaquettes of CaV_4O_9, $S = 1/2$ chains of $CuGeO_3$, NaV_2O_5, and $NaTiSi_2O_6$, $S = 1$ chains of Y_2BaNiO_5 and $PbV_2Ni_2O_8$, ladders of $SrCu_2O_3$, and an orthogonal mesh of $SrCu_2(BO_3)_2$ dimers.

In this review we discuss only those metaloxide compounds in which the ground state is separated from the excited states by a spin gap. In many low-dimensional compounds such a state is not achieved because the interactions between remote fragments of the magnetic structure at low temperatures lead to the establishment of a long-range—antiferromagnetic or ferromagnetic—order.

1. DIMERS

The simplest system in which a singlet ground state can be realized at low temperatures is an isolated pair of magnetic ions—a dimer. In the Heisenberg model the Hamiltonian of a dimer has the form

$$\hat{H} = J(\hat{\mathbf{S}}_1 \cdot \hat{\mathbf{S}}_2), \tag{1}$$

where $\hat{\mathbf{S}}_1$ and $\hat{\mathbf{S}}_2$ are the spin operators of the two magnetic ions forming the dimer, and J is the exchange interaction parameter. This Hamiltonian has the eigenstates $E = (J/2) \times [S(S+1) - S_1(S_1+1) - S_2(S_2+1)]$, where S is the total spin of the system. For $J > 0$ (antiferromagnetic coupling) the ground state of the dimer formed by two spins $S_1 = S_2 = 1/2$ is a spin singlet $E(S=0) = -\frac{3}{4}J$ with the wave function $\{1/\sqrt{2}\,(|\uparrow\downarrow\rangle - |\downarrow\uparrow\rangle)\}$, and the excited state $E(S=1) = +\frac{1}{4}J$ is a spin triplet described by the three wave functions $\{|\uparrow\uparrow\rangle;\ 1/\sqrt{2}\,(|\uparrow\downarrow\rangle + |\downarrow\uparrow\rangle);|\downarrow\downarrow\rangle\}$. The value of the energy

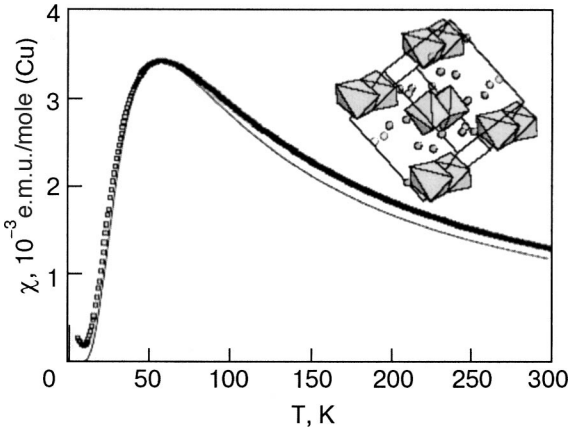

FIG. 1. Temperature dependence of the magnetic susceptibility of $CuTe_2O_5$. The solid curve shows $\chi(T)$ after subtraction of the temperature-independent (Van Vleck) component and the impurity (Curie) component. The crystal structure of $CuTe_2O_5$ is shown in the inset.

gap between these states is $\Delta = E(S=1) - E(S=0) = J$. For $J<0$ (ferromagnetic coupling) the singlet and triplet states exchange places.

The isothermal magnetic susceptibility of a mole of ions in a dimerized state is determined by the equation[1]

$$\chi = \frac{N_A g^2 \mu_B^2}{kT} \frac{1}{3 + e^{J/kT}}, \tag{2}$$

where N_A is Avogadro's number, g is the gyromagnetic ratio, μ_B is the Bohr magneton, and k is Boltzmann's constant. For $J>0$ the temperature dependence of the susceptibility $\chi(T)$ has a maximum at a temperature $T \approx 0.625J/k$ determined by the condition $\partial\chi/\partial T = 0$. In the high-temperature region ($J \ll kT$) the susceptibility obeys the Curie-Weiss law $\xi = C/(T-\theta)$, where $\theta = -J/4k$. For $T \to 0$ the susceptibility goes exponentially to zero.

The magnetic heat capacity of a mole of ions in the dimerized state is equal to[2]

$$C = 3R\left(\frac{J}{kT}\right)^2 \frac{e^{-J/kT}}{[1+3e^{-J/kT}]^2}. \tag{3}$$

The $C(T)$ curve passes through a maximum, and at high temperatures the magnetic heat capacity is proportional to T^{-2}.

A considerable number of metaloxide compounds are known to have a structure containing weakly intercoupled dimers, so that the thermodynamic properties of the material is determined almost wholly by the interaction within the dimer. As the temperature is lowered, however, the role of interdimer interactions increases, as a result of which at a certain temperature T_N a long-range magnetic order can be established in the whole system. Without claiming completeness of the list of dimer compounds, let us mention some of them.

1.1. $CuTe_2O_5$

In the structure of $CuTe_2O_5$, shown in the inset in Fig. 1, the Cu^{2+} ions ($S=1/2$), which are found in highly distorted CuO_6 edge–sharing octahedra form dimers which are distant from each other.[3] The bond angle Cu–O–Cu in the $CuTe_2O_5$ dimers is close to the critical angle for compensation of the ferromagnetic and antiferromagnetic interactions. At high temperatures, as is shown in Fig. 1, the magnetic susceptibility χ obeys the Curie-Weiss law with a Weiss constant $\theta = -41$ K, which indicates that the antiferromagnetic exchange is dominant. With decreasing temperature the $\chi(T)$ curve reaches a maximum at $T=56$ K, after which the susceptibility falls off rapidly. From the behavior of $\chi(T)$ one can estimate a value $J=90$ K for the magnetic interaction parameter in the dimers.[4] The slight increase of the magnetic susceptibility at low temperatures is not inherent to low-dimensional systems specifically and is due to impurities and imperfection of the crystal lattice. It is observed to some degree or other in all the compounds described below and will not be discussed further.

1.2. CsV_2O_5

In the structure of CsV_2O_5 the layers containing the magnetic V^{4+} ($S=1/2$) and nonmagnetic V^{5+} ($S=0$) vanadium ions alternate with Cs layers.[5] The $V^{4+}O_5$ pyramids, joined along an edge in the basal plane, form dimers. These dimers are separated from each other by $V^{5+}O_4$ tetrahedra, which leads to weakening of the interdimer coupling. It follows from analysis of the temperature dependence of the magnetic susceptibility of CsV_2O_5 that the gap in the spectrum of magnetic excitations has the value $\Delta = 146$ K.[6] It should be noted, however, that the appearance of the gap in the spectrum of magnetic excitations of CsV_2O_5 admits a different interpretation. Calculations of the band structure of CsV_2O_5 suggest that the magnetic exchange between the V^{4+} ions occurs across the $V^{5+}O_4$ complex also.[7] In that case the magnetic subsystem of CsV_2O_5 can be represented as an alternating chain with exchange J within a dimer and αJ between dimers. An estimate of the exchange interaction parameters from the $\chi(T)$ curve gives $J=146$ K, $\alpha = 0.25$.[7]

1.3. $CaCuGe_2O_6$

In the structure of $CaCuGe_2O_6$ the Cu^{2+} ions form zigzag chains along the c axis, while in the ab plane these ions form pairs.[8] The magnetic susceptibility of this compound exhibits a broad maximum at $T \sim 40$ K and falls off exponentially with decreasing temperature. However, calculations according to the dimer model for this compound deviate noticeably from the experimental data in the region of the maximum; this indicates a complex hierarchy of magnetic interactions in $CaCuGe_2O_6$. In principle, each Cu^{2+} ion can interact not only with two nearest neighbors but also with two next-nearest neighbors in the chain, and also in the ab plane with the nearest neighbors from other chains. The best agreement with experimental data for $CaCuGe_2O_6$ is achieved when a weak antiferromagnetic interaction between dimers is included.[9]

2. CLUSTERS IN $Ca_{0.85}CuO_2$

$Ca_{0.85}CuO_2$ has orthorhombic symmetry with lattice parameters $a=2.807$ Å, $b=6.324$ Å, $c=10.573$ Å.[10] In the crystal structure of this compound the copper ions are found in a planar environment of oxygen ions, forming CuO_2 chains extending along the a axis. These chains are separated by Ca ions. The O^{2-} ion from neighboring copper-oxygen

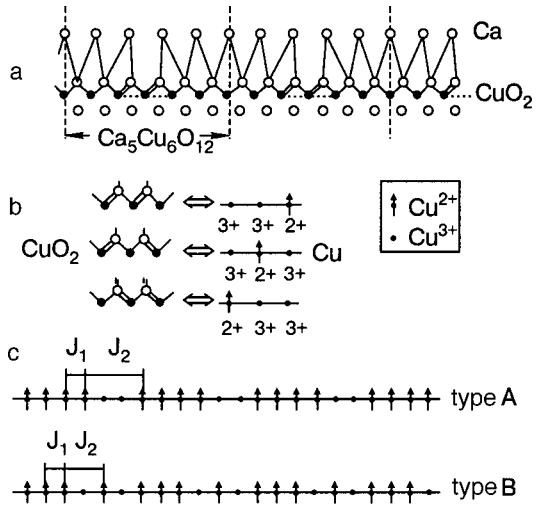

FIG. 2. Magnetic structure of $Ca_{0.833}CuO_2$: diagram of the chemical bonds in the CuO_2 chain (a); three versions of the arrangement of nonmagnetic ions in the $Ca_5Cu_6O_{10}$ segments (b); two types of magnetic structure of the CuO_2 chains (c).

chains can be joined into octahedra partially occupied by Ca^{2+} ions. If it were possible to synthesize the stoichiometric compound $CaCuO_2$, then the center of every-other octahedron would be occupied by a Ca^{2+} ion, and the CaO_6 octahedra would be joined along an edge. The stoichiometric composition is unstable, and the ratio Ca/Cu=0.85 is the highest possible value, since the Ca^{2+} ions cannot be found closer together than 3.2 Å in the crystal lattice.[11] In $Ca_{0.85}CuO_2$ only a percentage 0.425 of the octahedra are occupied, and the presence of vacancies causes the Ca^{2+} ions to be shifted in the direction of the ''tunnel'' along the *a* axis, and a more uniform distribution of the ions is formed. The structure of the Ca and Cu chains is incommensurate, and the mean distances between ions $5d_{\text{Ca-Ca}} \approx 6d_{\text{Cu-Cu}}$. The case of exact equality is realized for the composition $Ca_{0.833}CuO_2$ ($Ca_5Cu_6O_{12}$).

The incommensurability has a decisive influence on the magnetic properties of $Ca_{0.85}CuO_2$. This compound is an insulator; the formal valence of copper is equal to +2.33, i.e., the magnetic Cu^{2+} ions constitute two-thirds and the nonmagnetic Cu^{3+} ions one-third of the total number. The holes in this compound are localized, and the magnetic coupling of Cu^{2+} in the chains takes place through Cu–O–Cu superexchange. Studies of the electron paramagnetic resonance and magnetic susceptibility have shown that the exchange in the chains is antiferromagnetic, $J=45$ K.[12] The temperature dependence of the magnetic susceptibility of $Ca_{0.85}CuO_2$ exhibits a broad maximum at $T\sim 40$ K and an exponential decline to zero as $T\to 0$. Such behavior is what would be expected for a system with a spin gap $\Delta=83$ K.

The formation of a singlet ground state in $Ca_{0.85}CuO_2$ can be explained from a simple geometric analysis of the structure of the spin chains. For convenience one can neglect the weak incommensurability of the periods and consider the system $Ca_{0.833}CuO_2$. In Fig. 2a (taken from Ref. 12), which illustrates the scheme of the chemical bond of the repeating $Ca_5Cu_6O_{12}$ segments, it is seen that every ''missing'' Ca^{2+} ion is compensated by two Cu^{3+} ions. Figure 2b shows three variant distributions of these ions within a segment of the chain, and Fig. 2c shows the two possible types of magnetic chains; the exchange interaction constants between spins located next to each other and between spins separated by a nonmagnetic ion are denoted by J_1 and J_2, respectively. The structure of type A is characterized by the presence of a quartet of spins separated by two holes. In the case $J_1>J_2$ this structure can be considered as a cluster, and the even number of spins makes for a nonmagnetic ground state separated by a gap $\Delta=2J_1$ from the excited states. The structure of type B contains alternating segments containing one or three spins separated by nonmagnetic ions. The interaction between spins within a segment J_1 is the same as in the type-A structure, while the interaction between segments J_2 is larger, since it is acting over a shorter distance. Such a spin configuration can be considered as a chain with an alternating interaction. Calculations of the magnetic susceptibility of $Ca_{0.85}CuO_2$ have been done using the dimer model and the Bonner-Fisher model for a ring of N spins.[15] Both models describe the behavior of $\chi(T)$ well in the region $T<60$ K, while at higher temperatures the curve calculated for the dimer model deviates noticeably from the experimental values, whereas the calculation in the Bonner-Fisher model with parameters $J=45$ K, $N=8$ gives a good description of $\chi(T)$ up to 120 K. Thus the temperature dependence of the magnetic susceptibility corresponds to the behavior of structure segments containing an even number of spins $S=1/2$ (model A).

3. *S*=1/2 CHAINS

Analysis of the Hamiltonian of a quasi-one-dimensional magnet in the Ising approximation

$$\hat{H}=J\sum_i \hat{S}_i^Z \hat{S}_{i+1}^Z \tag{4}$$

shows that an isolated infinite chain of magnetic atoms does not order at any finite temperature.[13] The ground state is reached only at $T=0$, and there is no gap in the energy spectrum of magnetic excitations. This result stems from the fact that long-range order in a chain of atoms coupled by an exchange interaction J is destroyed by the flip of a single spin. Here the magnetic energy increases by $2J$, while the entropy increases by $k\ln N$. The change of the free energy upon the flip of a spin is written

$$\Delta F=2J-kT\ln N \tag{5}$$

and can be made negative at arbitrarily low temperature if the number of links N in the chain is chosen large enough.

The magnetic susceptibility of an Ising chain has the form[14]

$$\chi_\parallel=\frac{Ng_\parallel^2\mu_B^2}{2J}\frac{J}{2kT}e^{J/kT},$$

$$\chi_\perp=\frac{Ng_\perp^2\mu_B^2}{4J}\left[\tanh\left(\frac{J}{2kT}\right)+\frac{J}{2kT}\operatorname{sech}^2\left(\frac{J}{2kT}\right)\right]. \tag{6}$$

The symbols $\parallel$ and $\perp$ denote the direction of the external field relative to the axis of quantization of the spins within the chain. The temperature dependence of the magnetic susceptibility of a linear system in the Ising model is shown in Fig. 3. It is seen that $\chi_\parallel(T)$ is an odd function of J (for

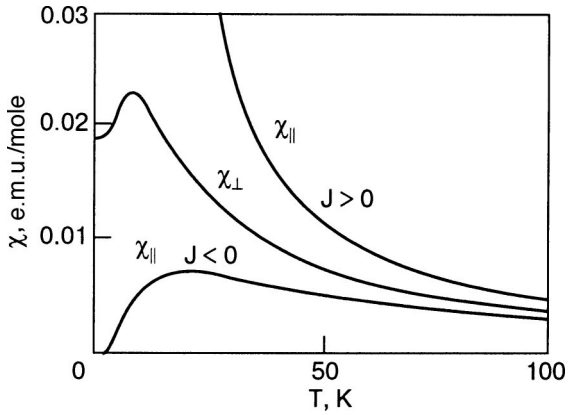

FIG. 3. Magnetic susceptibility of a linear $S=1/2$ chain, calculated according to the Ising model for $J>0$ and $J<0$.

$J>0$ it increases as $T\to 0$, and for $J<0$ it passes through a broad maximum and goes to zero for $T\to 0$). The perpendicular component $\chi_\perp(T)$ is an even function of J and is no different in the cases $J>0$ and $J<0$.

Following the solution of the Ising problem it was shown that Heisenberg chains of half-integer spins

$$\hat{H}=J\sum_i (\hat{\mathbf{S}}_i\cdot\hat{\mathbf{S}}_{i+1}) \tag{7}$$

do not order at finite temperatures either.[15] Such a chain has a degenerate singlet ground state and a triplet excited state. The magnetic excitation in the chain is a pair of spins propagating via the exchange interaction upon a spontaneous spin flip in the disordered chain. Such an excitation of the spins does not require additional energy, since there is no gap in the spectrum of magnetic excitations.

A calculation of the magnetic susceptibility of a ring of N Heisenberg spins was carried out in Ref. 15. The curve obtained in the limit $N\to\infty$ is shown in Fig. 4. The smooth maximum on the curve is determined by the relations

$$\frac{\chi_{\max}|J|}{g^2\mu_B^2}\approx 0.7346, \quad \frac{kT_{\max}}{|J|}\approx 1.282. \tag{8}$$

In the overwhelming majority of quasi-one-dimensional compounds with large values of the exchange interaction constants a three-dimensional magnetic ordering occurs at a

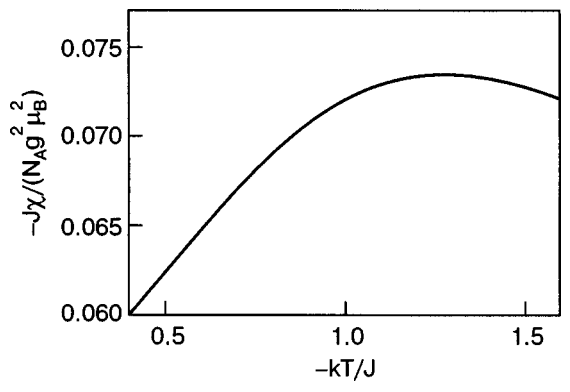

FIG. 4. Magnetic susceptibility of a linear $S=1/2$ chain calculated according to the Heisenberg model for $J>0$.

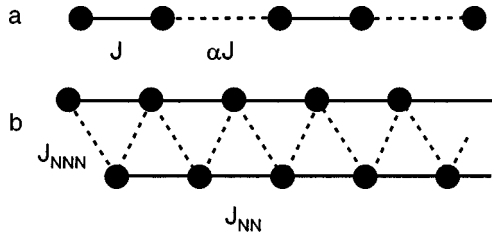

FIG. 5. Schematic models of a chain with alternating interaction (a) and with the interaction with next-nearest neighbors taken into account (b).

certain temperature.[1)] Such a transition is brought on by any type of anisotropy and weak interactions between chains.

As a criterion of "one-dimensionality" of the system we can use the ratio of the interactions between chains J' to the exchange integral in a chain. For isolated chains $J'/J\to 0$. When the interchain coupling is taken into account the Néel temperature T_N can be estimated from the formula[16]

$$J'=\frac{kT_N}{1.28}\sqrt{\ln\frac{5.8J}{kT_N}}. \tag{9}$$

If the exchange interaction within a linear chain of magnetic ions depends on the positions of the ion, then this is a chain with an alternating interaction (Fig. 5a). In the general case such a chain can be described by a Hamiltonian in the form

$$\hat{H}=J\sum_i (\hat{S}_{i-1}\hat{S}_i+\alpha\hat{S}_i\hat{S}_{i+1}),$$

where $\alpha<1$.[19] If $\alpha=0$, then such a chain transforms to a system of noninteracting dimers with a singlet ground state, while if $\alpha=1$ a chain with uniform exchange and a gapless spectrum is realized. The scale of the alternating exchange interaction in a chain is conveniently represented through the introduction of the parameter $\delta=(1-\alpha)/(1+\alpha)$.

Numerical calculations of the magnetic sucsceptibility χ and heat capacity C of alternating Heisenberg chains were carried out in Ref. 19. The results of these calculations are presented in Fig. 6. For any values of the parameter α a broad maximum is present on the $\chi(T)$ and $C(T)$ curves. The position of the maximum on the $\chi(T)$ curve is independent of α, while that on the $C(T)$ curves depends on α but not on J. For $T\to 0$ the behavior of $\chi(T)$ and $C(T)$ is described by an exponential decline, indicating the presence of a gap in the spectrum of magnetic excitations of the alternating chain.

In many real systems containing isolated chains of magnetic ions the behavior of the magnetic susceptibility is not described by simple models for a uniform or alternating chain. Agreement of the calculated results and experimental data is achieved by taking into account not only the interaction with nearest-neighbor ions, J_{NN}, but also the interaction with next-nearest neighbors, J_{NNN}. Such a system can be considered as two coupled chains or a zigzag chain, as is shown in Fig. 5b. Depending on the ratio J_{NN}/J_{NNN} different variants of the ground state are realized (long-range magnetic order, a spiral spin structure, or a spin-liquid state).[19–24] There exists an exact solution of this problem in the case

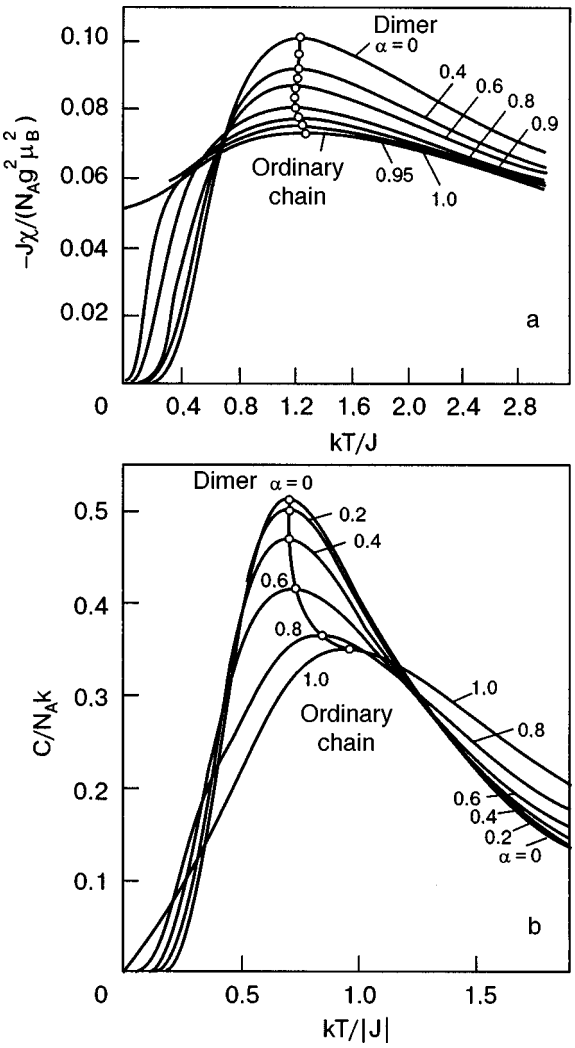

FIG. 6. Calculation of the magnetic susceptibility (a) and heat capacity (b) of chains with half-integer spin with different degrees of alternation.

$J_{NN}/J_{NNN}=1/2$; the ground state of such a chain is singlet and is separated from the first excited state by a gap in the magnetic excitation spectrum.[21]

An additional antiferromagnetic exchange interaction J_{NNN} of the same sign as J_{NN} is frustrating, i.e., it hinders the formation of an ordered ground state. In the region $J_{NN}<4J_{NNN}$ a dimerized state with a spin gap $\Delta\sim\exp\{-J_{NNN}/J_{NN}\}$ is realized. In the parameter region $J_{NN}<2J_{NNN}$ a spiral magnetic structure, which in the general case is incommensurate with the lattice, can form in the chain. A ferromagnetic exchange interaction J_{NNN} can lead to the formation of long-range magnetic order (Ref. 23).[2)]

In chains of half-integer spins a number of different scenarios for reaching the singlet ground state are realized, some of which will be described below.

3.1. $(VO)_2P_2O_7$

This compound, which contains two close-lying chains of magnetic V^{4+} ions, was long considered to be the first representative of a family of spin ladders. However, according to the present understanding, it is more aptly treated as a compound containing two types of alternating spin chains. This is the picture described below. The crystal structure of $(VO)_2P_2O_7$ is shown in Fig. 7. The unit cell contains eight

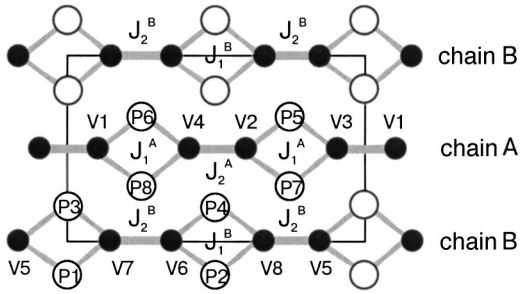

FIG. 7. Diagram of the crystal structure of $(VO)_2P_2O_7$.

inequivalent positions each for vanadium and phosphorus. Both types of alternating chains (A and B) are directed along the *b* axis, and each type contains pairs of VO_5 pyramids joined along an edge, which are separated by PO_4 tetrahedra.[27]

Nuclear magnetic resonance (NMR) studies of $(VO)_2P_2O_7$ have revealed a curious evolution of the spectrum of ^{31}P, shown in Fig. 8.[28] At the lowest temperatures one observes only one peak, corresponding to the nonmagnetic ground state of the compound. With increasing temperature this peak shifts and splits first into two and then into four lines. This behavior indicates that the eight phosphorus positions in the $(VO)_2P_2O_7$ structure are divided into four groups that are acted upon by different internal fields produced by the V ions. At high temperatures a single peak is again observed in the spectrum. The shift and nonmonotonic variation of the amplitudes of the individual lines with temperature presupposes the existence of several spin components having different temperature dependence of the magnetic sucsceptibility. The large value of the Knight shift at low temperatures indicates the presence of gaps in the spec-

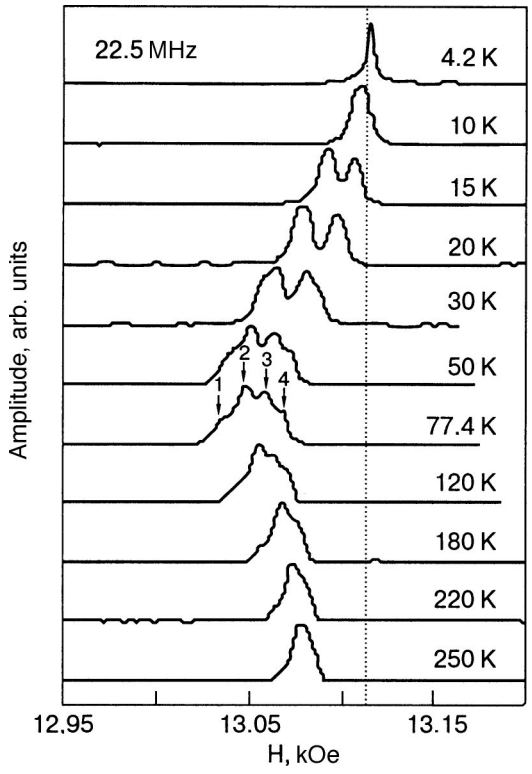

FIG. 8. Nuclear magnetic resonance spectrum of ^{31}P in $(VO)_2P_2O_7$.

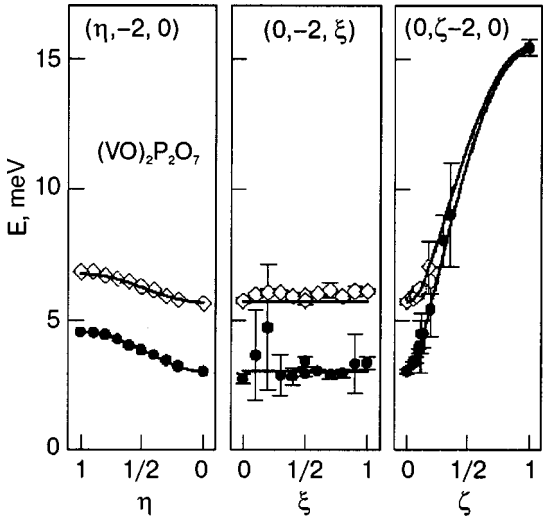

FIG. 9. Dispersion curves of the magnetic excitations in $(VO)_2P_2O_7$.

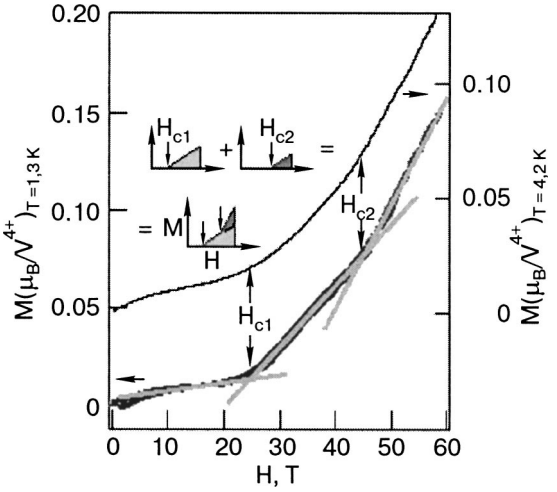

FIG. 10. Field dependence of the magnetization of $(VO)_2P_2O_7$.

tra of magnetic excitations of both chains. An estimate of the gaps for each of the four spin components was made according to the low-temperature trend of the Knight shift on the assumption of a quadratic magnon dispersion relation. It turned out that the four lines in the NMR spectrum are divided into two groups with different temperature dependence of the Knight shift and different values of the gap. For one group of peaks $\Delta = 35$ K, and for the other group $\Delta = 52$ K. We note that the spectrum of ^{51}V has only a single peak, and the value of the gap determined from its Knight shift is $\Delta = 68$ K. The discrepancy in the values of the gaps determined from the Knight shifts of ^{31}P and ^{51}V is due to the fact that the phosphorus ion is acted upon by the internal field of vanadium ions belonging to different chains.

As can be seen in Fig. 9, inelastic neutron scattering studies[29] have revealed two dispersion curves and, accordingly, two gaps $\Delta_1 = 36$ K and $\Delta_2 = 69$ K. Both dispersion curves indicate a large value of the antiferromagnetic exchange parameter along the *b* axis. At the Brillouin zone boundary in this direction the energies of the two branches become equal, reaching a value $E \sim 180$ K. The structural unit cell coincides with the magnetic unit cell, and therefore the dispersion of magnetic excitations is observed throughout the Brillouin zone. Using the dispersion relation for an alternating chain $E = \sqrt{\Delta^2 + (\pi/2J)^2 \sin^2 q}$ (q is the wave vector) and the values of the energy of the two branches at the Brillouin zone boundary, we can estimate the mean value of the antiferromagnetic exchange parameter $J = (J_1 + J_2)/2$ for each of the two chains. The scale of alternation in each chain, $\delta = (1-\alpha)/(1+\alpha)$, where $\alpha = J_2/J_1$, is determined from the expression $\Delta(\delta)/J \approx 2\delta^{3/4}$. The results of calculations for chains of types A and B are presented in Table I.

TABLE I.

Type of chain	Gap Δ, K	Alternation, α	Exchange J_1, K	Exchange J_2, K
A	68	0.67	136	92
B	35	0.83	124	103

The presence of two gaps in the magnetic excitation spectrum of $(VO)_2P_2O_7$ is manifested clearly in the field dependence of the magnetization of this compound at low temperatures[30] (Fig. 10). It is seen that this curve has kinks at two different fields: $H_{c1} = 25$ T, and $H_{c2} = 46$ T. The values of the gaps estimated from the relation $\Delta_{1,2} = g\mu_B H_{c1,2}/k$, come to $\Delta_1 = 33$ K and $\Delta_2 = 62$ K, in good agreement with the inelastic neutron scattering data. The slope of the magnetization curve in the region $H_{c1} \ll H < H_{c2}$ is about half as large as in the region $H_{c2} < H$. This means that the contributions of the two kinds of chains to the magnetization of $(VO)_2P_2O_7$ are comparable.

3.2. $CuGeO_3$

This compound is apparently the only currently known representative of metaloxides that undergo a spin-Peierls transition. This transition is realized in crystals containing isolated chains of half-integer spins. Uniform chains of such spins do not have gaps in the spectrum of magnetic excitations, but the total energy of the crystal can be lowered on account of alternation of the exchange interaction. At the spin-Peierls transition a doubling of the crystal lattice period occurs and a gap opens up in the spectrum of magnetic excitations.

$CuGeO_3$ has an orthorhombic structure with the lattice parameters $a = 4.81$ Å, $b = 8.43$ Å, $c = 2.95$ Å and contains two formula units per unit cell.[31] This compound has a structure in which chains of CuO_6 octahedra and chains of GeO_4 tetrahedra separating them extend along the *c* axis. The carriers of the spin magnetic moment $S = 1/2$ are Cu^{2+} ions with unfilled *d* shells.

A spin-Peierls transition in $CuGeO_3$ has been observed in an experimental study of the magnetic susceptibility of single crystals of this compound.[32] As is shown in Fig. 11, with decreasing temperature the broad maximum of the magnetic sucsceptibility which is characteristic for low-dimensional systems is observed at $T_m \sim 56$ K, and at $T_c \sim 14$ K a sharp decrease of the susceptibility occurs along all of the crystallographic axes. From a comparison with the model of a quantum half-integer ($S = 1/2$) chain of spins,[33] one can obtain an estimate of the exchange integral in accor-

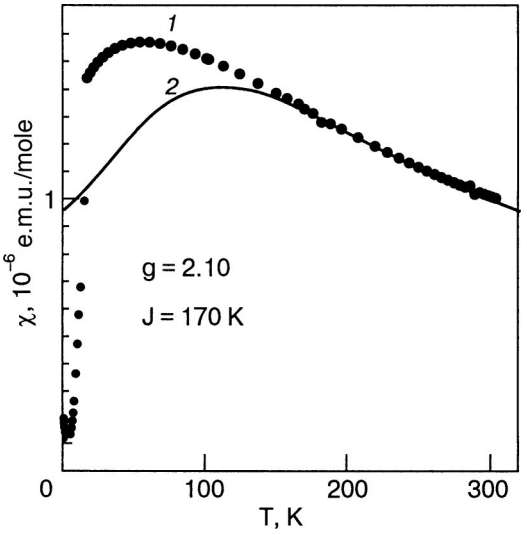

FIG. 11. Temperature dependence of the magnetic susceptibility of polycrystalline $CuGeO_3$ (*1*) and an approximation of this dependence by the Bonner–Fisher curve (*2*).

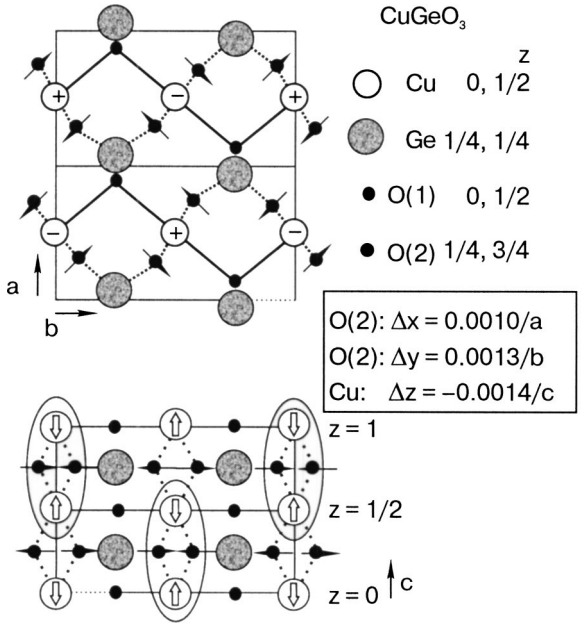

FIG. 12. Diagram of the atomic displacements at the spin-Peierls transition in $CuGeO_3$.

dance with the expression $T_m = 0.64J_C$: $J_C \sim 88$ K. The values of the exchange integrals characterizing the interaction of the next-nearest neighbors along the chain, J_C', and also the interaction between chains along the principal crystallographic directions, J_A and J_B, have been estimated in neutron scattering experiments. For $J_C = 120$ K it was found[34] that $J_C'/J_C = 0.2$, $J_A = 0.1J_C$, and $J_B = 0.01J_C$. These last relationships characterize the degree of one-dimensionality of the magnetic structure of copper germanate. From the trend of the magnetic susceptibility at $T < T_c$ one can estimate the value of the energy gap opening in the spectrum of elementary magnetic excitations of the dimerized system according to the Bulaevskiĭ model, $\Delta(T) = 1.64\delta(T)J_C$, and determine the alternation parameter δ of the exchange integral in the chain, $J_C^{1,2}(T) = J_C\{1 \pm \delta(T)\}$. For copper germanate it turns out that $\delta(0) = 0.17$, i.e., $J_C^1/J_C^2 = 1.41$, and $\Delta(0) = 24$ K.

The spin-Peierls transition in $CuGeO_3$ is accompanied by pronounced anomalies of many physical properties. For example, in the heat capacity this transition is manifested as a distinct anomaly of the λ type,[35] and the coefficients of thermal expansion exhibit markedly anisotropic behavior.[36,37] A fundamental feature of the spin-Peierls transition, as we have said, is the appearance of static distortions of the crystal lattice. Such distortions, which accompany the period doubling of the crystal cell, have indeed been observed in x-ray measurements and neutron diffraction experiments.[38] The largest displacements at the spin-Peierls transition in $CuGeO_3$ are suffered by the Cu^{2+} ions, which move along the *c* axis, and the $O^{2-}(2)$ ions, which move in the *ab* plane. It turns out that the values of the displacements causing the radical changes of the magnetic properties of copper germanate are very small:

$$u_{Cu}^C \sim -0.0014,\ u_{O(2)}^A \sim 0.0010,\ u_{O(2)}^B \sim 0.0013.$$

The resulting lattice strain can be represented as an alternating rotation of the germanium-oxygen tetrahedra about an axis joining the apical oxygen ions. Such rotations cause alternating negative and positive displacements of the copper ions along the *c* axis and, ultimately, even give rise to small displacements of the germanium ions along the *b* axis. As is seen in Fig. 12, the chains belonging to the same unit cell are dimerized in antiphase, and doubling of the crystal lattice occurs not only along the *c* axis but also along the *a* axis.

The behavior of copper germanate in a magnetic field can be described with the aid of the phase diagram shown in Fig. 13.[39] Regions *U*, *D*, and *I* in this diagram correspond to uniform, dimerized, and incommensurate phase states. In the *U* phase there is only short-range magnetic order in the chains, antiferromagnetic according to the sign of the exchange integral. In the *D* phase there is no macroscopic magnetic moment, but one does appear in the *I* phase, and the period of the magnetic system is in the general case incommensurate with the period of the crystal structure. The incommensurate *I* phase is incommensurate not only with the

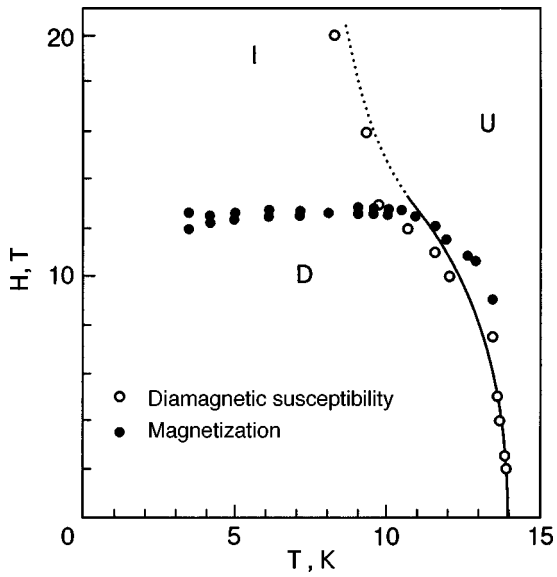

FIG. 13. Phase diagram of a spin-Peierls magnet.

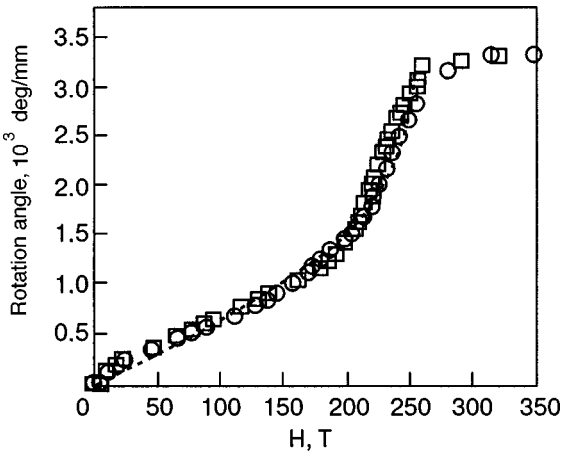

FIG. 14. Field dependence of the Faraday rotation angle in $CuGeO_3$ at $T=6$ (□) and 10 K (○); the dotted line shows the theoretical curve; $\lambda=1152$ nm (1.08 eV).

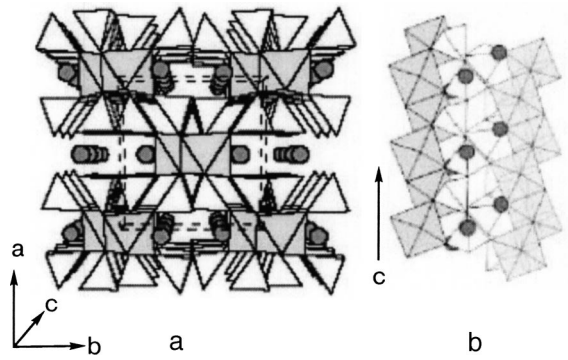

FIG. 15. a) Crystal structure of $NaTiSi_2O_6$; the gray and white polyhedra represent the $Ti^{3+}O_6$ octahedra and SiO_4 tetrahedra; the Na ions are indicated by gray circles. b) One-dimensional screw chain of TiO_6 octahedra joined along an edge.

uniform U phase but also with the dimerized D phase. In the absence of a static magnetic field a second-order phase transition from the U to the D phase occurs at $T=T_c$, and at the first critical field H_{c1} at low temperatures there is a first-order transition from the D to the I phase. The temperature of the U-D transition at $T_c=14.3$ K ($H=0$) corresponds to the field of the D-I transition, $H_{c1}=12.5$ T ($T=0$). The triple point L on the magnetic phase diagram of $CuGeO_3$ lies at $T_L=11.5$ K, $H_L=13$ T. On cooling of a spin-Peierls magnet in a field $H>H_L$ there is a second-order phase transition from the uniform to the incommensurate state.

The first critical field is related to the temperature of the spin-Peierls transition and the value of the gap in the spectrum of magnetic excitations by the simple relations

$$H_{c1}\sim 1.48\frac{kT_c}{9\mu_B}\sim 0.84\frac{\Delta}{g\mu_B},$$

and in weak fields the critical temperature decreases in proportion to the square of the magnetic field:

$$\frac{\Delta T}{T_c}\sim -\left(\frac{g\mu_B H}{2kT_c(0)}\right)^2.$$

The anisotropy of the spectroscopic splitting factor ($g_A=2.06$, $g_B=2.27$, $g_C=2.15$) is manifested in a difference of the values of the critical fields in the different crystallographic directions.[40,41] At low temperatures the field dependence of the magnetization in the region of the first critical field exhibits pronounced hysteresis, the value of which in $CuGeO_3$ is around 0.1 T. As is shown in Fig. 14, the jump of the magnetization (or of the Faraday rotation angle, which is proportional to it) in copper germanate at the first critical field H_{c1} is accompanied by subsequent monotonic growth, and in a field ~ 250 T the magnetization of $CuGeO_3$ reaches saturation.[42]

The physical picture of the processes occurring in spin-Peierls magnets in a magnetic field is as follows. When the field reaches the first critical value H_{c1} some of the dimers are destroyed (about 2% of them in $CuGeO_3$), and the ''normal'' magnetic moments that are formed are spaced equidistantly along the chain. The hysteresis of the field dependence of the magnetization in the region of the first critical field is indicative, in particular, of a possible pinning of the normal magnetic moments at structural defects. The number of unpaired magnetic moments and the distance between them are determined by the magnetic field. With increasing magnetic field the number of such moments increases and the distance between them decreases. Self-organization of the incommensurate phase of spin-Peierls magnets is observed in x-ray diffraction studies from the appearance of an additional period of the crystal lattice, controlled by the magnetic field. The dimerized state is completely destroyed only at the second critical field H_{c2}, the value of which turns out to be comparable to twice the value of the exchange integral in the chain, $2J_C$. For $H>H_{c2}$ the substance is again found in a uniform state, in which, however, all the magnetic moments are pointed in the same direction.

3.3. $NaTiSi_2O_6$

This compound has a monoclinic crystal lattice with space group $C2/c$, which is common to the whole family of pyroxenes. The lattice parameters at room temperature are $a=9.692$ Å, $b=8.874$ Å, $c=5.301$ Å, and angle $\beta=106.85°$ (Ref. 43). The pyroxene structure contains isolated zigzag chains of TiO_6 octahedra joined along an edge, as is shown in Fig. 15. These chains are separated by SiO_4 tetrahedra, which leads to substantial weakening of the interchain interactions. Since all the titanium positions in the structure are equivalent, the chains of TiO_6 octahedra at room temperature are chains of half-integer spins with a uniform exchange along the c axis.

The temperature dependence of the magnetic susceptibility of $NaTiSi_2O_6$ in a field $H=1$ T is shown in Fig. 16.[44] The $\chi(T)$ curve in the high-temperature region obeys the Curie-Weiss law and exhibits a sharp drop at $T<210$ K. At low temperatures a marked growth of the susceptibility occurs due to impurities and defects. The inset in Fig. 17 shows the susceptibility χ_m of $NaTiSi_2O_6$ after subtraction of the impurity contribution χ_i. Below $T\sim 210$ K χ_m falls off rapidly and remains practically unchanged at low temperatures. The residual susceptibility $\chi_0=6\times 10^{-5}$ e.m.u./mole is comparable in value to the magnetic susceptibility of other spin-Peierls systems in the ground state (NaV_2O_5, MgV_2O_5, CaV_2O_5, and CsV_2O_5), which suggests that the ground state of $NaTiSi_2O_6$ is a spin singlet. An estimate of the value of

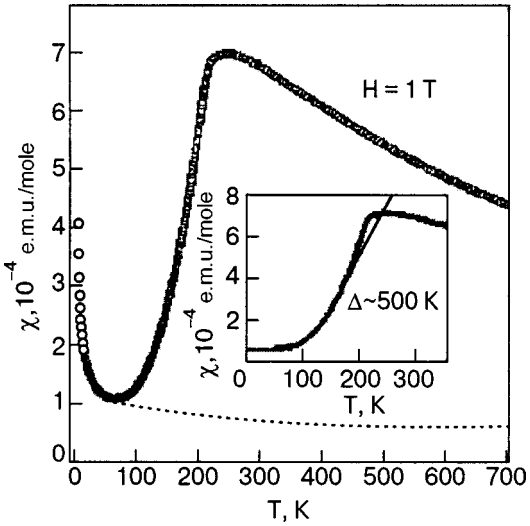

FIG. 16. Magnetic susceptibility of $NaTiSi_2O_6$. The dashed curve shows the approximation by the Curie law for impurities. The inset shows $\chi(T)$ after subtraction of the impurity contribution; the solid curve is the result of calculations that permit estimation of the value of the gap.

the spin gap $\Delta/k \sim 500$ K is obtained from the low-temperature part of the magnetic susceptibility $\chi_m \sim \exp(-\Delta/kT)$.

In the high-temperature region the $\chi(T)$ curve obeys the Curie-Weiss law, but deviations from that law begin to appear already at temperatures $T \sim 400$ K, as is seen in Fig. 17. The solid curve in Fig. 17 is the result of a calculation by the Bonner–Fisher formula for an antiferromagnetic chain of Heisenberg ions with spin $S=1/2$ and the parameters $g=2$ and $J/k=295$ K. The $\chi(T)$ curve is estimated well by that formula in the region $T>250$ K. A sharp decrease of the susceptibility occurs below 210 K, somewhat higher than the maximum on the Bonner-Fisher curve (~ 180 K). This means that the formation of a spin gap occurs prior to the formation of short-range magnetic order in the chain.

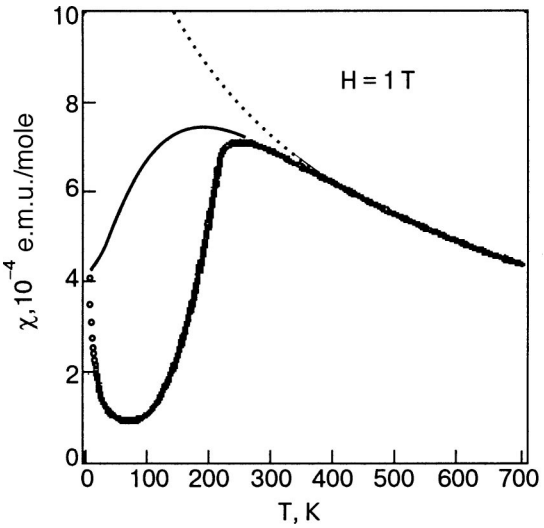

FIG. 17. Magnetic sucsceptibility of $NaTiSi_2O_6$: the dashed curve is the approximation by the Curie–Weiss law in the high-temperature region ($C=0.375$ e.m.u.·K/mole, $\theta=255$ K). The solid curve is the result of calculations by the Bonner-Fisher model ($g=2.0$, $J/k_B=295$ K).

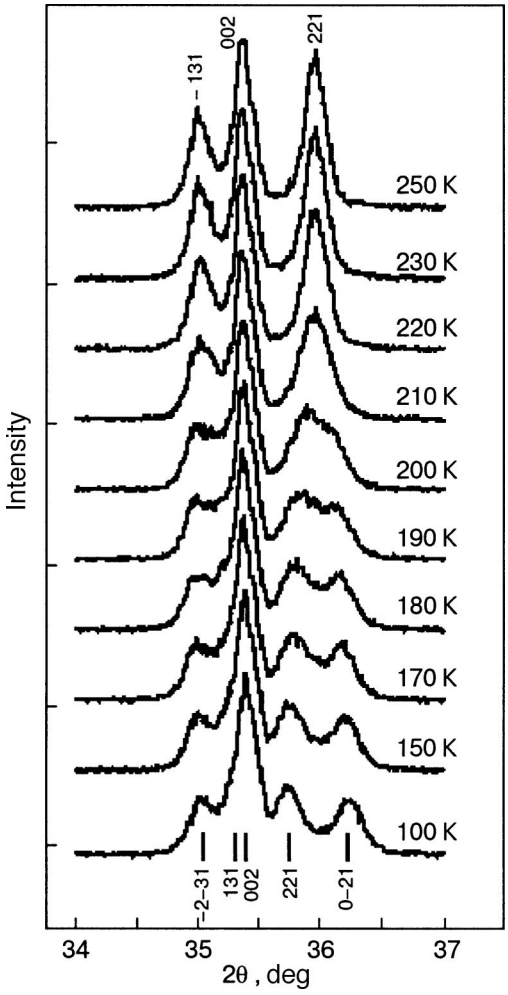

FIG. 18. Temperature dependence of the x-ray reflections $(-1\,3\,1)$, $(0\,0\,2)$, and $(2\,2\,1)$ in $NaTiSi_2O_6$.

The evolution of the x-ray spectrum of $NaTiSi_2O_6$ is shown in Fig. 18. Some of the diffraction peaks split at $T \sim 210$ K, attesting to a lowering of the crystal symmetry from monoclinic to triclinic.[44] The crystal lattice parameters at 10 K are $a=6.63$ Å, $b=8.83$ Å, $c=5.29$ Å, and angles $\alpha=90.2°$, $\beta=102.3°$, and $\gamma=47.1°$.

Although the transition in $NaTiSi_2O_6$ shows some of the signs of a spin-Peierls transition, it originates from orbital ordering. The TiO_6 octahedra in $NaTiSi_2O_6$ are joined along an edge formed by an apical and a basal oxygen ion. By virtue of the structural features of the $NaTiSi_2O_6$ two of the three t_{2g} orbitals of the Ti^{3+} ion are degenerate. They share a single electron that provides magnetic interaction along the chain. Here both orbitals are involved in the exchange. The Jahn-Teller situation is unstable, and at $T_c=210$ K a structural phase transition occurs which is accompanied by lifting of the degeneracy. In the low-temperature phase the electron on the d shell of titanium occupies the lowest-energy orbital d_{xy}, and a strong alternation of the exchange interaction in the chain occurs. In places where the d_{xy} orbitals overlap, a dimer is essentially formed. The transition to the singlet state brings about a sharp decrease of the magnetic susceptibility at T_c.

4. $S=1$ CHAIN

In Ref. 45 Haldane conjectured that the ground states of chains of half-integer spins and of integer spins are fundamentally different. A description of the low-energy excitations by magnons alone is incorrect for systems with easy-axis anisotropy, and it is necessary to take the existence of solitons into account. While a magnon in the case of strong anisotropy can be interpreted as the flipping of a single spin, a soliton is a collective excitation of the whole system, i.e., the spin flip occurs not at a single site but involves a certain (always odd) number of spins. Since a soliton includes an odd number of spins of the lattice, the admissible value of the soliton spin depends on the chain in which it forms. The spin of a soliton will be integer if the spins in the chain are integer spins and half-integer if they are half-integer.

In Ref. 45 the Hamiltonian for an easy-axis antiferromagnetic was analyzed in the form

$$\hat{H}=|J|\sum_i\ [\hat{S}_i^Z\hat{S}_{i+1}^Z+\lambda\hat{S}_i^Z\hat{S}_{i+1}^Z+\mu(\hat{S}_i^Z)^2], \tag{10}$$

where λ and μ are the anisotropic and zero-field splitting coefficients. For a complete description of the system it is necessary to introduce a nonlinear correction to the Hamiltonian describing solitons. The appearance of this ''topological'' term causes the properties of the chains of integer and half-integer spins to be different.

The soliton energy in the isotropic limit is

$$E_m(P)=\sqrt{(m^2+S^2)[(\hbar\omega_0)^2+c^2P^2]}\geqslant S\hbar\omega_0, \tag{11}$$

where P and ω_0 are the momentum and frequency of the soliton, and m is a number corresponding to quantization of the ''precession frequency'' of the soliton ($S_z=m\hbar$).

Description of the system in a semiclassical picture of the solitons and magnons is correct only in the region of weak but finite anisotropy, when the nonlinear dynamical fluctuations in the system are suppressed on account of anisotropy: $Se^{-\pi S}\ll\sqrt{\lambda-\mu}\ll 1$. Then the low-energy excitations in the chain are described by the appearance of $m=0$ solitons in the case of integer spins and $m=\pm 1/2$ if S is half-integer. It follows from such an assumption that a chain of integer spins has a singlet ground state separated by a gap Δ from the first excited state, containing $m=1$ solitons. The correctness of this assertion was justified in Ref. 46 and has been confirmed experimentally.

An estimate of the value of the gap in a Haldane chain has been made in a number of theoretical papers and amounts to $\Delta\approx 0.41J$.[47] The gap exists in the case $\mu=0$ for $0\leqslant\lambda\leqslant 1.18$, and outside this interval the state of the system is gapless. If $\mu\neq 0$ then the gap exists for $-0.25\leqslant\mu/2J\leqslant 0.8$, and the value of Δ falls off rapidly with increasing $\mu<0$.[48]

The Haldane theory achieved its furthest development in Ref. 49, in which it was shown that in the ground state of a chain of integer spins ($S=1$) resonance valence bonds are realized. The ground state of a chain of spins $S=1$ with only a nearest-neighbor interaction can be represented as simple valence bonds joining each pair of spins $S=1/2$ (the ''two parts'' of the spin $S=1$). The translational symmetry is not broken, and a singlet ground state with a spin gap is realized.

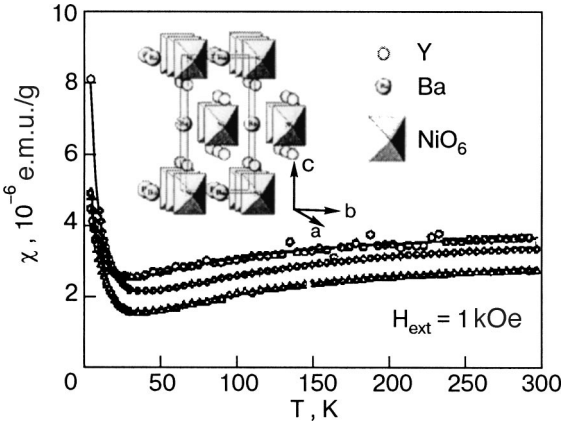

FIG. 19. Crystal structure and magnetic susceptibility of Y_2BaNiO_5 along the a ($\diamond$), b ($\triangle$), and c ($\bigcirc$) axes.

The Hamiltonian of the system can be solved exactly and is a sum of projection operators onto states with spin $S=0$, $S=2$ for each pair of spins:[49]

$$\hat{H}=\sum_i\ \left[\frac{1}{2}\hat{S}_i\hat{S}_{i+1}+\frac{1}{6}(\hat{S}_i\hat{S}_{i+1})^2+\frac{1}{3}\right]. \tag{12}$$

In real crystals there are dangling bonds, and the spin chains have a finite length (defects, impurity, boundaries of the crystal). In Haldane systems as the temperature is lowered one observes a drop of the magnetic susceptibility $\chi(T)\sim e^{-\Delta/kT}$ and then a sharp rise, which is due to the existence of dangling valence bonds at the ends of the chains, and its value can be used to estimate the length of the chains of magnetic ions in a real crystal.

4.1. Y_2BaNiO_5

The crystal structure of Y_2BaNiO_5 is shown in Fig. 19. In this compound chains of NiO_6 octahedra joined by the vertex extend along the a axis and are separated in the bc plane by Y and Ba ions.[50] The $\chi(T)$ curve has a maximum at $T\sim 410$ K due to one-dimensional interactions in the chain; for $T<25$ K an exponential decline of $\chi(T)$ is observed, and ultimately the susceptibility increases due to defects and the dangling bonds at the ends of the chains.[50] This compound has a strong planar anisotropy, and from the behavior of $\chi(T)$ at low temperatures in the cases $\mathbf{H}\|a$ and $\mathbf{H}\perp a$ one can estimate the values of the energy gaps $\Delta_\|=118$ K, $\Delta_\perp=104$ K.[51] Thus the mean value of the gap calculated according to the formula $\Delta=(2\Delta_\perp+\Delta_\|)/3$ is $\Delta\sim 109$ K.

4.2. $PbNi_2V_2O_8$

The crystal structure and magnetic susceptibility of the compound $PbNi_2V_2O_8$ are shown in Fig. 20.[52] This substance has tetragonal symmetry; the Ni^{2+} ions ($S=1$) are found in NiO_6 octahedra which are joined along an edge and form screwlike chains along the c axis. These chains are separated from each other by Pb^{2+} ions and VO_4 tetrahedra. The distance between nearest Ni ions in the chain is 2.8 Å, and the distance between chains is 5.9 Å.[53] The magnetic susceptibility of $PbNi_2V_2O_8$, shown in Fig. 20, exhibits a broad maximum at $T\sim 120$ K and falls off exponentially as the temperature approaches zero. The value of the exchange

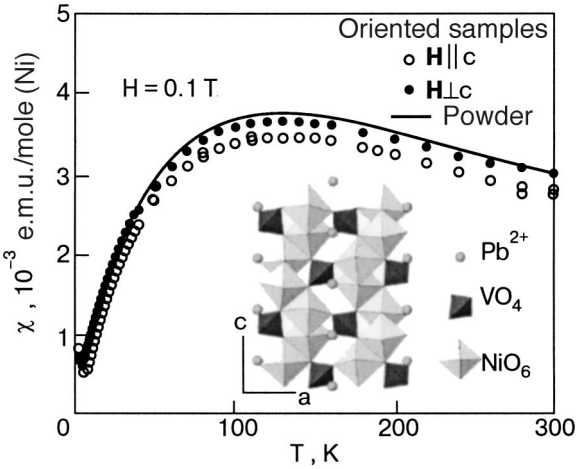

FIG. 20. Crystal structure and magnetic susceptibility of $PbNi_2V_2O_8$.

interaction in the chain, estimated from the high-temperature part of the $\chi(T)$ curve, is $J=95$ K. An estimate of the value of the energy gap for noninteracting chains according to the formula $\Delta \approx 0.41J$ gives a value $\Delta \approx 39$ K, which correlates with the data of neutron diffraction studies ($\Delta = 46$ K) and with an estimate from the decline of the magnetic susceptibility ($\Delta \sim 30$ K).[52] The best agreement between calculations and experimental results is achieved when an interaction between chains $J' \sim 1$ K and an anisotropy parameter $D=3$ K are taken into account. According to the values of these parameters, the ground state of $PbNi_2V_2O_8$ on the $D-J'$ phase diagram is found in a spin-gap disordered phase but close to the boundary of the spin-gap and ordered phases.[54] Because of this even a small content of nonmagnetic impurities substituting for the Ni^{2+} ions will push the system $Pb(Ni_{2-x}M_x)_2V_2O_8$ (M=Mg, Mn, Co) to antiferromagnetic ordering.[52–57] At present $PbNi_2V_2O_8$ is the only known compound in which long-range magnetic order is induced by a nonmagnetic dilution of $S=1$ chains.

5. SPIN LADDERS

Spin ladders are formed by spin chains lying close together. Their magnetic properties are determined by both the exchange along the legs and along the rungs. The properties of ladders with even and odd numbers of legs are fundamentally different. The spectrum of magnetic excitations of ladders with an even number of legs has a gap, and their ground state is a spin liquid characterized by short-range (falling exponentially to zero) spin pair correlations. The spectrum of magnetic excitations of a ladder with an odd number of legs does not contain a gap. The ground state in this case is characterized by spin-spin correlations that fall to zero by a power law.

The simplest variety of spin ladder is one with two legs formed by Heisenberg ions with spin $S=1/2$. The state of such a ladder with antiferromagnetic interactions J' along the rungs and J along the legs (Fig. 21) is described by the Hamiltonian[58]

$$\hat{H} = J \sum_{a=1,2} \sum_i \hat{S}_{i,a}\hat{S}_{i+1,a} + J' \sum_i \hat{S}_{i,1}\hat{S}_{i,2}, \qquad (13)$$

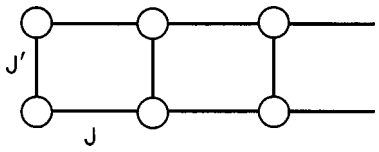

FIG. 21. Schematic model of a spin ladder with exchange interaction J' along the rungs and J along the legs.

where $\hat{S}_{i,a}$ is the spin operator at site i of the ladder on rung a.

The relationship between J and J' has an important influence on the mechanism of formation of the ground state, on the dispersion relation, and on the value of the gap separating the monmagnetic ground state from the first excited state.

In a ladder with $J' \gg J$ the singlet ground state corresponds to dimerization along the rungs. In the ground state the total spin of the ladder $S=0$, since each rung is found in the singlet state. The excited state of the ladder corresponds to the transition of one of the dimers to the triplet state ($S=1$). The exchange interactions along the legs leads to excitation transfer along the ladder, giving rise to an $S=1$ magnon band with the dispersion relation

$$E(q) = J' + J\cos q. \qquad (14)$$

Since the spin gap represents the minimum excitation energy, corresponding to $q=\pi$, to a first approximation $\Delta = J' - J$.

If $J' \geqslant J$ then the singlet ground state of the system can be represented in the form of dimers on each rung, coupled with the dimers on the neighboring rungs by a weak antiferromagnetic coupling (resonant valence bond).[59] In this case the dispersion relation has the form

$$E(q) = [\Delta^2 + 4a\Delta(1+\cos q)]^{1/2}, \qquad (15)$$

where $a = (1/2)d^2E/dq^2$ characterizes the spin-wave propagation velocity. Here the minimum energy corresponds to $q=\pi$.

In the limit $J' \ll J$ the two chains are not coupled to each other. It was assumed previously that the excitation spectrum of such a ladder, as in the case of an isolated chain of half-integer spins, does not have a gap. However, it was shown in Ref. 48 that the spin gap vanishes only at $J'/J=0$ and has a finite value for any ratio $J'/J>0$. Here the spin-wave band has a minimum at $q=\pi$ and a maximum at $q=\pi/2$ (for $J'/J=0$) or $q=0$ (for $J'/J=\infty$). The width of the band is determined by the antiferromagnetic interaction parameter along the rung, J', and varies from $\pi J/2$ (for $J'/J \to 0$) to $2J$ (for $J'/J \to \infty$). The value of the gap depends on the ratio of the exchange parameters J and J'. If the values of the exchange constants along the rungs and along the legs are comparable, one has $\Delta \approx 0.5J$.[58,60–62]

A change in the form of the dispersion relation for different values of the ratio J'/J is due to the fact that with decreasing J'/J the distance along the axis of the ladder over which an excitation arising on one rung can shift. For example, near the minimum of the dispersion curve the dispersion relation is characterized by a quadratic dependence for $J' \gg J$ and a linear dependence (as in a chain) for $J' \ll J$. At high temperatures the correlation length ξ in the distribution of the spin moments is the same for an isolated chain and a

spin ladder. With decreasing temperature, ξ becomes larger in the ladder, since the correlations in it increase faster because of the larger number of nearest neighbors. Therefore in the low-temperature region the dispersion relation for a ladder can be assumed quadratic.

The character of the dependence $E(q)$ is determined by the form of the structure factor, the spin-lattice relaxation rate, the susceptibility, and the heat capacity. For example, the dependence of the susceptibility $\chi(T)$ over a wide range of temperatures is determined by the form of the dispersion relation $E(q)$:[63]

$$\chi=\beta\frac{z(\beta)}{1+3z(\beta)}, \tag{16}$$

where $\beta=1/T$, $z(\beta)=1/2\pi\int_{-\pi}^{\pi}e^{-\beta(E(q)}dq$.

In the case of a quadratic dispersion relation one can estimate the gap in the magnetic interaction spectrum from the temperature dependence of the susceptibility χ and of the heat capacity C at low temperatures ($T\ll\Delta$):

$$\chi(T)=\frac{1}{2\sqrt{\pi aT}}e^{-\Delta/T}, \tag{17}$$

$$C(T)=\frac{3}{4}\left(\frac{\Delta}{\pi a}\right)^{1/2}\left(\frac{T}{\Delta}\right)^{-3/2}\left[1+\frac{T}{\Delta}+\frac{3}{4}\left(\frac{T}{\Delta}\right)^{2}\right]e^{-\Delta/T}. \tag{18}$$

The magnetic susceptibility and heat capacity at high temperatures ($T\gg\Delta$) can be used to estimate the values of the energy integrals along the rungs and along the legs of the ladder:

$$\chi(T)=1/4\,T^{-1}-1/8(J+1/2\,J')T^{-2}+3/64\,JJ'T^{-3}, \tag{19}$$

$$C(T)=3/16(J^2+1/2\,JJ')T^{-2}. \tag{20}$$

A spin ladder with an antiferromagnetic interaction along the legs ($J>0$) and a ferromagnetic interaction along the rungs ($J'<0$) also has a spin gap.[64] In the case of weak coupling along the rungs ($|J'|/J\ll1$) the susceptibility is determined by the same expression (17) as for a ladder with an antiferromagnetic interaction along the rungs. In the case of a strong ferromagnetic coupling along the rungs a two-leg ladder can be represented as a chain of spins $S=1$ coupled by an antiferromagnetic interaction $J/2$ along the chain. An estimate of the gap $\Delta=0.41J$ for this case is in good agreement with estimates of the gap for Haldane chains.

Together with the uniform spin ladders described above, it is possible to have spin ladders with half-integer spin in which the exchange interaction along the legs is alternating, with $J>0$ while J' can have either sign.[65] In this situation it is also possible to reach a singlet ground state separated from the excited states by a spin gap. The way in which the ground state is realized depends on the value and sign of the alternation parameter α. For $\alpha\to0$ the spin ladder separates into plaquettes of four spins. In the case of an alternation of antiferromagnetic and ferromagnetic exchanges along the legs ($\alpha<0$) a spin ladder with $S=1/2$ can be represented as a ladder formed by integer spins with $S=1$ ($J'>0$) or as a uniform chain with spin $S=2$ ($J'<0$).

In layered compounds based on Cu^{2+} and V^{4+} one encounters structural motifs of spin ladders lying close together. In the absence of interaction between layers no long-range magnetic order is achieved at finite temperatures, but interactions between ladders can decrease the value of the spin gap substantially.

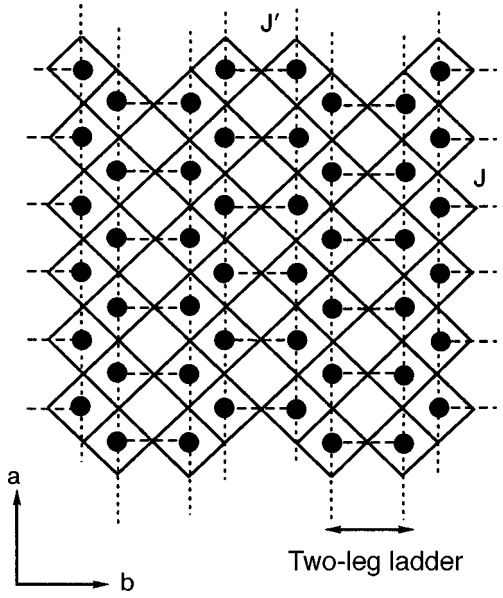

FIG. 22. In $SrCu_2O_3$ the Cu^{2+} ions, with spin $S=1/2$ (indicated by the symbol ●) are found in a square environment of O^{2-} ions.

5.1. $SrCu_2O_3$

The structure of $SrCu_2O_3$ is presented in Fig. 22.[66] In this compound the Cu_2O_3 planes alternate with Sr planes. The Cu^{2+} ions are found in a square environment of O^{2-} ions. The overlap of the $d_{x^2-y^2}$ orbitals of the copper ions with the p_x and p_y orbitals of the oxygen ions lead to 180° antiferromagnetic Cu–O–Cu exchange along the a and b axes. As a result, spin ladders with legs along a and rungs along b are formed in $SrCu_2O_3$. The coupling between copper ions of neighboring ladders corresponds to 90° ferromagnetic Cu–O–Cu exchange, which is further weakened by frustration. It follows from the temperature dependence of the magnetic susceptibility of $SrCu_2O_3$ (Fig. 23) that the system is found in a singlet ground state at low temperatures. An estimate of the spin gap from the low-temperature part of

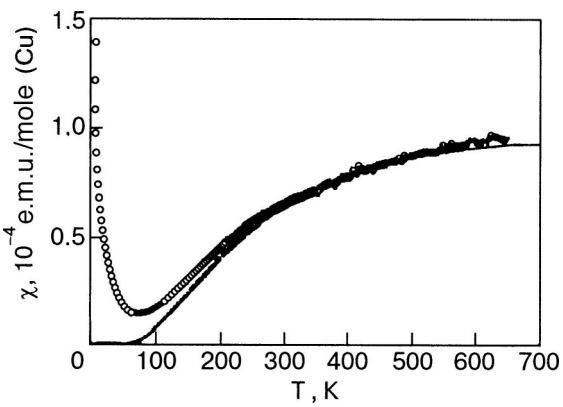

FIG. 23. Magnetic sucsceptibility of $SrCu_2O_3$. The solid line was obtained by subtraction of the diamagnetic contribution, the Van Vleck paramagnetism, and the contribution of paramagnetic impurities from the experimental dependence.

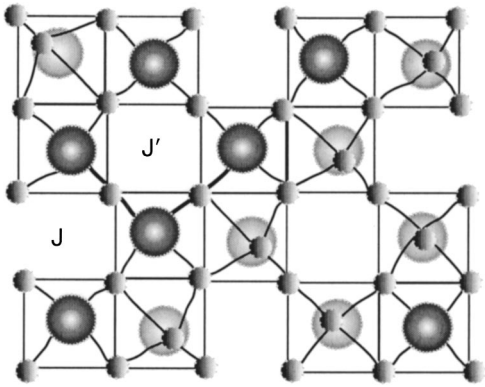

FIG. 24. Crystal structure of CaV_2O_5: J' and J denote the exchange path along a rung and along a leg, respectively.

$\chi(T)$ (after subtraction of the impurity contribution) in accordance with formula (17) gives $\Delta = 420$ K.[67] The value obtained for this same quantity from the temperature dependence of the spin-lattice relaxation rate in an experimental study of NMR on ^{63}Cu is 680 K.[68] Finally, from inelastic neutron scattering data the spin gap in $SrCu_2O_3$ was found to be $\Delta \approx 380$ K.[69] A similarly large scatter is seen in the estimated values of the exchange integrals along the legs ($J = 800-2000$ K) and along the rungs ($J' = 750$-100 K).[70–72] This situation is apparently due to the difficulties of synthesizing $SrCu_2O_3$ with reproducible parameters.

5.2. CaV_2O_5

The orthorhombic crystal lattice of CaV_2O_5 contains layers of square VO_5 pyramids with Ca^{2+} ions lying between these layers (see Fig. 24).[73] At the center of the pyramids are vanadium ions V^{4+} with spin $S = 1/2$. The VO_5 pyramids are joined along an edge in the base and form a mesh structure. The vertices of the pyramids (and, hence, the vanadium ions) lie on both sides of the basal plane ab. The strongest interaction is between nearest-neighbor V^{4+} ions lying on the same side of the plane. Those ions form a spin ladder with two legs. In each ladder the pyramids are joined by the corner both along the rungs and along the legs. The $3d$ electrons of V^{4+} occupy the d_{xy} orbital, and the interaction is of an antiferromagnetic character both along the rungs and along the legs. The pyramids belonging to neighboring ladders are joined along an edge, so that the interaction J'' between ladders takes place via a 90° V–O–V bond and is ferromagnetic and weak.

A spin-singlet ground state in CaV_2O_5 has been established[74] by NMR measurements on ^{51}V. A spin gap $\Delta = 616$ K was determined from the spin–lattice relaxation rate. The temperature dependence of the magnetic susceptibility can be approximated in the model of isolated dimers with equal values of the exchange and gap: $J = \Delta = 660$ K.[75] The estimates of the exchange integrals obtained for CaV_2O_5 by different methods also exhibit scatter: the exchange along the legs $J = 67-122$ K, the exchange along the rungs $J' = 608-670$ K, the exchange between ladders in the same plane $J'' = -28-45$ K, and the exchange between ladders in different planes $J''' \sim 20$ K.[70,76–78] Even when the scatter in the estimates is taken into consideration it it seen that strong anisotropy of the exchange interaction is realized in CaV_2O_5 and that the main exchange is along the rungs.

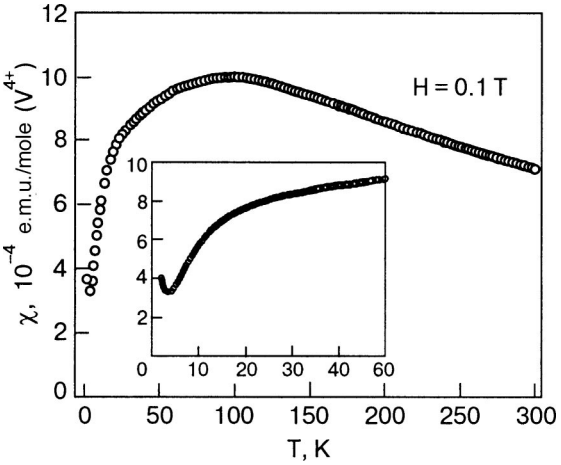

FIG. 25. Temperature dependence of the magnetic sucsceptibility of MgV_2O_5.

5.3. MgV_2O_5

The compound MgV_2O_5 has a structure analogous to that of CaV_2O_5 with the difference that the plane of the VO_5 pyramids in MgV_2O_5 is considerably more corrugated than in CaV_2O_5 (Ref. 79). The temperature dependence of the magnetic susceptibility of MgV_2O_5 exhibits the characteristic broad maximum for low-dimensional systems at $T \sim 100$ K (Fig. 25).[80] The temperature of this maximum is lower than in CaV_2O_5 by a factor of four, and therefore the values of the main exchange interactions in MgV_2O_5 must be smaller than in CaV_2O_5 by approximately the same factor. The spin gap estimated from an analysis of the temperature dependence of the susceptibility is ~ 15 K.[81] Inelastic neutron scattering shows a gap $\Delta = 20$ K at wave vector (π, π), which, because of the strong frustration of the exchange interactions, is not the minimum of the dispersion curve. The small value of the gap determined in that experiment suggests the possibility of an external-field-induced transition to a gapless state. Such a transition has indeed been observed on the field dependence of the magnetization at low temperatures, as is seen in Fig. 26.[80] Below and above the critical

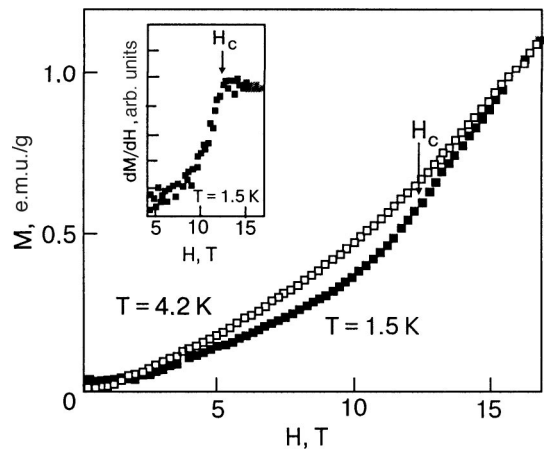

FIG. 26. Field dependence of the magnetization of MgV_2O_5.

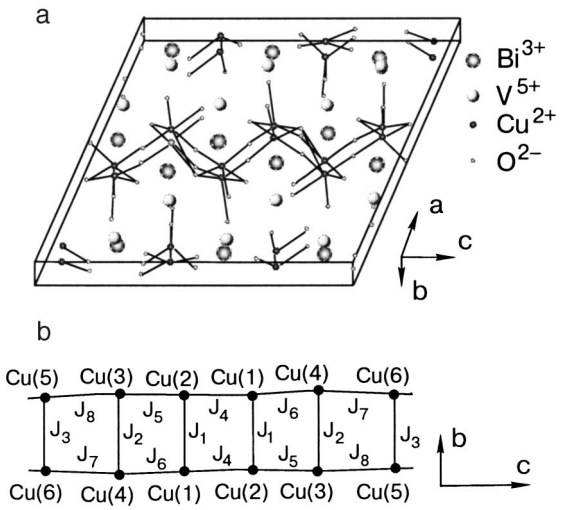

FIG. 27. Diagrams of the crystal lattice of $BiCu_2VO_6$ (a) and of the exchange interactions in it (b).

field $H_c \sim 12.5$ T the magnetization depends linearly on field but with different slopes. The dependence of the value of the gap on the field is given by the relation $\delta(H) = \Delta - g\mu_B H$, where Δ is the value of the gap at zero field. For $H \geqslant H_c$ there is no gap in the spectrum of magnetic excitations. An estimate of the gap from the field dependence of the magnetization gives $\Delta \sim 17$ K, in good agreement with the neutron data. From the temperature dependence of the magnetic susceptibility of MgV_2O_5 the following estimates have been obtained for the exchange integrals, in the same notation as was used for the CaV_2O_5 case: $J' \sim 92$ K, $J \sim 144$ K, $J'' \sim 60$ K, $J''' \sim 19$ K.[76,80,82] The comparable values of the exchange integrals along the rungs and legs of the ladder lead to a small value of the gap.

The substantial difference of the gap values of the structurally similar compounds CaV_2O_5 ($\Delta \sim 500$ K) and MgV_2O_5 ($\Delta \sim 20$ K) is due to the fact that the exchange interaction parameter depends strongly on the tilt of the VO_5 pyramids in the plane. Since the ionic radius of Mg is substantially smaller than that of Ca, the tilt of the VO_5 pyramids in MgV_2O_5 is greater.[32] This leads to a sharp decrease in the main exchange (along the rungs) in MgV_2O_5 in comparison with CaV_2O_5.

5.4. $BiCu_2VO_6$

The structure of the monoclinic crystal lattice of $BiCu_2Vo_6$ is shown in Fig. 27a.[84] The Cu^{2+} ions with spin $S = 1/2$ form a zigzag spin ladder with two legs parallel to the c axis. The rungs of the ladder are directed along the b axis. The ladders are separated from each other by the nonmagnetic ions V^{5+} and Bi^{3+}. In the structure of the ladder there are six inequivalent copper positions, which form eight different Cu–O–Cu bonds, each of which is characterized by an exchange interaction parameter J_i ($i = 1...8$) (Fig. 27b).

The temperature dependence of the magnetization of $BiCu_2VO_6$ indicates the presence of a spin gap in the magnetic excitation spectrum of this compound.[85] The abundance of exchange interaction parameters for the spin ladder in $BiCu_2VO_6$ does not permit the use of simple models for describing such structures. A dimer model approximation of

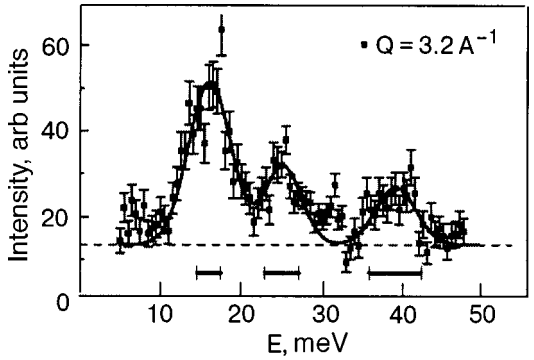

FIG. 28. Energy dependence of the inelastic neutron scattering intensity in $BiCu_2VO_6$.

$\chi(T)$ gives the order of magnitude of the gap in this compound ($\Delta \sim 16$ MeV). The absence of anomalies on the temperature dependence of the heat capacity indicates that the nonmagnetic ground state is inherent to this system and not the result of a structural transformation.

Inelastic neutron scattering studies in $BiCu_2VO_6$ have shown that for different values of the wave vector q the energy dependence of the scattering intensity (Fig. 28) shows three pronounced peaks, at energies ~ 190, 290, and 450 K. These features are explained by the presence of three types of weakly interacting clusters found in the singlet state. The simplest form of such clusters may be dimers on the rungs of a spin ladder, for example. The lowest value of the gap determined in this experiment is in good agreement with an estimate of the gap from magnetic measurements.

6. HYBRID SYSTEMS. $Sr_{14}Cu_{24}O_{41}$

The structure of the quasi-one-dimensional compound $Sr_{14}Cu_{24}O_{41}$, shown in Fig. 29, contains both spin chains and spin ladders. Layers containing chains and ladders alternate along the b axis. The chains are slightly shifted with respect to each other in the ac plane, and the ladders are shifted with respect to each other by a half period along the c axis. The periods of the chains and ladders along the c axis are incommensurate: $10c_{\text{chain}} \approx 7c_{\text{ladder}}$; the 24 Cu ions are apportioned between ladders and chains in the ratio 14:10. The Cu ions in both ladders and chains are found in a planar

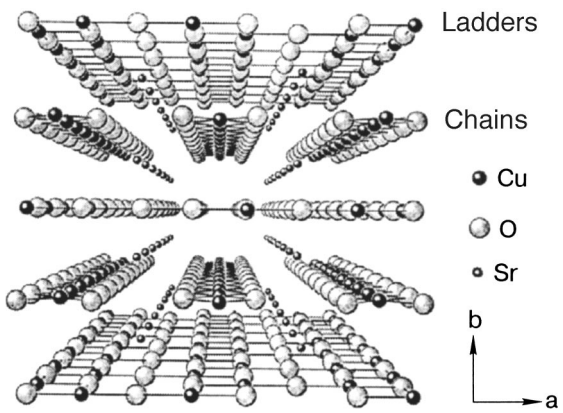

FIG. 29. Crystal structure of $Sr_{14}Cu_{24}O_{41}$.

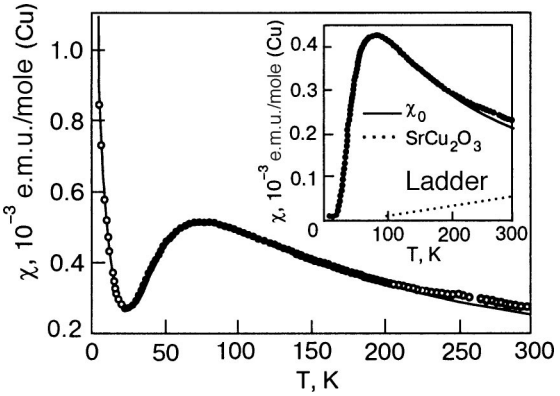

FIG. 30. Magnetic susceptibility of $Sr_{14}Cu_{24}O_{41}$. The inset shows $\chi(T)$ after subtraction of the paramagnetic and Van Vleck contributions. For comparison the dotted curve shows the susceptibility of the ladders.

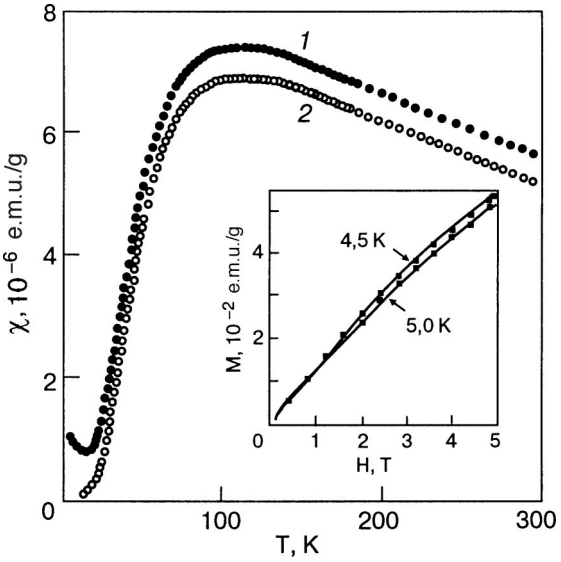

FIG. 31. Temperature dependence of the magnetic susceptibility of CaV_4O_9: *1*—experimental data; *2*—after subtraction of the paramagnetic and Van Vleck contributions. The inset shows the field dependence of the magnetization at $T=4.5$ and 5 K.

CuO_4 environment. The distance between Cu ions along the legs of the ladders is 1.90 Å, along the rungs 1.97 Å, and along the chains 2.75 Å.[86]

The magnetic susceptibility of $Sr_{14}Cu_{24}O_{41}$ is determined by the contributions of the ladders and chains, the paramagnetic contribution of defects, and the temperature-independent Van Vleck term.[87] The $\chi(T)$ curve shown in Fig. 30 has a broad maximum at $T\sim 80$ K followed by a noticeable decline of the susceptibility with decreasing temperature. Such behavior is due to the fact that the copper ions in the spin ladders of this compound are coupled by strong 180° antiferromagnetic exchange ($J\sim 1400$ K) and form a singlet ground state. The values of the exchange interaction parameters along the legs and rungs of the spin ladders are comparable and correspond to the parameters in $SrCu_2O_3$. At $T<400$ K the magnetic sucsceptibility is determined mainly by the contribution of the CuO_2 chains.

In $Sr_{14}Cu_{24}O_{41}$ the magnetic ions in the chains are separated by nonmagnetic $Cu^{3+}-O$ segments. The decline of the magnetic sucsceptibility for $T<80$ K can be described by the dimer model (4). According to estimates,[87] the number of dimers with spin $S=1/2$ is 1.47 per formula unit, and the exchange within the dimer has the value $J=140$ K.

According to NMR data, charge ordering of the Cu^{2+} and Cu^{3+} ions in the chains occurs at $T<80$ K.[88] Neutron scattering experiments register two maxima of the spin density, corresponding to dimerization in the chain, where, according to these data, the dimer is formed not by the nearest neighbors but by atoms lying at distances of 2 and 4 periods of the chain ($d_C=5.48$ Å).[89] Possibly dimers of this size are formed from two magnetic ions separated by nonmagnetic $Cu^{3+}-O_2$ segments. The ground state of the system is an ordered arrangement of such dimers in the chains. The interactions between dimers in a chain and between two nearest dimers in neighboring chains are close in value: $J_C\approx J_A\sim 10$ K.

7. TWO-DIMENSIONAL SYSTEMS

The most complex configurations of spins forming a singlet ground state are realized in two-dimensional systems, when the ensembles of exchange-coupled spin ladders considered above form strictly two-dimensional systems. There are also pronounced effects of frustration of the antiferromagnetic interaction in the planes.

7.1. CaV_4O_9

Spin-gap behavior in a quasi-two-dimensional system was first observed in CaV_4O_9. This compound has a simple tetragonal lattice ($a=8.333$ Å, $c=5.008$ Å) with two formula units per unit cell.[90] The CaV_4O_9 structure can be represented in the form of VO_5 pyramid layers separated by Ca ions. In each VO_5 plane there is a regular arrangement of V vacancies. The rarefaction of V in the magnetic subsystem makes for a $\sqrt{5}\times\sqrt{5}$ increase in the unit cell size, which itself is $\sqrt{2}\times\sqrt{2}$ times larger than the unit cell of the square VO lattice. The VO_5 pyramids with the apical O ion lying above (or below) the plane form chains connected by a corner. Pyramids with differently directed apical O ions are joined along an edge. The Ca ions lie above (or below) the V vacancies. The VO planes are highly deformed. The V ions are displaced by ± 0.625 Å along the direction toward the apical O ions in the corresponding pyramids.

The temperature dependence of the magnetic susceptibility of CaV_4O_9 is shown in Fig. 31.[91] The value of the energy gap in the magnetic excitation spectrum determined from these data, $\Delta\approx 110$ K, has been confirmed by spin-lattice relaxation studies in an NMR experiment.[91] The same value of Δ was obtained in inelastic neutron scattering experiments.[92]

The origin of the gap in CaV_4O_9 has been the subject of numerous theoretical papers.[93–97] At first it was assumed on the basis of the features of the crystal structure shown in Fig. 32 that the lattice can be represented in the form of simple plaquettes connected by dimer couplings; in this case the ground state realized in the system is one in which the spin configurations in each plaquette of the lattice are configurations of resonant valence bonds. It turns out, however, that the features in the arrangement of V ions in the plane and the

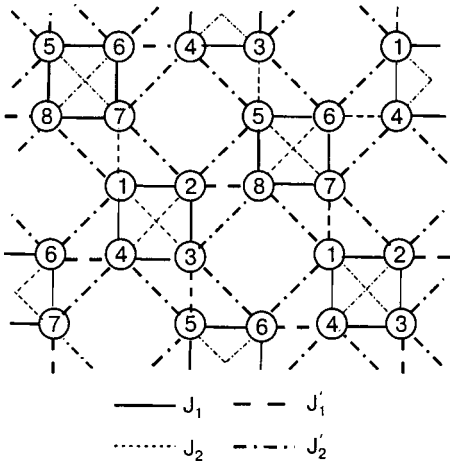

FIG. 32. Diagram of the couplings in CaV_4O_9.

analysis in terms of their exchange interaction does not agree with this simple picture.

The Heisenberg Hamiltonian for CaV_4O_9 with allowance for the interactions of nearest neighbors (nn and nn') and next-nearest neighbors (nnn and nnn') can be written as

$$\hat{H}=J_1\sum_{nn}\hat{\mathbf{S}}_i\cdot\hat{\mathbf{S}}_j+J_1'\sum_{nn'}\hat{\mathbf{S}}_i\cdot\hat{\mathbf{S}}_j+J_2\sum_{nnn}\hat{\mathbf{S}}_i\cdot\hat{\mathbf{S}}_j+J_2'\sum_{nnn'}\hat{\mathbf{S}}_i\cdot\hat{\mathbf{S}}_j. \tag{21}$$

The terms with J_1 and J_2 describe the interactions of spins within a single plaquette, while the terms with J_1' and J_2' describe the interactions of spins belonging to different plaquettes.[97]

Calculations of the spin-density distribution[90,97] show that the only uncoupled vanadium spin occupies the d_{xy} orbital. In this situation the exchange interaction with the next-nearest neighbor is dominant over the exchange interaction with the nearest neighbor. Then the singlet is formed on the metaplaquette shown by the heavy dotted line in Fig. 32. Here the dominant exchange is J_2'. The results of the theoretical studies are in good agreement with an inelastic neutron scattering experiment.[92] The exchange integrals obtained in those measurements had the values: $J_1=78.9$ K, $J_1'=78.9$ K, $J_2=19.7$ K, $J_2'=162.5$ K. The interactions with metaplaquettes is formed mainly by the V–O–V superexchange via the $2p$ orbitals of oxygen. The metaplaquette spins lying above the basal plane interact with the spin metaplaquettes lying below the plane, forming a unified two-dimensional state of resonant valence bonds.

7.2. NaV_2O_5

The features of the formation of the ground state in sodium divanadate have been actively studied since the time of discovery of a phase transition at $T_c\sim 34$ K in this compound.[98] According to the present ideas, at that temperature a redistribution of electric charge between vanadium positions occurs, accompanied by structural distortions and the onset of an energy gap in the magnetic excitation spectrum.[98,99]

At high temperatures this compound has tetragonal symmetry with space group *Pmmn*. The crystal structure of NaV_2O_5 is formed by corrugated layers of VO_5 pyramids

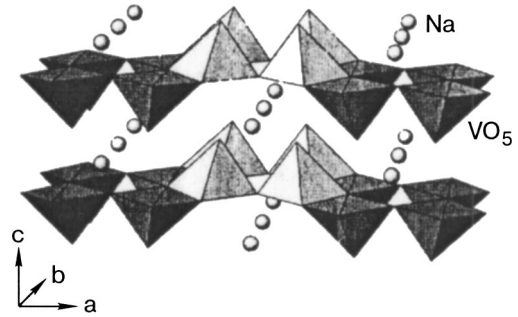

FIG. 33. Crystal structure of NaV_2O_5.

separated from each other by Na atoms (Fig. 33). The parameters of the crystal cell are $a=11.318$ Å, $b=3.611$ Å, $c=4.797$ Å. At $T>T_c$ all the vanadium positions are equivalent, and its formal valence is $V^{+4.5}$ (Ref. 100). This means that the only $3d$ electron that does not participate in the formation of ionic-covalent bonds is shared between two nearest-neighbor vanadium ions and is located on a V–O–V bonding molecular orbital.[101] These orbitals form the rungs of spin ladders displaced a half period with respect to each other along the b axis in the ab plane (Fig. 34). In an ordinary spin ladder the spins should be located at every site, and therefore at high temperatures the model of a ladder with every-other site occupied is used for NaV_2O_5. It is also possible to treat the two-dimensional system of vanadium-oxygen planes as a set of noninteracting spin chains shifted by a half period. The interaction in the chain is estimated as $J=280$ K.[98]

The physical properties of NaV_2O_5 have anomalies at the phase transition temperature. Fig. 35 shows the temperature dependence of the magnetic susceptibility of this compound.[98] With decreasing temperature the $\chi(T)$ curve displays a broad maximum at $T\sim 350$ K, corresponding to the establishment of spin correlations in the chains. In this temperature range the dependence is described well by the Bonner-Fisher model for noninteracting $S=1/2$ chains. Then, in the region $T<150$ K the experimental curve deviates from the calculated dependence in a wide temperature region, probably because of the development of spin fluctuations preceding the phase transition. At $T_c=34$ K a sharp isotropic drop of the magnetic susceptibility to zero is observed, due to the formation of a gap in the spectrum of magnetic excitations.

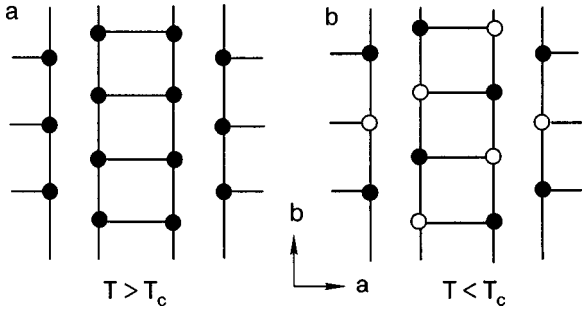

FIG. 34. Structure of spin ladders in the ab plane in NaV_2O_5 for $T>T_c$ (a). Zigzag structure in NaV_2O_5 for $T<T_c$. The magnetic V^{4+} ions (●) and nonmagnetic V^{5+} ions (○) are shown in (b).

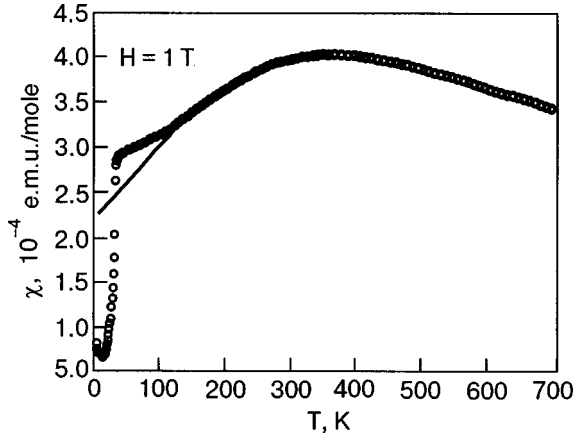

FIG. 35. Temperature dependence of the magnetic susceptibility of NaV_2O_5. The solid curves shows a calculation according to the Bonner-Fisher model in the interval 100–700 K.

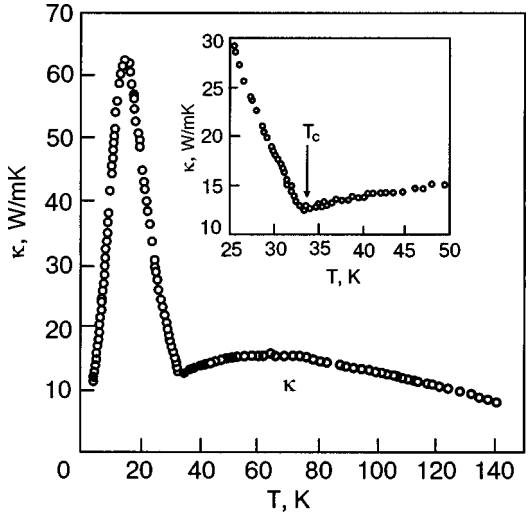

FIG. 37. Temperature dependence of the thermal conductivity of NaV_2O_5 along the *c* axis.

On the temperature dependence of the heat capacity of NaV_2O_5, shown in Fig. 36, the phase transition at T_c is accompanied by a sharp anomaly of the λ type.[102] The heat capacity in the region $T<T_c$ is well approximated by two terms corresponding to the contributions from the lattice and magnons: $C=\beta T^3+A_0\exp(-\Delta/kT)$. A giant increase of the heat capacity of this compound at T_c has also been observed (see Fig. 37),[103] due to a decrease in the scattering of thermal phonons on spin fluctuations at the phase transition.

A feature of the formation of the spin gap in NaV_2O_5 is the circumstance that the underlying cause of this effect is charge ordering of the vanadium ions, causing both a magnetic and a structural transformation. At low temperatures there are two inequivalent vanadium positions in the NaV_2O_5 structure, with formal valences $V^{4.5-\delta}$ and $V^{4.5+\delta}$, where δ determines the deviation of the valence from the mean value (below we have used the notation V^{4+} and V^{5+} for these ions).[104] The magnetic V^{4+} and nonmagnetic V^{5+} ions have a zigzag arrangement in the spin ladders (Fig. 34b). Such an arrangement of the magnetic and nonmagnetic ions in one spin ladder considered individually does not lead to the formation of a spin gap in its energy spectrum, but the influence of neighboring ladders causes results in an alternating exchange interaction. According to Ref. 105 this leads to the formation of a spin gap $\Delta=114$ K[106] in the magnetic excitation spectrum of NaV_2O_5.

At $T<T_c$ a superstructure $(a-b)\times 2b\times 4c$, having monoclinic symmetry with space group C_2^3-$A112$ (Refs. 107, 108) forms in NaV_2O_5. The appearance of inequivalent positions for the V^{4+} and V^{5+} ions in the region $T<34$ K is explained by a change in period along the *a* and *b* axis ($a_m=a-b$, $b_m=2b$). Figure 38 shows the distribution of the magnetic and nonmagnetic V ions within a layer. It is seen that there are 4 variant distributions of the dimers formed by magnetic ions; these configurations are denoted by the letters A, A′, B, and B′. For the formation of a

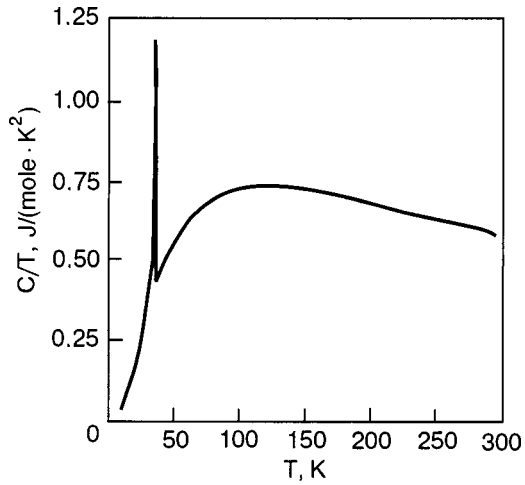

FIG. 36. Temperature dependence of the heat capacity of NaV_2O_5.

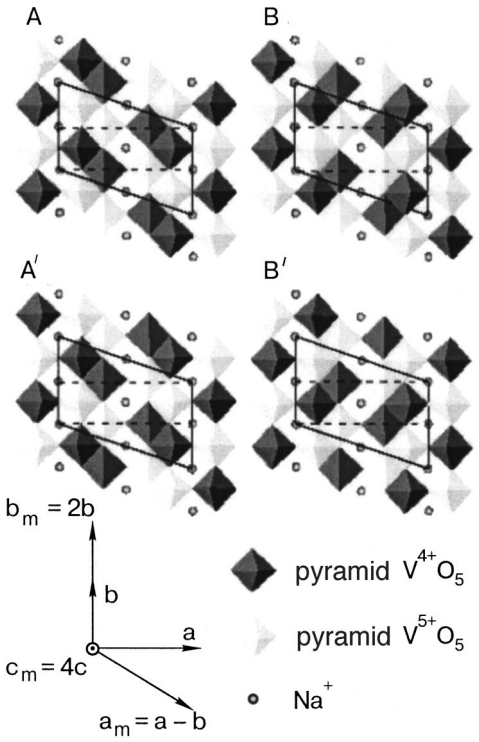

FIG. 38. Four variant distributions of dimers formed by the magnetic ions in NaV_2O_5.

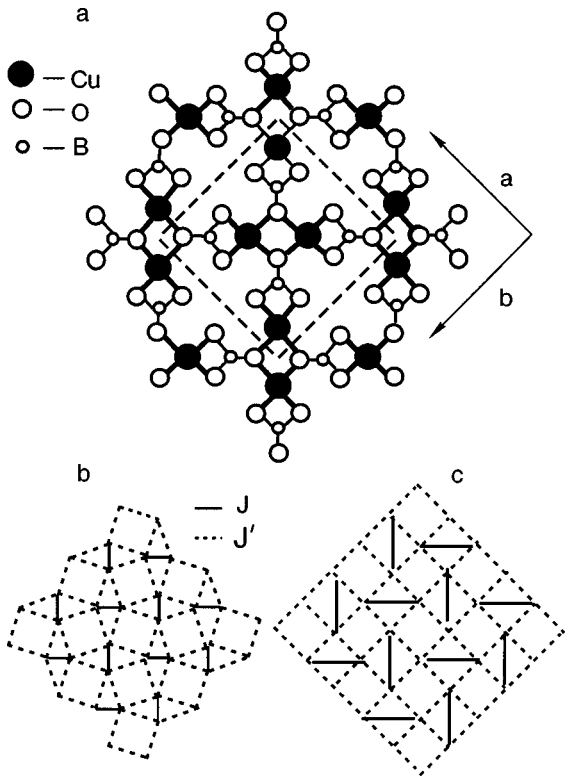

FIG. 39. Crystal structure (a) and arrangement of the magnetic dimers (b) in $SrCu_2(BO_3)_2$ and in the Shastry-Sutherland model (c).

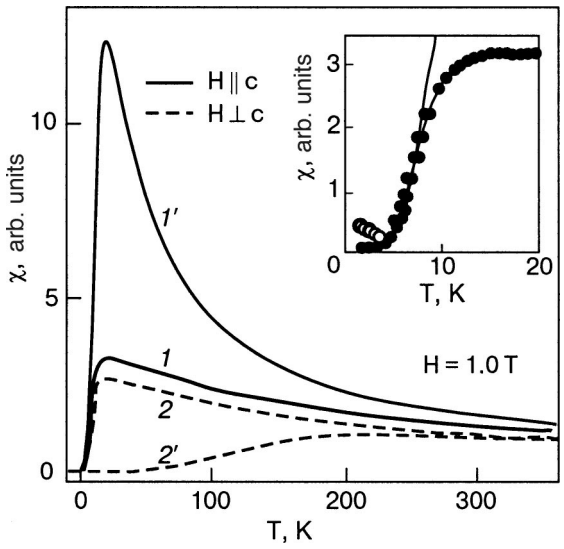

FIG. 40. Magnetic susceptibility of $SrCu_2(BO_3)_2$ for different directions of the magnetic field. Curves 1′ and 2′ are the theoretical calculation. The symbols in the inset show the experimental results; the solid line shows the activation approximation for determining the spin gap.

superstructure with period $c_m = 4c$ along the c axis the layers must alternate in the order ABA′B′ (Ref. 107) or AAA′A′ (Ref. 108). According to subsequent studies of resonant x-ray scattering[108] the structure of the type AAA′A′ best describes the spectra obtained.

7.3. $SrCu_2(BO_3)_2$

Included in the list of compounds with a spin gap is $SrCu_2(BO_3)_2$, the magnetic subsystem of which is a two-dimensional network of orthogonal dimers ($S=1/2$). $SrCu_2(BO_3)_2$ has tetragonal structure with unit cell constants $a=8.995$ Å, $c=6.649$ Å at room temperature.[109] In the $CuBO_3$ plane, shown in Fig. 39, rectangular planar CuO_4 complexes are connected to each other by BO_3 groups. The $CuBO_3$ layers are separated by spacers of nonmagnetic Sr^{2+} ions. All of the Cu^{2+} have spin $S=1/2$ and are found in crystallographically equivalent positions. The nearest Cu^{2+} ions, lying at a distance of 2.905 Å from each other, form magnetic dimers. The coupling between dimers, which are separated by a distance 5.132 Å, takes place via B^{3+} ions. The dimers in each layer do not lie strictly in the same plane: the vertical dimers are displaced slightly along the c axis with respect to the horizontal dimers.

By virtue of of the pronounced two-dimensionality of the $SrCu_2(BO_3)_2$ crystal its magnetic properties should be described well by the Heisenberg model with exchange constants J and J' inside and between dimers, respectively. An important role in this is played by frustration of the magnetic interaction stemming from the triangular arrangement of one J and two J' bonds. This frustration occurs independently of the sign of J' if the interaction J is antiferromagnetic ($J>0$). An attractive feature of a network of orthogonal dimers is the possibility of exact calculation of the ground state.[110] One of the results of this calculation was the conclusion that triplet excitations of the network of orthogonal dimers are extremely localized. Localization of the triplet excitations in $SrCu_3(BO_3)_2$ was confirmed experimentally by the existence of a series of plateaus on the magnetization curve.[111]

An indication of the presence of a spin gap in the spectrum of magnetic excitations was obtained from measurements of the magnetic susceptibility of the substance[112] and then confirmed by a number of independent methods. The temperature dependence of the magnetic susceptibilities parallel $\chi_\parallel$ and perpendicular $\chi_\perp$ to the layers of magnetic dimers in $SrCu_2(BO_3)_2$ is presented in Fig. 40. The magnetic anisotropy observed in these measurements is due to anisotropy of the g factor. With decreasing temperature the susceptibility reaches a maximum at 15 K and then falls rapidly to zero. After the contributions due to impurities and temperature-independent terms were separated out from the experimental curves, the contribution from just the dimers could be found. When this distribution is approximated at low temperatures by a function $\propto \exp(-\Delta/T)$ one obtains a value of the spin gap $\Delta = 34$ K.

The presence of a spin gap in a network of orthogonal dimers is naturally expected for $J'=0$. If this energy is neglected ($J'=0$), the system simplifies to a model of isolated dimers with spin $S=1/2$, which is the simplest model for all materials with a spin gap and is applicable to certain substances containing complexes of divalent copper Cu^{2+}. Attempts to approximate the experimental data by this model so as to achieve matching of the maxima of $\chi_\parallel(T)$ in the theory and experiment (~ 15 K) led to substantial disagreement, as is seen in Fig. 40 (curve 1′). If the theory and experiment are matched at high temperatures, then such an approximation (curve 2′) leads to too large a value of the spin gap Δ. These facts indicate that the interaction between dimers cannot be neglected: the dimers must be strongly correlated in each layer, and the whole system must be highly frustrated. In Ref. 113 a model of the formation of the spin

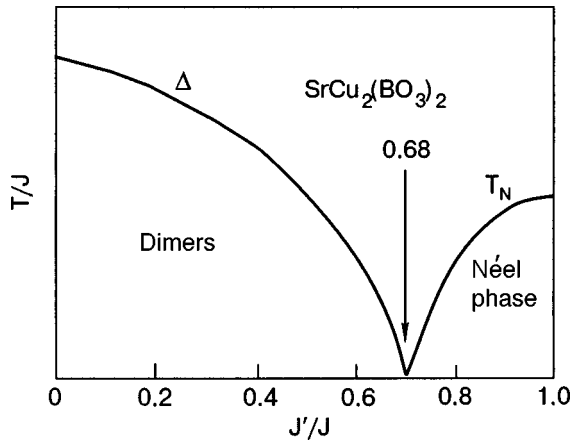

FIG. 41. Phase diagram of a network of orthogonal dimers.

gap for correlated dimers was proposed which describes the experimental curves quite accurately. The phase diagram constructed in the framework of this model for a network of orthogonal dimers is shown schematically in Fig. 41. For small values of the parameter J'/J the system is described satisfactorily by a model of isolated dimers. With increasing ratio J'/J a first-order phase transition to an antiferromagnetically ordered state occurs at $(J'/J)_c = 0.70$ (or 0.69). The existence of antiferromagnetic ordering for $J'/J > (J'/J)_c$ is clear from the fact that for $J=0$ the magnetic subsystem reduces to a simple square lattice. The value $J'/J = 0.68$ in $SrCu_2(BO_3)_2$ is extremely close to the critical value $(J'/J)_c$.

Figure 42 shows the magnetization curves of $SrCu_2(BO_3)_2$ measured in pulsed fields. No hysteresis was observed in the application and removal of magnetic field. With increasing magnetic field H the low-lying triplet excited states cross the spin-singlet ground state at ~ 20 T. Then the magnetization M grows, but the presence of steps on the $M(H)$ curves for $SrCu_2(BO_3)_2$ makes it fundamentally distinguished from classical spin systems, in which the magnetization increases monotonically. Plateaus are seen on the $M(H)$ curves at magnetizations of 1/8 and 1/4 of the total magnetic moment of the Cu^{2+} ions. The phase boundaries for the 1/8 plateau were determined by extrapolation to be 30.1–31.7 T for $\mathbf{H} \| c$ and 26.7–28.6 T for $\mathbf{H} \perp c$. For the

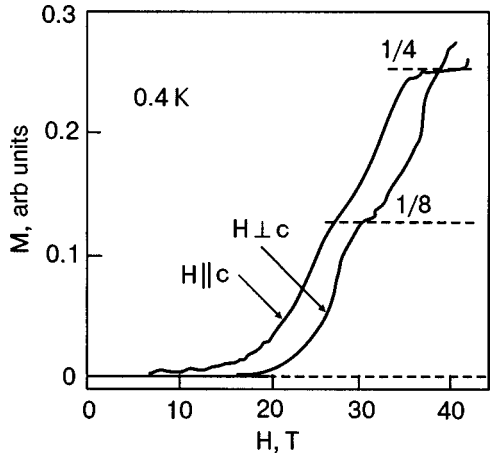

FIG. 42. Magnetization curves of $SrCu_2(BO_3)_2$, taken in pulsed fields.

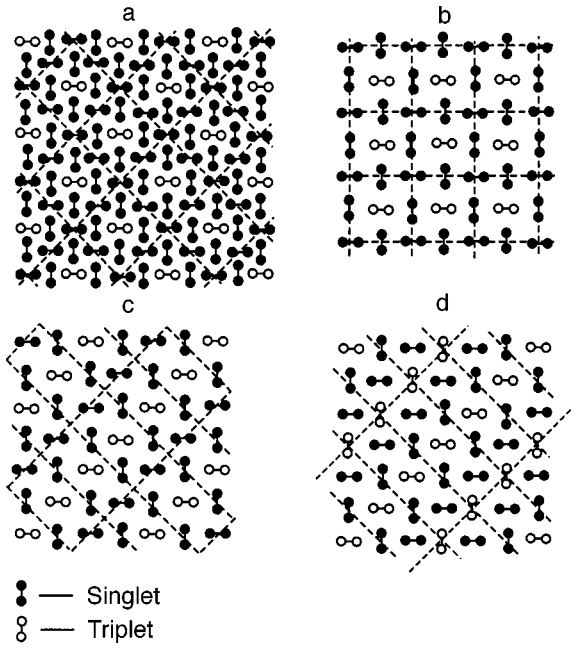

FIG. 43. Distribution of singlet and triplet states in a structure corresponding to destruction of the singlet states in 1/8 (a), 1/4 (b,c), and 1/3 (d) of all dimers and to the formation of the 1/8, 1/4, and 1/3 plateaus.

1/4 plateau these values were 39.1–41.6 T for $\mathbf{H} \| c$ and 35.0–39.0 T for $\mathbf{H} \perp c$. With increasing magnetic field the system passes successively through states with a spin gap and gapless states. In the plateau regions $SrCu_2(BO_3)_2$ has energy gaps between the ground and lowest excited states, while between plateaus the system does not have a gap in the spectrum of spin excitations, and the magnetization increases monotonically.

The fact that the triplets prefer an ordered state to a disordered state is apparently due to the orthogonality of the nearest-neighbor dimers. The transition of a triplet excitation from one crystallographic position to another within the same plane is possible only in the sixth order of perturbation theory. With allowance for the tetragonal symmetry of the $SrCu_2(BO_3)_2$ crystal a necessary condition for the formation of an ordered structure of magnetic triplets is the presence of a square magnetic unit cell, and this condition is met for the 1/8 and 1/4 plateaus, as is shown in Fig. 43a,b. This same requirement is met for the 1/2, 1/10, 1/16, and 1/32 plateaus in a crystal with tetragonal symmetry.

Theoretical calculations have shown[114,115] that the triplet–triplet interaction with second-order (next-nearest) neighbors is substantially weaker than the interactions with neighbors of the third order. It is therefore possible that the 1/4 plateau does not have a square magnetic lattice but is formed by magnetic stripes, as is shown in Fig. 43c. In such a case the unit cell in the plane is a rectangular parallelepiped in which there is no place for third-order neighbors. Another stripe structure, shown in Fig. 43d, has been proposed for the 1/3 plateau. Since the 1/3 plateau cannot appear in a square magnetic lattice, the observation of such a plateau is unambiguous proof of the existence of stripe structures. Soon after this prediction the presence of a 1/3 plateau was confirmed in an experiment at fields fields up to 60 T.[116]

CONCLUSION

Recent research has substantially widened the circle of materials having a spin gap in the spectrum of magnetic excitations. The experimental study of their properties has created the prerequisites for the formation of new theoretical models describing the mechanisms by which such a state is reached at low temperatures. The properties of low-dimensional magnets described in this review are close in a number of parameters to those of metaloxide superconductors and compounds characterized by charge density waves. Continuation of research on this topic will undoubtedly make it possible to formulate concepts describing quantum cooperative phenomena in solids from unified point of view.

This work was supported by grants RFFI 03-02-16108 and CRDF RU-P1-2599-MO-04.

*E-mail: anvas2000@yahoo.com

[1)]An example of a metaloxide compound containing isolated linear chains of Heisenberg spins $S=1/2$ is $CuSr_2O_3$. In the structure of this compound the Cu^{2+} ions are found in a planar oxygen environment, and the magnetic interaction is realized via 180° exchange along the Cu–O–Cu bonds. The scale of the exchange interaction in these chains is estimated as $J\sim 2500$ K, and the Néel temperature $T_N\sim 5$ K.[17,18]

[2]An example of a compound with chains of magnetic atoms with a frustrated interaction is $SrCuO_2$. The structure of that compound contains chains of Cu^{2+} ions, extending along the c axis, in a planar oxygen environment (CuO_4).[25] Two exchange interactions compete in the chains: a ferromagnetic 90° Cu–O–Cu exchange between nearest neighbors (J_{NN}) and an antiferromagnetic 180° Cu–O–Cu exchange between next-nearest neighbors (J_{NNN}). The exchange integral $J_{NNN}=1800$ K, and $J_{NN}/J_{NNN}=-0.1$.[26] Long-range magnetic order is established in the system at $T_c\sim 2$ K.

[1] Yu. V. Rakitin and V. T. Kalinnikov, *Modern Magnetochemistry* [in Russian], Nauka, St. Petersburg (1994).
[2] R. L. Carlin, *Magnetochemistry*, Springer-Verlag, Berlin (1986), Mir, Moscow (1989).
[3] K. Hanke, V. Kupcik, and O. Lindqvist, Acta Crystallogr. B **29**, 963 (1973).
[4] B. Bleaney and K. D. Bowers, Proc. R. Soc. Lon. Ser. A **214**, 451 (1952).
[5] K. Waltersson and B. Forslund, Acta Crystallogr., Sect. B: Struct. Crystallogr. Cryst. Chem. **33**, 789 (1975).
[6] M. Isobe and Y. Ueda, J. Phys. Soc. Jpn. **65**, 3142 (1996).
[7] R. Valenti and T. Saha-Dasgupta, Phys. Rev. B **65**, 144445 (2002).
[8] Y. Sasago, M. Hase, K. Uchinokura, M. Tokunaga, and N. Miura, Phys. Rev. B **52**, 3533 (1995).
[9] A. Zheludev, G. Shirane, Y. Sasago, M. Hase, and K. Uchinokura, Phys. Rev. B **53**, 11642 (1996).
[10] O. T. G. Babu and C. Greaves, Mater. Res. Bull. **26**, 499 (1991).
[11] T. Siegrist, R. S. Roth, C. J. Rawn, and J. J. Ritter, Chem. Mater. **2**, 192 (1990).
[12] J. Dolinsek, D. Arcon, P. Cevc, O. Milat, M. Miljak, and I. Aviani, Phys. Rev. B **57**, 7798 (1998).
[13] E. Ising, Z. Phys. **31**, 253 (1925).
[14] M. E. Fisher, Physica (Amsterdam) **26**, 618 (1960).
[15] J. C. Bonner and M. E. Fisher, Phys. Rev. **135**, A 640 (1964).
[16] H. J. Schulz, Phys. Rev. Lett. **77**, 2790 (1996).
[17] T. Ami, M. K. Crawford, R. L. Harlow, Z. R. Wang, D. C. Johnston, Q. Huang, and R. W. Erwin, Phys. Rev. B **51**, 5994 (1995).
[18] N. Motoyama, H. Eisaki, and S. Uchida, Phys. Rev. Lett. **76**, 3212 (1996).
[19] J. C. Bonner, S. A. Friedberg, H. Kobayashi, D. L. Meier, and H. W. J. Blote, Phys. Rev. B **27**, 248 (1983).
[20] C. K. Majumdar and D. K. Ghosh, J. Math. Phys. (N.Y.) **10**, 1388 (1969).
[21] B. S. Shastry and B. Sutherland, Phys. Rev. Lett. **47**, 964 (1981).
[22] F. D. M. Haldane, Phys. Rev. B **25**, 4925 (1982).
[23] S. R. White and I. Affleck, Phys. Rev. B **54**, 9862 (1996).
[24] A. A. Aligia, C. D. Batista, and F. H. L. Essler, Phys. Rev. B **62**, 3259 (2000).
[25] M. Matsuda, K. Katsumata, K. M. Kojima, M. Larkin, G. M. Luke, J. Merrin, B. Nachumi, Y. J. Uemura, H. Eisaki, N. Motoyama, S. Uchida, and G. Shirane, Phys. Rev. B **55**, R11953 (1997).
[26] I. A. Zaliznyak, C. Broholm, M. Kibune, M. Nohara, and H. Takagi, Phys. Rev. Lett. **83**, 5370 (1999).
[27] P. T. Nguyen, R. D. Hoffman, and A. W. Sleight, Mater. Res. Bull. **30**, 1055 (1995).
[28] J. Kikuchi, K. Motoya, T. Yamauchi, and Y. Ueda, Phys. Rev. B **60**, 6731 (1999).
[29] A. W. Garrett, S. E. Nagler, D. A. Tennant, B. C. Sales, and T. Barnes, Phys. Rev. Lett. **79**, 745 (1997).
[30] T. Yamauchi, Y. Narumi, J. Kikuchi, Y. Ueda, K. Tatani, T. C. Kobayashi, K. Kindo, and K. Motoya, Phys. Rev. Lett. **83**, 3729 (1999).
[31] H. Vollenkle, A. Wittmann, and H. Nowotny, Monatsh. Chem. **98**, 1352 (1967).
[32] M. Hase, I. Terasaki, and K. Uchinokura, Phys. Rev. Lett. **70**, 3651 (1993).
[33] L. N. Bulaevskiĭ, Fiz. Tverd. Tela (Leningrad) **11**, 1132 (1969) [Sov. Phys. Solid State **11**, 921 (1969)].
[34] M. Nishi, O. Fujita, and J. Akimitsu, Phys. Rev. B **50**, 6508 (1994).
[35] T. Lorenz, U. Ammerahl, R. Ziemes, B. Buchner, A. Revcolevschi, and G. Dhallen, Phys. Rev. B **55**, R15610 (1996).
[36] H. Winkelmann, E. Gamper, B. Buchner, M. Braden, A. Revcolevschi, and G. Dhalenne, Phys. Rev. B **51**, 12884 (1995).
[37] K. Takehana, M. Oshikiri, G. Kido, M. Hase, and K. Uchinokura, J. Phys. Soc. Jpn. **65**, 2783 (1996).
[38] K. Hirota, D. E. Cox, J. E. Lorenzo, G. Shirane, J. M. Tranquada, M. Hase, K. Uchinokura, H. Kojima, Y. Shibuya, and I. Tanaka, Phys. Rev. Lett. **73**, 736 (1994)
[39] M. Hase, I. Terasaki, K. Uchinokura, M. Tokunaga, N. Miura, and H. Obara, Phys. Rev. B **48**, 9616 (1993).
[40] H. Ohta, S. Imagawa, H. Ushiroyama, M. Motokawa, O. Fujita, and J. Akimitsu, J. Phys. Soc. Jpn. **63**, 2870 (1996).
[41] G. A. Petrakovskiĭ, K. A. Sablina, A. M. Vorotynov, A. I. Kruglik, A. G. Klimenko, A. D. Balaev, and S. S. Aplesnin, Zh. Éksp. Teor. Fiz. **98**, 1382 (1990) [Sov. Phys. JETP **71**, 772 (1990)].
[42] H. Nojiri, Y. Shimamoto, N. Miura, M. Hase, K. Uchinokura, H. Kojima, I. Tanaka, and Y. Shibuya, Phys. Rev. B **52**, 12749 (1995).
[43] H. Ohashi, T. Fujita, and T. Osawa, J. Jpn. Assoc. Mineral. Petrol. Econ. Geol. **77**, 305 (1982).
[44] M. Isobe, E. Ninomiya, A. N. Vasil'ev, and Y. Ueda, J. Phys. Soc. Jpn. **71**, 1423 (2002).
[45] F. D. M. Haldane, Phys. Rev. Lett. **50**, 1153 (1983).
[46] F. D. M. Haldane, Phys. Rev. Lett. **61**, 1029 (1988).
[47] R. Botet, R. Jullien, and M. Kolb, Phys. Rev. B **28**, 3914 (1983).
[48] R. Botet and R. Jullien, Phys. Rev. B **27**, 613 (1983).
[49] I. Affleck, T. Kennedy, E. H. Lieb, and H. Tasaki, Phys. Rev. Lett. **59**, 799 (1987).
[50] J. Darriet and L. P. Regnault, Solid State Commun. **86**, 409 (1993).
[51] T. Yokoo, T. Sakaguchi, K. Kakurai, and J. Akimitsu, J. Phys. Soc. Jpn. **64**, 3651 (1995).
[52] Y. Uchiyama, Y. Sasago, I. Tsukada, K. Uchinokura, A. Zheludev, T. Hayashi, N. Miura, and P. Boni, Phys. Rev. Lett. **83**, 632 (1999).
[53] A. Lappas, V. Alexandrakis, J. Giapintzakis, V. Pomjakushin, K. Prassides, and A. Schenck, Phys. Rev. B **66**, 014428 (2002).
[54] T. Sakai and M. Takahashi, Phys. Rev. B **42**, 4537 (1990).
[55] T. Masuda, K. Uchinokura, T. Hayashi, and N. Miura, Phys. Rev. B **66**, 174416 (2002).
[56] A. I. Smirnov, V. N. Glazkov, H.-A. Krug von Nidda, A. Loidl, L. N. Demianets, and A. Ya. Shapiro, Phys. Rev. B **65**, 174422 (2002).
[57] A. Zorko, D. Arčon, A. Larras, J. Giarintzakis, C. Saylor, and L. C. Brunel, Phys. Rev. B **65**, 144449 (2002).
[58] T. Barnes, E. Dagotto, J. Riera, and E. Swanson, Phys. Rev. B **47**, 3196 (1993).
[59] S. Gopalan, T. M. Rice, and M. Sigrist, Phys. Rev. B **49**, 8901 (1994).
[60] S. White, R. Noack, and D. Scalapino, Phys. Rev. Lett. **73**, 886 (1994).
[61] R. Noack, S. White, and D. Scalapino, Phys. Rev. Lett. **73**, 882 (1994).
[62] M. Azzouz, L. Chen, and S. Moukouri, Phys. Rev. B **50**, 6233 (1994).
[63] M. Troyer, H. Tsunetsugu, and D. Wurtz, Phys. Rev. B **50**, 13515 (1994).
[64] S. Larochelle and M. Greven, cond-mat/0310714, v. 2 (2004).
[65] K. Totsukat and M. Suzuki, J. Phys.: Condens. Matter **7**, 6079 (1995).
[66] Z. Hiroi, M. Azuma, M. Takano, and Y. Bandol, J. Solid State Chem. **95**, 230 (1991).
[67] M. Azuma, Z. Hiroi, M. Takano, K. Ishida, and Y. Kitaoka, Phys. Rev. Lett. **73**, 3463 (1994).

[68] K. Ishida, Y. Kitaoka, K. Asayama, M. Azuma, Z. Hiroi, and M. Takano, J. Phys. Soc. Jpn. **63**, 3222 (1994).
[69] M. Azuma, M. Takano, and R. S. Eccleston, J. Phys. Soc. Jpn. **67**, 740 (1998).
[70] D. C. Johnston, M. Troyer, S. Miyahara, D. Lidsky, K. Ueda, M. Azuma, Z. Hiroi, M. Takano, M. Isobe, Y. Ueda, M. A. Korotin, V. I. Anisimov, A. V. Mahajan, and L. L. Miller, cond-mat/0001147 (2000).
[71] K. Magishi, S. Matsumoto, Y. Kitaoka, K. Ishida, K. Asayama, M. Ueda, T. Nagata, and J. Akimitsu, Phys. Rev. B **57**, 11533 (1998).
[72] K. Ishida, Y. Kitaoka, Y. Tokunaga, S. Matsumoto, M. Azuma, Z. Hiroi, and M. Takano, Phys. Rev. B **53**, 2827 (1996).
[73] J.-C. Boulloux and J. Galy, Solid State Chem. **16**, 385 (1976).
[74] H. Iwase, M. Isobe, Y. Ueda, and H. Yasuoka, J. Phys. Soc. Jpn. **65**, 2397 (1996).
[75] M. Onoda and N. Nishiguchi, J. Solid State Chem. **127**, 359 (1996).
[76] M. A. Korotin, I. S. Elfimov, V. I. Anisimov, M. Troyer, and D. I. Khomskii, Phys. Rev. Lett. **83**, 1387 (1999).
[77] B. Normand and T. M. Rice, Phys. Rev. B **56**, 8760 (1997).
[78] S. Miyahara, M. Troyer, D. C. Johnston, and K. Ueda, cond-mat/9807127 (1998).
[79] J.-C. Boulloux and J. Galy, J. Solid State Chem. **16**, 393 (1976).
[80] M. Isobe, Y. Ueda, K. Takizawa, and T. Goto, J. Phys. Soc. Jpn. **67**, 755 (1998).
[81] P. Millet, C. Satto, J. Bonvoisin, B. Normand, K. Penc, M. Albrecht, and F. Mila, Phys. Rev. B **57**, 5005 (1998).
[82] M. Onoda and A. Ohyama, J. Phys.: Condens. Matter **10**, 1229 (1998).
[83] M. A. Korotin, V. I. Anisimov, T. Saha-Dasgupta, and I. Dasgupta, J. Phys.: Condens. Matter **12**, 113 (2000).
[84] I. Radosavljevic, J. S. O. Evans, and A. W. Sleight, J. Solid State Chem. **141**, 149 (1998).
[85] T. Masuda, A. Zheludev, H. Kageyama, and A. N. Vasiliev, Europhys. Lett. **63**, 757 (2003).
[86] M. Matsuda, K. Katsumata, H. Eisaki, N. Motoyama, S. Uchida, S. M. Shapiro, and G. Shirane, Phys. Rev. B **54**, 12199 (1996).
[87] M. Matsuda and K. Katsumata, Phys. Rev. B **53**, 12201 (1996).
[88] D. E. Cox, T. Iglesias, K. Hirota, G. Shirane, M. Matsuda, N. Motoyama, H. Eisaki, and S. Uchida, Phys. Rev. B **57**, 10750 (1998).
[89] R. S. Eccleston, M. Uehara, J. Akimitsu, H. Eisaki, N. Motoyama, and S. Uchida, Phys. Rev. Lett. **81**, 1702 (1998).
[90] W. E. Pickett, Phys. Rev. Lett. **79**, 1746 (1997).
[91] S. Taniguchi, T. Nishikawa, Y. Yasui, Y. Kobayashi, M. Sato, T. Nishioka, M. Kontani, and K. Sano, J. Phys. Soc. Jpn. **64**, 2758 (1995).
[92] K. Kodama, H. Harashina, H. Sasaki, Y. Kobayashi, M. Kasai, S. Taniguchi, Y. Yasui, M. Sato, K. Kakurai, T. Mori, and M. Nishi, J. Phys. Soc. Jpn. **66**, 793 (1997).
[93] K. Ueda, H. Kontani, M. Sigrist, and P. A. Lee, Phys. Rev. Lett. **76**, 1932 (1996).
[94] I. Bose and A. Ghosh, Phys. Rev. B **56**, 3149 (1996).
[95] M. Troyer, H. Kontani, and K. Ueda, Phys. Rev. Lett. **76**, 3822 (1996).
[96] O. A. Starykh, M. E. Zhitomirsky, D. I. Khomskii, R. R. P. Singh, and K. Ueda, Phys. Rev. Lett. **77**, 2558 (1996).
[97] C. Stephen Hellberg, W. E. Pickett, L. L. Boyer, Harold T. Stokes, and M. J. Mehl, J. Phys. Soc. Jpn. **68**, 3489 (1999).
[98] M. Isobeand and Y. Ueda, J. Phys. Soc. Jpn. **65**, 1178 (1996).
[99] T. Ohama, H. Yasuoka, M. Isobe, and Y. Ueda, Phys. Rev. B **59**, 3299 (1999).
[100] H.-G. von Schnering, Y. U. Grin, M. Kaupp, M. Samer, R. K. Kremer, O. Jepsen, T. Chatterji, and M. Weiden, Z. Kristallogr. **213**, 246 (1998).
[101] M. Cuoco, P. Horsch, and F. Mack, Phys. Rev. B **60**, R8438 (1999).
[102] A. N. Vasil'ev, M. M. Markina, M. Yu. Kagan, M. Isobe, and Yu. Ueda, JETP Lett. **73**, 357 (2001).
[103] A. N. Vasil'ev, V. V. Pryadun, D. I. Khomskii, G. Dhalenne, A. Revcolevschi, M. Isobe, and Y. Ueda, Phys. Rev. Lett. **81**, 1949 (1998).
[104] S. Ravy, J. Jegoudez, and A. Revcolevschi, Phys. Rev. B **59**, R681 (1999).
[105] M. V. Mostovoy and D. I. Khomskii, Solid State Commun. **113**, 159 (2000).
[106] Y. Fujii, H. Nakao, T. Yoshihama, M. Nishi, K. Nakajima, K. Kakurai, M. Isobe, H. Sawa, and Y. Ueda, J. Phys. Soc. Jpn. **66**, 326 (1997).
[107] H. Sawa, E. Ninomiya, T. Ohama, H. Nakao, K. Ohwada, Y. Murakami, Y. Fujii, Y. Noda, M. Isobe, and Y. Ueda, J. Phys. Soc. Jpn. **71**, 385 (2002).
[108] K. Ohwada, Y. Fujii, Y. Katsuki, J. Muraoka, H. Nakao, Y. Murakami, H. Sawa, E. Ninomiya, M. Isobe, and Y. Ueda, cond-mat/0408210 (2004).
[109] R. W. Smith and D. A. Keszler, J. Solid State Chem. **93**, 430 (1991).
[110] B. S. Shastry and B. Sutherland, Physica B **108**, 1069 (1981).
[111] H. Kageyama, K. Onizuka, T. Yamauchi, Y. Ueda, S. Hane, H. Mitamura, T. Goto, K. Yoshimura, and K. Kosuge, J. Phys. Soc. Jpn. **68**, 1821 (1999).
[112] H. Kageyama, K. Yoshimura, R. Stern, N. V. Mushnikov, K. Onizuka, M. Kato, K. Kosuge, C. P. Slichter, T. Goto, and Y. Ueda, Phys. Rev. Lett. **82**, 3168 (1999).
[113] S. Miyahara and K. Ueda, Phys. Rev. Lett. **82**, 3701 (1999).
[114] S. Chen and B. Han, Eur. Phys. J. B **31**, 63 (2003).
[115] S. Miyahara and K. Ueda, J. Phys.: Condens. Matter **15**, R327 (2003).
[116] H. Kageyama, Y. Ueda, Y. Narumi, K. Kindo, M. Kosaka, and Y. Uwatoko, Suppl. Prog. Theor. Phys. **145**, 17 (2002).

Translated by Steve Torstveit

Simulation of the adsorption of simple gases on transition metals (Review)

N. V. Petrova, I. N. Yakovkin,* and Yu. G. Ptushinskiĭ

Institute of Physics of the National Academy of Sciences of Ukraine, pr. Nauki 46, Kiev 03028, Ukraine
(Submitted July 12, 2004; revised September 28, 2004)
Fiz. Nizk. Temp. **31**, 300–322 (March–April 2005)

Results from simulations of the adsorption of gases on transition metal surfaces are presented. Attention is devoted mainly to the adsorption of hydrogen on the (110) surfaces of W and Mo, the structures and adsorption kinetics of oxygen and CO on the Pt(111) surface, and the catalytic reaction of CO oxidation. The choice of these systems is motivated not only by their practical importance and fundamental interest but also by the fact that substantial progress has been made toward understanding the processes of adsorption and the formation of film structures for them with the use of the Monte Carlo method. One of the main requisites for simulation of the adsorbed film structures is to adequately incorporate the lateral interaction between adsorbed molecules, which includes both a direct interaction (electrostatic and exchange) and indirect (via electrons of the substrate). The correct description of the lateral interaction in the simulation has permitted explanation of the mechanisms of formation of the structures of CO films on platinum. At the same time, the complexity of the interaction between adsorbed atoms has at yet precluded the development of a consistent model for the formation of the structure of adsorbed oxygen on the platinum surface. It can be hoped that this problem will soon be solved, making it possible to refine the model of the catalytic reaction of CO oxidation. © *2005 American Institute of Physics.* [DOI: 10.1063/1.1884424]

1. INTRODUCTION

The basic principles of the modern concepts of the physics of adsorption were set forth back in the early twentieth century by Irving Langmuir. Despite the enormous progress in our understanding of the process of gas adsorption on various surfaces, many of its important details and interrelationships require clarification. Interest in the adsorption of gases on transition metals stems not only from the possible importance of such research (it suffices to mention the necessity of achieving further progress on the problems of heterogeneous catalysis, for example, the problem of removing pollutants from the exhaust gases of automobiles and the comprehensive decontamination of the atmosphere), but also from the possibility of carrying out multifaceted research on such adsorption systems for the purpose of obtaining new information about the properties of surfaces. For example, low-energy electron diffraction (LEED) and scanning tunneling microscopy (STM) are used to study the structure of the surface and of the adsorbed film, and photo- and x-ray-electron spectroscopy are used to study the electronic structure. Infrared spectroscopy yields information about the types of adsorption sites and bonds and their symmetry, and experiments on diffusion, temperature programmed desorption, particle scattering, and adsorption kinetics can determine the adsorption energy and binding force of the molecules and atoms with the surface.

Progress in research on the adsorption of gases on transition metals demands the use of novel comprehensive techniques in addition to conventional methods. For example, for studying molecular adsorption of hydrogen by the molecular beam method (for purposes of studying the adsorption kinetics and to obtain information about the interaction potential between the incoming particle and the solid surface) the substrate must be cooled to liquid helium temperature. Obviously, purposeful investigation of the properties of adsorption systems also requires theoretical studies. Unfortunately, the possibilities for rigorous theoretical calculations of the interaction parameters of particles with metal surfaces are extremely limited because of the necessity of taking into account a large number of different factors, such as the presence of precursor states, accommodation, the character of the adsorption bond (ionic, covalent), the types of lateral interaction, and the rate of surface diffusion. Since many experiments on gas adsorption are done under equilibrium (or quasi-equilibrium) conditions, one can in principle employ thermodynamic methods to estimate the kinetic characteristics, but the accuracy of such estimates is insufficient for direct comparison with experimental data.

Using modern methods of calculation (in the framework of electron density functional theory) one can quite reliably estimate the binding energy of an atom or molecule with the surface, determine the most favorable adsorption centers, and estimate the interaction energy between adsorbed particles (the lateral interaction). However, significant difficulties arise when one attempts to compare the results of such model calculations with experimental data on adsorption. This to a large degree is due to the fact that experiments usually measure the integrated characteristics (sticking coefficient and diffusion coefficient, the heat of adsorption, etc.), whereas calculations give numerical values of the interaction parameters between particles and the surface and therefore cannot always be used directly for interpretation of the results of studies of the adsorption kinetics.

The complexity of calculations of the interaction with the surface for incoming gas molecules can be illustrated by the example of the so-called ''six-dimensional potential

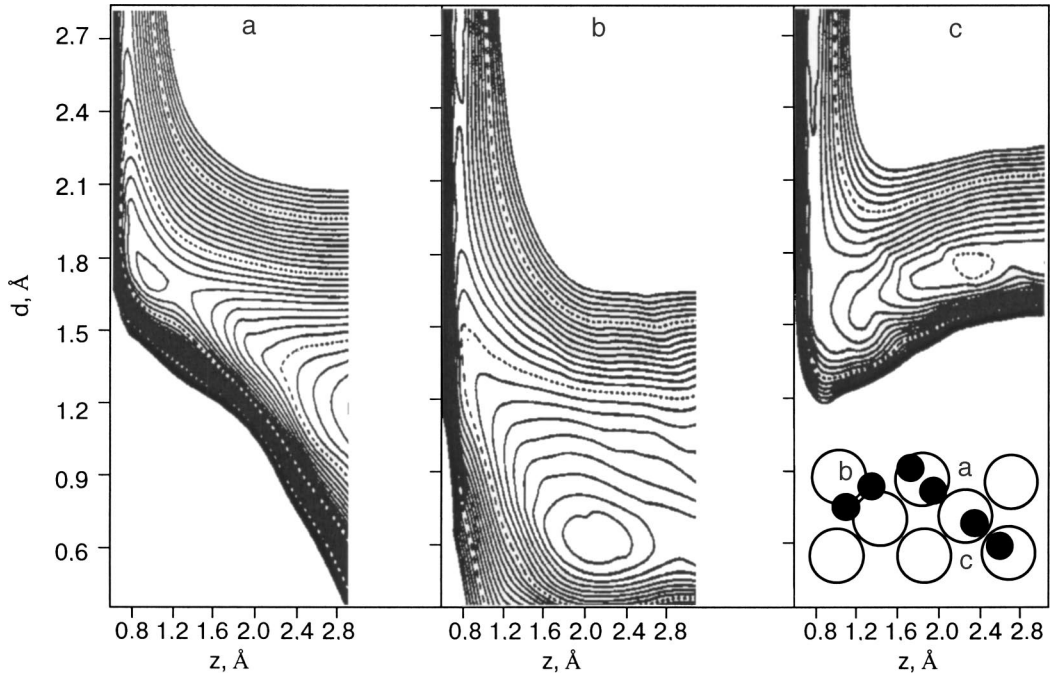

FIG. 1. Potential energy surfaces for hydrogen molecules on W(100) from Ref. 8: for molecules above an on-top center the axis of the molecule is parallel to the direction between two bridge positions on the substrate—barrierless desorption (a); for a molecule above a bridge adsorption center with the axis of the molecule parallel to the direction between two positions of threefold symmetry—barrierless desorption (b); for a molecule above a bridge position with the axis of the molecule parallel to the direction on the surface between two on-top positions (c). The barrier for desorption is 0.3 eV.

model.'' The molecular dynamics method is used to calculate the forces of interaction with the surface for different orientations (and sometimes velocities) of the molecules, and potential energy surfaces (PESs) are constructed.[1–7] As an example, Fig. 1 shows the PES calculated in Ref. 8 for hydrogen on W(100). In this model the growth of the initial sticking coefficient with decreasing energy of the incident hydrogen molecule is explained by a decrease in the speed of rotation owing to an orientation (or steering) of the incoming molecule. As a result of steering the molecule is oriented with respect to the surface in such a way that the probability of breaking the molecular bond becomes maximum. Thus, if a molecule oriented along the surface approaches an on-top or bridge position on the surface there is no potential barrier for chemisorption. However, if the axis of the molecule is perpendicular to the surface, the molecule cannot be chemisorbed in an on-top site (the potential barrier in this case is practically infinite), while the barrier for chemisorption in the bridge position is 0.3 eV. For dissociative chemisorption of a molecule in a position of threefold symmetry a potential barrier exists for any orientation of the incoming molecule.

For describing probabilistic processes in systems with a large number of particles it is resonable to make use of statistical simulation (the Monte Carlo method). The Monte Carlo method is widely used for studying the interaction of particles with a solid surface, crystal growth, adsorption, diffusion, and ordering of adsorbed atoms and molecules, and also chemical reactions on a surface. With this method one can do a computer experiment (simulation) based on physical concepts obtained as a result of experimental and theoretical studies of a given adsorption system. This not only allows one to check the correctness of existing ideas about the system but also to propose new concepts for interpreting the experimental data and, in a number of cases, to predict the behavior of systems under some particular conditions or other.

In this review we discuss the possibilities of the Monte Carlo method and the prospects for its use in modeling the adsorption of gases on transition metals. We present and analyze the results of simulations of the low-temperature adsorption of hydrogen (with precursor states and the phenomenon of enhanced accommodation taken into account), adsorption, the formation of structures of adsorbed films of oxygen and CO on platinum, and the catalytic reaction of CO oxidation.

2. ROLE OF PRECURSOR STATES IN LOW-TEMPERATURE ADSORPTION OF HYDROGEN ON TRANSITION METALS

2.1. Accommodation of molecules and the initial sticking coefficient

The probability of adsorption of a molecule on a surface (the initial sticking coefficient) depends on the energy of the particle, the direction of incidence, and the temperature of the substrate. At a low substrate temperature the probability of physisorption is determined mainly by the efficiency of transfer of the kinetic energy of the molecules to atoms of the surface in collision (accommodation of the molecule), after which the molecule is trapped by the surface, where its energy is close to the value of the minimum of the van der Waals potential (see Fig. 2). Accommodation of the molecule is explained by the loss of energy to excitation of one or several phonons in the substrate and, in some cases, the formation of electron–hole pairs also.[9] For particles with low energies the second process has a low probability and is usu-

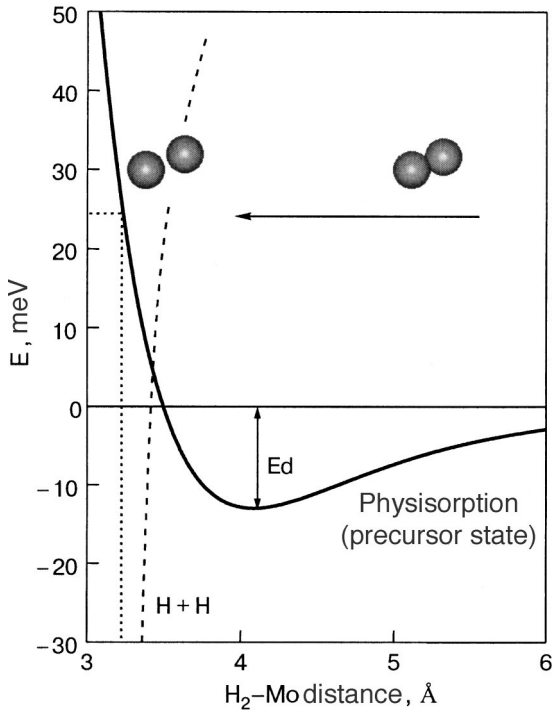

FIG. 2. One-dimensional interaction potential of a hydrogen molecule with the Mo(110) surface, calculated in the classical approximation.[47]

ally neglected. Taking a classical approach, one can estimate the scattering probability in the case of one- and two-phonon processes.[9–13] However, for typical energies of the hydrogen molecules in a molecular beam (25 meV) the scattering length has a value of the order of the lattice period on the surface of a transition metal, and that leads to significant diffraction effects.[9] Thus for a realistic description of the scattering of hydrogen molecules one must use a quantum-mechanical approach, which is practical only for a one-phonon process.[9,13,14] In Ref. 9 an analysis of the dependence of the sticking coefficient on the energy of the incident particle, $S(E)$, was done both from a classical standpoint and with quantum effects taken into account. It was shown that at low energies of the incident particles $(E \to 0)$ in the classical description $S(E) \to 1$, while in the case when quantum effects—in particular, quantum reflection—are included, the dependence has the form $S(E) \sim E^{1/2}$ for neutral atoms.

Clearly the adsorption of hydrogen on a metal surface can substantially alter the surface contribution to the phonon spectrum of the system, and therefore the estimates made are only of a qualitative character. For example, in the adsorption of a monolayer of hydrogen on the W(110) and Mo(110) surfaces one observes anomalies in the scattering spectrum of He atoms in comparison with scattering on the clean surface.[15] Softening of a phonon mode is due to electron–phonon coupling, which is enhanced on account of adsorption-induced surface states. This explanation is confirmed by calculations of the atomic and electronic structure, the vibrational spectra, and the spectra of excitation of electron–hole pairs in these systems in the framework of density functional theory.[16,17] Unfortunately, the necessity of taking into account a large number of factors influencing the accommodation makes it impossible the estimate the initial sticking coefficient to the accuracy necessary for comparison with experiment.

2.2. Precursor states and steering

Hydrogen can be adsorbed on transition metals in a process involving dissociation of the molecules and subsequent chemisorption of the individual atoms or at low temperatures in a weakly bound physisorbed molecular state.[18–28] The activation energy for dissociative chemisorption of hydrogen on W(110) and Mo(110), as follows from the growth of the sticking coefficient with decreasing energy of the incident molecules, is extremely insignificant, so that one can observe atomic chemisorption even at a temperature of 5 K. After an atomic layer is filled the further adsorption of hydrogen takes place in molecular form. The highest degree of coverage θ by hydrogen at $T = 5$ K in dynamic equilibrium with the incident hydrogen beam is $\theta = 1.5$, which corresponds to the formation of a complete molecular monolayer (ML) of hydrogen on top of the atomic monolayer (the degree of coverage is defined as the number of hydrogen molecules per adsorption site on the W(110) or Mo(110) surface, so that $\theta = 0.5$ corresponds to a filled atomic monolayer).

The chemisorption barrier for hydrogen adsorption on noble metals (Au, Cu) and transition metals (Pd, Rh, Pt, W, Mo) are substantially different. For noble metals typically there is a high activation barrier for dissociation. In contrast, for hydrogen adsorption on Ni(111) and Pt(111) the activation barrier is 50–100 meV, and for hydrogen adsorption on Rh(111) activationless chemisorption of hydrogen is observed. The value of the barrier for dissociation of hydrogen is determined by the crossing of the repulsive part of the physisorption potential and the attractive region of the chemisorption potential for atomic hydrogen (see Fig. 2). The difference between the surface potentials of transition and noble metals is apparently due to their different electronic structure (especially the difference between the surface states).[20,29–31]

Apparently the mechanism of dissociative chemisorption consists in the following. Electrons of the substrate escaping to vacuum can occupy antibonding states of the molecule and cause its dissociation[32,33] and the subsequent chemisorption of the individual atoms. Obviously an important role in this is played by the intrinsic and extrinsic precursor states.[10,22–25,34–37] A molecule trapped in a precursor state can move along the surface and come upon a favorable adsorption site, and this leads to its dissociation and the chemisorption of the atoms at two adjacent adsorption centers. At the same time, a molecule trapped in a precursor state can also desorb, in contradistinction to the model of direct dissociative chemisorption.[8,38–42]

The existence of intrinsic precursor states is still in dispute. For highly activational chemisorption, as is characteristic of the adsorption of hydrogen on simple and noble metals,[11,12,42,43] the existence of extrinsic precursor states is confirmed by the presence of both atomic and molecular hydrogen on the surface even at very low coverages. In this situation the molecular physisorbed state can serve as a precursor state for the subsequent dissociative chemisorption. Whereas dissociative adsorption of hydrogen is observed at

low energies of the incident molecules, the presence of intrinsic precursor states can be confirmed only indirectly.[19–21,23,26–28,34–37,43]

At the same time, the steering effect can account for some experimental data on the sticking coefficient of hydrogen without any need for invoking the concept of precursor states, and for that reason the existence of intrinsic precursor states has been called into question.[44] However, it follows from the calculations of Refs. 8 and 38–41 that the hydrogen molecules have a high mobility along the surface and thus spend a significant time near the surface before reflecting or dissociating.[8,39–41] Furthermore, the barrierless (direct) chemisorption of hydrogen on the W(100) surface, as follows from the calculations of Ref. 8, is observed only for certain orientations of the molecules with respect to the surface, and for other orientations this barrier is quite significant (see Fig. 1). Such a state in a two-dimensional model of the surface potential can be considered to be an intrinsic precursor state.[18,29,45,46] Thus the concept of precursor states as a temporary molecular state prior to chemisorption does not really contradict the steering-effect model, since in both models it is assumed that the molecule spends a significant time near the surface prior to its dissociation or return to the gas phase.

2.3. Effective two-dimensional potential

For qualitative description of the motion of a molecule it is advisable to use a one-dimensional potential model averaged over the surface. Two approaches are usually taken in the commonly used software packages based on methods of quantum chemistry: 1) classical Newtonian mechanics; 2) semiempirical potentials using universal parameters for the overlap integrals; 3) *ab initio* calculations (by the Hartree–Fock method, with the configuration interaction also taken into account if necessary), and 4) calculations using density functional theory. The interaction with the model surface can be described in terms of classical molecular mechanics or quantum mechanics. Quantum-mechanical calculations using the semiempirical approximation yield rather reliable estimates for the interaction parameters. In Newtonian mechanics the hydrogen molecule is treated as a classical particle in the fields of a van der Waals potential near the surface, while the semiempirical potential, which takes the electronic structure of the molecule into account, also permits modeling of its dissociation.

The interaction potential of the hydrogen molecule with the Mo(110) surface, calculated in the classical approximation, is shown in Fig. 2.[47] A particle approaching the surface is attracted by the van der Waals forces to a distance at which it begins to feel the ''tail'' of metal electrons escaping to vacuum. The interaction with these electrons leads to the formation of a repulsive potential and can lead to reflection of the particle. However, the molecule may lose kinetic energy (e.g., owing to excitation of phonons in the substrate)[9–13] and, as a result, be trapped in a potential near the surface, corresponding to a state of physical adsorption. The depth of the physisorption well for hydrogen on Mo(110) is only around 15 meV,[47,20] and therefore a stable molecular layer of physisorbed hydrogen can be obtained only at low substrate temperatures.

2.4. Monte Carlo simulation of adsorption kinetics of hydrogen

In both physical and chemical adsorption the atoms and molecules generally occupy certain sites or adsorption centers. This position is determined by the interaction potential of the particle with the surface, and it is therefore logical to assume that the geometry of the arrangement of adsorption centers is determined by the potential relief of the surface. Indeed, in an atomic adsorbed layer the limiting concentration of hydrogen atoms is equal to the surface concentration of atoms of the substrate, which can present as a lattice of adsorption centers, each of which can be occupied by one atom. Clearly the presence of an atomic layer on a surface can influence the binding of the molecules of the second layer with the surface. Nevertheless, the molecular adsorption of hydrogen can also be described by a lattice-gas model, inasmuch as it has been observed in experiment that the second (molecular) layer is saturated at the same concentration of hydrogen molecules as the surface concentration of substrate atoms. This feature allows one to describe the molecular and dissociative adsorption of hydrogen by the Monte Carlo method, which gives a transparent description of the process and enables one to elucidate the role of the various factors influencing the effective sticking coefficient.

It has been observed in molecular beam experiments at low temperatures (5 K) that the adsorption kinetics of hydrogen demonstrates a strong dependence of the sticking coefficient S and of the limiting dynamic-equilibrium coverage on the molecular flux.[28] For example, at high fluxes a significant maximum of S is observed at coverages in the region corresponding to molecularly adsorbed hydrogen, while at low fluxes this maximum is very slight or absent altogether. Furthermore, the limiting equilibrium coverage at high fluxes equals 1, while at low fluxes it is 0.2.

The dependence of the sticking coefficient on the degree of coverage is given by the relation

$$S(\theta)=1-k(\theta)-\theta n_0 W(\theta)/F, \tag{1}$$

where θ is the degree of coverage, defined as $\theta=n/n_0$ [n_0 is the density of adsorption sites, 1.4×10^{15} cm^{-2} in the case of the W(110) or Mo(110) surface], $k(\theta)$ is the coefficient of reflection of a molecule from the surface, $W(\theta)=\nu\exp(-E_{\text{eff}}/k_bT)$ is the desorption probability, $E_{\text{eff}}=E_d+U$ (E_d is the activation energy for desorption, U is the energy of the lateral interaction of neighboring atoms), ν is the frequency factor, and F is the particle flux. The influence of the flux on $S(\theta)$ is explained by enhancement of the accommodation for particles that in the process of their adsorption collide with previously adsorbed molecules.[48–51] Indeed, in the collision of a molecule with a heavy substrate atom, because of the mass mismatch of the colliding particles, it is harder for a molecule to lose sufficient energy to become trapped in the physisorption well, and upon collision with an already adsorbed molecule, owing to the equality of the masses, the exchange of energy will be much more efficient, and therefore the probability of adsorption will be higher. The situation can be modeled as follows. If a molecule collides with a substrate atom, then the probability of adsorption is determined by the initial sticking coefficient S_0 (the simulation can be done using the value of S_0 obtained from ex-

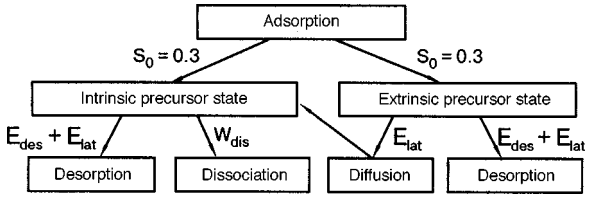

FIG. 3. Scheme of the simulation of adsorption of hydrogen on a transition metal.

periment), while if it collides with an adsorbed molecule when an unoccupied adsorption site is among the nearest neighbors, then the adsorption probability is taken equal to unity.

The scheme of the Monte Carlo simulation of hydrogen adsorption in Ref. 47 was as follows (Fig. 3):

1. An adsorption center is selected at random. If the center is unoccupied or occupied by a chemisorbed atom, then the molecule with a certain probability W_A (determined by the initial sticking coefficient S_0) is trapped in an intrinsic or extrinsic precursor state, respectively.

2. A molecule trapped into this precursor state can either dissociate (with a probability W_{diss}) with the instantaneous chemisorption of the hydrogen atoms (in the presence of an unoccupied adsorption center) or can make several diffusion hops or be desorbed. At low coverages and low temperatures desorption of a molecule is considerably less probable than diffusion, and the desorption of atoms from a chemisorbed state is practically impossible at low temperatures.

3. If the chosen center is occupied by a molecule, than it is assumed that the accommodation of molecules in this case is significantly enhanced on account of the equality of the particle masses. This circumstance is taken into account with the aid of a modeling of the possibility for such a molecule to occupy the nearest center not occupied by another molecule, and in that case the desorption probability is equal to 1.

The result of the Monte Carlo simulation of hydrogen adsorption on W(110) and Mo(110) with diffusion and the lateral interaction between molecules and also the enhanced accommodation[45] taken into account is in good agreement with the experimental $S(\theta)$ curves in the entire range of coverages studied and at all values of the flux of hydrogen molecules (Fig. 4a). The calculated $S(\theta)$ curve reproduces well such experimentally observed features as enhancement of sticking and growth of the limiting dynamic-equilibrium coverage with increasing flux of hydrogen molecules onto the surface. The growth of the sticking coefficient with increasing flux here is due to the enhanced accommodation for the hydrogen molecules at high fluxes, and the increase in the limiting coverage is due to a change in the ratio of the desorption flux to the incident flux [see Eq. (1)]. It should be noted that in using this model it is unnecessary to include other parameters in order to get the growth of the sticking coefficient at high coverages and fluxes. Such agreement with the experimental data can be obtained only if the role of the intrinsic and extrinsic precursor states is adequately taken into account. For example, control calculations of the functions $S(\theta)$ without the precursor states have revealed the absence of experimentally observable dependence of the sticking coefficient on the flux at coverages of around 0.5 (Fig. 4b).

For hydrogen adsorption on Mo(110) the dependence of the sticking coefficient on the degree of coverage is qualitatively different from the case of H_2 adsorption on W(110) and of deuterium adsorption on Mo(110). Only for the system H/Mo(110) is a sharp decrease of the sticking coefficient observed at coverage $\theta = 0.5$ (Fig. 5). In Refs. 27 and 52 this difference in the behavior of $S(\theta)$ was explained by the anomalously high mobility of hydrogen on Mo(110). On the basis of the results of a simulation[47] an alternative explanation was proposed for the different behavior of $S(\theta)$ in the cases of hydrogen and deuterium adsorption on Mo(110). For example, when only the difference of the activation energies for desorption of hydrogen and deuterium on Mo(110) is taken into account, one observes a tendency to form a minimum (Fig. 5).

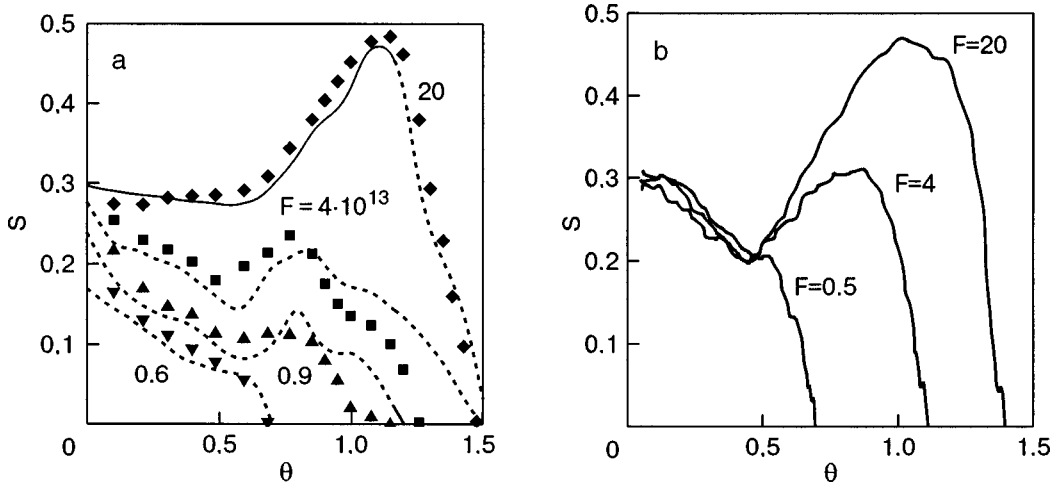

FIG. 4. Dependence of the sticking coefficient of hydrogen on W(110) on the degree of coverage for different values of the incident particle flux (the dashed curves show the experimental results, and the symbols the result of a simulation[47] including precursor states) (a); the results of a simulation for different fluxes in the case of direct chemisorption (b).

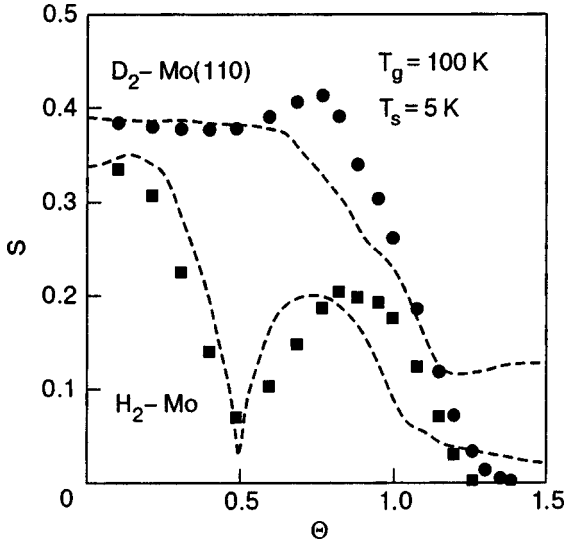

FIG. 5. Dependence of the sticking coefficient on the degree of coverage for hydrogen and deuterium on Mo(110) (the dashed curve is experimental, the symbols the results of a simulation[47]).

2.5. Simulation of hydrogen desorption

An effective method for investigating the interaction of an adsorbate with a surface is temperature programmed desorption (TPD). For interpretation of the TPD spectra one usually uses the Polanyi–Wigner equation for the rate of desorption:

$$R_{\mathrm{des}} = \theta^n \nu \exp(-E_{\mathrm{eff}}/k_B T),$$

where R_{des} is the rate of desorption, ν is a pre-exponential factor, $E_{\mathrm{eff}} = E_{\mathrm{des}} + E_{\mathrm{lat}}$ is the effective activation energy for desorption with the lateral interaction taken into account, and n is the order of desorption.[53,54]

The presence of the lateral interaction between adsorbed particles has a sensitive influence on the position of the peaks in the TPD spectrum. A Monte Carlo simulation of the desorption process in real time permits one to determine the influence of the lateral interaction on the position and shape of the TPD peaks and also to estimate the value of this interaction. In Ref. 55 an algorithm was proposed for Monte Carlo simulation of the TPD spectra in real time and to analyze the influence on the TPD spectra of the substrate geometry and the lateral interaction between particles. It was shown that the presence of a repulsive interaction leads to the appearance of two peaks in the TPD spectra, corresponding to desorption from different ordered phases on the surface, the larger splitting of the peaks corresponding to the stronger lateral repulsion. For a weak repulsion one observes some broadening of the desorption peak. The presence of an attractive interaction for the next-nearest neighbors when the nearest neighbors have a repulsive interaction leads to sharpening of the TPD peak. In Ref. 45 a simulation of the TPD and isothermal desorption spectra of the system $H_2/W(110)$ was done for the cases of different initial degrees of coverage (see Fig. 6). The values obtained for the activation energy of desorption and the lateral interaction from the results of a simulation[45] for the systems $H_2/W(110)$, $H_2/Mo(110)$, and $D_2/W(110)$ are in good agreement with experiment, and so the algorithm developed can be used for simulation of the adsorption and desorption processes for the different systems and can also be used to explain the coverage dependence of the sticking coefficient of CO and oxygen on Pt(111), the

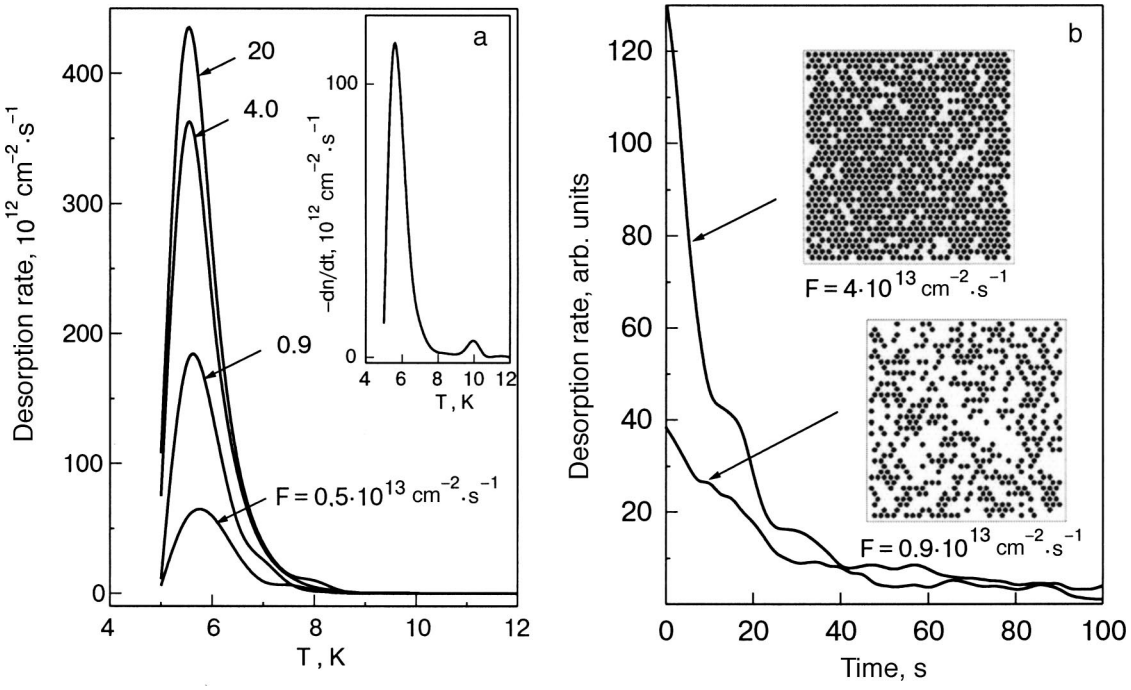

FIG. 6. Temperature programmed desorption (TPD) spectrum for the system H_2-W(110), obtained as a result of the simulation for different fluxes (the inset shows the TPD spectrum obtained in an experiment[26] at a molecular flux $F = 0.9\times10^{13}$ cm^{-2} s^{-1}) (a); the distribution of the hydrogen molecules at the equilibrium coverages on W(110), obtained for $F = 0.9\times10^{13}$ and 4×10^{13} cm^{-2} s^{-1} and the spectra of isothermal molecular desorption (in relative units), obtained as a result of a simulation[45] for 5 K (b).

structural ordering of adsorbed CO molecules,[56] and the catalytic reaction of CO oxidation on the platinum surface.

3. SIMULATION OF THE CO OXIDATION REACTION ON Pt(111)

A huge number of studies devoted to the adsorption of CO on platinum is due not only to the importance of the development of fundamental concepts but also to the search for possible ways of perfecting platinum catalysts for removing pollutants from the exhaust gases of automobiles. The catalytic reaction of CO oxidation takes place by the Langmuir–Hinshelwood mechanism (a bibliography may be found in Imbihl's excellent review[57] of oscillatory reactions on the surfaces of single crystals). Clearly the electronic and catalytic properties depend substantially on the structure of the substrate surface and of the adsorbed layer. From a practical standpoint the surface of greatest interest is that of polycrystalline Pt, which on annealing acquires a (111) texture. This fact accounts for the significant interest in studying the adsorption of CO and the joint adsorption of CO and oxygen on specifically the Pt(111) surface.[58–67]

For simulation of the catalytic reaction of CO oxidation on the platinum surface the Monte Carlo method with the ZGB algorithm, proposed by Ziff, Gulary, and Barshad,[68] is widely used. This mechanism consists in the following: 1) in accordance with the relative concentration of the gas in the mixture the choice of a candidate for adsorption—CO or O_2—is made; 2) an unoccupied adsorption center is selected at random and is filled in the case of CO adsorption or is filled together with an adjacent unoccupied adsorption center in the case of oxygen adsorption; 3) in the case when the CO molecule and an O atom occur in adjacent adsorption centers on the surface, a reaction takes place between them (with the instantaneous evaporation of CO_2), and both adsorption centers become unoccupied. The results of a calculation in this model give a strictly bounded region of relative pressures of CO in which a reaction is possible: $P_{CO}/P_{O_2}=0.39-0.53$. To the left of this region the model predicts poisoning of the surface by oxygen, and to the right, by CO. Experimentally, however, poisoning of the platinum surface by oxygen is not observed, and the degree of suppression of the reaction because of CO adsorption is strongly temperature dependent.

Thus the given algorithm has a number of important shortcomings, and for that reason several refined versions have been proposed to take into account the parameters of the diffusion, desorption of CO, and lateral interactions in the system.[69–72]

In Refs. 70 and 72 the Monte Carlo method was used to investigate the influence of desorption and diffusion of CO molecules on the characteristics of the hysteresis in the CO oxidation reaction. In particular, it was shown that the diffusion of CO leads, on the one hand, to separation of the unoccupied pairs of adsorption sites needed for adsorption of oxygen, and thereby decreases its adsorption probability. On the other hand, diffusion increases the probability of the CO_2 formation reaction, which leads to a decrease of the amount of oxygen on the surface. In addition, the presence of diffusion leads to significant broadening of the hysteresis loop in the dependence of the reaction rate on the CO partial pressure. The presence of CO desorption is also one of the mechanisms that empty the adsorption sites for subsequent adsorption of reactants, and the increase of the CO desorption probability leads to narrowing of the hysteresis loop.

It should be noted that the factors listed still do not avoid the oxygen poisoning of the surface that is obtained in the ZGB model. For this reason the algorithm used to describe the adsorption kinetics was substantially modified in Ref. 67. As a result, the dependence of the CO oxidation reaction rate on Pt(111) on the relative pressure of CO was found to be in good agreement with experiment for the entire range of relative pressures of the reactants. The influence of lithium adsorption on the course of the CO oxidation reaction on the Pt(111) surface was investigated in that paper. It was shown that because of their small size, Li adatoms occupy the active centers on the surface, leading to an effective decrease of its area. At the same time, the possible enhancement of oxygen adsorption at low Li coverages is small because of the small value of the dipole moment of the adatoms. At close to monolayer coverages, when the mutual depolarization of the dipoles causes metallization of the adsorbed Li layer, the rate of oxygen adsorption decreases rapidly, as a result of which the oxidation reaction is suppressed. The validity of this qualitative explanation of the role of Li in the reaction has been confirmed by Monte Carlo simulation of the reaction with the use of the ZGB model. Besides desorption and diffusion of the CO molecules, the probability of oxygen adsorption was also taken into account in the model, by the introduction of an initial sticking coefficient taken from experiment. In contrast to the usual way of modeling the desorption probability,[68,72,73] in this model an attempt at desorption was made whenever there was no attempt at adsorption because the site was occupied. Thus an implicit description of the growth of desorption with increasing degree of coverage is achieved. Incorporation of a sticking coefficient as well as desorption and diffusion made it possible to obtain good agreement between the calculated and experimental dependence of the reaction rate on the relative pressure of CO (Fig. 7). Here it should be noted that the calculated position of the maximum rate agrees with the experimentally observed rate at $T=480$ K, a feat that had not been achieved previously in a simulation of the reaction on the Pt(111) surface.[72]

The adsorption of alkali metals was incorporated in the simulation with the assumption that they occupy the same adsorption sites as CO and O. The influence of an alkali metal on the adsorption of oxygen is described by a corresponding change of the initial sticking coefficient. The results of the simulation for different Li coverages are presented in Fig. 7. Despite the increase of the initial sticking coefficient for oxygen in the presence of Li, which leads to a shift of the reaction rate maximum to higher CO relative pressures, the reaction rate falls off rapidly with increasing Li coverage. Thus it was shown[67] that the influence of Li on CO oxidation on the Pt(111) surface presupposes the existence of two competing effects: the increase of the sticking coefficient for oxygen (aiding the reaction) and, on the other hand, a decrease of the number of adsorption centers, which leads to a decrease of the CO and oxygen adsorption probabilities.

Nevertheless, in all the studies mentioned on the subject

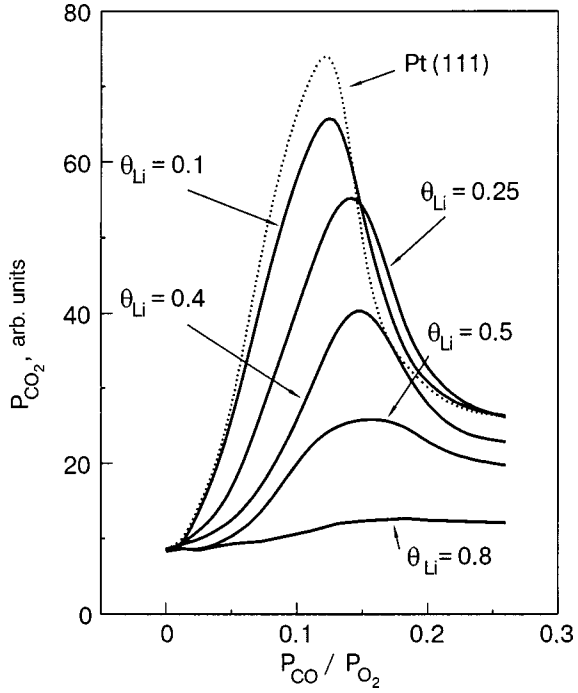

FIG. 7. Results of a simulation[67] of the CO oxidation reaction on the Pt surface in the presence of Li at a temperature of 480 K. P_{CO_2}, P_{O_2}, and P_{CO} are the partial pressures of the components in the gas phase, θ_{Li} is the degree of coverage by Li on Pt(111).

of simulation of the CO oxidation reaction on the platinum surface it was impossible to obtain the correct values of the maximum coverages in the limiting cases of separate adsorption of oxygen or CO. Consequently, the algorithm used in simulation of the reaction is in need of further refinement, which can be achieved with a more realistic description of both the lattice of adsorption centers on the surface and the lateral interaction between molecules.

4. STRUCTURE FORMATION AND ADSORPTION KINETICS OF CO ON Pt(111)

The CO film structures formed at different coverages on Pt(111) have been investigated in a number of studies and, it would seem, the basic rules governing adsorption and the sequence of structures formed with increasing coverage should be well established. For example, it was found by Ertl *et al.*[58] that at coverage $\theta=1/3$ a $(\sqrt{3}\times\sqrt{3})R30°$ structure is formed. This structure is observed only at reduced temperatures (170 K)[59] and is practically absent at room temperature.[58,59] However, it is stated in Ref. 60 that the diffuse reflections of the $(\sqrt{3}\times\sqrt{3})R30°$ structure, which is observed at 100 K even at considerably lower coverages, are split and actually correspond to a more complex film structure.

At $\theta=0.5$ a diffraction pattern (Fig. 8) corresponding to a well-ordered structure of the CO film on Pt(111) is observed even at room temperature. The observed diffraction pattern is usually interpreted,[59–65] following Ref. 58, as the formation of $c(4\times2)$ structure of the adsorbed film. It should be noted that similar diffraction patterns for CO on the similar surface Cu(111) were interpreted in Ref. 74 as the formation of the $(1.5\times1.5)R18°$, which corresponds to the

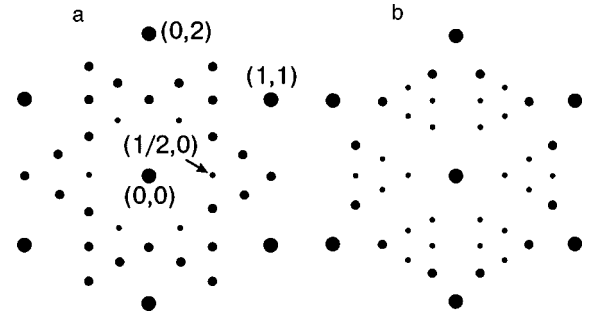

FIG. 8. Diagrams of the arrangement of reflections on the diffraction patterns for CO on Pt(111) at $\theta=0.5$ (a) and 0.6 (b).[58,59] The different diameters of the circles correspond to different intensity of the reflections.

stoichiometric concentration $\theta=0.44$. On the Ni(111) surface[75–81] at coverage $\theta=1/3$ the $(\sqrt{3}\times\sqrt{3})R30°$ structure forms, as on Pt(111), and for $\theta=0.5$ the $c(4\times2)$ structure, but upon further increase in coverage the CO film takes on the structure $(\sqrt{7}/2\times\sqrt{7}/2)R19.1°$, which differs from the structure observed on Pt(111) (see Fig. 8). The $(\sqrt{3}\times\sqrt{3})R30°$ structure is also observed in the adsorption of CO on the hexagonal faces Rh(111) (Refs. 29, 82, and 83) and Ru(0001) (Refs. 84 and 85).

Since the Pt(111) surface has a hexagonal structure, the structure of the adsorbed films is usually also designated in terms of the size and orientation of the experimental lattice with respect to the substrate.[58,82] In a number of cases, however, a rectangular cell can be chosen in the adsorbed layer, and then it is more convenient to use a notation in which the size of the unit cell and the number of particles in it are indicated explicitly.[78] Thus another notation for the structure $c(4\times2)$, which contains two CO molecules in the unit cell ($\theta=0.5$), is $c(2\times\sqrt{3})rect$ [under the condition that the CO molecules at the center of the rectangular unit cells of size $2a\times\sqrt{3}a$] or $(2\times\sqrt{3})rect$-2CO. In these systems of notation the structure of a CO film on Pt(111) at $\theta=0.6$ (the maximum stable coverage for this system at a temperature of 160 K)[59] is characterized as $c(5\times\sqrt{3})rect$-3CO.

There is also disagreement[48,59,74–80] as to the type of adsorption centers occupied by CO molecules at different coverages on Pt(111) and Ni(111). For example, in some papers it is stated that the CO molecules on Ni(111) occupy positions at the centers of triangles formed by surface atoms,[77] while in other papers[78] it is emphatically argued that the CO molecules lie above substrate atoms and in bridge positions between two surface atoms. The situation with the adsorption of CO on Pt(111) is somewhat more definite in this regard. For Pt(111) the most reliably justified model is apparently one in which the filling of centers with increasing CO coverage occurs in the following order. Below a coverage $\theta=0.33$ adsorption centers corresponding to the on-top position are filled.[59,61–66] With increasing coverage the bridge centers are also filled, and a redistribution of molecules occurs such that at $\theta=0.5$ the number of occupied on-top centers is equal to the number of occupied bridge centers.[59,61,85–87] Such a sequence of filling of adsorption centers follows both from theoretical estimates[62–66] and from the data of a vibrational spectroscopy study[61] of CO on Pt(111).

It is reliably established (see, e.g., the review[57] and references cited therein) that on the Pt(111) surface the CO molecules stand vertically, with the oxygen atom upward, and thus their dipole moments are oriented parallel to each other. The adsorption of CO on Pt(111) causes an initial decrease of the work function,[58,60] i.e., CO acts as an electropositive adsorbate. An estimate by the Helmholtz formula gives a dipole moment $\mu \approx 0.2$ D [the intrinsic dipole moment of the bond in the CO molecule is 0.74 D for a single bond (C–O) and 2.3 D for a double bond (C=O)]. Hence it follows that the lateral interaction between CO molecules will have the character of dipole–dipole repulsion. The presence of repulsion between adsorbed CO molecules is also attested to by the decrease of the heat of adsorption with increasing coverage[58] and also by the a number of theoretical estimates.[62–66,85–87] At the same time, the formation of complex structures in the films and also an analysis[88] of the phase diagrams of the oxidation reaction of CO on Pt(111) indicates the presence of attraction between the adsorbed CO molecules at certain distances between them.[84–87] This long-range attraction is apparently due to the so-called indirect interaction,[89–91] i.e., the interaction of CO molecules via electrons of the substrate. The mutual depolarization of neighboring dipoles with increasing concentration on the surface also leads to a change of the value and character of the interaction, and at small distances between adsorbed molecules the direct exchange interaction between them also becomes important.[63,89–91]

Thus the interaction between adsorbed CO molecules on Pt(111) has a complex, nonmonotonic character and depends substantially on the coverage. In this situation the reliability of the interpretation of experimental data can be improved significantly by the use of mathematical simulations.[48,55,92–97] After a particular character of the lateral interaction is conjectured on the basis of an analysis of the sequence of structures observed in the adsorbed films, the reproduction of these structures in the mathematical simulation can be achieved. For this one should obviously choose the appropriate interaction parameters, which are determined on the basis of the requirement that the properties obtained match those observed in experiment.

4.1. Interpretation of the diffraction patterns for CO on Pt(111)

Whereas the diffraction pattern at a CO coverage $\theta = 0.33$ on Pt(111) or Ni(111) clearly corresponds to the $(\sqrt{3} \times \sqrt{3})R30°$ structure with the CO molecules at equivalent adsorption centers, the interpretation of the patterns for $\theta = 0.5$ and 0.6 (see Fig. 8) is ambiguous and remains in dispute.[58–65] The point of contention is that the position of the reflections is determined by the symmetry of the two-dimensional lattice of the structure, while the distribution of the intensity of the reflections is determined by the position of the molecules in the unit cell. The lattice corresponding to the LEED pattern for $T = 0.5$ can be designated as $c(4\times 2)$ or $(\sqrt{e}\times 2)rect$, but in that case for one atom in the unit cell a coverage $\theta = 0.25$ is obtained. To see that such a structure gives the correct distribution of reflections in the diffraction pattern, one can estimate the relative influence of the low-energy electron reflection:

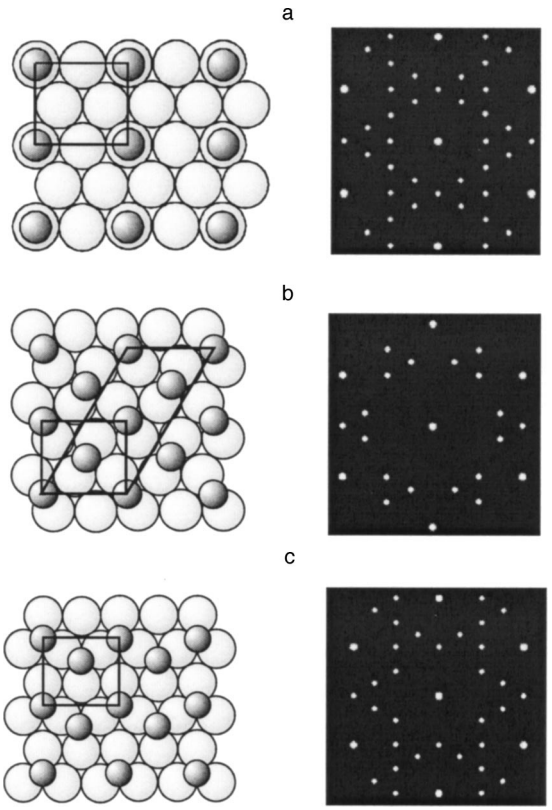

FIG. 9. Position of the atoms in a two-dimensional lattice with component $c(4\times 2)$ ($\theta = 0.25$) and the calculated diffraction pattern for the three equivalent orientations of such a lattice (a). The structure proposed for explaining the diffraction pattern observed[58] in CO films on Pt(111) (b). The structure of CO on Ni(111) proposed in Ref. 77 for $\theta = 0.5$ (c). The large, light circles represent atoms of the metal, and the small, dark circles represent CO molecules.

$$I(h,k) = \left| \sum_n \exp\{2\pi i(hx_n + ky_n)\} \right|^2 \qquad (2)$$

and obtain the simulated diffraction pattern (Fig. 9a). The summation in this formula is over discrete coordinates of the molecules, expressed in fractions of the size of the simulated part of the surface, and h and k denote the coordinates in a two-dimensional reciprocal space. For a hexagonal lattice the strong reflections of electrons is obtained only when the sum of h and k is equal to an even number. By choosing arbitrary values of h and k one can model the intensity distribution on the screen of the LEED display.[93,98,99] Here one can trace the transformations of the patterns during the ordering of the structures and, if the step is chosen small enough, the variation of the width of the reflection upon variation of the size of the islands or the size of the simulated part of the surface (in Ref. 56 a part of the Pt(111) surface containing 36×30 atoms and approximately 100×100 Å in size[99] was chosen, corresponding to the coherence length for the standard LEED device).

An imitation of the LEED patterns was done by the following method. To indicate the brightness the reflections are represented by circles of radius proportional to the relative intensities of the electron reflection estimated by formula (2). For clarity the reflections coinciding with reflections from the substrate are represented by circles of slightly larger diameter.

An important feature of the LEED pattern calculated for the three equivalent orientations of the $c(4\times2)$, or $(2\times\sqrt{3})rect$, structure ($\theta=0.25$) (Fig. 9a), is the equality of the intensities of all 6 additional reflections forming the characteristic triangles. It is expected that the addition of molecules to the unit cell might lead to a decrease of the relative intensity of certain reflections owing to the effect of the structure factor. In particular, the reflection (1/2,0) on the experimental patterns for $\theta=0.5$ is considerably weaker than the other reflections (see Fig. 8), and this property can serve as an indicator of the correctness of the choice of unit cell.

Figure 9b,c shows the structures proposed in Refs. 58, 76, and 77 for explanation of the diffraction patterns observed in CO films on Pt(111) and Ni(111) at $\theta=0.5$ (a diagram of the disposition of the reflections for this pattern is shown in Fig. 8). As is seen in the figure, the diffraction patterns calculated for all three orientations of the lattices are substantially different from those observed in experiment. Because of the location of the CO molecules at the center of the rectangular unit cell,[58] some of the experimentally observed reflections are suppressed by the structure factor and vanish from the pattern. We note that an analogous calculation[77] for this structure for CO and Ni(111) gave exactly the same results, since the diffraction pattern is obviously not affected by a displacement of the adsorbed layer such that the molecules occupy the positions characteristic for Ni(111), at centers with threefold symmetry. Nor is the situation rescued by displacement of the molecules along a symmetry axis of the rectangle—certain reflections vanish, as before. In Ref. 77 these missing reflections were artificially drawn in as if they were reflections appearing as a result of multiple reflection, which cannot be taken into account in the kinematic approximation. However, in the experiments of Refs. 58–60 these reflections were only slightly weaker than the others and can scarcely be due to multiple reflection. In order to obtain a diffraction pattern corresponding to the experimental one at $\theta=0.5$ it is necessary to displace the CO molecules from the symmetric position. To preserve equality of the number of molecules in the two types of adsorption centers, on-top and bridge, it is advisable to consider the movement of molecules from the bridge positions at the center of the cells to the neighboring bridge centers (Fig. 10a). The choice of such centers is dictated by the following considerations. First, symmetry of the unit cell in even one direction inevitably leads to suppression of the corresponding reflection, and therefore the cell should be completely asymmetric. Second, the disposition of two molecules in the on-top position and the bridge center nearest to it is improbable because the minimum distance observed for adsorbed CO molecules (3.2–3.4 Å)[58,59] is considerably greater than the distance between such centers (1.38 Å). Satisfaction of these requirements leads to the situation that when the corner molecules are placed in a rectangular unit cell at on-top centers, the proposed structure of the CO film on Pt(111) for $\theta=0.5$ (Fig. 10a) is actually the only one possible (the disposition of molecules at the other three analogous centers, which corresponds to reflections in the symmetry planes of the rectangle, leads to equivalent unit cells). Each of the three possible orientations of the lattice corresponds to 2 pairwise symmetric unit cells, so that 6 equivalent domains (and not 3, as in the case of a centered cell) contribute to the diffraction pattern. For this reason the calculated diffraction pattern (Fig. 10a) is in excellent agreement with the experimentally observed pattern not only in respect to the distribution of superstructural reflections but also their relative intensities. In particular, reflections of the type (1/2, 0) in the bases of the characteristic triangles turn out to be noticeably weaker than the rest, as is well seen on the experimental patterns for CO on Pt(111) at $\theta=0.5$.[58–60]

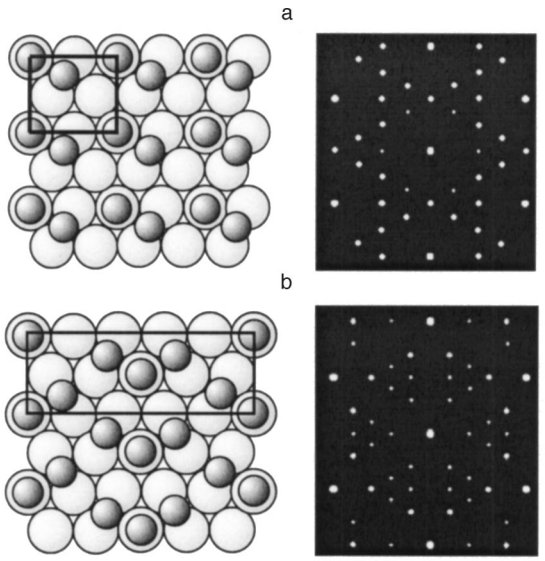

FIG. 10. The $(2\times\sqrt{3})rect$-2CO structure of a CO film on Pt(111) for $\theta=0.5$.[56] The molecules at the corners of the rectangular unit cell are located at on-top centers, while those inside the rectangle are located at bridge positions. There are 6 equivalent domains of this structure which contribute to the diffraction pattern (right-hand panel) (a). The $c(5\times\sqrt{3})rect$-3CO film of CO on Pt(111) for $\theta=0.6$ (b).

Thus the proposed model of the structure of a CO film on Pt(111) at $\theta=0.5$ can explain the observed diffraction patterns without the need for invoking addition assumptions involving multiple reflection. The correctness of the choice of asymmetric unit cell is also indicated by recent STM observations for the similar system CO on Ni(111) at $\theta=0.5$. The STM patterns presented in Ref. 78 clearly reveal the asymmetry of the unit cell, although the authors interpret it as the symmetric cell structure $c(4\times2)$, explaining the asymmetry as instrumental distortions.

At a degree of coverage $\theta=0.6$ the diffraction pattern observed in experiment is obtained by adding the contributions from the six domains of the $c(\sqrt{5}\times\sqrt{3})rect$-3CO structure, illustrated in Fig. 10b. The CO molecules at the center and corners of the rectangular unit cell are located in on-top adsorption centers, while the rest are in bridge positions. Interestingly, this structure of the CO film on Pt(111) at $\theta=0.6$ is observed by the addition of a third molecule to the characteristic pair of molecules at a distance $a\sqrt{3}/2$.

4.2. Monte Carlo simulation of the ordering of a structure

At first glance it seems that the dipole–dipole interaction between adsorbed molecules is in itself sufficient to bring about the formation of the $(\sqrt{3}\times\sqrt{3})R30°$ structure, since this structure is most rarefied at $\theta=0.33$. However, the small value (0.2 D) of the dipole moment μ estimated from the

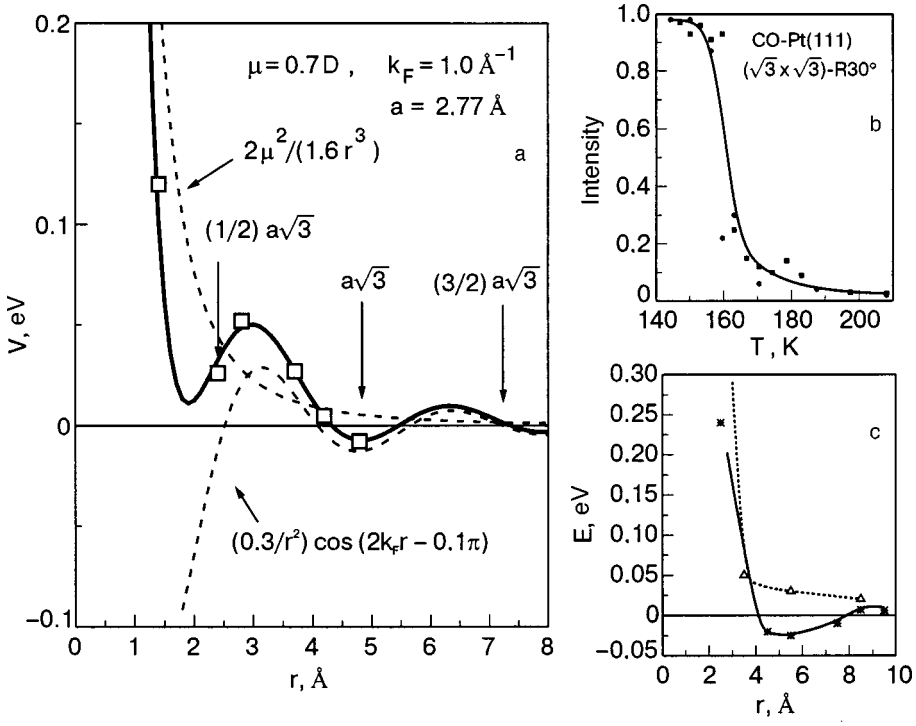

FIG. 11. Dependence of the model lateral interaction potential on the distance between CO molecules on the Pt(111) surface. The effective potential is constructed by adding together the dipole–dipole and an oscillatory indirect interaction. The symbols show the values of the interaction parameters obtained in the simulation (a). The temperature dependence of the intensity of a diffraction peak for the $(\sqrt{3}\times\sqrt{3})R30°$ structure[56] (b). The energies of the lateral interaction for CO on Pt(111), calculated in Ref. 63 (c).

initial decrease of the work function[58] turns out to be insufficient to account for the stability of the structure at 160 K, which is clearly seen in experiment. The disordering of the structure occurs at a temperature at which the energy kT of the fluctuations is of the order of the energy of the lateral interaction per particle. According to the results of the simulation, to obtain an order–disorder phase transition in the $(\sqrt{3}\times\sqrt{3})R30°$ structure at a temperature of 170 K it is necessary to postulate the presence of a dipole moment of around 2 D, which is much greater than the experimental value. This means that even at low coverages the interaction between adsorbed molecules has a more complex character. Since the $(\sqrt{3}\times\sqrt{3})R30°$ structure in CO films on Pt(111) is also observed[59] at $\theta=0.27$, this is indicative of island growth of the structure, apparently due to the attraction between CO molecules at distances $c=a\sqrt{3}$. It is important to note that the distance $c=a\sqrt{3}$, corresponding to the lattice constants for the $(\sqrt{3}\times\sqrt{3})R30°$ structure, is preserved at the transition from one structure to another. Indeed, this same value is shared by the height of the triangle formed by molecules at the on-top centers in the $(2\times\sqrt{3})rect$-2CO and $c(5\times\sqrt{3})rect$-3CO structures, which correspond to coverages $\theta=0.5$ and $\theta=0.6$. The presence of a quantity $(c=a\sqrt{3})$ conserved in the structural transformations indicates that it is favorable for the molecules to lie at such a separation, i.e., it implies the existence of a local minimum of the lateral interaction potential.

The denser structures $(2\times\sqrt{3})rect$-2CO and $c(5\times\sqrt{3})rect$-3CO, which have lower symmetry than the surface, also inevitably presuppose the presence of a complex interaction that depends nonmonotonically on the distance between molecules.[62–64,85–87] At larger distances between molecules the effective attraction can come about only through indirect interaction.[89–91] The indirect interaction potential oscillates with distance r between molecules, the period of the oscillations being determined by the Fermi wave vector k_F:

$$V=Cr^{-n}\cos(2k_Fr+\delta). \tag{3}$$

The asymptotics of the interaction is determined by the parameter n, which depends on the shape of the Fermi surface and the presence of bands of surface states crossing E_F. In the latter case $n=2$ and the indirect interaction is quite efficient.[91,100] Starting from the value of the modulus of the Fermi wave vector averaged over directions, $k_F\approx 1$ Å^{-1}, one can estimate the period of the Friedel oscillations as $T=\pi/k_F\approx 3.1$ Å. We assume further that the attraction between CO molecules at a distance of $a\sqrt{3}$ is due to the minimum of the indirect interaction potential. This determines the choice of the initial phase, and for $\delta=-0.1\pi$ the second minimum of the potential will be at a distance of $a\sqrt{3}$ from a molecule located at the coordinate origin (Fig. 11). It should be emphasized that here the first minimum lies at a distance close to $a\sqrt{3}/2$, which agrees with the distance between nearest-neighbor molecules in the structures $(2\times\sqrt{3})rect$-2CO and $c(5\times\sqrt{3}3)rect$-3CO proposed for explaining the diffraction pattern at $\theta=0.5$ and $\theta=0.6$, respectively (see Fig. 10). We also note that the distance to the center of the rectangular cell, 3.66 Å, corresponds to a maximum of the indirect interaction potential, that can explain why the structure with the centered unit cell is energetically unfavorable and, consequently, does not form. Assuming that the lateral interaction between adsorbed CO molecules can be divided conventionally into a dipole–dipole (direct) and an indirect part, one can represent the result of their addition graphically as in Fig. 11a. The dipole–dipole repulsion between molecules smoothes out the first minimum of the potential somewhat at a distance $a\sqrt{3}/2$. This is apparently determined, in turn, by the absence of structures denser than $(\sqrt{3}\times\sqrt{3})R30°$ at $\theta=0.33$. Thus the lateral interaction at θ

$=0.33$ in the model adopted here is described by dipole–dipole repulsion with energy $2\mu/r^3$ (Ref. 90) and by the indirect interaction of the potential (3). For estimating the absolute values of the parameters of these interactions with the aid of a Monte Carlo simulation, one can use the data on the disordering of the $(\sqrt{3}\times\sqrt{3})R30°$ structure with increasing temperature. For example, at $T=160$ K this structure is distinct and apparently well ordered,[59] while for $T=170$ K the brightness of the reflections is somewhat lower,[58] indicating a partial disordering, and at $T=300$ K this structure is essentially no longer visible for CO on Pt(111).[58] The values of the interaction parameters chosen for the simulations of the structure formation are shown by the symbols in Fig. 11a, and the calculated temperature dependence of the intensity of the diffraction peak for the $(\sqrt{3}\times\sqrt{3})R30°$ structure for those values is shown in Fig. 11b. As is seen in the figure, the values of the interaction parameters for different distances between CO molecules on Pt(111) are well described by the sum of the dipole–dipole and indirect interactions for $\mu=0.7$ D and $C=0.3$ eV·Å^2.

As we have said, the sequence of filling of the adsorption centers with increasing CO coverage on Pt(111) attest to the advantage of the on-top centers. It is natural to assume that these centers are energetically more favorable than the bridge centers, because of the different energy of the adsorption bond for the CO molecules in these two types of centers. According to estimates made in Ref. 86 on the basis of quantum-mechanical calculations by the electron density functional method for different configurations of the clusters, the binding energy of a CO molecule with the Pt(111) surface in the on-top position is 1.64 eV, which is close to the experimental value 1.5 eV.[60] In the bridge position the binding energy is somewhat smaller, as is obvious from the fact that at low coverages the molecules occupy only on-top centers, and the difference in energy can be estimate only crudely as some hundredths of an electron-volt.[58,63] The presence of two types of adsorption centers on the surface permits one to use a modified lattice gas model in which the difference of the energies of the particles in sites of different types is taken into account (the energy benefit obtained when a CO molecule moves from a bridge to an on-top position was taken equal to 0.01 eV[56]).

Starting from the arguments adduced above, we chose for the simulation of the ordering of the adsorbed layer a matrix contains 72 rows and 120 columns for description of the two types of adsorption centers, which corresponds to a simulated piece of the Pt(111) surface approximately 100 $\times 100$ Å in size. This size of the simulated region approximates the coherence length of electrons for the standard LEED device and is therefore convenient for comparison of the simulated LEED patterns with the experimental ones, and it gives satisfactory statistics upon averaging over the particle distributions obtained after thermodynamic equilibrium is reached. It is assumed that the chosen part of the surface simulates an infinite Pt(111) surface, and so periodic boundary conditions were imposed.

The ordering procedure[56,68–70,93,94] is carried out as follows. First the particles were distributed randomly over adsorption centers, creating a specified coverage, and then, with a probability $\exp(-\Delta E/k_BT)$, a randomly chosen particle is moved to a neighboring adsorption center. The energy difference is calculated with allowance for the lateral interaction and the difference of the adsorption energies at the two types of centers. If the move is energetically favorable ($\Delta E<0$) or is the probability $\exp(-\Delta E/k_BT)$ is greater than a random number from the range (0–1), then the move is made. Otherwise the particle remains at the initial center. The number of moves made on average per particle is tallied. After 15–20 such moves, thermodynamic equilibrium is established in the system (corresponding to a minimum of the free energy; the total energy fluctuates about a minimum value that depends on temperature). If the temperature is below the temperature of the order–disorder transition, then domain structures corresponding to the chosen concentration are formed in the film, while at higher temperatures the film is disordered. Since the probability of a particle displacement is determined by the ratio $\Delta E/k_BT$, the values of the interaction parameters can be chosen so as to make the transition temperature match that observed in experiment (by the LEED method). Thus one can determine the numerical values of the parameters used in the simulation.

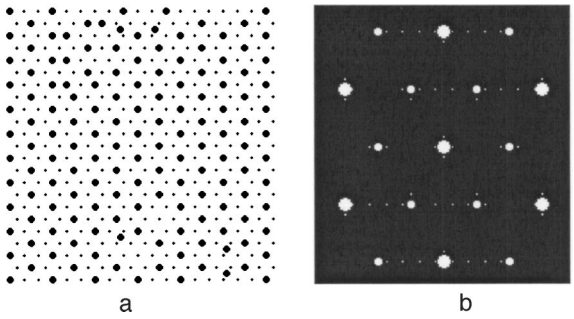

FIG. 12. Typical equilibrium distribution of particles on the model surface (a "snapshot") obtained at $\theta=0.33$ at a temperature below the disordering temperature[56] (a). The diffraction pattern calculated in the kinematic approximation agrees with the experimentally observed LEED pattern[58] at a temperature of 170 K (b).

Figure 12 shows a typical equilibrium distribution of the particles over the model surface (a snapshot) at a coverage $\theta=0.33$ and temperature 160 K, i.e., below the ordering temperature. The formation of a $(\sqrt{3}\times\sqrt{3})R30°$ domains structure with characteristic point defects (due to fluctuations) is clearly seen. The overwhelming majority of the particles occupy on-top adsorption centers, in agreement with the experimental data for CO on Pt(111). The diffraction pattern calculated in the kinematic approximation (according to formula (22)) is also in good agreement with the observed LEED pattern for this CO coverage at a temperature of 170 K.[58]

It is important to emphasize that the simulation of the $(\sqrt{3}\times\sqrt{3})$ structure formation was done with the parameter values obtained from summing the dipole–dipole and indirect interaction potentials (see Fig. 11a). The parameter values shown by the symbols were also used in a simulation of the disordering of this structure (Fig. 11b) followed by the formation of denser structures at coverages of 0.5 and 0.6. The energies of the lateral interaction found in this way are in excellent agreement with the data of quantum-chemistry calculations from first principles[63] for the interaction energies between CO molecules at definite adsorption centers for

different distances between them (Fig. 11c). Here it should be noted that to explain the nonmonotonic[62] lateral interaction and the attraction between molecules at characteristic distances of 5–6 Å it is not necessary to invoke ternary interactions, as had previously been considered unavoidable.[63]

Apparently the ternary interactions become important in the formation of the $(2\times\sqrt{3})rect$-2CO structure. As is seen in Fig. 11a, the first (local) minimum of the pair interaction potential can lead to the formation of the characteristic pairs of molecules for this structure, which lie at different adsorption centers a distance $a\sqrt{3}/2$ apart. Clearly this position of the molecules, which probably coincides with the smallest possible distance between them, should lead to a redistribution of the electron density in the system. This may involve the partial depolarization of the dipoles and the corresponding changes in the parameters for the screening by substrate electrons. In this situation one would hardly expect that the indirect interaction potential created by a given pair on the surface would correspond to the sum of potentials formed by individual molecules.

In our study the ternary interaction was taken into account in the following way. In the direction along the pair of molecules the potential is assumed to be weakened (this was simulated by turning on an attraction due to the indirect pair interaction potential at a distance of $a\sqrt{3}$, and thus the interaction anisotropy arising in the formation of the $(2\times\sqrt{3})rect$-2CO structure can be described in a natural way. As a result of the ordering of the film after approximately 30 displacements per particle, domains of this structure form, with a definite orientation of the lattice with respect to the Pt(111) surface (a small part of the simulated surface is shown in Fig. 13). It is probably the ternary interaction that leads to the formation of the domains of the $(2\times\sqrt{3})rect$-2CO structure with the same definite arrangement of the molecules in the rectangular unit cells as is seen in the STM images[78] for such a structure of CO on Ni(111).

Indeed, in considering an individual unit cell it seems obvious that four similar structures with the same energy (and, hence, the same probability of formation) can be formed, namely, the given structure and the three structures obtained by reflection in the planes passing through the centers of the sides of the rectangular unit cell. The structures obtained by successive reflection in both planes (or by a 180° rotation about the center of the cell) are pairwise equivalent in the sense that they produce the same diffraction pattern (see Fig. 13), but the presence of other symmetric pairs of structures leads to a decrease of the intensity of certain reflections.

Thus the formation of domains of one orientation of the structure $(2\times\sqrt{3})rect$-2CO requires the formation of initial nuclei of that orientation, ''turning on'' the ternary interactions. In the simulation such nuclei can be formed in a random manner (as was done in the case of the formation of the domains of the $(2\times\sqrt{3})rect$-2CO structure), shown in Fig. 13) or can be specially introduced, imitating defects of a real surface. The diffraction pattern contains averaged information about a rather large part of the surface, with a size of the order of the electron beam diameter, within which several parts of area 100×100 Å with different orientations of the

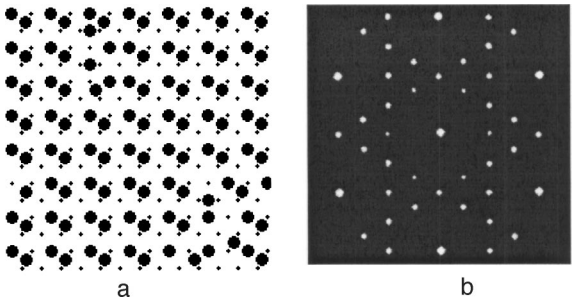

FIG. 13. Results of a simulation of the formation of the $(2\times\sqrt{3})rect$-2CO structure: the equilibrium distribution of particles at a temperature of 300 K (a) and the diffraction pattern corresponding to it[56] (b).

domains of the $(2\times\sqrt{3})rect$-2CO structure move about freely. Domains of this size are entirely sufficient to form a rather sharp diffraction pattern, which is obtained as a result of summing the contributions from structures with different orientations with respect to the three equivalent directions on the Pt(111) surface (Fig. 13).

4.3. Kinetics of CO adsorption on Pt(111)

The most important disagreement between the results of the simulation of the CO oxidation reaction on the platinum surface with experiment remains the value of the limiting coverage ($\theta=1$) obtained with the use of the ZGB algorithm[68–72] for CO adsorption in the absence of oxygen. Apparently the reason for this may be inadequate account of the lateral interaction between CO molecules and also the extremely simplified description of the surface as a lattice of adsorption centers of one type. Both of these shortcoming have been eliminated in a model proposed in Ref. 56, which holds forth the hope of a more correct description of the kinetics of CO adsorption on Pt(111).

A method of simulating the adsorption of gases in real time is described in detail in Ref. 45 and discussed above, and we shall therefore discuss only the details which are important for the kinetics of CO adsorption on Pt(111). At a fixed CO pressure the flux of particles to the surface is estimated by the Hertz–Knudsen formula and is expressed in fractions of a monolayer (i.e., the degree of coverage under the condition that the sticking coefficient S is equal to 1) per second. This allows one to express the exposure used in the simulation in langmuirs and to compare directly the adsorption isobars obtained with those observed in experiment.

The initial sticking coefficient of CO on Pt(111) was taken equal to 0.9 in accordance with experiment.[101,102] This is described in the simulation by an adsorption probability of 0.9 at a randomly chosen center on the clean surface (when the lateral interaction has not yet appeared, and all the centers are unoccupied). The role of extrinsic precursor states is also taken into account: a molecule striking the surface at an occupied center can be adsorbed at an unoccupied neighboring center.

After the adsorption has gone on for a certain time an ordering of the film occurs in the manner described in the previous Section, and then the desorption of molecules is simulated. Here it is assumed that the probability of desorption is determined by the Polanyi–Wigner equation with an

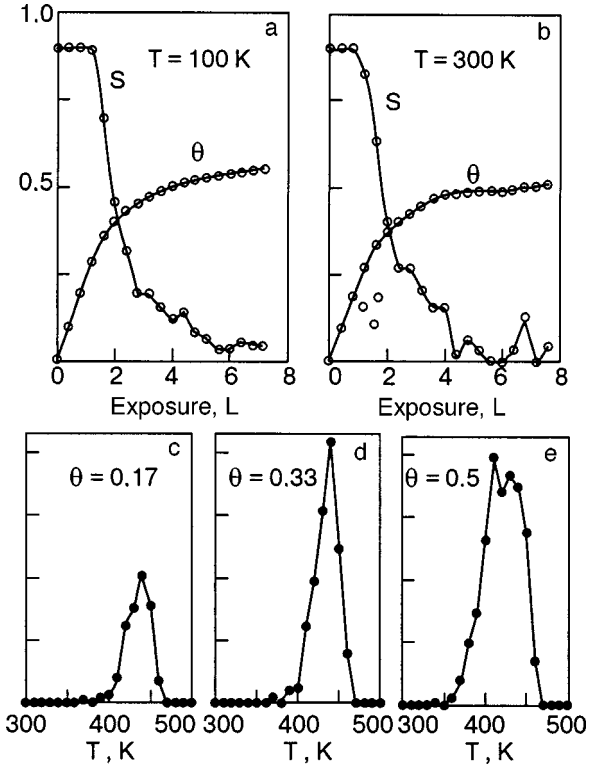

FIG. 14. Calculated dependence of the sticking coefficient S and degree of coverage θ on the exposure (a,b), and the TPD spectra[56] for CO on Pt(111) obtained for different initial degrees of CO coverage (c,d,e).

activation energy that depends on the lateral interaction of the molecules.[45,102] In the description[45] of the kinetics of adsorption of molecular hydrogen on W(110) this algorithm demonstrated its ability to reproduce correctly both the dependence of the sticking coefficient on the coverage and the limiting coverages at different temperatures. The resulting dependence of the sticking coefficient S and coverage θ on the exposure for CO on Pt(111) is shown in Fig. 14. As in experiment,[58,60,101,102] at low coverages the sticking coefficient is practically constant, attesting to the important role of extrinsic precursor states and the correctness of their description in the model used. As the coverage grows, S rapidly decreases, primarily because of the lateral interaction between adsorbed CO molecules and also the decrease of the number of unoccupied centers. As a result of the establishment of dynamic equilibrium, the CO coverage equals approximately 0.5, and for $T=300$ K it remains practically unchanged with time, while in the case of adsorption on a cooled surface ($T=100$ K) it continues to increase slowly, tending toward a value of around 0.6.

Using the standard Monte Carlo technique for simulating the temperature dependence of the desorption rate,[45,55,96] for the same kinetic parameters and interaction energies one can to good accuracy reproduce the spectrum observed[60] by temperature programmed desorption for CO on Pt(111) (Fig. 14). To facilitate comparison with experiment[60] the adsorption was simulated at $T=100$ K and was stopped after a a specified coverage (0.17, 0.33, and 0.5) was reached, whereupon the substrate temperature was increased linearly at a rate of 15 K/s. At $\theta=0.17$, when the lateral interaction as yet has practically no effect on the heat of adsorption, the maximum on the TPD spectrum occurs at $T=480$ K. At larger coverages the lateral interaction, which is on average repulsive, becomes substantial and leads to a shift of the start of desorption to lower temperatures (Fig. 14), in good agreement with experiment.[60]

The temperature dependence of the limiting coverage obtained in the simulation is in good agreement with that observed experimentally for CO on Pt(111).[58–60,101,102] The kinetic parameters used in the simulation (desorption activation energy $E_d=1.2$ eV at a frequency factor $\nu=10^{13}$ s^{-1}) also agree with those estimated in Refs. 58, 60–65, and 102.

5. STRUCTURE FORMATION AND ADSORPTION KINETICS OF OXYGEN ON Pt(111)

In the temperature range 25–150 K oxygen is adsorbed on the Pt(111) surface in molecular form, occupying adsorption sites with bridge type symmetry. The desorption peak of molecular oxygen is observed at 140–150 K, in agreement with the desorption activation energy ~0.36–0.38 eV.[104] Desorption of oxygen occurs from this molecular precursor state at a temperature above 150 K. First-principles calculations of the desorption energy with the use of the VASP code give a value of the barrier in the range 0.3 eV,[105] 0.38 eV,[106] 0.43 eV,[107] and, for different configurations of the position of the oxygen molecule relative to the Pt(111) surface, 0.3–1.5 eV.[108] Here atomic oxygen is adsorbed at adsorption sites with threefold symmetry and binds strongly with the surface. The TPD spectrum for oxygen displays two peaks: one corresponding to desorption from the molecule phase at a temperature of 140–150 K, and the other corresponding to dissociative desorption from the atomic state in the temperature region 600–1000 K.[60,104,109] Apparently the dissociation of the oxygen molecule near the metal surface is ultimately due to the occupation of the antibonding $2\pi^*$ orbital.[110,111] On the hexagonal face of Pt(111) there are two types of adsorption centers of threefold symmetry, fcc and hcp, and the binding energy of atomic oxygen with the substrate is substantially different for the two types of sites. It is shown in Ref. 112 that the fcc centers are the stabler for the adsorption of oxygen, and the calculated activation energies of diffusion fcc←hcp and fcc→hcp are 0.13 and 0.58 eV, respectively.

The initial sticking coefficient for oxygen on Pt(111) is only 0.06.[113–115] One can alter the sticking coefficient substantially by the adsorption of active atoms and molecules that strongly affect the electron density distribution on the substrate surface. In the adsorption of alkali metals on Pt(111) their partial ionization leads to a redistribution of the electron density and creates local electric fields.[111,116,117] This results in a significant lowering of the potential barrier for chemisorption (the activation energy) and, in a number of cases, the probability of dissociative adsorption of oxygen can reach unity.[118]

It was shown in Refs. 119–124 that the presence of an electronegative adsorbate on the surface leads to a strong decrease in the rate of dissociative adsorption and in the limiting coverage and also to a significant change in the desorption parameters. The linear decrease of the initial sticking coefficient with increasing degree of coverage by an electronegative adsorbate attests to blocking of the mobile

precursor states for dissociative adsorption on the adsorbate-modified surface.[113]

Atomic oxygen on Pt(111) at temperatures in the range 200 K$<T<$350 K forms the ordered structure $p(2\times2)$, corresponding to a coverage of 0.25.[59] The limiting coverage achieved under different conditions of oxygen adsorption ranges from 0.22 to 0.28 ML.[59,125]

In order to obtain the correct value of the limiting coverage for system in a simulation one usually introduces parameters describing the desorption probability,[69,72] which makes it possible to avoid the complete poisoning of the model surface. It should be noted, however, that the oxygen desorption rate from the platinum surface at a temperature of the order of 400 K is negligible, and therefore the introduction of a desorption parameter can scarcely be justified physically; for this reason Sander and Ghaisas[71] have proposed (somewhat artificially) that oxygen requires three unoccupied neighboring sites for dissociative adsorption.

The results of a dynamic Monte Carlo simulation of the adsorption of molecular and atomic oxygen in the temperature range 100–200 K with dissociation, diffusion, and desorption taken into account are reported in Ref. 126. Also taken into account were the presence of a repulsive interaction up to third-nearest neighbors and the preference for adsorption of an oxygen atom at adsorption centers of fcc symmetry. A necessary condition for a molecular-oxygen desorption event is the presence of two unoccupied nearest adsorption centers of threefold symmetry. These conditions lead to a limitation of the possibility of adsorption at large coverages, and the limiting coverage obtained in such a model is 0.26, in good agreement with experiment. However, the experimentally observed $p(2\times2)$ structure could not be obtained in the simulation, probably because of inadequate account of the lateral interaction in the model used.

It should be noted that the observed $p(2\times2)$ structure is extremely rarefied, and for it to form at 300 K it is necessary to have a substantial interaction between adsorbed atoms. What sort of interaction can give rise to the formation of such structures? This lateral interaction might be dipole–dipole repulsion, although simple estimates show that if the formation of the $p(2\times2)$ structure at room temperature were due solely to the dipole–dipole interaction, it would require a dipole moment of the oxygen adatom of 5 D, which is considrably larger than the value of the dipole moment of an oxygen atom on platinum estimated from the change of the work function.[115]

The indirect interaction between adatoms obviously plays an important role in the formation of oxygen structures on Pt(111). In the simulation, however, significant difficulties arise in the choice of initial parameters of the indirect interaction owing to the substantial variation of the electronic structure of the substrate with increasing oxygen concentration on the surface. This effect is due to the significant electronegativity of oxygen. For example, by means of self-consistent calculations of the electrostatic potential on the surface near an adsorbed electronegative atom in the jellium model, it was shown in Ref. 127 that the degree of poisoning of the surface increases with increasing electronegativity. The region in which the electrostatic potential acts is of the order of 3–4 Å, which corresponds to the distance to the third- or fourth-nearest adsorption centers. Interestingly, the self-poisoning of the Pt(111) surface by oxygen does not prevent the adsorption of carbon monoxide, forming a $c(2\times2)$ structure with the CO molecules located at the on-top center in the middle of the cell formed by oxygen adatoms.

The complexity of the interaction between adsorbed oxygen atoms on Pt(111) apparently is the reason why there are still no consistent and physically justified models for the formation of the observed structures. One expects that the solution of this pressing problem will open up new possibilities not only for deepening our understanding of the dissociative adsorption process for oxygen on a transition metal but will also broaden substantially the existing ideas as to the role of different factors in the kinetics of the catalytic reaction of CO oxidation.

6. CONCLUSION

The criteria of applicability and efficiency of a mathematical model include its ability to reproduce the main characteristics of the observed effects and also the degree to which it approximates the conditions of an experiment and the transparency of the results obtained. In this regard the Monte Carlo method of mathematical attempts is particularly well favored, since in many cases it not only makes it possible to explain many of the relationships observed in experiments but also to predict the behavior of the system under new conditions not yet investigated. It should be stressed that the simulation must always be based on firmly established facts, and its results must admit comparison with the data of real (or future) experiments—otherwise the simulation is of little value, since there are no other criteria for assessing the reliability of the results obtained and the conclusions drawn from them.

Examples of the efficient use of the Monte Carlo method for elucidating the properties of adsorption systems include the papers discussed in this review on the simulation of the low-temperature adsorption of hydrogen on W(110) and Mo(110), the adsorption and structure formation of CO films, and the catalytic reaction of CO oxidation on the platinum surface. For example, the model of molecular adsorption involving extrinsic precursor states has been validated and refined by simulations, and the activation energy for desorption of hydrogen molecules on the tungsten surface has been determined; this is important for the development of the theory of gas adsorption.

An important feature of the simulation methods described is the trend toward a detailed (to the degree possible) reproduction of the real conditions of an experiment and the incorporation of the most important factors governing the behavior of the system. This has made it possible to estimate the value and to elucidate the role of the lateral interaction in the establishment of thermodynamic equilibrium between the incident and desorbing fluxes of hydrogen molecules and also, with the aid of a real-time simulation algorithm developed, to propose an alternative explanation of the reason for the radical difference in the dynamics of oxygen adsorption on W(110) and Mo(110).

The use of a complex lattice of adsorption centers and the incorporation of the lateral interaction in the simulation of the formation of CO films on Pt(111) have made it pos-

sible not only to propose a novel (correct, i.e., in agreement with the experimentally observed sequence of diffraction patterns) arrangement of the molecules in the unit cell of the surface structures of CO on Pt(111), but also to obtain numerical values of the parameters of the indirect interaction that leads to the formation of those structures. By using the algorithm for the real-time simulation of the kinetic processes we have been able to obtain a correct value for the limiting CO coverage on Pt(111) and to reproduce the exposure dependence of the sticking coefficient.

The information obtained with the aid of simulations as to the structures of adsorbed CO films on Pt(111) and the parameters of the lateral interaction will obviously be useful for further studies of the catalytic reaction of CO oxidation and will open up new possibilities for a more detailed and realistic description of this reaction with the aid of refined simulation algorithms.

Note added in proof: Monte Carlo simulations using an advanced model for CO oxidation in Pt(111) have recently been carried out by N. V. Petrova and I. N. Yakovkin, Surf. Sci. **578**, 162 (2005).

*E-mail: yakov@iop.kiev.ua

[1]G. J. Kroes, Prog. Surf. Sci. **60**, 1 (1999).
[2]A. Gross, Surf. Sci. **500**, 347 (2002).
[3]S. Wilke and M. Scheffler, Phys. Rev. Lett. B **53**, 4296 (1996).
[4]A. Gross, M. Scheffler, M. J. Mehl, and D. A. Papaconstantopoulos, Phys. Rev. Lett. **82**, 1209 (1999).
[5]A. Gross and M. Scheffler, Phys. Rev. Lett. B **57**, 1293 (1999).
[6]G. Wiesenekker, G. J. Kroes, and E. J. Baerends, J. Chem. Phys. **104**, 7344 (1996).
[7]C. M. Wei, A. Gross, and M. Scheffler, Phys. Rev. Lett. B **57**, 15572 (1998).
[8]J. A. White, D. M. Bird, and M. C. Payne, Phys. Rev. Lett. B **53**, 1667 (1996).
[9]W. Kohn, Surf. Rev. Lett. **1**, 129 (1994).
[10]H. J. Kreuzer, S. H. Payne, A. Drozdiwski, and D. Menzel, J. Chem. Phys. **110**, 6982 (1999).
[11]G. R. Darling and S. Holloway, Surf. Sci. **321**, L189 (1994).
[12]S. Holloway and G. R. Darling, Surf. Rev. Lett. **1**, 115 (1994).
[13]M. Persson and S. Andersson, Surf. Rev. Lett. **1**, 187 (1994).
[14]M. Bonn, A. W. Kleyn, and G. J. Kroes, Surf. Sci. **500**, 475 (2002).
[15]E. Hulpke and J. Ludecke, Phys. Rev. Lett. **68**, 2846 (1992).
[16]B. Kohler, P. Ruggerone, and M. Scheffler, Surf. Sci. **368**, 213 (1996).
[17]B. Kohler, P. Ruggerone, and M. Scheffler, Phys. Rev. Lett. B **56**, 13503 (1997).
[18]Yu. G. Ptushinskiĭ, Fiz. Nizk. Temp. **30**, 3 (2004) [Low Temp. Phys. **30**, 1 (2004)].
[19]V. V. Dvurechenskikh, V. D. Osovskii, Yu. G. Ptushinskii, V. G. Sukretnyi, and B. A. Chuikov, JETP Lett. **54**, 40 (1991).
[20]J. Harris and S. Andersson, Phys. Rev. Lett. B **55**, 1583 (1985); S. Andersson, L. Wilzen, M. Persson, and J. Harris, *ibid.* **40**, 8146 (1989).
[21]W. Friess, H. Schlichting, and D. Menzel, Phys. Rev. Lett. **74**, 1147 (1995).
[22]K. D. Rendulic, G. Anger, and A. Winkler, Surf. Sci. **208**, 404 (1989).
[23]H. F. Berger, C. Resch, E. Grosslinger, G. Eilmsteiner, A Winkler, and K. D. Rendulic, Surf. Sci. **275**, L627 (1992).
[24]D. A. Butler, B. E. Hayden, and J. D. Jones, Chem. Phys. Lett. **217**, 423 (1994).
[25]D. A. Butler and B. E. Hayden, Chem. Phys. Lett. **232**, 542 (1995).
[26]V. D. Osovskii, Yu. G. Ptushinskii, V. G. Sukretnyi, and B. A. Chuikov, JETP Lett. **67**, 959 (1998).
[27]B. A. Chuikov, V. D. Osovskii, Yu. G. Ptushinskii, and V. G. Sukretnyi, Surf. Sci. Lett. **448**, L201 (2000).
[28]B. A. Chuikov, V. D. Osovskii, Yu. G. Ptushinskii, and V. G. Sukretnyi, Surf. Sci. **473**, 143 (2001).
[29]M. Beutl, J. Lesnik, and D. K. Rendulic, Surf. Sci. **429**, 71 (1999).
[30]Ch. Resch, H. F. Berger, K. D. Rendulic, and E. Bertel, Surf. Sci. **316**, L1105 (1994).
[31]D. A. Papaconstantopoulos, *Handbook of the Band Structure of Elemental Solids*, Plenum Press, New York (1986).
[32]Y. Xu and I. I. Fabrikant, Appl. Phys. Lett. **78**, 2598 (2001).
[33]T. O. O'Malley, Phys. Rev. Lett. B **150**, 150 (1966).
[34]P. W. Tamm and L. D. Schmidt, J. Chem. Phys. **54**, 4775 (1971).
[35]K. Christmann, Surf. Sci. Rep. **9**, 1 (1988).
[36]P. Alnot, A. Cassuto, and D. A. King, Surf. Sci. **215**, 29 (1989).
[37]K. D. Rendulic, Surf. Sci. **272**, 34 (1992).
[38]A. Gross, S. Wilke, and M. Scheffler, Phys. Rev. Lett. **75**, 2718 (1995).
[39]M. Kay, G. R. Darling, S. Holloway, J. A. White, and D. M. Bird, Chem. Phys. Lett. **245**, 311 (1995).
[40]H. F. Busnengo, W. Dong, and A. Salin, Chem. Phys. Lett. **320**, 328 (2000).
[41]M. A. Di Cesare, H. F. Busnengo, W. Dong, and A. Salin, J. Chem. Phys. **118**, 11226 (2003).
[42]M. R. Hand and J. Harris, J. Chem. Phys. **92**, 7610 (1990).
[43]H. Schlichting and D. Menzel, Surf. Sci. **272**, 27 (1992).
[44]A. Gross, Surf. Sci. **363**, 1 (1996).
[45]N. V. Petrova, I. N. Yakovkin, and Yu. G. Ptushinskii, Surf. Sci. **497**, 349 (2002).
[46]Yu. G. Ptushinskiĭ and B. A. Chuĭkov, Poverkhnost' **9**, 5 (1992).
[47]N. V. Petrova, I. N. Yakovkin, and Yu. G. Ptushinskii, Eur. Phys. J. B **38**, 525 (2004).
[48]V. D. Osovskii, Yu. G. Ptushinskii, V. G. Sukretnyi, and B. A. Chuikov, JETP Lett. **60**, 569 (1994).
[49]V. D. Osovskii, Yu. G. Ptushinskii, V. G. Sukretnyi, and B. A. Chuikov, Low Temp. Phys. **23**, 587 (1997).
[50]H. Schlichting, D. Menzel, T. Brunner, and W. Brenig, J. Chem. Phys. **97**, 4453 (1992).
[51]M. Head-Gordon, J. C. Tully, H. Schlichting, and D. Menzel, J. Chem. Phys. **95**, 9266 (1991).
[52]V. D. Osovskiĭ, Yu. G. Ptushinskiĭ, V. G. Sukretnyi, and B. A. Chuĭkov, Fiz. Nizk. Temp. **27**, 1138 (2001) [Low Temp. Phys. **27**, 843 (2001)].
[53]C. M. Chan, R. Aris, and W. H. Weinberg, Appl. Surf. Sci. **1**, 360 (1978).
[54]J. L. Taylor and W. H. Weinberg, Surf. Sci. **78**, 259 (1978).
[55]B. Meng and W. Y. Weinberg, J. Chem. Phys. **100**, 5280 (1994).
[56]N. V. Petrova and I. N. Yakovkin, Surf. Sci. **519**, 90 (2002).
[57]R. Imbihl, Prog. Surf. Sci. **44**, 185 (1993).
[58]G. Ertl, M. Neumann, and K. M. Streit, Surf. Sci. **64**, 393 (1977).
[59]P. R. Norton, J. A. Davies, and T. E. Jackman, Surf. Sci. Lett. **122**, L593 (1982).
[60]H. Steininger, S. Lehwald, and H. Ibach, Surf. Sci. **123**, 264 (1982).
[61]B. N. J. Persson and R. Ryberg, Phys. Rev. Lett. **40**, 20173 (1989).
[62]D. C. Skelton, D. H. Wei, and S. D. Kevan, Surf. Sci. **320**, 77 (1994).
[63]D. R. Jennison, P. A. Schultz, and M. P. Sears, Phys. Rev. Lett. **77**, 4828 (1996).
[64]R. Brako and D. Sokcevic, Surf. Sci. **401**, L388 (1998).
[65]K. L. Kostov, P. Jakob, and D. Menzel, Surf. Sci. **377–379**, 802 (1997).
[66]F. Debecq, Surf. Sci. **389**, L1131 (1997).
[67]I. N. Yakovkin, V. I. Chernyi, and A. G. Naumovets, Surf. Sci. **442**, 81 (1999).
[68]R. M. Ziff, E. Gulary, and Y. Barshad, Phys. Rev. Lett. **24**, 2553 (1986).
[69]J. Mai, W. von Niessen, and A. Blumen, J. Chem. Phys. **93**, 3685 (1990).
[70]R. Chakarova, Surf. Sci. **389**, 234 (1997).
[71]L. M. Sander and S. V. Ghaisas, Surf. Sci. **391**, 125 (1997).
[72]M. Ehsasi, M. Matloch, O. Frank, J. H. Block, K. Christmann, F. S. Rys, and W. Hirschwald, J. Chem. Phys. **91**, 4949 (1989).
[73]V. K. Medvedev, Yu. Suchorski, and J. H. Block, Appl. Surf. Sci. **76/77**, 136 (1994).
[74]P. Hollins and J. Pritchard, Surf. Sci. **99**, L389 (1980).
[75]K. Chrestmann, O. Schober, and G. Ertl, J. Chem. Phys. **60**, 4719 (1974).
[76]H. Conrad, G. Ertl, J. Kuppers, and E. E. Latta, Surf. Sci. **57**, 475 (1976).
[77]L. Becker, S. Aminpirooz, B. Hillert, M. Pedio, J. Haase, and D. L. Adams, Phys. Rev. Lett. B **47**, 9710 (1993).
[78]Norihito Ikemiya, Toshiaki Suzuki, and Masatoki Ito, Surf. Sci. **466**, 119 (2000).
[79]R. Davis, R. Toomes, D. P. Woodruff, O. Schaff, V. Fernández, K.-M. Schindler, Ph. Hofmann, K.-U. Weiss, R. Dippel, V. Fritzsche, and A. M. Bradshaw, Surf. Sci. **393**, 12 (1997).
[80]L. D. Mapledoram, M. P. Bessent, A. Wander, and D. A. King, Chem. Phys. Lett. **228**, 527 (1994).
[81]L. Surnev, Z. Xu, and J. T. Yates, Jr., Surf. Sci. **201**, 1 (1988).
[82]M. Giere, A. Barbieri, M. A. Van Hove, and G. A. Somorjai, Surf. Sci. **391**, 176 (1997).

[83]D. H. Wei, D. C. Skelton, and S. D. Kevan, Surf. Sci. **381**, 49 (1997).
[84]B. Reidmuller, I. M. Ciobica, D. C. Papageorgopoulos, B. Berenbak, R. A. van Santen, and A. W. Kleyn, Surf. Sci. **465**, 347 (2000).
[85]J. J. Mortensen, B. Hammer, and J. K. Norskov, Surf. Sci. **414**, 315 (1998).
[86]Y. Morikawa, J. J. Mortensen, B. Hammer, and J. K. Norskov, Surf. Sci. **386**, 67 (1997).
[87]Hideaki Aizawa and Shinji Tsuneyuki, Surf. Sci. **399**, L364 (1998).
[88]N. Pavlenko, P. P. Kostrobij, Yu. Suchorski, and R. Imbihl, Surf. Sci. **489**, 29 (2001).
[89]T. B. Grimley, Proc. Phys. Soc. London **90**, 751 (1967).
[90]T. L. Einstein, CRC Crit. Rev. Sol. St. and Mat. Sci. **7**, 261 (1978).
[91]O. M. Braun and V. K. Medvedev, Sov. Phys. Usp. **32**, 328 (1989).
[92]T. T. Tsong, Surf. Sci. **122**, 99 (1982).
[93]J. Kuppers, Vacuum **21**, 393 (1971).
[94]I. N. Yakovkin, Surf. Sci. **282**, 195 (1993).
[95]I. Hasegawa and S. Ino, Phys. Rev. Lett. **68**, 1192 (1992).
[96]B. Lehner, M. Hohage, and P. Zeppenfeld, Surf. Sci. **454–456**, 251 (2000).
[97]K. Fichthorn, E. Gulari, and R. Ziff, Surf. Sci. **243**, 273 (1991).
[98]L. D. Roelofs, R. L. Park, and T. L. Einstein, J. Vac. Sci. Technol. **16**, 478 (1979).
[99]V. K. Medvedev and I. N. Yakovkin, Sov. Phys. Solid State **19**, 1515 (1977).
[100]O. M. Braun, L. G. Ilchenko, and E. A. Pashitsky, Sov. Phys. Solid State **22**, 1649 (1980).
[101]I. N. Yakovkin, V. I. Chernyi, and A. G. Naumovets, J. Phys. D: Appl. Phys. **32**, 841 (1999).
[102]M. Kiskinova, G. Pirug, and H. P. Bonzel, Surf. Sci. **133**, 321 (1983).
[103]C. Puglia, A. Nilsson, B. Hernnas, O. Karis, P. Bennich, and N. Martensson, Surf. Sci. **342**, 119 (1995).
[104]A. Winkler, X. Guo, H. R. Siddiqui, P. L. Hagans, and J. T. Yates, Surf. Sci. **201**, 419 (1988).
[105]T. Li and P. B. Balbuena, J. Phys. Chem. B **105**, 9943 (2001).
[106]J. L. Gland, Surf. Sci. **93**, 487 (1980).
[107]C. T. Campbell, G. Ertl, H. Kuipers, and Segner, J. Surf. Sci. **107**, 220 (1981).
[108]A. Eichler and J. Hafner, Phys. Rev. Lett. **79**, 4481 (1997).
[109]X.-Y. Zhu, S. R. Hatch, A. Campion, and J. M. White, J. Chem. Phys. **91**, 5011 (1989).
[110]A. Zangwill, *Physics at Surfaces*, Cambridge Univ. Press, Cambridge (1986), Mir, Moscow (1990).
[111]M. Kiskinova, *Studies in Surface Science and Catalysis*, Elsevier (1992), Vol. 70, p. 1.
[112]A. Bogicevic, J. Stromquist, and B. I. Lundqvist, Phys. Rev. Lett. **B57**, R4289 (1998).
[113]M. P. Kiskinova, Surf. Sci. Rep. **8**, 359 (1988).
[114]L. Surnev, *Physics and Chemistry of Alkali Metal Adsorption*, Elsevier (1989).
[115]G. Pirug, H. P. Bonzel, and G. Broden, Surf. Sci. **122**, 1 (1982).
[116]J. K. Brown and N. Lunz, Chem. Phys. Lett. **186**, 125 (1991).
[117]J. Norskov, S. Holloway, and N. D. Lang, Surf. Sci. **137**, 65 (1984).
[118]H. P. Bonzel, Surf. Sci. Rep. **84**, 3 (1988).
[119]M. Kiskinova and D. W. Goodman, Surf. Sci. **109**, L555 (1981).
[120]M. Kiskinova and D. W. Goodman, Surf. Sci. **108**, 64 (1981).
[121]D. W. Goodman and M. Kiskinova, Surf. Sci. **105**, L256 (1981).
[122]S. Johnson and R. J. Madix, Surf. Sci. **108**, 77 (1981).
[123]E. I. Ko and R. J. Madix, Surf. Sci. **109**, 221 (1981).
[124]K. D. Rendulic and A. Winkler, Surf. Sci. **74**, 318 (1978).
[125]A. Szabo, M. Kiskinova, and J. T. Yates, Jr., J. Chem. Phys. **90**, 4604 (1989).
[126]D. S. Mainardi, S. R. Calvo, A. P. J. Jansen, J. J. Lukkien, and P. B. Balbuena, Chem. Phys. Lett. **382**, 553 (2003).
[127]N. D. Lang, S. Holloway, and J. K. Norskov, Surf. Sci. **150**, 24 (1985).

Translated by Steve Torstveit

SUPERCONDUCTIVITY, INCLUDING HIGH-TEMPERATURE SUPERCONDUCTIVITY

Boundary line of the transition into the pseudogap state in thulium cuprates

E. B. Amitin,* K. R. Zhdanov, A. G. Blinov, M. Yu. Kameneva, Yu. A. Kovalevskaya, L. P. Kozeeva, and I. E. Paukov

A. V. Nikolaev Institute of Inorganic Chemistry, Siberian Branch of the Russian Academy of Sciences, 3 prosp. Lavrent'eva, Novosibirsk 630090, Russia

(Submitted August 12, 2004; revised November 5, 2004)
Fiz. Nizk. Temp. **31**, 323–326 (March–April 2005)

Precision measurements of the heat capacity of 1-2-3 thulium cuprates with oxygen content ranging from 6.3 to 6.92 were performed in the temperature range 6–300 K. Analysis of the experimentl data showed anomalies in the temperature dependence of the electronic heat capacity. It is conjectured that the anomalies are due to a transition from the normal metallic into the pseudogap state. © *2005 American Institute of Physics.* [DOI: 10.1063/1.1884425]

In memory of E. S. Borovik

1. INTRODUCTION

The many works published in the last few years still leave open the question of why the electron density of states in underdoped cuprates decreases near the Fermi level (see the review Ref. 1 and the references cited there), a phenomenon which has been termed a ''pseudogap.'' The question of whether or not the pseudogap state (PGS) has anything to do with high-temperature superconductivity remains open. In the literature several different models explaining the origin of the PGS are being discussed and the question of the boundaries of existence of the pseudogap state is being examined.[1–3]

Even though various properties of the PGS have been studied in an entire series of investigations it is difficult to say definitively whether or not singularities occur in the thermodynamic properties at the transition through the normal metal-PGS boundary and whether or not the transition into the PGS is a phase transition.[1–3]

Measurements of the heat capacity of yttrium cuprates in a wide range of oxygen content and temperatures have not shown any anomalies, due to a transition into the pseudogap state, in the thermodynamic properties.[4,5] This has served as grounds for believing that a line of phase transitions does not exist[1] and that the pseudogap state is not a thermodynamic phase.

We have performed measurements of the temperature dependence of the heat capacity of the single-phase thulium cuprates $TmBa_2Cu_3O_X$ at temperatures ranging from 6 to 300 K for different values of the oxygen content. Anomalies in the temperature dependence of the electronic heat capacity were found in oxygen-underdoped samples at temperatures of about 210–230 K. These anomalies are attributed to the formation of a PGS.

2. EXPERIMENTAL PART

The standard method of solid-phase synthesis from the oxides Tm_2O_3 (Tm-3 grade), BaO, and CuO (ultrapure grade) was used to obtain $TmBa_2Cu_3O_X$ ceramic samples with different oxygen content ($X=6.92$, 6.7, 6.5, and 6.3). We have described the special features of the heat treatment and oxygen saturation of the samples in Ref. 6.

The $TmBa_2Cu_3O_X$ system was chosen because its content of impurity aluminum, which enters the ceramic during synthesis in corundum crucibles, is ten times lower than that of $YBa_2Cu_3O_X$. X-Ray phase analysis (XPA) showed that all $TmBa_2Cu_3O_X$ samples obtained were nearly single-phase. The main impurity phases, whose content did not exceed 2–3%, were Tm_2BaCuO_5 and $BaCuO_3$. The XPA data showed that the impurity content was independent of the oxygen content. It should be noted that analysis of the structural factors which are sensitive to the uniformity of oxygen distribution (the orthorhombicity parameters and the half-widths of the basal reflections) showed all samples to be highly uniform.

The temperature dependences of the heat capacity of thulium cuprates $TmBa_2Cu_3O_X$ with $X=6.92$, 6.70, 6.50, and 6.30 were invetigated using an automated low-temperature vacuum adiabatic calorimeter. The accuracy of the measurements was $\pm 2\%$ at 6–10 K, 0.5% in the range 10–30 K, 0.2% from 30 to 60 K, and 0.5% from 60 to 310 K. The magnitude of the temperature rise in an individual calorimetric experiment in the temperature range 100–300 K was 5 K. The average variance of the experimental values of the heat capacity according to several series of measurements was about 0.02% for the indicated interval. As temperature decreased, the variance increased up to the order of 1% at 10 K. Three to four hundred calorimetric experiments were performed for each sample. The mass of the samples was about 16 g.

Figure 1 shows the temperature dependences of the heat capacity C_p of four samples with different oxygen content. The heat capacities are close in value. At high temperatures the heat capacity is all the higher the greater the content of oxygen in the sample, and at low temperatures lower values of the heat capacity correspond to higher values of X. The

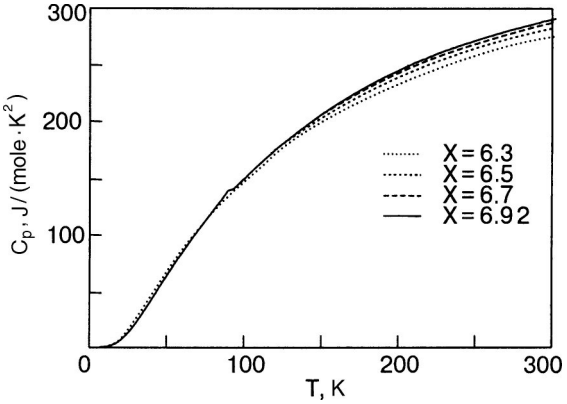

FIG. 1. Temperature dependences of the heat capacity of thulium cuprates $TmBa_2Cu_3O_X$ with different oxygen content X.

differences are due to the lattice and electronic components.

It is quite difficult to identify the anomalous contribution, due to the formation of the PGS, to the electronic heat capacity because the effect is so small. The electronic contribution to the heat capacity in the temperature range of interest to us is only 2–3% of the total heat capacity. The anomalous part is another order of magnitude smaller, 0.2–0.3% of the total value. Such a small anomalous part can be extracted by comparing the heat capacities of the samples. Making such a comparison requires samples which do and do not undergo a transition into the pseudogap state. In addition the electronic components must be compared. The lattice components of the heat capacity of all experimental samples are close but not so close that the difference can be neglected.

The lattice heat capacity was calculated using the phonon density of states. The density of states, in turn, was determined from the calorimetric data. The procedure for doing this is described in detail in Refs. 6 and 7. Since the phonon spectrum determines the heat capacity of a crystal in an integral manner, small uncertainties in the determination of the density of states should not produce large errors when determining the lattice heat capacity. The uncertainty in the calculation of the phonon density of states has only a weak effect on the computed values of the lattice contribution[8] and has no effect on the character of the anomaly in the electronic heat capacity.

The values obtained for the phonon density of states were used to calculate the lattice heat capacity of the samples. The electronic component C_{el} of the heat capacity was determined as the difference between the experimental and computed lattice values (the anharmonic contribution was neglected).

For clarity in presenting the data the values of the electronic heat capacity coefficient $\gamma = C_{el}/T$ were calculated. Figure 2 displays the temperature dependences of the difference of the coefficients $\Delta\gamma = \gamma(X=6.92) - \gamma(X)$ for a sample with oxygen content near optimal doping and for samples in an underdoped state. It was assumed that the pseudogap state does not exist at the point of optimal doping ($X=6.92$), so that the sample with $X=6.92$ is taken as the basal sample. The figure shows weakly expressed anomalies for samples with $X=6.7$ and $X=6.5$ with singularities at $T \approx 220-225$ K (minima in Fig. 2). The positions of the extrema are essentially independent of oxygen content. The anomalies are weak but exceed the experimental variance. No singularities were observed for the sample with $X=6.3$ to within the experimental variance. It should be noted that anomalies cannot be due to the uncertainties in the calculation of the lattice heat capacity. The observed singularities also cannot be due to the anharmonic contribution which was neglected.

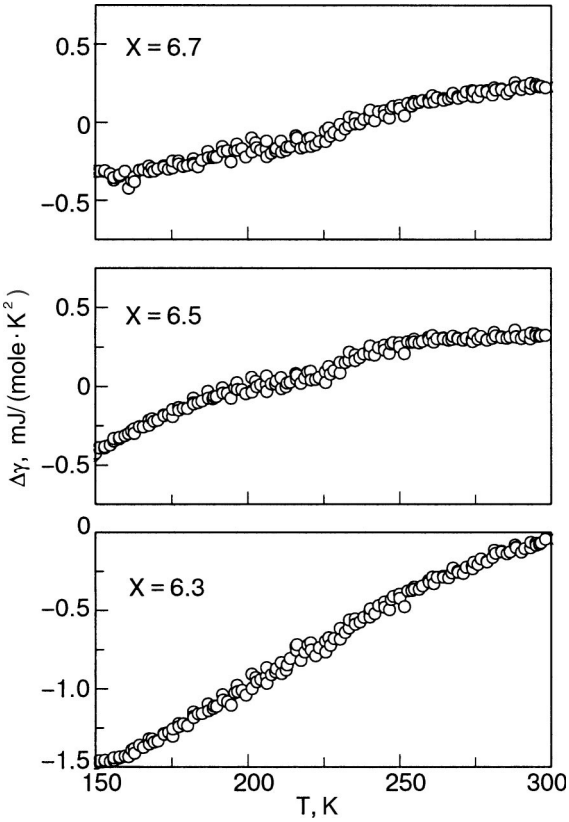

FIG. 2. Temperature dependences of the difference of the electronic heat capacity coefficient of thulium cuprates with different oxygen content X. The basal sample is a sample with oxygen content near the point of optimal doping ($X=6.92$).

3. CONCLUSIONS

The phase diagram of all states in high-temperature superconductors of the 1-2-3 system has not been adequately studied. This concerns especially the boundaries of the pseudogap phase. In theoretical works the diagram is represented, mainly, only schematically. The phase diagram also has not been adequately studied experimentally. The different behavior of the line separating the normal-metal state from the pseudogap state is discussed. Specifically, a possible form of the phase diagram is studied in Ref. 9. The authors propose the existence of two boundary lines—a ''strong pseudogap'' line $T^*(X)$ and a ''weak pseudogap'' line $T^*(X_2)$. The first line is due to the interaction of charge carriers with antiferromagnetic or structural fluctuations of the short-range order.[1] As the tetra-ortho phase transition is approached, the magnetic fluctuations become stronger and the temperature of the transition into the pseudogap phase increases (''strong pseudogap phase'').

The boundary line $T^*(X_2)$ of the transition from a ''strong pseudogap'' to a ''weak pseudogap'' behaves differently—it is essentially independent of the degree of doping.

In Refs. 10 and 11 it is proposed that the line $T^*(X)$ is the line of phase transitions with a change in symmetry in the *d* electron subsystem. A study of the symmetry characteristics of the cuprates investigated near the line $T^*(X)$ could confirm the existence of phase-transition phenomena in this region of the phase diagram.

Anomalies in the temperature dependence of the heat capacity are always associated with phase transitions. Our calorimetric investigations indicate the presence of phase transitions at $X=6.7$ and $X=6.5$ with $T\approx 220$ K and $T\approx 225$ K, respectively. However, the calorimetric data cannot answer the question of the nature of the phase transformations in matter. It can be conjectured that the anomalies in the temperature dependence of the heat capacity are due to a transition from a high-temperature normal phase into a low-temperature pseudogap phase and lie on the interface between phases in the oxygen-content—temperature plane. Only two points are plotted in this phase diagram (no heat-capacity anomalies are found in the sample with $X=6.3$: either because there is no phase transition or the phase transition occurs at a different temperature). Additional investigations of underdoped cuprates with different oxygen content are needed to obtain the complete phase diagram.

This work was supported by a program of the Ministry of Science of the Russian Federation under State Contract No. 40.012.1.1.11.1356.

*E-mail: amit@che.nsk.su

[1] M. V. Sadovskiĭ, Usp. Fiz. Nauk **171**, 539 (2001).
[2] M. Sadovskiy and E. Z. Kuchinski, Physica C **341–348**, 879 (2000).
[3] V. B. Geshkenbein, L. B. Ioffe, and A. I. Larkin, Phys. Rev. B **55**, 3173 (1997).
[4] J. W. Loram, J. L. Tallon, and G. V. M. Williams, Physica C **338**, 9 (2000).
[5] J. W. Loram and J. L. Tallon, Physica C **349**, 53 (2001); ArXiv: cond-mat/0005063.
[6] E. B. Amitin, K. R. Zhdanov, M. Yu. Kameneva, Yu. A. Kovalevskaya, L. P. Kozeeva, I. E. Paukov, and A. G. Blinov, Fiz. Nizk. Temp. **28**, 926 (2002) [Low Temp. Phys. **28**, 669 (2002)].
[7] K. R. Zhdanov, F. S. Rakhmenkulov, V. E. Fedorov, and A. V. Mishchenko, Fiz. Tver. Tela (Leningrad) **30**, 1119 (1988) [Sov. Phys. Solid State **30**, 649 (1988)].
[8] K. R. Zhdanov, V. E. Fedorov, and P. P. Samoĭlov, Élektronnyĭ zhurnal ''Issledovano v Rossii,'' **031**, 327 (2002); http://zhurnal.ape.relarn.ru/articles/2002/031.pdf.
[9] J. Schmalian, D. Pines, and B. Stojkovich, Phys. Rev. Lett. **80**, 3839 (1998); Phys. Rev. B **60**, 667 (1999).
[10] S. Chakravarty, R. B. Laughlin, D. K. Morr, and Ch. Nayak, ArXiv: cond-mat/0005443.
[11] V. Emery, S. A. Kivelson, and O. Zahar, Phys. Rev. B **56**, 6120 (1997).

Translated by M. E. Alferieff

Commensurate vortex lattices and oscillation effects in superconducting Mo/Si and W/Si multilayers

M. Yu. Mikhailov* and O. I. Yuzephovich

B. Verkin Institute for Low Temperature Physics and Engineering of the National Academy of Sciences of Ukraine, 47 Lenin Ave., Kharkov 61103, Ukraine

Yu. V. Bomze

B. Verkin Institute for Low Temperature Physics and Engineering of the National Academy of Sciences of Ukraine, 47 Lenin Ave., Kharkov 61103, Ukraine; Solid State Institute, Technion, Haifa, 32100 Israel

E. I. Buchstab and N. Ya. Fogel

Solid State Institute, Technion, Haifa, 32100 Israel

(Submitted August 6, 2004)
Fiz. Nizk. Temp. **31**, 327–338 (March–April 2005)

We report experimental results of a vortex lattice structure investigation in artificial superconducting Mo/Si and W/Si superlattices. Resistance R and critical current I_c measurements in parallel magnetic fields are performed as well as measurements in tilted magnetic fields. At temperatures where the condition of strong layering is satisfied the dependences $I_c(H_\parallel)$ and $R(H_\parallel)$ exhibit oscillatory behavior. It is shown that the appearance of oscillations and of reentrant behavior (vanishing of the resistivity in definite ranges of $H_\parallel$) are due to the strong intrinsic pinning and to the effect of commensurability between the vortex lattice period and multilayer wavelength. The locations of $I_c(H_\parallel)$ and $R(H_\parallel)$ extrema correspond to the stable states of a commensurate vortex lattice. Our experimental data are in good quantitative agreement with the Ivlev, Kopnin, and Pokrovsky (IKP) theory. It is shown that the values of the commensurability fields depend exclusively on the superlattice period s and anisotropy coefficient γ and do not depend on the type of materials used for multilayer preparation. A memory effect, i.e., dependence of the oscillation pattern on the magnetic history of the sample, is observed. It is shown experimentally that the state of the vortex matter in the layered superconductors is essentially different from that of type-II superconductors with a random distribution of the pinning centers. Investigation of oscillation and reentrance behavior may be used as a new tool for the study of the vortex lattice arrangement in layered superconductors. The essential advantage of this method is connected with its simplicity and with the possibility of using it in arbitrary large fields. Investigations of the commensurate states may be used for rather precise determination of the anisotropy coefficient γ. © *2005 American Institute of Physics.* [DOI: 10.1063/1.1884426]

INTRODUCTION

The vortex lattice (VL) structure in layered superconductors differs in many aspects from the simple triangular one observed in homogeneous type-II superconductors, unless the magnetic field **H** is parallel to the **c** axis of the system considered. Different types arrangements of VL are predicted theoretically for the cases when the applied magnetic field is parallel or inclined with respect to the layer planes. The first theory concerning VL structure in the layered superconducting systems consisting of alloys with periodic modulation of the component concentration appeared many years ago.[1] It was shown that the spatial variation of the impurity concentration might be considered as a regular pinning potential. Ami and Maki[1] have studied the stability of different VL configurations in the Ginzburg-Landau (GL) approximation for parallel magnetic field $H_\parallel$, taking into account that the ''resonance conditions,'' i.e., the commensurability between vortex lattice parameter and layered structure period, plays an important role. In the vicinity of the upper critical field H_{c2} in the commensurate state the triangular VL, with different orientations of the vortex unit cell vector with respect to the layers, appeared to be stable. The values of magnetic fields H_Δ corresponding to the resonance conditions have been obtained. In the framework of this theory they depend exclusively on the superlattice period s. At these fields the maxima of the critical current I_c should be observed. It appeared that the Ami and Maki model described fairly well the dependence of I_c on $H_\parallel$ obtained on the modulated PbBi alloys.[2]

Interest in the commensurability effect and in the properties of the VL structure has been renewed after discovery of the high-temperature superconductivity in the layered oxide compounds. Especially essential progress was achieved in the area of the vortex lattice structure theory. Different theoretical approaches, including anisotropic three-dimensional (3D) London and GL models as well as the Lawrence-Doniach (LD) model, were used. According to the results of Ref. 3 obtained within the London approximation,

in the field domain $H_{c1} \ll H \ll H_{c2}$ the unit cell of the flux line lattice should be strongly distorted with respect to the equilateral triangle. Choosing the primitive cell of the VL as a hexagon, Campbell, Doria, and Kogan[3] obtained the unit cell parameters of VL, which depend intrinsically on the anisotropy parameter $\gamma=(M/m)^{1/2}$ and the angle between **H** and the anisotropy axis. Here M is the effective electron mass along the **c** axis, and m is the in-plane mass. The commensurability effect remained outside the scope of this work. The latter was considered in the papers of Ivlev, Kopnin, and Pokrovsky.[4–6] It was shown[4] that in the case of parallel field, when the intrinsic pinning energy E_p is much greater than the elastic energy of a VL shear deformation E_{el}, the vortices cannot cross the layers. In this situation the period Z_0 along the **c** axis is fixed, and it is determined by the initial conditions under which the VL was formed. This means that the VL should always be commensurable with the layered structure period s (the distance between vortices in the direction orthogonal to the layers $Z_0=Ns$, with N an integer). It is independent of the external field, while the unit cell area varies with field only due to the vortex displacements along the layers. In the opposite limiting case the VL parameters are determined by the external magnetic field. It was shown that the free energy of the rhombic lattice in the commensurate state as a function of H displays two minima corresponding to the different orientations of the unit cell vectors with respect to the layer planes.[4] There are a lot of metastable states in the instability region of the rhombic lattice corresponding to the different displacements of the vortex rows relative to each other in the neighboring interlayers.[4,7] The number of such states grows at low magnetic fields. They can be dynamically accessible upon H variation.[7] In the framework of the LD approach for relatively high parallel magnetic fields a sequence of first-order phase transitions between VLs with different N is predicted.[8] The domain of stability of the VL structures with the different orders of commensurability N was investigated theoretically in Ref. 9.

For the tilted magnetic fields many types of vortex arrangement are suggested.[10–19] The idea of an independent response of the layered superconductor to the parallel and perpendicular components of magnetic field[20] is exploited in many works. The most exotic among possible VL configurations in the tilted magnetic fields is the so-called combined lattice consisting of two vortex ''species'' oriented in different directions (see, for example, Refs. 10–15, 18, 19, 21). Such a configuration of the VL may appear only in a case of a rather large γ.[10,12] One of the coexisting sublattices is oriented along the **c** axis; another may be parallel to the layers[13] or oriented along the external field.[11] In the vicinity of H_{c1} for the tilted magnetic fields a vortex configuration consisting of flux-line chains is predicted.[17] Such vortex chains in the weak field range have been observed in decoration experiments on high-T_c superconductors.[22–24]

Obviously, due to the nonstandard VL structure and intrinsic pinning, many unusual effects can arise in layered superconductors. First of all, in a tilted field the direction of the magnetization vector **M** in many cases does not coincide with the external field direction.[3,16,25] Depending on the misorientation angle, anisotropy parameter, and magnetic field domain, the vector **M** may be oriented either closely to the **c** direction of the layered structure,[3] along the layer planes,[11,25] or along the applied field direction.[11] Even magnetization **M** antiparallel to the external field **H** is possible.[3,26] In parallel magnetic fields due to the intrinsic pinning and commensurability effect the critical current (when the transport current flows in the layer planes) should be an oscillating function of magnetic field.[1,4] This result was obtained experimentally, as was mentioned above, on alloys with a spatial modulation of the component concentration[2] and on Nb/Ta multilayers.[27] The theoretical results cited above have been obtained mostly for high-T_c superconductors. These results should be relevant for the artificial multilayers as well. The essential advantage of the artificial superlattices for the VL structure study is their tunability, i.e., the possibility of easily changing their periodicity and anisotropy parameter. Moreover, the present-day technology of their preparation is very sophisticated, and exceptionally perfect superstructures may be obtained.

Here we report on a new effect observed on Mo/Si and W/Si artificial superlattices, whose origin may be connected with the intrinsic pinning, the commensurability phenomenon, and the specifics of the VL structure in layered superconductors. In a parallel magnetic field and in tilted fields at relatively small tilt angles with respect to the layer planes a reentrance to the state with zero resistivity with increase of the magnetic field is observed. The reentrance phenomenon is detected by the resistive method. The resistivity versus magnetic field H curves below a certain temperature T_0 become nonmonotonic. At some value of the external magnetic field a resistance minimum appears which becomes more pronounced with decreasing temperature and transforms into a large zero-resistance region (ZRR) at still lower temperatures. After the ZRR the resistance reappears. These effects are very sensitive to the magnetic field orientation. It is shown that all the features of the reentrance behavior may be explained quantitatively if one takes into account different possible realizations of VL structure in layered superconductors. It is suggested that the reentrance phenomenon discovered could be used as a new powerful instrument for the VL structure investigations, which, in distinction from other known methods, is valid for arbitrary high fields. A brief report about some of the results described below for Mo/Si SLs has been published in Ref. 28.

SAMPLE PREPARATION AND EXPERIMENTAL METHODS

For the experiments we chose Mo/Si and W/Si multilayered samples in which only the spacer thickness and, correspondingly, the anisotropy parameter are varied (Table I). For such a choice it is mainly the parameter γ that changes, and it allows one to study the evolution of the reentrant and oscillatory resistive behavior with γ variation. The interlayer coupling energy changes exponentially with the spacer thickness,[29] and the anisotropy changes quickly as well.

The Mo/Si multilayers were prepared by dc magnetron sputtering in argon onto glass substrates. The W/Si multilayers were prepared by e-beam evaporation onto oxidized Si(100) wafers. More details may be found in Refs. 29–31. The sample wavelength and individual layer thicknesses are determined from small-angle x-ray diffractometry with an

TABLE I. Parameters of multilayered samples.

Sample	Multilayer type	Mo layer thickness d_{Mo}, Å	W layer thickness d_W, Å	Si layer thickness d_{Si}, Å	Number of bilayers	γ	T_c, K
A	Mo/Si	22		28	50	5.7	4.17
B	Mo/Si	22		34	50	11.8	3.67
C	Mo/Si	22		44	50	23.5	4.15
D	W/Si		20	30	10	3.2	3.32
E	W/Si		20	40	10	15.2	2.92

accuracy of 0.1 Å. The Si layers in the multilayers are amorphous. The metal layers have fine crystalline structure.

Measurements were performed with a 5 T superconducting magnet. At all orientations of **H** with respect to the layer planes the transport current **I** directed along the layers was always perpendicular to **H**. The precision of **H** alignment with the layer planes was about 0.2°. The stabilization of the temperature during a field sweep was no worse than 10^{-3} K. The zero-field resistive transition width for the all samples was no more than 0.15 K.

The values of the anisotropy parameter γ were obtained from measurements of the critical magnetic fields $H_{c\parallel}(T)$ and $H_{c\perp}(T)$.

EXPERIMENTAL RESULTS AND DISCUSSION

In Fig. 1 the resistance as a function of magnetic field at different temperatures for angle $\theta=0°$ is shown for Mo/Si sample B with the wavelength 56 Å ($\theta=0°$ for magnetic field parallel to the layers). Starting at some reduced temperature ($t=0.96$ in this case) steps appear on the R versus H curves, which at lower temperatures develop into minima. With further decrease of T instead of resistance minima, zero-resistance regions (ZRR) appear (Fig. 1b), which manifest the reentrance of superconductivity with the increase of the applied field. After the ZRR at still larger fields the resistance reappears. As we keep going down in temperature, the ZRR becomes wider, and in the low-temperature limit, the R maximum dividing the two minima vanishes (plot *5*, Fig. 1b). Thus, reentrance behavior exists in a limited temperature range between T_0 and some lower temperature T'. For understanding the reentrance phenomenon scale it should be mentioned that the low-temperature normal resistance of sample B is 42.4 Ohm.

The resistance as a function of parallel magnetic field for Mo/Si sample A with a wavelength 50 Å is shown in Fig. 2. A similar plot for sample C ($s=66$ Å) has been presented in Ref. 28. For all samples the magnetic field values corresponding to the ZRRs and to the resistance minima are different.

It is noteworthy that different patterns of the R versus $H_\parallel$ curves may be obtained on the same sample. The reentrance phenomenon is sensitive to the magnetic history. For example, when one starts measurements with the first switching on of the magnetic field sweep at sufficiently low temperature, another realization of the R versus H curves at $\theta=0°$ in the same field range may be obtained. Such another realization for sample B is shown in Fig. 3. As follows from this figure, the reentrance of superconductivity may arise twice during one magnetic field sweep. The third realization for this sample is shown in Fig. 4. None of the patterns observed on sample B coincides with those registered for other samples.

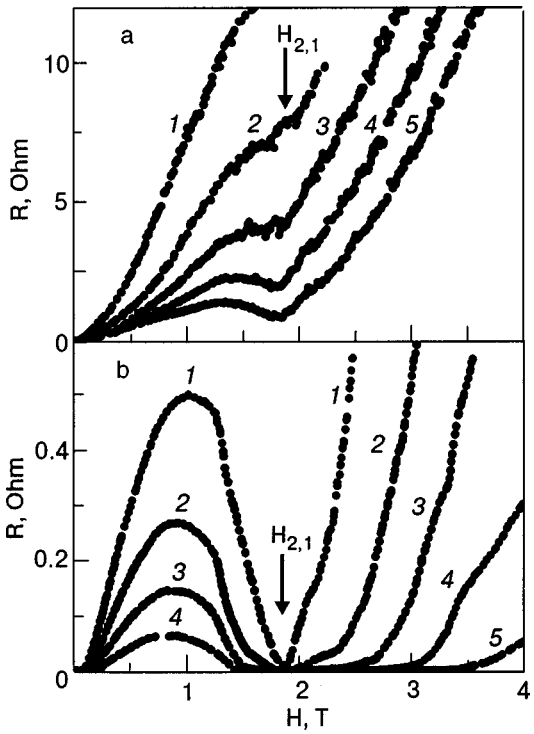

FIG. 1. Resistance as a function of magnetic field for Mo/Si sample B (angle $\theta=0°$) at different temperatures T [K]: (a) 3.557 (*1*); 3.535 (*2*); 3.520 (*3*); 3.508 (*4*); 3.495 (*5*); (b) 3.456 (*1*); 3.420 (*2*); 3.377 (*3*); 3.314 (*4*); 3.214 (*5*).

The features of the resistive curves in a parallel magnetic field depend essentially on the transport current (Fig. 5). At relatively small currents (plot *1* in Fig. 5) the resistive state

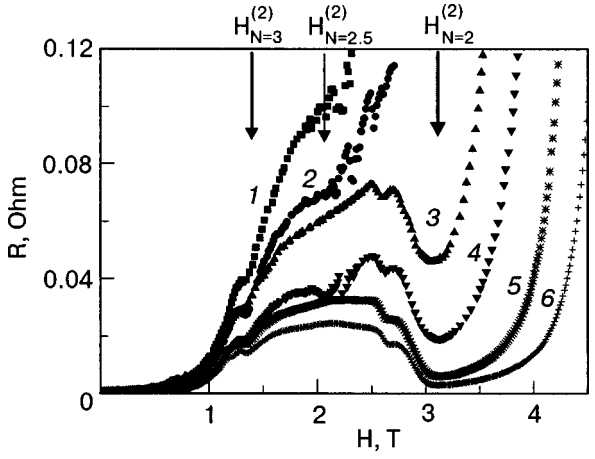

FIG. 2. Resistance as a function of parallel magnetic field for Mo/Si sample A at different temperatures T [K]: 3.788 (*1*); 3.779 (*2*); 3.765 (*3*); 3.750 (*4*); 3.731 (*5*); 3.711 (*6*).

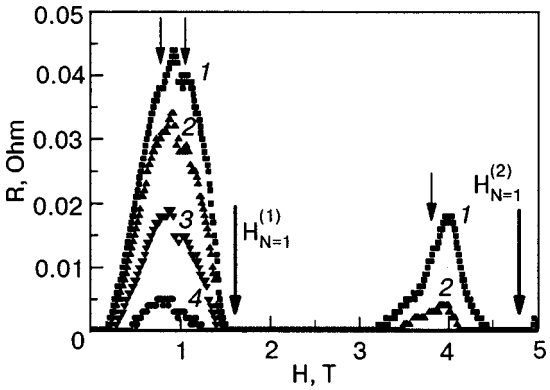

FIG. 3. Resistance as a function of magnetic field for Mo/Si sample B (another realization) at different temperatures T [K]: 3.236 (*1*); 3.218 (*2*); 3.172 (*3*); 3.077 (*4*).

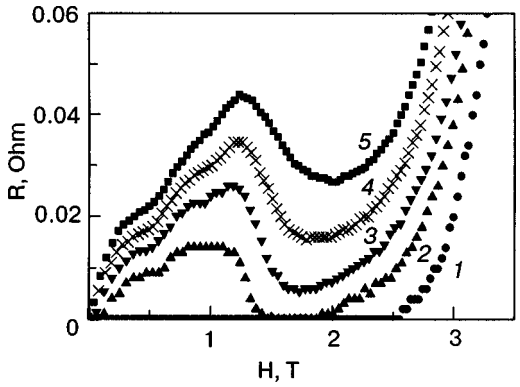

FIG. 5. Resistance as a function of magnetic field for Mo/Si sample B at $T=3.37$ K for different transport currents [mA]: 0.5 (*1*); 1.0 (*2*); 1.5 (*3*); 2.0 (*4*); 2.5 (*5*).

first appears at a rather large magnetic field. Until this field the Lorentz force is too small for overcoming of the pinning barrier. At a higher current (plot *2*) the resistance is already observed in the weak field range, but at intermediate fields the reentrance of superconductivity is observed. Further current increase leads to the appearing of a resistance minimum (plot *3*) instead of the ZRR. Thus the correct choice of the transport current value is crucial for the observation of the ZRR and nonmonotonic R versus $H_{\|}$ behavior. As we will see below, the most informative are the resistive curves of the plot *3* kind.

From comparison of Figs. 4 and 5 it follows that diminishing of temperature and diminishing of the transport current give rise to similar evolution of the resistive transitions. In the former case the pinning barrier increases, while in the latter case the Lorentz force decreases. Because the Lorentz force should counterbalance intrinsic pinning for the vortex motion, it is obvious that both factors influence the resistive behavior identically. If one wants to investigate a larger part of the $H_{\|}$-T phase diagram, it is necessary to enhance the transport current value at a reduced temperature. The temperature T' is a function of transport current, and this temperature may be set as low as one wishes.

In the temperature range between T_0 and T' hysteretic behavior was observed. Some examples of hysteretic curves are shown in Fig. 6. Though the resistance in the increasing and decreasing magnetic fields differs markedly, the positions of the extrema, as a rule, coincide. Similar hysteretic behavior is observed for all samples and for all detected realizations.

The R versus $H_{\|}$ dependences at different temperatures for W/Si sample D ($s=50$ Å) are shown in Fig. 7. The resistive curve patterns obtained on this and other W/Si SLs are similar to those obtained on Mo/Si samples. In the resistive transition realization presented in Fig. 7, the resistance minima and ZRRs appear at three different fields. On W/Si

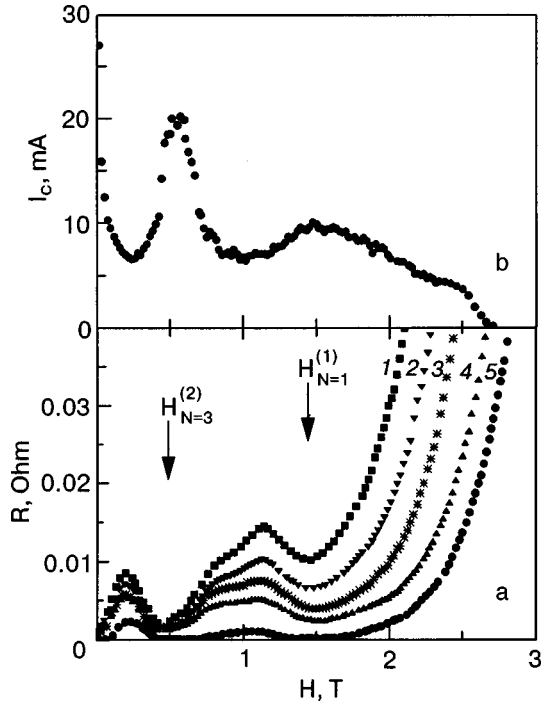

FIG. 4. a—Resistance as a function of magnetic field for Mo/Si sample B (the third realization) at different temperatures T [K]: 3.462 (*1*); 3.459 (*2*); 3.453 (*3*); 3.447 (*4*); 3.441 (*5*). b—Critical current as a function of magnetic field for this sample at $T=3.4$ K.

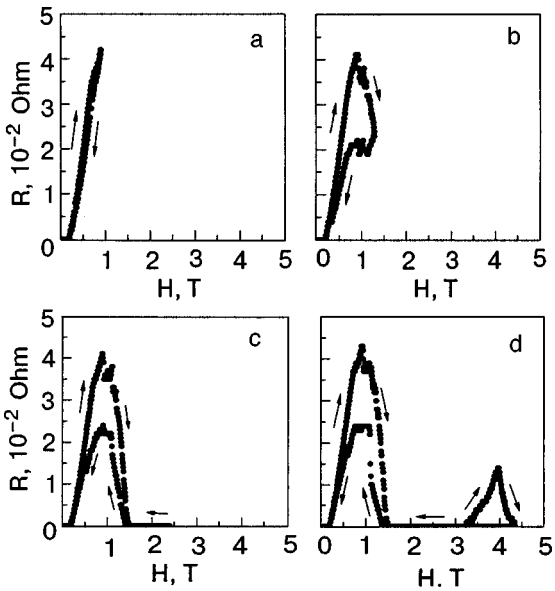

FIG. 6. Hysteretic behavior of resistance for Mo/Si sample B at temperature $T=3.236$ K.

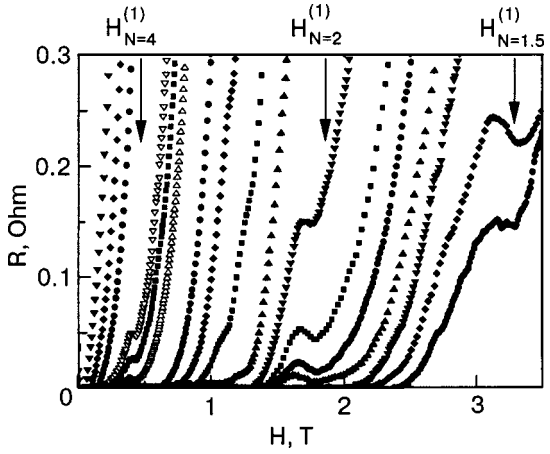

FIG. 7. Resistance as a function of magnetic field at different temperatures for W/Si sample D in the temperature range 2.895–2.488 K.

multilayers the hysteretic behavior and the transport-current dependence of the resistive curve are akin to those observed on Mo/Si SLs.

The reentrance behavior is sensitive to the deviation of magnetic field orientation from parallel to the layer planes. It is illustrated by Fig. 8 where the resistance as a function of magnetic field is shown for different angles θ. When the misorientation angles between **H** and the layer planes are very small the resistance increases with angle growth, but all the features of the resistance transition at $\theta=0°$ hold, the positions of the R minima do not shift (Fig. 8a), and the

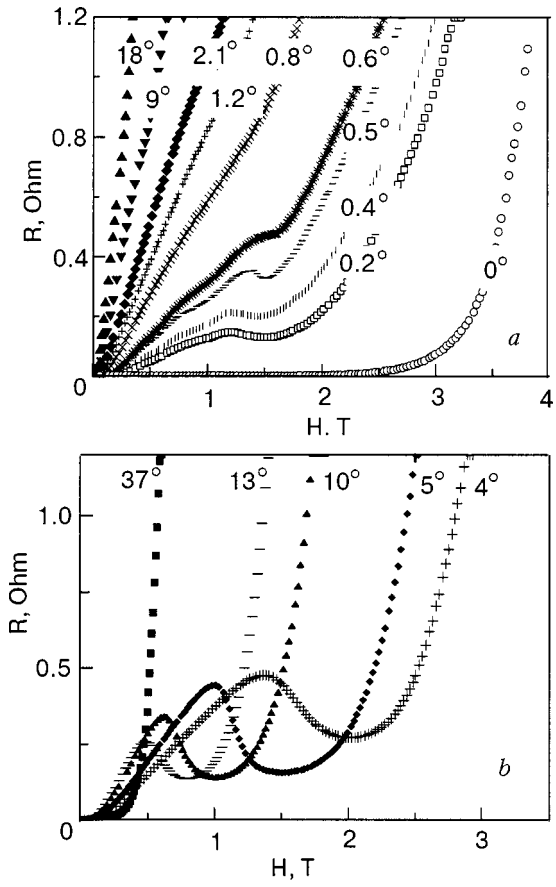

FIG. 8. Resistance as a function of magnetic field for different angles θ at $T=3.440$ (a) and 3.193 K (b) (Mo/Si sample B).

reentrance phenomenon also takes place. It has been shown[32] that such behavior on Mo/Si multilayers is an indication of the lock-in transition at small angles $\theta<\theta_{cr}$. In this θ range the vortices are trapped in a position parallel to the layers even though the applied magnetic field is tilted with respect to the layers. The θ_{cr} is usually defined as the angle where the directions of the external magnetic field and of the induction in the sample begin to coincide. The maximal value of θ_{cr} for sample B is about 2°. At the larger angles in a case of sufficiently low temperatures the minimum position as well as all resistive curves shift to the smaller **H** side, and this shift increases with growth of θ (Fig. 8b). At another critical angle θ^*_{cr} the resistance minimum disappears. Both angles θ_{cr} and θ^*_{cr} depend on the temperature. Most probably, the observation of patterns similar to those typical for commensurate states in a parallel field[28] over a wide range of angles may be considered as evidence of the existence of the combined vortex lattice predicted in Refs. 10–17. This question will be discussed in detail elsewhere.

As was natural to expect, oscillations of the critical current I_c are observed along with the resistivity oscillations (Fig. 4b). The positions of the minima on the R versus $H_\parallel$ curves coincide with the locations of the maxima on the I_c versus $H_\parallel$ curves and vice versa. The dependences of the critical current on $H_\parallel$ display hysteretic behavior, too. Thus the explanation of the unusual patterns characteristic for the R versus $H_\parallel$ dependences is very simple. Provided there are oscillations on the I_c versus H curves, one may expect that for the fields around the I_c maximum the fixed transport current I will be less than I_c, and correspondingly resistance is absent (ZRR state). In the meantime, in magnetic fields around the I_c minimum the condition $I>I_c$ may be satisfied, and a nonzero resistance should be observed in this field range. The data in Fig. 5 also serve as confirmation of the explanation presented above.

For a detailed interpretation of the data obtained let us begin with the determination of the physical meaning of the temperature T_0 where the signs of developing ZRR states appear. It follows from the experimental data that at this temperature the transverse coherence length $\xi_\perp(T)$ becomes equal to or less than $s/2$ ($s=d_{met}+d_{Si}$ is the SL wavelength), i.e., beginning at this temperature a confinement of the vortices between superconducting layers starts to develop. For sample B the value $\xi_\parallel(0)=63$ Å, $\gamma=11.8$, $\xi_\perp(0)=5.5$ Å. At $T_0=3.52$ K the value $\xi_\perp(T_0)=27$ Å, $2\xi_\perp(T_0)\leqslant s=56$ Å. When the vortex cores fit into the insulating interlayers, intrinsic pinning should become well pronounced,[33] and a transition to the limit $E_p>E_{el}$ may be expected. Thus, T_0 manifests by itself the transition to the regime of strong layering.[4] It should be mentioned that the temperature T_0 is practically the same as the 3D–2D crossover temperature determined from the temperature dependence of the critical magnetic field $H_{c\parallel}$. The same situation is observed for other samples. The appearance of nonmonotonic I_c versus $H_\parallel$ dependence only below the crossover temperature is also reported in Ref. 27.

Following up on a suggestion[28] that the phenomena observed are a manifestation of the existence of commensurate vortex lattices, let us analyze the data obtained in detail. In the beginning let us compare the results of different theories

based on various approaches. The Ami-Maki theory[1] considers only dirty superconductors, and its domain of validity is restricted to fields close to H_{c2}. It is assumed that the spatial variation of the impurity content is relatively small (on a scale of the electron mean free path), and among all superconductor parameters only the diffusion coefficient has significant spatial dependence on the impurity concentration. For the specific fields H_Δ satisfying the ''resonance condition'' (i.e., the condition that the Abrikosov lattice parameter a is commensurate with the modulation period s) the following simple expression is obtained:[1]

$$H_\Delta = \frac{\sqrt{3}\pi\Phi_0}{2s^2}(N^2+L^2+NL)^{-1}. \tag{1}$$

Here N and L are integers. This solution suggests that not only variation of the vortex density is possible, but rotation of the vortex unit cell with respect to the equiconcentrational planes as well. Formula (1) satisfactorily describes the experimental data obtained by Raffi *et al.*[2] on PbBi alloys with periodically modulated concentration. The consistency of the experimental results of Broussard *et al.*[34] (Nb/Ta artificial multilayers) with the Ami-Maki predictions is substantially worse. It is clear that the Ami-Maki approximation is valid only for the case of weak anisotropy. As our numerical estimates show, there is nothing in common between the calculated H_Δ values and the experimental values H_N of the I_c maxima and R minima on the resistive curves for the Mo/Si and W/Si samples investigated.

The serious extension of the Ami-Maki model appeared much later, after the discovery of high-T_c superconducting layered compounds. The conception of the intrinsic pinning associated with the periodic layered structure was formulated for vortices parallel to the layer planes.[33,35] High-T_c compounds are usually considered as the periodic stacking of the strongly and weakly superconducting (or normal) layers.[35] The origin of the intrinsic pinning is connected with the fact that the most energetically favorable position of the vortex line, which is parallel to the layers, corresponds to its location in a weakly superconducting, either normal or insulating, interlayer. In this case, the gain in the vortex free energy is about equal to the condensation energy in the volume of the vortex cores. Moreover, the vortices are pinned along their entire length. When the distance between vortices in the direction orthogonal to the layers matches with the layered structure period, all the vortices are locked between superconducting layers. This configuration corresponds to strong pinning. If the magnetic field and transport current both lie in the layer plane and orthogonal to each other, the vortices should move under the influence of the Lorentz force across the layers, i.e., overcome the high potential barriers associated with the variation of the condensation energy. Such a movement is strongly hindered and occurs by finite steps at rather high currents.[6] The important role of the intrinsic pinning, determining the orientational dependence of the critical current I_c, has been confirmed experimentally.[36–38] Intrinsic pinning also gives rise to such phenomenon as a lock-in transition.[25]

Due to intrinsic pinning an essential modification of the vortex lattice structure in comparison with the Abrikosov one is also expected. Recently, the influence of the commensurability effect on the vortex arrangement in a parallel magnetic field has been considered in theoretical works.[3–6,8,39] At a given magnetic field, one can make the VL be commensurate with the underlying layered structure by the compressing the VL along the normal to the layers and introducing the necessary shear deformation.[4] However, if the energy $E_{\rm el}$ of such a deformation exceeds the pinning energy E_p, the VL parameters are determined by the applied magnetic field. Then it is the value of the external magnetic field that would prescribe whether or not the lattice is commensurate with the underlying periodic pinning potential. This is a situation which should be characteristic for weakly layered systems. This situation does not differ basically from that considered by Ami and Maki. However, in the case of comparatively large values of the anisotropy parameter γ the final result for the ''resonant'' fields[4] turns out to be different from (1):

$$H_N = \frac{\sqrt{3}}{2}\frac{\Phi_0}{N^2 s^2 \gamma}; \quad \gamma = \left(\frac{M}{m}\right)^{1/2}. \tag{2}$$

Here $N=1,2,3...$ is the order of commensurability. Formula (2) corresponds to the simplest case of a rhombic VL with one of its unit-cell vectors parallel to the layers. It is easy to see that formula (2) differs from the Ami-Maki expression for the case $L=0$ only by the factor γ, which is absent in the Ami-Maki expression for H_Δ because of very insignificant anisotropy incorporated in their model. The depinning current should oscillate, reaching maximal values at the integer Z_0/s values. If other pinning centers are absent, the critical current should be zero at all H values where the ratio Z_0/s is not close to an integer.

The intrinsic pinning energy increases with the lowering of temperature as at any other pinning mechanism. Moreover, as was mentioned above, it turns out more pronounced when the vortex core size in the direction orthogonal to the layers $\xi_\perp(T)$ becomes comparable to or smaller than the superstructure period. In this case the vortex cores fit easily between two neighboring superconducting layers. Taking into account the ratio between $\xi_\perp(T)$ and s, Ivlev, Kopnin, and Pokrovsky[4] (IKP) have classified all layered systems as superconductors with weak layering ($\xi_\perp(T) \gg s$) and strong layering ($\xi_\perp(T) \ll s$). According to IKP, the regime of strong pinning is accessible for any type of layering, and in both the cases of weak and strong layering there are regions of the H-T diagram where the elastic deformation energy is smaller than the pinning energy.[4] For weakly layered superconductors ($\xi_\perp(T) \gg s$) such regions are determined by the conditions:

$$\begin{aligned} &1-\frac{H}{H_{c2}} \ll \left(\frac{\xi_c}{s}\right)^3 \exp\left(-\frac{8\xi_c^2}{s^2}\right); \\ &\frac{H}{H_{c2}} \ll \left(\frac{\xi_c}{s}\right)^3 \exp\left(-\frac{8\xi_c^2}{s^2}\right), \end{aligned} \tag{3}$$

while for highly layered structures ($\xi_\perp(T) \ll s$) they are determined by the conditions:

$$1-\frac{H}{H_{c2}} \ll 1; \quad \frac{H}{H_{c2}} \ll 1. \tag{4}$$

The estimates by formula (3) show that for weakly layered superconductors the regions of strong pinning are unrealisti-

cally narrow. Thus a more realistic statement is that for the layered systems with $\xi_\perp(T=0)>s$ the pinning is relatively weak at all T and H. If $\xi_\perp(T=0)<s$, then at elevated temperatures $\xi_\perp(T)$ may become $\geqslant s$, and a transition between the situation of strong and weak layering may occur. It is clear that in the framework of the above-mentioned classification the concentrationally modulated alloys and artificial superlattices of the S/S′ and S/N types (S is a superconductor, S′ is a superconductor with T_c smaller than that of S, and N is a normal metal) should belong to the weakly layered systems. Superlattices of the S/I type (I is a semiconductor or an insulator) may belong either to the weakly or to the strongly layered systems. This depends on the anisotropy parameter and, accordingly, on the interlayer Josephson coupling energy. Both situations may be expected in high-T_c superconductors. The authors of Refs. 4 and 5 noted that $YBa_2Cu_3O_x$, in particular, could be a favorable object for investigation of commensurability effects. Indeed, such experimental observations on $YBa_2Cu_3O_x$ and on $RBa_2Cu_3O_x$ (R=Y,Nd) have appeared later.[40–43] In the work of Oussena *et al.*[40] oscillations in the magnetization of a $YBa_2Cu_3O_x$ single crystal were observed when the magnetic field was parallel to its **a** or **b** axis. The positions of the magnetization maxima were temperature independent. It was clear evidence that the oscillations are connected with the matching between vortex lattice parameter and regular layered structure. The large number of maxima on the magnetization curves (the magnetic field was varied up to 12 T) allowed the authors to determine the anisotropy parameter in $YBa_2Cu_3O_x$ to good accuracy using formula (2) for the case of weak layering. In particular, using the data of Fig. 3 of Ref. 40 (upper panel), presented for **H** parallel to the **a** axis and $T=60$ K, one can easily determine the orders of commensurability present on this plot. The maxima fit to the orders N from 5 to 11. The maxima corresponding to the smaller $N=1-4$ should be observed at $\mathbf{H}>12$ T. Because of the relatively large wavelengths in our multilayers the H_N values belonging to the low orders of commensurability get in the accessible range of magnetic fields in distinction to the high-temperature compounds with small s values. At 60 K the additional peak on the magnetization oscillation curve is observed which does not obey the above-mentioned classification and was not explained by the authors. We will present the interpretation of this extra peak below. It is somewhat surprising that the M oscillation amplitude diminishes at lower temperatures. This probably means that background pinning on another type of defects grows with decreasing T faster than the intrinsic pinning. In the work of Gordeev *et al.*[41] the oscillations of resistance with parallel magnetic field have been observed on YBCO samples with a transition temperature of 60 K. The features of the resistive transitions on this sample are similar to those observed on our SLs.

As was mentioned above, in the situation of the strong layering and strong pinning, the VL should be commensurate with the SL wavelength at all magnetic field values.[4] According to IKP, the stable states of the commensurate lattice correspond to the rhombic lattice with the rational values of the apex angle $\pi/3$ and $2\pi/3$ (in the frame of the reduced coordinates $x, z\sqrt{M/m}$; here x is the direction along the layers, and z is along the **c** axis). The conditions of stability look as follows:[4]

$$p=\pi/\sqrt{3}, \quad p=\pi\sqrt{3}. \tag{5}$$

Here p is the reduced magnetic field:

$$p=2\pi N^2 s^2 \gamma H/\Phi_0. \tag{6}$$

Correspondingly, the dependence of the free energy of the given commensurate lattice on magnetic field has two minima at the H values:

$$H_N^{(1)}=\frac{\Phi_0}{2\sqrt{3}N^2 s^2 \gamma}, \quad H_N^{(2)}=\frac{\Phi_0\sqrt{3}}{2N^2 s^2 \gamma}. \tag{7}$$

Note that the $H_N^{(2)}$ values coincide with H_N for weakly layered structures. We have already mentioned above that the patterns of the resistance minima obtained in the different R versus $H_\parallel$ realizations have nothing in common with calculated values of the Ami-Maki fields H_Δ. As follows from the above argumentation about the temperature range in which the resistance minima and ZRR states are observed on Mo/Si samples investigated, for both Mo/Si and W/Si SLs we are dealing with the case of highly layered superconductors. That is why a comparison with IKP theory considering this limiting case is the most reasonable. Figure 9 shows the dependences of the Gibbs energy on magnetic field calculated according to IKP for different orders of commensurability for Mo/Si sample B, with the γ value of 11.8. A comparison of the pattern of Fig. 9 with the data obtained on this sample reveals quite satisfactory consistency with the IKP theoretical predictions. In Fig. 3 the two regions of the ZRR states correspond to the two stable states for $N=1$. The H_N values are shown in this figure by the thick arrows. The minima in Fig. 4 correspond to $N=3$, the second stable state, and $N=1$, the first stable state. The stable state with $N=2$ is also obtained in one of the realizations. All the R versus $H_\parallel$ realizations observed correspond to the definite initial conditions under which the vortex lattice was formed. As was mentioned above, the realization shown in Fig. 3 is observed in a case when the external magnetic field is switched on first at sufficiently low temperature. The first ZRR state in this case corresponds to $N=1$. It is obvious that in such a case the appearance of the states with the larger N in the increasing

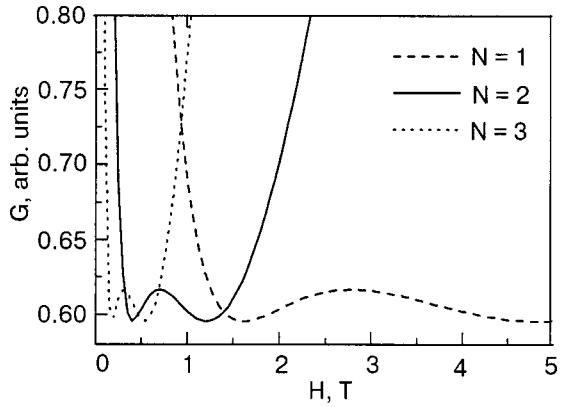

FIG. 9. Dependences of the Gibbs free energy on magnetic field for different orders of commensurability for Mo/Si sample B calculated according to IKP theory.

field is impossible. When the measurements of the resistive curves are started from T_c, the realizations of such types as presented in Figs. 1 and 4 take place. The positions of the IKP fields H_N in these figures are also indicated by the thick arrows.

For Mo/Si sample A, with smaller s and γ values, we have the following values of the IKP matching field at two stable states: for $N=1$, 4.2 T and 12,6 T; for $N=2$, 1.05 T and 3.15 T; for $N=3$, 0.47 T and 1.4 T. Comparison of these values with Fig. 2 shows that the R minima corresponding to $N=3$ and $N=2$ (for both minima it is the second stable state) are distinctively seen. They are indicated by the thick arrows.

Between these two minima there is additional minimum at a field of 2.02 T (it is shown in Fig. 2 by the thin arrow), which corresponds fairly well to the IKP stable state with a half-integer order of commensurability $N=2.5$. From our point of view, such commensurate arrangements are also allowed in the strongly layered superconductors. One should simply contemplate the possibility that another kind of commensurate states exists, when half of the vortex chains are confined to the spacers while the other half are located on the superconducting layers. It is a regular vortex lattice consisting of Josephson and Abrikosov vortices. Additional evidence for the existence of such VLs follows from data obtained on Mo/Si SLs with thick spacers, where only magnetic interlayer coupling is essential, and avalanche-type jumps of resistance correspond to phase transitions between different commensurate states.[44] It is known that a single flux line sitting on a superconducting layer is unstable.[45] However, in a case when half of the vortices are trapped in the spacers and fixed by the strong periodic pinning potential, the entire vortex system is commensurate with this potential and is stable. A similar observation in commensurability magnetization experiments on high-T_c samples was reported in Ref. 43. This situation is also reminiscent of one which occurs in the case of a superconducting film with an antidote lattice, where in the matching field all of the vortex ensemble is strongly pinned, though only part of the vortices are trapped at pinning sites.[46]

Two observed R minima on sample C may be identified as IKP stable states for $N=1$ and $N=3$.[28] Sometimes, as particularly in the latter case and the case illustrated in Fig. 4 for sample B, the stable state with $N=2$ is not observed experimentally. The possible explanation of this fact might be as follows. The rearrangement of the VL at the transition from the lattice with $N=3$ to the lattice with $N=2$ is rather complicated, while the transition $N=3\rightarrow N=1$ occurs simply by the dividing of one vortex chain into three. Nevertheless, this transition is observed on sample A.

A fairly good consistency with the IKP theory is obtained on W/Si samples as well. On the sample with $s=50$ Å the first two R minima correspond to $N=4$ and $N=2$, the first stable state (Fig. 7). The third minimum fits as in a case with Mo/Si sample A to a half-integer number 1.5. On the W/Si sample with $s=60$ Å the R minima corresponding to two stable states with $N=4$ are found. The minimum corresponding to $N=3$, which should appear between these two minima, does not reveal itself. The reason for this might be the above-mentioned difficulty with the rearranging of the VL in the situation when two N values are not multiples of each other.

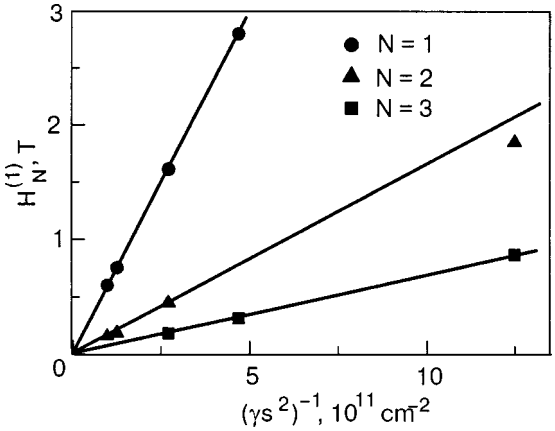

FIG. 10. Experimental values of the commensurate magnetic fields for samples with different wavelengths and anisotropy parameters.

Additional confirmation that the resistive transition patterns reflect the properties of the commensurate lattices may be provided by data such as those presented in Fig. 10. Here the examples of the dependence of experimental values of H_N on the parameter $(\gamma s^2)^{-1}$ characterizing the individuality of the layered sample are shown. As follows from formula (7), the data for different samples lie on straight lines passing through the zero point. Thus by changing the spacer thickness at a constant metal layer thickness, one obtains additional evidence of the perfect applicability of the IKP theory for the interpretation of the oscillation phenomena and ZRR states.

Analysis of the data of Oussena *et al.*[40] has shown that the extra peak in magnetization observed on YBCO at the relatively low temperature 60 K is the peak corresponding to IKP field for a strongly layered system with $N=9$ (the second stable state). Thus, the second stable states begin to appear at lower temperatures.

Besides the stable VL configurations considered by IKP, rather different VL states might exist, as was mentioned above, which are dynamically accessible upon the variation of the magnetic field.[4,6,7] Under conditions of strong pinning and relatively small magnetic fields, shear instability of the commensurate lattice leads to the breaking of symmetry: neighboring vortex chains locked between superconducting layers may be shifted with respect to one another.[6,7] Many of these ''shifted'' lattices correspond to metastable states, i.e., to local minima of the free energy. The positions of all the free energy local minima have a hierarchical structure, which is described by a set of Farey numbers.[7] Due to this hierarchy the number of metastable states grows with magnetic field decrease. The trajectory of the dynamically accessible minimum, which starts from the symmetric VL (the lattice without shear), goes through a sequence of bifurcation and quasibifurcation points, and this trajectory is not uniquely defined. As the magnetic field varies, the trace of the absolute minimum jumps in a complicated way between different metastable states.[7] One may believe that metastable states of the VL may be probed in dynamic experiments, i.e., by resistive or critical-current measurements. We suggest that a number of additional features observed on the R versus H

and I_c versus H curves (like steps, kinks, or abrupt changes of curvature; see, for example, the thin arrows in Fig. 3) along with the main maxima and minima, may be evidence of a manifestation of dynamically accessible metastable states. Sometimes the H values where the features mentioned appear are the same in different experiments, and sometimes these values change, i.e., other trajectories of dynamically accessible minima are realized.

An interesting aspect of the oscillation phenomena observed on Mo/Si and W/Si multilayers is a memory effect. It manifests itself in the repetition of the same $R(H_\parallel)$ curve patterns during all experiments made in the same run of the cooling down of the sample. If one wishes to obtain another realization of the resistive behavior, it is necessary to heat the sample above the transition temperature. The memory effect has been observed on all samples investigated. Subsequently to the diminishing of the magnetic field down to zero, part of the vortices stay frozen in all interlayers where they were during the previous field sweep. Evidence of that is the hysteretic behavior. This predetermines the appearance of the same resistive pattern at each following field sweep at lower temperatures. It seems that during the decrease of the field and, correspondingly, of the vortex density, the VL might pass through another sequence of transformations. For example, if on increasing field, H_i, one observes a transition between commensurate VL phases with $N=3$ and $N=1$, and it seems that nothing should preclude the transition $N=1 \rightarrow N=2$ in the decreasing field H_d. However, this never happens, and the resistive curves in field H_d repeat the pattern observed in field H_i. Therefore one arrives at the conclusion that the previous location of the vortex rows in definite interlayers modifies in some way the intrinsic pinning behavior. To eliminate this subtle modification the sample should be returned to the virgin state, i.e., be put in the normal state. It is noteworthy that the memory effect concerns the metastable states as well (see, for example, Figs. 3 and 6). For a full understanding of the memory effect, additional experiments are needed.

Attention must also be paid to the fact that the set of the different $R(H_\parallel)$ realizations on each sample constitutes a unique ''fingerprint,'' which characterizes the possible stable VL states for a given multilayer. This fingerprint depends exclusively on the anisotropy parameter and SL period (more exactly, on the value γs^2), and does not depend on the type of materials used for preparation of the multilayer. Obviously, it is possible to imagine the eventuality of the existence of the ''twin'' samples with different values of γ and s, but with equal values of γs^2 magnitude. However, as a matter of fact, such coincidence is highly improbable due to the very strong dependence of the anisotropy parameter on the spacer thickness.[29] Thus, the investigations of the commensurate states in layered superconductors may be used for determination of the anisotropy parameter γ. The same conclusion follows from the magnetization experiments of Oussena *et al*. However, it is better to deal with samples having a rather large number of layers because in the layered thin films commensurability with the full sample thickness is possible as well.[47] The interplay between the two commensurability effects leads to the appearance of special selection rules. This makes the interpretation of the oscillation data more complicated.

The predictions about the VL structure in layered superconductors obtained in the paper of Bulaevskii and Clem[8] (BC) in the framework of the LD model, which takes into account the Josephson nature of the interlayer coupling, are rather different from those obtained on the basis of the 3D anisotropic London or GL approach. The series of first-order phase transitions between different commensurate phases should occur at definite magnetic field values $H_{n,n-1}$, which also depend on the anisotropy parameter and SL wavelength. For this effect the value of the characteristic field $H_0 = \Phi_0/\gamma s^2$ where the Josephson cores of the vortices begin to overlap is essential.

For sample B this characteristic field H_0 is equal to 5.51 T. The transition between commensurate phases corresponding to $Z_0=s$ and $Z_0=2s$ should occur in the field $H_{2,1} = H_0/3 = 1.84$ T, and another transition (between the phases with $Z_0=2s$ and $Z_0=3s$) in the field $H_{3,2}=H_0/8=0.69$ T. The position of the large minimum in Fig. 1 is just consistent with the field $H_{2,1}$ estimated above on the basis of the LD model results of BC.[8] However, at fields close to $H_{3,2} = 0.69$ T there is only a peculiarity on the derivative dR/dH (data of Fig. 1a). The second shallow minimum in Fig. 5, showing another run under the same conditions for sample B, is closer to the IKP field $H_3^{(2)}$.

It is necessary to note here that the values of the IKP and BC fields are rather close to each other numerically. The ratio of the fields $H_0/H_N^{(2)} = 2N^2/\sqrt{3} \approx 1$ in the case $N=1$ and the ratio $H_{2,1}/H_N^{(1)}$ are equal to the same value. It is quite natural that the BC transition fields may be seen in the same magnetic field range as the IKP stable commensurate states. In the IKP work the properties and stability of a given commensurate state are considered, but transitions between different commensurate states are outside the framework of this theory. Oppositely, in BC theory only the transitions between different commensurate VL states are under consideration. The approaches used in both papers mentioned are rather distinct, but the authors of these works are actually considering different sides of the same phenomenon, i.e., evolution of the mixed state in strongly layered superconductors. It is clear that at the appropriate choice of the current the both IKP and BC scenarios may be observed on the same sample. It appears that the location of the minima in Fig. 1a cannot be explained in the IKP GL model, while they are in excellent agreement with the results of the LD model of BC. In the meantime, the data of the other figures with the oscillating R versus H dependences are consistent only with the IKP theory predictions.

In conclusion, the new type of reentrance phenomenon discovered on Mo/Si multilayers, occurring if the magnetic field is aligned along the layers or slightly inclined with respect to the layer planes, has been studied in detail on series of Mo/Si and W/Si multilayered samples. The reentrance behavior is connected with the influence of intrinsic pinning and with the specifics of the VL structure in layered superconductors. Locations of the R versus H minima and ZRR correspond either to the stable states of a commensurate VL or to transitions between two commensurate lattices with different Z_0. Examination of the results obtained allows one to

conclude that investigation of the reentrance behavior may be used as a new tool for studying the VL arrangement in layered superconductors. The investigations of the dependences of the critical current on $H_{\|}$ and of the resistive transitions give practically the same results. However, the latter method seems more attractive because it is substantially simpler, and it allows one to cover a larger area of the $H_{\|}$-T diagram.

It has been shown experimentally that the state of the vortex matter in layered superconductors differs essentially from that in type-II superconductors with a random distribution of pinning centers.

This research was supported in part by Grant N 351/99 from the Israel Science Foundation and The Center for Absorption in Science, Ministry of Immigrant Absorption, State of Israel. The authors are grateful to L. Bulaevskii, V. Kogan, and V. L. Pokrovsky for valuable discussions and to S. A. Yulin and R. Senderak for assistance in sample preparation.

*E-mail: mikhailov@ilt.kharkov.ua

[1] S. Ami and K. Maki, Prog. Theor. Phys. **53**, 1 (1975).
[2] H. Raffy, J. C. Renard, and E. Guyon, Solid State Commun. **11**, 1679 (1972).
[3] L. J. Campbell, M. M. Doria, and V. G. Kogan, Phys. Rev. B **38**, 2439 (1988).
[4] B. I. Ivlev, N. B. Kopnin, and V. L. Pokrovsky, J. Low Temp. Phys. **80**, 187 (1990).
[5] B. I. Ivlev and N. B. Kopnin, Phys. Rev. Lett. **64**, 1828 (1990).
[6] B. I. Ivlev and N. B. Kopnin, J. Low Temp. Phys. **80**, 161 (1990).
[7] L. S. Levitov, Phys. Rev. Lett. **66**, 224 (1991).
[8] L. Bulaevskii and J. R. Clem, Phys. Rev. B **44**, 10234 (1991).
[9] M. Ichioka, Phys. Rev. B **51**, 9423 (1995).
[10] D. A. Huse, Phys. Rev. B **46**, 8621 (1992).
[11] L. N. Bulaevskii, M. Ledvij, and V. G. Kogan, Phys. Rev. B **46**, 366 (1992).
[12] A. Sudbø, E. H. Brandt, and D. A. Huse, Phys. Rev. Lett. **71**, 1451 (1993).
[13] L. L. Daemen, L. J. Campbell, A. Yu. Simonov, and V. G. Kogan, Phys. Rev. Lett. **70**, 2948 (1993).
[14] G. Preosti and P. Muzikar, Phys. Rev. B **48**, 9921 (1993).
[15] E. Sardella and M. A. Moore, Phys. Rev. B **48**, 9664 (1993).
[16] A. V. Balatskii, L. I. Burlachkov, and L. P. Gor'kov, Zh. Éksp Teor. Fiz. **90**, 1478 (1986) [Sov. Phys. JETP **63**, 866 (1986)].
[17] A. I. Buzdin and A. Yu. Simonov, JETP Lett. **51**, 191 (1990).
[18] A. E. Koshelev, Phys. Rev. Lett. **83**, 187 (1999).
[19] A. N. Grigorenko, S. J. Bending, A. E. Koshelev, J. R. Clem, T. Tamegai, and S. Ooi, Phys. Rev. Lett. **89**, 217003 (2002).
[20] P. H. Kes, J. Aarts, V. M. Vinokur, and C. J. van der Beek, Phys. Rev. Lett. **64**, 1063 (1990).
[21] M. Benkraouda and M. Ledvij, Phys. Rev. B **51**, 6123 (1995).
[22] C. A. Bolle, P. L. Gammel, D. G. Grier, C. A. Murray, and D. J. Bishop, Phys. Rev. Lett. **66**, 112 (1991).
[23] I. V. Grigorieva, J. W. Steeds, and K. Sasaki, Phys. Rev. B **48**, 16865 (1993).
[24] G. J. Dolan, F. Holtzberg, C. Feild, and T. R. Dinger, Phys. Rev. Lett. **62**, 2184 (1989).
[25] D. Feinberg and C. Villard, Phys. Rev. Lett. **65**, 919 (1990).
[26] A. M. Grishin, A. Yu. Martynovich, and S. V. Yampol'skii, Zh. Éksp. Teor. Fiz. **97**, 1930 (1990) [Sov. Phys. JETP **70**, 1089 (1990)].
[27] C. Coccorese, C. Attanasio, L. V. Mercaldo, M. Salvato, L. Maritato, J. M. Slaughter, C. M. Falco, S. L. Prischepa, and B. I. Ivlev, Phys. Rev. B **57**, 7922 (1998).
[28] N. Ya. Fogel, M. Yu. Mikhailov, Yu. V. Bomze, and O. I. Yuzephovich, Phys. Rev. B **59**, 3365 (1998).
[29] M. Yu. Mikhailov, O. I. Yuzephovich, A. S. Pokhila, Yu. V. Bomze, N. Ya. Fogel, I. M. Dmitrenko, S. A. Yulin, A. S. Sidorenko, O. B. Moldovan, and E. I. Buchstab, Fiz. Nizk. Temp. **25**, 850 (1999) [Low Temp. Phys. **25**, 635 (1999)].
[30] E. I. Bukhshtab, V. Yu. Kashirin, V. V. Kondratenko, A. I. Fedorenko, N. Ya. Fogel, V. G. Cherkasova, and S. A. Yulin, Fiz. Nizk. Temp. **19**, 704 (1993) [Low Temp. Phys. **19**, 506 (1993)].
[31] N. Ya. Fogel, E. I. Buchstab, A. S. Pokhila, A. I. Erenburg, and V. Langer, Phys. Rev. B **53**, 71 (1996).
[32] O. I. Yuzephovich, Yu. V. Bomze, M. Yu. Mikhailov, I. M. Dmitrenko, and N. Ya. Fogel, Fiz. Nizk. Temp. **26**, 142 (2000) [Low Temp. Phys. **26**, 103 (2000)].
[33] M. Tachiki and S. Takahashi, Solid State Commun. **70**, 291 (1989).
[34] P. R. Broussard and T. H. Geballe, Phys. Rev. B **37**, 68 (1988).
[35] M. Tachiki and S. Takahachi, Solid State Commun. **72**, 1083 (1989).
[36] B. Roas, L. Schultz, and G. Saemann-Ischenko, Phys. Rev. Lett. **64**, 479 (1990).
[37] P. Schmitt, P. Kummeth, L. Schultz, and G. Saemann-Ischenko, Phys. Rev. Lett. **67**, 267 (1991).
[38] A. Walkenhorst, C. Tome-Rosa, C. Stolzel, G. Jacob, M. Schmitt, and H. Adrian, Physica C **177**, 165 (1991).
[39] V. Prokic, D. Davidovic, and L. Dobrosavljevic-Grujic, Phys. Rev. B **51**, 6013 (1995).
[40] M. Oussena, P. A. J. de Groot, R. Gagnon, and L. Taillefer, Phys. Rev. Lett. **72**, 606 (1994).
[41] S. N. Gordeev, A. A. Zhukov, P. A. J. de Groot, A. G. M. Jansen, R. Gagnon, and L. Taillefer, Phys. Rev. Lett. **85**, 4594 (2000).
[42] H. Kupfer, G. Ravikumar, T. Wolf, A. A. Zhukov, A. Will, H. Leibrock, R. Mtetr-Himer, H. Wuhl, and P. A. J. de Groot, Phys. Rev. B **66**, 64512 (2002).
[43] H. Kupfer, G. Ravikumar, A. A. Zhukov, P. A. J. de Groot, C. Meingast, A. I. Rykov, S. Tajima, and Th. Wolf, Physica C **404**, 215 (2004).
[44] O. I. Yuzephovich, Yu. V. Bomze, M. Yu. Mikhailov, E. I. Buchstab, and N. Ya. Fogel, Physica C **361**, 59 (2001).
[45] T. Koyama, N. Takezawa, and M. Tachiki, Physica C **172**, 501 (1991).
[46] V. V. Metlushko, L. E. DeLong, M. Baert, E. Rosseel, M. J. van Bael, K. Temst, and V. V. Moshchalkov, Europhys. Lett. **41**, 333 (1998).
[47] N. Ya. Fogel, E. I. Buchstab, V. G. Cherkasova, O. I. Yuzephovich, M. Yu. Mikhailov, and A. N. Stetzenko, Fiz. Nizk. Temp. **27**, 1019 (2001) [Low Temp. Phys. **27**, 752 (2001)].

This article was published in English in the original Russian journal. Reproduced here with stylistic changes by AIP.

Microwave impedance of $YBa_2Cu_3O_{7-\delta}$ high-temperature superconductor films in a magnetic field

V. M. Pan,* D. A. Luzhbin, A. A. Kalenyuk, A. L. Kasatkin, and V. A. Komashko

G. V. Kurdyumov Institute of Metal Physics, Ukrainian National Academy of Sciences, 36 bul'v. Akad. Vernadskogo, Kiev 03142, Ukraine

A. V. Velichko and M. Lancaster

University of Birmingham, School of Electronic, Electrical and Computer Engineering, B15 2TT, United Kingdom

(Submitted August 3, 2004)
Fiz. Nizk. Temp. **31**, 339–349 (March–April 2005)

The temperature, field, and intensity (amplitude) dependences of the surface impedance of magnetron-sputtered $YBa_2Cu_3O_{7-\delta}$ quasi-single-crystal films on a sapphire substrate with a CeO_2 buffer layer were measured. The measurements were performed with a coplanar resonator at 5.25 GHz in a weak constant magnetic field $0<B<12$ mT in the temperature range 13 K $<T<80$ K. They made it possible to obtain the surface resistance and penetration depth versus the temperature and the magnetic field strength and to determine the contribution of Abrikosov vortices to the impedance. The cases with a frozen magnetic field and zero-field cooling with the field subsequently switched on at temperatures below the critical value were investigated separately. A substantial difference in the behavior of the high-frequency response of the vortices in these two cases was found. The Coffey-Clem and Brandt theories were used to study the linear response and the critical state model the nonlinear response of the vortices. © *2005 American Institute of Physics.* [DOI: 10.1063/1.1884427]

1. INTRODUCTION

The discovery of high-temperature superconductors (HTSCs) has greatly rekindled interest in studying the high-frequency properties of superconducting materials.[1] In addition to the possibility of investigating the fundamental physical properties of these materials, the possible application of HTSCs as components in various passive and active microwave devices is also very promising.[2,3] The main advantage of HTSC materials for applications is their very low surface resistance (compared with pure Au, Ag, or Cu) at temperatures below the temperature of liquid nitrogen and the low thermal-noise level, which will make it possible in the future to produce commercial microwave devices which operate at liquid-nitrogen temperatures, possess uniquely high sensitivity and selectivity, and have extremely low losses.

There is still great interest in studying the fundamental properties of HTSC materials, such as, the symmetry of the superconducting order parameter, the characteristics of the superfluid electronic condensate, and the relationship between these properties and the stoichiometry and the defect and impurity structures of HTSCs.[4] Since all known HTSC materials are type-II superconductors with very low first critical fields ($\sim 10^{-2}$ T for bulk superconductors), the influence of the vortex ensemble on the microwave properties of HTSCs must be taken into account when performing measurements, even in comparatively weak magnetic fields. The great variety of crystalline structures of various HTSC compounds, the high working temperatures, and the diversity of various phase states of the vortex ensemble in HTSC materials[5,6] have led to a situation where the study of the properties of the mixed state (vortex matter),[5–9] specifically, the high-frequency response of Abrikosov vortices,[10–26] has become a separate subfield of the physics of superconductivity.

Investigations of the microwave properties of HTSC materials can be conventionally divided into two regions: in the absence and presence of a constant magnetic field. In the first case the internal electronic properties and the factors determining them (presence of defects of various types and sizes, Josephson weak links, anisotropy, superconducting condensate parameters, quasiparticle scattering time, and so on) are predominating features for the microwave response (surface impedance) of a superconductor.[4] At the same time effects due to the presence of vortices in the interior volume of a superconductor (flux creep, elastic properties of the vortex ensemble, vortex pinning on various defects, thermally activated motion of vortices, phase transitions in the vortex ensemble, and so on) are important in the second case.[7] In turn, the high-frequency response of superconductors can also be divided into linear and nonlinear. Different experimental methods are used to study these responses. A description of these methods can be found in Refs. 4 and 27–30.

There are many experimental[10–19] and theoretical[20–26,31] works investigating the high-frequency response of superconductors in the linear regime (where the response of a superconductor is independent of the amplitude of the high-frequency field) in magnetic fields $B>B_{c1}$. It is shown in these works that the linear response of a superconductor can be quite completely described on the basis of a phenomenological theory which takes account of the high-frequency dynamics of the vortices,[20–26,31] and the presence of a vortex medium modifies the effective ac resistance of the supercon-

ductor, which becomes a function of the magnetic induction in the superconductor (i.e. the concentration of vortices) and the temperature and microwave frequency: $\rho_{ac} = \rho_{ac}(B,T,\omega)$. The form of the dependence $\rho_{ac}(B,T,\omega)$ is determined by the specific properties of the vortex ensemble: its phase state, the type of pinning, the presence of creep, and so on. The surface impedance is determined in terms of the modified resistance in the standard manner:[20] $Z_s = R_s + iX_s = \sqrt{i\omega\mu_0\rho_{ac}}$. It has been shown that for a uniform ordered vortex lattice (which can be obtained by cooling a superconductor in a constant uniform magnetic field—the field cooling regime, FC) the resistivity of a bulk superconductor can be represented in the form[23,24]

$$\rho_{ac} = i\omega\mu_0\lambda^2 + \rho_{TAFF}\frac{1+i\omega\tau}{1+i\omega\tau_0}, \qquad (1)$$

where λ is the London penetration depth, $\rho_{TAFF} = \rho_{FF}\tau_0/\tau \approx \rho_{FF}\exp(-U_p/k_BT)$, ρ_{TAFF} is the resistance in the thermally activated flow regime, ρ_{FF} is the resistance in the viscous flow regime, $\tau_0 = \eta/\alpha_L$ is the characteristic relaxation time for a pinned vortex lattice, $\tau \approx \tau_0\exp(U_p/k_BT)$ is the time constant for thermally activated creep of vortices, U_p is the activation energy of pinned vortices (the depth of the pinning potential row), $\alpha_L \approx 2U_p/r_p^2$ (r_p is the characteristic size of the potential well $U_p(r)$) is the Labush parameter characterizing the pinning strength, and η is the viscosity coefficient for moving vortices. The quantities α_L and η (per unit length of a single vortex) depend on the temperature,[10,14] and in sufficiently strong fields ($B \geqslant 0.1$ T), they also depend on the magnitude of the applied magnetic field.[14] In the proposed phenomenological models the specific temperature and field dependences of U_p, α_L, and η are determined either experimentally, as adjustable parameters, or are taken from the corresponding microscopic theories. Thus, specifically, the different form of the symmetry of the superconducting order parameters can also be taken into account.[11]

It can be shown that the following dependences for the surface resistance at low temperatures in weak magnetic fields follow from the expression (1):

$$\Delta R_s = R_s(B) - R_s(0) \cong \frac{B\Phi_0}{2\lambda\alpha_L}\frac{\omega^2}{\omega_0(1+(\omega/\omega_0)^2)}, \qquad (2)$$

where $\omega_0 = \tau_0^{-1}$ and for HTSCs lies in the range 10^{10}–10^{12} s^{-1}.[10] When additional effects are taken into account (specifically, the surface pinning, surface barrier, gyroscopic and size effects, presence of normal quasiparticles, finite sizes of the superconducting sample, and other factors[25,32–35]), the expression (1) is modified, which, correspondingly, changes the field, frequency, and temperature dependences of the surface resistance as compared with Eq. (2).

Thus, in principle, the characteristics of the vortex ensemble and the internal parameters of a superconducting material can be determined by comparing the theoretical dependences $\rho_{ac}(B)$ with the experimental data. Specifically, the temperature dependence, obtained in a number of experiments[16,19] by measuring the imaginary part of the surface impedance, of the London penetration depth $\lambda(T)$ agrees with the two-fluid model $\lambda(T) = \lambda_0[1-(T/T_c)^n]^{-1/2}$ with $n = 4$. In a number of other experiments the best agreement with the experimental data was obtained for values of n in the range $1.4 \leqslant n \leqslant 2.45$.[12,36]

When other measurement regimes are used, specifically, cooling in a zero magnetic field after which a field is switched on (zero field cooling, ZFC), the surface distribution of the vortices becomes substantially nonuniform. This alos results in a spatial nonuniformity of the high-frequency resistivity $\rho_{ac} = \rho_{ac}(B(\mathbf{r}))$. One consequence of the nonuniform distribution of vortices is hysteresis of the dependence $Z_s(B)$ when the constant magnetic field is cycled.[15] Using the critical-state model to describe the nonuniform vortex ensemble produced by a magnetic field in ZFC experiments[37,38] makes it possible to extract the transport characteristics of a superconductor, such as, the critical-currrent density and its temperature and field dependences $J_c(T,B)$, from the high-frequency measurements.

Investigations of the nonlinear high-frequency properties of HTSC materials (the dependence of the response on the magnitude of the applied signal) is of fundamental and applied value, since practical applications of HTSC materials in microwave technology are limited, first and foremost, by their nonlinear properties. Even though the nonlinear response of superconductors has been studied in a large number of experimental[39–45] and theoretical[31,46–49] works, today, there is no clear understanding of the mechanisms of and reasons for the nonlinear response. Probable reasons for the nonlinearities are considered to be the existence of weak links, depairing of supercurrent carriers, generation of vortices by an external high-frequency field, presence of flux creep, local superheating with high external currents, and other mechanisms, which in turn can depend on the presence of impurities, crystal-lattice defects, oxygen content, mechanical treatment of the sample, and other factors.[27] As a rule, a quadratic (in the magnitude of the ac magnetic field H_{ac}) dependence of the quantities $R_s(H_{ac})$ and $X_s(H_{ac})$ for comparatively low amplitudes of the high-frequency field is observed experimentally. As the field amplitude increases, the exponent increases. The quantities $R_s(H_{ac})$ and $X_s(H_{ac})$ in many cases exhibit correlated behavior (i.e. their dependence on H_{ac} is of the same form), but for a number of samples uncorrelated dependences have been observed.[27] In a number of experiments an ''anomalous nonlinear response'' in which the quantity Z_s (R_s or X_s and sometimes R_s and X_s simultaneously) decreases with increasing amplitude of the ac field was also observed.[39] This behavior has still not been given a generally accepted explanation. The possible reasons for and mechanisms of the nonlinearities of HTSC films are reviewed in greater detail in Ref. 27.

The present work is devoted to the study of the dynamical properties of the mixed state in highly perfect quasi-single-crystal $YBa_2Cu_3O_{7-\delta}$ (YBCO) films in the microwave range. The experiments were performed using a coplanar resonator,[28,29] made from the YBCO films studied, at frequency 5.25 GHz in the temperature range 13 K$< T <$80 K in the presence of a perpendicular external constant magnetif field $0 < B < 12.63$ mT. The linear and nonlinear responses of a YBCO film in FC and ZFC regimes were investigated. The results of an investigation of the temperature, field, and intensity (amplitude) dependences of the sur-

face impedance (real and imaginary parts) of YBCO films are presented. The phenomenological model of Refs. 21–24 was used for the theoretical description in order to explain the characteristic features of the response in the linear regime in FC and ZFC experiments; in addition, the nonuniform distribution of the vortices in the ZFC regime is taken into account using the critical-state model.[37,38] The critical-state model extended to the variable-field case was used to describe the response in the nonlinear regime.[48,49]

In the present work, when analyzing the linear response to a microwave field (in addition to what was done in Refs. 10–19) the influence of the uniformity of the static distribution of vortices over the width of the film on the microwave properties of the film in the mixed state is also investigated. It is shown that the response in the FC regime is substantially different from that in the ZFC regime. Indeed, in the FC regime, where the static distribution of vortices in the film can be assumed to be relatively uniform over the film width, in the linear (in the amplitude H_{ac} of the microwave field) case a correction B, linear in the magnitude of the constant field, to the surface impedance is observed; this correction is due to the contribution of the fluctuating vortices, in agreement with the theory of the linear response of vortices to an ac field (compare with the expression (2)).[21–24] In the ZFC regime the vortex correction to the impedance is found to be a non-single-valued function of the applied constant magnetic field—when the magnetic field is cycled from 0 to $B_{\max}$ (12.63 mT) and back hysteresis of $R_s(B)$ is observed. The nonlinear response in a zero constant field and in the FC regime was investigated for quite large amplitudes of the ac field ($H_{ac} > 5.2$ kA/m, in zero external magnetic field). It is shown that a barrier prevents vortices from entering the sample; the field and temperature dependences of the barrier are found. Application of the critical-state model extended to the case of an ac field[48,49] made it possible to calculate the critical current density J_c. The functions $J_c(T)$ found are in good agreement with the data obtained from transport measurements, and measurements of the dynamical magnetic susceptibility and also the magnetization performed with a SQUID magnetometer.[50–53]

2. EXPERIMENTAL PROCEDURE

The experiments in which the surface impedance was measured were performed using YBCO thin films with critical temperature $T_c \approx 90$ K. The films were deposited by noncoaxial magnetron sputtering, using ac current, on a single-crystal sapphire substrate (r cut) with a 25 nm thick CeO_2 buffer layer. YBCO was deposited at substrate temperature 740 °C.[52] The films were investigated by high-resolution electron microscopy, atomic force microscopy, and low-frequency magnetic (induction) methods, in which the dynamical magnetic susceptibility in a low-frequency ac field was studied and the real and imaginary parts of the susceptibility were determined as a function of temperature, the amplitude of the ac magnetic field, and the intensity of the applied constant magnetic field. The results of these investigations showed that the films obtained had a high degree of perfection and structural uniformity.[51–54] Independent

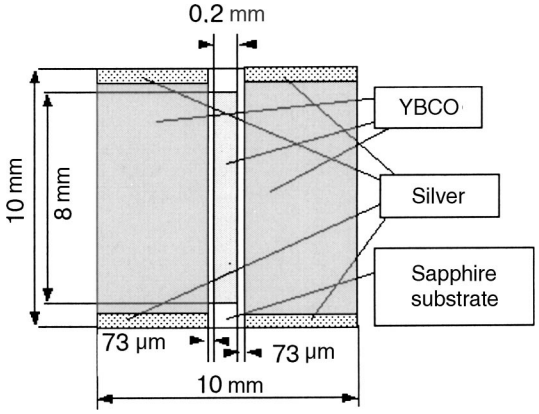

FIG. 1. Topology of a coplanar resonator.

experiments[51,53] showed that the critical current density in the films in the absence of a field is $(2-3)\cdot 10^6$ A/cm^2 at $T \approx 77$ K.

Coplanar resonators, whose topology is shown in Fig. 1, were fabricated using ion-etching technology and YBCO films with a thickness of about 350 nm. After the resonator was built, a thin strip of silver was deposited on its edge, as shown in Fig. 1, by vacuum sputtering in order to obtain a good ohmic contact between the YBCO film and the ''ground'' (ground plane) of the microwave coaxial feed cable. Next, this resonator was placed inside a copper holder with coupling antennas (Fig. 2.) The silver contact was clamped to the ground plane via a layer of thin indium foil.

A thick flat insulator layer was clamped by means of a spring to the bottom of substrateto improve heat removal from the resonator and ensure an electrical contact between the resonator and the ''ground.'' The copper holder with the sample was placed inside a closed-cycle cryostat. This made it possible to vary the temperature of the cold duct from room temperature down to 12 K. The temperature was measured on the top and bottom parts of the holder; when the temperature difference dropped below 0.5 K the temperature was assumed to be reliably set and the measurements commenced.

The resonance frequency f_0 and the width f_B of the resonance curve at half power of the line, were measured in the experiments. These values were used to determine the load factor $Q_L = f_0/f_B$ and the change in the resonance frequency as a function of temperature: $\Delta f = f(T_0) - f(T)$, where T_0 is

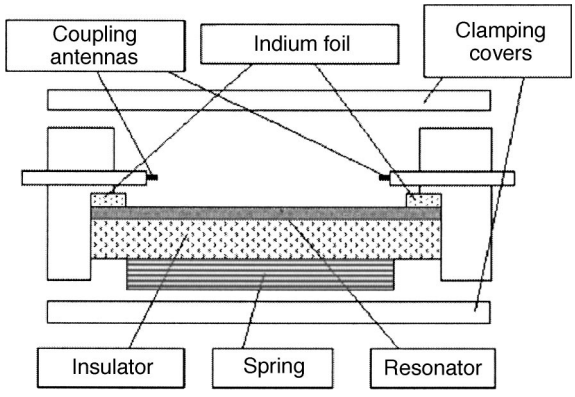

FIG. 2. Resonator holder with mobile coupling antennas.

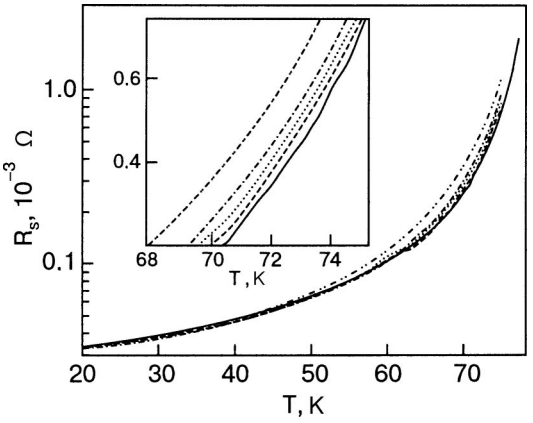

FIG. 3. Temperature dependences of the impedance of a YBCO film in the FC regime for different values of the external magnetic field B, mT: 0 (——), 1.58 (— — —), 3.16 (····), 6.32 (–·–), 12.63 (–···–). Inset: magnified section for 68 K$<T<$75 K.

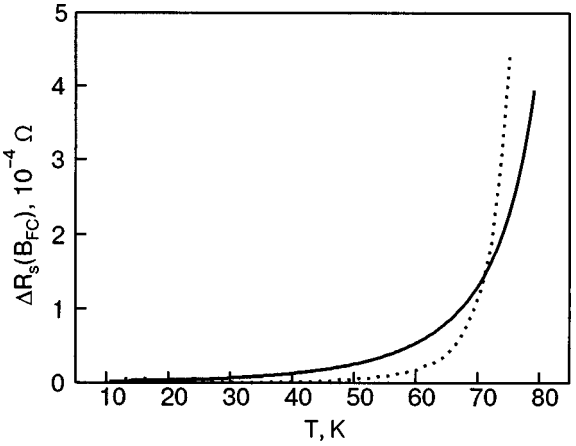

FIG. 4. Theoretical (——) and experimental (····) dependences $\Delta R_s(B) = R_s(B) - R_s(0)$ in the field $B_{FC} = 12.63$ mT.

a fixed temperature, in our case equal to the lowest temperature reached in the experiment 12 K. The real and imaginary parts of the surface impedance, R_s and X_s, and the penetration depth λ were extracted from the measured dependences.[28,29]

The magnetic system was made in the form of an outer removable solenoid, which produced an external constant magnetic field perpendicular to the sample with induction up to 12.63 mT. The solenoid was removed from the cryostat when measurements were performed in a zero external magnetic field.

3. MEASUREMENT RESULTS

A. Linear response in the frozen magnetic field regime

The temperature dependences of the surface resistance of a YBCO film in the FC regime are displayed in Fig. 3. Before the magnetic field was switched to a new value the resonator was heated up to a temperature above T_c and then cooled to the required temperature.

The dependence presented in Fig. 3 shows that the surface resistance is essentially independent of the magnitude of the frozen field down to temperature ~45 K. As the temperature increases further, the difference in the values of R_s obtained with different values of the magnetic field becomes even greater. The change in the surface resistance $\Delta R_s(B) = R_s(B) - R_s(0)$ is directly proportional to the magnitude of the frozen magnetic flux (i.e. the magnitude of the external static magnetic field): $\Delta R_s(B) \propto B$, in complete agreement with Eq. (2). The direct applicability of the expressions (1) and (2) follows from the assumption that the distribution of the static magnetic flux in the film in the FC regime is approximately uniform. The temperature dependence obtained can be explained as follows. The temperature dependence of the surface resistance is determined by the temperature dependences of the quantities $\alpha_L(T)$, $\eta(T)$, and $\lambda(T)$, which are described by the following relations:[10]

$$\alpha_L(t) = \alpha_L(0)(1-t)^{4/3}(1+t)^2 \exp(-3.14t).$$

where $\alpha_L(0) = 3\times 10^5$ N/m^2,

$$\eta(t) = \eta(0)(1-t^2)/(1+t^2),$$

where $\eta(0) = 1.2\times 10^{-6}$ Ns/m^2, $t = T/T_c$.

The function $\lambda(T)$ is described by the relation (3). The effect of the finite thickness of the film was taken into account by the relation $Z_s(d) = Z_s \coth(i\omega\mu_0 d/Z_s)$, where Z_s is the surface impedance of a bulk superconductor.[12,27]

Figure 4 displays the theoretical and experimental (calculated on the basis of the experimental data shown in Fig. 3) dependences of the surface resistance in a magnetic field, which follow from the indicated temperature dependences $\alpha_L(T)$, $\eta(T)$, and $\lambda(T)$. The quite good agreement between theory and experiment shows that the temperature dependence of the surface resistance of the films in a magnetic field is determined by the temperature dependences of the quantities $\alpha_L(T)$, $\eta(T)$, and $\lambda(T)$ (the fact that in Fig. 4 the curves do not coincide completely is probably due to the empirical character of the dependences $\alpha_L(T)$ and $\eta(T)$ used, which can vary depending on the defect structure of the films). The experimentally observed zero point of ΔR_s ($T \leqslant 45$ K, Fig. 3) is determined by the sensitivity of the measurement setup.

The experimentally obtained temperature dependence of the penetration depth $\lambda(T)$ is described well by the expression

$$\lambda(T) = \frac{\lambda_0}{\sqrt{1-t^n}} \tag{3}$$

with exponent $n \simeq 2$, which agrees with the data obtained in other experimental works.[12,16,36] In Eq. (3) λ_0 is the penetration depth of the magnetic field at $T = 0$, equal to 238 nm.

No H dependence of λ was observed in the experiment in the FC regime.

B. Linear response in the zero field cooling regime

The dependences obtained for the surface resistance of YBCO films in the ZFC regime at four different fixed temperatures 13, 20, 35, and 50 K are displayed in Fig. 5. The ZFC regime was obtained by cooling the resonator in a zero external magnetic field. After the prescribed temperature was reached the external magnetic field was increased from 0 to $B_{max} = 12$ mT in fixed steps. After B_{max} was reached the external magnetic field was once again decreased to zero in

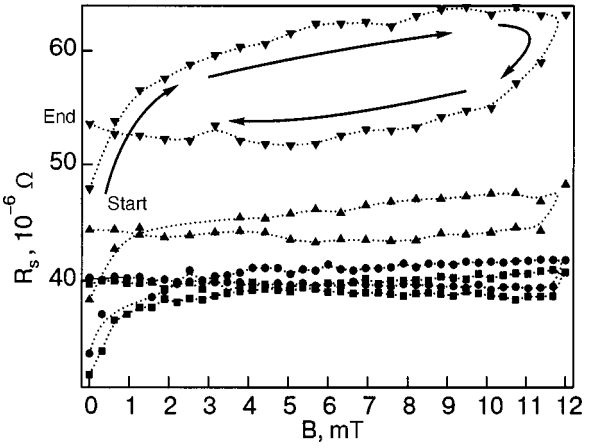

FIG. 5. Dependence of the surface resistance of YBCO films in the ZFC regime for T, K: 13 (■), 20 (●), 35 (▲), and 50 (▼).

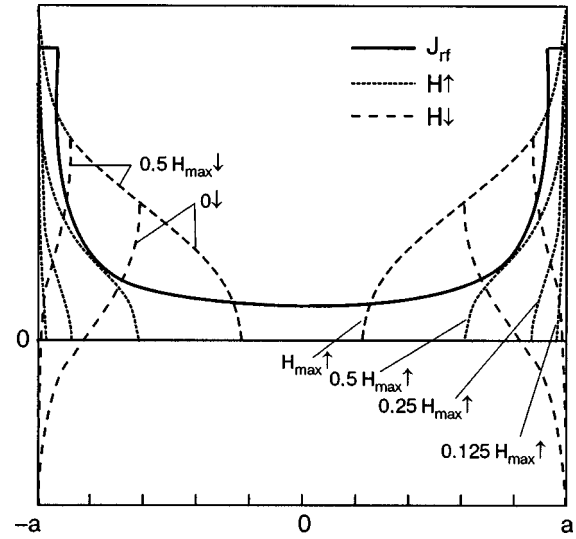

FIG. 6. Magnetic flux penetration into a superconducting film of width $2a$ with increase and subsequent decrease of the external magnetic field in the critical-state model (— — —);[37,38] distribution of the high-frequency current over the film width (——).[28,29]

steps. After each series of measurements at a prescribed temperature the resonator was heated up to a temperature above T_c and then cooled in zero field to the prescribed temperature.

Figure 5 shows that the dependences of the surface resistance on the external magnetic field exhibit hysteresis. Initially, R_s grows rapidly with increasing strength of the external applied magnetic field. Then the dependence $R_s(B)$ smoothly becomes virtually linear with R_s depending on the field B all more weakly the lower the temperature. After the maximum value of the external magnetic field is reached in a given cycle, at the very start of the decrease of B the quantity R_s drops rapidly and subsequently manifests a weak field dependence down to $B=0$. The value of R_s at the initial point of each measurement cycle (start) is different from that at the final point (end): the initial value of R_s is 10–12 $\mu\Omega$ less than the final value.

In the ZFC experiments the distribution of vortices in the film is strongly nonuniform and for low temperatures can be described by the critical-state model (it is assumed that the microwave current in this case does not destroy the critical state).[37,38]

Figure 6 shows the form of the profiles of the magnetic flux produced in the film as the external magnetic field B is increased from zero to some maximum value $B_{\max}$ and then decreased back down to zero, following from the critical-state model.[37,38] Under such cycling of the external field a trapped nonuniform magnetic flux remains in the film. As already mentioned, this results in local changes of the high-frequency properties of the material, specifically, the microwave resistivity of the vortex flow becomes dependent on the coordinate y and therefore the local surface resistance becomes coordinate-dependent $R_{\rm loc}(y)=\sqrt{\omega\mu_0\rho_{ac}(y)/2}$.

Taking account of the nonuniformity of the distribution of the high-frequency current over the width of the film, as shown in Fig. 6 (and, correspondingly, the high-frequency field $H_{ac}(y)$), the expression for the integral surface resistance in this case can be written in the form[55]

$$R_s=\frac{\int_{-a}^{a}R_{\rm loc}(y)H_{ac}^2(y)dy}{\int_{-a}^{a}H_{ac}^2(y)dy}, \qquad (4)$$

where $H_{ac}(y)$ is the tangential component of the high-frequency microwave field on the film surface and $2a$ is the width of the film. Using the explicit form of the expressions for $B(y)$ and $H_{ac}(y)$,[37,38] Eq. (4) was used to calculate the field dependence of the surface resistance in the ZFC experiments. This dependence exhibits hysteresis, similar to that displayed in Fig. 5. The dependence obtained is shown in Fig. 7.

C. Nonlinear response in the frozen magnetic field regime

For sufficiently large amplitudes of the ac field (in our experiment for $H_{ac}>5.2$ kA·m^{-1} in zero external magnetic field) the response of superconducting films becomes nonlinear: the surface resistance increases with the amplitude of the high-frequency field H_{ac}. As already mentioned, the most diverse factors can result in a nonlinearity of this type. However, the coplanar-resonator method used makes it possible to take account of one of them, specifically, the preferred mechanism whereby the vortices generated by an external high-frequency field enter through the sample edge. Indeed, as calculations show,[11,12] the microwave current density near the film edges is much higher than the average current density in the resonator (to a first approximation the current density at the edges is characterized by a square-root divergence). Thus even for relatively low levels of the input signal the field at the sample edges is higher than the critical field for nucleation of vortices, which then move under the action of the microwave current into the interior of the resonator. Since the density of the generated vortices depends on the amplitude of the microwave signal, this results in a natural manner in the nonlinearity of the type being considered.

A series of curves $R_s(T,H_{ac},B_{FC})$ was measured for samples cooled in a constant magnetic field $B_{FC}=0$, 1.58, 3.16, 6.32, and 12.63 mT for temperatures $T=13$, 20, 35, and 50 K.

Figure 8 shows curves of the surface resistance of a coplanar resonator versus the magnitude of the ac magnetic

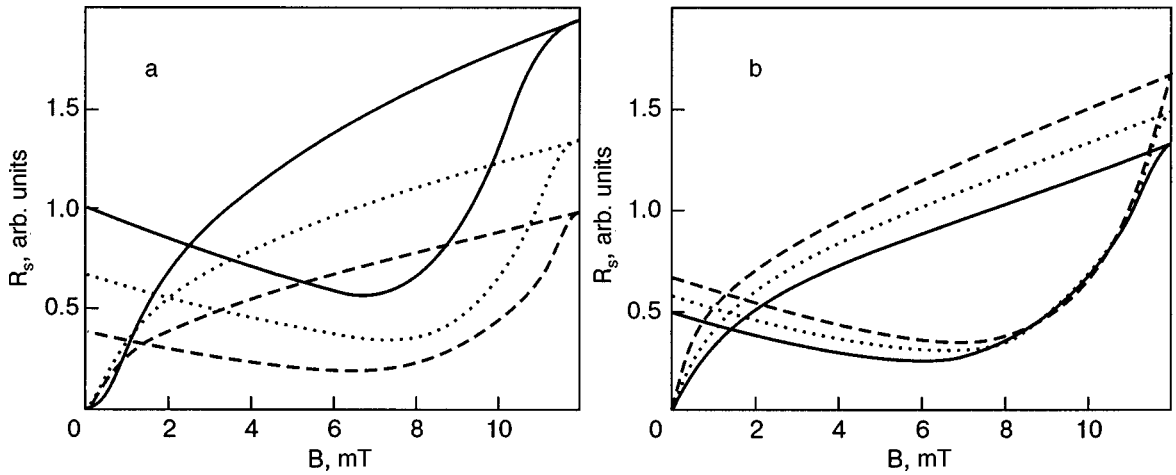

FIG. 7. Hysteresis of the surface resistance with cycling of a magnetic field from 0 to $B_{max}=12$ mT, obtained from the linear-response theory for the critical state of a film with the following values used in the calculation: $\lambda_0=250$ nm; $J_c=1\times10^7$ (——), 5×10^6 (····), 2.5×10^6 (— — —) A·cm^{-2} (a); $J_c=2.5\times10^6$ A·cm^{-2}, $\lambda_0=500$ (——), 250 (····), 125 nm (— — —) (b).

field which were obtained at $T=20$ K for different values of B_{FC}. Figure 9 shows similar curves for a resonator cooled in the field $B_{FC}=12.63$ mT for various temperatures. The characteristic feature of both dependences is the presence of a linear section where R_s is independent of the ac field amplitude and a nonlinear section where the surface resistance is described well by the relation $R_s \propto H_{ac}^2$.

The presence of a linear section in the dependences $R_s(T,H_{ac},B_{FC})$ attests to the presence of an edge barrier, on account of which vortex starts in fields exceeding a certain critical value: $H_{ac} \geqslant H_b$. We shall characterize the barrier by the current I_b. Correspondingly, vortex entry through the film edge starts for values of the microwave current at the sample edges exceeding I_b.

We shall use the critical-state model developed in Refs. 37 and 38 to give a theoretical description of the data obtained. When the current at the film boundary reaches a value of the order of the critical value (J_c) Abrikosov vortices start to enter the film through the boundary and a region $b<|x|<a$ where current flows with density $J=J_c$ arises at the film boundary; as the current increases further this region expands toward the center of the film. Detailed expressions for the distribution of currents and fields in the film and their dependence on the field B_{FC} can be found in Refs. 37 and 38.

For the subsequent calculations we shall use the amplitude I_0 of the microwave current in the resonator, determined by the relation[28,29]

$$I_0 = \sqrt{\frac{4P_{\text{in}}Q_L S_{21}}{q\pi Z_0}}. \tag{5}$$

where $S_{21}=10^{I_L/20}$, I_L are the measured coupling losses, Q_L is the loaded Q factor measured according to the half-width of the resonance curve, P_{in} is the entering microwave power taking account of losses in the feed line, q is the number of the resonance mode ($q=1$), and Z_0 is the characteristic impedance of the resonator ($Z_0=50\ \Omega$).

The microwave response of the critical state taking account of the barrier and the nonuniform (over the resonator length) distribution of the microwave current is described by the integral relation[41,49]

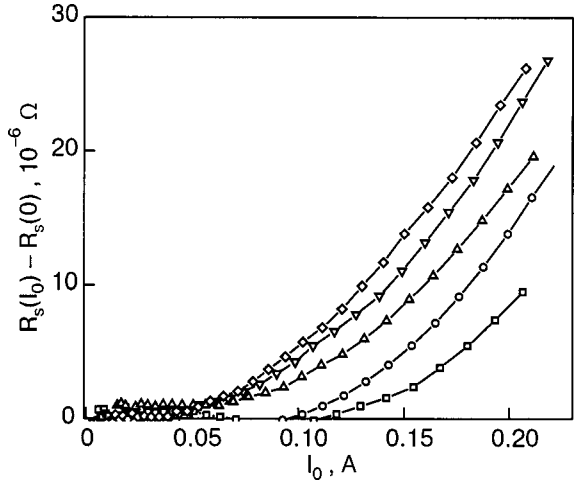

FIG. 8. R_s versus the amplitude of the microwave current at fixed temperature $T=20$ K for different values of the magnetic field B_{FC}, mT: 0 (□), 1.58 (○), 3.16 (▽), 6.32 (△), and 12.63 (◇).

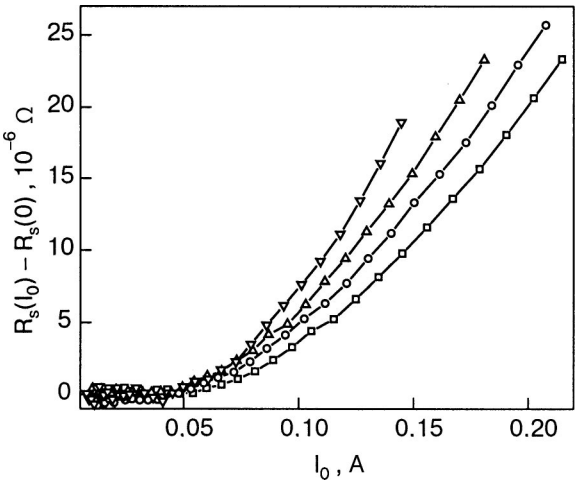

FIG. 9. R_s versus the amplitude of the microwave current with a fixed magnetic field $B_{FC}=12.63$ mT for different values of T, K: 13 (□), 20 (○), 35 (△), and 50 (▽).

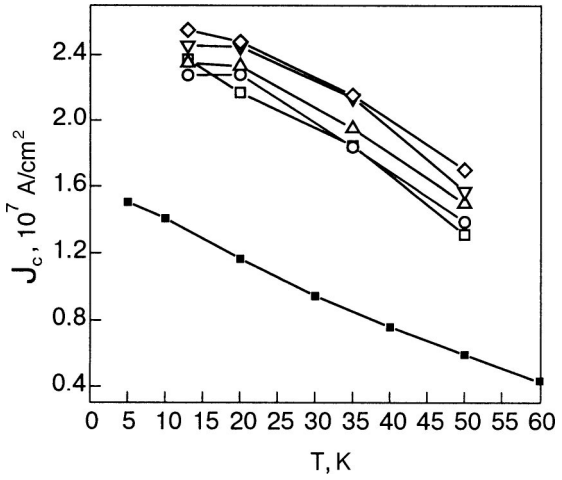

FIG. 10. Temperature dependence of the critical current J_c obtained on the basis of the critical-state model with B, mT: 0 (□), 1.58 (○), 3.16 (△), 6.32 (▽), and 12.63 (◇). The bottom curve was obtained by measuring the magnetization with a SQUID magnetometer on an equivalent film.[51,53]

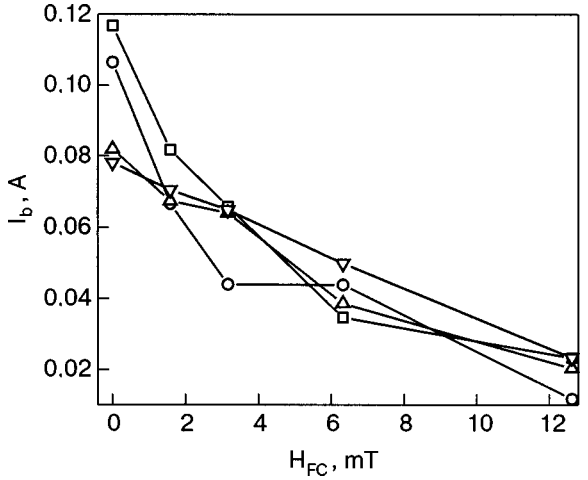

FIG. 11. Barrier I_b versus the field B_{FC} frozen in the sample at T, K: 13 (□), 20 (○), 35 (△), and 50 (▽).

$$R_s = \frac{8 f \mu_0 a}{\pi} \frac{\int_{z_1}^{z_2} F(x g(z)) dz}{x^2 \int_{z_1}^{z_2} g^2(z) dz}, \tag{6}$$

where the function $F(x)$ describes the hysteresis losses to the entry-exit of vortices and $g(z)$ is the distribution of the microwave current along the resonator. In our experiments the resonator was used at the fundamental mode of the oscillations (half-wave regime), for which in the absence of hysteresis

$$g(z) = \sin(\pi z/l).$$

In Eq. (6)

$$F(x) = (1-x)\ln(1-x) + (1+x)\ln(1+x) - x^2,$$

$$x = (I_a - I_b)/I_{\max}, I_{\max} = 2aJ_c,$$

$$g(z) = (I_0 \sin(\pi z/l) - I_b)/(I_0 - I_b),$$

$$z_1 = l \arcsin(I_b/I_0)/\pi,$$

$$z_2 = l(\pi - \arcsin(I_b/I_0))/\pi,$$

and l is the length of the resonator. The experimentally observed relation $R_s(I_0) \propto (I_0 - I_b)^2$ follows from Eq. (6).

The quantities $I_b(T)$, $I_b(B_{FC})$, and $J_c(T)$ calculated according to Eq. (6) from the measured dependences (Figs. 8 and 9) are displayed in Figs. 10–12. According to Fig. 10 the critical current obtained in this manner is somewhat higher than its values obtained by the direct method of transport measurements and by measuring the magnetization with a SQUID magnetometer.[51–53] The main reason for this could be that the critical-state model[37,38] is applicable in pure form in the quasistatic case in a strip (and not coplanar) geometry. In addition, in order to use it in the microwave regime the real (i.e. viscous) motion of the vortex lattice and the inertial properties of the vortices must be taken into account. Nonetheless, the quite good agreement of the experimentally determined magnitudes of the critical current shows that the nonlinear response of the superconducting resonator is indeed caused by vortices generated by the microwave field. The response to these vortices can be described by the critical-state model, at least for qualitative estimation of the phenomenon described.

It is evident that in our case the barrier current is different from the critical current (Figs. 10–12). This justifies introducing it as a parameter which is independent of J_c. The dependences displayed in Fig. 11 could be due to a decrease in the effective curvature of the edge of the superconducting film in the presence of a magnetic field because of vortex curvature near the edges of the resonator, which decreases the barrier.[56] The weaker temperature dependence of the barrier current in the presence of a magnetic field as compared with experiments in the absence of a constant field (Fig. 12) is explained in this case by the different nature of the barrier in both cases: in the absence of a field the barrier is determined by the temperature dependence of the critical current density, and in the presence of a magnetic field it is determined by the geometry of the sample and is essentially temperature-independent.[56]

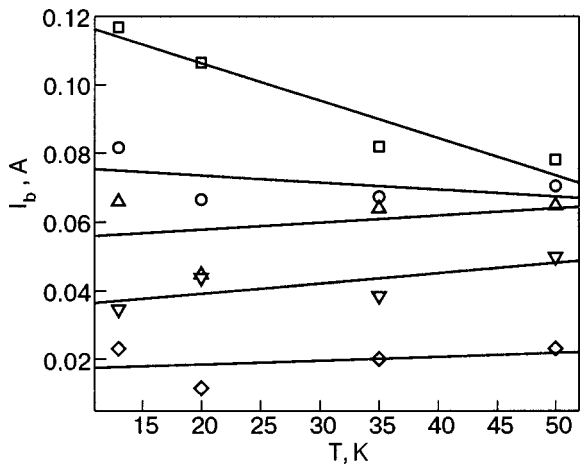

FIG. 12. Temperature dependence of the barrier with B_{FC}, mT: 0 (□), 1.58 (○), 3.16 (△), 6.32 (▽), and 12.63 (◇).

4. CONCLUSIONS

The temperature and field dependences of the surface impedance and penetration depth of the magnetic field for YBCO single crystal films at 5.25 GHz in the linear and nonlinear regimes were found. The contribution of the Abrikosov vortices, oscillating in a high-frequency field, to the surface resistance in a mixed state of the film was determined. It was shown that the microwave response of uniformly distributed vortices is different from that of nonuniformly distributed vortices, as measured in FC and ZFC experiments. It was suggested that the observed behavior be described on the basis of the theory of linear high-frequency response of vortices using the critical-state model to take account of the distribution of frozen (trapped) vortices, which is nonuniform over the film width, for the case of ZFC experiments. It was shown that the linear-response theory for the mixed state[25–28] describes the observed dependences well; the hysteresis part, obtained in the ZFC regime, can be explained within the critical-state model.[37,38] The nonlinear response of the resonator can also be described on the basis of the critical-state model for the entry of vortices generated by the high-frequency field, modified taking account of the barrier preventing entry of vortices and the nonuniform distribution of the microwave field along the sample.[41,49] The nonlinear part of the surface resistance is characterized by the barrier preventing entry of vortices into the film. The field and temperature dependences of the magnitude of the barrier, which are different from the analogous dependences of the critical field, were determined on the basis of the model employed. It was shown that the values of the critical current which were obtained on the basis of this approach are characterized by the same temperature dependence as the values determined for equivalent films by the SQUID-magnetometry method. It was concluded that in the geometry considered (coplanar resonator) the predominant mechanism of the microwave nonlinearity is the generation and motion of Abrikosov vortices under the action of a microwave field.

We thank A. V. Semenov for stimulating discussions in the course of the analysis of the experimental data. One of us (D. A. Luzhbin) is grateful for the support provided by an INTAS Young Scientist Fellowship (Grant No. 03-55-2036).

*E-mail: pan@imp.kiev.ua

[1] J. G. Bednorz and K. A. Müller, Z. Phys. B: Condens. Matter **64**, 189 (1986).
[2] J. M. Rowell, IEEE Trans. Appl. Supercond. **9**, 2837 (1999).
[3] A. I. Braginski, IEEE Trans. Appl. Supercond. **9**, 2825 (1999).
[4] M. R. Trunin, Usp. Fiz. Nauk **168**, 931 (1998).
[5] G. Blatter, M. V. Feigel'man, V. B. Geshkenbein, A. I. Larkin, and V. M. Vinokur, Rev. Mod. Phys. **6**, 1125 (1994).
[6] P. Chaddah and S. B. Roy, Curr. Sci. **80**, 1036 (2001) (cond-mat/0005311).
[7] E. H. Brandt, Rep. Prog. Phys. **58**, 1465 (1995).
[8] T. Giamarchi and S. Bhattacharya, cond-mat/0111052.
[9] Y. Yeshurun, A. P. Malozemoff, and A. Shaulov, Rev. Mod. Phys. **68**, 911 (1996).
[10] M. Golosovsky, M. Tsidlekht, and D. Davidov, Semicond. Sci. Technol. **9**, 1 (1996).
[11] E. Silva, R. Fastampa, M. Giura, R. Marcon, D. Neri, and S. Sarti, Semicond. Sci. Technol. **13**, 1186 (2000).
[12] M. I. Tsindlekht, E. B. Sonin, M. A. Golosovsky, D. Davidov, X. Castel, M. Guilloux-Viry, and A. Perrin, Phys. Rev. B **61**, 1596 (2000).
[13] N. Belk, D. E. Oates, D. A. Feld, G. Dresselhaus, and M. S. Dresselhaus, Phys. Rev. B **53**, 3459 (1996).
[14] I. S. Ghosh, L. F. Cohen, and J. C. Gallop, Semicond. Sci. Technol. **10**, 936 (1997).
[15] B. A. Willemsen, J. S. Derov, and S. Sridhar, Phys. Rev. B **56**, 11989 (1997).
[16] S. Revenaz, D. E. Oates, D. Labbe-Lavigne, G. Dresselhaus, and M. S. Dresselhaus, Phys. Rev. B **50**, 1178 (1994).
[17] J. R. Powell. A. Porch, R. G. Humphreys, F. Wellhöfer, M. J. Lancaster, and C. E. Gough, Phys. Rev. B **57**, 5474 (1998).
[18] V. A. Berezin, E. V. Il'ichev, V. A. Tulin, E. B. Sonin, A. K. Tagantsev, and K. B. Traito, Phys. Rev. B **49**, 4331 (1994).
[19] M. Golosovsky, M. Tsindlekht, H. Chayet, and D. Davidov, Phys. Rev. B **50**, 470 (1994).
[20] L. P. Gor'kov and N. B. Kopnin, Usp. Fiz. Nauk **116**, 413 (1975) [Sov. Phys. Usp. **18**, 496 (1975)].
[21] M. W. Coffey and C. R. Clem, Phys. Rev. Lett. **67**, 386 (1991).
[22] M. W. Coffey and J. R. Clem, Phys. Rev. B **48**, 342 (1993).
[23] E. H. Brandt, Phys. Rev. Lett. **67**, 2219 (1991).
[24] E. H. Brandt, Physica C **195**, 1 (1992).
[25] E. B. Sonin and K. B. Traito, Phys. Rev. B **50**, 13547 (1994).
[26] B. Palacais, P. Mathieu, Y. Simon, E. B. Sonin, and K. B. Traito, Phys. Rev. B **54**, 13083 (1996).
[27] A. V. Velichko and M. J. Lancaster, in *Proceedings of the 5th International Symposium on Physics and Engineering of Microwaves, Millimeter, and Submillimeter Waves*, edited by A. Kostenko, Kharkov, Ukraine (2004), p. 78.
[28] M. J. Lancaster, *Passive Microwave Device Applications of High Temperature Superconductors*, Cambridge University Press, United Kingdom (1997).
[29] A. Porch, M. J. Lancaster, and R. G. Humphreys, IEEE Trans. Microwave Theory Tech. **43**, 306 (1995).
[30] D. E. Oates, A. C. Anderson, D. M. Sheen, and S. M. Ali, IEEE Trans. Microwave Theory Tech. **39**, 1522 (1991).
[31] C. J. van der Beek, V. B. Geshkenbein, and V. M. Vinokur, Phys. Rev. B **48**, 3393 (1993).
[32] D. A. Luzhbin, A. L. Kasatkin, and V. M. Pan, Fiz. Nizk. Temp. **27**, 455 (2001) [Low Temp. Phys. **27**, 333 (2001)].
[33] D. A. Luzhbin, Fiz. Nizk. Temp. **27**, 1232 (2001) [Low Temp. Phys. **27**, 909 (2001)].
[34] N. V. Zhelezina and G. M. Maksimov, Fiz. Tver. Tela (St. Petersburg) **43**, 1939 (2001) [Phys. Solid State **43**, 2018 (2001)].
[35] A. Kasatkin and B. Rosenstein, Phys. Rev. B **60**, 14907 (1999).
[36] I. B. Vendik, E. K. Gol'man, S. V. Razumov, A. A. Svishchev, and A. V. Tumarkin, Pis'ma Zh. Tekh. Fiz. **23**, 79 (1997) [Tech. Phys. Lett. **23**, 608 (1997)].
[37] E. H. Brandt and M. Indenbom, Phys. Rev. B **48**, 12893 (1993).
[38] E. Zeldov, J. R. Clem, M. McElfresh, and M. Darwin, Phys. Rev. B **49**, 9802 (1994).
[39] A. V. Velichko, M. J. Lancaster, R. A. Chakalov, and F. Wellhofer, Phys. Rev. B **65**, 104522 (2002).
[40] P. P. Nguyen, D. E. Oates, G. Dresselhaus, and M. S. Dresselhaus, Phys. Rev. B **48**, 6400 (1993).
[41] P. P. Nguyen, D. E. Oates, G. Dresselhaus, M. S. Dresselhaus, and A. C. Anderson, Phys. Rev. B **51**, 6686 (1995).
[42] N. Belk, D. E. Oates, D. A. Feld, G. Dresselhaus, and M. S. Dresselhaus, Phys. Rev. B **56**, 11966 (1997).
[43] J. R. Powell, A. Porch, A. P. Kharel, M. J. Lancaster, R. G. Humphreys, F. Wellhöfer, and C. E. Gough, J. Appl. Phys. **86**, 2137 (1999).
[44] A. P. Kharel, A. V. Velichko, J. W. Powell, A. Porch, M. J. Lancaster, and R. G. Humphreys, Phys. Rev. B **58**, 11189 (1998).
[45] M. A. Hein, R. G. Humphreys, P. J. Hirst, S. H. Park, and D. E. Oates, J. Supercond. **16**, 895 (2003).
[46] J. Halbritter, J. Supercond. **8**, 691 (1995).
[47] A. V. Velichko and A. Porch, Phys. Rev. B **63**, 094512 (2001).
[48] T. Dasgupta, D. P. Choudhury, and S. Sridhar, cond-mat/9905063.
[49] S. Sridhar, Appl. Phys. Lett. **65**, 1054 (1994).
[50] V. M. Pan, Usp. Fiz. Met. **1**, 49 (2000).
[51] Yu. V. Fedotov, E. A. Pashitskii, S. M. Ryabchenko, A. V. Semenov, A. V. Pan, S. X. Dou, C. G. Tretiatchenko, V. A. Komashko, Yu. V. Cherpak, and V. M. Pan, Physica C **401**, 316 (2004).
[52] V. A. Komashko, A. G. Popov, V. L. Svetchnikov, A. V. Pronin, V. S. Melnikov, A. Yu. Galkin, V. M. Pan, S. L. Snead, and M. Suenaga, Semicond. Sci. Technol. **13**, 209 (2000).
[53] V. M. Pan, E. A. Pashitskii, S. M. Ryabchenko, V. A. Komashko, A. V.

Pan, S. X. Dou, A. V. Semenov, C. G. Tretiatchenko, and Y. V. Fedotov, IEEE Trans. Appl. Supercond. **13**, 3714 (2003).
[54] V. L. Svetchnikov, V. P. Pan, Ch. Tracholt, and H. W. Zandbergen, IEEE Trans. Appl. Supercond. **7**, 1396 (1997).
[55] A. N. Reznik, IEEE Trans. Appl. Supercond. **7**, 1474 (1997).
[56] E. Zeldov, A. I. Larkin, V. B. Geshkenbein, M. Konczykowski, D. Majer, B. Khaykovich, V. M. Vinokur, and H. Shtrikman, Phys. Rev. Lett. **73**, 1428 (1994)

Translated by M. E. Alferieff

Negative thermal expansion of HTSC-type structures: low temperature structure measurements on $Eu_{1+x}(Ba_{1-y}R_y)_{2-x}Cu_3O_{7-d}$ compounds and theoretical treatment

V. V. Eremenko,* S. B. Feodosyev, I. A. Gospodarev, V. A. Sirenko, and M. Yu. Shvedun

B. Verkin Institute for Low Temperature Physics and Engineering of the National Academy of Sciences of Ukraine, 47 Lenin Ave., Kharkov 61103, Ukraine

W. McCallum

Ames Laboratory, Ames, Iowa, USA

M. Tovar

Berlin Neutron Scattering Center, Hahn-Meitner-Institute, Germany

(Submitted November 4, 2004)
Fiz. Nizk. Temp. **31**, 350–355 (March–April 2005)

The temperature dependences of the lattice parameters are investigated on the perovskite-like structures $Eu_{1+x}(Ba_{1-y}R_y)_{2-x}Cu_3O_{7-d}$ with Ba substitution by light rare earth, using x-ray diffraction techniques. A negative thermal expansion effect is observed and explained in detail. © *2005 American Institute of Physics.* [DOI: 10.1063/1.1884428]

BACKGROUND

Negative thermal expansion (NTE) has been known for some time in several compounds such as perovskite ferroelectrics[1] and layered superconductors.[2] This phenomenon is the result of unusual lattice dynamics. In such multilayer structures the lattice parameter in one of the crystallographic directions is much greater than the characteristic radius of interatomic interaction. This weakens the influence of regularity in the crystal atom distribution on the phonon spectrum and vibrational properties of the crystal. Structures of this type take an intermediate state between crystals and disordered systems. We consider this effect for the HTSC perovskite-like system $Eu_{1+x}(Ba_{1-y}R_y)_{2-x}Cu_3O_{7-d}$ with Ba substitution by the light rare earth La. It was shown recently that the structural distortions in $Eu(Ba_{1-x}R_x)Cu_3O_{7+d}$ caused by a rare earth (R=La, Nd, Pr) on a Ba site include a crystallographic transition from orthorhombic to tetragonal symmetry, changes of the ''buckling angle'' at the CuO_2 plane layer, and changes in ionic bond lengths.[3] This results in suppression of high-temperature superconductivity in these compounds and a number of specific effects in the vicinity of the superconducting transition, which merit a comprehensive study. The present work is part of such a study.

EXPERIMENTAL PART

Experiment details

We studied HTSCs with rare earth substitutions for Ba, corresponding to different levels of doping (concentration of carriers),[4] in order to check the attribution of volume changes at low temperatures (below the superconducting transition) to phase transitions. The crystal structure contains layers of Eu, CuO_2, BaO, and CuO_{1-d}. Characterization of the samples has shown that the preparation procedure provided perfect location of the substituting La atoms in Ba positions. A study of the neutron diffraction patterns (NDPs) above and below T_c, including measurements in magnetic field up to 4 T, was performed, together with low-temperature x-ray measurements. The x-ray spectra $I(\Theta)$ were registered on a DRON-2.0 diffractometer, using the Bragg—Brentano scheme of focusing (Θ–2Θ scheme). The complete spectra of the diffracted radiation were obtained, with a subsequent identification of the unit cell system and parameters. The accuracy of the intensity measurements was 0.5%. The lattice parameters were determined to accuracy within $\pm 0.01\%$. The error bars are shown on the measured curves. The DRON-2.0 diffractometer was also used in the cryogenic experiments: in this case a small-size cryostat for x-ray powder measurements in a temperature range 4.2–300 K was installed. In the experiment an x-ray tube with a copper anode was used ($\lambda_{CuK\alpha}=1.54178$ Å). The spectra were registered in the angle range $2\Theta=20°-60°$.

Experimental results

The typical measured diffraction patterns are shown in Fig. 1. The calculated lattice parameters are summarized in

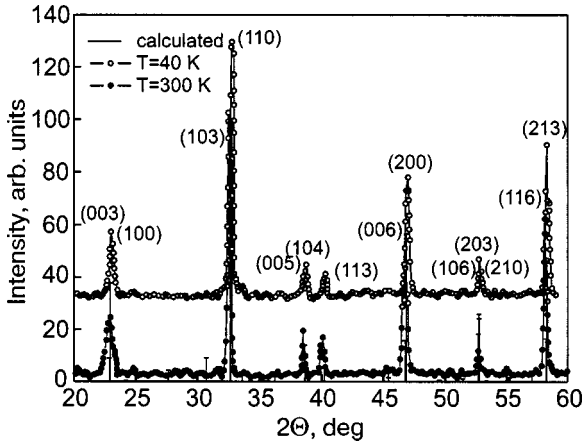

FIG. 1. X-ray diffraction patterns for $Eu(Ba_{0.85}La_{0.15})_2Cu_3O_{7-d}$.

TABLE I. The calculated lattice parameters of the perovskite-like structures $Eu_{1+x}(Ba_{1-y}R_y)_{2-x}Cu_3O_{7-d}$.

T, K	a, Å			b, Å		c, Å			V, Å^3		
	$EuBa_2Cu_3O_{7-d}$	$Eu(Ba_{0.85}La_{0.15})_2Cu_3O_{7-d}$	$Eu(Ba_{1-x}Nd_x)_2Cu_3O_{7-d}$	$EuBa_2Cu_3O_{7-d}$	$Eu(Ba_{1-x}Nd_x)_2Cu_3O_{7-d}$	$EuBa_2Cu_3O_{7-d}$	$Eu(Ba_{0.85}La_{0.15})_2Cu_3O_{7-d}$	$Eu(Ba_{1-x}Nd_x)_2Cu_3O_{7-d}$	$EuBa_2Cu_3O_{7-d}$	$Eu(Ba_{0.85}La_{0.15})_2Cu_3O_{7-d}$	$Eu(Ba_{1-x}Nd_x)_2Cu_3O_{7-d}$
300	3.8313		3.8186	3.8900	3.8868	11.6699		11.5687	173.9254		171.7042
280		3.8912					11.6481			176.3690	
260		3.8905					11.6534			176.3858	
240	3.8305	3.8888		3.8893		11.6764	11.6571		173.9546	176.2876	
220		3.8877					11.6617			176.2574	
200		3.8839					11.6753			176.1182	
180	3.8295	3.8836		3.8873		11.6791	11.6761		173.8599	176.1030	
160		3.8830					11.6774			176.0682	
140		3.8824	3.8187		3.8904		11.6789	11.5851		176.0364	172.1114
120	3.8243	3.8800		3.8855		11.6838	11.6871		173.6133	175.9423	
100		3.8777					11.6894			175.7683	
80	3.8243	3.8775		3.8841		11.6862	11.6908		173.1325	175.7713	
60		3.8768					11.6930			175.7409	
40		3.8721	3.8184		3.8892		11.7064	11.5871		175.5159	172.0745

Table I and illustrated by Fig. 2 for $Eu(Ba_{0.85}La_{0.15})_2Cu_3O_{7-d}$ as an example. The space groups and discrepancy factors for these compounds are: $EuBa_2Cu_3O_{7-d}$:

$Pmmm$, $R_p=4.2\%$, $R_{wp}=5.4\%$, $R_B=6.2\%$;

$Eu(Ba_{0.85}La_{0.15})_2Cu_3O_{7-d}$:

$P4/mmm$, $R_p=4.6\%$, $R_{wp}=5.6\%$, $R_B=6.4\%$;

$Eu(Ba_{1-x}Nd_x)_2Cu_3O_{7-d}$:

$Pmmm$, $R_p=4.4\%$, $R_{wp}=5.6\%$, $R_B=6.2\%$.

The data in Table I show a weak orthorhombicity in the *Pmmm* structures.

Here we address ourselves to the problem of anisotropic negative expansion, illustrated by Fig. 2 for $Eu(Ba_{0.85}La_{0.15})_2Cu_3O_{7-d}$ as an example. The same tendency is observed for the non-substituted compound $Eu_1Ba_2Cu_3O_{7-d}$, as our x-ray measurements revealed. The corresponding numerical data are presented in Table I.

DISCUSSION

Strong anisotropy of the thermal expansion when, at positive volumetric expansion, the lattice is compressed along any crystal axes (or planes), testifies, first of all, to strong anisotropy of the interatomic interaction.

The possibility of negative values of the linear thermal expansion coefficient (LTEC) along a direction of strong coupling of layered or chained structures (so-called ''membrane effect'') was first predicted by Lifshits[3] for strongly anisotropic compounds, the phonon spectra of which reveal

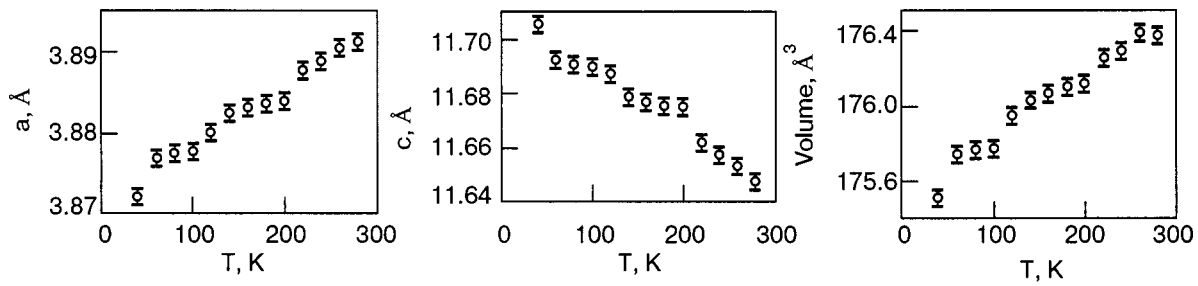

FIG. 2. Temperature dependence of the unit cell parameters for $Eu(Ba_{0.85}La_{0.15})_2Cu_3O_{7-d}$.

the so-called bending vibrations with a quadratic dispersion law $\omega(k)$ at $k\to 0$. Later, negative values of the LTEC have been found (see, for example,[5]) for strongly anisotropic layered crystals containing modes with characteristic ''quasi-bending'' curvature in a long-wavelength region of the vibration spectrum (for example, graphite), and for compounds (such as GaSe, GaS, InSe) in which the phonon spectra exibit either a weaker corresponding curvature or the latter is not revealed at all. Recently, similar features were observed on advantageous superconductors like MgB_2. A more general analysis, based on microscopic consideration, of the reasons causing negative LTEC along directions of strong coupling in crystals with strong anisotropy of the interatomic interaction and elastic properties has been proposed in Refs. 6 and 7.

In such strongly anisotropic crystals the amplitude of the atomic vibrations along directions of weak coupling (perpendicular to layers or chains) is much higher than in directions of strong coupling. Displacement of an atom along a direction of weak coupling leads to an increase in the distance between atoms within a layer (or chain) of magnitude Δl proportional to the square of this displacement. Consequently, within a layer a compressive force proportional to Δl arises, which is the reason for the anisotropic negative expansion alike the ''membrane effect.'' We suggest the following microscopic description for these compressive forces.

If the potential energy Φ of a lattice is expanded in a number of components u_i of a small displacement of the atoms from equilibrium position up to the cubic term, then the temperature dependence of the principal values of the LTEC tensor $\alpha_{ii}(T)$ in view of the translational invariance of the lattice are described by the following expression:

$$D_i\alpha_{ii}(T)=-\frac{1}{2}\sum_{\substack{\mathbf{r},\mathbf{r}'\\k,l}}\Phi_{ikl}(\mathbf{r},\mathbf{r}')\langle u_k(\mathbf{r})u_k(\mathbf{r}')\rangle_T, \qquad (1)$$

where

$$D_i=\sum_{\mathbf{r}}\Phi_{ik}(\mathbf{r})|x_k|,$$

$$\Phi_{ik}(\mathbf{r})=\Phi_{ik}(\mathbf{r}-\mathbf{r}')=\frac{\partial^2\Phi}{\partial u_i(\mathbf{r})\partial u_k(\mathbf{r}')}$$

are the elements of a force matrix,

$$\Phi_{ikl}(\mathbf{r},\mathbf{r}')=\Phi_{ik}(\mathbf{r}-\mathbf{r}'',\mathbf{r}'-\mathbf{r}'')=\frac{\partial^3\Phi}{\partial u_i(\mathbf{r})\partial u_k(\mathbf{r}')\partial u_l(\mathbf{r}'')}$$

x_i are the components of the radius vectors $\mathbf{r}$ of the equilibrium positions of the atoms; the symbol $\langle u_i(\mathbf{r})u_k(\mathbf{r}')\rangle_T$ is the correlator of the atomic displacements, calculated in the harmonic approximation.

In considering effects nonlinear in the vibrations of a crystal lattice (see, for example, Ref. 8) it is necessary to take into account anharmonicity only in the terms connected to the largest forces of interatomic interaction, while the potential energy of the weak forces of interlayer (or interchain) interactions, as well as noncentral forces, should be considered in the harmonic approach. Therefore in (1) it is possible to neglect the summands containing correlators of the atomic displacements from different layers or chains, i.e., correlators of the $\langle u_x(\mathbf{r})u_y(0)\rangle_T$ type. Besides, as in the majority of crystals the central interaction between atoms decreases with distance quickly enough, it is possible to neglect in (1) the summands containing correlators between the second and more-distant neighbors of the same layer or a chain. Correlators of the $\langle u_\mu(\mathbf{r})u_\mu(0)\rangle_T$ type for the nearest neighbors (the direction μ is chosen along the strong coupling) grow with temperature not faster than the mean-square displacement $\langle u_\mu^2(\mathbf{r})\rangle_T$, and both these temperature dependences are similar (this follows, for example, from the expressions obtained in Ref. 9). Therefore the behavior of the temperature dependence of the LTEC along a direction of strong coupling of a layered or chained crystal can be described by the rather simple expression:

$$\alpha_\parallel(T)=\alpha_{\mu\mu}(T)=A\frac{\partial}{\partial T}\langle u_\mu^2\rangle_T\left\{\delta-\frac{\dfrac{\partial}{\partial T}\langle u_\perp^2\rangle_T}{\dfrac{\partial}{\partial T}\langle u_\mu^2\rangle_T}\right\}. \qquad (2)$$

Here $\langle u_\perp^2\rangle_T$ is the mean-square displacement of atoms along a direction of weak coupling, that is, $\langle u_\perp^2\rangle_T=\langle u_c^2\rangle_T$ for layered crystals (if ab is the plane of the layers) and $\langle u_\perp^2\rangle_T=\langle u_a^2\rangle_T+\langle u_b^2\rangle_T$ for chained (with the chains built along the **c** axis). The parameters A and δ appearing in (2) are obviously expressed in terms of the anharmonic constants $\Phi_{ikl}(\mathbf{r},\mathbf{r}')$, but the explicit form of the corresponding expressions is not presented here for reasons of space.

Let us analyze the temperature dependence of the quantity

$$\Delta(T)=\frac{\dfrac{\partial}{\partial T}\langle u_\perp^2\rangle_T}{\dfrac{\partial}{\partial T}\langle u_\mu^2\rangle_T}. \qquad (3)$$

For strongly anisotropic crystals the quantities $\langle u_\perp^2\rangle_T$ are not only much greater than $\langle u_\mu^2\rangle_T$ but also at lower temperatures are outside of the classical limit. Thus, near the temperature $T_\perp$ (the temperature at which the quantity $\langle u_\perp^2\rangle_T$ approaches the classical limit) the function $\Delta(T)$ has a maximum, the size of which is proportional to $\exp(\gamma^{-1/2})$, where γ is the ratio of the weak interlayer or interchain interaction to the strong interaction along the layers or chains, respectively. Therefore, near this temperature the LTEC $\alpha_\parallel$ is anomalously small and may have negative values.

The values of the temperatures of the maxima obtained in Refs. 6 and 7 for the quantities ΔT have shown good agreement with the temperatures of the minima on the measured dependences of the LTEC $\alpha_\parallel(T)$ of strongly anisotropic layered crystals.[5]

We should note at once that for the crystal structures considered in Refs. 5–7 the strong anisotropy of the interatomic interaction remains in the long-range order and manifests itself, in particular, in anisotropy of the elastic constants. In crystals such as 1–2–3 HTSCs the anisotropy of the elastic constants is insignificant and, moreover, has the other sign, as the sound velocity along the layers is higher than in the direction normal to the layers.[10] At the same time, in such multilayered compounds the lattice period along the **c** axis is not only higher than along axes a and b, but it also

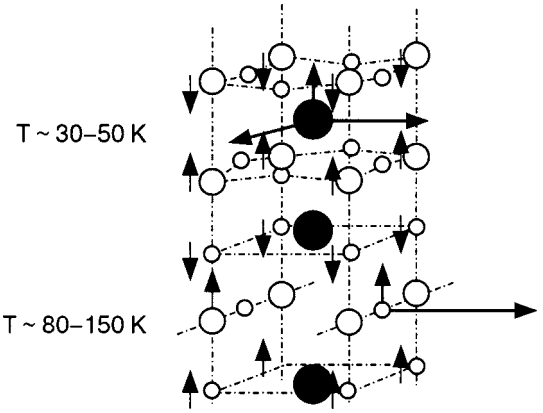

FIG. 3. Schematic presentation of the causes of negative thermal expansion along the **c** axis in the $EuBa_2Cu_3O_{7-d}$ structure. The thick arrows indicate the comparative amplitudes of atomic vibrations in different crystallographic directions. The thin arrows demonstrate compression of the corresponding interlayer spacings.

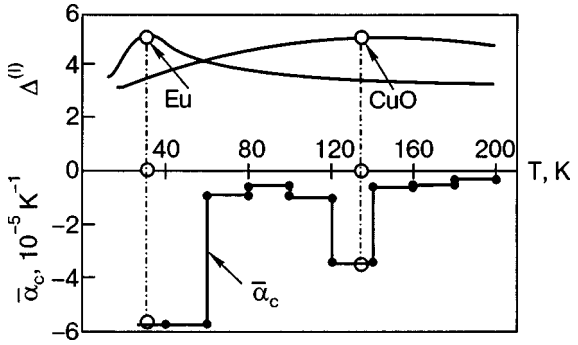

FIG. 4. Temperature dependences of the $\Delta^{(l)}(T)$ values for Eu and CuO layers of the compound $EuBa_2Cu_3O_7$ and the temperature dependence of the LTEC $\overline{\alpha_c}(T)$ averaged over temperature intervals between experimental points.

substantially exceeds the characteristic radius of interatomic interaction. This leads to a weakening effect of the crystal structure regularity on the character of quasiparticle excitations. The spectral characteristics of such crystals display the features common to disordered systems. In particular, for the phonon spectra of multilayered structures the presence of quasi-local (weakly dispersed) modes[11–13] is typical. Consequently, the propagation of excitations along the **c** axis in such systems will be complicated in comparison with their propagation in the layers.

In multilayered lattices, even those for which the macroscopic characteristics are not distinguished by appreciable anisotropy (as, for example, HTSCs of the 1–2–3 type), the interaction between separate atoms or atomic groups can be strongly anisotropic. The ''damped'' propagation of the interaction between layers inherent in substances of the specified class may result in appreciable manifestation of such local anisotropy both in the phonon spectrum[14] and in the behavior of some vibrational characteristics, in particular the mean-square displacement of atoms from separate layers along various crystal directions.

Some multilayered HTSC, for example $Bi_2Sr_2CaCu_2O_x$, show the anisotropy of elastic constants inherent to layered crystals, and negative thermal expansion in the direction of the layers,[15] which can be described by the formula (2). At the same time, for multilayered structures such as 1–2–3 HTSC, where the interlayer interaction between all layers is of the same order, and the intralayer interaction varies substantially from layer to layer. Local anisotropy of the ''chain'' type is characteristic for layers with weak intralayer interaction (a layer of the rare earth and a layer of Cu–O chains), that is, in these layers the mean-square displacements of the atoms in the layer plane are appreciably higher than the mean-square displacements of the same atoms in the direction normal to the layers and lie outside the classical limit at lower temperatures. Therefore there can exist temperature intervals, in which the interlayer distances Cu_2O–Eu–Cu_2O and BaO–CuO–BaO compress with temperature increase, which is the possible reason for the negative values of LTEC along the **c** axis (Fig. 3).

The temperature dependence of each spacing change can be described by some local thermal expansivity $\alpha_c^{(l)}(T)$ for which a relation of the form (2) is true, namely:

$$\alpha_c^{(l)}(T)=A\frac{\partial}{\partial T}\langle(u_c^l)^2\rangle_T\{\delta^{(l)}-\Delta^{(l)}(T)\}, \tag{4}$$

where the index l numbers the atomic layers (R or CuO, respectively), and the functions $\Delta^{(l)}(T)$ are defined similarly to (3) by the addition of the index l for the corresponding mean-square displacements. Then $\langle(u_i^l)^2\rangle_T$ $(i=a,b,c)$ means either the mean-square displacement $\langle u_i^2\rangle_T^R$ itself for the layers of rare-earth elements, or the half-sum $\frac{1}{2}\{\langle u_i^2\rangle_T^{Cu}+\langle u_i^2\rangle_T^{O}\}$ for the CuO layers.

Calculation of the temperature dependences $\Delta^{(l)}(T)$ was made by the method of J matrices (see, for example, Refs. 16–18). Necessary data on force constants are obtained on the basis of the data of Refs. 19–22.

Results of the calculation are presented in a Fig. 4 along with the temperature dependence of the average values of the LTEC along the **c** axis on each of the temperature intervals between the experimental points (see Table I and Fig. 2):

$$\overline{\alpha_c}(T\in[T_i,T_{i+1}])=\frac{2}{T_{i+1}-T_i}\frac{c(T_{i+1})-c(T_i)}{c(T_{i+1})+c(T_i)}.$$

The temperatures of the maxima on the $\Delta^{(l)}(T)$ curves fall on intervals of the least values of $\overline{\alpha_c}(T)$ where the rate of decrease of the lattice parameter c is the greatest (see Table I; partial replacement of Ba by La does not lead to appreciable change of the phonon spectrum and oscillatory characteristics considered here). The good agreement of the results of calculation and experiment certainly testifies in favor of the mechanism offered here for the negative thermal expansion along the **c** axis in the compound considered, based on the crystal lattice dynamics in the quasi-anharmonic approach. At temperatures $T\leqslant 50$ K negative thermal expansion is caused by compression of the interlayer spacings $Cu_2O\leftrightarrow Eu\leftrightarrow Cu_2O$, and at 80 K$\leqslant T\leqslant$150 K by those of $BaO\leftrightarrow CuO\leftrightarrow BaO$ (see Fig. 3). At temperatures above 200 K an even faster linear decrease of the parameter c with temperature is observed, which is not explained by the proposed model (in the temperature range 260–280 K the crystal size decreases), as in this temperature range the quasiharmonic lattice dynamics becomes inapplicable. It should be noted that it follows from the experimental curves that at $T\leqslant 180$ K the LTEC becomes practically zero. This attests to

independent mechanisms responsible for the negative thermal expansion at high (above 200 K) and low temperatures $T \leqslant 140$ K, as considered by us, or at least for a weak effect of the ''high-temperature'' mechanism on the thermal expansion at $T \leqslant 180$ K. The results do not show any significant contribution of the BaO layers to the negative expansion.

This work was supported by MES of Ukraine (Grant #M/257-2004).

*E-mail: eremenko@ilt.kharkov.ua

[1] G. Shirane and S. Hoshina, J. Phys. Soc. Jpn. **6**, 265 (1951).
[2] N. V. Anshukova, B. M. Bulychev, A. I. Golovashkin, L. I. Ivanova, I. B. Krynetskiĭ, A. A. Minakov, and A. P. Rusakov, Zh. Exsp. Teor. Fiz. **124**, 80 (2003) [JETP **97**, 70 (2003)].
[3] I. M. Lifshits, Zh. Eksp. Teor. Fiz. **22**, 475 (1952).
[4] Xu. Youwen, M. J. Kramer, K. W. Dennis, H. Wu, A. O'Connor, R. W. McCallum, S. K. Malik, and W. B. Yelon, Physica C **341–348**, 613 (2000).
[5] G. L. Belen'kiĭ, R. A. Suleĭmanov, N. A. Abdullaev, and V. Ya. Shteĭnshraĭber, Fiz. Tverd. Tela **26**, 3560 (1984) [Sov. Phys. Solid State **26**, 2142 (1984)].
[6] S. B. Feodosyev, I. A. Gospodarev, and E. S. Syrkin, Phys. Status Solidi B **150**, K19 (1988).
[7] S. B. Feodos'ev, E. S. Syrkin, I. A. Gospodarev, V. P. Popov, A. A. Gurskas, and N. M. Nesterenko, Fiz. Tverd. Tela **31**, 186 (1989) [Sov. Phys. Solid State **31**, 102 (1989)].
[8] A. M. Kossevich, *The Crystal Lattice (Phonons, Solitons, Dislocations)*, WILEY-VCH Verlag Berlin GmbH, Berlin (1999).
[9] S. B. Feodosyev, I. A. Gospodarev, M. A. Strzhemechny, and R. J. Hemley, Physica B **300**, 186 (2001).
[10] Ming Lei, J. L. Sarrao, W. M. Visssher, T. M. Bell, J. D. Thompson, A. Migliory, U. W. Welp, and B. W. Veal, Phys. Rev. B **47**, 6154 (1993).
[11] E. S. Syrkin and S. B. Feodos'ev, Fiz. Nizk. Temp. **17**, 1055 (1991) [Sov. J. Low Temp. Phys. **17**, 549 (1991)].
[12] A. M. Kosevich, E. S. Syrkin, and S. B. Feodosyev, Phys. Lett. A **167**, 94 (1992).
[13] I. A. Gospodarev, A. M. Kosevich, E. S. Syrkin, and S. B. Feodosyev, Fiz. Nizk. Temp. **22**, 593 (1996) [Low Temp. Phys. **22**, 457 (1996)].
[14] S. B. Feodosyev, I. A. Gospodarev, A. M. Kosevich, and E. S. Syrkin, Phys. Low-Dimens. Semicond. Struct. **10/11**, 209 (1995).
[15] I. A. Gospodarev, A. P. Isakina, A. I. Prokhvatilov, E. S. Syrkin, and S. B. Feodosyev, Fiz. Nizk. Temp. **16**, 673 (1990) [Sov. J. Low Temp. Phys. **16**, 396 (1990)].
[16] V. I. Peresada, in *Physics of the Condensed State* [in Russian], B. Verkin Institute for Low Temp. Phys. and Eng., Kharkov (1968), Vol. **2**, p. 172.
[17] V. I. Peresada, V. N. Afanas'ev, and V. S. Borovikov, Fiz. Nizk. Temp. **1**, 461 (1975) [Sov. J. Low Temp. Phys. **1**, 227 (1975)].
[18] R. Haydock, Solid State Phys. **35**, 129 (1980) [H. Ehrenreich, F. Seitz, and D. Turnbull (eds.), Academic Press, New York].
[19] S. Mass, T. Jasuda, Y. Horie, M. Kusada, and T. Fukami, J. Phys. Soc. Jpn. **57**, 1024 (1988).
[20] V. K. Fedotov, A. I. Kolesnikov, V. I. Kulakov, E. G. Ponyatovskio, I. Natkanets, Yu. Maoer, and Ya. Kravszyk, Fiz. Tverd. Tela (St. Petersburg) **35**, 310 (1993) [Phys. Solid State **38**, 156 (1993)].
[21] L. Pintschovius, N. Pyka, W. Reichard, A. Yu. Rumiantsev, N. L. Mitrifanov, A. S. Ivanov, G. Golin, and A. Bourges, Physica B **174**, 323 (1991).
[22] J. J. Rhyne, D. A. Neumann, J. A. Gitaas, and F. Beech, Phys. Rev. B **36**, 2294 (1991).

This article was published in English in the original Russian journal. Reproduced here with stylistic changes by AIP.

LOW-TEMPERATURE MAGNETISM

Hexagonal ferrite: from macro- to nanocrystal

Yu. A. Mamluĭ and L. P. Ol'khovik*

V. N. Karazin Kharkov National University, 4 Svobody Sq., Kharkov 61077, Ukraine
(Submitted July 8, 2004)
Fiz. Nizk. Temp. **31**, 356–366 (March–April 2005)

The directions and most important results of studies of the fundamental magnetic properties of hexagonal ferrites performed at Kharkov National University over the last 50 years are reviewed. The influence of the basic factors (size, surface, and collective) specific to small particles and ensembles of small particles on the evolution of the magnetic properties under a transition from a macro- to a nanocrystal is analyzed in a section devoted to the topical subjects ''Nanophysics and nanotechnology of barium ferrite.'' © *2005 American Institute of Physics.* [DOI: 10.1063/1.1884429]

1. ESTABLISHMENT OF FERRITE STUDIES AT KHARKOV UNIVERSITY

Hexagonal barium ferrite is a ferrimagnetic oxide with *M*-type structure. Synthesized more than 50 years ago by specialists at the Dutch company Phillips, this high-energy magnetic material was not only widely used for permanent ceramic magnets but it has long occupied an appreciable niche in research.

The Kharkov school of physicists which Professor Evgeniĭ Stanislavovich Borovik, a Corresponding Member of the Soviet Academy of Sciences, founded has made a large contribution to the establishment of ferrite science in this country and throughout the world. The first single- and polycrystalline samples of the new compositions of hexagonal ferrites were synthesized and the study of their magnetic properties was started under the leadership of Professor Borovik at Kharkov National University, now named for V. N. Karazin, in 1955–1957.[1–5]

The new compounds were found to be good objects for scientific research. This is because the oxygen packing, forming the framework of the crystal structure of ferrites, contains diverse interstitial positions occupied by iron ions Fe^{3+} and (or) uni- and divalent metals. The possibility of introducing dia- or paramagnetic ions made it possible to influence in a definite manner the physical parameters of ferrites and, as a result, enriched the natural compound (known since 1938[6]) magnetoplumbite $PbFe_{7.5}Mn_{3.5}Al_{0.5}Ti_{0.5}O_{19}$ with an extremely wide spectrum of magnetic properties. A subsequent generation of researchers developed in the 1970–1990s a systematized databank of the fundamental magnetic characteristics and technically important parameters of hexagonal ferrites with *M*, *S*, *W*, *Y*, *Z*, and *U* structures. The diamagnetic substitution method developed was a key point in the study of the main mechanisms responsible for the formation of the magnetic properties of ferrites: exchange interaction, magnetocrystalline anisotropy, and magnetostriction.

Methods for performing an integrated study of the physical parameters in static magnetic fields (magnetization, anisotropy and magnetostriction constants) and in high-frequency fields (anisotropy field, effective *g* factor, FMR linewidth) were developed and used to obtain the most complete information about various properties of ferrites. Information about local parameters of Fe^{3+} ions localized in nonequivalent crystallographic positions has been obtained by Mössbauer spectroscopy and nuclear magnetic resonance.

A spectrometer with an innovative construction making it possible to detect signals by a stationary method and by the spin-echo method in the temperature range 4.2–295 K and in magnetic fields up to 16 kOe was developed to investigate NMR on ^{57}Fe nuclei in domains and domain walls.[7]

A magnetometer construction making it possible to detect magnetization changes $\sim 0.1\%$ in a sample by performing measurements in a wide temperature range 4.2–500 K and in magnetic fields up to 24 kOe was proposed to study the special features of orientational phase transitions.[8]

The lattice parameters and the elastic and thermal properties of, first and foremost, model objects were taken into account.

We shall discuss in greater detail the most important directions of experimental studies of highly anisotropic *M*-type hexaferrites and also *W*-type hexaferrites which are rich with spin-reorientation phase transitions.

The unit cell of an *M*-type hexaferrite consists of two formula units, 12 ions in each of which is localized in five crystallographically nonequivalent positions with two variants of the directions of the magnetic moments relative to the hexagonal axis of the crystal:

$$\uparrow 2a(D_{3d}) + \uparrow 12k(C_s) + 2b(D_{3h})$$

and $$\downarrow 4f_1(C_{3v}) + \downarrow 4f_2(C_{3v}).$$

The possibility of systematic purposeful elimination of Fe^{3+} ions from the five sublattices was used to determine the role of each of the five sublattices in the formation of the magnetic structure and magnetocrystalline anisotropy of ferrite. To this end the trivalent In^{3+}, Sc^{3+}, Al^{3+}, and Ga^{3+} metal ions were used as the substituting ions.

The values of the exchange integrals corresponding to the most important pair interactions in M-type hexaferrite were calculated using the method of diamagnetic substitutions in a three-sublattice model: J_{2b-4f_2}, J_{12k-4f_1}, J_{12k-4f_2}, $J_{4f_2-4f_2}$, and $J_{12k-12k}$. This established that the main exchange interaction determining the character of the magnetic structure of ferrite is the interaction $\mathrm{Fe}(2b)-\mathrm{Fe}(4f_2)$.[9–11]

A series of works[12–23] presents the results of static and resonance studies of the magnetic anisotropy[12–17] and magnetostriction[18–23] of M- and W-type hexagonal ferrites.

The anisotropy constants up to sixth order were determined for the systems $BaFe_{12-x}In_xO_{19}$, $BaCo_2Ti_2Fe_8O_{19}$, $Ni_{2-y}Co_yBaFe_{16}O_{27}$, and $Zn_{2-y}Co_yBaFe_{16}O_{27}$ in the temperature range from 77 K to T_C. The intervals of existence of the various types of anisotropy were established and the temperature dependences of each of the contributions to the anisotropy energy, which are due to dipole-dipole interaction and spin-orbit interaction of Fe^{3+} and Co^{2+} ions, were determined for these systems.

The role of Fe^{3+} ions, occupying low-symmetry positions, in the formation of the anisotropic properties of hexaferrites is investigated in Refs. 24–26. For $La_{0.5}Na_{0.5}Fe_{12}O_{19}$ and $Ba_{0.5}Ca_{0.5}Fe_{12}O_{19}$ crystals with an unsubstituted magnetic matrix, in contrast to $BaFe_{12}O_{19}$, it was found that second- and fourth-order anisotropy constants appear.

Mössbauer studies of these crystals made it possible to determine the reason for the observed effect. It is due to the change in the energy state of the Fe^{3+} ions in definite positions as a result of a lowering of the local symmetry of the $2b$ pentahedron from D_{3h} to C_i and a change in the local distortions of the $12k$ octahedra with structural ordering of nonequivalent La^{3+} and Na^{+} ions and Ba^{2+} and Ca^{2+} ions in the basal plane of the R structural block.

This direction of the studies made it possible to formulate a new principle for matching technically important characteristics: high level of magnetization and thermal stability of the anisotropy field and coercive force in the working temperature range. The crux of the principle is a purposeful change in the single-ion contributions of $Fe^{3+}(2b)$ and $Fe^{3+}(12k)$ with the magnetic matrix of the ferrite as a whole being preserved. This idea was used as a basis to develop a number of fundamental materials[27–29] for use in producing systems with high local uniformity of the magnetizing field and also new types of carriers for vertical magnetic recording.

A fruitful stage in the study of the nature of the magnetic anisotropy of M-type hexagonal ferrites was a direct study of the anisotropy of local magnetic fields on ^{57}Fe-enriched single crystals.[30–32] It was shown that the magnitude of the magnetocrystalline anisotropy constant is due to the interionic magnetic dipole-dipole interaction. A combined analysis of the data on the anisotropic magnetic properties and the latest information on local NMR characteristics made it possibe to determine all sublattice contributions to the anisotropy constants of hexaferrites. At low temperatures $\mathrm{Fe}(12k)$, $\mathrm{Fe}(4f_2)$, and $\mathrm{Fe}(2b)$ make the largest contribution.

The investigation of various types of noncollinear magnetic structures formed in substituted M- and W-type ferrites under the influence of external actions (magnetic field, pressure, and temperature) and the determination of the temperature-field range of their existence made it possible to determine the precise exchange interactions with whose appearance they are associated and the role of the magnetocrystalline anisotropy energy in the dynamics of the change in the equilibrium states of the magnetization.

A theoretical analysis and experimental results of investigations of several hexaferrites from the systems $BaFe_{12-x}In_xO_{19}$,[15] $BaCo_2Ti_2Fe_8O_{19}$,[23] $Ni_{2-y}Co_yBaFe_{16}O_{27}$,[13,14] $Zn_2Ba_2Fe_{12}O_{23}$,[33] and $Co_2Ba_3Fe_{24}O_{41}$,[34] among which the compositions undergoing spin-reorientational phase transitions were determined, made it possible to construct the orientational phase diagrams of the anisotropy for crystals of M-, W-, Y-, and Z-type ferrites.[33–36].

The use of the physical principles of a model computer experiment, based on an analysis of the anisotropic part of the thermodynamic Gibbs potential (taking account of terms up to sixth order in the expansion and the Zeeman energy), to investigate the equilibrium states of the spontaneous magnetization made it possible to model directly the phase diagrams, the characteristic anisotropy surfaces and their sections, the magnetization isotherms, and the transformation of the magnetic structure of a crystal of any structural type under the influence of an external action.[37] The effectiveness of this approach, containing large potential possibilities for predicting the magnetic properties, subsequently proved itself in the study of ultrasmall objects and the determination of the mechanisms of the formation of their specific magnetic properties.

2. NANOCRYSTALS AND SOME RESULTS OF INVESTIGATIONS OF THE NATURE OF THEIR UNUSUAL PROPERTIES

One direction of the works which are now being performed on ferrites in the magnetism laboratory is the study of the evolution of the properties of the highly anisotropic ferrimagnet $BaFe_{12}O_{19}$ with a transition from a macro- to a nanocrystal.

It is well known that the properties of small particles are dominated by the so-called finite-size effects—the influence of an open surface as a structural defect and the closeness of the volume of the particles to the critical value V_S at which a transition occurs from a magnetostable (MS) into a superparamagnetic (SPM) state. The experimental study of an ensemble of particles also introduces collective effects due to interparticle magnetic interaction. Consequently, in order to determine the role of each of the factors listed above in the specific nature of the magnetic properties of the highly dispersed system studied it was first necessary to develop a technology for obtaining nanocrystals which best satisfy the requirements for the model object: the composition of the particles must consist of a single phase, the structure of the particles must be perfect, there must be no conglomerates in the powder, the particles must be granulometrically uniform, and the linear dimensions of the particles must correspond to the criterion of single-domainness. Since the particles in a real system always have a size distribution irrespective of the method used to obtain the particles, the system studied must at least correspond to the Pfeiffer classification[38] with respect to the volumes of small particles, based on the definite char-

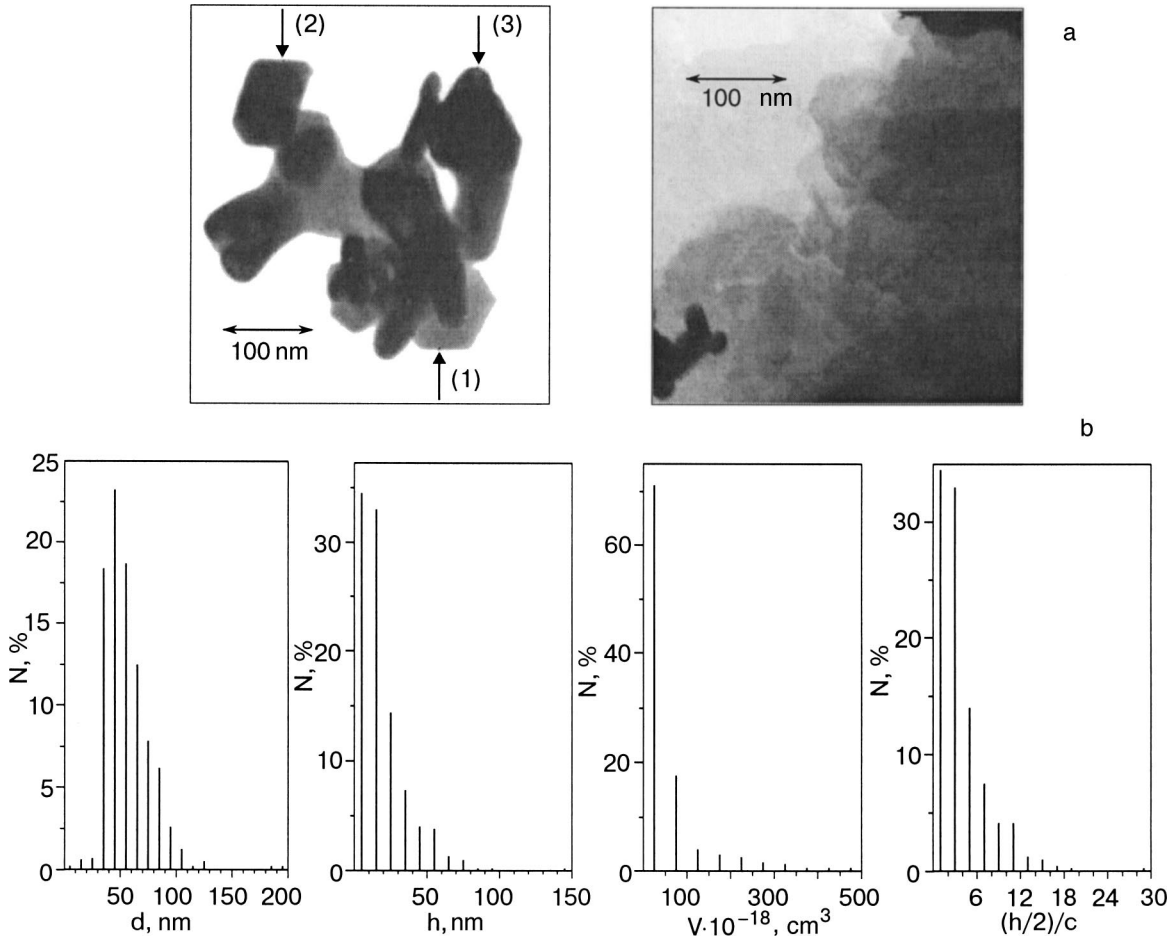

FIG. 1. Electron-microscopic photograph of $BaFe_{12}O_{19}$ nanocrystals (a). Size distribution of particles in a nanocrystalline powder: d—diameter, h—thickness, V—volume of the particles, c—crystal lattice parameter. Sample with $N = 520$ particles (b).

acter of their magnetic behavior. Thus for small Stoner-Wohlfarth (SW) particles the volume limitation is given by the condition $V \leqslant 100V_S$ and for large SW particles $100V_S < V \leqslant 1000V_S$.

The methods developed to obtain nano- and microcrystalline $BaFe_{12}O_{19}$ particles employed elements of cryochemical[39–42] and radiation-thermal[43,44] technologies to ensure high chemical uniformity of the initial ferrite-forming mixtures. These methods made it possible to produce highly dispersed model systems of particles in two size ranges: 10–100 nm and 0.1–1 μm (in diameter) with the aspect ratio regulatable from 1 to 15.

Figure 1 displays photomicrographs of nanocrystalline particles illustrating their morphological features of the particles (plate shape in the form of a hexagon, whose hexagonal axis **c** is the axis of easy magnetization) and the particle size distribution (d—diameter, h—thickness, V—volume). If the thickness of the particles is normalized with respect to the lattice parameter c, then for the nanometer range it is only 1–10 lattice parameters. The closeness of the particle volumes to the critical value is confirmed by the fact that in the actually attainable range of temperatures and magnetic fields ~50% of the particles of the experimental system are capable of transforming from a magnetically stable into a superparamagnetic state. A generalized diagram of the magnetic state of a nanodispersed system of $BaFe_{12}O_{19}$ particles (Fig. 2) gives an idea of the degree to which and how the properties of an ultrasmall highly anisotropic crystal are transformed as compared with the macroscopic analog.

In the first variant of the $H-T$ diagram obtained for the magnetic state of this nanodispersed system[45,46] we neglected

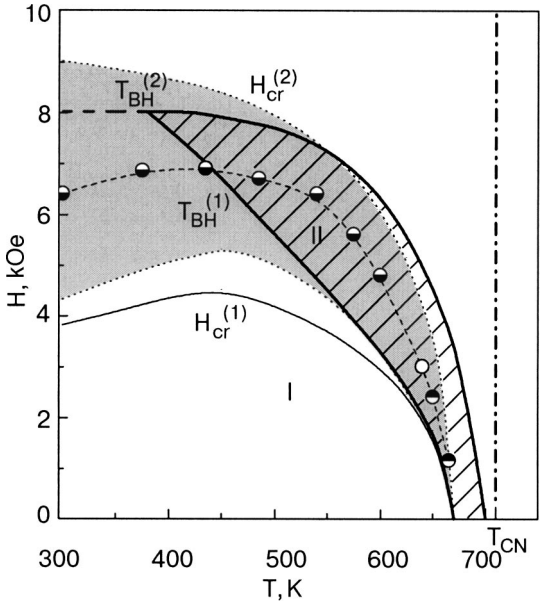

FIG. 2. Diagram of the magnetic state of a system of nanocrystals (packing factor $p = 0.4$).

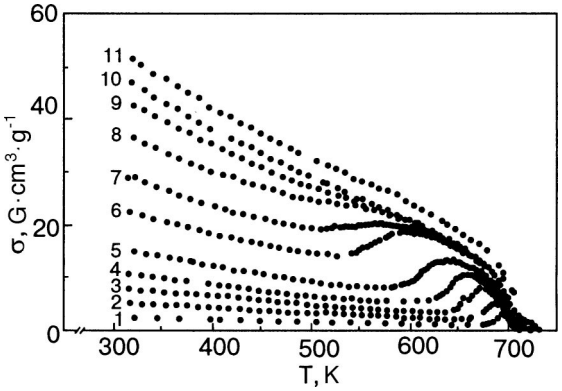

FIG. 3. Temperature dependences of the specific magnetization for different values of the magnetic field H, kOe: 0.5 (1), 2.2 (2), 3.5 (3), 4.1 (4), 4.6 (5), 6.0 (6), 6.5 (7), 7.0 (8), 7.5 (9), 8.0 (10), and 10.0 (11).

the interparticle magnetic interaction, making the assumption that this interaction is negligible for particles of highly anisotropic hexaferrite.

Before characterizing the corresponding regions of the diagram we shall give a brief exposition of the method used to determine and results of the determination of the critical parameters $T_B^{(1),(2)}$ and $H_{\rm cr}^{(1),(2)}$.

According to Ref. 47, as the temperature increases, a characteristic anomaly in the form of a peak (Fig. 3) is observed in the temperature dependence of the magnetization σ (for $H \ll H_a$) as a result of the particles in the system making a transition into the SPM state.

The temperature at which σ increases sharply is called the blocking temperature T_B. The temperature shift of the peak is due to the dependence of T_B on the applied magnetic field:

$$T_{BH} = T_{BO}(1 - H/H_a)^2, \tag{1}$$

where T_{BO} and T_{BH} correspond to $H=0$ and $H \neq 0$.[48]

For a system with a particle volume distribution the SPM transition occurs in the temperature range $T_{BH}^{(1)} - T_{BH}^{(2)}$. Following Pfeiffer[47] we determined the transition onset temperature $T_{BM}^{(1)}$ from the position of the minimum in the curve $\sigma(T)$ and the temperature $T_{BH}^{(2)}$ at the end of the transition from the position of the maximum.

The lines of the critical fields $H_{\rm cr}^{(1),(2)}(T)$, which bound the region of reversible and irreversible magnetization processes (low- and high-field regions), were determined from an analysis of the isotherms of the field dependence of the specific magnetization[49] and the particular hysteresis loops for various temperatures.

As a result a number of regions of the magnetic state which are uncharacteristic for the macroanalog were designated in the diagram. In the first place there is the region II, which is quite extended in temperature and magnetic field, of existence of a superparamagnetic state of the system of nanocrystals, in contrast to the macroanalog which remains in the magnetostable state right up to the Curie temperature T_C.[50] The SPM state is nonuniform within the region II. Even though the smallest experimental particles are close in size to the lower limit of single-domainness, because of the high magnetocrystalline anisotropy energy the transition into the SPM state in the absence of a magnetic field solely as a result of thermal fluctuations is possible only within 30 K of the Curie temperature ($T_{CN}=710$ K). Fields $H \leqslant 2$ kOe influence the magnetic state of the system comparatively weakly. Increasing the magnetic field appreciably decreases the blocking temperature to 400 K. It should be underscored that for 2 kOe$< H \leqslant 6$ kOe the field as an additional factor with respect to the thermal energy stimulates unblocking of the particles and then itself creates a blocking effect.

A state where the magnetic moments of all particles (superparamagnetic and magnetically stable) are blocked by a magnetic field is reached in fields $H_{\rm cr}^{(2)}(T)$. The region of higher fields can be regarded as a region of suppression of local noncollinearity of the magnetic moments of Fe^{3+} ions localized on the surface and in near-surface layers.

The observation of a so-called ''canted'' magnetic structure in $BaFe_{12}O_{19}$ crystals using depth-selective conversion electron Mössbauer spectroscopy[51] and the determination of the parameters characterizing it (thickness of the layer and average angle of deviation of the magnetic moment from the **c** axis) subsequently played a strategic role in the study of surface anisotropy.

A nonuniform magnetic state not only in the system but also in individual $BaFe_{12}O_{19}$ nanocrystals has been observed in a study of their properties near T_C.[52]

The concretization of the magnetic states in the high-temperature region which are due to size and surface factors simultaneously, was achieved by comparing the high-temperature fragment of the $H-T$ diagram of the magnetic state of a nanodispersed system and data from Mössbauer studies of the near-surface region of a macroscopic analog. It should be noted that the thickness of the latter region at temperatures $T>600$ K increases by two orders of magnitude compared with the value for 300 K and is ~ 200 nm, i.e. the thickness of the largest nanocrystals in the experimental system.

According to Fig. 4 a the temperature range 650–740 K is saturated with magnetic phase transitions. Three magnetic phases occur within 100 K: magnetostable, superparamagnetic, and paramagnetic (PM). The temperature $T_{CN}=710 \pm 2$ K, determined from the temperature dependence of the magnetization in a weak field ($H \sim 25$ Oe),[53] was taken as the Curie temperature of a nanocrystalline powder sample.

The high-temperature data obtained by simultaneous γ, x-ray, and electron Mössbauer spectroscopy (Fig. 4b),[52] show a gradual transition (680–732 K) of the near-surface region of the crystal into the paramagnetic state. In this connection we interpret the temperature $T=680$ K as the Curie temperature T_{CS}^0 of an open surface. The paramagnetic phase nucleates primarily on an open surface with iron vacancies[54] and, correspondingly, broken exchange bonds. The density of broken bonds within the surface layer decreases monotonically with depth; this gives rise to a gradual expansion of the temperature range of the paramagnetic phase. The temperature at which the Zeeman-splitting lines, which were obtained by detecting the conversion and Auger electrons from a ~ 200 nm thick region at the surface, vanish completely was taken as the Curie temperature of the surface layer T_{CS}. According to Fig. 4b T_{CS} is only 3 K lower than the Curie temperature T_{CV} in the bulk of the crystal.

As a result the magnetic state of the system for the high-

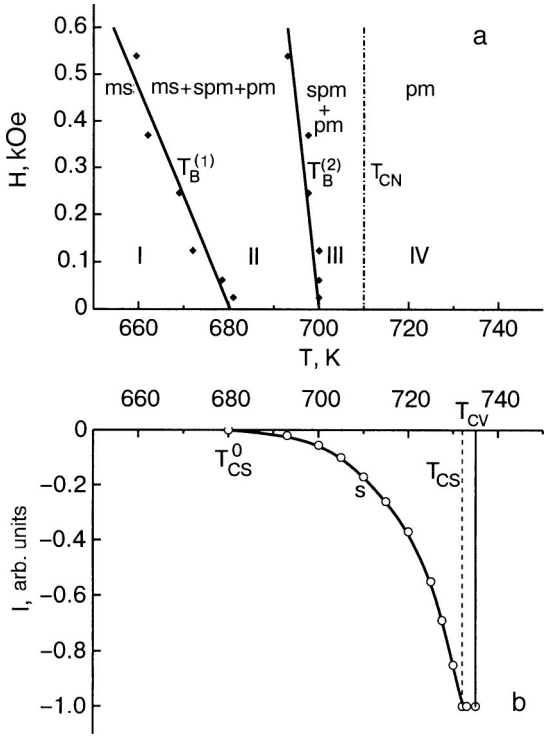

FIG. 4. High-temperature fragment of the $H-T$ diagram of the magnetic state of a system of nanocrystals (a). The temperature dependence of the intensity of the paramagnetic line in the Mössbauer spectrum from a near-surface region of the macrocrystal (b). MS—magnetostable state, SPM—superparamagnetic state, PM—paramagnetic state.

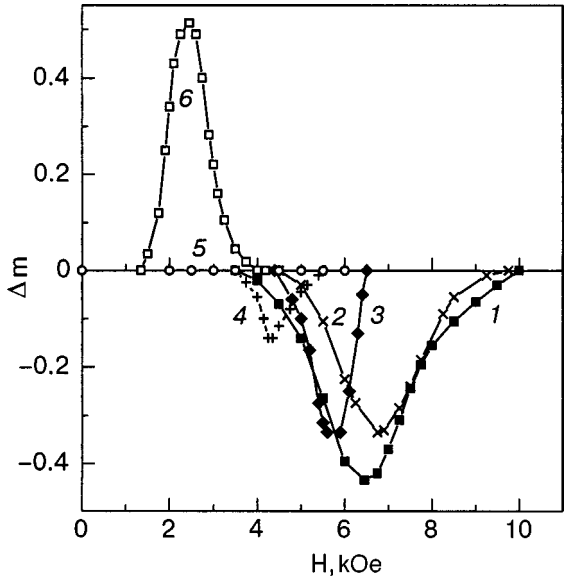

FIG. 6. Interparticle magnetic interaction parameter as a function of the magnitude of the external magnetic field (Kelly plot) for different temperatures T, K: 300 (1), 360 (2), 550 (3), 592 (4), 612 (5), and 621 (6).

temperature fragment of the diagram presented in Fig. 4a turned out to be even more complicated than for the superparamagnetic region as a whole. The magnetic states MS + SPM + PM coexist in region II and SPM + PM in region III. In region IV all particles, irrespective of their past history, have crossed into the PM state.

To be completely sure that taking account of the interparticle magnetic interaction in a system of highly anistropic particles should not change the form of the $H-T$ diagram presented for the magnetic state we studied this question in detail using electron-microscopic and magnetic measurements. The electron-microscopic studies of ferrite powders with different dispersity[55] showed that particle aggregation differs even in uncompacted powders which are demagnetized beforehand. The illustrations of replicas of microcrystalline particles presented in Fig. 5 are especially obvious. Accumulations in the form of ''stacks'' (Fig. 5a) as elements of closed ''ing'' structures (Fig. 5b) can be identified in different variants of particle arrangement. Such configurations are a result of the morphological features of the particles (plate shape), the magnetocrystalline anisotropy (the easy-magnetization axis is also the hexagonal axis **c** of the crystal), and ultimately the minimization of the demagnetization energy. The sign and magnitude of the resulting interaction between the magnetic moments of the particles in the system depend on the disbalance of the positive component (in a stack) and the negative component (between stacks).[56]

One parameter characterizing the interparticle interaction is[57]

$$\Delta m = m_d(H) - (1 - 2m_r(H)). \tag{2}$$

According to Ref. 58 two residual magnetization curves are measured to determine this parameter: $m_r(H) = \sigma_r(H)/\sigma_r(\infty)$ and $m_d(H) = \sigma_d(H)/\sigma_d(\infty)$.

The curves presented in Fig. 6 of the parameter Δm versus the magnitude of the external magnetic field for vari-

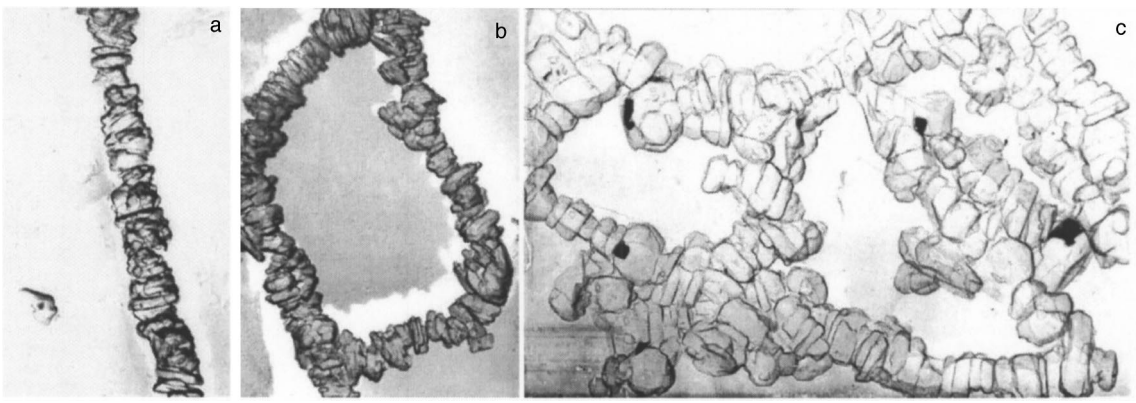

FIG. 5. Typical collections of particles in barium hexaferrite powder.

ous temperatures made it possible to see the sign-alternating character of the dependence $\Delta m^{\max}=f(T)$ and to determine the $H-T$ space which is significant with respect to the magnitude of the parameter Δm. The latter is designated in the diagram of the magnetic state by the shaded region (see Fig. 2). As expected, the space encompassed by the interaction remains within the region of irreversible magnetization processes, i.e. beyond the line of the critical fields $H_{\rm cr}^{(1),(2)}(T)$. The points connected by the dashed line passing along the central line of the $H-T$ space with $\Delta m\neq 0$ correspond to the maximum values of $|\Delta m|$. In the range $300\ {\rm K}\leqslant T<630\ {\rm K}$ the resulting interparticle interaction is negative ($\Delta m<0$); near 630 K $\Delta m\approx 0$; and, for $630\ {\rm K}<T\approx 650\ {\rm K}$ $\Delta m>0$. Comparing the $H-T$ space where $\Delta m\neq 0$ with the $H-T$ region of existence of the SPM state in the system showed that an interparticle interaction which is average in magnitude does not influence the critical parameters of the change in the magnetic state in a system of highly anisotropic nanoparticles.

It should be noted that the parameter Δm turned out to be quite sensitive to the appearance of any processes induced in the system of nanoparticles by the action of temperature and magnetic fields. Thus a transformation of the $H-T$ space of the interparticle interaction was found for a series of critical temperatures in the initial diagram: as the temperature at which the transition of the system into the SPM state starts ($T_{BH}\approx 400$ K) is approached the boundaries of the $H-T$ space rapidly narrow to the SPM region; within 50 K of the Curie temperature, when the open surface of the particles transforms into a paramagnetic state,[52] the $H-T$ space of the interparticle interaction ''prematurely'' leaves the zone of overlapping with the SPM region, collapsing at $T=660$ K virtually to a point. The latter fact makes it possible to draw the fundamentally important conclusion that the collective effect observed in a system of highly anisotropic particles is due to the interaction of the magnetic moments of primarily surface atoms.

Investigations of the behavior of a system of $BaFe_{12}O_{19}$ nanoparticles in a magnetic field confirmed that not only the interparticle magnetic interaction but also the surface anisotropy, as one of the main specific features of small particles, must also be taken into account.

Surface anisotropy arises as a result of structural distortions on an open surface (with disrupted stoichiometry) and in layers lying close to it.[54] The method of depth-selective conversion electron Mössbauer spectroscopy was used to establish that for a $BaFe_{12}O_{19}$ macrocrystal the thickness of the surface layer with the perturbed (''canted'') magnetic structure along the **c** axis is 2–5 nm at 300 K,[51] i.e. it is comparable with the thickness of the nanoparticles of the experimental system. In this connection, to characterize the surface anisotropy we introduced the constant K_S as the energy referred to not unit surface area (the generally accepted definition introduced by Néel[59]) but rather unit volume. The estimates made of K_S at 300 K showed that the surface magnetic anisotropy constant has the opposite sign from the magnetocrystalline anisotropy constant K_1 of ferrite and is comparable to it in magnitude.[60] Near 550 K K_S changes sign, reaching its maximum positive value $\sim 0.5\cdot 10^6$ erg/cm^3 at $T\approx 650$ K. Being crystallographic in nature, the surface anisotropy is due to the single-ion contributions of Fe^{3+}, occupying positions with lowered symmetry relative to identical positions in the bulk of the crystal. In this case, by analogy to $La_{0.5}Na_{0.5}Fe_{12}O_{19}$ single crystals, where, as mentioned in Sec. 1, the lowering of local symmetry was due to the appearance of a constant K_2 whose temperature-dependence is sign-alternating and which is of the same order of magnitude as K_S,[29] we made the following assumption. The constant K_S was introduced as K_2 in the anisotropic part of the free energy of a hexagonal single crystal. Then, taking account of all basic forms of the magnetic anisotropy energy of $BaFe_{12}O_{19}$ nanoparticles:

magnetocrystalline

$$W(\theta)=K_1\sin^2\theta, \tag{3}$$

magnetostatic

$$W_{\rm dem}=\frac{I_S^2}{2}(N_b-N_a)\sin^2\theta=K_N\sin^2\theta \tag{4}$$

and surface

$$W_S=K_S\sin^4\theta, \tag{5}$$

the anisotropic part of the free energy can be written in the form

$$F_A(\theta)=(K_1-K_N)\sin^2\theta+K_S\sin^4\theta+\dots\ . \tag{6}$$

This equation was used as the basis for the analytical description of magnetization processes in nanocrystals and obtaining an equation for the basic magnetization curve or an equation for the magnetic state of a hexagonal crystal. To solve these problems the Zeeman energy

$$F=F_A(\theta)-I_SH\cos(\theta_H-\theta) \tag{7}$$

was included in the expression for the free energy. Here and in Eqs. (3)–(6) I_S is the saturation magnetization, θ and θ_H are the angles between the **c** axis of the crystal and the directions of magnetization and the external magnetic field, respectively; and, N_a and N_b are demagnetizing factors.

Using the orientational phase diagram for the case $K_1>0$ and $K_2<0$[37] and concrete values of $|K_2|/K_1$ we employed the ''Kristall'' computer program to perform a computer simulation of the dynamics of magnetization processes accompanying a transition from a macro- to a nanocrystal and to predict the possibility of the existence of angular magnetic structure and a spin-reorientational phase transition in a $BaFe_{12}O_{19}$ nanocrystal.[61] Examples of the models obtained for the basic magnetization curves for different orientations of the external magnetic field relative to the crystallographic **c** axis of the crystal are presented in Fig. 7. According to Fig. 7a the magnetization curve for $\theta_H=90°$ has the characteristic form for a uniaxial macrocrystal. Any deviation of the external magnetic field from the basal plane sharply increases the technical saturation field (Figs. 7b, c). At $\theta_H=65°$ it is about eight times greater than the anisotropy field.

The models of the basic magnetization curves of a barium ferrite nanocrystal, which correspond to the experimental value $|K_2|/K_1=0.6$ (300 K), are presented in Figs. 7d–f. All curves for cases where the external field orientation lies in the range $65°<\theta_H<90°$ contain a feature in the form of a ''jump'' in the magnetization. For $\theta_H<65°$ the magne-

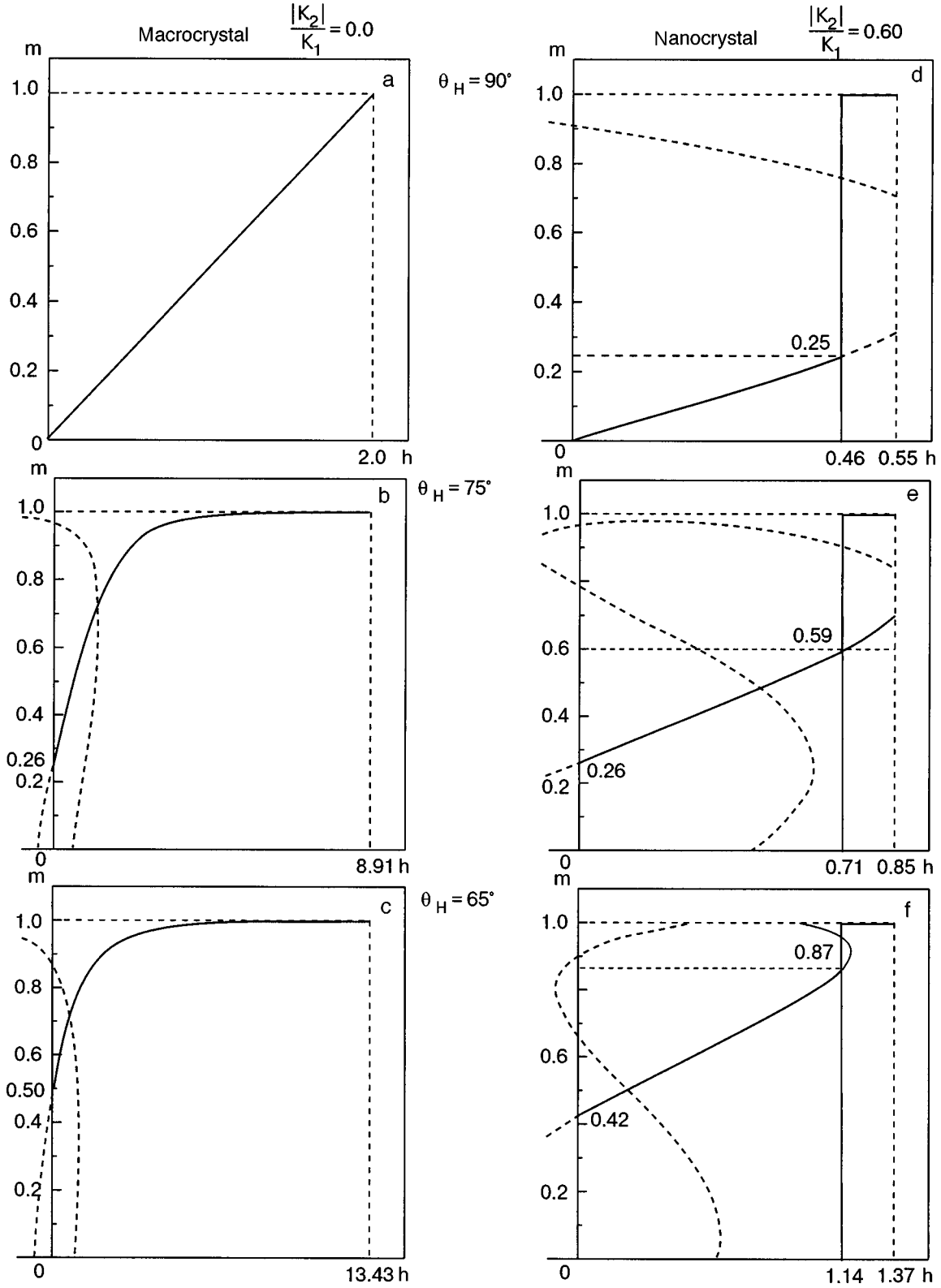

FIG. 7. Computer models of the magnetization curves of a macrocrystal $|K_2|/K_1 = 0$ (a–c) and nanocrystal $|K_2|/K_1 = 0.6$ (d–f) for different orientations of the external magnetic field relative to the crystal axis **c**. Dashed curves—solution of the equation for the main magnetization curve.[61] $h = 2H/H_a$, where H_a is the anisotropy field.

tization curves of a nanocrystal become similar to the corresponding curves of a macrocrystalline sample. For $\theta_H = 90°$ the value of the jump field is 0.34 times the average value of the anisotropy field in the experimental system of nanocrystals.[60] The fact that this value agrees with the experimentally observed value shows that we have used an adequate approach to describe the magnetic anisotropy of a barium hexafluoride nanocrystal.

The contribution of the surface anisotropy, manifested in the form of a spin-reorientation phase transition for nanoparticles in the basic magnetization curve as an additional transition in the Stoner-Wohlfarth model,[62] was determined by

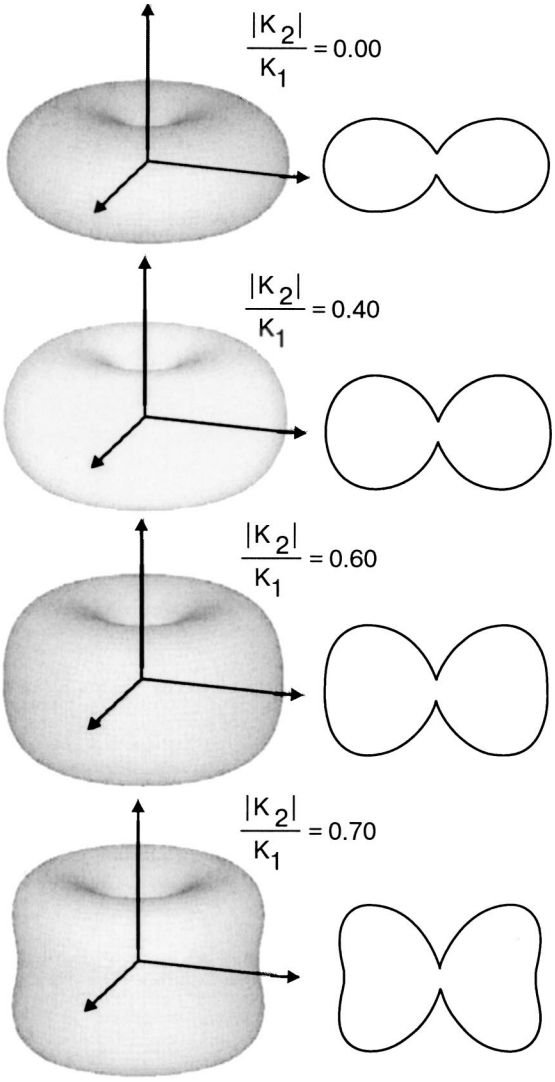

FIG. 8. Evolution of the characteristic surfaces and vector diagrams of anistropy with a transition from a macro- to a nanocrystal.

taking account of the influence of the interparticle magnetic interaction occurring in a close-packed system of particles.[55]

In Ref. 61, to determine why a spin-reorientation phase transition occurs in a nanocrystal of hexagonal barium ferrite, characteristic anisotropy surfaces and their sections—vector diagrams of the anisotropy—were obtained. These diagrams give a graphic representation of the special features of the spatial distribution of the anisotropy energy in a $BaFe_{12}O_{19}$ nanocrystal. The cases studied for $|K_2|/K_1$ ranging from 0 to 0.7 are presented in Fig. 8.

The vector diagram of a macrocrystal ($|K_2|/K_1=0$) contains an absolute minimum and an absolute maximum of anisotropy energy, corresponding to angles $\theta=0$ and 90°. These angles correspond to the directions of easy and hard magnetization. As the ratio of the constants increases (the case of a nanocrystal), the anisotropy energy in the basal plane gradually decreases, and a local energy minimum appears for $|K_2|/K_1 \geqslant 0.2$. The depth of this minimum increases as the ratio of the constants increases further. The absolute and local minima are separated by an absolute maximum, whose position shifts from $\theta=90°$ to $\theta \approx 60°$. The direction of easiest magnetization is once again along the **c** axis; the new direction of easy magnetization which arises lies in the basal plane; and, the direction of hard magnetization moves out of the plane. This signifies a change in the magnetic structure accompanying a transition from a macro- to a nanocrystal.

3. CONCLUSIONS

Following the directions of the scientific investigations performed in the original works cited in the literature we have attempted to convey, as much as possible, the complexity and multifaced nature of the properties of the basic classes of ferimagnetic oxides chosen as the object of investigation, to note the advantages of the methods developed for obtaining highly dispersed ferrite systems, to reveal the problems of small particles for the example of hexagonal barium ferrite, to show the integrated approach used to study these problems, which made it possible to obtain fundamentally new generalizing data—in the form of the $H-T$ diagram of the magnetic state of a system of nanocrystals, taking account of all basic effects specific to small particles and their ensembles (size, surface, and collective effects), and in the form of a spin-reorientation phase diagram with specification of the regions of existence of equilibrium states of magnetization of a nanocrystal as compared with a macroscopic analog.

*E-mail: Larisa.P.Olkhovik@univer.kharkov.ua

[1] E. S. Borovik and Yu. A. Mamaluĭ, Fiz. Met. Metalloved. **9**, 36 (1960).
[2] E. S. Borovik and Yu. A. Mamaluĭ, Fiz. Met. Metalloved. **9**, 828 (1960).
[3] E. S. Borovik and Yu. A. Mamaluĭ, Fiz. Met. Metalloved. **14**, 146 (1962).
[4] E. S. Borovik and Yu. A. Mamaluĭ, Fiz. Met. Metalloved. **15**, 300 (1963).
[5] E. S. Borovik and Yu. A. Mamaluĭ, Izv. Akad. Nauk SSSR, Ser. Fiz. **30**, 1079 (1966).
[6] V. Adelskold, Ark. Kemi. Mineral. Geol. **12A**, 1 (1938).
[7] Inventor's Certificate 1397960 SSSR, MKN G 09 V 23/26. *A Device for Studying Magnetic Resonance*, S. P. Kuntsevich, A. A. Bezlepkin, and E. E. Tuluzova (SSSR) No. 3873516/31–32; priority date December 29, 1984; published May 23, 1988, Byul. No. 19, p. 8.
[8] Inventor's Certificate 983601 SSSR, m. kl. 3 G 01 R 33/02; *Vibrating Coil Magnetometer*, V. N. Gorbach and Yu. A. Mamaluĭ, Claim N2776189, priority date February 23, 1982, Byul. No. 47.
[9] N. N. Efimova and Yu. A. Mamaluĭ, Izv. Akad. Nauk SSSR, Ser. Fiz. **34**, 979 (1970).
[10] N. N. Efimova and Yu. A. Mamaluĭ, Zh. Éksp. Teor. Fiz. **61**, 1073 (1971) [JETP **34**, 572 (1972)].
[11] N. N. Efimova and Yu. A. Mamaluĭ, Ukr. Fiz. Zh. (Russ. Ed.) **18**, 1114 (1973).
[12] Yu. A. Mamaluĭ and A. A. Murakhovskiĭ, Zh. Éksp. Teor. Fiz. **60**, 1418 (1971) [JETP **33**, 768 (1971)].
[13] Yu. A. Mamaluĭ, A. A. Murakhovskiĭ, and L. V. Burakova, Élektronnaya tekhnika: Nauchno-tekhn. sbornik TSNII ''Élektronika,'' Moskva **42**, 45 (1971).
[14] Yu. A. Mamaluĭ and A. A. Murakhovskiĭ, Ukr. Fiz. Zh. (Russ. Ed.) **17**, 393 (1972).
[15] Yu. A. Mamaluĭ and A. A. Murakhovskiĭ, Fiz. Tver. Tela (Leningrad) **14**, 1968 (1972) [Sov. Phys. Solid State **14**, 1703 (1973)].
[16] Yu. A. Mamaluĭ and A. A. Murakhovskiĭ, Ukr. Fiz. Zh. (Russ. Ed.) **19**, 468 (1974).
[17] Yu. A. Mamaluĭ, A. A. Murakhovskiĭ, and L. P. Ol'khovik, Kristallografiya **20**, 351 (1975) [Sov. Phys. Crystallogr. **20**, 215 (1975)].
[18] S. P. Kuntsevich and V. P. Palekhin, Ukr. Fiz. Zh. (Russ. Ed.) **21**, 409 (1976).
[19] S. P. Kuntsevich, A. A. Bezlepkin, and V. P. Palekhin, Izv. Vyssh. Uchebn. Zaved. Fiz. **9**, 106 (1985).
[20] S. P. Kuntsevich and V. P. Palekhin, Fiz. Tver. Tela (Leningrad) **15**, 3460 (1973) [Sov. Phys. Solid State **15**, 2314 (1974)].

[21] A. A. Bezlepkin, S. P. Kuntsevich, and V. P. Palekhin, Izv. Vyssh. Uchebn. Zaved. Fiz. **7**, 111 (1987).
[22] S. P. Kuntsevich and V. P. Palekhin, Fiz. Tver. Tela (Leningrad) **20**, 2869 (1978) [Sov. Phys. Solid State **20**, 1661 (1978)].
[23] T. D. Duczmal, S. P. Kuntsevich, V. P. Palekhin, and J. Pietrzak, Phys. Status Solidi A **67**, K125 (1982).
[24] Yu. A. Mamaluĭ, L. P. Ol'khovik, and L. F. Checherskaya, in *Abstracts of Reports at the 15th All-Union Conference on the Physics of Magnetic Phenomena* (1981), p. 32.
[25] Yu. A. Mamaluĭ, L. P. Ol'khovik, L. F. Checherskaya, and M. N. Shipko, Ukr. Fiz. Zh. (Russ. Ed.) **27**, 1580 (1982).
[26] Yu. A. Mamaluĭ, L. P. Ol'khovik, and L. F. Checherskaya, Fizika i tekhnika vysokikh davleniĭ **12**, 17 (1983).
[27] Inventor's Certificate 1152046 SSSR, MKI N 01 F1/10, C 04 B 35/26, *Ferrite Material*, Yu. A. Mamaluĭ and L. P. Ol'khovik, Claim No. 3675284, priority date December 19, 1983, Published December 22, 1984.
[28] Inventor's Certificate 1499582 SSSR, MKI N 01 F 1/00, F 1/11/; L. P. Ol'khovik, Z. V. Golubenko, T. G. Kuz'micheva, and Yu. A. Mamaluĭ, Claim No. 4268362, priority date June 26, 1987, published April 15, 1989.
[29] Yu. A. Mamaluĭ and L. P. Ol'khovik, Ukr. Fiz. Zh. (Russ. Ed.) **33**, 287 (1988).
[30] S. P. Kuntsevich, A. A. Bezlepkin, and Yu. A. Popkov, Zh. Éksp. Teor. Fiz. **88**, 1820 (1985) [JETP **61**, 1079 (1985)].
[31] S. P. Kuntsevich, Fiz. Nizk. Temp. **24**, 754 (1998) [Low Temp. Phys. **24**, 568 (1998)].
[32] S. P. Kuntsevich, Visnik Kharkivs'kogo derzhavnogo universitetu. Ser. fizika **440**, 125 (1999).
[33] I. Onyskiewicz, T. Duczmal, J. Pietrzak, and A. Murachovskii, Acta Magnetica **1**, 111 (1984).
[34] J. Hankiewicz, Z. Pajak, and A. Murachovskii, J. Magn. Magn. Mater. **101**, 103 (1991).
[35] Yu. A. Mamaluĭ and L. P. Ol'khovik, Ukr. Fiz. Zh. (Russ. Ed.) **24**, 3431 (1982).
[36] Yu. A. Mamaluĭ, V. N. Gorbach, and L. P. Ol'khovik, Fizika i tekhnika vysokikh davleniĭ **14**, 10 (1983).
[37] A. A. Murachovskii, S. N. Zinenko, and J. Pietrzak, in *Proceedings of the 5th International Conference on Magnetic Materials*, edited by W. Gorzkowski, Madralin, Poland (1990), p. 243.
[38] H. Pfeiffer, Phys. Status Solidi A **120**, 233 (1990).
[39] Patent N17244584 Ukraine C01G49/00. Claim N4843538. T. G. Kuz'micheva, L. P. Ol'khovik, and V. P. Shabatin (Russia), priority date June 28, 1990.
[40] N. M. Borisova, Z. V. Golubenko, T. G. Kuz'micheva, L. P. Ol'khovik, and V. P. Shabatin, J. Magn. Magn. Mater. **114**, 317 (1992).
[41] T. G. Kuz'micheva, L. P. Ol'khovik, and V. P. Shabatin, IEEE Trans. Magn. **31**, 800 (1995).
[42] L. P. Ol'khovik, N. M. Borisova, T. G. Kuz'micheva, and V. P. Shabatin, Functional Materials **3**, 84 (1996).
[43] Inventor's Certificate 94011245 Ukraine-Russia, MPK 6 B 22 F9/16, N01 F1/11; N. M. Borisova (Ukraine), V. P. D'yakov, A. S. Kamzin (Russia), L. P. Ol'khovik (Ukraine), O. G. Fisenko (Russia); claim N94-0/1245/02; priority date March 22, 1994; patent awarded January 5, 1996.
[44] L. P. Ol'khovik, N. M. Borisova, A. S. Kamsin, and O. G. Fisenco, J. Magn. Magn. Mater. **154**, 365 (1996).
[45] L. P. Ol'khovik, Z. I. Sizova, Z. V. Golubenko, and T. G. Kuz'micheva, J. Magn. Magn. Mater. **183**, 181 (1998).
[46] L. P. Ol'khovik, Phys. Status Solidi A **172**, 201 (1999).
[47] H. Pfeiffer and W. Schuppel, J. Magn. Magn. Mater. **130**, 92 (1994).
[48] R. W. Chantrell, M. El-Hilo, and R. O'Grady, IEEE Trans. Magn. **27**, 3570 (1991).
[49] Z. V. Golubenko, A. S. Kamzin, L. P. Ol'khovik, and Z. I. Sizova, Fiz. Tver. Tela (St. Petersburg) **40**, 1294 (1998) [Phys. Solid State **40**, 1178 (1998)].
[50] J. Smit and H. P. J. Wijn, *Ferrites*, Wiley, New York (1959) [Russian translation, Izd. Inostr. Lit., Moscow (1962)].
[51] A. S. Kamzin, B. Stahl, R. Gellert, G. Klingelhofer, E. Kankeleit, and L. P. Ol'khovik, Fiz. Tver. Tela (St. Petersburg) **4**, 5 (2000) [*sic*].
[52] L. P. Ol'khovik, Z. I. Sizova, and A. S. Kamzin, Fiz. Tver. Tela (St. Petersburg) **45**, 2033 (2003) [Phys. Solid State **45**, 2136 (2003)].
[53] L. P. Ol'khovik, T. G. Kuz'micheva, Yu. A. Mamaluĭ, and A. S. Kamzin, Fiz. Tver. Tela (St. Petersburg) **38**, 3420 (1996) [Phys. Solid State **38**, 1865 (1996)].
[54] A. S. Kamsin, V. L. Rozenbaum, L. P. Ol'khovik, and E. D. Kovtun, J. Magn. Magn. Mater. **161**, 139 (1996).
[55] L. P. Ol'khovik, M. M. Khvorov, N. M. Borisova, Z. V. Golubenko, Z. I. Sizova, and E. V. Shurinova, Fiz. Tver. Tela (St. Petersburg) **45**, 643 (2003) [Phys. Solid State **45**, 675 (2003)].
[56] G. W. D. Spratt, N. Kodama, H. Jnoue, Y. Uesaka, and M. Katsumoto, IEEE Trans. Magn. **27**, 4660 (1991).
[57] E. P. Wohlfarth, Phys. Status Solidi **29**, 595 (1958).
[58] P. E. Kelly, K. O'Grady, P. I. Mayo, and R. W. Chantrell, IEEE Trans. Magn. **25**, 3881 (1989).
[59] L. Neel, C. R. Acad. Sci. **237**, 1468 (1953).
[60] Z. V. Golubenko, A. S. Kamzin, L. P. Ol'khovik, Yu. A. Popkov, and Z. I. Sizova, Fiz. Tver. Tela (St. Petersburg) **40**, 1894 (1998) [Phys. Solid State **40**, 1718 (1998)].
[61] S. N. Zinenko, A. A. Murakhovskiĭ, L. P. Ol'khovik, Z. I. Sizova, E. V. Shurinova, and A. S. Kamzin, Zh. Éksp. Teor. Fiz., **123**, 1073 (2003) [JETP **96**, 945 (2003)].
[62] E. S. Stoner and E. P. Wohlfarth, IEEE Trans. Magn. **27**, 3469 (1991)

Translated by M. E. Alferieff

Natural behavior of the magnetization under spontaneous reorientation: $TmFeO_3$, $ErFeO_3$

L. T. Tsymbal*

A. A. Galkin Donetsk Institute of Physics and Engineering, Ukrainian National Academy of Sciences, 72 ul. R. Lyuksemberg, Donetsk 83114, Ukraine; Department of Physics, Ohio State University, Columbus, OH, USA

Ya. B. Bazaliĭ

A. A. Galkin Donetsk Institute of Physics and Engineering, Ukrainian National Academy of Sciences, 72 ul. R. Lyuksemberg, Donetsk 83114, Ukraine; IBM Almaden Research Center, San Jose, CA, USA

G. N. Kakazeĭ

Department of Physics, Ohio State University, Columbus, Ohio USA; Institute of Magnetism, Ukrainian National Academy of Sciences, bul. Akad. Vernadskogo 36-b, Kiev 03142, Ukraine

Yu. I. Nepochatykh

A. A. Galkin Donetsk Institute of Physics and Engineering, Ukrainian National Academy of Sciences, ul. R. Lyuksemberg 72, Donetsk 83114, Ukraine

P. E. Wigen

Department of Physics, Ohio State University, Columbus, OH, USA

(Submitted September 20, 2004)
Fiz. Nizk. Temp. **31**, 367–373 (March–April 2005)

A SQUID magnetometer is used to study the behavior of the magnetization of $TmFeO_3$ single crystals along the **a** and **c** principal crystallographic axes in the $\Gamma_4-\Gamma_{24}-\Gamma_2$ spin reorientation range. The temperature dependences are obtained as the moduli of the magnetization vector **M** and its turn angle θ in the reorientation range. The results are compared with the same results for $ErFeO_3$. It is shown that even though the experimental dependences $|\mathbf{M}|(T)$ and $\theta(T)$ are qualitatively different in $TmFeO_3$ and $ErFeO_3$ they can all be convincingly described on the basis of a modified mean-field theory previously proposed by the authors. Since the theoretical analysis does not include any parameters which are not known from experiment, the agreement between theory and experiment confirms that the model proposed for describing $\Gamma_4-\Gamma_{24}-\Gamma_2$ phase transitions in orthoferrites is a general model. *Dedicated to E. S. Borovik—Scientist and Humanitarian "Who can say what influence the silent presence of one person has on another?" Walter De la Mar*
[DOI: 10.1063/1.1884430]

1. INTRODUCTION

Rhombic rare-earth (RE) orthoferrites $RFeO_3$ (where R is a rare-earth or yttrium ion) are classical model materials for studying second-order orientational phase transitions in ferrites.

A characteristic feature of orthoferrites is the presence of two magnetic subsystems: the *d* electrons of iron and the *f* electrons of rare-earth ions. The magnetic structure of orthoferrites is complicated, but in the temperature range of interest to us it can be described using a simplified scheme: the magnetic moments of iron below the Néel temperature $T_N = 620-740$ K form a weakly canted antiferromagnetic structure with Néel vector **G** and weak ferromagnetism vector **F**, and the rare-earth subsystem remains paramagnetic right down to temperatures of the order of 10 K, below which some of the rare-earth ions also undergo ordering. The interaction of the magnetic subsystems and the change in the effective anisotropy constants under actions characterized by different kinds of external parameters (temperature, field, and pressure) results in the existence of a series of orientational phase transitions in such materials.

For all orthoferrites the basal magnetic structure of the iron subsystem just below T_N corresponds to an irreducible representation $\Gamma_4(G_x,F_z)$ with the vector **F** oriented along the **c** axis ($\mathbf{c}\|\mathbf{z}$) ($T_2<T_1<T_N$) of the crystal and the vector **G** directed along the **a** axis ($\mathbf{a}\|\mathbf{z}$). For crystals with magnetically inert RE ions (R=La,Lu, or Y) the $\Gamma_4(G_x,F_z)$ configuration remains right down to the lowest temperatures. For other RE ions spin reorientation occurs on cooling, most often (for example, in $ErFeO_3$, $TmFeO_3$, $YbFeO_3$, $SmFeO_3$, and $NdFeO_3$) according to the type

$$\Gamma_4(G_x,F_z)\rightarrow\Gamma_{24}(G_{x,z},F_{x,z})\rightarrow\Gamma_2(G_z,F_x).$$

Such a reorientation consists in a gradual rotation of the spin system of iron as a whole relative to the crystallographic axes. As temperature decreases, the vector **F** rotates in the (**ac**) plane from the **c** axis to the **a** axis in the interval T_2-T_1

($T_2 < T_1 < T_N$). When the temperature T_2 is reached the system switches into another symmetric configuration $\Gamma_2(G_z, F_x)$ with $\mathbf{F} \| \mathbf{a}$. Ordinarily, the interval of reorientation temperatures is quite wide (~ 10 K), and its limits at temperatures T_1 and T_2 are points of second-order phase transitions. It is supposed that the magnetic subsystem of iron is saturated in the reorientation temperature range. This assumption is justified for T_1, T_2 (~ 100 K) $\ll T_N$, because the d-d exchange energy is three orders of magnitude greater than the energy of the d-f and f-f interaction energies.

Although the range of orientational phase transitions has been investigated by diverse methods in many orthoferrites, the specific question of the behavior of the magnetization in the reorientation range has been little studied. The experimental results are often incomplete, sometimes contradictory, are not accurate enough and cannot be described satisfactorily either by the standard form of the Landau theory[1–3] or the theoretical models proposed by the authors.

The first high-accuracy measurements of the temperature dependence of the magnetic moment performed on a $ErFeO_3$ single crystal with a SQUID magnetometer in the range of spontaneous reorientation along the principal crystallographic axes **a** and **c** were performed in Refs. 4 and 5. These measurements made it possible to extract the temperature dependences of the amplitude of the total magnetic moment $|\mathbf{M}|(T)$ of an $ErFeO_3$ crystal and the turn angle $\theta(T)$ of the vector **M** relative to the **c** axis in the temperature range $T_2 - T_1$ in zero magnetic field.

A modified mean-field theory has been proposed to describe the results obtained. This theory, in contrast to the classic approach used in Refs. 1–3, takes account of the anisotropy of paramagnetism of rare-earth ions and gives excellent agreement with experiment. It has been suggested that the model constructed is suitable for describing the reorientation range in other magnets exhibiting similar phase transitions.

The purpose of the present work is to study in detail the behavior of $|\mathbf{M}|(T)$ and $\theta(T)$ for $TmFeO_3$ single crystals and compare the results with those for $ErFeO_3$. Indeed, the initial characteristics of $TmFeO_3$ are closest to $ErFeO_3$. $TmFeO_3$ is characterized by the same type of phase transition $\Gamma_4 \rightarrow \Gamma_{24} \rightarrow \Gamma_2$ and virtually the same range of reorientation temperatures $T_2 - T_1$. On this basis $TmFeO_3$ is an ideal object for checking the correctness and applicability of the modified mean-field theory for describing the region of a $\Gamma_4 \rightarrow \Gamma_{24} \rightarrow \Gamma_2$ phase transformation in magnets.

2. EXPERIMENT

The measurements were performed on $TmFeO_3$ single crystals. Sample 1 is a $3.05 \times 4.16 \times 2.5$ mm parallelepiped with mass 0.2482 g. Sample 2 is oval in shape with mass 0.0047 g. Sample 3 is nearly spherical with mass 0.03 g. The results obtained on different samples confirm one another.

Since the magnetic anisotropy conditions control the reorientation phenomenon, it is not surprising that the chemical, thermal, and other processes influencing anisotropy also change the transition temperature. The reorientation interval in a real crystal is sensitive to the purity, perfection, and growth conditions of the crystal and can vary somewhat from one sample to another. In this connection, for a quantitative analysis of the results it is desirable to determine the specific values of the temperatures T_1 and T_2 for the experimental samples.

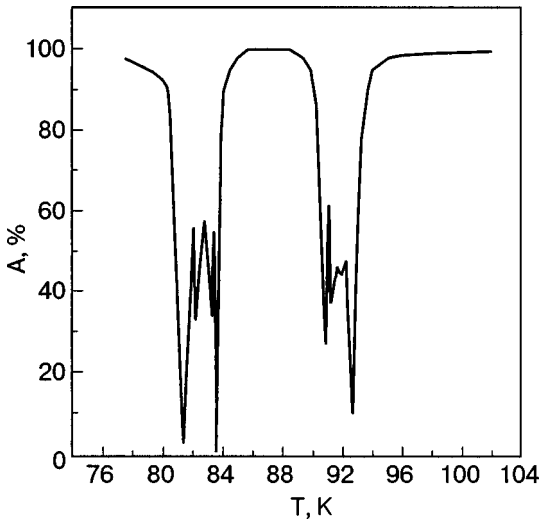

FIG. 1. Temperature dependence of the amplitude of microwave power absorption in the reorientation range for $TmFeO_3$ (sample 3, $f = 38.2$ GHz).

To this end, specifically, use resonance experiments using a direct-amplification microwave spectrometer can be used. Indeed, it is well known (see, for example, Ref. 6), that near phase transitions in $TmFeO_3$ softening of the acoustic branches of the oscillations of the magnetic d subsystem of the iron ion occurs. This results in resonance absorption of microwave power at a fixed frequency at two points which are almost symmetric relative to the temperature of each transition. To determine the temperatures T_1 and T_2 more accurately the form of the temperature-frequency dependence of the position of the resonance absorption lines[6] and the absorption anomalies between them must be taken into account. Figure 1 displays an example of an experimental trace for sample 3 fabricated from the same $TmFeO_3$ single crystals as sample 1. The absorption of microwave power at 38.2 GHz, reflected from a waveguide-shortening piston with the sample placed at the center of the waveguide, were recorded. The direction of the magnetic component of the linearly polarized microwave field relative to the crystallographic axes was chosen from the condition that the soft modes are excited simultaneously at the transition $\Gamma_2 - \Gamma_{24}$ and at the transition $\Gamma_4 - \Gamma_{24}$. The four deepest minima in the curve in Fig. 1 determine the resonance absorption points. The temperatures T_1 and T_2 are determined to within ± 0.5 K. The values $T_1 \approx 92$ K and $T_2 \approx 82$ K were taken on the basis of an analysis of all experimental measurements.

The magnetic moment **M** of the crystal was studied using a Quantum Design MPMS-5S SQUID magnetometer in the temperature range 60–120 K and magnetic fields in the range $H = \pm 1000$ Oe. The saturation magnetization was determined by two methods: 1) by analyzing the hysteresis loops of $M(H)$ measured at definite temperatures and 2) by directly measuring the magnetization $M(T)$ in the weakest external magnetic field sufficient for reaching a single-domain state of the sample. The latter measurements were possible because it was found that for our experimental

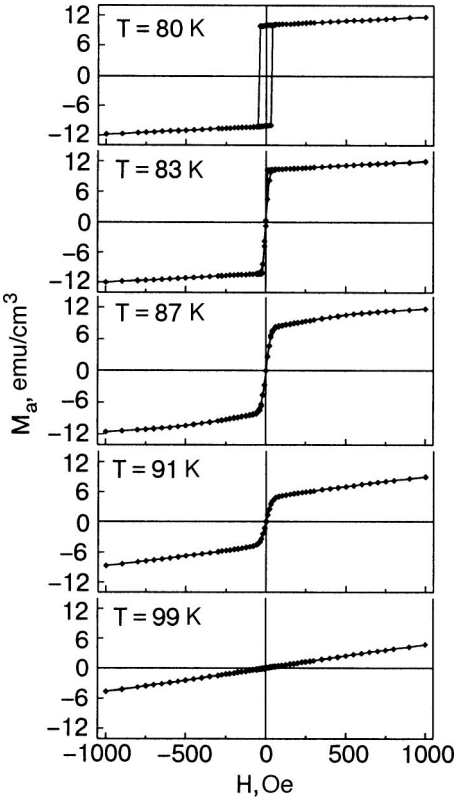

FIG. 2. Experimental traces of the magnetization curves $M_a(H)_{T=\text{const}}$ obtained with a SQUID magnetometer for $TmFeO_3$ (**a** axis, sample 1).

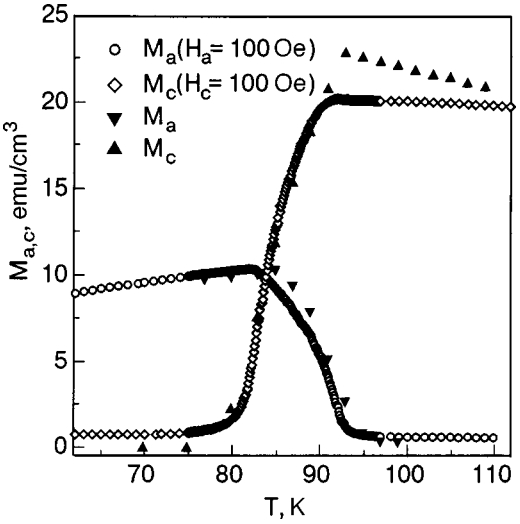

FIG. 3. Magnetizations $M_{a,c}(T)$, calculated on the basis of the magnetization curves (filled symbols) and measured by scanning the temperature in an external magnetic field $H=100$ Oe (open symbols), for a $TmFeO_3$ single crystal (sample 1).

samples the magnetization in a negligible field of the order of 50–100 Oe is, in practice, close to the true saturation magnetization. Being sufficiently accurate, the second method greatly simplifies the measurement procedure and makes it possible to perform measurements with a small temperature step.

For analyzing hysteresis loops we recall the following. The H-T phase diagram of orthoferrites with the magnetic field strictly oriented along the crystallographic axes, $\mathbf{H}\|\mathbf{a}$ or $\mathbf{H}\|\mathbf{c}$, has been widely studied. Analysis of this diagram shows that when the external magnetic field varies in the range $\pm H$ the intersection of the line $H=0$ in the reorientation temperature range T_2-T_1 with $\mathbf{H}\|\mathbf{a}$ and with $\mathbf{H}\|\mathbf{c}$ corresponds to a first-order phase transition. A first-order phase transition also occurs on crossing the line $H=0$ in the temperature range above T_1 with $\mathbf{H}\|\mathbf{c}$ and in the temperature range below T_2 with $\mathbf{H}\|\mathbf{a}$. Evidently, the precise geometry cannot be achieved in a real experiment. Analysis of the three-dimensional phase diagram[4,7] shows that for an inclined field any intersection of the line $H=0$ in an arbitrary direction corresponds to a first-order transition. A jump of at least one component of the magnetic moment should be observed and, correspondingly, the hysteresis loop for this component is square. Thus the initially expected form of the hysteresis loop is square.

Figure 2 shows experimental traces of hysteresis loops which were obtained for $TmFeO_3$ sample 1 in the experimental geometry $\mathbf{H}\|\mathbf{a}$. It is evident that, just as in the case of $ErFeO_3$,[4] square hysteresis loops are indeed observed outside the orientation interval with $T<T_2$. Their shape is explained by the assumption that magnetic domains are not formed in this temperature interval and the magnetization of the sample switches coherently with **H** changing sign. Deep inside the reorientation interval T_2-T_1 the square loops become S-shaped magnetization curves. Just as in $ErFeO_3$,[4] this is probably due to the formation of a polydomain magnetic structure in the nonsymmetric phase and a sharp change in energy and mobility of domain walls in the reorientation region.[8] Finally, a straight line $M(H)$ due to the paramagnetism of the thulium ions in an external magnetic field is observed for $T>T_1$.

On the basis of the above-indicated transformation of the form of the magnetization curves measurements of the saturation magnetization M in the reorientation range were performed for each value of the temperature by extrapolating the linear sections of the curves $M(H)_{T=\text{const}}$ observed in high fields to zero magnetic field. The point of intersection of the extrapolated straight line and the vertical axis $H=0$ gives the value of M. The experimental values $M_a(T)$ and $M_c(T)$ obtained in this manner are displayed in Fig. 3 (filled symbols). According to Fig. 2 the width of the S-shaped sections of the magnetization curves does not exceed 100 Oe, and the magnetization in this field is indeed close to the value obtained by extrapolating the high-field rectilinear section of the magnetization curve. The results obtained in this manner are displayed in Fig. 3 (open symbols).

The measured values of $M_a(T)$ and $M_c(T)$ make it possible to reconstruct the temperature dependence of the absolute magnitude $|\mathbf{M}|$ and the rotation angle θ of the magnetization according to the formulas

$$|\mathbf{M}|=\sqrt{M_a^2+M_c^2},\quad \theta=\tan^{-1}\left(\frac{M_a}{M_c}\right).$$

The results of an analysis of the experiment are presented in Figs. 4a and 5a. For comparison the analogous results for $ErFeO_3$ are presented in Figs. 4b and 5b.[4,5]

According to Figs. 3–5, as temperature decreases the total magnetization of the crystal behaves as follows:

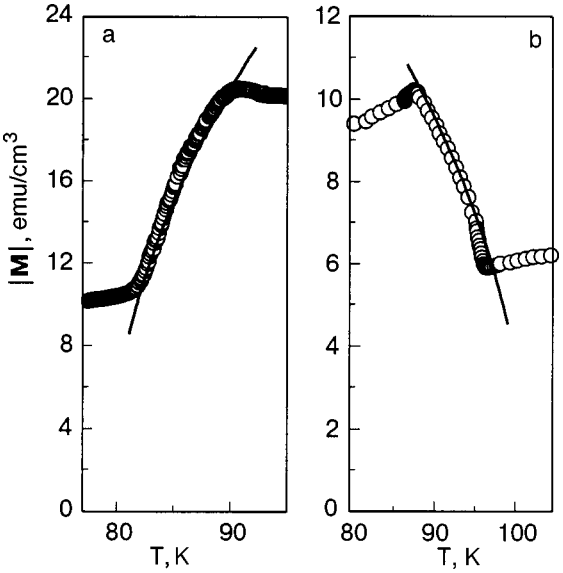

FIG. 4. Experimentally measured absolute values of the magnetization $|\mathbf{M}|(T)$: for $TmFeO_3$ (a) and $ErFeO_3$ (from Ref. 5) (b). Solid curves—calculation using Eq. (2).

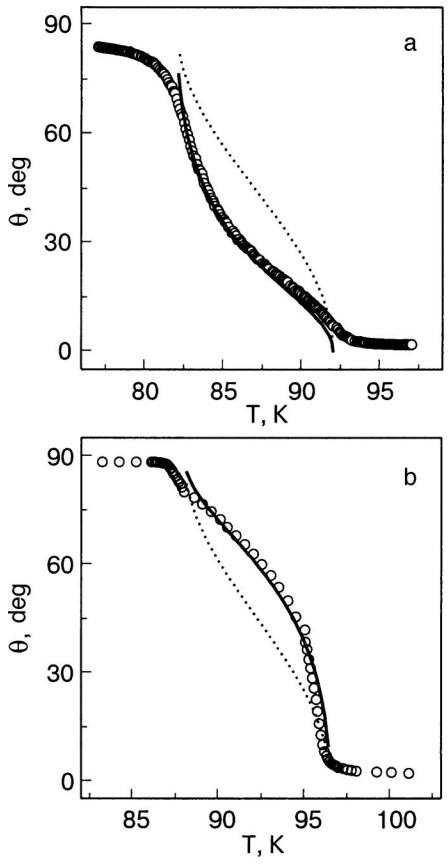

FIG. 5. Rotation angle of the crystal magnetization vector for $TmFeO_3$ in the reorientation range. The angle calculated from the components of **M** measured for sample 1 in a 100 Oe field. Solid curve—theoretical result obtained taking account of the magnetization of Tm and its anisotropy (9); dotted curve—result of a standard approximation (2) (a). The rotation angle of the crystal magnetization vector for $ErFeO_3$ in the reorientation range. The angle was calculated from the components of **M** measured in a 50 Oe field. Solid curve—theoretical result obtained taking account of the magnetization and anisotropy (9) of Er; dotted curve—the result of the standard approximation (2) (b).[4,5]

—as temperature decreases from T_N to T_1 the total magnetization of the crystal increases smoothly in agreement with Ref. 9; this confirms the fact that the magnetic moment of the thulium subsystem is formed parallel to the magnetic moment of the iron subsystem;

—conversely, as temperature decreases below T_2 the total magnetization of the crystal decreases in agreement with Ref. 9, indicating that in this configuration the magnetic moment of the thulium subsystem is formed antiparallel to the magnetic moment of the iron subsystem;

—a catastrophic decrease ($\sim 100\%$) of the total magnetization of the crystal with decreasing temperature is observed in the narrow reorientation temperature interval T_2-T_1;

—the rotation angle of the magnetization vector changes smoothly in the reorientation interval T_2-T_1;

—the behavior of $|\mathbf{M}|(T)$ and $\theta(T)$ in the reorientation range is qualitatively different for $TmFeO_3$ and $ErFeO_3$ crystals; indeed, the magnetization of a $TmFeO_3$ crystal in this narrow interval decreases considerably with decreasing temperature, while for $ErFeO_3$ it increases substantially; the behavior of $\theta(T)$ is just as divergent (see Figs. 4 and 5); however, it must be underscored that the measured values for both crystals exhibit a general behavior—in the entire interval T_2-T_1 the rotation angles $\theta(T)$ vary smoothly and the amplitudes $|\mathbf{M}|(T)$ vary very substantially but also smoothly;

—the behavior of $\theta(T)$ in the interval T_2-T_1 is different from the substantially nonsymmetric behavior previously presented for $TmFeO_3$ in Ref. 10 and $ErFeO_3$ in Ref. 11; this could be due to the large error, indicated by the authors of Refs. 10 and 11, in the amplitude measurements performed using the NMR method to determine $\theta(T)$ and by a lack of information on the large change in $M(T)$ in the reorientation interval.

3. ANALYSIS

Spin reorientation is often described on the basis of the Landau theory (see, for example, Refs. 1–3). In this theory it is assumed that the absolute magnitude of the magnetization of the iron subsystem remains constant under a $\Gamma_4 \rightarrow \Gamma_{24} \rightarrow \Gamma_2$ phase transition and the free energy of the system depends only on the angle of rotation of the magnetization. Under this assumption the angle of rotation of the magnetization vector is determined by minimizing the expression for the free energy

$$F = F_0 + \frac{1}{2} K_U(T)\cos(2\theta) + K_b(T)\cos(4\theta). \tag{1}$$

Under minimal assumptions concerning the temperature dependence of the phenomenological constants in a narrow neighborhood of the reorientation interval, specifically, $K_b = \text{const}$, K_u varies linearly as a function of temperature, passing through the value $K_u = 0$, minimization gives

$$\tan\theta = \sqrt{\frac{1+\xi}{1-\xi}}, \tag{2}$$

where $\xi(T) = (T_1+T_2)/2 - T/(T_1-T_2)/2$.

The dependences obtained from Eq. (2) for $TmFeO_3$ and $ErFeO_3$ are shown in Figs. 5a and 5b (dotted lines). It is evident that in the experiment on both crystals neither the assumption that $|\mathbf{M}|(T)$ is constant (Fig. 4) nor the behavior of $\theta(T)$ predicted by Eq. (2) (Fig. 5) is confirmed.

On the whole this is not surprising because the above-described approach ignores the RE subsystem, even though it is well known that paramagnetic rare-earth ions are often magnetized by the molecular field of iron, and the RE subsystem acquires its own magnetic moment **m**. Therefore the total moment of the crystal becomes $\mathbf{M}=\mathbf{F}+\mathbf{m}$. According to the modified mean-field model[4,5] the magnetic moment **F** of the iron subsystem itself indeed remains unchanged under reorientation, remaining in a saturation state for $T_1, T_2 \ll T_N$. The key feature of the model is the anisotropy of the paramagnetic susceptibility of the rare-earth subsystem to the molecular field of iron

$$m_a=\chi_a^R F_a, \quad m_c=\chi_c^R F_c, \tag{3}$$

where $\chi_a^R \neq \chi_c^R$.

Susceptibility anisotropy has been observed in resonance experiments and could be responsible for the spin-reorientation transition,[2,9,12,13] but it was never taken into account in previous calculations of the temperature dependence of the rotation angle of the magnetization vector of the crystal.

Taking this anisotropy into account the interaction energy between the iron and rare-earth subsystems can be written in the form

$$\tilde{F}=\tilde{F}_0+\frac{1}{2}K_u\cos(2\theta_F)+K_b\cos(4\theta_F)-\beta(F_a\chi_a^R m_a + F_c\chi_c^R m_c)+\frac{\beta}{2}m^2. \tag{4}$$

Minimizing with respect to m_a, m_c, and m gives an equation whose form is similar to that of Eq. (2):

$$\tilde{F}=\tilde{F}_0'+\frac{1}{2}K_u'\cos(2\theta_F)+K_b\cos(4\theta_F). \tag{5}$$

Here θ_F is the rotation angle of the magnetization vector of the iron subsystem and once again satisfies Eq. (2), and K_u' is a new effective anisotropy constant,

$$K_u'=K_u-\frac{\beta F^2}{2}((\chi_c^R)^2-(\chi_a^R)^2). \tag{6}$$

The experimentally measured angle is now determined as

$$\tan\theta=\frac{M_a}{M_c}=\left(\frac{1+\chi_a^R}{1+\chi_c^R}\right)\frac{F_a}{F_c}=\left(\frac{1+\chi_a^R}{1+\chi_c^R}\right)\tan\theta_F. \tag{7}$$

Since

$$M(T_1)=M_c(T_1)=(1+\chi_c^R)F \quad \text{and}$$
$$M(T_2)=M_a(T_2)=(1+\chi_a^R)F, \tag{8}$$

the function $\theta(T)$ can be determined from the expression

$$\tan\theta=r\sqrt{\frac{1+\xi}{1-\xi}}, \quad \text{where} \quad r=\frac{M_a(T_2)}{M_c(T_1)}. \tag{9}$$

The expression for determining the absolute magnitude of the magnetization is

$$M=\sqrt{M_a^2+M_c^2}=\sqrt{(1+\chi_a^R)^2\sin\theta_F^2+(1+\chi_c^R)^2\cos\theta_F^2}$$
$$=M_c(T_1)\sqrt{\frac{r^2(1+\xi)+(1-\xi)}{2}}. \tag{10}$$

Here $M_a(T_2)$ and $M_c(T_1)$ are, respectively, the magnetization of the crystal along the **a** axis at temperature T_2 and the **c** axis at temperature T_1. The expressions (9) and (10) do not contain any unknown adjustable parameters, since the quantities T_1, T_2, $M_a(T_2)$, and $M_c(T_1)$ are determined from experiment. The quantities $M_a(T_2)$ and $M_c(T_1)$ were chosen according to more accurate measurements—according to the hysteresis curves of magnetization. The value of r obtained for $TmFeO_3$ was 0.47. According to Figs. 4 and 5, constructed using Eqs. (9) and (10), the theoretical curves demonstrate convincing agreement with the experimental results obtained for $TmFeO_3$ and $ErFeO_3$. We note that the deviation of the experimental values from the theoretical curves near the edges of the reorientation interval is due to the well-known fact that the dependences $M(T)$ flatten out in the reorientation range in the presence of an external magnetic field.[14]

We underscore once again that analysis of the dependences $|\mathbf{M}|(T)$ and $\theta(T)$ using the model of Ref. 4, in the first place, is valid only in the reorientation temperature interval T_2-T_1 and, in the second place, is independent of the origins of the reorientation. The expressions (1) and (10) are applicable in all cases where the effective second-order anisotropy constant $K_u'(T)$ can be approximated by a linear function, irrespective of whether or not such a dependence is determined by the iron subsystem, the R-Fe interaction, the behavior of the susceptibility of the RE ions, or other factors. Since a linear variation of $K_u'(T)$ in orthoferrites has been observed experimentally[14,15] and it is shown in Ref. 16 that the microscopic theory of Ref. 17 predicts such behavior, the model of Ref. 4 could have wide applications.

4. CONCLUSIONS

The first direct measurements of the temperature dependences of the absolute values $|\mathbf{M}|(T)$ and rotation angle $\theta(T)$ of the magnetization were performed for $TmFeO_3$ crystals in the range of the orientational phase transition $\Gamma_4 \rightarrow \Gamma_{24} \rightarrow \Gamma_2$. It was established that the induced magnetic moment of the thulium subsystem is comparable to that of the iron subsystem and the total magnetization of the system in the unsymmetric phase varies smoothly almost by a factor of 2 with a smooth variation of its rotation angle as a function of temperature. It was shown that on the basis of a modified mean-field theory the experimental results for $TmFeO_3$ crystals can be described just as well as for $ErFeO_3$ crystals even though the extrinsic difference in the behavior of $\theta(T)$ and $|\mathbf{M}|(T)$ is substantial between $TmFeO_3$ and $ErFeO_3$ crystals. The results obtained provide a strong argument in favor of taking into account the anisotropy of the susceptibility of RE ions to the molecular field of iron as the basis of the model in Ref. 4 and the applicability of this model for describing orientational transitions of the type $\Gamma_4(G_x,F_z)\rightarrow\Gamma_{24}(G_{x,z},F_{x,z})\rightarrow\Gamma_2(G_z,F_x)$ in different orthoferrites.

This work at the Donetsk Institute of Physics and Engineering of the Ukrainian National Academy of Sciences was supported in part by the State Foundation for Fundamental Research, project F7/203-2004. Ya. Bazaliĭ was supported by DARPA/ARO under contract No. DAAD19-01-C-006.

*E-Mail: tsymbal@sova.fti.ac.donetsk.ua

[1] J. R. Shane, Phys. Rev. Lett. **20**, 728 (1968); H. Horner and C. M. Varma, *ibid.* **20**, 845 (1968).
[2] J. Sirvardiere, Solid State Commun. **7**, 1555 (1969).
[3] K. P. Belov, A. K. Zvezdin, A. M. Kadomtseva, and R. V. Levitin, *Orientational Transitions in Rare-Earth Magnetic Materials*, Nauka, Moscow (1979).
[4] Ya. V. Bazaliy, L. T. Tsymbal, G. N. Kakazei, A. I. Izotov, and P. E. Wigen, Phys. Rev. B **69**, 104429 (2004).
[5] Ya. B. Bazaliy, L. T. Tsymbal, G. N. Kakazei, and P. E. Wigen, J. Appl. Phys. **95**, 6622 (2004).
[6] V. D. Buchel'nikov, N. K. Dan'shin, L. T. Tsymbal, and V. G. Shavrov, Usp. Fiz. Nauk **166**, 585 (1996).
[7] V. G. Bara'yakhtar, A. N. Bogdanov, and D. A. Yablonskiĭ, Usp. Fiz. Nauk **156**, 47 (1988) [Sov. Phys. Usp. **31**, 810 (1988)].
[8] F. C. Rossol, J. Appl. Phys. **39**, 5263 (1968); *ibid.* **40**, 1082 (1969).
[9] R. White, J. Appl. Phys. **40**, 1061 (1969).
[10] V. D. Doroshev, A. S. Kharnachev, N. M. Kovtun, E. E. Soloviev, F. Ya. Chervonenkis, and A. A. Shemyakov, Phys. Status Solidi B **51**, K31 (1972).
[11] N. M. Kovtun, A. S. Karnachev, E. E. Solov'ev, A. Ya. Chervonenkis, and A. A. Shemyakov, Fiz. Tver. Tela (Leningrad) **14**, 2150 (1972) [Sov. Phys. Solid State **14**, 1856 (1972)].
[12] D. Treves, J. Appl. Phys. **36**, 1033 (1965).
[13] T. Yamaguchi, J. Phys. Chem. Solids **35**, 479 (1974).
[14] M. Abe, M. Gomi, K. Shomo, Ya. Mori, and S. Nomura, Jpn. J. Appl. Phys., Part 1 **16**, 279 (1977).
[15] K. P. Belov, R. A. Volkov, B. N. Goranskiĭ, A. M. Kadomsteva, and V. V. Uskov, Fiz. Tver. Tela (Leningrad) **11**, 1148 (1969) [Sov. Phys. Solid State **11**, 935 (1969)].
[16] W. J. Schaffer, R. W. Bene, and R. M. Walser, Phys. Rev. B **10**, 255 (1974).
[17] L. M. Levinson, M. Luban, and S. Shtrikman, Phys. Rev. **187**, 715 (1969).

Translated by M. E. Alferieff

Low-temperature deviations from Bloch's law in $BaFe_{12}O_{19}$ hexaferrite

A. A. Bezlepkin* and S. P. Kuntsevich

V. N. Karazin Kharkov National Universty, 4 pl. Svobody, Kharkov 61077, Ukraine
(Submitted September 27, 2004)
Fiz. Nizk. Temp. **31**, 374–376 (March–April 2005)

The NMR method is used to study the temperature variations of local fields on ^{57}Fe nuclei in the octahedral positions $12k$, $4f_2$, and $2a$ of the iron ions in the ferrite $BaFe_{12}O_{19}$. The possibility of applying Bloch's spin-wave theory to describe the temperature variations of the local fields on the iron nuclei is examined. Deviations from Bloch's 3/2 power law are found in the temperature range 4.2–77 K. These deviations cannot be described on the basis of the behavioral characteristics due to the presence of an energy gap in the acoustic magnon spectrum. © *2005 American Institute of Physics.* [DOI: 10.1063/1.1884431]

1. INTRODUCTION

The investigation of the magnetic resonance of nuclei in multiple-sublattice ferrimagnets makes it possible to obtain data on the temperature dependence of the sublattice magnetizations. These dependences reflect the special features of the spin dynamics and carry information about the character of the energy spectra with excitation of spin waves. The hexaferrite $BaFe_{12}^{3+}O_{19}$ contains as magnetoactive ions only Fe^{3+} ions in five crystallographically nonequivalent positions, which have octahedral ($12k$, $2a$, $4f_2$), tetrahedral ($4f_1$), and bipyramidal ($2b$) oxygen environments.[1] The bipyramidal environment is trigonal and consists of two pseudotetrahedral sites. The local fields on ^{57}Fe nuclei in bipyramidal and tetrahedral positions of the crystal lattice of the ferrite BaM in the temperature range 4.2–295 K were studied in Ref. 2. In the present work NMR was used to investigate the temperature variations of the local fields on iron nuclei in the $12k$, $2a$, and $4f_2$ positions in the ferrite BaM. Deviations from Bloch's law were found at low temperatures. These deviations cannot be explained on the basis of the behavioral characteristics due to the presence of an energy gap in the acoustic magnon spectrum.

2. SAMPLES AND MEASUREMENT PROCEDURE

The $BaFe_{12}O_{19}$ hexaferrite samples were synthesized by the fluxed solution method with the flux $BaO \cdot B_2O_3$. Crystallization was performed on a rotating seed in the temperature range 1420–1300 K. X-Ray diffraction was used to monitor the phase composition of the crystals. The crystal lattice constants at room temperature are $a = 0.589$ nm and $c = 2.19$ nm. The crystals were 95% enriched with the isotope ^{57}Fe. The stationary method described in Ref. 3 was used to study NMR on iron nuclei in near-domain layers of Bloch walls. The measurements were performed at low rf power. The exciting voltage on the circuit containing the experimental sample did not exceed 10^{-2} V. The frequencies of the NMR lines obtained from near-domain layers by the stationary method at 77 K were the same to within 0.2% as the line frequencies obtained from nuclei in domains by the spin-echo method. The error in determining the frequencies of the peaks at the NMR signals did not exceed 0.1%.

3. EXPERIMENTAL RESULTS AND DISCUSSION

The temperature dependences of the local fields H_i (i is the sublattice index) on ^{57}Fe nuclei for all crystallographically nonequivalent positions $12k$, $2a$, $4f_2$, $4f_1$, and $2b$ of trivalent iron ions, corresponding to the a, b, c, d, and e sublattices, are shown in Fig. 1. (For the c and e sublattices the results from Ref. 2 are presented.) According to Fig. 1, an anomalous decrease of the local field on the nuclei in the e ($2b$) sublattice occurs as the temperature decreases in the range 4.2–77 K. The reasons for this decrease are examined in Ref. 2. For all other sublattices there is no such anomaly, and monotonic growth of the field as temperature decreases from 295 to 4.2 K is observed. It is well known that the uncompensated spins of the electron shell of the magnetically active ion make the largest contribution to the local field H_i of a sublattice, so that to a first approximation the local field of a definite sublattice is proportional to the magnetization of this sublattice.[4] If the interionic dipole-dipole interaction is neglected, then at low temperatures a quadratic dispersion law obtains for acoustic magnons.[5] In M-type hexaferrites the dipole magnetic fields due to the interionic

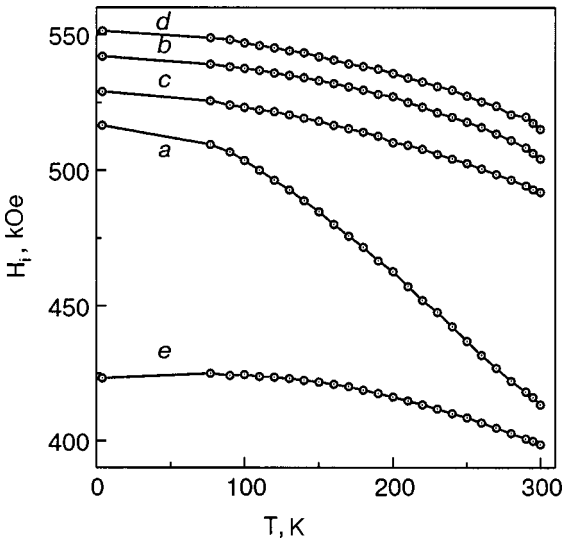

FIG. 1. Temperature dependences of local fields on ^{57}Fe nuclei in the hexaferrite $BaFe_{12}O_{19}$.

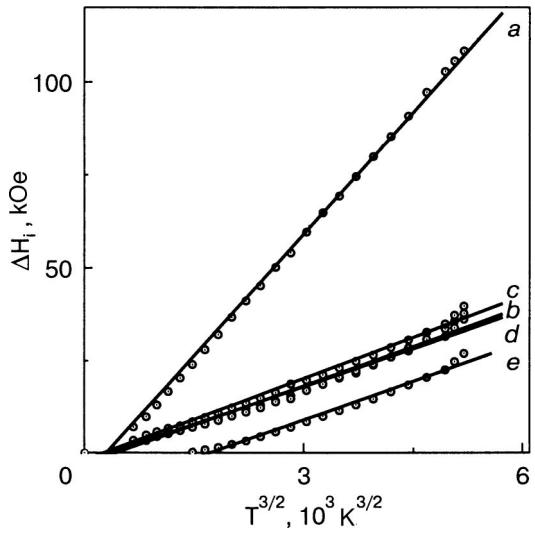

FIG. 2. Temperature variations of local fields on ^{57}Fe nuclei in the hexaferrite $BaFe_{12}O_{19}$.

dipole-dipole interaction are much weaker than the effective exchange fields.[6] Consequently, Bloch's 3/2 power law should hold for the temperature dependences of the sublattice magnetizations M_i. Since $M_i(T) \sim H_i(T)$,

$$H_i(0) - H_i(T) = \Delta H_i(T) = B_i T^{3/2}, \tag{1}$$

where $H_i(0)$ is the local field for the ith sublattice as $T \to 0$, $H_i(T)$ is the local field at temperature T, and B_i is a temperature-independent constant.

The quantities $\Delta H_i(T^{3/2})$, calculated from the experimental data on $H_i(T)$ for the interval 4.2–295 K, are presented in Fig. 2. It is evident that a deviation from Bloch's law occurs in the temperature range 4.2–200 K for the e sublattice and 4.2–77 K for the a, b, c, and d sublattices. The reasons for this deviation from Bloch's law for the e sublattice are examined in Ref. 2. It is shown in this work that the observed features are due to the redistribution of the spin and electron densities as a result of the low-temperature evolution of potential barriers near pseudotetrahedral sites in the bipyramidal positions of the iron ions. The observed feature is not associated with the specific nature of the spin dynamics, but it manifests formally in the plot $\Delta H_i = f(T^{3/2})$ as a deviation from Bloch's law.

The mechanism examined above cannot explain the deviation from Bloch's law for the a, b, c, and d sublattices in the interval 4.2–77 K for the following reasons.

In the first place the distortions of the crystal lattice near bipyramidal sites are local. In the second place the temperature ranges where Bloch's law is violated for the sublattices e and a, b, c and d differ substantially. According to Fig. 2 the dependences $\Delta H_i(T^{3/2})$ for the a, b, c, and d sublattices are of a "threshold" character. Extrapolating the dependences to the point $\Delta H_i = 0$ gives the temperature $T_s = 55$ K.

In magnetically uniaxial crystals the dispersion law for acoustic magnons in a ferrimagnet can be represented in the form[7]

$$\varepsilon_k = \varepsilon_0 + Aa^2k^2, \tag{2}$$

where ε_k is the magnon energy, ε_0 is the gap energy, A is the exchange parameter, a is the crystal lattice parameter, and k is the wave number.

Bloch's law should hold in the temperature range[8]

$$\frac{\varepsilon_0}{\chi} < T \ll \Theta_C, \tag{3}$$

where χ is Boltzmann's constant and Θ_C is the Curie temperature.

Deviations from Bloch's law should be observed for $T < \varepsilon_0/\chi$. The energy gap can be represented in the form

$$\varepsilon_0 = H_a \mu, \tag{4}$$

where H_a is the anisotropy field and $\mu = 5\mu_B$ is the magnetic moment of the Fe^{3+} ion (μ_B is the Bohr magneton).

For the hexaferrite BaM at 77 K $H_a \approx 16$ kOe.[9] Using the values of μ and H_a we obtain for the effective gap temperature $T_{\text{eff}} = \varepsilon_0/\chi \approx 5$ K, which is an order of magnitude less than the temperature T_s. Consequently the deviations observed for the a, b, c, and d sublattices from Bloch's law at low temperatures are not associated with the presence of a gap in the spin-wave spectrum.

The behavior examined in this paper indicate the existence of a "threshold" mechanism which changes the spin dynamics in the temperature interval 4.2–55 K.

*E-mail: bezlepkiny@bk.ru

[1] W. D. Nownes, J. H. Fang, and A. J. Perrota, Z. Kristallogr. B **125**, 437 (1967).
[2] A. A. Bezlepkin and S. P. Kuntsevich, Fiz. Tver. Tela (St. Petersburg) **45**, 2048 (2003) [Phys. Solid State **45**, 2152 (2003)].
[3] S. P. Kuntsevich, A. A. Bezlepkin, and Yu. A. Popkov, Zh. Éksp. Teor. Fiz. **88**, 1820 (1985) [JETP **61**, 1079 (1985)].
[4] E. A. Turov and M. P. Petrov, *Nuclear Magnetic Resonance in Ferro- and Antiferromagnetic Materials*, Nauka, Moscow (1969).
[5] S. P. Kuntsevich and A. A. Bezlepkin, Fiz. Tver. Tela (St. Petersburg) **43**, 754 (2000) (*sic*).
[6] S. P. Kuntsevich Fiz. Nizk. Temp. **24**, 754 (1998) [Low Temp. Phys. **24**, 568 (1998)].
[7] E. A. Turov, *Physical Properties of Magnetically Ordered Crystals*, Nauka, Moscow (1963).
[8] E. M. Lifshitz and L. P. Pitaevskiĭ, *Statistical Physics*, Nauka, Moscow (1978), Pt. 2.
[9] S. P. Kuntsevich, Visnik KHDU, No. 440, Ser. "Fizika," No. **3**, 125 (1999).

Translated by M. E. Alferieff

ELECTRONIC PROPERTIES OF METALS AND ALLOYS

Level statistics for quantum Hall systems

V. Kagalovsky*

Negev Academic College of Engineering, Beer-Sheva 84100, Israel

B. Horovitz and Y. Avishai

Department of Physics, Ben-Gurion University of the Negev, Beer-Sheva 84105, Israel

(Submitted July 12, 2004)
Fiz. Nizk. Temp. **31**, 377–381 (March–April 2005)

Level statistics for two classes of disordered systems at criticality are analyzed in terms of different realizations of the Chalker-Coddington network model. These include: 1) Re-examination of the standard $U(1)$ model describing dynamics of electrons on the lowest Landau level in the quantum Hall effect, where it is shown that after proper local unfolding the nearest-neighbor spacing distribution (NNSD) at the critical energy follows the Wigner surmise for Gaussian unitary ensembles (GUE). 2) Quasi-particles in disordered superconductors with broken time reversal and spin rotation invariance (in the language of random matrix theory this system is a representative of symmetry class D in the classification scheme of Altland and Zirnbauer). Here again the NNSD obeys the Wigner surmise for GUE, reflecting therefore only ''basic'' discrete symmetries of the system (time reversal violation) and ignoring particle-hole symmetries and other finer details (criticality). In the localized regime level repulsion is suppressed. [DOI: 10.1063/1.1884432]

1. INTRODUCTION

The statistics of energy levels in a disordered system is an important tool in determining its transport properties as well as its critical behavior. A central quantity in this study is the nearest-neighbor spacing distribution (NNSD) denoted by $p(s)$. Here the random variable s is the (fluctuating) level spacing under the proviso that the local average of the density of states is energy independent (otherwise, a proper unfolding procedure is required). The distribution $p(s)$ involves all N point correlation functions of the pertinent Green function and hence, it is generally not available in a closed form.

In dealing with disordered systems, it is useful to distinguish between systems undergoing an Anderson type metal-insulator transition, and those characterized by a quantum Hall (QH)-like transition where, in the thermodynamic limit, critical state energies are isolated points occurring between continuous intervals of localized state energies. As for level statistics pertaining to disordered systems of the Anderson metal-insulater transition kind, there are a couple of important properties which are well established: 1) Under certain conditions it is expected to be represented (on the metallic side) by random matrix spectra.[1] To be more precise, it is well described by one of the corresponding Gaussian ensembles, Gaussian orthogonal (GOE), Gaussian unitary (GUE) and Gaussian simplectic (GSE), depending on the symmetry class to which the physical system belongs. The main condition is that the corresponding energy intervals are smaller than the Thouless energy. 2) It has been shown[2] that in the limit of an infinite system there are only three types of distributions $p(s)$. They are the Poisson law for the insulating regime, the Wigner surmise for the metallic domain, and a third one for the critical region. On the other hand, for systems in the second group (such as the quantum Hall effect) there is no similar analysis. The main difficulty is related to the fact that in the absence of a metallic regime, it is not possible to approach the critical point from the metallic regime using the powerful tool of expansion in the small parameter $1/g$ (here g is the dimensionless conductance). Common sense suggests that the distribution follows the Poisson law in the insulating part of the spectra while again, the distribution in the critical region is different, and related to the relevant universality class. For the quantum Hall transition this is supported by numerous numerical calculations.[3]

Recently, it has been noticed that the second group contains, besides the systems belonging to the quantum Hall effect universality class, other disordered systems whose phase diagram is much richer. They are related to the physics of disordered superconductors[4] and comprise four novel universality classes, determined according to the symmetry properties of the corresponding Bogoliubov-de Gennes Hamiltonian under spin rotation and time reversal. Some of these new phase diagrams have already been exposed, mainly in class C (where time reversal symmetry is broken while spin rotation invarinace is preserved). So far, the level statistics in the critical regions of the four new universality classes has not yet been studied. The goal of the present work is to fill this gap, starting by elucidating the level statistics of one of these new classes, namely class D, for which both symmetries (spin rotation and time reversal) are violated.

Some of the disordered systems in the second group can

be mapped on a network model. The most studied one is the quantum Hall system which is mapped on the Chalker-Coddington network model (CCNM).[5] The CCNM is designed to describe transition between plateaus in the QH system using transfer matrix algorithm in an infinite cylinder geometry (in the Landauer sense). It was later suggested that if, instead of studying transport properties, the system is closed up as a torus, then the eigenvalue problem can be addressed and the level statistics can be studied[6] (although no Hamiltonian is specified). In our previous works, a somewhat modified CCNM has been constructed which can describe noninteracting quasiparticles in disordered superconductors.[7,8] It appears that such a description can serve as an appropriate physical realization of the new random matrix universality classes.[4]

It is then natural to attempt an investigation of level statistics of these new symmetry classes by using the CCNM. Our main results are summarized below. 1) As a starting reference point we revisit the familiar QH system by repeating calculations for the original $U(1)$ model 6. The results of Ref. 6 are indeed reproduced ($p(s)$ deviates slightly from the Wigner surmise for GUE). Moreover, we show that after proper local unfolding, the NNSD of the $U(1)$ model at the critical energy is exactly identical with the Wigner surmise. In order to stress the necessity of unfolding we argue that the density of states (DOS) averaged over all samples is indeed uniform, whereas it has some structure for each sample. 2) We then present results for class D of disordered superconductors that have neither time-reversal nor spin-rotation invariance. Once again NNSD at the critical energy (after unfolding) coincides with the Wigner surmise. We find the DOS to have a periodic structure (period $\pi/2$), as one would expect from the form of the unitary operator. Beside the critical region, we also present results for the localized regime and show that level repulsion disappears. Thus, although the $U(1)$ and class D models considered here describe different systems and have different phase diagrams, yet the NNSD in the critical region is the same, depending only on the broken time-reversal symmetry. The fact that class D obeys particle-hole symmetry is not reflected in its NNSD. Our findings are in agreement with recent works[9] where it is argued that k-body embedded Gaussian ensembles of random matrices for sufficiently high rank k of the random interaction behave generically (i.e., in order to have exact RMT results it is not necessary for the Hamiltonian to be a full random matrix).

2. THE $U(1)$ NETWORK MODEL

In the original CCNM, electrons move along unidirectional links forming closed loops in analogy with semiclassical motion on equipotential contours. Scattering between links is allowed at nodes in order to map tunneling through saddle-point potentials. Propagation along links yields a random phase φ, and thus links are represented by diagonal matrices with elements in the form $\exp(i\varphi)$ (hence the notation $U(1)$ model). The transfer matrix for one node relates a pair of incoming and outgoing amplitudes on the left to a corresponding pair on the right; it has the form

$$\mathbf{T}=\begin{pmatrix}\cosh\theta & \sinh\theta\\ \sinh\theta & \cosh\theta\end{pmatrix}. \tag{1}$$

The node parameter θ is related to the electron energy in the following way:

$$\varepsilon=-\frac{2}{\pi}\ln(\sinh\theta), \tag{2}$$

where ε is the relative distance between the electron energy and the barrier height.

If the network forms a torus, then on every link the electron motion appears once as an outgoing one and once as an incoming one. The collection of relations between incoming and outgoing amplitudes defines the system's S matrix or rather, a discrete-time unitary evolution operator, $U(\varepsilon)$ (Ref. 6). The eigenphases of U serve as input for level statistics analysis. For a square network of $N\times N$ nodes, U is a $(2\times N^2)\times(2\times N^2)$ unitary matrix. The action of U on a vector Ψ of flux amplitudes defined on the start of each link maps the system onto itself, providing therefore an *implicit* eigenvalue equation $U(\varepsilon)\Psi=\Psi$. Since the dependence of the matrix elements of U on ε is complicated, it is practically impossible to find solutions of that equation (even numerically). Instead, it has been suggested[6] to find the eigenvalues of the equation

$$U\Psi_n=\exp[i\omega_n(\varepsilon)]\Psi_n \tag{3}$$

and to study statistics of ω_n for a given ε. The rationale behind it is twofold. First, there are sufficiently many states even in a narrow window near a particular energy ε to provide good statistics. Second, the behavior of the curves $\omega_n(\varepsilon)$ is rather smooth, and therefore the statistics of ω_n for a given ε is expected to be the same as the statistics of ε_n for $\omega=0$ (which are the true energy eigenvalues). We argue that the second hypothesis is justified only after a proper unfolding procedure is executed. Indeed, from the RMT point of view the eigenvalue problem of Eq. (3) belongs to the circular unitary ensemble (CUE). In the standard CUE all the eigenvalues lie on the unit circle and are equally spaced, so there is no need for unfolding of the spectra. However, Eq. (3) represents a physical problem in which not all the elements of U are independent random variables. Therefore, the question of whether the $U(1)$ model is a *bona fide* CUE should be examined. Our calculations show that the averaged (over 50 samples) DOS is indeed uniform, whereas it has some pronounced structure for each particular sample. Since the level statistics should be manifested for each individual sample (as in the study of nuclear spectra), the spectrum of each sample should then be properly unfolded. Here we make use of the fact that the dimensionless unfolded distance between two levels is

$$\Delta s_n=2k\frac{E_{n+1}-E_n}{E_{n+k}-E_{n-k}}, \tag{4}$$

where k is a number of neighbors to be optimized by the requirement of having a constant DOS. This procedure encodes the important local fluctuations of level spacing. We have checked that for $k\geqslant 6$ the result is practically independent of k, provided of course that $k\ll 2\times N^2$. To substantiate this point we plot in Fig. 1 the DOS of a single sample (at the

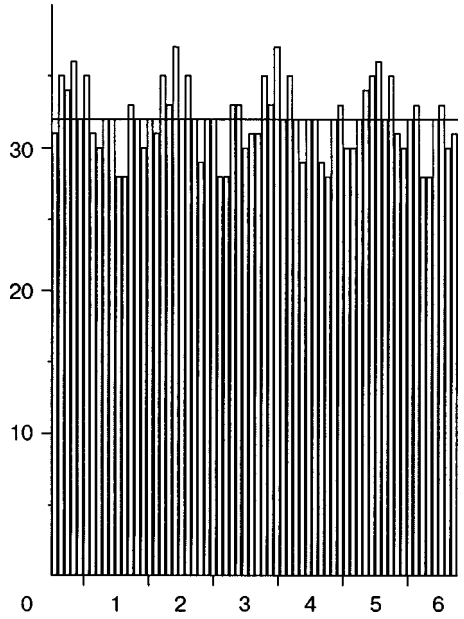

FIG. 1. Histogram for the DOS of a single sample at the critical point $\varepsilon=0$ for the $U(1)$ model without unfolding.

critical point $\varepsilon=0$) without unfolding. It shows indeed that the averaged DOS is not constant in energy. On the other hand, after averaging over 50 samples, Fig. 2 indicates that the average DOS is constant, as expected for random matrices belonging to CUE. The corresponding NNSD are displayed in Fig. 3. Raw data without unfolding reproduce the results obtained in Ref. 6, whereas after local unfolding the NNSD nearly coincides with the Wigner surmise for GUE (expected to be true also for CUE at large N). Finally, we assert in Fig. 4 that in the localized regime ($\varepsilon=1$) the NNSD follows the Poisson statistics $p(s)=e^{-s}$.

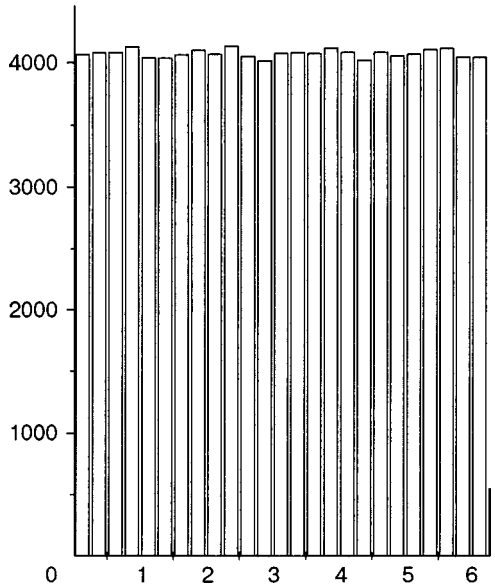

FIG. 2. Histogram for the DOS of 50 samples at the critical point $\varepsilon=0$ for the $U(1)$ model.

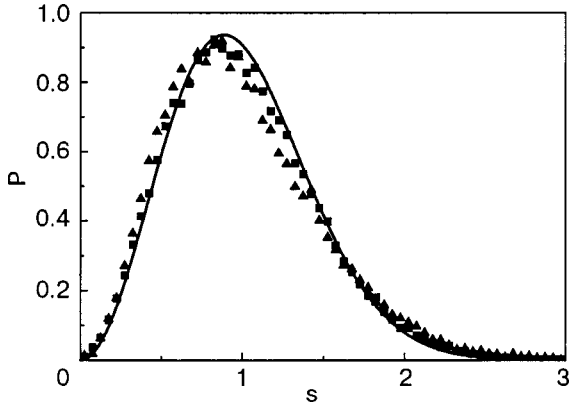

FIG. 3. Nearest neighbor spacing distribution $P(s)$ for the $U(1)$ model at $\varepsilon=0$ (critical regime). The curve is the Wigner surmise for the GUE; without unfolding Mettzer–Klesse (▲), ± 3 neighbor local unfolding (■).

3. DISORDERED SUPERCONDUCTORS: CLASS D

The properties of quasiparticles in disordered superconductors have been the subject of much recent interest. The Hamiltonians of such systems are representatives of a set of symmetry classes different from the three classes which are familiar both in normal disordered conductors and in the Wigner-Dyson random matrix ensembles. A list of additional random matrix ensembles, determined by these new symmetry classes, has been established.[4] Below we present numerical results on statistics of energy levels for a certain two-dimensional system with a particularly rich phase diagram. In the nomenclature of Ref. 4 the corresponding symmetry is denoted as class D. It can be realized in superconductors with broken time-reversal invariance, and either broken spin-rotation invariance (as in d-wave superconductors with spin-orbit scattering) or spinless or spin-polarized fermions (as in certain p-wave states). A particular realization of class D (which will be adopted here) is the Cho-Fisher (CF) model[10] which has a rich phase diagram. Each realization has two parameters: a disorder strength W ($0\leqslant W\leqslant 1$), and a tunneling amplitude ε, which controls the value of the thermal Hall conductance at short distances. The phases on the links on the two sides of the same node (which are either π with probability W or 0 with probability $1-W$) are correlated: the

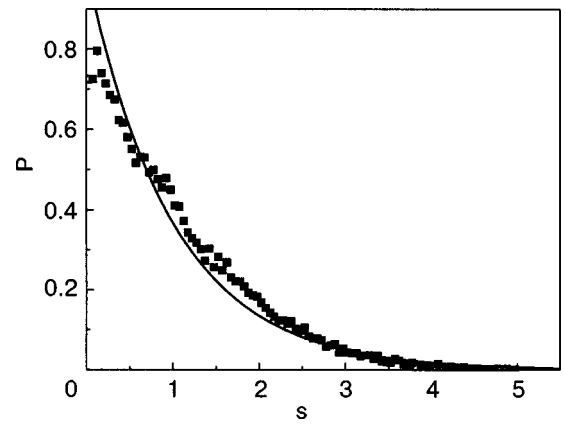

FIG. 4. Nearest-neighbor spacing distribution $P(s)$ for the $U(1)$ model at $\varepsilon=1$ (localized regime). The curve is the Poissonian statistics; data after unfolding (■).

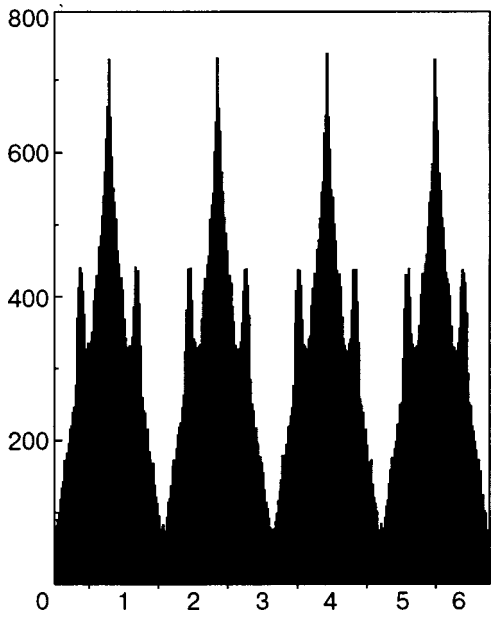

FIG. 5. Histogram for the DOS of 50 samples for the CF model at the critical point $\varepsilon=0$ and $W=0.1$.

same random phase appears on both sides. It is equivalent to attributing random sign to the off-diagonal elements of the transfer matrix. The phase diagram in the (ε, W) plane contains a region of metallic states, and two distinct localized domains, which can be identified as regions with different quantized thermal Hall conductance. There is a critical state at $\varepsilon=0$ for any W. The detailed structure of the phase diagram has been presented elsewhere.[8]

In our numerical simulations we have studied 50 different network systems, of size $(2\times32^2)(2\times32^2)$, on the critical line $\varepsilon=0$ and for disorder strength parameter $W=0.1$. The raw DOS appears to be a periodic function of ω with period $\pi/2$ reflecting the cubic symmetry of the CF model (Fig. 5). The NNSD is presented in Fig. 6 and are compared with the Wigner surmise for GUE. The agreement is rather evident, and it could not be achieved without unfolding. We are thus convinced that the critical form of the NNSD at the critical line of the CF model (in fact of class D in general)

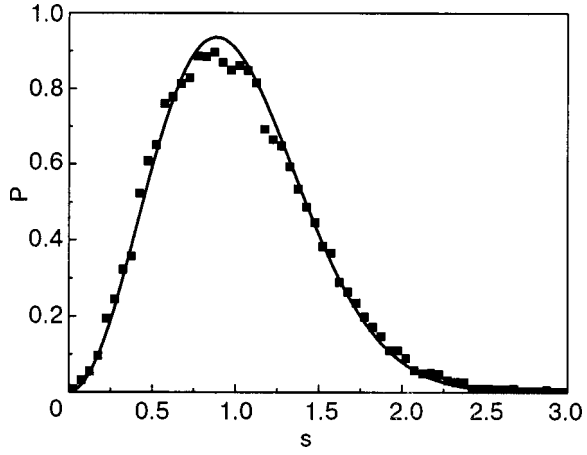

FIG. 6. Nearest-neighbor spacing distribution $P(s)$ for the CF model at $\varepsilon=0$ and $W=0.1$ (metallic regime). The curve is the Wigner surmise for the GUE.

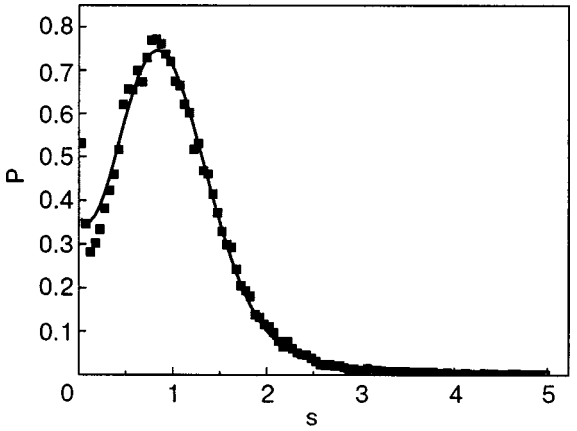

FIG. 7. Nearest-neighbor spacing distribution $P(s)$ for CF model at $\varepsilon=1$ and $W=0.1$ (localized regime). The curve is the Berry-Robnick fit for the transition from GUE to Poissonian statistics.

coincides with the GUE. Next, we move away from the critical line and put $\varepsilon=1$, keeping the same value $W=0.1$, which, according to our phase diagram, is well within a localized domain. The results are shown in Fig. 7. They are fitted by the Berry-Robnick approximation.[11] Usually the large-s behavior is more sensitive to localization than the small-s behavior. In other words, even deep inside the localized regime one still finds level repulsion $p(0)=0$. Remarkably, for the CF model we find $p(0.025)\approx0.53$, which cannot be attributed just to statistical error in view of the fact that we study almost 10^6 energy levels. We have also calculated the compressibility η of the spectrum and have found an extremely small value ≈0.01, which is in agreement with the classical result for the GUE, where $\eta\to0$ for large system sizes.

In conclusion, although mapping of a physical problem on a network model results in correlated and sparse matrices of unitary evolution operators, the results for NNSD seem to agree with the predictions of RMT which assume non-sparse matrices with uncorrelated matrix elements.[9] In the cases studied here this agreement is achieved after a proper local unfolding of the spectra is executed.

The main physical result is the following: Despite the occurrence of ten different random matrix symmetry classes according to time-reversal, spin-rotation, and particle-hole symmetries, with many different physical properties, some basic characteristics remain intact, depending only on time reversibility and spin rotation invariance. There have been numerous attempts to check whether the form of $p(s)$ in QH-like systems deviates from that of GUE.[12] Our results indicate that as far the network model realization is concerned, $p(s)$ is satisfactorily accounted for by the Wigner surmise for the unitary ensemble. The violation of time reversal invariance either by a magnetic field (in QH systems) or spontaneously in unconventional superconductors is the dominant factor, which masks finer details such as quantum criticality.

This study was supported in part (V.K.) by the Sacta-Rashi foundation. V.K. appreciates stimulating discussions with Hans Weidenmüller, Thomas Seligman, Yoram Althassid, Richard Berkovits, and Alexander Mirlin.

*E-mail: victork@nace.ac.il

[1] B. L. Al'tshuler and B. I. Shklovskiĭ, Zh. Éksp. Teor. Fiz. **91**, 220 (1986) [Sov. Phys. JETP **64**, 127 (1986)].
[2] B. I. Shklovskii, B. Shapiro, B. R. Sears, P. Lambrianides, and H. B. Shore, Phys. Rev. B **47**, 11487 (1993).
[3] B. Huckestein, Rev. Mod. Phys. **67**, 357 (1995).
[4] A. Altland and M. R. Zirnbauer, Phys. Rev. B **55**, 1142 (1997); M. R. Zirnbauer, J. Math. Phys. **37**, 4986 (1996).
[5] J. T. Chalker and P. D. Coddington, J. Phys. C **21**, 2665 (1988).
[6] R. Klesse and M. Metzler, Europhys. Lett. **32**, 229 (1995); R. Klesse and M. Metzler, Phys. Rev. Lett. **79**, 721 (1997).
[7] V. Kagalovsky, B. Horovitz, Y. Avishai, and J. T. Chalker, Phys. Rev. Lett. **82**, 3516 (1999).
[8] J. T. Chalker, N. Read, V. Kagalovsky, B. Horovitz, Y. Avishai, and A. W. W. Ludwig, Phys. Rev. B **65**, 012506 (2001).
[9] L. Benet, T. Rupp, and H. A. Weidenmüller, Phys. Rev. Lett. **87**, 010601 (2001); L. Benet, T. Rupp, and H. A. Weidenmüller, Ann. Phys. **292**, 67 (2001).
[10] S. Cho and M. P. A. Fisher, Phys. Rev. B **55**, 1025 (1997).
[11] M. Robnik, J. Phys. A **20**, 495 (1987).
[12] M. Feingold, Y. Avishai, and R. Berkovits, Phys. Rev. B **52**, 8400 (1995); V. E. Kravtsov, I. V. Lerner, B. L. Altshuler, and A. G. Aronov, Phys. Rev. Lett. **72**, 888 (1994).

This article was published in English in the original Russian journal. Reproduced here with stylistic changes by AIP.

Contribution to the theory of galvanomagnetic phenomena in polycrystalline metals

I. M. Kaganova*

L. F. Vereshchagin Institute of High-Pressure Physics, Russian Academy of Sciences, Troitsk, Moscow District 142190, Russia

M. I. Kaganov**

7 Agassiz Ave #1, Belmont, Massachusetts 02478 USA
(Submitted November 8, 2004)
Fiz. Nizk. Temp. **31**, 382–404 (March–April 2005)

An algorithm is constructed for calculating the effective conductivity tensor of polycrystals in a magnetic field from the values of the galvanomagnetic characteristics of crystallites. The algorithm is based on a series expansion in powers of the deviations of the tensors from their average values. The effective conductivity tensor is calculated in two limiting cases: in a weak magnetic field for metals with any electronic energy spectrum and in a strong magnetic field for metals with a closed Fermi surface (in this case the initial equations come from the theory of galvanomagnetic phenomena which employs the solution of the classical Boltzmann equation for the distribution function of electrons with an arbitrary dispersion law). The formulas obtained for polycrystals of cubic metals in a weak magnetic field and metals with closed Fermi surfaces in strong fields have the same accuracy as the initial expressions. © *2005 American Institute of Physics.* [DOI: 10.1063/1.1884433]

1. INTRODUCTION

The theory of galvanomagnetic phenomena (GMP), which I. M. Lifshitz and his students constructed in the 1950s,[1–3] posed the problem of determining the extent to which the electronic energy spectrum of a metal determines the asymptotic behavior of the transverse (relative to the magnetic field) components of the resistance tensor in strong magnetic fields. These works established that the asymptotic behavior of the magnetic field dependence of the resistance is entirely determined by the topology of the Fermi surface (FS) of metals. The work of E. S. Borovik provided, to a large extent, the initial impetus for the construction of a theory of GMP.[4,5] We shall be pleased if the present paper is published in the issue of this journal that is dedicated to the 90th birthday anniversary of Evgeniĭ Stanislavovich.

The most important result of the work performed in the 1950s on the theory of GMP is understanding the role of open FS. This made it possible to determine the contours of the topological structure of the FS of many metals on the basis of measurements of the GMP characteristics. Yu. P. Gaĭdukov's review,[6] in the form of Appendix III in Ref. 7, is the culmination of this approach.

A direction of the electronic theory of metals (not only the theory of GMP) which was termed *fermiology* was formulated in the 1950s and somewhat later. Fermiology is primarily concerned with the *spectroscopic possibilities of various phenomena* in metals. Theoreticians and experimentalists preferred phenomena which make it possible to construct the FS completely or partially and determine the velocity of the Fermi electrons on the basis of the experimentally obtained data.

In this respect the de Haas-van Alphen and Shubnikov-de Haas quantum effects were found to be most fruitful. Details concerning the investigations of oscillation effects and information obtained on the energy spectrum of metals using these effects can be found in D. Shoenberg's monograph.[8]

Fermiology has always given priority to the most perfect single crystals. Defects, including intercrystalline interlayers, were viewed as nuisances. On the other hand an enormous amount of experimental information on GNP had already been accumulated by the 1950s, and most of these results were obtained for polycrystals.

Specifically, the well-known *Kapitza law*—the linear growth of resistivity versus magnetic field in sufficiently strong fields—was discovered by P. L. Kapitza while he was studying the influence of a magnetic field on the resistance of polycrystals.[9] This is why Kapitza did not observe quantum oscillations of the resistance even though he performed measurements on bismuth where Shubnikov and de Haas discovered oscillations.[10]

According to Borovik[5] the linear magnetic field dependence of the resistance of metals is an approximation to a smooth function describing the transitional section between a quadratic dependence in weak fields and either saturation or another quadratic dependence in strong fields. Of course, Borovik's results (specifically, the classification of metals into different groups according to their behavior in strong magnetic fields) did not take account of the fact that metals in different groups could have FS with different topology: at the time nothing was known about the role of the topology of FS in GMP.

Kapitsa's law for polycrystals of metals with open FS (copper and gold-type metals) was explained in the first works on the theory of AMP by I. M. Lifshitz and V. G. Peschanskiĭ.[2] They showed that the linear dependence of the resistance on a strong magnetic field is directly related with the *polycrystallinity* and arises because of averaging of the

resistance tensor, which has a gigantic anisotropy as is characteristic for single crystals of metals with open FS in strong magnetic fields. It should be noted that in Ref. 2 the average resistance was calculated for a thin sample (wire) whose cross section accommodates one crystallite.

In a later work Yu. A. Dreĭzin and A. M. Dykhne calculated the effective resistance of bulk polycrystals of metals with open FS in extremely strong magnetic fields.[11] Using a diffusion analogy they showed that the effective resistance of a polycrystal depends on the type of openness of the FS and on whether or not the metals have an unequal numbers of electrons n_e and holes n_h or are compensated ($n_e = n_h$). Fermi surfaces in the form of a ''spatial network'' and ''fluted cylinder'' were studied. For example, in the case of a FS of the fluted-cylinder type, when the neck of the cylinder is not too small with respect to the size of the reciprocal-lattice cell, the effective transverse resistance $\rho_\perp^{\text{eff}} \propto H^{2/3}$ for $n_e \neq n_h$ and $\rho_\perp^{\text{eff}} \propto H^{4/3}$ for $n_e = n_h$. We recall that in strong magnetic fields the resistance of compensated metals with closed FS is proportional to H^2.

The first works on the theory of GMP and the present status of the theory are reviewed in detail in Ref. 12. The interest in GMP in polycrystals has a long history. There are few special theoretical works which relate the galvanomagnetic characteristics of polycrystals with the characteristics of crystallites. Aside from the works noted above,[2,11] as far as we know there is only our work Ref. 13 where formulas suitable in a strong magnetic fields for polycrystalline metals with closed FS are derived and the case of an uncompensated metal is examined. Formulas for metals with equal numbers of electrons and holes are derived in the present work. We have not encountered in the literature a derivation of formulas for GMP in polycrystals in weak magnetic fields, employing expressions which are valid for single-crystals-crystallites. Section 3 is devoted to this question.

The magnetoresistance and the Hall effect are two of the most important properties of metals. The need for formulas describing GMP in polycrystals is obvious. It seems to us that our work will be helpful in filling the current lacuna in the theory.

Work on the theory of polycrystals is often limited to giving a *description* without providing any details. In such cases a textureless polycrystal is assumed to be an isotropic body. Obviously, such an approach simplifies the *description*: the number of moduli is smaller, rank-2 tensors become scalars, and so on. When the electronic properties of polycrytalline metals are described in this manner the true FS is often replaced by a sphere. As a result, one actually returns to the Drude-Lorenz-Sommerfeld model. Sometimes this is justified, since it is possible to introduce in a reasonable manner the parameters (density n_e, effective mass m_e, and mean-free path length l_e) characterizing conduction electrons and to *describe* with their help the thermal, galvanic, and thermoelectric properties of polycrystalline metals.

Polycrystals can be treated as a widely occurring case of nonuniform disordered solids. The nonuniformity and disorder are due to the random orientation of individual single-crystal grains. In cases where the intercrystallite interlayers play a small role[1)] polycrystals can be regarded as a conglomerate of single-crystal grains whose axes are oriented differently, and the structure of the polycrystal can be interpreted as the character of the orientation of the axes of the crystallites—the statistics of directions, as it is customarily said.

The spatial fluctuations of most characteristics serve as a measure of the disordering of a polycrystal. Not all characteristics of a polycrystal exhibit spatial fluctuations. Of course, the scalar characteristics of a polycrystal are uniform (the heat capacity, as an example). A more interesting example of the absence of spatial fluctuations are metals where the crystallites possess cubic symmetry. The conductivity tensor of each cubic crystallite in the absence of a magnetic field degenerates into a scalar and is independent of the direction of the axes of the crystallites. The electric conductivity of a polycrystal is uniform. This is a scalar, equal to the value of the conductivity of an individual crystallite. Naturally, this last assertion pertains not only to the conductivity but also to any property of a cubic polycrystal which can be described by a symmetric rank-2 tensor. For example, the thermal conductivity, permittivity, and magnetic permeability tensors also degenerate into scalars.

The properties of polycrystals are described by introducing *effective* quantities. The main problem of the theory of polycrystals is to introduce and calculate these quantities. The initial quantities are those that characterize a given property of a crystallite, and it is assumed that for a given metal the characteristics of the crystallites are identical to those of macroscopic single crystals.

The last assumption must be justified in each specific case. Is a direction-averaged characteristic of crystallites an effective characteristic of the polycrystal? In general, the answer is no.

An effective characteristic of a polycrystalline, in contrast to an average characteristic, takes account of stray fields due to nonuniformities. Consequently, the effective characteristics for a medium with spatial fluctuations must be calculated by first averaging the exact equation that contains the fluctuating coefficient and describes the phenomenon being studied. The first works where a method was formulated for calculating the effective characteristics of polycrystals on the basis of the values of local quantities describing crystallites is probably the work of I. M. Lifshitz and his students. It is shown in Ref. 14, which is devoted to the theory of the static elastic properties of polycrystals, that the averaged elastic moduli of crystallites in general are only the zeroth approximation in the anisotropy to the effective moduli.

This method was subsequently extended to the dynamic theory of elasticity[15] and the dielectric properties of crystallites.[16] In Refs. 15 and 16 the characteristics of acoustic and electromagnetic waves propagating in polycrystals were calculated.

In all above-cited works on the theory of polycrystals specific results were obtained for unbounded samples in the first nonvanishing approximation of the perturbation theory by averaging the static and dynamic equations of the theory of elasticity[14,15] and Maxwell's equations in a dielectric.[16]

The application of the first approximation of perturbation theory means that the average values of the squared spatial fluctuations are taken into account. The anisotropy of the tensor properties serves as a measure of fluctuations: in a

fixed laboratory coordinate system tied to the sample the coefficients of the averaged equation are functions of the coordinates, fluctuating from one crystallite to another.

Starting in 1992 the properties of polycrystals have been investigated in detail in Refs. 17–19. In these works the theory was extended to the case of a half-space. The propagation of a Rayleigh wave in a polycrystal was studied,[17] the problem of the normal and anomalous skin effects was solved,[18] and the dispersion law for surface polaritons was calculated.[19] The authors of these works assumed the anisotropy to be small and calculated the first nonvanishing correction in the anisotropy to the quantity studied.

A. M. Dykhne and I. M. Kaganova showed that it is possible to go beyond the theory where the anisotropy is assumed to be small.[21] They derived a formula for the effective impedance of a polycrystal, which, when Leontovich's local boundary conditions are applicable,[21] is identical to the formula derived for the impedance of a single crystal. This formula, which was somewhat conditionally obtained, was said to be *exact*, and we shall adhere to this term. An *exact* formula was obtained in Ref. 20 for the effective impedance of a polycrystal under the conditions of the normal skin effect and in Ref. 22 for the anomalous skin effect. In both cases the anisotropy of the impedance[27] from one crystallite to another can be arbitrary: the accuracy of the result is not associated with the magnitude of the anisotropy. The accuracy is determined by something else—by the fact that for the entire surface (for each crystallite on the surface) the Leontovich local boundary conditions are assumed to hold and by the fact that for good metals the components of the impedance tensor are much less than one. As a result, the correlation terms are much smaller than the main terms and can be dropped, and the structure of the *exact* formula for the impedance is simple: the effective impedance of a polycrystal is simply the average value of the impedance of the crystallites.

The impedance is small because the ratio δ/λ, where δ is the depth of the skin layer and λ is the wavelength in vacuum, is small. It is precisely the smallness of the surface impedance that makes it possible in most problems to use the so-called impedance boundary conditions (see, for example, Ref. 23). In order for the impedance boundary conditions to be local (the Leontovich local boundary conditions hold) one other inequality must be satisfied: the size of a surface nonuniformity must be much greater than δ. For a polycrystal with a flat surface this means that the following condition must be satisfied: the average size a of the crystallites is much greater than the depth δ of the skin layer. The two- and multiple-point correlation functions of the fluctuation terms which are neglected when calculating the effective impedance are small because the ratios δ/λ and δ/a are small.

Small parameters are also present in the theory of GMP for weak or extremely strong magnetic fields. When constructing a theory of GMP for polycrystals it is often possible to use these small parameters to obtain *exact* solutions, i.e. solutions which are identical to the expansions of the corresponding characteristics in small parameters.

2. FORMULATION OF THE PROBLEM

For calculating the effective characteristics of the GMP of polycrystals we shall remain within the basic assumptions of the so-called *classical* theory of GMP, and we shall neglect *quantum oscillations*, remaining strictly within the framework of the theory of GMP.[1–3]

The Drude-Lorenz-Sommerfeld model is unsuitable for describing GMP in polycrystals. If the FS is assumed to be spherical, then it is impossible to describe the main features of GMP—the magnetic field dependence of the resistance and the difference of the Hall ''constants'' in weak and strong magnetic fields (for some metals the sign of the Hall ''constant'' changes). True, if a more complicated model is used, making the assumption that not only electrons but also holes with a set of parameters n_h, m_h, l_h, and charge $-e$ are present, then such an approach for metals with closed FS could be successful: good agreement between theory and the experimental data can be achieved.

The deficiency of such a theory is obvious: the parameters introduced must be related to the characteristics of the conduction electrons of the crystallites. The characteristics of a metal in a magnetic field are sensitive to the structure of the electronic spectrum. It is well known that the FS of virtually all metals, except for certain group-I metals, are very different from a sphere.

In order to neglect crystallite sizes when calculating the effective characteristics of GMP and assume the crystallites to be infinite single crystals the inequality $l \ll a$ must be satisfied. Then $l \ll r_H$ in weak fields and $r_H \ll l$ in strong fields (l is the average mean-free path length of a conduction electron and r_H is the radius of an electron orbit in a magnetic field).

The theory of GMP of polycrystals proposes to calculate the following effective tensors: the conductivity tensor σ_{ik}^{eff} (ECT) and the resistance tensor ρ_{ik}^{eff} (ERT). Both tensors are functions of the magnetic field $\mathbf{H}$ and are reciprocals of one another, i.e., $\sigma_{ik}^{\text{eff}}=\sigma_{ik}^{\text{eff}}(\mathbf{H})$, $\rho_{ik}^{\text{eff}}=\rho_{ik}^{\text{eff}}(\mathbf{H})$, and $\sigma_{ik}^{\text{eff}}\rho_{ik}^{\text{eff}}=\delta_{ik}$, where δ_{ik} is the Kronecker symbol.

The tensor σ_{ik}^{eff}, by definition, relates quantities which are uniform over the entire polycrystal—the current density $\langle \mathbf{j} \rangle$ and the electric field strength $\langle \mathbf{E} \rangle$:

$$\langle j_i \rangle = \sigma_{ik}^{\text{eff}}(\mathbf{H}) \langle E_k \rangle. \tag{1}$$

The components of the effective tensor $\sigma_{ik}^{\text{eff}}(\mathbf{H})$ must be expressed in terms of the components of the local conductivity tensor (LCT) $\sigma_{ik}(\mathbf{r},\mathbf{H})$ of the crystallites in a constant and uniform magnetic field $\mathbf{H}$. The components of the LCT depend on the radius vector $\mathbf{r}$ because $\sigma_{ik}(\mathbf{r},\mathbf{H})$ changes from one crystallite to another, in the first place, because the axes of the tensor rotate relative to the laboratory coordinate system and, in the second place, because the orientation of the magnetic field $\mathbf{H}$ with respect to the axes of a specific crystallite is different. Ordinarily, the laboratory coordinate system is chosen so that one of its axes (as a rule, the z axis) is oriented in the same direction as the magnetic field.

If the values of the components $\sigma_{ik}(\mathbf{r},\mathbf{H})$ are assumed to be known, then the difference in calculating σ_{ik}^{eff} for $H \neq 0$ and $H=0$ is due to two factors: 1) the tensor characteristics obtained by averaging are anisotropic, they are expressed not only in terms of the tensor δ_{ik} and the unit antisymmetric rank-3 tensor e_{ikl} but also in terms of the components of the vector $\mathbf{H}$; 2) for $H=0$ the conductivity σ is a symmetric rank-2 tensor and in a magnetic field the symmetry principle

for the kinetic coefficients[24] requires a much more complicated symmetry:

$$\sigma_{ik}(\mathbf{H}) = \sigma_{ki}(-\mathbf{H}). \quad (2)$$

It is well known that the antisymmetric part of the conductivity tensor describes the Hall effect.

Neither circumstance prevents separating the average value from the tensor $\sigma_{ik}(\mathbf{r},\mathbf{H})$:

$$\sigma_{ik}(\mathbf{r},\mathbf{H}) = \langle \sigma_{ik}(\mathbf{H}) \rangle + \Delta_{ik}(\mathbf{r},\mathbf{H}), \quad \langle \Delta_{ik}(\mathbf{r},\mathbf{H}) \rangle = 0. \quad (3)$$

The tensor $\Delta_{ik}(\mathbf{r},\mathbf{H})$ describes the part of the LCT which varies as $\mathbf{r}$ passes from one crystallite to another. The brackets denote averaging over an ensemble of all possible realizations of the nonuniform medium (polycrystal). The calculation of $\sigma_{ik}^{\text{eff}}(\mathbf{H})$ essentially reduces to taking account of the contribution of multiple-point correlation functions of the type $\langle \Delta_{ik}(\mathbf{r},\mathbf{H}) \Delta_{lm}(\mathbf{r}_1,\mathbf{H}) \ldots \rangle$, arising when averaging the equations

$$\frac{\partial \sigma_{ik}(\mathbf{r},\mathbf{H}) E_k}{\partial x_i} = 0, \quad \mathbf{E} = 0, \quad (4)$$

to the ECT.

When solving electrostatic equations one often switches from the electric field to the potential φ: $E_i(\mathbf{r}) = -\partial \varphi(\mathbf{r})/\partial x_i$, combining the equations in Eq. (4). In contrast to the average potential, the average field $\langle \mathbf{E} \rangle$ is independent of the coordinates by definition. If the average value, determining $\langle \mathbf{E} \rangle$, and a random correction which vanishes on averaging, is separated from the potential, then care must be taken to see whether or not the random field $\mathbf{E} - \langle \mathbf{E} \rangle$ also vanishes on averaging. In this connection it will be more convenient for us to use the equations for the electric field directly.

The result of a perturbation-theory calculation of the ECT performed in Ref. 13 is presented in Appendix I. The expansion is made in powers of the deviations $\Delta_{ik}(\mathbf{r},\mathbf{H})$. The calculation employs the Fourier method (the functions $\Delta_{ik}(\mathbf{H})$ are expanded in plane waves). The equation (I.1) is a solution if the series appearing in it converge. Then the value of $\sigma_{ik}^{\text{eff}}(\mathbf{H})$ can be obtained in the form of an expansion in powers of the correlation functions of the tensors $\Delta_{ik}(\mathbf{r},\mathbf{H})$ to any degree of accuracy. Checking the convergence of the series is a separate problem (see, for example, Ref. 25, where this question is discussed for the case $\mathbf{H} = 0$).

The calculation of multiple-point correlation functions for polycrystals is described in Appendix II. As already mentioned above, the initial assumptions are that the crystallographic axes of individual crystallites are oriented randomly (there is no texture) and the directions of the axes of the crystallites are statistically independent of one another. The components of the tensors describing the properties of the crystallites, if they are given in the same laboratory coordinate system, are random functions of the coordinates. The scalar characteristics, which do not depend on the magnetic field orientation, are the same in all crystallites.

The expressions written out in Appendix I and formally solving the above-posed problem of calculating $\sigma_{ik}^{\text{eff}}(\mathbf{H})$ need to be concretized.

The theory of GMP on which we are relying has certain characteristic features which need to be indicated.

The application of the classical Boltzmann equation, including the Lorentz force, only in principle makes it possible to indicate an algorithm for calculating the conductivity tensor of a single-crystal of a metal to an arbitrary degree of accuracy. The actual exact calculation is very difficult and requires solving integral equations of a nonstandard type. As far as we know this problem has never been solved for metals with Fermi surfaces with a complicated shape in a magnetic field of arbitrary magnitude.

The theory of GMP geared toward determining the role of the *topology* of the Fermi surface of a metal considers only strong magnetic fields ($r_H \ll l$) where the role of the topology is determining. In application to our problem the result of this theory is the determination of the dependence of the components $\sigma_{ik}(\mathbf{H})$ on $\mathbf{H}$. The coefficients of the powers of the magnetic field in the expressions obtained are tensors whose structure is known but the values of the components are known, strictly speaking, only in order of magnitude. It is these *tensor coefficients* that serve as the random functions which must be averaged over the directions of the crystallites when calculating the ECT.

The magnetic field dependence of the LCT in weak magnetic fields ($l \ll r_H$) can be established by expanding in powers of the components of the vector $\mathbf{H}$. The expansion takes account of the symmetry of the conductivity tensor (2) and the crystal lattice (the symmetry class to which it belongs).

Limiting cases make it possible to separate the magnetic field dependence of the expressions for the components of the tensor $\Delta_{ik}(\mathbf{r},\mathbf{H})$. It is important that here there arises a criterion for estimating the terms in these expressions, containing H raised to different powers. The criterion is valid irrespective of the magnitude of the anisotropy. The fact that the accuracy of the effective expressions for polycrystals must match the accuracy of the initial formulas of the theory of GMP for single crystals is the basis for the substantial simplifications made in many cases.

The results obtained are discussed on the basis of formulas which are valid in the limiting cases of weak and strong magnetic fields.

3. EFFECTIVE CONDUCTIVITY TENSOR IN A WEAK MAGNETIC FIELD

For weak fields we shall use an expansion of the LCT in powers of the components of the magnetic field, retaining the linear and quadratic terms. Of course, this acutally means an expansion in the dimensionless small parameter l/r_H. In agreement with the symmetry principle for the kinetic coefficients, the expansion has the form

$$\sigma_{ik}(\mathbf{H},\mathbf{r}) = \sigma_{ik}^{(0)}(\mathbf{r}) + H e_{ikl} a_{lm}(\mathbf{r}) \kappa_m + H^2 S_{ik,lm}(\mathbf{r}) \kappa_l \kappa_m, \quad (5)$$

where $\kappa_i = H_i/H$ is a unit vector in the direction of the magnetic field $\mathbf{H}$ and the tensors a_{ik} and $S_{ik;lm}$ are independent of the magnetic field.

The expression (5) is written in an invariant form. All indices refer to the common laboratory coordinate system. We recall that it is precisely because of the random orientation of the grains that in Eq. (5) the components of the tensors are random functions of the coordinates. In the crystal-

lographic system of axes the number of independent components of these tensors is determined by the symmetry class to which a given metal belongs.

The electric conductivity tensor $\sigma_{ik}^{(0)}$ for $H=0$ is symmetric. The symmetry principle for the kinetic coefficients does not impose any restrictions on the tensor a_{ik} appearing in the Hall term. However, in most cases the symmetry of a nonmagnetic metal is such that a rank-2 tensor which is independent of the magnetic field cannot have an antisymmetric part. Metals with virtual axial symmetry (for example, β plutonium possesses this property[26]) are an exception. For simplicity, we shall assume that $a_{ik}=a_{ki}$.

The symmetry principle for the kinetic coefficients requires that $S_{ik;lm}=S_{ki;lm}$. Since the tensor $S_{ik;lm}$ appears in the expression (5) in the form of a contraction with the symmetric tensor $\kappa_l\kappa_m$, it can be symmetrized with respect to the indices l and m. Then $S_{ik;lm}=S_{ik;ml}$. However, $S_{ik;lm}\neq S_{lm;ik}$.[3)]

Naturally, the formula for the ECT should have a structure that is characteristic for an isotropic body in weak magnetic fields:

$$\sigma_{ik}^{\rm eff}(\mathbf{H})=\sigma^{\rm eff}(0)\,\delta_{ik}+A_H e_{ikl}\kappa_l H + [\alpha_\parallel\kappa_i\kappa_k+\alpha_\perp(\delta_{ik}-\kappa_i\kappa_k)]H^2, \tag{6}$$

where $\sigma^{\rm eff}(0)$ is the effective conductivity of a polycrystal for $\mathbf{H}=0$, the coefficient A_H describes the Hall effect, $\alpha_\parallel$ takes account of the dependence of the longitudinal (relative to the field) conductivity on the magnetic field, and $\alpha_\perp$ is the transverse conductivity. Our problem is to calculate these quantities.

In accordance with the general formula (I.1) the calculation of $\sigma_{ik}^{\rm eff}(\mathbf{H})$ starts with the decomposition of the LCT into average and fluctuating parts. Averaging the expression (5) gives

$$\langle\sigma_{ik}(\mathbf{H})\rangle=\sigma_0\delta_{ik}+Hae_{ikl}\kappa_l+H^2(S_1\delta_{ik}+2S_2\kappa_i\kappa_k). \tag{7a}$$

Here $\sigma_0=\sigma_H^{(0)}/3$ and $a=a_H/3$ are obtained by averaging the tensors $\sigma_{ik}^{(0)}$ and a_{ik}, respectively, and the invariants S_1 and S_2 determine the average value of the tensor $S_{ik;lm}$:

$$\langle S_{ik,lm}\rangle=S_1\delta_{ik}\delta_{lm}+S_2(\delta_{im}\delta_{kl}+\delta_{il}\delta_{km}), \tag{7b}$$

$$S_1=\frac{1}{15}(2S_{pp;qq}-S_{pq,pq});\quad S_2=\frac{1}{30}(3S_{pq,pq}-S_{pq;qq}). \tag{7c}$$

The random part of the LCT is $\Delta_{ik}(\mathbf{H},\mathbf{r})=\sigma_{ik}(\mathbf{H},\mathbf{r})-\langle\sigma_{ik}(\mathbf{H})\rangle$:

$$\Delta_{ik}(\mathbf{H},\mathbf{r})=\Delta_{ik}^{(0)}(\mathbf{r})+He_{ikl}\delta a_{lm}(\mathbf{r})\kappa_m + H^2\delta S_{ik;lm}(\mathbf{r})\kappa_l\kappa_m, \tag{8}$$

where

$$\Delta_{ik}^{(0)}(\mathbf{r})=\sigma_{ik}^{(0)}(\mathbf{r})-\sigma_0\delta_{ik};\quad \delta a_{ik}(\mathbf{r})=a_{ik}(\mathbf{r})-a\,\delta_{ik};$$

$$\delta S_{ik;lm}(\mathbf{r})=S_{ik;lm}(\mathbf{r})-\langle S_{ik;lm}\rangle.$$

Evidently, $\langle\Delta_{ik}^{(0)}\rangle=\langle\delta a_{lm}\rangle=\langle\delta S_{ik;lm}\rangle=0$ and therefore $\langle\Delta_{ik}(\mathbf{H},\mathbf{r})\rangle=0$. Having determined $\langle\sigma_{ik}(\mathbf{H},\mathbf{r})\rangle$ and $\Delta_{ik}(\mathbf{H},\mathbf{r})$ an expression can be obtained for the ECT to arbitrary accuracy in the anisotropy. In accordance with Eq. (I.1), the fluctuation corrections to $\langle\sigma_{ik}(\mathbf{H},\mathbf{r})\rangle$ in the ECT are determined by series which contain the correlation functions of the tensors $\Delta_{ik}(\mathbf{H},\mathbf{r})$.

In the expression (5) we limited the expansion of the components of the LCT to terms which are quadratic in the field. Therefore the terms containing higher powers of the magnetic field must be dropped in the calculations. Retaining such terms exceeds the accuracy of the approximation used.

To calculate the fluctuation correction of nth order in the anisotropy to the ECT the tensor $w_{ik}^{(n)}(\mathbf{H},\mathbf{r})$ (see Eq. (I.3)) must be calculated up to terms $O(H^2)$. To the accuracy indicated the components of this tensor are determined by the average integrals

$$\left\langle\Delta_{il_1}(\mathbf{r})\Delta_{j_1l_2}(\mathbf{r}_1)\ldots\Delta_{j_{n-1}k}(\mathbf{r}_{n-1})\prod_{s=1}^{n-1}q_{l_sj_s}^{(s)}\right\rangle = \langle T_{ik}^{(0,n)}\rangle+H\langle T_{ik,p}^{(1,n)}\rangle\kappa_p+H^2\langle T_{ik,pq}^{(2,n)}\rangle\kappa_p\kappa_q, \tag{9}$$

where to the same degree of accuracy the tensor $q_{ik}^{(s)}$ (see Eq. (I.4)) is

$$q_{ik}^{(s)}=\frac{n_i^{(s)}n_k^{(s)}}{\sigma_0}\left(1-H^2\frac{S_1+2S_2}{\sigma_0}(\kappa\mathbf{n}^{(s)})^2\right).$$

We recall that aside from the coordinate dependence each of the tensors $\Delta_{j_sl_s+1}$ in Eq. (9) also depends on the constant vector $\mathbf{H}$.

Let $Q_{ik}^{(0,n)}$, $Q_{ik,p}^{(1,n)}$, and $Q_{ik;pq}^{(2,n)}$ be the contributions of each of the tensors $w_{ik}^{(n)}(\mathbf{H})$, respectively, to $\langle T_{ik}^{(0,n)}\rangle$, $\langle T_{ik,p}^{(1,n)}\rangle$, and $\langle T_{ik;pq}^{(2,n)}\rangle$. Since these are isotropic tensors with known symmetry properties under a transposition of indices, their structure is also known:

$$Q_{ik}^{(0,n)}=Q^{(0,n)}\delta_{ik},\quad Q^{(0,n)}=\frac{1}{3}\langle Q_{kk}^{(0,n)}\rangle;$$

$$Q_{ik,p}^{(1,n)}=Q^{(1n)}e_{ikp},\quad Q^{(1,n)}=\frac{1}{6}Q_{ik,p}^{(1,n)}e_{ikp};$$

$$Q_{ik,pq}^{(2,n)}=Q_1^{(2,n)}\delta_{ik}\delta_{pq}+Q_2^{(2,n)}(\delta_{ip}\delta_{kq}+\delta_{iq}\delta_{kp}); \tag{10}$$

$$Q_1^{(2,n)}=\frac{1}{15}(2Q_{kk,qq}^{(2,n)}-Q_{kq,kq}^{(2,n)}),$$

$$Q_2^{(2,n)}=\frac{1}{30}(3Q_{kq,kq}^{(2,n)}-Q_{kk,qq}^{(2,n)}).$$

The calculation of the contractions appearing in Eqs. (10) is much simpler than the calculation of the tensors $\hat{Q}^{(r,n)}$ $(r=0,1,2)$ themselves. However, even after these simplifications are made very cumbersome expressions are obtained for arbitrary value of n, so that we shall not present them. In the formula for the ECT we shall retain terms which are quadratic and cubic in the correlation functions of the tensors $\Delta(\mathbf{H},\mathbf{r})$ $(n=2,3)$.

Another reason why we confine ourselves to terms $O(\Delta^3)$ in calculating the ECT in weak fields is that, just as in the case $H=0$ (see, for example, Ref. 25), for $n\geqslant 3$ the fluctuation corrections depend on the form of the multiple-point correlation functions describing the statistics of the orientations of the crystallographic axes of individual grains.

This means that for $n \geqslant 3$ we cannot perform the calculation without using model assumptions about the form of these correlation functions.

We shall present only the expressions for $Q^{(0,2)}$ and $Q^{(0,3)}$, to demonstrate the dependence of the fluctuation corrections to the ECT for $n>2$ on the form of the correlation functions, and the coefficients entering in the expression for $\sigma_{ik}^{\text{eff}}(\mathbf{H})$ (see Eq. (6)) up to terms which are cubic in the anisotropy. The derivation of the expressions obtained is presented in the Appendix III.

For $n=2$ it follows from Eqs. (III.1) and (I.3) that

$$Q^{(0,2)}=\frac{1}{3(2\pi)^3\sigma_0}\int d^3k_1 n_{j_1}^{(1)} n_{l_1}^{(1)} \times \int d^3r_1 \exp[-i\mathbf{k}_1(\mathbf{r}_1-\mathbf{r})]\langle \Delta_{kl_1}^{(0)}(\mathbf{r})\Delta_{j_1k}^{(0)}(\mathbf{r}_1)\rangle. \tag{11a}$$

In accordance with Eq. (II.4) the average $\langle \Delta_{kl_1}^{(0)}(\mathbf{r})\Delta_{j_1k}^{(0)}(\mathbf{r}_1)\rangle = D_2\delta_{j_1l_1}W_2(|\mathbf{r}_1-\mathbf{r}|)/3$, where the invariant $D_2=\Delta_{kl}^{(0)}\Delta_{lk}^{(0)}$. Hence

$$Q^{(0,2)}=\frac{D_2}{9\sigma_0}\int d^3k_1 W_2(k_1)=\frac{D_2}{9\sigma_0}. \tag{11b}$$

The integral appearing in Eq. (11b) equals the value of the correlation function $W_2(|\mathbf{r}|)$ at $\mathbf{r}=0$. Therefore it is equal to 1.

We shall use Eqs. (II.5)–(II.7) to calculate $Q^{(0,3)}$. Then

$$Q^{(0,3)}=-\frac{1}{3(2\pi)^6\sigma_0^2}\int d^3k_1\int d^3k_2 n_{j_1}^{(1)}n_{l_1}^{(1)}n_{j_2}^{(2)}n_{l_2}^{(2)} \times \int d^3r_1\int d^3r_2 \exp[-i\mathbf{k}_1(\mathbf{r}_1-\mathbf{r})] \times \exp[-i\mathbf{k}_2(\mathbf{r}_2-\mathbf{r}_1)] \times \langle \Delta_{kl_1}^{(0)}\Delta_{j_1l_2}^{(0)}\Delta_{j_2k}^{(0)}\rangle W_3([\mathbf{r},\mathbf{r}_1,\mathbf{r}_2]), \tag{12}$$

where $W_3([\mathbf{r},\mathbf{r}_1,\mathbf{r}_2])$ is the probability that the vectors $\mathbf{r}$, $\mathbf{r}_1$, and $\mathbf{r}_2$ lie in the same crystallite; the average

$$\langle \Delta_{kl_1}^{(0)}\Delta_{j_1l_2}^{(0)}\Delta_{j_2k}^{(0)}\rangle = \frac{D_3}{30\sigma_0^2}[-2\delta_{j_1l_2}\delta_{j_2l_1} + 3(\delta_{j_1j_2}\delta_{l_1l_2}+\delta_{j_1l_1}\delta_{j_2l_2})];$$

and, $D_3=\Delta_{pq}^{(0)}\Delta_{qr}^{(0)}\Delta_{rp}^{(0)}$ is an invariant. Therefore

$$Q^{(0,3)}=-\frac{D_3}{30\sigma_0^2}(1+F_3^{(\text{st})}),$$

and $F_3^{(\text{st})}$ depends on the form of the correlation function

$$F_3^{(\text{st})}=\frac{1}{9}(7-6J_3^{(\text{st})}), \tag{13}$$

where

$$J_3^{(\text{st})}=1-\frac{1}{2}\int\int dk_1^3 dk_2^3 (\mathbf{n}_1\mathbf{n}_2)^2 W_2(|\mathbf{k}_1-\mathbf{k}_2|)(W_2(k_1)+W_2(k_2)).$$

In Ref. 25 the value of $J_3^{(\text{st})}$ is calculated for different model assumptions about the form of the two-point correlation function $W_2(r)$:

$J_3^{(\text{st})}=0.028$, when $W_2=\exp(-r^2/a^2)$;

$J_3^{(\text{st})}=0.136$, when $W_2=\exp(-r/a)$;

$J_3^{(\text{st})}=0.052$, when $W_2=1/(1+r^2/a^2)$.

The value of $J_3^{(\text{st})}$ is very small in all cases examined. It is evident from the expressions and Eqs. (III.21) and (III.22) presented below that the function $F_3^{(\text{st})}$ appears in the expression for third-order fluctuation corrections for all coefficients in the expression (6) for the ECT. Therefore although in third-order perturbation theory the statistical properties of polycrystals influence the magnitude of the components of the ECT, this influence is very weak. The dependence of the fluctuation corrections in the statistics was not investigated for $n>3$.

Taking account of terms of order $O(\Delta^3)$ we obtain the coefficients appearing in the expression (6) for σ_{ik}^{eff} in the form

$$\sigma^{\text{eff}}(0)=\sigma_0-\frac{1}{9\sigma_0}\left\{D_2-\frac{3D_3}{5\sigma_0}(1+F_3^{(\text{st})})\right\},$$
$$A_H=a+\frac{1}{9\sigma_0}\left\{A_2+\frac{A_3}{5\sigma_0}(1-3F_3^{(\text{st})})\right\}. \tag{14}$$

Here $A_2=\Delta_{lk}^{(0)}\delta a_{ik}$ and $A_3=\Delta_{kl}^{(0)}\Delta_{lm}^{(0)}\delta a_{mk}$ are second- and third-order invariants, respectively. Finally,

$$\alpha_{\parallel}=S_1+\beta_{\parallel}^{(1)}+\beta_{\parallel}^{(2)}F_3^{(\text{st})},$$
$$\alpha_{\perp}=(2S_2+S_1)+\beta_{\perp}^{(1)}+\beta_{\perp}^{(2)}F_3^{(\text{st})}. \tag{15}$$

The values of $\beta_{\parallel}^{(1)}$, $\beta_{\parallel}^{(2)}$, $\beta_{\perp}^{(1)}$, and $\beta_{\perp}^{(2)}$ are expressed in terms of all possible second- and third-order invariants that can be constructed from the tensors $\Delta_{ik}^{(0)}$, δa_{ik}, and $\delta S_{ik;lm}$. Explicit expressions for these quantities are presented in the Appendix III.

A. Polycrystals of metals with cubic symmetry

Very many metals possess cubic symmetry (according to Ref. 27 there are more than 30). The formulas derived above simplify substantially for crystallites with cubic symmetry: rank-2 tensors degenerate into scalars. Thus in Eq. (5) for the LCT of polycrystals of cubic metals

$$\sigma_{ik}^{(0)}=\sigma_0\delta_{ik}, \quad a_{lm}=a\,\delta_{ik}, \tag{16}$$

and therefore

$$\Delta_{ik}^{(0)}(\mathbf{r})=\delta a_{ik}(\mathbf{r})=0.$$

A consequence of Eqs. (16) is that although in the formula (5) the rank-4 tensor $S_{ik;lm}(\mathbf{r})$ can possess arbitrary anisotropy (its components change from one crystallite to another), in weak magnetic fields the correlation part of $\sigma_{ik}^{\text{eff}}(\mathbf{H})$ for polycrystals of cubic metals vanishes to all orders in the anisotropy parameter. Thus the expression for the effective conductivity becomes (see Eq. (7a))

$$\sigma_{ik}^{\text{eff}}(\mathbf{H})=\langle\sigma_{ik}(\mathbf{H})\rangle = \sigma_0\delta_{ik}+Hae_{ikl}\kappa_l+H^2(S_1\delta_{ik}+2S_2\kappa_i\kappa_k), \tag{17}$$

where the coefficients S_1 and S_2 are given by Eqs. (7c). We underscore that Eq. (17) is just as accurate as Eq. (5): its accuracy is due not to the smallness of the anisotropy but rather the weakness of the magnetic field, i.e. the inequality $l/r_H \ll 1$. The equation (17) is *exact* in the same sense as the equation obtained for the surface impedance in Ref. 20 for a polycrystal is said to be *exact*. In Sec. 5 we shall present explicit expressions for the tensors describing the GMP properties of single crystals in weak fields and, with their help, the effective characteristics of polycrystals of cubic metals. The expressions employ an approximate solution of the classical Boltzmann equation containing the Lorentz force.[28] The accuracies of the dispersion law for conduction electrons and of the collision integral are not improved.

4. EFFECTIVE CONDUCTIVITY TENSOR IN A STRONG MAGNETIC FIELD (CLOSED FS)

For strong magnetic fields the theory of GMP[1–3] is limited to calculating the leading terms in the expansion in powers of the reciprocal of the magnetic field or, more accurately, powers of the dimensionless parameter $r_H/l \ll 1$. For a metal with a closed FS the conductivity tensor has the form

$$\sigma_{ik}(\mathbf{H})|_{r_H \ll l} = S(\kappa)\kappa_i\kappa_k + \frac{1}{H} e_{ikl} a_{lm}^{(1)}(\kappa)\kappa_m + \frac{1}{H^2} s_{ik}(\kappa). \tag{18}$$

Once again $\kappa_i = H_i/H$. In the laboratory coordinate system $\boldsymbol{\kappa} = (0,0,1)$. The tensors s_{ik} and $a_{ik}^{(1)}$ are symmetric. The first tensor is symmetric in agreement with the symmetry principle for Onsager's kinetic coefficients, and the second tensor is symmetric because we have limited our analysis to the most common crystals (see preceding section).

The scalar $S(\boldsymbol{\kappa})$ in the expression for $\sigma_{ik}(\mathbf{H})|_{r_h \ll l}$ is equal to the main term in the longitudinal conductivity and is independent of the magnitude of the magnetic field. The Hall conductivity, determined by the tensor $a_{ik}^{(1)}$, is proportional to $1/H$. The tensor s_{ik} gives the main contribution of order $1/H^2$ to the transverse conductivity.

The purpose of our calculation is to determine the main terms in the components of the ECT: the effective longitudinal conductivity is calculated up to terms which are independent of H, the effective Hall conductivity with accuracy $O(1/H)$, and the effective transverse conductivity with accuracy $O(1/H^2)$.

The equation (18) gives the components of the LCT for polycrystals. The tensors appearing in Eq. (18) and the scalar $S(\kappa)$ are random functions which vary from one crystallite to another: $S(\kappa)$ because κ depends on the direction of the magnetic field with respect to the crystallographic axes and the components of the tensors because of the dependence on κ and because in each crystallite the orientation of the crystallographic axes with respect to the laboratory coordinate system is random (the argument $\mathbf{r}$ is dropped to simplify the expressions).

Ordinarily, the term *gigantic anisotropy* is used when describing GMP in metals with open FS, having in mind the difference of the asymptotic behavior with respect to the magnetic field of the two transverse components of the conductivity (resistance) tensor in cases where the open trajectories do or do not contribute to the conductivity. According to Eq. (18) different components of the tensor $\sigma_{ik}(\mathbf{H})|_{r_H \ll l}$ exhibit substantially different asymptotic behavior. This is also definite evidence of the gigantic anisotropy of the conductivity tensor for metals with closed FS.

The values of the GNP characteristics in strong magnetic fields ($r_H/l \ll 1$) depend not only on the topology of the FS. If the FS are closed, it is important whether the metal is compensated ($n_e = n_h$) or uncompensated ($n_e \neq n_h$). In the first case the transverse *resistance* increases quadratically with the magnetic field, and in the second case it saturates. In addition for a metal with an unequal number of electrons and holes the Hall constant R becomes a true constant:

$$R_\infty = \frac{1}{ec(n_e - n_h)}. \tag{19}$$

The index ∞ shows that R_∞ is the asymptotic value of the Hall constant.

In terms of the conductivity tensor the difference between compensated and uncompensated metals does not appear to be so dramatic. If $n_e \neq n_h$, then in the laboratory coordinate system the Hall conductivity $\sigma_{12}^{(H)} = 1/HR_\infty$ is the same for all directions of the crystallographic axes relative to the magnetic field. In accordance with Eq. (18) it follows from this that the contraction

$$a_{ik}^{(1)}\kappa_i\kappa_k = \frac{1}{R_\infty} \tag{20}$$

is the same for all crystallites. However, if $n_e = n_h$, then $a_{lm}^{(1)}\kappa_l\kappa_m = 0$. This means that in the laboratory coordinate system a term of order $1/H$ of the components of the Hall conductivity $\sigma_{xy}(\mathbf{H}) = \sigma_{yx}(\mathbf{H}) = 0$.

We shall consider polycrystals of uncompensated metals first. It is shown in Ref. 13 that the specific form (18) of the LCT of polycrystals of metals with closed FS makes it possible, in the leading approximation in $r_H/l \ll 1$, to calculate *exactly* the components of the ECT by perturbation theory methods (see Appendix I). In this case it is possible not only to calculate for arbitrary n the leading order terms of the components of the tensors $w_{ik}^{(n)}(\mathbf{H})$ (see Eq. (I.3)) but also to sum the series (I.2) for the components of the tensor W_{ik}.

We shall write the tensor for the average conductivity using Eq. (18). We shall use Eq. (II.8) to average the tensors $a_{ik}^{(1)}(\mathbf{r},\kappa)$ and $s_{ik}(\mathbf{r},\kappa)$.

Since the average value of the tensor $a_{lm}^{(1)}$ can be written in the form $\langle a_{lm}^{(1)}\rangle = A_1\delta_{lm} + A_2\kappa_l\kappa_m$, from Eq. (20) we have the contraction $\langle a_{lm}^{(1)}\rangle\kappa_m = (A_1 + A_2)\kappa_l = \kappa_l/R_\infty$. Then

$$\langle \sigma_{ik}(\mathbf{H})\rangle|_{r_H \ll l} = \langle S(\mathbf{r},\kappa)\rangle\kappa_i\kappa_k + \frac{1}{HR_\infty} e_{ikm}\kappa_m + \frac{1}{H^2}(S_1\delta_{ik} + S_2\kappa_i\kappa_k), \tag{21}$$

$$S_1 = \frac{1}{2}(\langle s_{kk}\rangle - \langle s_{ik}\rangle\kappa_i\kappa_k),$$
$$S_2 = \frac{1}{2}(3\langle s_{ik}\rangle\kappa_i\kappa_k - \langle s_{kk}\rangle) \tag{22}$$

are the coefficients appearing in the expression for $\langle s_{ik}\rangle$.

Let $S=\langle S\rangle+\delta S$, $a_{ik}^{(1)}=\langle a_{ik}^{(1)}\rangle+\delta a_{ik}^{(1)}$ and $s_{ik}=\langle s_{ik}\rangle+\delta s_{ik}$ ($\langle\delta S\rangle=\langle\delta s_{ik}\rangle=0$). The equation (20) makes it obvious that the components of the tensor $\delta a_{ik}^{(1)}$ satisfy, aside from the equality $\langle\delta a_{ik}^{(1)}\rangle=0$, the condition

$$\delta a_{ik}^{(1)}\kappa_i\kappa_k=0. \tag{23}$$

The equality (23) is important for all subsequent calculations.

The fluctuating part of the LCT is given by the expression

$$\Delta_{ik}(\mathbf{H},\mathbf{r})\big|_{r_c\ll l}=\delta S(\kappa,\mathbf{r})\kappa_i\kappa_k+\frac{1}{H}e_{ikl}\delta a_{lm}(\kappa,\mathbf{r})\kappa_m + \frac{1}{H^2}\delta s_{ik}(\kappa,\mathbf{r}). \tag{24}$$

Let us consider the expression for the nth fluctuation correction $w_{ik}^{(n)}(\mathbf{H})$ (Eq. (I.3)). Aside from the n-point correlation function of the tensors $\hat{\Delta}$, this expression contains the tensors $q_{l_sj_s}^{(s)}$ determined by Eq. (I.4). We shall write out these tensors explicitly for strong magnetic fields.

In accordance with Eq. (21)

$$Q^{(s)}=\langle\sigma_{ik}(\mathbf{H})\rangle n_i^{(s)}n_k^{(s)}=\langle S\rangle[(1+\alpha_2^2)(\kappa n_s)^2+\alpha_1^2];$$

$$\alpha_i^2=\frac{S_i}{\langle S\rangle H^2}\ll 1, \tag{25}$$

where $i=1$, 2, and S_i are given by Eqs. (22). Dropping α_2^2 compared with 1 we obtain

$$q_{l_sj_s}^{(s)}=\frac{n_{l_s}^{(s)}n_{j_s}^{(s)}}{\langle S\rangle}\times\frac{1}{((\kappa\mathbf{n}_s)^2+\alpha_1^2)}. \tag{26}$$

Therefore in the leading order approximation the contraction

$$q_{l_sj_s}^{(s)}\kappa_{l_s}\kappa_{j_s}=1/\langle S\rangle \tag{27}$$

is a constant. If only the contraction (27) appears in the expression for the tensors $w_{ik}^{(n)}(\mathbf{H})$, then α_1^2 in the denominator of the expression (26) for the components of the tensor $q_{l_sj_s}^{(s)}$ can be dropped.

It should be noted that for an isotropic, randomly nonuniform conductor, whose conductivity in strong magnetic fields is given by the formula

$$\sigma_{ik}(\mathbf{r})=(\sigma_0+\Delta(\mathbf{r}))\left[\kappa_i\kappa_k+\frac{1}{h}e_{ikl}\kappa_l+\frac{1}{h^2}\delta_{ik}\right], \tag{28}$$

$\Delta(\mathbf{r})$ is a random function and $\langle\Delta(\mathbf{r})\rangle=0$, $h=\omega_c\tau=eH\tau/mc$ (τ is the relaxation time), it is precisely the presence of poles in the components of the tensors $q_{l_sj_s}^{(s)}$ that causes the perturbation-theory series for the transverse components of the ECT to converge, only if the value of the magnetic field is limited by the condition $h\langle\Delta^2\rangle/\sigma_0^2\ll 1$. For strong magnetic fields the perturbation-theory series diverges because of the anomalously large contribution of the fluctuations of the Hall components, which can be seen even when calculating the first nonvanishing fluctuation correction $w_\perp^{(2)}(\mathbf{H})$ (see Ref. 11). A qualitative calculation performed by Dreĭzin and Dykhne has shown that for such conductors the transverse effective conductivity is anomalously large: $\sigma_\perp^{\text{eff}}\sim 1/H^{4/3}$ (instead of $\sigma_\perp^{\text{eff}}\sim 1/H^2$). Comparing Eqs. (18) and (28) shows that in Eq. (28) the fluctuations of the Hall conductivity are described by the tensor $\delta a_{ik}^{(1;is)}\sim\Delta(\mathbf{r})\delta_{ik}$. Evidently, the equality (23) does not hold for the tensor $\delta a_{ik}^{(1;is)}$.

In the polycrystals of metals with closed FS, because of the inequality (23) the fluctuations of the Hall components do not make an anomalously large contribution to the effective transverse conductivity. The expressions for $w_\perp^{(2)}(\mathbf{H})$ for an isotropic nonuniform conductor and a polycrystal are compared in the Appendix IV. In addition, we have shown by direct calculation that for polycrystals the contribution of only the Hall terms to $w_\perp^{(3)}(\mathbf{H})$ is zero, and in $w_\perp^{(4)}(\mathbf{H})$ this contribution is of the order of $1/H^3$.

When other terms in the fluctuation part of the LCT are taken into account the effective transverse conductivity becomes of the order of $1/H^2$.[13] The estimates made suggest that the contribution of the Hall components to the fluctuation corrections of higher order ($n>4$) in the reciprocal of the magnetic field is small compared to terms of order $1/H^2$. If this conjecture is correct, then the expression obtained below for $\sigma_\perp^{\text{eff}}$ is *exact* within the approximation considered.

On this basis we shall calculate the tensor $w_{ik}^{(n)}(\mathbf{H})$ (see Eq. (I.3)) for arbitrary n to order $O(1/H^2)$. We write $w_{ik}^{(n)}(\mathbf{H})$ in the form

$$w_{ik}^{(n)}=w_{ik}^{(n;L)}+w_{ik}^{(n;A)}/H+w_{ik}^{(n;T)}/H^2. \tag{29}$$

To calculate $w_{ik}^{(n;L)}$, $w_{ik}^{(n;A)}$, and $w_{ik}^{(n;T)}$ we write the product

$$\Delta_{il_1}(\mathbf{H},\mathbf{r})\Delta_{j_1l_2}(\mathbf{H},\mathbf{r}_1)\ldots\Delta_{j_{n-1}k}(\mathbf{H},\mathbf{r}_{n-1})$$

up to terms of order $1/H^2$:

$$\Delta_{il_1}(\mathbf{H},\mathbf{r})\Delta_{j_1l_2}(\mathbf{H},\mathbf{r}_1)\ldots\Delta_{j_{n-1}k}(\mathbf{H},\mathbf{r}_{n-1}) =\left(\hat{L}^{(n)}+\frac{1}{H}\hat{A}^{(n)}+\frac{1}{H^2}\hat{T}^{(n)}\right)\hat{P}^{(n)}, \tag{30}$$

where the cap indicates a collection of indices, and $\hat{P}^{(n)}=\Pi_{q=1}^{n-1}\kappa_{l_q}\kappa_{j_q}$. By virtue of Eq. (27), to leading order the contraction

$$q_{l_1j_1}^{(1)}q_{l_2j_2}^{(2)}\ldots q_{l_{n-1}j_{n-1}}^{(n-1)}\hat{P}^{(n)}=1/\langle S\rangle^{n-1}. \tag{31}$$

Each term on the right-hand side of the expression (29) is determined by one of the operators on the right-hand side of Eq. (30). The tensor $\hat{L}^{(n)}\hat{P}^{(n)}$ in Eq. (31) corresponds to a product of n tensors of the form $\delta S(\mathbf{r}_q)\kappa_{j_q}\kappa_{l_{q+1}}$: $\hat{L}^{(n)}=\kappa_i\kappa_k\delta S(\mathbf{r})\Pi_{p=1}^{n-1}\delta S(\mathbf{r}_p)$. Substituting this expression into Eq. (I.3) and using the equality (31) we obtain

$$\begin{aligned}w_{ik}^{(n;L)}=&\frac{(-1)^n\kappa_i\kappa_k}{\langle S\rangle^{n-1}(2\pi)^{3(n-1)}}\int\ldots\int d^3r_1\ldots d^3r_{n-1}\\ &\times\left\langle\delta S\langle\mathbf{r})\prod_{p=1}^{n-1}\delta S(\mathbf{r}_\rho)\right\rangle\\ &\times\int\ldots\int d^3k_1\ldots d^3k_{n-1}\exp[-i\mathbf{k}_1(\mathbf{r}_1-\mathbf{r})]\\ &\times\exp[-i\mathbf{k}_2(\mathbf{r}_2-\mathbf{r}_1)]\ldots\\ &\times\exp[-i\mathbf{k}_{n-1}(\mathbf{r}_{n-1}-\mathbf{r}_{n-2})].\end{aligned} \tag{32}$$

Integrating over $\mathbf{k}_j$ ($j=1,2,...,n-1$) leads to the appearance of the functions $\delta(\mathbf{r}_j-\mathbf{r}_{j-1})$ in the integrand, which reduce the multiple-point average $\langle \delta S(\mathbf{r})\Pi_{p=1}^{n-1}\delta S(\mathbf{r}_p)\rangle$ to the constant $\langle(\delta S)^n\rangle$. As a result

$$w_{ik}^{(n;L)}=w_{\parallel}^{(n)}\kappa_i\kappa_k, \quad w_{\parallel}^{(n)}=(-1)^n\frac{\langle(\delta S)^n\rangle}{\langle S\rangle^{n-1}}. \tag{33}$$

The structure of the tensors $w_{ik}^{(n;L)}$ shows that they contribute to the longitudinal part of the tensor W_{ik}.

The tensor $\hat{A}^{(n)}\hat{P}^{(n)}$ corresponds to all possible products, including one of the tensors $\delta a_{mn}^{(1)}(\mathbf{r}_s)$ and the $(n-1)$ tensor $\delta S(\mathbf{r}_q)\kappa_{j_q}\kappa_{l_{q+1}}$. We shall not write out the expression for $\hat{A}^{(n)}$, since, as shown in Ref. 13, for all $n\geqslant 2$ this tensor does not contribute to $w_{ik}^{(n)}(\mathbf{H})$ because of Eq. (23).

Terms proportional to $1/H^2$ appear in Eq. (30) because of

1) all possible products of one tensor $\delta s_{j_q l_{q-1}}(\mathbf{r}_{n-1})$ and the $(n-1)$ tensor $\delta S(\mathbf{r}_q)\kappa_{j_q}\kappa_{l_{q+1}}$;

2) all possible products of two tensors $\delta a_{mn}^{(1)}(\mathbf{r}_s)$ and $(n-2)$ tensors $\delta S(\mathbf{r}_q)\kappa_{j_q}\kappa_{l_{q+1}}$.

The complete expression for the tensor $\hat{T}^{(n)}$ is very complicated. We shall write out only the portion of this tensor that makes a nonzero contribution to the leading order term in the effective transverse conductivity:

$$\hat{T}^{(n)}=e_{il_1m_1}e_{j_{n-1}km_2}\frac{1}{\kappa_{l_1}\kappa_{j_{n-1}}}\delta a_{m_1n_1}^{(1)}(\mathbf{r})\,\delta a_{m_2n_2}^{(1)} \times(\mathbf{r}_{n-1})\kappa_{n_1}\kappa_{n_2}\prod_{p=1}^{n-2}\delta S(\mathbf{r}_p)+\dots\,. \tag{34}$$

The dots signify terms which have been dropped.

Calculating the tensor $w_{ik}^{(n;T)}$ we keep in mind that this is a rank-2 isotropic tensor whose components depend on the fixed vector κ. According to Eq. (II.8) $w_{ik}^{(n;T)}=w_{\perp}^{(n)}\delta_{ik}+w_{\parallel}^{(n;T)}\kappa_i\kappa_k$. The term $w_{\parallel}^{(n;T)}\kappa_i\kappa_k$ gives a correction $O(1/H^2)$ to the longitudinal part of the tensor $w_{ik}^{(n)}$. In our approximation this term must be dropped. The expression for $w_{\perp}^{(n)}$ has the form

$$w_{\perp}^{(n)}=\frac{1}{2}(w_{kk}^{(n;T)}-w_{ik}^{(n;T)}\kappa_i\kappa_k). \tag{35}$$

Using Eqs. (34) and (35) we obtain from Eq. (I.3)

$$\begin{aligned}w_{\perp}^{(n)}=&\frac{(-1)^n}{2\langle S\rangle^{n-3}}\frac{1}{(2\pi)^6}(e_{rl_1m_1}e_{j_{n-1}}rm_2\\ &-e_{rl_1m_1}e_{j_{n-1}sm_2}\kappa_r\kappa_s)\\ &\times\int\int d^3k_1d^3k_{n-1}\kappa_{j_1}\kappa_{l_{n-1}}q_{l_1j_1}^{(1)}q_{l_{n-1}j_{n-1}}^{(n-1)}\\ &\times\int\int d^3r_1d^3r_{n-1}\exp[-i\mathbf{k}_1(\mathbf{r}_1-\mathbf{r})]\\ &\times\exp[-i\mathbf{k}_{n-1}(\mathbf{r}_{n-1}-\mathbf{r}_1)]\langle\delta a_{m_1n_1}^{(1)}\\ &\times(\mathbf{r})\kappa_{n_1}(\delta S(\mathbf{r}_1))^{n-2}\delta a_{m_2n_2}^{(1)}(\mathbf{r}_{n-1})\kappa_{n_2}\rangle.\end{aligned} \tag{36}$$

We shall calculate the average in Eq. (36) using the equations from Appendix II and Eq. (23):

$$\begin{aligned}&\langle\delta a_{m_1n_1}^{(1)}(\mathbf{r})\kappa_{n_1}(\delta S(\mathbf{r}_1))^{n-2}\delta a_{m_2n_2}^{(1)}(\mathbf{r}_{n-1})\kappa_{n_2}\rangle\\ &\quad=N_{m_1n_2}\{Y_1W_3([\mathbf{r},\mathbf{r}_{n-1}],\mathbf{r}_1)+Y_2W_3([\mathbf{r},\mathbf{r}_1,\mathbf{r}_{n-1}])\},\end{aligned} \tag{37}$$

where

$$N_{m_1m_2}=(\delta_{m_1m_2}-\kappa_{m_1}\kappa_{m_2}), \quad Y_1=\frac{1}{2}\langle A\rangle\langle(\delta S)^{n-2}\rangle,$$

$$Y_2=\frac{1}{2}\langle A(\delta S)^{n-2}\rangle, \quad A=\delta a_{mp}^{(1)}\delta a_{mq}^{(1)}\kappa_p\kappa_q. \tag{38}$$

Substituting the expression (38) into Eq. (36) gives

$$w_{\perp}^{(n)}=-\frac{(-1)^n}{\langle S\rangle^{n-1}}\{Y_1W_3([\mathbf{r},\mathbf{r}],\mathbf{r})+Y_2W_3([\mathbf{r},\mathbf{r},\mathbf{r}])\}.$$

Since, by definition (see Appendix II), the probabilities $W_3([\mathbf{r},\mathbf{r}],\mathbf{r})=0$ and $W_3([\mathbf{r},\mathbf{r},\mathbf{r}])=1$, we obtain finally

$$w_{\perp}^{(n)}=-\frac{(-1)^n}{2\langle S\rangle^{n-1}}\langle A(\delta S)^{n-2}\rangle. \tag{39}$$

Thus, in the laboratory coordinate system the $w_{ik}^{(n)}$ for the terms in the series W_{ik} (see Eq. (I.1)) are given by

$$w_{ik}^{(n)}=w_{\parallel}^{(n)}\delta_{i3}\delta_{k3}+\frac{w_{\perp}^{(n)}}{H^2}(\delta_{ik}-\delta_{i3}\delta_{k3}), \tag{40}$$

where to leading order $w_{\parallel}^{(n)}$ is given by Eq. (33) and $w_{\perp}^{(n)}$ by Eq. (39).

The expressions for $w_{\parallel}^{(n)}$ and $w_{\perp}^{(n)}$ are independent of the correlation functions associated with the spatial fluctuations at different points of the medium. This is a rarely encountered situation, which makes it possible to obtain the *exact* solution for the ECT. There are several reasons why there is no dependence on the correlation functions. In the first place the form of the leading order term in the expansion of the fluctuation part of the LCT in power of $1/H$ is comparatively simple: in accordance with Eq. (24) this term is independent of $1/H$ and equals $\delta S(\kappa,\mathbf{r})\kappa_i\kappa_k$. In the second place Eq. (27) for the contractions $q_{l_sj_s}^{(s)}\kappa_{l_s}\kappa_{j_s}$ makes it possible to perform in the limit $H\to\infty$ the integration in Eq. (36) over almost all vectors $\mathbf{k}_m$. Finally, and most importantly, $\delta a_{ik}^{(1)}\kappa_i\kappa_k=0$, which holds for polycrystals of metals. As noted above, when this equality is satisfied, the perturbation-theory series converges and the expansion (30) can be used to calculate the product

$$\Delta_{il_1}(\mathbf{H},\mathbf{r})\Delta_{j_1l_2}(\mathbf{H},\mathbf{r}_1)\dots\Delta_{j_{n-1}k}(\mathbf{H},\mathbf{r}_{n-1}).$$

Using Eq. (40) we shall write the expression for the tensor W_{ik} in the laboratory coordinate system

$$W_{ik}=W_{\parallel}\delta_{i3}\delta_{k3}+\frac{W_{\perp}}{H^2}(\delta_{ik}-\delta_{i3}\delta_{k3}), \tag{41a}$$

where

$$W_{\parallel}=\sum_{n=2}^{\infty}w_{\parallel}^{(n)}=\langle S\rangle\left\{\langle S\rangle\left\langle\frac{1}{S}\right\rangle-1\right\};$$

$$W_{\perp}=\sum_{n=2}^{\infty}w_{\perp}^{(n)}=-\frac{1}{2}\left\langle\frac{A}{S}\right\rangle. \tag{41b}$$

In deriving the expressions (41) we employed the fact that $\langle \delta S\rangle = 0$, and the formula for the sum of a geometric progression

$$\sum_{n=0}^{\infty} (-1)^n (\delta S(\mathbf{r})/\langle S\rangle)^n = \langle S\rangle / S(\mathbf{r}),$$

which converges if $|\delta S(\mathbf{r})/\langle S\rangle| < 1$ for all orientations of the crystallites. Our solution is valid at least as long as the anisotropy of the longitudinal component of the LCT satisfies this inequality. If this condition holds, then Eqs. (41) give the *exact* expression for the tensor W_{ik} within the approximation used.

In order to use Eq. (I.1) for the ECT it remains to calculate the tensors I_{ik} and V_{ik}. According to the definition (I.6) I_{ik} is an isotropic rank-2 tensor whose components depend on κ. Therefore $I_{ik} = I_0\delta_{ik} + I_1\kappa_i\kappa_k$. In strong magnetic fields the leading order terms in the expansion $I_0 = -I_1 \sim H$, and the leading term in the expansion of the sum $I_0 + I_1 = 1/\langle S\rangle$.

According to the definition (I.5) and Eq. (41),

$$V_{ik} = V_{\parallel}\kappa_i\kappa_k + V_{\perp}(\delta_{ik} - \kappa_i\kappa_k),$$

$$V_{\parallel} = W_{\parallel}(I_0 + I_1) + \frac{W_{\perp}}{H^2} I_1, \quad V_{\perp} = 1 + \frac{W_{\perp}}{H^2} I_0.$$

Using these formulas we shall calculate V_{ik}^{-1} and then the ECT. To the accuracy of interest to us, in the laboratory coordinate system

$$\sigma_{ik}^{\text{eff}}(\mathbf{H})\big|_{r_c \ll l} = \sigma_{\parallel}^{\text{eff}}\delta_{i3}\delta_{k3} + \frac{1}{HR_{\infty}} e_{ik3} + \sigma_{\perp}^{\text{eff}}(\delta_{ik} - \delta_{i3}\delta_{k3}), \tag{42a}$$

$$\sigma_{\parallel}^{\text{eff}} = \frac{1}{\langle 1/S\rangle}; \quad \sigma_{\perp}^{\text{eff}} = \frac{s_{\perp}^{\text{eff}}}{H^2}, \quad s_{\perp}^{\text{eff}} = S_1 + \frac{1}{2}\left\langle \frac{A}{S}\right\rangle, \tag{42b}$$

where S_1 is given by Eq. (22) and $A = \delta a_{mp}^{(1)}\delta a_{mq}^{(1)}\kappa_p\kappa_q$.

The result for $\sigma_{\parallel}^{\text{eff}}$ is obvious. If only the components of ECT which do not vanish as $H\to\infty$ are calculated, then in the laboratory coordinate system only one component of the LCT needs to be retained—σ_{zz}. In the invariant representation $\sigma_{ik}(\mathbf{H},\mathbf{r}) = S(\kappa,\mathbf{r})\kappa_i\kappa_k$. For a nonuniform conductor where all current lines are parallel (in this case, directed along the magnetic field), the average conductivity is known (see, for example, Ref. 29): it is the reciprocal of the average resistance.

It follows from Eq. (42b) that the value of the effective Hall conductivity is the same as in a single-crystal metal: in strong magnetic fields the spatial fluctuations do not affect its magnitude. The result for the effective transverse conductivity can be obtained only by indirect calculation.

A. Compensated metal

Let us now consider polycrystals of compensated metals ($n_e = n_h$). The derivation of the formulas for ECT differ little from the derivation presented above. However, for $n_e = n_h$, as already mentioned, the terms σ_{xy} and σ_{yx}, which are proportional to $1/H$, are zero in the laboratory coordinate system. The expansion of these Hall components starts with the term $O(1/H^3)$. Consequently, the expression for the LCT must be supplemented by a term proportional to $1/H^3$. Thus, for $n_e = n_h$ the following expression for the LCT serves as the starting point instead of Eq. (18):

$$\sigma_{ik}(\mathbf{H})\big|_{r_c \ll l} = S(\kappa)\kappa_i\kappa_k + \frac{1}{H} e_{ikl} a_{lm}^{(1)}(\kappa)\kappa_m + \frac{1}{H^2} s_{ik}(\kappa) + \frac{1}{H^3} e_{ikl} a_{lm}^{(2)}(\kappa)\kappa_m. \tag{43}$$

In the invariant representation the condition $n_e = n_h$ imposes a constraint on the components of the tensor $a_{lm}^{(1)}$:

$$a_{lm}^{(1)}\kappa_l\kappa_m = 0. \tag{44}$$

To calculate $\langle \sigma_{ik}(\mathbf{H})\rangle$ using Eq. (43) we take account of the fact that $\langle a_{lm}^{(1)}(\kappa)\kappa_m\rangle = \langle a_{pq}^{(1)}\kappa_p\kappa_q\rangle\kappa_l = 0$ (compare with Eq. (20)). Then

$$\langle \sigma_{ik}(\mathbf{H})\rangle\big|_{r_c \ll l} = \langle S\rangle\kappa_i\kappa_k + \frac{1}{H^2}(S_1\delta_{ik} + S_2\kappa_i\kappa_k) + \frac{A_2}{H^3} e_{ikl}\kappa_l, \tag{45}$$

where, just as in Eq. (21), the values of S_1 and S_2 are determined by Eqs. (22), and

$$\langle a_{lm}^{(2)}(\kappa)\kappa_m\rangle = \langle a_{pq}^{(2)}\kappa_p\kappa_q\rangle\kappa_l = A_2\kappa_l. \tag{46}$$

The fluctuation part of the LCT is given by the expression

$$\Delta_{ik}(\mathbf{H},\mathbf{r})\big|_{r_c \ll l} = \delta S(\kappa,\mathbf{r})\kappa_i\kappa_k + \frac{1}{H} e_{ikl} a_{lm}^{(1)}(\kappa,\mathbf{r})\kappa_m + \frac{1}{H^2}\delta s_{ik}(\kappa,\mathbf{r}) + \frac{1}{H^3} e_{ikl}\delta a_{lm}^{(2)}(\kappa,\mathbf{r})\kappa_m. \tag{47}$$

Here, just as in Eq. (24), $\langle \delta S\rangle = \langle \delta s_{ik}\rangle = 0$ and, of course, $\langle \delta a_{lm}^{(2)}\rangle = 0$.

Instead of Eq. (29) we shall write out the expansion for $w_{ik}^{(n)}(\mathbf{H})$ taking account the term of order $O(1/H^3)$:

$$w_{ik}^{(n)} = w_{ik}^{(n;L)} + w_{ik}^{(n;A_1)}/H + w_{ik}^{(n;T)}/H^2 + w_{ik}^{(n;A_2)}/H^3. \tag{48}$$

To calculate the tensors appearing in Eq. (48), instead of the expression (30), the product of tensors

$$\Delta_{il_1}(\mathbf{H},\mathbf{r})\Delta_{j_1l_2}(\mathbf{H},\mathbf{r}_1)\ldots\Delta_{j_{n-1}k}(\mathbf{H},\mathbf{r}_{n-1})$$

must be written up to terms of order $1/H^3$. The expression for the longitudinal $w_{ik}^{(n;L)}$ and transverse $w_{ik}^{(n;T)}$ components of the tensors $w_{ik}^{(n)}$ is identical to the calculation presented above. We note that even though the equality (44) holds, the contraction $A = \delta a_{mp}^{(1)}\delta a_{mq}^{(1)}\kappa_p\kappa_q$ appearing in the expression for $\sigma_{\perp}^{\text{eff}}$ is different from zero. In addition, in the expression for $w_{ik}^{(n)}$ the term $O(1/H)$ vanishes.

The only difference is that the tensor $w_{ik}^{(n;A_2)}$ must be calculated. We have shown that

$$w_{ik}^{(n;A_2)} = \frac{(-1)^n}{\langle S\rangle^{n-1}} e_{ikl}\langle B\,\delta S^{n-2}\rangle\kappa_l, \quad B = a_{pq}^{(1)}\kappa_p\delta s_{qr}\kappa_r. \tag{49}$$

We shall now sum the expressions for $w_{ik}^{(n)}$ over all n using Eqs. (33), (39), and (49). The result is

$$W_{ik}=W_{\parallel}\kappa_i\kappa_k+\frac{1}{H^2}W_{\perp}(\delta_{ik}-\kappa_i\kappa_k)$$

$$+\frac{1}{H^3}W_H e_{ikl}\kappa_l, \quad W_H=-\left\langle\frac{B}{S}\right\rangle, \tag{50}$$

and $W_{\parallel}$ and $W_{\perp}$ are given by the expressions (41b).

Now, calculating the tensors I_{ik} and V_{ik} we shall find, using Eq. (I.1), the ECT for a compensated metal. In the laboratory coordinate system

$$\sigma_{ik}^{\text{eff}}(\mathbf{H})|_{r_c\ll l}=\sigma_{\parallel}^{\text{eff}}\delta_{i3}\delta_{k3}+\sigma_{\perp}^{\text{eff}}[\delta_{ik}-\delta_{i3}\delta_{k3}]+\sigma_H^{\text{eff}}e_{ik3}, \tag{51}$$

where $\sigma_{\parallel}^{\text{eff}}$ and $\sigma_{\perp}^{\text{eff}}$ are given by Eqs. (42b), and

$$\sigma_H^{\text{eff}}=\frac{a_{\text{eff}}}{H^3}; \quad a_{\text{eff}}=\langle a_{pq}^{(2)}\kappa_p\kappa_q\rangle+\left\langle\frac{B}{S}\right\rangle. \tag{52}$$

We note that for $n_e=n_h$, in contrast to the case of an uncompensated metal, the fluctuation corrections influence the leading order term of the effective Hall conductivity.

5. EXPLICIT EXPRESSIONS FOR THE COMPONENTS OF THE EFFECTIVE CONDUCTIVITY TENSOR (WEAK FIELDS)

We have underscored that the problem of the present paper is to derive formulas for the effective characteristics of the GMP in polycrystals in terms of the characteristics of crystallites—single crystals. This was done in preceding sections. It seems to us that to develop the theory further the formulas obtained above need to be specified for polycrystals of various metals. The implementation of this program will require using simplifying models and computer calculations. This falls outside the scope of our problem.

On the other hand the experience of fermiology teaches that writing the characteristics in the form of integrals over the FS in cases where the integrand contains quantities which have a clear physical meaning is (or, better said, may be) very helpful. Consequently, we shall present the expressions for the characteristics of the GMP for weak magnetic fields. We shall focus our attention on polycrystals of metals with cubic symmetry, for which the ECT is described by an *exact* formula: the expression (17) for polycrystals is no less accurate than the formula (5) for single crystals. The theory of GMP[1–3] uses an expansion in the reciprocal of the magnetic field for solving the Boltzmann equation—calculating the conduction electron distribution function, and with its help the conductivity tensor. Reference 28 is an extension of these works. In Ref. 28 an expansion of the distribution function is also obtained in powers of the magnetic field, which makes it possible to calculate the tensors a_{ij} and $S_{ik,lm}$ appearing in Eq. (5).

One problem of the present section is to make the formulas transparent. Consequently, we shall say a few words about the notation. The nonequilibrium part of the distribution function f_1, just as the entire distribution function itself, is a scalar. It is convenient to represent f_1 in the form

$$f_1=-e\left(\frac{\partial f_F}{\partial\varepsilon}\right)\mathbf{l}(\mathbf{p})\mathbf{E}$$

(the standard notation is used). The vector $\mathbf{l}(\mathbf{p})$ is the solution of the Boltzmann equation. The notation chosen must underscore that $\mathbf{l}(\mathbf{p})$ must/can be regarded as a vector mean-free path length for conduction electrons. Indeed,

$$\mathbf{l}(\mathbf{p})=\hat{W}_{\mathbf{p}}^{-1}\mathbf{v}, \tag{53}$$

where $\hat{W}_{\mathbf{p}}$ is the collision operator, and the conductivity tensor

$$\sigma_{ik}=\langle v_i l_k\rangle_F; \quad \langle\ldots\rangle_F=-\frac{2e^2}{(2\pi h)^3}\int\frac{\partial f_F}{\partial\varepsilon}dp^3, \tag{54}$$

the brackets $\langle\ldots\rangle_F$ denote integration over the quasimomentum space. Replacing $-\partial f_F/\partial\varepsilon$ with a δ function, the integration extends over the FS.

If the FS is a sphere, then $\mathbf{v}$ is a characteristic function of the collision operator and $\mathbf{l}(\mathbf{p})=\tau(\varepsilon)\mathbf{v}$ always, where $\tau(\varepsilon)$ is the relaxation time or the free flight time of an electron with energy ε. In the general case with an arbitrary dispersion law $\varepsilon=\varepsilon(\mathbf{p})$ the replacement of $\hat{W}_{\mathbf{p}}^{-1}$ by $\tau(\varepsilon)$ is called the τ approximation, though essentially this is not an approximation but rather it fixes the dimension and order of magnitude of $\mathbf{l}(\mathbf{p})$, if τ is, in order of magnitude, the free flight time of a conduction electron.

For a spherical FS, replacing $(-\partial f_F/\partial\varepsilon)$ in the expression (54) by a δ function gives immediately $\sigma_{ik}=\sigma\delta_{ik}$, where $\sigma=ne^2\tau/m_{\text{eff}}$ (n is the conduction electron density, $m_{\text{eff}}=p_F/v_F$ is the effective mass, and the index F indicates that the energy ε equals the Fermi energy ε_F).

When the form of the FS is complicated the average mean-free path length can be introduced:

$$l_p=\int \mathrm{d}S_F|\mathbf{l}(\mathbf{p})|/S_F,$$

where the integration extends over the FS and S_F is the area of the FS. Using this notation and Eq. (54) the specific conductivity of a crystal with cubic symmetry in field $H=0$ can be written in the form

$$\sigma_{ik}=\sigma\delta_{ik}, \quad \sigma=\frac{2e^2S_Fl_p}{3(2\pi\hbar)^3}. \tag{55}$$

The advantage of this representation is its transparency.

We shall now use the results of Ref. 28. We write out the expressions for the symmetric $\sigma_{ik}^s=\sigma_{ik}^{(0)}+S_{ik;lm}H_lH_m$ and antisymmetric $\sigma_{ik}^a=e_{iklm}a_{lm}H_m$ parts of the conductivity tensor $\sigma_{ik}(\mathbf{H})$

$$\sigma_{ik}^a=\frac{e}{c}\left\langle[\mathbf{vH}]_q\frac{\partial l_i}{\partial p_q}l_k\right\rangle; \tag{56}$$

$$\sigma_{ik}^s-\sigma_{ik}^{(0)}=\frac{e^2}{c^2}\left\langle[\mathbf{vH}]_q\frac{\partial l_i}{\partial p_q}\hat{W}^{-1}[\mathbf{vH}]_m\frac{\partial l_k}{\partial p_m}\right\rangle. \tag{57}$$

These formulas show the quantities which are used when writing down the expressions for the characteristics of GMP in weak fields. The rank-2 tensor $u_{ik}=\partial l_i/\partial p_k$ can be called a *generalized mobility tensor*. In our case the tensor u_{ik} is asymmetric. In the τ approximation (when τ is a constant) this tensor is symmetric:[4)]

$$u_{ik}=\tau\frac{\partial v_i}{\partial p_k}=\tau\frac{\partial^2\varepsilon}{\partial p_i\partial p_k}=\tau\left(\frac{1}{m}\right)_{ik}, \tag{58}$$

$1/m_{ik}$ is the tensor of the reciprocals of the effective masses. The expression (58) is a typical generalization of the isotropic mobility $u=\tau/m$ (m is the electron mass).

The tensor u_{ik} appears in Eqs. (56) and (57) together with the velocity vector **v**. Consequently, it is convenient to consider the rank-3 tensor $\gamma_{ikl}=v_i(\partial l_k/\partial p_l)$ as the main element and express the tensors a_{ik} and $S_{ik;lm}$ in terms of this tensor. We obtain from Eqs. (55)

$$a_{ik}=\frac{e}{2c}e_{pqi}e_{rsk}\langle\gamma_{spr}l_q\rangle_F;$$

$$S_{ik,lm}=-\frac{e^2}{2c^2}e_{pql}e_{rsm}\langle\gamma_{qip}\hat{W}^{-1}\gamma_{skr}+\gamma_{qkp}\hat{W}^{-1}\gamma_{sir}\rangle_F. \tag{59}$$

These formulas are not too transparent, but in the τ approximation they can be substantially simplified.

We shall now say a few words about polycrystalline cubic metals. As already noted above, for them $\sigma_{ik}^{(0)}=\sigma_0\delta_{ik}$ and $a_{ik}=a\delta_{ik}$, which makes it possible to calculate the ECT *exactly*.

Let us compare the expression (17) with the conductivity tensor $\sigma_{ik}^{(is)}$ for an isotropic body with a spherical FS. In weak fields

$$\sigma_{ik}^{(is)}=\sigma_0^{(is)}[\delta_{ik}+he_{ikl}\kappa_l-h^2(\delta_{ik}-\kappa_i\kappa_k)], \tag{60}$$

where $h=\omega_H\tau=eH\tau/mc$.

Now, according to Eqs. (59), in Eq. (17)

$$a=\frac{a_{ll}}{3}=\frac{e}{6c}(\langle\gamma_{spp}l_s\rangle-\langle\gamma_{pps}l_s\rangle), \tag{61}$$

and according to Eqs. (7c) the coefficients S_1 and S_2 are

$$S_1=-\frac{e^2}{15c^2}\left\{2[\langle(\gamma_{skr}-\gamma_{rks})\hat{W}^{-1}\gamma_{skr}\rangle_F]-\frac{1}{2}e_{pql}e_{rsk}(\langle\gamma_{qlp}\hat{W}^{-1}\gamma_{skr}+\gamma_{qkp}\hat{W}^{-1}\gamma_{slr}\rangle_F)\right\}, \tag{62}$$

$$S_2=-\frac{e^2}{30c^2}\left[\frac{3}{2}e_{pql}e_{rsk}(\langle\gamma_{qlp}\hat{W}^{-1}\gamma_{skr}+\gamma_{qkp}\hat{W}^{-1}\gamma_{slr}\rangle_F)-\langle(\gamma_{skr}-\gamma_{rks})\hat{W}^{-1}\gamma_{skr}\rangle_F\right]. \tag{63}$$

Let us compare Eqs. (17) and (60). It is evident that in Eq. (17) the coefficients of the terms which are linear and quadratic in the magnetic field have a much more complicated structure than in Eq. (60). It is well known that in an isotropic body the symmetric part of the resistance tensor is completely independent of the magnetic field (see, for example, Ref. 16): $\rho_{ik}^{(is)}=(\delta_{ik}-he_{ikl}\kappa_l)/\sigma_0^{(is)}$. For calculating the ECT using Eq. (17) it is easy to show that for a polycrystal the Hall part does not compensate the quadratic term. This shows once again that even for polycrystals of cubic metals the effective GMP characteristics do not correspond to a metal with a spherical FS.

In the τ approximation all quantities appearing in Eq. (17) can be put into a form which is similar to their form in Eq. (60). But this will require introducing four different effective masses. Only when the FS is a sphere are they equal to one another and the same as $m_{\text{eff}}=p_F/v_F$.

6. CONCLUSIONS

The main result of this paper is the derivation of the formulas making it possible to calculate the characteristics of the GMP of polycrystals to any degree of accuracy in the anisotropy of the characteristics of the crystallites. All formulas needed to calculate the ECT are presented in the text (see Appendix I and Secs. 3 and 4). As a rule, experimentalists use the resistance tensor instead of the conductivity tensor to describe GMP. We shall present formulas for the ECT and ERT for polycrystals, which are isotropic on the average, in an arbitrary magnetic field. In this case the ECT is determined by the expression

$$\sigma_{ik}^{\text{eff}}(\mathbf{H})=s_1(\delta_{ik}-\kappa_i\kappa_k)+\tilde{a}e_{ikl}\kappa_l+s_3\kappa_i\kappa_k, \tag{64}$$

where the coefficients s_1, s_3, and $\tilde{a}$ depend on the magnitude of the magnetic field H. For the ERT we obtain from this expression

$$\rho_{ik}^{\text{eff}}(\mathbf{H})=\frac{s_1}{s_1^2+\tilde{a}^2}(\delta_{ik}-\kappa_i\kappa_k)-\frac{\tilde{a}}{s_1^2+\tilde{a}^2}e_{ikl}\kappa_l+\frac{1}{s_3}\kappa_i\kappa_k. \tag{65}$$

Analysis of the solutions of the Boltzmann equation (see Refs. 28, 30, and 31) has revealed the relations in form of inequalities between different characteristics of GMP. It is still not clear which of them hold in polycrystals.

Of course, when the ECT is described by *exact* formulas the formulas for the ERT are just as *exact*. Our exact solutions give

1) the ERT of polycrystals of cubic metals in weak magnetic fields:

$$\rho_{ik}^{\text{eff}}(\mathbf{H})=\frac{1}{\sigma_0}\left\{\delta_{ik}-\frac{aH}{\sigma_0}e_{ikl}\kappa_l-\frac{1}{\sigma_0}[(S_1+a^2/\sigma_0)\delta_{ik}+(2S_2-a^2/\sigma_0)\kappa_i\kappa_k]\right\}, \tag{66}$$

where Eqs. (61)–(63) give the values of a, S_1, and S_2.

2) the ERT of polycrystals of metals with closed FS in strong magnetic fields:

uncompensated metals ($n_e\neq n_h$)

$$\rho_{ik}^{\text{eff}}(\mathbf{H})=s_\perp^{\text{eff}}R_\infty^2(\delta_{ik}-\kappa_i\kappa_k)-R_\infty He_{ikl}\kappa_l+\frac{1}{\sigma_\parallel^{\text{eff}}}\kappa_i\kappa_k; \tag{67}$$

compensated metals ($n_e=n_h$)

$$\rho_{ik}^{\text{eff}}(\mathbf{H})=\frac{H^2}{s_\perp^{\text{eff}}}(\delta_{ik}-\kappa_i\kappa_k)-\frac{a_{\text{eff}}}{s_\perp^{\text{eff}}}He_{ikl}\kappa_l+\frac{1}{\sigma_\parallel^{\text{eff}}}\kappa_i\kappa_k. \tag{68}$$

In Eqs. (67) and (68) $s_\perp^{\text{eff}}$ and $\sigma_\parallel^{\text{eff}}$ are given by Eq. (42b) and a_{eff} is given by Eq. (52).

Of course, as expected, averaging did not produce anything unexpected. All four GMP of single crystals of metals with closed FS remain: saturation of the transverse resistance

with increasing magnetic field for metals with unequal numbers of electrons and holes and quadratic growth in metals with $n_e = n_h$.

We underscore that the present investigation can serve as one of the few examples where the problem of calculating the characteristics of real disordered media—in this case polycrystals—can be solved exactly.

We are grateful to Academician A. M. Dykhne and Professor A. V. Chaplik for valuable remarks and helpful discussions during the course of this work. I. M. K. was supported by grant No. 02-02-17226 from the Russian Foundation for Fundamental Research.

7. APPENDIX I. ECT: PERTURBATION THEORY SERIES

The formal perturbation-theory solution of the problem has the form (see Ref. 13):

$$\sigma_{ik}^{\text{eff}} = \langle \sigma_{ik}(\mathbf{H}) \rangle - V_{ij}^{-1}(\mathbf{H}) W_{jk}(\mathbf{H}), \tag{I.1}$$

where

$$W_{ik} = \sum_{n=2}^{\infty} w_{ik}^{(n)}; \tag{I.2}$$

$$\begin{aligned} w_{ik}^{(n)}(\mathbf{H}) = {} & \frac{(-1)^n}{(2\pi)^{3(n-1)}} \int \ldots \int d^3k_1 \ldots d^3k_{n-1} \\ & \times q_{l_1 j_1}^{(1)} q_{l_2 j_2}^{(2)} \ldots q_{l_{n-1} j_{n-1}}^{(n-1)} \\ & \times \int \ldots \int d^3r_1 \ldots d^3r_{n-1} \exp[-i\mathbf{k}_1(\mathbf{r}_1 - \mathbf{r})] \\ & \times \exp[-i\mathbf{k}_2(\mathbf{r}_2 - \mathbf{r}_1)] \ldots \\ & \times \exp[-i\mathbf{k}_{n-1}(\mathbf{r}_{n-1} - \mathbf{r}_{n-2})] \ldots \\ & \times \langle \Delta_{il_1}(\mathbf{H}, \mathbf{r}) \Delta_{j_1 l_2}(\mathbf{H}, \mathbf{r}_1) \ldots \Delta_{j_{n-1} k}(\mathbf{H}, r_{n-1}) \rangle. \end{aligned} \tag{I.3}$$

The tensors $q^{(s)}$ appearing in Eq. (I.3) are

$$q_{ik}^{(s)} = \frac{n_i^{(s)} n_k^{(s)}}{Q^{(s)}}, \quad \mathbf{n}^{(s)} = \frac{\mathbf{k}^{(s)}}{k},$$

$$Q^{(s)} = \langle \sigma_{ik}(\mathbf{H}) \rangle n_i^{(s)} \mathbf{n}_k^{(s)}. \tag{I.4}$$

The tensor V_{ij} in Eq. (I.1) is given by the expression

$$V_{ik} = \delta_{ik} + W_{im} I_{mk}, \tag{I.5}$$

$$I_{ik}(\mathbf{H}) = \int d^3k q_{ik}(\mathbf{H}) \delta(\mathbf{k}). \tag{I.6}$$

The method for calculating the multiple-point correlation functions appearing in Eq. (I.3) is described in Appendix II.

The equation (I.1) makes it possible to calculate the ECT, to any degree of accuracy in the anisotropy, characterized by the tensor $\hat{\Delta}(\mathbf{r}, \mathbf{H})$, if the series (I.2) for W_{ik} converges.

The compact representation of the solution, Eq. (I.1), should not hide the complexity of the result obtained: the expression for the ECT contains two series. As the number n increases, the integrands in Eq. (I.3) for the terms in the series (I.2) $w_{ik}^{(n)}(\mathbf{H})$ become more complicated. In addition, ordinarily, for $n > 2$ the components of these tensors depend on the statistics of the directions of the crystallographic axes (see Sec. 3). It is also difficult to write out a series for $\hat{V}^{-1}$ for arbitrary values of the field. In general, apparently, it is virtually impossible to sum the series. An exception is the solution presented above for polycrystals of metals with closed FS in strong magnetic fields, where the smallness of the parameter r_H/l makes it possible to sum the terms of the series (I.2), leaving only terms $O((r_H/l)^2)$.

8. APPENDIX II. CALCULATION OF MULTIPLE-POINT CORRELATION FUNCTIONS

The formulas presented in Appendix I contain multiple-point correlation functions of random functions whose average values are zero. For simplicity we shall calculate first the correlation functions of scalar functions $a(\mathbf{r})$, $b(\mathbf{r})$, $c(\mathbf{r})$, and so on ($\langle a(\mathbf{r}) \rangle = \langle b(\mathbf{r}) \rangle = \langle c(\mathbf{r}) \rangle \ldots = 0$). We recall that we take into account the nonuniformity of a polycrystal that is due solely to the disorientation of grains. Other sources of nonuniformity are neglected.

The only property of polycrystals that influences an ensemble-averaged quantity is the rotation of the crystallographic axes of the crystallites: averaging over an ensemble is equivalent to averaging over all possible rotations of the crystallites.

Let all rotations in an ensemble be statistically independent. Then, when calculating a two-point correlation function $\langle a(\mathbf{r}) b(\mathbf{r}_1) \rangle$ two cases must be considered:

1) the vectors $\mathbf{r}$ and $\mathbf{r}_1$ lie in the same grain,

2) the vectors $\mathbf{r}$ and $\mathbf{r}_1$ lie in different grains.

Let $W([\mathbf{r}, \mathbf{r}_1])$ be the probability of the case 1. The brackets indicate that the vectors $\mathbf{r}$ and $\mathbf{r}_1$ lie in the same crystallite. If the medium is statistically homogeneous and isotropic, then $W_2([\mathbf{r}, \mathbf{r}_1]) = W_2(|\mathbf{r} - \mathbf{r}_1|)$. The probability of case 2 is $W_2([\mathbf{r}], [\mathbf{r}_1]) = 1 - W_2([\mathbf{r}, \mathbf{r}_1])$. Obviously, $W_2([\mathbf{r}, \mathbf{r}_1] = 1$ when $\mathbf{r} = \mathbf{r}_1$. Since in case 2 the two-point average

$$\langle a(\mathbf{r}) b(\mathbf{r}_1) \rangle = \langle a(\mathbf{r}) \rangle \langle b(\mathbf{r}_1) \rangle = 0,$$

we obtain

$$\begin{aligned} \langle a(\mathbf{r}) b(\mathbf{r}_1) \rangle &= \langle ab \rangle W_2([\mathbf{r}, \mathbf{r}_1]) + \langle a \rangle \langle b \rangle W_2([\mathbf{r}], [\mathbf{r}_1]) \\ &= \langle ab \rangle W_2([\mathbf{r}, \mathbf{r}_1]). \end{aligned} \tag{II.1}$$

The averages where arguments are not indicated denote single-point averages. For example, $\langle ab \rangle = \langle a(\mathbf{r}) b(\mathbf{r}) \rangle$.

To calculate the average of three quantities $\langle a(\mathbf{r}) b(\mathbf{r}_1) c(\mathbf{r}_2) \rangle$ we let $W_3([\mathbf{r}_a, \mathbf{r}_b], \mathbf{r}_c)$ be the joint conditional probability that the vectors $\mathbf{r}_a$ and $\mathbf{r}_b$ lie in the same crystallite and the vector $\mathbf{r}_c$ lies in a different crystallite. The probability $W_3([\mathbf{r}_a, \mathbf{r}_b], \mathbf{r}_c)$ eliminates the possibility that all three vectors lie in the same crystallite. According to our representation $W_3([\mathbf{r}_a, \mathbf{r}_b, \mathbf{r}_c])$ is the probability that all three vectors lie in the same crystallite. Then

$$\begin{aligned} \langle a(\mathbf{r}) b(\mathbf{r}_1) c(\mathbf{r}_2) \rangle = {} & \langle a \rangle \langle bc \rangle W_3([\mathbf{r}_1, \mathbf{r}_2], \mathbf{r}) + \langle b \rangle \\ & \times \langle ac \rangle W_3([\mathbf{r}, \mathbf{r}_2], \mathbf{r}_1) + \langle c \rangle \\ & \times \langle ab \rangle W_3([\mathbf{r}, \mathbf{r}_1], \mathbf{r}_2) \\ & + \langle abc \rangle W_3([\mathbf{r}, \mathbf{r}_1, \mathbf{r}_2]). \end{aligned}$$

If each average $\langle a \rangle = \langle b \rangle = \langle c \rangle = 0$, then, evidently,

$$\langle a(\mathbf{r})b(\mathbf{r}_1)c(\mathbf{r}_2)\rangle = \langle abc\rangle W_3([\mathbf{r},\mathbf{r}_1,\mathbf{r}_2]). \tag{II.2}$$

The average of four scalar functions which depend on four different vectors can be written in the form

$$\begin{aligned}\langle a(\mathbf{r})b(\mathbf{r}_1)c(\mathbf{r}_2)d(\mathbf{r}_3)\rangle = {}& \langle ab\rangle\langle cd\rangle W_4([\mathbf{r},\mathbf{r}_1],[\mathbf{r}_2,\mathbf{r}_3]) \\ & + \langle ac\rangle \\ & \times\langle bd\rangle W_4([\mathbf{r},\mathbf{r}_2],[\mathbf{r}_1,\mathbf{r}_3]) \\ & + \langle ad\rangle \\ & \times\langle bc\rangle W_4([\mathbf{r},\mathbf{r}_3],[\mathbf{r}_2,\mathbf{r}_1]) \\ & + \langle abcd\rangle W_4([\mathbf{r},\mathbf{r}_1,\mathbf{r}_2,\mathbf{r}_3]).\end{aligned} \tag{II.3}$$

$W_4([\mathbf{r}_a,\mathbf{r}_b],[\mathbf{r}_c,\mathbf{r}_d])$ is the probability that the vectors $\mathbf{r}_a$ and $\mathbf{r}_b$ lie in the same crystallite and simultaneously the vectors $\mathbf{r}_c$ and $\mathbf{r}_d$ lie in a different crystallite ($W_4([\mathbf{r}_a,\mathbf{r}_b],[\mathbf{r}_c,\mathbf{r}_d])=0$, if, for example, the vectors $\mathbf{r}_a$ and $\mathbf{r}_c$ lie in the same crystallite); $W_4(\mathbf{r},\mathbf{r}_1,\mathbf{r}_2,\mathbf{r}_3)$ is the probability that all four vectors lie in the same crystallite.

If we are calculating multiple-point correlation functions of tensor quantities, then the coefficients in Eqs. (II.1)–(II.3) are isotropic tensors of the corresponding rank. These tensors have the same symmetry under transposition of indices as the random tensors being averaged. The coefficients in the expressions for multiple-point correlation functions can depend only on the invariants of the tensors beng averaaged.

For example, let $\hat{B}$ be a symmetric rank-2 tensor whose components are random functions of the coordinates. Such a tensor possesses three independent invariants: a first-order invariant $B_1=B_{kk}/3$ and a second-order invariant $B_2=B_{pq}B_{pq}$. Two quadratic invariants which can be constructed from the components of such a tensor are B_1^2 and B_2. If $B_1=\langle B_{ik}\rangle$, then

$$\begin{aligned}&\langle B_{kl}(\mathbf{r})B_{mn}(\mathbf{r}_1)\rangle = \frac{B^2}{30}F_{kl;mn}W_2(|\mathbf{r}_1-\mathbf{r}|); \\ &F_{kl;mn} = -2\delta_{kl}\delta_{mn}+3(\delta_{km}\delta_{ln}+\delta_{kn}\delta_{lm}).\end{aligned} \tag{II.4}$$

If $B_1=0$, then the only nonzero invariant of order 3 which can be constructed from the components of the tensor $\hat{B}$ is $B_3=B_{rs}B_{st}B_{tr}$. Then the three-point correlation function

$$\langle B_{ik}(\mathbf{r})B_{lm}(\mathbf{r}_1)B_{pq}(\mathbf{r}_2)\rangle = \frac{B_3}{210}F_{ik;lm;pq}W_3([\mathbf{r},\mathbf{r}_1,\mathbf{r}_2]), \tag{II.5}$$

where the tensor $F_{ik;lm;pq}$ is given by the expression

$$\begin{aligned}F_{iklm;pq} = {}& 16\delta_{ik}\delta_{lm}\delta_{pq}-12[\delta_{ik}(\delta_{pl}\delta_{mq}+\delta_{ql}\delta_{pm}) \\ & +\delta_{lm}(\delta_{ip}\delta_{kq}+\delta_{iq}\delta_{kp})+\delta_{pq}(\delta_{il}\delta_{km} \\ & +\delta_{im}\delta_{kl})]+9[\delta_{lq}(\delta_{im}\delta_{kp}+\delta_{ip}\delta_{km}) \\ & +\delta_{mq}(\delta_{il}\delta_{kp}+\delta_{ip}\delta_{kl})+\delta_{mq}(\delta_{il}\delta_{kp}+\delta_{ip}\delta_{kl}) \\ & +\delta_{lp}(\delta_{im}\delta_{kq}+\delta_{iq}\delta_{km})].\end{aligned} \tag{II.6}$$

In Ref. 25 the three-point correlation function $W_3([\mathbf{r},\mathbf{r}_1,\mathbf{r}_2])$ was expressed in terms of W_2:

$$\begin{aligned}W_3 = {}& \frac{1}{3}(W_2(|\mathbf{r}-\mathbf{r}_1|)W_2(|\mathbf{r}-\mathbf{r}_2|)+W_2(|\mathbf{r}_1-\mathbf{r}|) \\ & \times W_2(|\mathbf{r}_1-\mathbf{r}_2|)W_2(|\mathbf{r}_2-\mathbf{r}|)W_2(|\mathbf{r}_2-\mathbf{r}_1|)).\end{aligned} \tag{II.7}$$

The equation (II.7) is used to calculate all three-point correlation functions.

For example, the three-point correlation function of two random tensors $\hat{B}$ and $\hat{C}$ ($\langle B_{ik}(\mathbf{r})\rangle=\langle C_{ik}(\mathbf{r})\rangle=0$), for example, $\langle B_{ik}(\mathbf{r})B_{lm}(\mathbf{r}_1)C_{pq}(\mathbf{r}_2)\rangle$, is given by the expression (II.5), where B_3 is replaced by the invariant $B_{rs}B_{st}C_{tr}$.

Thus far we have been studying the averages of quantities whose components depend only on the coordinates. Let the averaged quantities also depend on the components of a prescribed vector κ_i. Since in different crystallites the components of this vector are oriented differently relative to the crystallographic axes, the scalar quantities also change from one crystallite to another.

If the components of the averaged tensor $\hat{R}$ depend on the vector κ_i, i.e., $R_{ik}(\mathbf{r},\kappa)$, then the formulas become more complicated. For example,

$$\langle R_{ik}\rangle = R_1\delta_{ik}+R_2\kappa_i\kappa_k, \tag{II.8}$$

where

$$R_1 = \frac{1}{2}[\langle R_{kk}\rangle - \langle R_{ik}\rangle\kappa_i\kappa_k],$$

$$R_2 = \frac{1}{2}[3\langle R_{ik}\rangle\kappa_i\kappa_k - \langle R_{kk}\rangle].$$

To calculate the averages of rank-4 tensors of the form $\langle\hat{R}(\mathbf{r},\kappa)\hat{R}(\mathbf{r},\kappa)\rangle$ the terms containing tensors constructed from the components of κ are added into the expression (II.4) for the tensors $F_{kl;mn}$:

$$A(\delta_{kl}\kappa_m\kappa_n+\delta_{mn}\kappa_k\kappa_l)+B(\delta_{km}\kappa_l\kappa_n+\delta_{kn}\kappa_l\kappa_m)$$

and $C\kappa_k\kappa_l\kappa_m\kappa_n$. To determine the coefficients A, B, and C, aside from the average invariants of the tensors themselves, the following averages are also used:

$$\langle R_{kk}(\mathbf{r},\kappa)R_{mn}(\mathbf{r}_1,\kappa)\kappa_m\kappa_n\rangle,$$

$$\langle R_{kl}(\mathbf{r},\kappa)R_{kn}(\mathbf{r}_1,\kappa)\kappa_l\kappa_n\rangle,$$

$$\langle R_{kl}(\mathbf{r},\kappa)R_{mn}(\mathbf{r}_1,\kappa)\kappa_k\kappa_l\kappa_m\kappa_n\rangle.$$

Similar formulas make it possible to calculate also the averages of tensors of higher rank. The coresponding formulas are too complicated to present here.

9. APPENDIX III. CALCULATION OF THE EFFECTIVE GALVANOMAGNETIC CHARACTERISTICS IN WEAK MAGNETIC FIELDS

To calculate the coefficients appearing in the expression (6) for the ECT up to terms of order $O(\Delta^3)$, we write the tensors $T_{ik}^{(0,n)}$, $T_{ik,p}^{(1,n)}$, and $T_{ik;pq}^{(2,n)}$ for $n=2,3$ up to terms which are quadratic in the magnetic field. Using the definition (9) and Eq. (8) it is easily shown that

$$T_{ik}^{(0,2)} = \frac{1}{\sigma_0}\Delta_{il_1}^{(0)}(\mathbf{r})\Delta_{j_1k}^{(0)}(\mathbf{r}_1)n_{j_1}^{(1)}n_{l_1}^{(1)}; \tag{III.1}$$

$$T_{ik}^{(0,3)}=\frac{1}{\sigma_0^2}\Delta_{il_1}^{(0)}(\mathbf{r})\Delta_{j_1l_2}^{(0)}(\mathbf{r}_1)\Delta_{j_2k}^{(0)}(\mathbf{r}_2)n_{j_1}^{(1)}n_{l_1}^{(1)}n_{j_2}^{(2)}n_{l_2}^{(2)}. \tag{III.2}$$

We recall that $n_i^{(s)}=k_i^{(s)}/k^{(s)}$. Next

$$T_{ik,p}^{(1,2)}=\frac{1}{\sigma_0}[e_{il_1p}\delta a_{pq}(\mathbf{r})\Delta_{j_1k}^{(0)}(\mathbf{r}_1)+e_{j_2kp}\delta a_{pq}(\mathbf{r}_1)\Delta_{il_1}^{(0)}\times(\mathbf{r})]n_{j_1}^{(1)}n_{l_1}^{(1)}; \tag{III.3}$$

$$\begin{aligned}T_{ik,p}^{(1,3)}=\frac{1}{\sigma_0^2}[&e_{il_1p}\delta a_{pq}(\mathbf{r})\Delta_{j_1l_2}^{(0)}(\mathbf{r}_1)\Delta_{j_2k}^{(0)}(\mathbf{r}_2)\\&+e_{j_1l_2p}\delta a_{pq}(\mathbf{r}_1)\Delta_{il_1}^{(0)}(\mathbf{r})\Delta_{j_2k}^{(0)}(\mathbf{r}_2)\\&+e_{j_2kp}\delta a_{pq}(\mathbf{r}_2)\Delta_{il_1}^{(0)}(\mathbf{r})\Delta_{j_1l_2}^{(0)}\\&\times(\mathbf{r}_1)]n_{j_1}^{(1)}n_{l_1}^{(1)}n_{j_2}^{(2)}n_{l_2}^{(2)}.\end{aligned} \tag{III.4}$$

It is convenient to represent $T_{ik;pq}^{(2,n)}$ as a sum of three terms:

$$T_{ik;pq}^{(2,n)}=X_{ik;pq}^{(0,n)}+X_{ik;pq}^{(1,n)}+X_{ik;pq}^{(2,n)}, \tag{III.5}$$

where the tensor $X_{ik;pq}^{(0,n)}$ is related with the dependence of the components of the tensor $q_{ik}^{(s)}$ on H^2:

$$X_{ik;pq}^{(0,n)}=-\frac{S_1+2S_2}{\sigma_0}T_{ik}^{(0,n)}\sum_{r=1}^{n-1}(n_p^{(r)}n_q^{(r)});\quad n=2,3, \tag{III.6}$$

the tensor $X_{ik;pq}^{(1,n)}$ includes terms containing two tensors $\delta\hat{a}$:

$$\begin{aligned}X_{ik;pq}^{(1,2)}&=\frac{1}{\sigma_0}e_{il_1r}e_{j_1ks}\delta a_{rp}(\mathbf{r})\,\delta a_{sq}(\mathbf{r}_1)n_{j_1}^{(1)}n_{l_1}^{(1)},\\X_{ik;pq}^{(1,3)}&=\frac{1}{\sigma_0^2}[e_{il_1r}e_{j_1l_2s}\delta a_{rp}(\mathbf{r})\,\delta a_{sq}(\mathbf{r}_1)\Delta_{j_2k}^{(0)}(\mathbf{r}_2)\\&\quad+e_{j_2kr}e_{j_1l_2s}\delta a_{rp}(\mathbf{r}_2)\,\delta a_{sq}(\mathbf{r}_1)\Delta_{il_1}^{(0)}(\mathbf{r})\\&\quad+e_{il_1r}e_{j_2ks}\delta a_{rp}(\mathbf{r})\,\delta a_{sq}(\mathbf{r}_2)\Delta_{j_1l_2}^{(0)}\\&\quad\times(\mathbf{r}_1)]n_{j_1}^{(1)}n_{l_1}^{(1)}n_{j_2}^{(2)}n_{l_2}^{(2)}.\end{aligned} \tag{III.7}$$

The tensor $X_{ik;pq}^{(2,n)}$ in Eq. (III.5) includes the tensor $\delta S_{ik;pq}(\mathbf{r})$:

$$\begin{aligned}X_{ik;pq}^{(2,2)}&=\frac{1}{\sigma_0}[\delta S_{il_1;pq}(\mathbf{r}))\Delta_{j_1}^{(0)}(\mathbf{r}_1)+\delta S_{j_1kpq}(\mathbf{r}_1))\Delta_{il_1}^{(0)}\\&\quad\times(\mathbf{r})]n_{j_1}^{(1)}n_{l_1}^{(1)},\\X_{ik;pq}^{(2,3)}&=\frac{1}{\sigma_0^2}[\delta S_{il_1;pq}(\mathbf{r})\Delta_{j_1l_2}^{(0)}(\mathbf{r}_1)\Delta_{j_2k}^{(0)}(\mathbf{r}_2)\\&\quad+\delta S_{j_1l_2;pq}(\mathbf{r}_1)\Delta_{il_1}^{(0)}(\mathbf{r})\Delta_{j_2k}^{(0)}(\mathbf{r}_2)\\&\quad+\delta S_{j_2k;pq}(\mathbf{r}_2)\Delta_{il_1}^{(0)}(\mathbf{r})\Delta_{j_1l_2}^{(0)}\\&\quad\times(\mathbf{r}_1)]n_{j_1}^{(1)}n_{l_1}^{(1)}n_{j_2}^{(2)}n_{l_2}^{(2)}.\end{aligned} \tag{III.8}$$

Having determined the tensors $T_{ik}^{(0,n)}$, $T_{ik,p}^{(1,n)}$, and $T_{ik;pq}^{(2,n)}$ for $n=2,3$ we shall now calculate the averages of the contractions of these tensors appearing in the tensor $\hat{Q}^{(0,n)}$. Since the values of $Q^{(0,n)}$ were calculated in Sec. 3 it remains to examine the cases $r=1$, 2. In accordance with Eq. (10), for $r=1$ the averages $\langle T_{ik,p}^{(1,n)}e_{ikp}/6\rangle$ must be calculated. The equations given in Appendix II yield

$$\frac{1}{6}\langle T_{ik,p}^{(1,2)}e_{ikp}\rangle=-\frac{A_2}{9\sigma_0}W_0(|\mathbf{r}-\mathbf{r}_1|);\quad A_2=\Delta_{kl}^{(0)}\delta a_{lk}; \tag{III.9}$$

$$\frac{1}{6}\langle T_{ik,p}^{(1,3)}e_{ikp}\rangle=\frac{A_3}{45\sigma_0^2}[1-3(\mathbf{n}_1,\mathbf{n}_2)^2]W_3([\mathbf{r},\mathbf{r}_1,\mathbf{r}_2]). \tag{III.10}$$

Here $A_3=\Delta_{kl}^{(0)}\Delta_{lm}^{(0)}\delta a_{mk}$. Substituting the expressions (III.9) and (III.10) into the integral (I.3) we obtain the expression for A_H presented in Eq. (14).

To calculate the coefficients $\beta_\parallel^{(1)}$, $\beta_\parallel^{(2)}$, $\beta_\perp^{(1)}$, and $\beta_\perp^{(2)}$, which determine the H dependence of the symmetric part of the ECT (see Eqs. (6) and (15)), we shall calculate the averages of the contractions of the tensors $X_{ik;pq}^{(0,n)}$, $X_{ik,pq}^{(1,n)}$, and $X_{ik;pq}^{(2,n)}$ required for calculating the coefficients $Q_1^{(2,n)}$ and $Q_2^{(2,n)}$ in Eq. (10).

For $n=2$ we obtain from Eqs. (III.6), (II.4), and (II.5)

$$\begin{aligned}\langle X_{kk;pp}^{(0,2)}\rangle&=-\frac{(S_1+2S_2)D_2}{3\sigma_0^2}W_2(|\mathbf{r}-\mathbf{r}_1|),\\\langle X_{kp;kp}^{(0,2)}\rangle&=-\frac{2(S_1+2S_2)D_2}{15\sigma_0^2}W_2(|\mathbf{r}-\mathbf{r}_1|).\end{aligned} \tag{III.11}$$

We recall that $D_2=\Delta_{kl}^{(0)}\Delta_{lk}^{(0)}$. For $n=3$ we obtain

$$\langle X_{kk;pp}^{(0,3)}\rangle=-\frac{(S_1+2S_2)D_3}{15\sigma_0^3}[1+3(\mathbf{n}_1\mathbf{n}_2)^2]W_3([\mathbf{r},\mathbf{r}_1,\mathbf{r}_2]),$$

$$\langle X_{pk;pk}^{(0,3)}\rangle=-\frac{(S_1+2S_2)D_3}{105\sigma_0^3}[19(\mathbf{n}_1\mathbf{n}_2)^2-3]\times W_3([\mathbf{r},\mathbf{r}_1,\mathbf{r}_2]).$$

Here $D_2=\Delta_{pq}^{(0)}\Delta_{qr}^{(0)}\Delta_{rp}^{(0)}$.

Next, we find from Eqs. (III.7)

$$\langle X_{kk;pp}^{(1,2)}\rangle=-\frac{2B_2}{3\sigma_0}W_2(|\mathbf{r}-\mathbf{r}_1|);\quad B_2=\delta a_{rp}\delta a_{rp}. \tag{III.12}$$

If δa_{rp} is a symmetric tensor, then $\langle X_{kp;kp}^{(1,2)}\rangle=0$.

$$\langle X_{kk;pp}^{(1,3)}\rangle=\frac{B_3}{30\sigma_0^2}[13-9(\mathbf{n}_1\mathbf{n}_2)^2]W_3([\mathbf{r},\mathbf{r}_1,\mathbf{r}_2]),$$

$$\langle X_{kp;kp}^{(1,3)}\rangle=-\frac{B_3}{6\sigma_0^2}[1-(\mathbf{n}_1\mathbf{n}_2)^2]W_3([\mathbf{r},\mathbf{r}_1,\mathbf{r}_2]),$$

where the invariant $B_3=\delta a_{rs}\delta a_{st}\Delta_{tr}^{(0)}$.

Finally, we obtain from Eqs. (III.8) for $n=2$

$$\begin{aligned}\langle X_{kk,pp}^{(2,2)}\rangle&=\frac{2Z_1^{(2)}}{3\sigma_0}W_2(|\mathbf{r}-\mathbf{r}_1|);\quad Z_1^{(2)}=\delta S_{kl;pp}\Delta_{kl}^{(0)},\\\langle X_{kp;kp}^{(2,2)}\rangle&=\frac{2Z_2^{(2)}}{3\sigma_0}W_2(|\mathbf{r}-\mathbf{r}_1|);\quad Z_2^{(2)}=\delta S_{kl;kp}\Delta_{lp}^{(0)}.\end{aligned} \tag{III.13}$$

Introducing

$$Z_1^{(3)}=\delta S_{st;rr}\Delta_{tu}^{(0)}\Delta_{su}^{(0)},\quad Z_2^{(3)}=\delta S_{rs;rt}\Delta_{tu}^{(0)}\Delta_{su}^{(0)},$$
$$Z_3^{(3)}=\delta S_{rr,st}\Delta_{tu}^{(0)}\Delta_{su}^{(0)},\quad Z_4^{(3)}=\delta S_{tu;rs}\Delta_{rt}^{(0)}\Delta_{us}^{(0)}, \qquad \text{(III.14)}$$

we obtain

$$\langle X_{kk,pp}^{(2,3)}\rangle=\frac{Z_1^{(3)}}{10\sigma_0^2}[3+(\mathbf{n}_1\mathbf{n}_2)^2]W_3([\mathbf{r},\mathbf{r}_1,\mathbf{r}_2]),$$

$$\langle X_{kp;kp}^{(2,3)}\rangle=\frac{1}{30\sigma_0^2}[\tilde{Z}+\tilde{Z}_u(\mathbf{n}_1\mathbf{n}_2)^2]W_3([\mathbf{r},\mathbf{r}_1,\mathbf{r}_2]),$$

where

$$\tilde{Z}=6Z_2^{(3)}-Z_3^{(3)}+3Z_4^{(3)};\quad \tilde{Z}_n=2Z_2^{(3)}+3Z_3^{(3)}+Z_4^{(3)}.$$

Substituting the expressions (III.9)–(III.14) into the integral determining $w_{ik}^{(2)}(\mathbf{H})$ and $w_{ik}^{(3)}(\mathbf{H})$ (see Eq. (I.3)) we obtain the series (I.2) with accuracy up to terms of order $O(\Delta^3)$ in the anisotropy and $O(H^3)$ in the magnetic field:

$$W_{ik}\approx w_{ik}^{(2)}(\mathbf{H})+w_{ik}^{(3)}(\mathbf{H}), \qquad \text{(III.15)}$$

where

$$w_{ik}^{(n)}(\mathbf{H})=w_0^{(n)}\delta_{ik}+Hw_1^{(n)}e_{ikq}\kappa_q+H^2(w_2^{(n;1)}\delta_{ik}+w_2^{(n;2)}\kappa_i\kappa_k).$$

Here

$$w_0^{(2)}=\frac{D_2}{9\sigma_0};\quad w_0^{(3)}=-\frac{D_3}{30\sigma_0^2}(1+F_3^{(\mathrm{st})}). \qquad \text{(III.16)}$$

$$w_1^{(2)}=-\frac{A_2}{9\sigma_0};\quad w_1^{(3)}=-\frac{2A_3}{15\sigma_0^2}(1-3F_3^{(\mathrm{st})}), \qquad \text{(III.17)}$$

$$w_2^{(2;1)}=\frac{2}{45}\left\{-\frac{4(S_1+2S_2)}{5\sigma_0^2}D_2+\frac{1}{\sigma_0}(2Z_1^{(2)}-Z_2^{(2)}-2B_2)\right\};$$
$$w_2^{(2;2)}=\frac{1}{45}\left\{-\frac{S_1+2S_2}{5\sigma_0^2}D_2+\frac{2}{\sigma_0}(-Z_1^{(2)}+3Z_2^{(2)}+B_2)\right\}. \qquad \text{(III.18)}$$

Finally,

$$w_2^{(3;1)}=-\frac{(S_1+2S_2)D_3}{35\sigma_0^3}\left(1-\frac{1}{9}F_3^{(\mathrm{st})}\right)+\frac{B_3}{450\sigma_0^2}(31-23F_3^{(\mathrm{st})})+\frac{1}{450\sigma_0^2}\times[(18Z_1^{(3)}-\tilde{Z})+(6Z_1^{(3)}-\tilde{Z}_n)F_3^{(\mathrm{st})}], \qquad \text{(III.19)}$$

$$w_2^{(3;2)}=\frac{2(S_1+2S_2)D_3}{105\sigma_0^3}\left(1-\frac{5}{3}F_3^{(\mathrm{st})}\right)-\frac{2B_3}{225\sigma_0^2}(7-6F_3^{(\mathrm{st})})+\frac{1}{150\sigma_0^2}\times[(-3Z_1^{(3)}+\tilde{Z})+(-Z_1^{(3)}+\tilde{Z}_n)F_3^{(\mathrm{st})}].$$

So, the equations (III.15)–(III.19) determine the tensor $W_{ik}(\mathbf{H})$ to $O(\hat{\Delta}^3)$. Now, to use Eq. (I.1) for the ETC the tensor $V_{ik}^{-1}(\mathbf{H})$ must be calculated in the same approximation. However, it follows from the expression (I.5) that $V_{ik}^{-1}(\mathbf{H})=\delta_{ik}+\delta V_{ik}^{-1}(\mathbf{H})$, where $\delta V_{ik}^{-1}(\mathbf{H})$ takes account of the anisotropy dependence of the components of this tensor. Just like the components of the tensor $W_{ik}(\mathbf{H})$, the components of the tensor $\delta V_{ik}^{-1}(\mathbf{H})$ contain terms of second and third order in the anisotropy. Therefore the components of the tensor $\delta V_{ij}^{-1}(\mathbf{H})W_{jk}(\mathbf{H})$ are at least of fourth order in the anisotropy. Taking account of such terms exceeds the accuracy of the approximation used. Thus, if only terms of third order in the anisotropy are used, then

$$\sigma_{ik}^{\mathrm{eff}}=\langle\sigma_{ik}(\mathbf{H})\rangle-W_{ik}(\mathbf{H}). \qquad \text{(III.20)}$$

In conclusion, we shall write out explicitly the formulas for $\beta_{\parallel}^{(1)}$, $\beta_{\parallel}^{(2)}$, $\beta_{\perp}^{(1)}$, and $\beta_{\perp}^{(2)}$ appearing in the coefficients $\alpha_{\parallel}$ and $\alpha_{\perp}$ describing the dependence of the symmetric part of the ECT on the magnetic field. For the longitudinal conductivity

$$\beta_{\parallel}^{(1)}=-\frac{S_1+2S_2}{25\sigma_0^2}\left(D_2+\frac{5D_3}{21\sigma_0}\right)+\frac{2}{45\sigma_0}(Z_1^{(2)}+2Z_2^{(2)}-2B_2^{(2)})+\frac{B_3}{150\sigma_0^2}+\frac{1}{150\sigma_0^2}\left(3Z_1^{(3)}+4Z_2^{(3)}-\frac{2}{3}Z_3^{(3)}+2Z_4^{(3)}\right), \qquad \text{(III.21)}$$

$$\beta_{\parallel}^{(2)}=-\frac{(S_1+2S_2)D_3}{35\sigma_0^3}+\frac{B_3}{450\sigma_0^2}+\frac{1}{150\sigma_0^2}\left(Z_1^{(3)}+\frac{4}{3}Z_2^{(3)}+2Z_3^{(3)}+\frac{2}{3}Z_4^{(3)}\right),$$

and for the transverse conductivity

$$\beta_{\perp}^{(1)}=-\frac{S_1+2S_2}{5\sigma_0^2}\left(\frac{8}{45}D_2+\frac{D_3}{7\sigma_0}\right)+\frac{2}{45\sigma_0}(2Z_1^{(2)}-Z_2^{(2)}-2B_2^{(2)})+\frac{17B_3}{450\sigma_0^2}+\frac{1}{300\sigma_0^2}\left(11Z_1^{(3)}+2Z_2^{(3)}-\frac{1}{3}Z_3^{(3)}+Z_4^{(3)}\right), \qquad \text{(III.22)}$$

$$\beta_{\perp}^{(2)}=\frac{(S_1+2S_2)D_3}{315\sigma_0^3}-\frac{11B_3}{450\sigma_0^2}+\frac{1}{300\sigma_0^2}\left(3Z_1^{(3)}+\frac{2}{3}Z_2^{(3)}+Z_3^{(3)}+\frac{1}{3}Z_4^{(3)}\right).$$

In Eqs. (III.21) and (III.22) the invariants D_2, D_3, B_2, and B_3 are given by Eqs. (III.11) and (III.12); $Z_1^{(2)}$ and $Z_2^{(2)}$ are determined by Eqs. (III.13) and $Z_r^{(3)}$ $(r=1,2,3,4)$ by Eq. (III.14).

10. APPENDIX IV. COMPARISON OF FLUCTUATION CORRECTIONS DUE TO THE HALL CONDUCTIVITY FOR AN ISOTROPIC NONUNIFORM METAL AND A POLYCRYSTAL (STRONG FIELDS)

It is shown in Ref. 11 that perturbation theory cannot be used to calculate the transverse effective conductivity of an isotropic nonuniform metal in strong magnetic fields. In such a conductor $\delta_\perp^{\text{eff}} \propto 1/H^{4/3}$. The source of the unusually large value of $\sigma_\perp^{\text{eff}}$ are fluctuations of the Hall component of the local conductivity tensor. To simplify the calculations we shall assume that only the Hall components of the conductivity tensor undergo fluctuations. We shall compare the values of $\omega_\perp^{(2)} = (w_{kk}^{(2)} - w_{ik}^{(2)}\kappa_i\kappa_k)/2$, due to such fluctuations, for an isotropic nonuniform metal and a polycrystal.

According to Eq. (28), in this case the LCT of an isotropic nonuniform metal is

$$\sigma_{ik}^{(is)}(\mathbf{H},\mathbf{r}) = \sigma_0\left[\kappa_i\kappa_k + \frac{1}{h}e_{ikl}\kappa_l + \frac{1}{h^2}\delta_{ik}\right] + \Delta_{ik}^{(is)} \times(\mathbf{H},\mathbf{r}); \quad \Delta_{ik}^{(is)}(\mathbf{H},\mathbf{r}) = \frac{\Delta(\mathbf{r})}{h}e_{ikl}\kappa_l. \quad \text{(IV.1)}$$

For a polycrystal we shall assume that the LCT is

$$\sigma_{ik}^{(p)}(\mathbf{H},\mathbf{r}) = \langle\sigma_{ik}^{(p)}(\mathbf{H})\rangle + \Delta_{ik}^{(p)}(\mathbf{r},\mathbf{H}); \quad \Delta_{ik}^{(p)}(\mathbf{r},\mathbf{H}) = \frac{1}{H}e_{ikl}\delta a_{lm}^{(1)}(\mathbf{r},\kappa)\kappa_m, \quad \text{(IV.2)}$$

where the tensor $\langle\sigma_{ik}^{(p)}(\mathbf{H})\rangle$ is given by Eq. (21) and the fluctuating tensor $\delta a_{lm}^{(1)}(\mathbf{r},\kappa)$ satisfies Eq. (23).

We shall now calculate the first fluctuation correction $\omega_\perp^{(is;2)}$ for an isotropic nonuniform metal (see Eq. (I.3)). The tensor $q_{ik}^{(is)}$ appearing in the expression for $\omega_\perp^{(is;2)}$ is

$$q_{ik}^{(is,1)} = \frac{n_i^{(1)}n_k^{(1)}}{\sigma_0[(\kappa\mathbf{n}^{(1)})^2 + 1/h^2]}. \quad \text{(IV.3)}$$

Using the expression (IV.1) it is easy to verify that the contraction

$$\Delta_{il_1}^{(is)}(\mathbf{r},\mathbf{H})\Delta_{j_1k}^{(is)}(\mathbf{r},\mathbf{H})\kappa_i\kappa_k = 0.$$

This means that $w_\perp^{(is;2)} = w_{kk}^{(is;2)}/2$. Assuming the conductor to be statistically homogeneous on the average and isotropic we have

$$\langle\Delta_{kl_1}^{(is)}(\mathbf{r})\Delta_{j_1k}^{(is)}(\mathbf{r}_1)\rangle = -\langle\Delta^2\rangle(\delta_{j_1l_1} - \kappa_{j_1}\kappa_{l_1})W_2(|\mathbf{r}-\mathbf{r}_1|),$$

where $W_2(|\mathbf{r}-\mathbf{r}_1|)$ is a correlation function, and we obtain

$$w_\perp^{(is;2)} = -\frac{\langle\Delta^2\rangle}{4\sigma_0h^2}\int_{-1}^{1}dx_1\frac{1-x_1^2}{x_1^2+1/h^2} \approx -\frac{\langle\Delta^2\rangle\pi}{4\sigma_0h}; \quad x_1 = \kappa\mathbf{n}^{(1)}. \quad \text{(IV.4)}$$

The derivation of Eq. (IV.4) took account of the equality

$$W_2(0) = \int d^3k W_2(k) = 1.$$

Therefore $w_\perp^{(is;2)} \propto 1/h$, while $\langle\sigma_\perp^{is}\rangle \propto 1/h^2$. It is evident that for $n>2$ the expressions for $w_\perp^{(is;n)}$ depend on the statistics of the distribution of the random function $\Delta(\mathbf{r})$. We have shown that if this random function is a Gaussian function (only the values of $w_\perp^{(is;n)}$ with even numbers n are different from zero), $w_\perp^{(is;4)} \propto \langle\Delta^2\rangle^2/\sigma_0^3$.

So, the average transverse conductivity is of the order of σ_0/h^2, and because of fluctuations of the Hall component of the LCT the terms $w_\perp^{(is;n)}$ in the series for the tensor W_{ik} are of the order of $(\langle\sigma^n\rangle)h^{n/2-2}$. For $h \gg 1$ this series converges only if $h\langle\Delta^2\rangle/\sigma_0^2 \ll 1$. This inequality corresponds to the limits of applicability indicated by Dreĭzin and Dykhne for the perturbation theory for calculating the effective transverse conductivity of an isotropic nonuniform conductor.

It could appear that even in polycrystals when the fluctuations of the Hall components of the LCT are taken into acount fully, resulting in the appearance of terms of the order of $1/H^n$ $(n>2)$ in the product

$$\Delta_{il_1}(\mathbf{H},\mathbf{r})\Delta_{j_1l_2}(\mathbf{H},\mathbf{r}_1)\ldots\Delta_{j_{n-1}k}(\mathbf{H},\mathbf{r}_{n-1})$$

terms which are large compared with terms of order $1/H^2$ will appear in the expressions for $w_\perp^{(n)}$. However, this is not so because $\delta a_{ik}^{(1)}\kappa_i\kappa_k = 0$.

To check this assertion it is sufficient to calculate the expressions for $w_\perp^{(p;2)}$ for the case where the fluctuations of the LCT are due to the tensor $\Delta_{ik}^{(p)}(\mathbf{r},\mathbf{H})$ (IV.2).

First we calculate $w_\perp^{(p;2)}$. In this case $\Delta_{il_1}^{(p)}(\mathbf{r})\Delta_{j_1k}^{(p)}(\mathbf{r}) = e_{il_1m}e_{j_1km_1}\delta a_{mn}^{(1)}\kappa_n\delta a_{m_1n_1}^{(1)}\kappa_{n_1}$. Since Eq. (23) is satisfied, the average

$$\langle\delta a_{mn}^{(1)}\kappa_n\delta a_{m_1n_1}^{(1)}\kappa_{n_1}\rangle = \frac{\langle A\rangle}{2}(\delta_{mn_1} - \kappa_m\kappa_{m_1}). \quad \text{(IV.5)}$$

Now, using the expression (26) for the tensor $q_{l_1j_1}^{(1)}$ we obtain

$$w_\perp^{(p;2)} = -\frac{\langle A\rangle}{2H^2\langle S\rangle}\int d^3k_1\frac{(\kappa\mathbf{n}_1)^2W_2(k_1)}{[(\kappa\mathbf{n}_1)^2+\alpha^2]} \approx -\frac{\langle A\rangle}{2H^2\langle S\rangle},$$

(compare with Eq. (IV.4)). Here A is given by the expression (38). The term $w_\perp^{(p;2)}$ was taken into account in the summation of the series (41) for $W_\perp$.

As we saw in Sec. 4, when the expansion (30) is used the values of $w_\perp^{(2n-1)}$ are different from zero (see Eq. (39)). However if the fluctuations of the LCT are given by the tensor $\Delta_{ik}^{(p)}(\mathbf{r},\mathbf{H})$, all odd corrections vanish $w_\perp^{(p;2n-1)} = 0$. This is because all averages of an odd number of vectors $\delta a_{mn}^{(1)}\kappa_n$ vanish because of Eq. (23). Specifically, $w_\perp^{(p;3)} = 0$.

The the method presented in Appendix II to calculate averages can be used to calculate the expressions for $w_\perp^{(p;2n)}$ for arbitrary n. However this is a very difficult task. We have verified that $w_\perp^{(p;4)} \sim 1/H^3$. It is hoped that because of the specific form of the averages $\langle\delta a_{mn}\delta a_{m_1n_1}\ldots\delta a_{m_{2n-1}n_{2n-1}}\kappa_n\kappa_{n_1}\ldots\kappa_{n_{2n-1}}\rangle$ the corrections $w_\perp^{(p;2n)}$ for all $n>2$ will be small in the parameter $1/H$ compared with terms of the order of $1/H^2$, taken into account in the expression (42b) for $W_\perp$. If so, then our expression (42b) for $\sigma_\perp^{\text{eff}}$ is *exact* within the approximation studied.

*E-mail: kaganova@hppi.troitsk.ru
**E-mail: MKaganov@compuserve.com

[1)] Usually, this occurs in the case of large-grain polycrystals. For example, in most cases, when describing the electronic properties of polycrystals of metals the electron mean-free path length l must be much shorter than the average crystallite size a.

[2)] The impedance is a rank-2 two-dimensional tensor.

[3)]It is this last inequality that distinguishes the symmetry under a transposition of the indices of the tensor $S_{ik;lm}$ from the symmetry of, for example, the tensor of elastic moduli of a single crystal.
[4)]The dependence of τ on ε does not destroy the symmetry of u_{ik}.

[1] I. M. Lifshitz, M. Ya. Azbel', and M. I. Kaganov, Zh. Éksp. Teor. Fiz. **31**, 63 (1956) [JETP **4**, 41 (1957)].
[2] I. M. Lifshitz and V. G. Peschanskiĭ, Zh. Éksp. Teor. Fiz. **35**, 1251 (1958) [JETP **8**, 875 (1959)].
[3] I. M. Lifshitz and V. G. Peschanskiĭ, Zh. Éksp. Teor. Fiz. **38**, 188 (1960) [JETP **11**, 137 (1960)].
[4] E. S. Borovik, Zh. Eksp. Teor. Fiz. **25**, 91 (1952).
[5] E. S. Borovik, Fiz. Met. Metalloved. **2**, 33 (1956).
[6] Yu. P. Gaĭdukov, *Topology of Fermi Surfaces (Reference Table)*. Appendix III to Ref. 7.
[7] I. M. Lifshitz, M. Ya. Azbel', and M. I. Kaganov, *Electron Theory of Metals*, Consultants Bureau, New York (1973) [Russian original, Nauka, Moscow (1971)].
[8] D. Shoenberg, *Magnetic Oscillations in Metals*, Cambridge University Press, New York (1984) [Russian translation, Mir, Moscow (1986)].
[9] P. L. Kapitza, *Change of the Electric Conductivity in Strong Magnetic Fields. Selected Works*, Nauka, Moscow (1988).
[10] L. V. Shubnikov and W. J. de Haas, Leiden Commun. **19**, 2071 (1930).
[11] Yu. A. Dreĭzin and A. M. Dykhne, Zh. Éksp. Teor. Fiz. **63**, 242 (1972) [JETP **36**, 127 (1973)].
[12] M. I. Kaganov and V. G. Peschanskii, Phys. Rep. **372**, 445 (2002).
[13] I. M. Kaganova and M. I. Kaganov, Lazar Physics **14**, 416 (2004).
[14] I. M. Lifshitz and L. N. Rozentsveĭg, Zh. Éksp. Teor. Fiz. **16**, 967 (1946).
[15] I. M. Lifshitz and G. D. Parkhomovskiĭ, Zh. Éksp. Teor. Fiz. **20**, 175 (1950).
[16] I. M. Lifshitz, M. I. Kaganov, and V. M. Tsukernik, in *Selected Works of I. M. Lifshitz*, Nauka, Moscow (1987).
[17] I. M. Kaganova and A. A. Maradudin, Phys. Scr. **T44**, 104 (1992).
[18] I. M. Kaganova and M. I. Kaganov, Fiz. Nizk. Temp. **22**, 929 (1996) [Low Temp. Phys. **22**, 712 (1996)].
[19] I. M. Kaganova, Phys. Rev. B **51**, 5333 (1995).
[20] A. M. Dykhne and I. M. Kaganova, Physica A **241**, 154 (1997).
[21] M. A. Leontovich in *Investigation of the Propagation of Radio Waves*, Gostekhizdat, Moscow (1948).
[22] I. M. Kaganova and M. I. Kaganov, Phys. Rev. B **63**, 054202 (2001).
[23] L. D. Landau and E. M. Lifshitz, *Electrodynamics of Continuous Media*, Pergamon Press, New York (1984) [Russian original, Nauka, Moscow (1982)].
[24] E. M. Lifshitz and L. P. Pitaevskiĭ, *Physical Kinetics*, Pergamon Press, New York (1981) [Russian original, Nauka, Moscow (1979)].
[25] I. M. Kaganova, Phys. Lett. A **312**, 108 (2003).
[26] M. I. Kaganov, Zh. Eksp. Teor. Fiz. **77**, 250 (1979) [JETP **50**, 128 (1979)].
[27] *Physical Encyclopedia*, Vol. 3, Bol'shaya Rossiĭskaya éntsiklopediya, Moscow (1992).
[28] M. I. Kaganov and V. G. Peschanskiĭ, *Investigation of the Electronic Spectrum in Metals*, Naukova dumka, Kiev (1965).
[29] A. G. Fokin, Usp. Fiz. Nauk **166**, 1096 (1966) (*sic*).
[30] G. T. Avanesyan and M. I. Kaganov, Zh. Éksp. Teor. Fiz. **63**, 1472 (1972) [JETP **36**, 780 (1973)].
[31] G. T. Avanesyan and M. I. Kaganov, Zh. Éksp. Teor. Fiz. **69**, 999 (1975) [JETP **42**, 508 (1975)].

Translated by M. E. Alferieff

Fluctuations and nonuniformities in strongly correlated electronic systems

L. A. Boyarskiĭ* and S. P. Gabuda

Institute of Inorganic Chemistry, Siberian Branch of the Russian Academy of Sciences, 3 pr. Akad. Lavrent'eva, Novosibirsk 630090, Russia; Novosibirsk State University, 2 ul. Pirogova, Novosibirsk, 630090, Russia

S. G. Kozlova

Institute of Inorganic Chemistry, Siberian Branch of the Russian Academy of Sciences, 3 pr. Akad. Lavrent'eva, Novosibirsk 630090, Russia

(Submitted June 9, 2004; revised August 11, 2004)
Fiz. Nizk. Temp. **31**, 405–411 (March–April 2005)

A general approach to describing a number of phenomena in strongly correlated electronic systems is examined. These phenomena are united by the fluctuation nature of the effects and the presence (or appearance) of nonuniform charge and/or spin densities. The following problems are discussed: the nature of ferromagnetism in *d* metals; the reasons for the appearance of metallic conductivity in oxides of heavy *p* metals; and, the nature of the pseudogap state in high-temperature superconductors. © *2005 American Institute of Physics.*
[DOI: 10.1063/1.1884434]

1. INTRODUCTION

The purpose of this work is to formulate a general approach to the description of phenomena, which at first glance appear to be of different nature, in strongly correlated electronic systems. These phenomena are united by the fluctuation nature of the effects on the one hand and the presence (or appearance) of nonuniform charge and/or spin density on the other.

We shall first indicate the range of phenomena which will be used to illustrate the discussions below.

A paradox due to the contradictory data from magnetic measurements on ferromagnetic metals above the Curie point and x-ray spectral experiments has been discussed for several decades in the literature. In the first case the magnetic susceptibility was described by the Curie-Weiss law, which attested to localized moments of unfilled shells, and in the second case the x-ray spectra indicated the presence of a conduction band containing these same electrons. This concerned, primarily, $3d$ metals but a similar though less evident divergence was also observed for rare-earth elements.

It is known that many oxides of transition elements possess metallic conductivity. At the same time the oxides of heavy *p* metals are insulators, which is consistent with the understanding of their band structure. However, the conductivity of lead dioxide is found to be quite high, essentially, ''metallic.'' [1] This is probably not the only case (some data indicate possible ''metallicity'' in Tl_2O_3 and Bi_2O_5).

Here are several other examples of the influence of nonuniform electronic states on the properties of a material. In his well-known work[2] R. O. Zaĭtsev calculated the phase diagram of the titanium-boron system and showed that the superconducting state in this system can arise only in nonstoichiometric compositions and definitely not in diboride. The nonuniform distribution of the $5f$ electron density results in curious effects in uranium compounds (systems with heavy fermions).[3,4]

Here is one other, and by no means the last, example. In high-temperature superconductors, according to the phase diagram, as the oxygen index changes the insulating antiferromagnetic phase is replaced by a metallic phase and then by a superconducting phase which does not possess an ordered magnetic structure. Above the superconducting transition point a pseudogap phase was observed to appear (a substantial decrease of the electronic density of states) for oxygen content below the optimal value. Many investigators interprete this phenomenon as a ''precursor'' to superconductivity—the appearance of uncorrelated Cooper pairs. However, different points of view also exist concerning the nature of this phenomenon.

It should be noted that these phenomena so far have not been given a sufficiently simple and, most importantly, general explanation. We believe that a general approach can be developed on the basis of the well-known Friedel model of virtual electronic levels,[5] which Friedel developed, generally speaking, while constructing a model of ferromagnetism of free electrons and also the magnetic properties of spin glasses. In light of the problems which we have examined it is only necessary to take into account in Friedel's model the possibility of a dynamical picture of the appearance and dissipation of virtual levels. These considerations in one form or another have been discussed repeatedly in the scientific literature but as far as we know a general approach to the phenomena described below has not been developed.

2. FERROMAGNETIC METALS

As already mentioned above, according to x-ray spectral measurements, in iron-group transition metals electrons of the partially filled $3d$ shell are delocalized and form a narrow band. However, magnetic measurements show that the susceptibility of elements in the iron triad satisfy the Curie-Weiss law above the Curie point, which attests to localization of the corresponding groups of electrons. The effective mag-

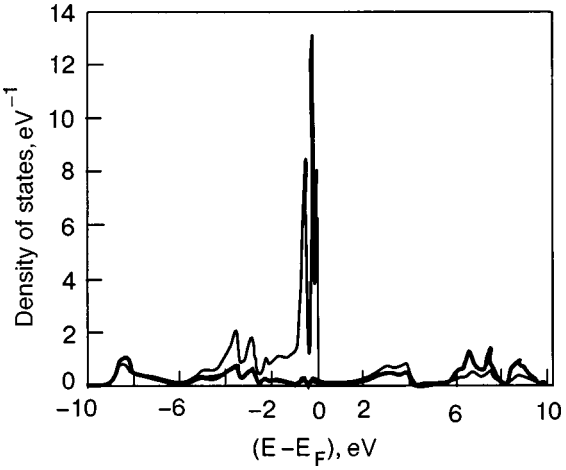

FIG. 1. Computed electron density of states in lead dioxide with stoichiometric composition: heavy line—Pb; fine line—O.[1]

netic moment per metal atom is found to be different from the nominal value. Ordinarily, this fact is attributed to the *s-d* exchange interaction (the well-known Vonsovskiĭ-Turov model). We believe that we are dealing with dynamic, time-averaged localization of electrons. Here delocalized *d* and *s* electrons can be trapped in *d* levels. The proposed hypothesis fits completely into Friedel's concept of virtual electronic levels.

The various models which are given in all monographs on ferromagnetism for the exchange interaction of conduction electrons and which admit the appearance of Curie-Weiss behavior of the paramagnetic susceptibility are well known. These models are based on a stationary ''distribution'' of *d* electrons (band-level). However, our considerations also appear to be valid.

It is not superfluous to note that the sensitivities of the magnetic and spectroscopic methods with respect to different states of electrons are different. Indeed, the ''Curie-Weiss'' susceptibility of localized $3d$ electrons is much greater than the Pauli contribution. At the same time spectroscopic methods ''feel'' delocalized electrons well.

The concept of partial delocalization also appears in recently published results concerning the states of $5f$ electrons in uranium compounds of the type UPt_3.[6] Fulde concluded that two $5f$ electrons remain localized and one moves into the conduction band.[3] Zvyagin has published more rigorous analysis.[4] He studied the influence of the anisotropy of hybridization of $5f$ electrons with itinerant electrons.

3. HEAVY-METAL OXIDES

We shall give the following example as an illustration of the influence of nonuniformities on the behavior of a strongly correlated system. Figure 1 shows the computed energy spectrum of stoichiometric lead dioxide.[1] It is evident that the Fermi level lies near the top boundary of the filled band. We believe that the deviations from stoichiometry result in electron tunneling into the valence band, i.e. the formation of virtual levels and, as a consequence, the appearance of metallic conductivity. This hypothesis agrees well with the fact that when lead dioxide is synthesized an entire set of oxides (up to 15) with different stoichiometric composition is always obtained.

The problem associated with the stoichioimetry of the synthesized compound arises quite often. A standard example is niobium stannide Nb_3Sn. For any synthesis technology it is always stoichiometric, while Nb_3Ge is obtained in a form corresponding to the formula presented only when doped with aluminum. However, this problem, in spite of its importance (and the fact that it has not been solved), falls outside the scope of the present paper. Of course, it can be conjectured that fluctuations of the electronic structure play an important role in this question. In this connection we should mention Ref. 7, which is devoted to an analysis of the experimental paradox: calculations show that the two compounds Ni_3Al and Ni_3Ga, which have very similar structures and electronic characteristics, should possess ferromagnetic properties. However, the first compound is a weak ferromagnet and the second is a paramagnet. The authors of the work cited attribute this paradox precisely to strong fluctuations in Ni_3Ga.

Here are two other standard examples of the special features appearing in the physical properties of materials as a result of spatial nonuniformities. It is well known that metallic samarium crystallizes in a modified hexagonal structure (the so-called ''samarium lattice''), which results in the presence of two types of sites which are coordinated differently with one another. The superexchange interaction in these two subsystems is so different that the metal exhibits two Néel points differing by a factor of approximately 10.

Here is a second example: at the metal-insulator phase transition in completely uniform and stoichiometric vanadium dioxide the tetravalent vanadium ions split into two groups—tri- and pentavalent.[8]

4. PSEUDOGAP STATES

We now turn to the problem of high-temperature superconductivity. We recall that the typical representatives of HTSCs—perovskite-like cuprates—are compounds which are by no means stoichiometric. Even the most perfect single crystals (no twins) cannot be regarded as uniform with respect to the concentrations of the components. This cannot help but affect the behavior of their charge subsystem.

In the last few years researchers have turned their attention to one specific region on the phase diagram of cuprate HTSCs (typical formula $YBa_2Cu_3O_{6+x}$). For suboptimal oxygen content (from the standpoint of superconducting properties), above the superconducting transition temperature right up to a certain value $T^*(x)$, where x is the oxygen index, a low electron density of states is observed experimentally. Spectroscopic and resonance methods of investigation were used. It is commonly assumed that at high (approximately from T_c up to $2T_c$) temperatures a pseudogap state, a kind of ''precursor'' to superconductivity, occurs. In a number of publications it was assumed *a priori* that incoherent Cooper pairs exist in this region. Looking ahead somewhat we note that many diagrams contain two phase boundaries—an ''upper'' pseudogap (temperature $T^{cr}(x)$—where deviations of the resistance from the linear

law start) and a ''lower'' pseudogap (temperature $T^*(x)$). We shall examine this question below.

Publications on this problem first appeared only ten years ago. That is when the idea of a decrease of the density of states in the normal phase of a superconductor arose. Since then tens if not hundreds of works have been published, but the question of the nature of the pseudogap state remains open. One of the first reviews of experimental works was published in 1999.[9] This review is devoted primarily to the question of the magnitude of the pseudogap. Among other things, the temperature-independence of the width of the pseudogap was examined; this did not correlate with the known fact that such a dependence occurs for the superconducting gap. It was asserted at the same time that both characteristics have a similar *d* nature. The authors base their conclusions on published experiments using angle-resolved photoemission (ARPES), tunneling spectroscopy, nuclear magnetic resonance, and the transport properties and heat capacity. The experiments were performed primarily on yttrium and bismuth cuprates. According to different data the values of the pseudogap, specifically, for the Bi-2221 cuprates, ranged from 20 to 40 meV depending on the degree of doping. We note that a very recently published work[10] gives approximately the same values for the pseudogap in the sodium-cobalt oxide system—$Na_{0.35}CoO_{2.1}3H_2O$ and $Na_{0.35}CoO_{2.0}7H_2O$.

Discussions of two questions are continuing in connection with the problem of the pseudogap state. One question asks whether the curve $T^*(x)$ is a phase transition line, and the second and more general question asks what the nature of this state is. We recall that the characteristic values of the superconducting transition temperature for yttrium cuprates do not exceed 98 K, and a pseudogap ''opens'' near 220 K.

The following can be said about the first question. An investigation of underdoped thulium cuprates[11] led to the discovery of a feature in the electronic contribution to the heat capacity that is characteristic for a phase transition. Measurements were performed on four samples with different oxygen indices. The signal point here is the fact that the anomaly sought was observed only for two samples with low oxygen content. At the same time, based on general considerations, the corresponding feature should be observed in all samples. We add that the authors of Ref. 12 did not observe any anomaly of the electronic contribution to heat capacity. It should be noted that by no means the entire charge system undergoes a transition into a new state; only a small part of the charge system does so. This makes it is difficult to expect anomalies with magnitudes that are commonly observed with phase transitions. However, irrespective of the specific difference between the high- and low-temperature phases it can only be concluded, as many investigators have, that the transition is of a fluctuation character. Incidently, the Hubbard model was recently ued to study the fluctuation nature of the pseudogap phenomenon.[13]

Quite a long time ago, in a description of a transition of liquid helium into the superfluid state, the idea was advanced that two forms of ordering exist in nature: spatial ordering (for example, crystallization) and velocity ordering (Bose condensation). Obviously, this general approach can also be used to analyze the genesis of a pseudogap state, if the appearance of this state is regarded as a phase transition. Indeed, two points of view concerning the mechanism resulting in a decrease of the electronic density of states predominate in the literature. According to one point of view, as noted above, some charge carriers in a special region of the phase diagram being studied form uncorrelated pairs (in other words, partial velocity ordering), which do not result in the appearance of a macroscopic superconducting phase. The other version is based on the idea that partial charge-carrier localization accompanied by the formation of comparatively long-lived antiferromagnetic clusters (magnetic ordering-spatial ordering) occurs in the pseudogap region. Which type of ordering occurs? For systems with many degrees of freedom the answer cannot be unique, because different mechanisms can have close energy characteristics.

Sadovskiĭ's review[14] contains many citations to experimental and theoretical works concerning the problem of a pseudogap in HTSCs. The most detailed information has been obtained from angle-resolved photoemission experiments. It should be noted that the experiments only confirm the presence of the indicated state above the superconducting transition point, but the ''genetic'' question remains unsolved, i.e., the results concern only the substantial decrease of the electron density of states when the temperature drops below T^*. However, the question of the nature of the pseudogap state remains open.

Sadovskiĭ believes that no phase transition occurs at the indicated temperature, and the quantity T^* merely determines the scale of the energy below which pseudogap features appear in the properties of matter. We believe that this result can be debated, because as noted above the fluctuation character of the phenomenon could be related with some ''partial'' phase transition of the electronic subsystem. In addition, an anomaly of the electronic contribution to the heat capacity has been observed experimentally.[11]

Returning to the question of the magnetic origin of the pseudogap, it should be noted that inelastic neutron scattering experiments have proved the existence of antiferromagnetic clusters.[15] These results were also confirmed subsequently.[16] One of the present authors, just as the author of Ref. 11, participated in an investigation of the magnetoresistance of underdoped YBCO single crystals.[17] It was shown that in the intermediate oxygen concentration range—between the boundary of the antiferromagnetic insulating state and the optimally doped cuprate—the magnetoresistance contains, in addition to a quadratic contribution, a contribution which is linear in the magnetic field intensity. This corresponds to the behavior of the indicated characteristic in antiferromagnetic metals.[18] Characteristically, the coefficient of the linear term in the magnetoresistance depends on the oxygen concentration—it decreases with decreasing oxygen concentration, becoming negligibly small at optimal doping. It can be concluded that the experiments performed confirm the results of Ref. 15 concerning the existence of antiferromagnetic dynamical clusters.

It can be inferred on the basis of the experimental facts cited above[15–17] that when the boundary of the region studied is crossed from the high-temperature side partial Bose condensation does not occur but rather partial carrier localization occurs, resulting in a decrease in the density of states on the

one hand and the appearance of fluctuating antiferromagnetic fragments on the other. In a number of works (see, for example, Refs. 19–21) pseudogap phenomena are discussed precisely from the ''magnetic'' point of view.

In summary, it is entirely possible that there exists a magnetic mechanism for the appearance of a pseudogap (fluctuation spatial ordering). Is this concept consistent with a phase transition at T^*? In our view, no. The important fact is that ordering (even though partial) and not a specific form of ordering is present. Does this preclude the mechanism of uncorrelated-pair formation (fluctuation velocity ordering)? In our view, also no. As indicated above, the energetics of both processes are probably very similar, and it is hardly possible today to draw an unequivocal conclusion. To complete the picture we note that the ''superconducting'' model for the appearance of a pseudogap is given its due in Refs. 22 and 23. It should be noted that the explanation of the anomalies observed in various properties of HTSCs in the normal phase within the framework of the model of uncorrelated Cooper pairs is based, as a rule, not on unequivocal experimental facts but rather on particular theoretical models. In this connection we note the recently published Ref. 24 where the anomalous behavior of the magnetic moment of lanthanum-strontium cuprate substantially above the superconducting transition temperature is described. It was noted that the moment changes by several percent, and the magnetic past history had a large influence on the effect. The results are strongly reminiscent of the behavior of a spin glass, which can probably be easily explained by the magnetic origin of the anomaly (localization). However, the authors of Ref. 24 believe that everything has to do with the appearance of uncorrelated Cooper pairs. However, no direct proof of this assertion is given. At the same time, in our opinion, the published result attests to the fact that partial carrier localization should not necessarily give rise to antiferromagnetic ordering. In nonuniform systems frustrations resulting in spin-glass freezing of magnetic moments are entirely likely. However, if the corresponding exchange interaction is weak, then we shall obtain an additional paramagnetic component of the moment.

When considering theoretical models of the genesis of a pseudogap one cannot help but turn to the works of Pines. These works are, essentially, an elaboration of an idea formulated by Friedel. In 1998 Pines *et al.*[25] proposed a spin-fermion model for the development of processes in the normal phase of HTSCs. Data on the temperature and concentration (oxygen) dependences of the single-particle spectral density were used. The resulting strong anisotropy of this density resulted in qualitatively different behavior of ''hot'' (near $k=(\pi,0)$) and ''cold'' (near $k=(\pi/2,\pi/2)$) quasiparticles in momentum space. The authors attribute the wide high-energy peak in the spectrum to strong antiferromagnetic correlations. These correlations greatly decrease the electron-phonon interaction constant in cuprate HTSCs, which could result in the lower, compared with the optimally doped cuprate, superconducting transition temperatures. At the same time it is the ''hot'' electrons that give rise to the pseudogap states—both ''weak'' and ''strong.'' Figure 2 shows a model phase diagram of cuprate HTSCs.[25] We believe that the bottom pseudogap cannot appear without the top pseudogap.

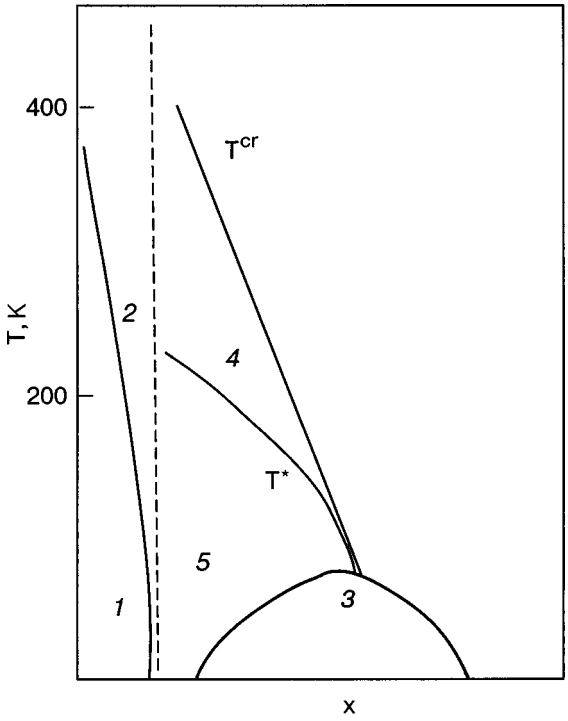

FIG. 2. Qualitative representation of the phase diagram of cuprate HTSCs.[25] 1—antiferromagnetic region (insulator); 2—insulator region; 3—superconductor region; 4—weak pseudogap region; 5—strong pseudogap region; T^{cr} and T^* are phase boundaries.

The ratio of the concentrations of the ''hot'' and ''cold'' electrons depends on the oxygen concentration. For optimal doping the number of ''hot'' electrons becomes negligibly small, which causes the pseudogap to vanish. The two-fluid model constructed by Pines was a logical extension of these ideas.

In his review[26] Pines formulated on the basis of an analysis of many experimental data the idea that the pseudogap state should be a new form of matter which coexists with a coherent electronic state in the normal phase and with the superconducting state below the transition temperature. He developed a phenomenological two-fluid model which makes it possible to explain the simple scaling behavior of the magnetic susceptibility in underdoped cuprates. It is asserted that a pseudogap state competes with the superconducting state, which, generally speaking, can result in the appearance of a quantum critical point. As indicated above, even earlier NMR and ARPES experiments led the authors of Ref. 25 to the conclusion that a pseudogap is engendered by ''hot'' (or, in other words, antinode) quasiparticles near $k=(\pi,0)$ in momentum space. At the same time analysis of spin-lattice relaxation and spin-echo damping data led to the conclusion[27] that T^* is the temperature at which the antiferromagnetic correlation length associated with the hot quasiparticles is one to two orders of magnitude greater than the lattice parameter a. In other words, here, there is a bridge to the idea of partial localization of free charge carriers. The opinion that nonuniformity of the composition and structure should play a substantial role in all of the processes described was also advanced. Unfortunately, the thermody-

namic characteristics of cuprates above the superconducting transition point, specifically, whether or not a phase transition occurs along the curves T^{cr} and T^*, are not discussed in the works cited. With respect to the first of these curves it is stated in Ref. 25 that here crossover, characterized by the appearance of appreciable antiferromagnetic correlations, arises here and that below the second curve the spin-fluctuation energy decreases because the spectral weight of the quasiparticles decreases.

In support of the model of the magnetic nature of the pseudogap we shall present examples of substances in which superconductivity does not occur but a pseudogap phase is observed. For example, analysis of the infrared absorption spectra and the Raman scattering in the quantum magnet ($S=1/2$) TiOCl has led to the conclusion that at temperatures below 135 K size crossover occurs in this material, resulting in dimerization of the ground state and the appearance of a pseudogap.[28]

The most interesting example is vanadium-doped chromium.[29] It is well known that below room temperature chromium is characterized by antiferromagnetic ordering. The magnetic structure is described by a wave of spin density ''organized'' by the moments of delocalized $3d$ electrons. Doping with vanadium results in partial localization of the free electrons (a process which is the inverse of the excitation of virtual Friedel levels) and, therefore, the appearance of a pseudogap.

We call attention to the work, performed by Pines' group,[30,31] using the two-fluid model to explain the anomalies in the Knight shift which occur in the NMR spectra of cerium, ytterbium, and uranium compounds and are associated with the formation of pseudogap states.

Finally, two other publications devoted to the pseudogap problem have appeared very recently.[32,33] In the first one the generalized Hartree-Fock method is used to study correlations in regions of weak and strong pseudogaps. The second work, performed by Canadian theoreticians, is also devoted to the problems of weak and strong pseudogaps. However, here the calculation is performed for a somewhat different system—the cuprate $Nd_{2-x}Ce_xCuO_4$—an electronic-type HTSC. Here the ''hot'' electrons occupy other ''angles'' in momentum space, but the conclusions of the authors correlate with the fluctuation model, presented above, of partial carrier localization resulting in the appearance of a pseudogap.

5. CONCLUSIONS

We have presented only several effects where nonuniformity of the spatial and electronic structure and fluctuations and generation and dissipation of dynamical virtual levels associated with fluctuations play a large role. It has turned out that the ideas developed by Friedel make it possible to suggest an explanation for the well-known paradox associated with the contradictory data on the nature of the ferromagnetism of transition metals, describe the mechanism of the appearance of metallic conductivity in heavy-metal oxides, and advance a number of arguments in favor of the localization mechanism of the formation of a pseudogap state in high-temperature superconductors. Naturally, the range of phenomena, long known and described in detail in the literature, associated with the physical properties of dilute alloys (the Kondo effect and spin glasses) is reflected in the extensive scientific literature and does not need a new analysis.

One of us (L. A. B.) wishes to pay his respects to the blessed memory of his teacher—Evgeniĭ Stanislavovich Borovik—with deep esteem and gratitude.

We thank E. B. Amitin for helpful discussions.

This work was supported by grant No. 02-03-32319 from the Russian Foundation for Fundamental Research.

*E-mail: boy@che.nsk.su

[1] L. A. Boyarskiĭ, S. P. Gabuda, S. G. Kozlova, and R. N. Pletnev, Fiz. Nizk. Temp. **28**, 958 (2002) [Low Temp. Phys. **28**, 691 (2002)].
[2] R. O. Zaĭtsev, Sverkhprovodimost: Fiz., Khim., Tekh. **2**, 36 (1989).
[3] G. Zwicknagl and P. Fulde, Cond-mat/0211706 (2002); G. Zwicknagl, A. N. Yaresko, and P. Fulde, Phys. Rev. B **65**, 081103(R) (2002).
[4] A. A. Zvyagin, Phys. Rev. B **63**, 014503 (2001).
[5] J. Friedel, J. Phys. Radium **19**, 573 (1958).
[6] J. Schoenes, O. Vogt, J. Lohle, F. Hulliger, and K. Mattenberger, Phys. Rev. B **53**, 14987 (1996).
[7] A. Aguayo, I. I. Mazin, and D. J. Singh, Cond-mat/0310629 (2003).
[8] L. A. Boyarskiĭ, S. P. Gabuda, and S. G. Kozlova, Fiz. Nizk. Temp. **26**, 197 (2000) [Low Temp. Phys. **26**, 147 (2000)].
[9] T. Timusk and B. Statt, Rep. Prog. Phys. **62**, 61 (1999).
[10] T. Shimojima, T. Yokoya, T. Kiss, A. Chainani, S. Shin, T. Togashi, C. Chen, S. Watanabe, K. Takada, T. Sasaki, H. Skurai, and E. Takayama-Muromachi, Cond-mat/0406632 (2004).
[11] E. B. Amitin, K. R. Zhdanov, M. Yu. Kameneva, Yu. A. Kovalevskaya, L. P. Kozeeva, I. E. Paukov, and A. G. Blinov, Fiz. Nizk. Temp. **28**, 926 (2002) [Low Temp. Phys. **28**, 669 (2002)].
[12] J. W. Loram and J. L. Tallon, Physica C **349**, 53 (2001).
[13] G. Litak, Cond-mat/0212337 (2002).
[14] M. V. Sadovskiĭ, Usp. Fiz. Nauk **171**, 539 (2001).
[15] J. Rossat-Mignod, L. P. Regnault, C. Vettier, P. Bourges, P. Burlet, J. Bossy, J. Y. Henry, and G. Lapertot, Physica C **185–189**, 86 (1991).
[16] H. A. Mook, Pengheng Dai, S. M. Hayden, A. Hiess, S.-H. Lee, and F. Dogan, Cond-mat/0402134 (2004).
[17] E. B. Amitin, A. G. Blinov, L. A. Boyarsky, V. Ya. Dikovsky, K. R. Zhdanov, M. Yu. Kameneva, O. M. Kochergin, V. N. Naumov, and G. I. Frolova, Phys. Rev. B **51**, 15388 (1995).
[18] E. A. Turov and V. G. Shavrov, Izv. Akad. Nauk SSSR, Ser. Fiz. **27**, 1487 (1963).
[19] V. N. Samovarov, V. L. Vakula, M. Yu. Libin, S. A. Uyutnov, and G. G. Sergeeva, Fiz. Nizk. Temp. **28**, 934 (2002) [Low Temp. Phys. **28**, 674 (2002)].
[20] P. Monthoux, Cond-mat/0301228 (2003).
[21] J. Friedel and M. Kohmoto, Cond-mat/0204337 (2002).
[22] T. Pereg-Barnea and M. Franz, Cond-mat/0606712 (2003).
[23] F. J. Ohkawa, Cond-mat/0305422 (2003).
[24] C. Panagopoulos, M. Majoros, and A. P. Petrovic, Phys. Rev. B **69**, 144508 (2004).
[25] J. Schmalian, D. Pines, and B. Stojkovic, Cond-mat/9804129 (1998).
[26] D. Pines, Cond-mat/0404151 (2004).
[27] V. Barzykin and D. Pines, Phys. Rev. B **52**, 13585 (1995).
[28] P. Lemmens, K. Y. Choi, G. Caimi, L. Degiorgi, N. N. Kovaleva, A. Seidel, and F. C. Chou, Cond-mat/0307502 (2003).
[29] C. Pepin and M. R. Norman, Cond-mat/0309580 (2003).
[30] N. J. Curro, B.-L. Young, J. Schmalian, and D. Pines, Cond-mat/0402179 (2004).
[31] S. Nakasuji, D. Pines, and Z. Fisk, Phys. Rev. Lett. **92**, 016401 (2004).
[32] Moshe Dayan, Cond-mat/0407090 (2004).
[33] V. Hankevych, B. Kyung, A.-M. Dare, D. Senechal, and A.-M. S. Tremblay, Cond-mat/0407085 (2004).

Translated by M. E. Alferieff

Pressure effect on the Fermi surface and electronic structure of $LuGa_3$ and $TmGa_3$

V. B. Pluzhnikov

International Laboratory of High Magnetic Fields and Low Temperatures, Gajowicka 95, 53-529 Wrocław, Poland; B. Verkin Institute for Low Temperature Physics and Engineering of the National Academy of Sciences of Ukraine, 47 Lenin Ave., Kharkov 61103, Ukraine

G. E. Grechnev*

B. Verkin Institute for Low Temperature Physics and Engineering of the National Academy of Sciences of Ukraine, 47 Lenin Ave., Kharkov 61103, Ukraine

A. Czopnik

W. Trzebiatowski Institute of Low Temperature and Structure Research, P.O. Box 1410, 50-950 Wrocław, Poland

O. Eriksson

Theoretical Magnetism Group, Department of Physics, University of Uppsala, Box 530, S-751 21 Uppsala, Sweden

(Submitted August 31, 2004)
Fiz. Nizk. Temp. **31**, 412–421 (March–April 2005)

The Fermi surfaces and cyclotron masses of $LuGa_3$ and $TmGa_3$ compounds are studied by means of the de Haas-van Alphen effect technique under pressure. Highly anisotropic pressure dependences of the de Haas-van Alphen frequencies and cyclotron masses are observed in both compounds. Concurrently, *ab initio* calculations of the volume-dependent band structures are been carried out for these compounds, including the ferromagnetic-configuration phase of $TmGa_3$, by employing a relativistic version of the full-potential linear muffin-tin orbital method within the local spin-density approximation. The experimental data are analyzed on the basis of the calculated volume-dependent band structures and compared with the corresponding pressure effects in the isostructural compound $ErGa_3$. © *2005 American Institute of Physics.* [DOI: 10.1063/1.1884445]

1. INTRODUCTION

In recent years the de Haas-van Alphen (dHvA) effect has been extensively studied in a number of RM_3 compounds (R is a rare earth, and M is a *p* element from the group-III series), including RGa_3 (Refs. 1–4), light RIn_3 (R = La–Gd),[5] heavy RIn_3 (R = Tb–Lu),[6] $TmAl_3$ (Ref. 7), and $CeIn_3$ (Ref. 8). The main objective of these studies was to determine the Fermi surface (FS) geometry and effective cyclotron masses in the representative series of RM_3 compounds. The role of magnetic ordering in reconstruction of the FS has been also addressed in Refs. 5 and 6 (RIn_3), Ref. 9 ($TmGa_3$), and Ref. 10 ($ErGa_3$).

In the present work we study the effect of pressure on the FS and cyclotron masses of the $LuGa_3$ and $TmGa_3$ compounds by means of the dHvA effect. The pressure derivatives of the dHvA frequencies and cyclotron masses are of particular interest due to their sensitivity to details of the exchange interaction and many-body effects in R systems. Therefore, the present investigation can provide a critical test for recently developed methods of *ab initio* calculations of electronic and magnetic structures, and to stimulate the formulation of improved theories of the electronic structure of rare earths.

This work represents an extension of our recent studies[1–3] of the FS and electronic structure in RGa_3 compounds at ambient pressure. Also, the pressure effect on the FS of $ErGa_3$ has been addressed in Ref. 4. Information on physical properties of $TmGa_3$ and $LuGa_3$ is scarce. These compounds crystallize in the AuCu3-type cubic structure. At $T_N = 4.26$ K $TmGa_3$ orders antiferromagnetically[11] to the multiaxial 3**k**-type magnetic structure.[12,13] It has been shown[14] that in the paramagnetic state the interaction between quadrupole moments of the $4f$ shells is strong, and it leads to their ordering just above T_N, and the leading mechanism appears to be the pair quadrupolar interaction via conduction electrons.

It can be expected that at low temperatures $TmGa_3$ reveals large and field-dependent magnetization, in the same manner as is the case for $ErGa_3$ (Refs. 3–4). As in the case of $ErGa_3$ (Ref. 4), it causes a number of difficulties in the Fourier analysis of dHvA oscillations. As a result, one has to study the dHvA effect in strong enough magnetic fields where magnetization tends to saturate. Obviously, these fields are required to be higher than the critical field destroying the antiferromagnetic order. Therefore, the dHvA effect can be studied in the paramagnetic phase of $TmGa_3$, in which sufficient magnetic fields lead to a quasi-ferromagnetic configuration of magnetic moments.

In this work, the experimental investigation of the dHvA effect under pressure is supplemented by *ab initio* calculations of the volume-dependent electronic structures of

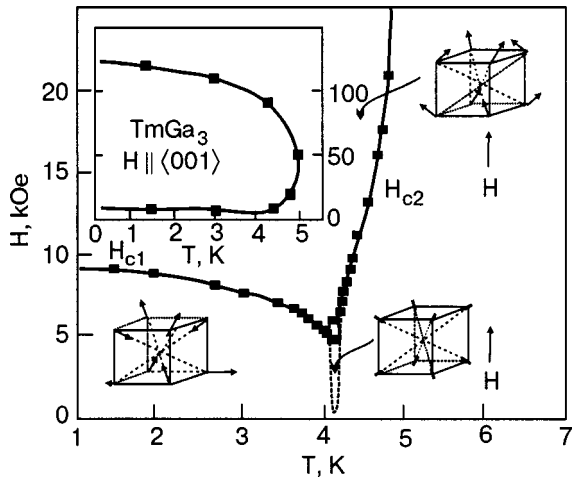

FIG. 1. Low-field magnetic phase diagram of $TmGa_3$ in magnetic field applied along the ⟨001⟩ axis (taken from Ref. 13). The inset shows the whole diagram.

$TmGa_3$ and the reference compound $LuGa_3$. This provides the possibility of estimating many-body enhancement of the ''bare'' cyclotron masses, and the mass enhancement factors λ can be evaluated with the observed (m_c^*) and calculated (m_c^b) cyclotron masses.

Also, a comparison of the dHvA data under pressure and the calculated volume-dependent band structures is expected to be very useful for development of advanced theoretical models for electronic spectra of rare-earth compounds. The evaluated parameters of the electronic structure of $TmGa_3$ and $LuGa_3$ and their pressure derivatives are compared with the corresponding results obtained for the isostructural $ErGa_3$ compound at high pressures.[4] This comparison provides the possibility of estimating the anisotropy and volume dependences of the FS and the many-body enhancement of the cyclotron masses in heavy RGa_3 rare-earth compounds.

A discussion is given on the role of different interactions (exchange splitting, magnetic quadrupolar excitations, spin waves, crystal field) in the revealed pressure effects on the FS and cyclotron masses.

2. EXPERIMENTAL DETAILS

Single crystals of $TmGa_3$ and $LuGa_3$ were grown by the flux method from a melt of the nominal composition 90 at.% Ga and 10 at.% Tm or Lu. The purity of the starting metals was 6N for Ga and 4N for Tm and Lu. The feed placed in an alumina crucible and sealed in a quartz tube in an argon atmosphere under a pressure of 150 Torr at room temperature, was heated in a resistance furnace up to 920 °C, held at this temperature for 48 h and then slowly cooled down at the rate 0.8 K/h. The synthesis was stopped at about 350 °C and then the sample was rapidly cooled down to room temperature to avoid the formation of RGa_6 in a peritectic reaction.[15] The resulting crystals of $TmGa_3$ and $LuGa_3$ were immersed in an excess of Ga which is easy to remove. The crystals obtained had the form of cubes with maximum dimensions $5\times5\times5$ mm. According to an x-ray examination the quality of the single crystals was very good.

The magnetic phase diagram of $TmGa_3$ in magnetic field parallel to the ⟨100⟩ axis is shown in Fig. 1 (cited from Ref. 13). The antiferroquadrupolar phase exists only in low fields up to 0.5 T and in the very narrow range of temperatures: $(T_Q-T_N)<0.1$ K. The critical lines $H_{c1}(T)$ and $H_{c2}(T)$ are the lines of metamagnetic transitions: at the field $H_{c1}(T)$ from the 3**k** phase to an intermediate one and at $H_{c2}(T)$ from the intermediate phase to a paramagnetic one. In a field applied along the other two principal crystallographic axes, ⟨110⟩ and ⟨111⟩, the phase diagrams are similar to that cited, but the critical field $H_{c2}(T)$ reaches much lower values and does not exceed 2.2 T.[13] At temperatures lower than T_N and in magnetic field higher than 7 T the magnetic moments reach an induced paramagnetic configuration, except for a small region of angles at the ⟨100⟩ axis. Above the second metamagnetic transition the magnetization is large and anisotropic. This fact has important consequences for analysis of the dHvA effect in $TmGa_3$.

First, in the Fourier analysis of the dHvA signal $V_{\rm osc}$ one must take into account the magnetic induction B in the Lifshits–Kosevich formula instead of the applied magnetic field $H_{\rm appl}$,

$$V_{\rm osc}\approx A\sin\left[\left(\frac{2\pi F}{B}\right)+\varphi\right], \tag{1}$$

where the dHvA frequency F is proportional to the extremal cross-sectional area of the FS, and the magnetic induction $B=H_{\rm appl}+4M(1-N)$ depends on the magnetization per unit volume M and on the demagnetizing factor N.

Secondly, the cyclotron effective mass m_c^* is determined from the temperature dependence of the dHvA amplitude A, namely, from the slope of the plot of $\ln\{A[1-\exp\times(-2\alpha m_c^*T/B)]/T\}$ versus T, where $\alpha=2\pi^2ck_B/e\hbar$. Therefore, one has to take into account the magnetic induction B instead of the applied magnetic field $H_{\rm appl}$.

Thirdly, in a strong magnetic field the magnetic moments of Tm^{3+} ions reach a spin-polarized paramagnetic configuration. Then the k-f exchange interaction leads to a splitting of the conduction band into sub-bands, and the value of this band splitting is proportional to the magnetic moment, density of states, and the k-f exchange integral.

The dHvA effect measurements for the magnetic $TmGa_3$ were performed on a spherical sample (diameter 2.5 mm) by using a standard field modulation technique at temperatures down to 1.5 K and in magnetic fields up to 13 T applied along the principal crystallographic axes. For a spherical sample, as we have used, one has $B=H_{\rm appl}+(8\pi/3)M$. The magnetization at the magnetic fields used for the dHvA-effect study depends rather weakly on the magnetic field strength. Complementary magnetization measurements were performed by a home-made vibrating-sample magnetometer.

A standard Cu–Be clamp was used for the pressure effect study with an extracted benzine solvent as the medium transmitting pressure to the sample. The maximum pressure employed was 6.4 kbar at 4.2 K. A small Manganin coil with a resistance of about 60 Ω was placed near the sample to measure the applied pressure. Preliminarily this coil had been trained to the cooling pressure and then calibrated by measuring the superconducting transition temperature of Sn.[16] The deviation of the Manganin coil resistance due to the residual magnetic field of the superconducting magnet has also been taken into account. The sample, the pick-up

coil, and the Manganin coil were all placed in a Teflon cell, filled with the extracted benzine solvent, and then the cell was put into the pressure clamp. The deviation from hydrostatic pressure and its effect on the measurements are estimated to be negligible by observing that the superconducting transition width of Sn does not change noticeably, and the amplitudes of the dHvA oscillations do not decrease substantially under the pressures used in this work. Since the pressure clamp is heated by the modulation field, there is a difference in temperatures between the helium bath and the sample in the pressure clamp. The modulation amplitude and frequency used in the measurements were 40 G and 38.5 Hz, respectively. These amplitude and frequency were chosen to produce a large enough dHvA signal, and, at the same time, to reduce the heating power, which leads to a temperature difference not exceeding 0.02 K.

The applied pressure modifies the magnitude and field dependence of the magnetization due to a pressure effect on the crystal field (CF) splitting, as well as on the exchange interaction.[2,3] It is known that the CF of metallic rare-earth compounds contains contributions from charges of surrounding ligands as well as from the direct Coulomb and exchange interactions of the R ion with conduction electrons. In order to estimate the influence of pressure on the CF we have restricted ourselves to the contribution from surrounding ligands within the point charge model. The applied pressure P brings about the volume dilatation $\delta V/V = -P/c_B$, where c_B is the bulk modulus. Under a pressure of 10 kbar $\delta V/V$ is estimated to be -0.013, provided the bulk modulus of $TmGa_3$ is taken from Ref. 14 ($c_B = 765$ kbar). The change of CF due to this dilatation causes a variation of the magnetic induction not larger than 20 G at 1.7 K in an applied field of 13 T. One can also estimate the change of the magnetization in $TmGa_3$ due to the variation of the exchange interaction parameter under pressure by using the data obtained for the isostructural RIn_3 compounds.[17,18] The corresponding variation of the magnetic induction at an applied pressure of 10 kbar is about -10 G at 1.7 K in a field of 15 T. Therefore, the total change of the magnetic induction reaches only 10 G, giving a relative variation of the dHvA frequency $\delta F/F \approx 2 \times 10^{-4}$ kbar^{-1}, which can be neglected in the Fourier analysis of the dHvA oscillations.

The dHvA-effect measurements were carried out in magnetic fields higher than 7 T, where the magnetization does not change appreciably and the Fourier analysis of the dHvA oscillations can be performed. Otherwise a dHvA frequency would change its value following the strength of the external magnetic field. Therefore, the dHvA effect studies were carried out in the paramagnetic phase well above the $H_{c2}(T)$ line of the antiferromagnetic-paramagnetic transition (Fig. 1), except for the ⟨100⟩ axis, for which the critical field reaches significant values. The magnetization in magnetic fields higher than 7 T tends to saturate, and the magnetic moments settle into a quasi-ferromagnetic configuration. Moreover, the magnetization along all directions in a magnetic field higher than 7 T appeared to be almost temperature independent in the range 1.7–4.2 K (Fig. 2, cited from Ref. 13).

The effects of the antiferromagnetic and antiferroquadrupolar order on the FS of $TmGa_3$ have not been examined in this study. For these phases the large magnetization value and its strong dependence on magnetic field have not allowed analysis of the dHvA oscillations. Also, a very narrow temperature range (<0.1 K) for the antiferroquadrupolar phase has prevented the corresponding study of the dHvA effect.

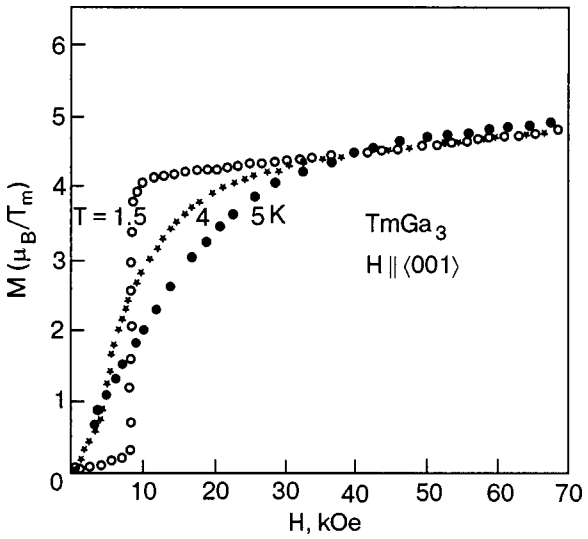

FIG. 2. Magnetization of $TmGa_3$ in a magnetic field applied along ⟨001⟩ at different temperatures (taken from Ref. 13).

3. DETAILS OF CALCULATIONS

A treatment of localized strongly correlated $4f$ electrons still presents a challenge to the band structure theory. The results of *ab initio* calculations (see, e.g., Refs. 2, 3 and 18–21) together with a wealth of experimental data (including bulk and FS properties) provide solid evidence that within the local spin-density approximation (LSDA)[22] a strict band treatment of the $4f$ states is inadequate for heavy rare earths. The f shell is not filled, and the $4f$ bands, which act as a sink for electrons, would always cut the Fermi level E_F, leading to absurd values of the specific heat coefficients[19] and wrong $4f$ occupancies, close to the divalent (i.e., atomic) configuration.[23]

According to the photoemission data,[23–25] the $4f$ spectral density for Er, Tm, and their compounds were observed about 5 eV below E_F. Therefore, in order to describe the band structure of the ground state of $TmGa_3$ near E_F, it is feasible to consider the $4f$ states as semi-localized core states, in line with Refs. 18, 20, 26. The bulk and magnetic properties calculated within this approach, as well as the Fermi surfaces of Gd, Tb,[20] and ErAs[21] appeared to be in agreement with experimental data. Actually, the standard rare-earth model[19] is employed in this work in the limit of large Hubbard repulsion U within the *ab initio* LSDA scheme[22] for the exchange-correlation effects. The localized f states of Tm were treated as spin-polarized outer-core wave functions, contributing to the total spin density, and the spin occupation numbers were fixed by applying the Russel-Saunders coupling scheme to the $4f$ shell, which was not allowed to hybridize with conduction electrons.

The *ab initio* band structure calculations were carried out for the paramagnetic configuration phase of $TmGa_3$ and non-

spin-polarized $LuGa_3$ by using the full potential linear muffin-tin orbital method (FP-LMTO).[27,28] In the case of $TmGa_3$, the spin density of the $4f$ states polarizes the ''spin-up'' and ''spin-down'' conduction electron states through the local exchange interaction. The exchange split conduction electron states interact with the localized f states at other sites, appearing as the medium for the indirect $f-f$ interaction.[18,26] In order to calculate FS orbits for both $TmGa_3$ and $LuGa_3$, the charge densities were obtained by including spin-orbit coupling at each variational step, as suggested in Refs. 19 and 20. The band structures and crystal potentials were calculated self-consistently on a uniform mesh of 455 **k** points in the irreducible wedge of the cubic Brillouin zone for a number of lattice parameters close to the experimental ones ($a=4.196$ Å and 4.180 Å for $TmGa_3$ and $LuGa_3$, respectively). The bulk moduli c_B were evaluated from the calculated total energies $E(V)$ as functions of volume V (i.e., from the theoretical equations of states, according to Ref. 27), and were estimated to be about 800 kbar for $TmGa_3$ and $LuGa_3$, which is close to the experimental value $c_B=765$ kbar ($TmGa_3$).[14] This is a rather normal overestimation of c_B, presumably due to the overbonding tendency of the LSDA.

The calculated total and partial densities of states (DOS) $N(E)$ for $LuGa_3$ are presented in Fig. 3. There are two fairly broad peaks (bonding and antibonding states) arising due to hybridization of $5d$ states of Lu and the p states of Ga. As can be seen in Fig. 3, these p states give a substantial contribution to the conspicuous peak in the total DOS at the Fermi energy E_F. The calculated total and partial DOS for $TmGa_3$ are in qualitative agreement with the $N(E)$ of $LuGa_3$, as well as with the previously calculated DOS of $TmGa_3$ (see Fig. 7 in Ref. 2). The intersections of the calculated FS of $LuGa_3$ with faces of the cubic Brillouin zone (Fig. 4) show an almost spherical electron FS centered at the R point and a complicated multiply connected hole FS centered at the Γ and X points, analogously to $TmGa_3$ and also $ErGa_3$ (Ref. 3). As a whole, the electron FS of RGa_3 is nearly spherical, whereas the hole FS is a complicated multiply connected surface.

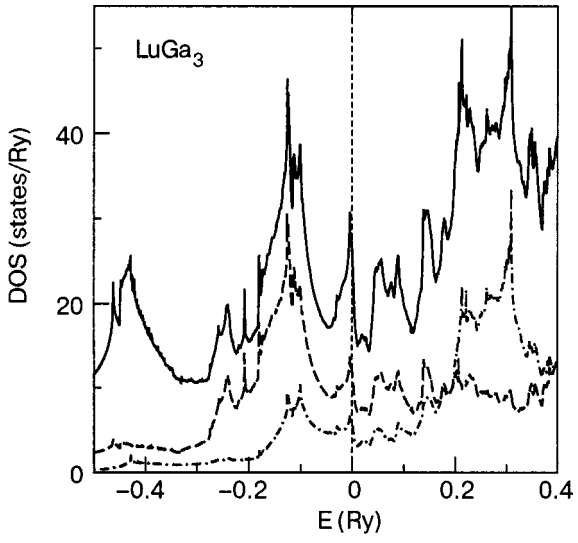

FIG. 3. Total (solid line) and partial densities of states (DOS) $N(E)$ relative to the Fermi energy $E_F=0$ for $LuGa_3$. The dashed line stands for the p states of Ga, and the dash-and-dot line represents d states of Lu.

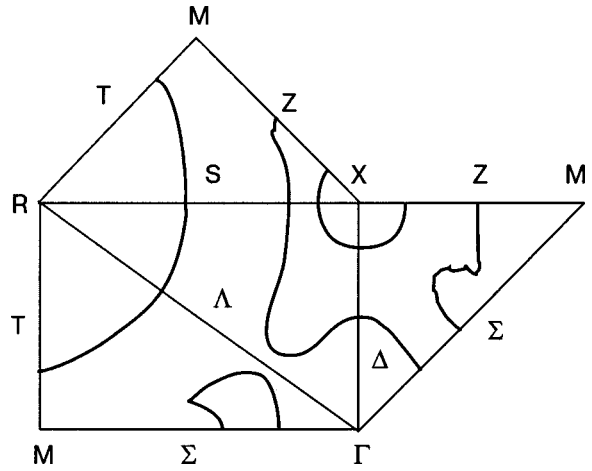

FIG. 4. Intersection of the Fermi surface for $LuGa_3$ with the Brillouin zone faces.

In agreement with the results of Ref. 20 for Gd and Tb, the incorporation of the spin-orbit coupling has a small effect on the calculated dHvA frequencies and cyclotron masses. It should be noted that for the field-induced quasi-ferromagnetic configuration of $TmGa_3$ the exchange splitting is larger than the spin-orbit splitting, and the dHvA spectrum of $TmGa_3$ can be compared with the results of band structure calculations for the spin-polarized state.

4. RESULTS AND DISCUSSION

The Fourier spectra of dHvA oscillations in $TmGa_3$, observed along the ⟨100⟩ axis at different pressures, are presented in Fig. 5, and the pressure effect on the corresponding dHvA frequencies is exhibited in Fig. 6. The branch a origi-

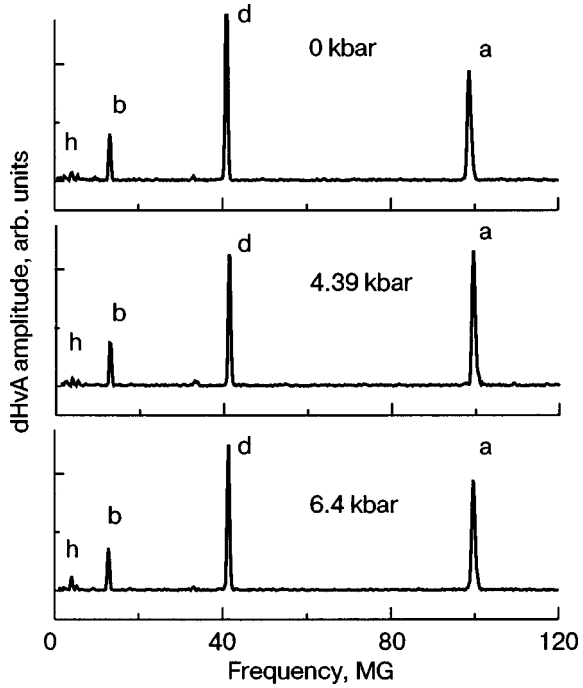

FIG. 5. Fourier spectra of the dHvA oscillations observed in $TmGa_3$ at 1.9 K for magnetic fields directed along ⟨001⟩ axis at different pressure.

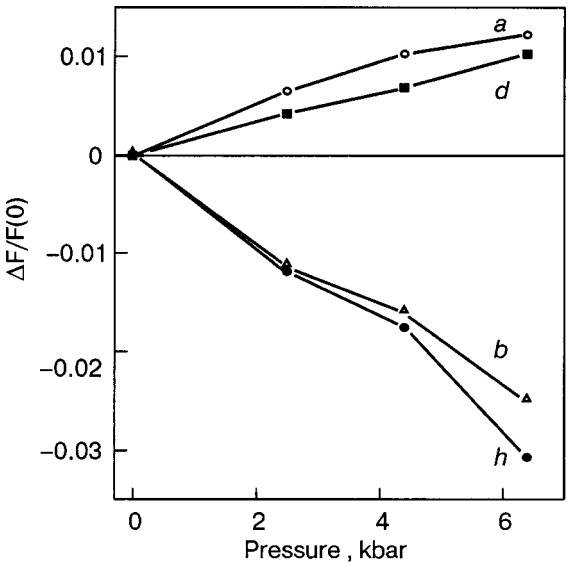

FIG. 6. Fractional changes of the dHvA frequencies, $\Delta F/F(0)=[F(P)-F(0)]/F(0)$, in $TmGa_3$ as a function of pressure for the ⟨001⟩ magnetic field direction at 1.9 K. The frequencies are labeled according to Ref. 2 and Fig. 5. The solid lines are guides for the eye.

nates from the belly orbit in the band 7 electron FS centered at the R point, whereas the *d* orbit comes from the nearly spherical part of the hole FS at the Γ point (see Fig. 4). The orbit *b* is associated with the FS centered at the X point, and the low-frequency orbits *h* are related to ''arms'' in the band 6 hole FS. At ambient pressure the experimental angular dependent dHvA frequencies turned out to be very close to those previously reported for $TmGa_3$ and $LuGa_3$ (Figs. 2 and 3 in Ref. 2, respectively), and also to the results of the present FP-LMTO calculations.

In the range of high dHvA frequencies (branches *a* and *d*) the spectra of $LuGa_3$ and $TmGa_3$ are very similar. In the low dHvA frequency range, instead of single *b* and *h* branches for $LuGa_3$, two *b*-and several *h*-type branches were observed for $TmGa_3$. For all principal crystallographic axes, ⟨100⟩, ⟨110⟩, and ⟨111⟩, the dHvA frequencies *F* at ambient pressure, their pressure derivatives, $d\ln F/dP$, and the corresponding cyclotron masses m_c^* together with their pressure derivatives, $d\ln m_c^*/dP$, are given in Tables I and II for $LuGa_3$ and $TmGa_3$, respectively. The pressure coefficients $d\ln F/dP$ are determined by fitting a straight line to each set of data in $\ln F$ versus *P* plots (see, e.g., Fig. 6). For comparison and further discussion, the analogous results on *F*, $d\ln F/dP$, and m_c^* in the isovalent $ErGa_3$ compound are taken from our paper[4] and shown in Table III. It is worth noting that the ''exchange-split'' dHvA oscillations, which should originate from the slightly spin-polarized sub-bands of $TmGa_3$, were not resolved in this work within the limits of the large experimental errors. In contrast to investigations of Refs. 2 and 3, in the present dHvA experiments additional errors emerged due to the weak signal from the pick-up coil, which had to be placed in the pressure clamp, and also due to possible nonhydrostatic pressure conditions at the sample. Therefore, only solid and reliable high pressure results are presented in the tables, while questionable data have been omitted.

As is seen from the tables, the larger dHvA frequencies *a* and *d* increase with pressure. On the other hand, for the hole FSs *b* and *h* the derivatives $d\ln F/dP$ turned out to be negative. Also, the observed pressure dependences of the dHvA frequencies are quite different among $ErGa_3$, $TmGa_3$, and the non-*f* reference compound $LuGa_3$. The experimental pressure derivatives $d\ln F/dP$, presented in Tables I and II, are rather large in comparison with the free-electron scaling prediction, which gives two-thirds of the volume compressibility, or 0.87×10^{-3} $kbar^{-1}$, provided the available value[14] of bulk modulus of $TmGa_3$ is accepted. This scaling estimate actually means that with increasing pressure, the volumes of the Brillouin zone and the FS increase, and one can also expect that both the hole and electron FS increase. However, this effect cannot explain the negative pressure derivatives for the hole FS.

In the framework of the band theory, the overlap of the wave functions between the 4*p* bands of Ga and the 5*d* bands of R increases with pressure, and the *p*-*d* hybridiza-

TABLE I. The dHvA frequencies *F* (in MG) and the corresponding cyclotron effective masses m_c^* (in units of the free electron mass) in $LuGa_3$ at ambient pressure, their logarithmic pressure derivatives (in 10^3 $kbar^{-1}$), and the mass enhancement factor λ.

Field direction, branch	*F*	$d\ln F/dP$		m_c^*		λ	$d\ln m_c^*/dP$	
	exper.	exper.	theory	exper.	theory		exper.	theory
⟨100⟩, *a*	98.06	+1.2(0.2)	1.0	0.74	0.38	0.95	–	–
d	41.3	+1.0(0.2)	1.3	0.63	0.48	0.31	−15(3)	−5
b	11.87	−3.4(0.1)	–	0.3	–	–	−6.5(0.3)	–
h	4.92	–	–	0.33	–	–	−38(9)	–
⟨110⟩, *a*	94.6	+1.2(0.2)	0.9	0.73	0.36	1.03	–	–
b'	14.9	−2.6(0.2)	–	0.36	–	–	+17(3)	–
b	12.76	−3.0(0.2)	–	0.47	–	–	+12(2)	–
h	3.97	−4.2(0.4)	–	0.23	–	–	+35(1)	–
⟨111⟩, *a*	88.6	+1.3(0.8)	1.0	0.57	0.36	0.58	−8.5(1)	−3
d	35.6	+1.6(0.2)	1.4	0.53	0.39	0.36	−5.5(2)	−4
h	4.8	−3.1(0.6)	–	0.24	–	–	−20(1)	–

TABLE II. The dHvA frequencies F (in MG) and the corresponding cyclotron effective masses m_c^* (in units of the free electron mass) in $TmGa_3$ at ambient pressure, their logarithmic pressure derivatives (in 10^3 $kbar^{-1}$), and the mass enhancement factor λ.

Field direct-ion, branch	F	$d \ln F / dP$		m_c^*		λ	$d \ln m_c^* / dP$	
	exper.	exper.	theory	exper.	theory		exper.	theory
⟨100⟩, *a*	98.68	+1.8(0.3)	1.2	1.24	0.41	2.0	+1.6(1.6)	−4
d	41.1	+2.0(0.4)	1.6	1.3	0.46	1.8	−14(3)	−7
b	11.61	−3.8(0.2)	–	0.83	–	–	+16(8)	–
h	3.58	−4.5(1.7)	–	–	–	–	–	–
⟨110⟩, *a*	94.41	+1.5(0.1)	1.1	1.04	0.38	1.7	−7(4)	−4
b′	14.46	−2.9(0.3)	–	–	–	–	–	–
b	12.66	−2.8(0.1)	–	0.96	–	–	−29(6)	–
h′	4.8	−2.3(0.2)	–	–	–	–	–	–
h	3.57	−4.3(0.3)	–	0.46	–	–	–	–
⟨111⟩, *a*	87.28	+1.8(0.3)	1.1	0.91	0.38	1.4	+22(10)	−3
d	34.24	+2.1(0.5)	1.5	0.83	0.42	1.0	+3.6(0.7)	−6
h	4.31	−6.0(0.3)	–	0.46	–	–	−22(6)	–

tion becomes stronger. Consequently, while the volume of the big spherical FS sheets increases, the volumes of small "arms" of the hole FS may decrease due to strong hybridization and substantial deviation from free-electron scaling, and this can provide the anisotropic dHvA frequency changes. Basically, there is qualitative agreement between the experimental and calculated derivatives $d \ln F/dP$ for the *a* and *d* orbits in $LuGa_3$ (again, the bulk modulus of $TmGa_3$ was used to convert the calculated volume derivatives to the pressure derivatives listed in the tables). However, this band approach cannot explain the discrepancy between the experimental and calculated pressure derivatives of the dHvA frequencies in $TmGa_3$.

It was originally suggested in Ref. 29 that in ferromagnetic systems there are two contributions to the pressure derivative of a dHvA frequency. The first ("potential") contribution comes from an atomic volume effect on the crystal potential, and also from a scaling effect due to the change of the Brillouin zone size. It can be approximated by the corresponding derivative for a nonmagnetic reference compound with a close value of the compressibility (in our case it can be $LuGa_3$). The second ("magnetic") contribution originates from the pressure-induced redistribution of conduction electrons between exchange-split sub-bands and the corresponding changes of the volume enclosed by the FS sheets. According to the present calculations, the Fermi surfaces of $TmGa_3$ do not change uniformly because of a strong **k**-dependent $p-d$ mixing effect on the exchange-split conduction band. As a result, the difference between pressure derivatives of the spin-split FS cross-sectional areas is inconsistent with simple estimates based on the Stoner-Wohlfarth model.

TABLE III. The dHvA frequencies F (in MG) at ambient pressure, their logarithmic pressure derivatives (in 10^3 $kbar^{-1}$), the corresponding cyclotron effective masses m_c^* (in units of the free electron mass), and the mass enhancement factor λ in the compound $ErGa_3$.

Field direct-ion, branch	F	$d \ln F/dP$		m_c^*		λ
	exper.	exper.	theory	exper.	theory	
⟨100⟩, *a*	98.71	+2.3(0.3)	1.3	0.96	0.40	1.4
d	41.07	+1.7(0.2)	2.0	0.91	0.46	0.98
b	12.66	−2.7(0.1)	− 2.8	0.44	–	–
h	4.35	–	–	0.55	–	–
⟨110⟩, *a*	95.17	+1.0(0.3)	1.1	0.89	0.37	1.4
b′	15.14	−1.1(0.1)	–	0.57	–	–
b	11.95	−2.4(0.2)	−2.0	0.84	–	–
h	3.37	−4.5(0.3)	–	0.28	–	–
⟨111⟩, *a*	87.58	+1.7(0.1)	1.2	0.80	0.37	1.16
d	35.47	+2.3(0.2)	1.9	0.70	0.40	0.75
h	4.21	–	–	0.51	–	–

Glancing at the experimental lattice parameters, which are very close in $TmGa_3$ and $LuGa_3$, one may assume that the crystal potential in the two compounds does not differ substantially, and that the differences in the dHvA frequencies derivatives of $TmGa_3$ and $LuGa_3$ compounds can be attributed to the unfilled $4f$ shell in $TmGa_3$. In the $4f$ spin-polarized state the differences can arise, first, from the exchange splitting of the conduction band of $TmGa_3$, and, secondly, from the magnetostriction effects due to the $\Gamma_5^{(1)}$ CF ground state of the $^3H_6$ multiplet of the Tm^{3+} ion. Unfortunately, at the present stage the differences in $d\ln F/dP$ cannot be ascribed confidently either to the conduction band splitting or to the magnetostriction.

The cyclotron masses m_c^* have been determined at ambient and high pressures for most of the dHvA frequencies for the field applied along the ⟨100⟩, ⟨110⟩, and ⟨111⟩ axes and are presented in Tables I and II. The band cyclotron masses m_c^b were calculated for the *a* and *d* branches and are also given in the tables. Also, the cyclotron masses measured and calculated for $ErGa_3$ in Refs. 3 and 4 are listed in Table III for comparison.

The mass enhancement factor λ, which is defined by the relation $m_c^*=m_c^b(1+\lambda)$, presents a measure of the interaction strength of the conduction electrons with low-energy excitations, and it can be determined by comparison of the experimental cyclotron effective masses with the corresponding calculated ones. The λ factors for electrons on the *a* and *d* orbits in $LuGa_3$, $TmGa_3$, and $ErGa_3$ are listed in the tables. In the nonmagnetic $LuGa_3$ the λ factor represents a measure of the electron-phonon interaction, whereas in $ErGa_3$ and $TmGa_3$ this factor also contains contribution(s) coming from magnetic excitations. As seen in Table I, in $LuGa_3$ the λ factor ranges from 0.3 (*d* branch) to about 1 (*a* branch). Assuming that the values of $\lambda_{e-\mathrm{ph}}$ in RGa_3 are close to the corresponding ones in $LuGa_3$, we estimated the magnetic contributions λ_{mag} in $ErGa_3$ to be 0.4–0.6 and 0.4–0.7 for the *a* and *d* orbits, respectively. In $TmGa_3$ the corresponding values of λ_{mag} are larger and more anisotropic, namely, 0.5–1 and 0.8–1.5.

Hybridization of conduction electrons with $4f$ states could contribute to the larger cyclotron masses observed in $TmGa_3$ and $ErGa_3$ as compared to $LuGa_3$. However, a strong hybridization with $4f$ bands in the framework of the LSDA would lead to a substantial reduction of the conduction band width in RGa_3 and thus to bulk properties remarkably different from those in $LuGa_3$. In fact, the lattice parameters decrease slightly in a linear fashion in the series $ErGa_3$, $TmGa_3$, and $LuGa_3$ due to the lanthanide contraction, and it can be expected that the conduction band widths are close in RGa_3, and therefore the band cyclotron masses should also be close. At the present stage more elaborated analysis is necessary to estimate the scale of the hybridization effects by employing modern theoretical schemes (like the LSDA+U approach) and additional experimental data (e.g., for related RIn_3 compounds).

One can also assume that the distinctions between effective masses in RGa_3 are probably due to the different ground state multiplets $^3H_6$ and $^4I_{15/2}$ of Tm^{3+} and Er^{3+} ions in the crystal field of $TmGa_3$ and $ErGa_3$, respectively. The triplet $\Gamma_5^{(1)}$ with intrinsic magnetic and quadrupolar moments is the ground state in $TmGa_3$ (Ref. 14), and most likely Γ_7 is the ground state in the crystal field of $ErGa_3$ (Ref. 30). Since the $\Gamma_5^{(1)}$ state exhibits a quadrupole moment and the Γ_7 state does not, one can expect large magnetostriction effects in $TmGa_3$ and none in $ErGa_3$.

In this connection one can expect that the presence of strong quadrupolar interactions increases the cyclotron effective masses. It is well known[31] that the quadrupolar excitations do not occur in compounds with the cubic symmetry. They may appear, however, in $TmGa_3$ as coupled magnetic-quadrupolar excitations in an applied magnetic field.[14] It was shown in Ref. 31 that the corresponding excitations contribute to the effective mass of the conduction electrons, and the effect appears to be large and magnetic field dependent. Also, in the quasi-ferromagnetic configuration of magnetic moments, the exchange splitting of the conduction bands can vary in $ErGa_3$ and $TmGa_3$ due to the difference in corresponding $4f$-shell spin occupation numbers. At the moment, however, one can not estimate the relative contributions of the conduction band splitting and the magnetostriction to the observed differences in cyclotron masses and the pressure dependences of the dHvA frequencies in $TmGa_3$ and $ErGa_3$.

Also, one more mechanism can affect the cyclotron masses in RGa_3. It was shown in Refs. 31–33 that virtual magnetic excitations can contribute substantially to the effective mass of the conduction electrons in rare-earth systems. These excitations are magnetic excitons in a paramagnetic system (e.g., praseodymium) and spin waves in magnetically ordered rare earths. The corresponding mass enhancement is expected to be large, magnetic-field dependent, and proportional to the static susceptibility of the magnetic system. According to estimates of the electronic specific-heat coefficients in Ref. 33, the corresponding effective masses increase in the series of heavy rare-earth metals. This trend is consistent with the relation between observed cyclotron masses in $ErGa_3$ and $TmGa_3$, and also in $ErIn_3$ and $TmIn_3$ compounds.[6] However, considerable work is needed to implement the findings of Refs. 32 and 33 for a quantitative description of the cyclotron masses in magnetic RM_3 compounds.

In conclusion it should be noted that the calculated LSDA band cyclotron masses m_c^b did not reproduce the highly anisotropic pressure derivatives of m_c^* in $TmGa_3$ (see Table II), which are presumably determined by various magnetic and many-body excitations. On the other hand, the calculated $d\ln m_c^b/dP$ in $LuGa_3$ turned out to be in qualitative agreement with the corresponding experimental data in Table I.

SUMMARY

As a whole, the present results on the dHvA effect and FS in $TmGa_3$ and $ErGa_3$ at ambient pressure are in good agreement with recent studies (Refs. 9 and 10, respectively) of the two-dimensional angular correlation of the positron annihilation radiation (2D-ACAR). The calculated pressure derivatives of the dHvA frequencies in $LuGa_3$ and $TmGa_3$ are in qualitative agreement with the experimental data, though the origin of some discrepancies found for $d\ln F/dP$ in $TmGa_3$ is not clear. The estimated magnetic contributions to the mass enhancement factor λ in $ErGa_3$ and $TmGa_3$

turned out to be large and magnetic field dependent. We admit that more work is needed to elucidate the nature of the large cyclotron masses observed in RGa_3 and, in particular, to evaluate the magnetic excitations effects on m_c^*. Also, the surprisingly large and highly anisotropic pressure effect on the cyclotron masses has been observed in $LuGa_3$ and especially in $TmGa_3$, which cannot be explained within the standard rare-earth model employed. It should be emphasized that different interactions (exchange splitting, CF and magnetic-quadrupolar excitations, spin waves) have to be taken into account in a further theoretical analysis of the revealed pressure effects on the FS and cyclotron masses in RGa_3. Also, at the present stage a more elaborated study is necessary to estimate the scale of the hybridization effects with $4f$ states in $ErGa_3$ and $TmGa_3$ within modern theoretical approaches (e.g. LSDA+U). These tasks apparently go beyond the aim of the present work, in which we tried to reach a true LSDA limit within the standard rare-earth model in order to explain the experimental dHvA data. It can be also beneficial to supplement such theoretical efforts with experimental study of the pressure effect on the dHvA frequencies and cyclotron masses in the related RIn_3 compounds.

The authors dedicate this work to the 90th anniversary of the birth of E. S. Borovik, who was one of pioneers of the Fermi surfaces studies.[34]

We are grateful to Professors J. Klamut, T. Palewski, V. Nizhankovskii, and I. V. Svechkarev for their kind support and fruitful scientific discussions.

This work has been partly supported by The Swedish Natural Science Research Council (VR) and The Swedish Foundation for Strategic Research (SSF).

*E-mail: grechnev@ilt.kharkov.ua

[1] V. B. Pluzhnikov, A. Czopnik, and I. V. Svechkarev, Physica B **212**, 375 (1995).
[2] V. B. Pluzhnikov, A. Czopnik, G. E. Grechnev, N. V. Savchenko, and W. Suski, Phys. Rev. B **59**, 7893 (1999).
[3] V. B. Pluzhnikov, A. Czopnik, and G. E. Grechnev, J. Phys.: Condens. Matter **11**, 4507 (1999).
[4] V. B. Pluzhnikov, A. Czopnik, O. Eriksson, G. E. Grechnev, and Yu. V. Fomenko, Fiz. Nizk. Temp. **25**, 894 (1999) [Low Temp. Phys. **25**, 670 (1999)].
[5] N. Nagai, I. Umehara, T. Ebihara, A. K. Albessard, H. Sugawara, T. Yamazaki, K. Satoh, and Y. Onuki, Physica B **186–188**, 139 (1993).
[6] S. Nojiri, Y. Katayama, D. Aoki, N. Suzuki, K. Sugiyama, R. Settai, Y. Inada, Y. Onuki, and H. Harima, Physica B **281–282**, 747 (2000).
[7] T. Ebihara, D. Aoki, Y. Inada, R. Settai, K. Sugiyama, Y. Haga, and Y. Onuki, J. Magn. Magn. Mater. **226–230**, 101 (2001).
[8] M. Biasini, G. Ferro, and A. Czopnik, Phys. Rev. B **68**, 094513 (2003).
[9] M. Biasini, G. Kontrym-Sznajd, M. A. Monge, M. Gemmi, A. Czopnik, and A. Jura, Phys. Rev. Lett. **86**, 4616 (2001).
[10] M. Biasini, G. Ferro, G. Kontrym-Sznajd, and A. Czopnik, Phys. Rev. B **66**, 075126 (2002).
[11] A. Czopnik, Cz. Bazan, N. Iliev, B. Stalinski, H. Madge, and R. Pott, Physica B & C **130**, 262 (1985).
[12] P. Morin, M. Giraud, P. L. Regnault, E. Roudaut, and A. Czopnik, J. Magn. Magn. Mater. **66**, 345 (1987).
[13] P. Morin, M. Giraud, P. Burlet, and A. Czopnik, J. Magn. Magn. Mater. **68**, 107 (1987).
[14] P. Morin, J. Rouchy, M. Giraud, and A. Czopnik, J. Magn. Magn. Mater. **67**, 95 (1987).
[15] J. Pelleg, G. Kimmel, and D. Dayan, J. Less-Common Met. **81**, 33 (1981).
[16] T. F. Smith, C. W. Chu, and M. B. Maple, Cryogenics **9**, 53 (1969).
[17] A. Czopnik, A. S. Panfilov, and I. V. Svechkarev, Fiz. Nizk. Temp. **20**, 48 (1999) [Low Temp. Phys. **20**, 39 (1994)].
[18] G. E. Grechnev, A. S. Panfilov, I. V. Svechkarev, K. H. J. Buschow, and A. Czopnik, J. Alloys Compd. **226**, 107 (1995).
[19] M. S. S. Brooks and B. Johansson, in *Ferromagnetic Materials*, Vol. **7**, K. H. J. Buschow (ed.), North-Holland, Amsterdam (1993), p. 139.
[20] R. Ahuja, S. Auluck, B. Johansson, and M. S. S. Brooks, Phys. Rev. B **50**, 5147 (1994).
[21] A. G. Petukhov, W. R. L. Lambrecht, and B. Segall, Phys. Rev. B **53**, 4324 (1996).
[22] U. von Barth and L. Hedin, J. Phys. C **5**, 1629 (1972).
[23] B. I. Min, H. J. F. Jansen, T. Oguchi, and A. J. Freeman, J. Magn. Magn. Mater. **61**, 139 (1986).
[24] J. F. Herbst and J. W. Wilkins, in *Handbook on the Physics and Chemistry of Rare Earths*, Vol. **10**, K. A. Gschneidner, Jr., L. Eyring, and S. Hufner (eds.), North-Holland, Amsterdam (1987), p. 321.
[25] A. J. Freeman, B. I. Min, and M. R. Norman, in *Handbook on the Physics and Chemistry of Rare Earths*, Vol. **10**, K. A. Gschneidner, Jr., L. Eyring, and S. Hufner (eds.), North-Holland, Amsterdam (1987), p. 165.
[26] M. S. S. Brooks, L. Nordstrom, and B. Johansson, Physica B **172**, 95 (1991).
[27] O. Eriksson and J. M. Wills, in *Electronic Structure and Physical Properties of Solids*, Hugues Dreysse (ed.) Springer, Berlin (2000), p. 247.
[28] G. E. Grechnev, A. S. Panfilov, I. V. Svechkarev, A. Delin, B. Johansson, J. M. Wills, and O. Eriksson, J. Magn. Magn. Mater. **192**, 137 (1999).
[29] G. Lonzarich and A. V. Gold, Can. J. Phys. **52**, 694 (1974).
[30] A. Murasik, A. Czopnik, L. Keller, and P. Fischer, J. Magn. Magn. Mater. **213**, 101 (2000).
[31] P. Fulde and M. Loewenhaupt, Adv. Phys. **34**, 589 (1986).
[32] R. M. White and P. Fulde, Phys. Rev. Lett. **47**, 1540 (1981).
[33] P. Fulde and J. Jensen, Phys. Rev. B **27**, 4085 (1983).
[34] E. S. Borovik, V. G. Volotskaya, and N. Ya. Fogel, Zh. Éksp. Teor. Fiz. **45**, 46 (1963) [Sov. Phys. JETP **18**, 34 (1963)]; E. S. Borovik and V. G. Volotskaya, Zh. Éksp. Teor. Fiz., **48**, 1554 (1965) [Sov. Phys. JETP **21**, 1041 (1965)].

This article was published in English in the original Russian journal. Reproduced here with stylistic changes by AIP.

New type of topological electronic transition in metals with a change in the Fermi energy

V. I. Makarov*

Scientific and Industrial Enterprise "Khartron-Plant," 1 ul. Proskury, Kharkov 61070, Ukraine

D. V. Bolotov and V. A. Gor'kavyĭ

B. N. Verkin Institute for Low Temperature Physics and Engineering, Ukrainian National Academy of Sciences, 47 pr. Lenina, Kharkov 61103, Ukraine

A. A. Yatsenko

National Scientific Center "Kharkov Physicotechnical Institute," 1 ul. Akademicheskaya, Kharkov 61108, Ukraine

(Submitted October 15, 2004; revised November 2, 2004)
Fiz. Nizk. Temp. **31**, 422–428 (March–April 2005)

A new type of electronic topological transition due to an abrupt change in the differential-geometric characteristics of the Fermi surface, whose topology remains unchanged, at some critical energy ε_d is predicted. This type of electronic topological transition differs from known electronic topological transitions due to a change in the topology of the Fermi surface in that the isoenergy surface $\varepsilon(p)=\varepsilon_d$ does not contain any singular points where the velocity of the electrons vanishes. It is shown that a feature common to both types of electronic topological transitions associated with an abrupt change in the topology of the Fermi surface and its differential-geometric characteristics with no change in topology is that a qualitative change occurs in the spherical image of the Fermi surface as a result of the abrupt change in the number of pre-images of a point under a spherical mapping. © *2005 American Institute of Physics.*
[DOI: 10.1063/1.1884435]

Electronic topological transitions associated with a change in the topology of the Fermi surface under the influence of an external action were predicted by Lifshitz[1] and first observed experimentally in Refs. 2–4. These investigations stimulated a long series of theoretical and experimental works on the influence of external actions on the electronic properties of metals and semimetals. A reliable indicator of the manifestation of electronic topological transitions is considered to be the observation of an abrupt change in the frequency spectrum of the oscillatory dependences of the macroscopic characteristics of conducting crystals as a function of the magnetic field or the observation of anomalies in the thermodynamic and kinetic characteristics as a result of singularities in the electron density of states with a change in the topology of the Fermi surface.

In the present paper a new type of electronic topological transition is studied. This transition is associated with an abrupt change in the differential-geometric characteristics of the Fermi surface at some critical energy ε_d with no change in the topology of the surface. This type of electronic topological transition is different from the well-known electronic topological transitions associated with a change in the topology of the Fermi surface in that the isoenergy surface $\varepsilon(p)=\varepsilon_d$ does not have any singular points where the electron velocity vanishes. It is shown that a feature common to both types of electronic topological transitions associated with abrupt changes in the Fermi surface topology and the differential-geometric characteristics of the Fermi surface with no change in topology is a qualitative change in the spherical image of the Fermi surface due to an abrupt change in the number of images of a point under a spherical mapping.

1. MODEL OF THE ELECTRONIC SPECTRUM OF A METAL

We shall consider a simple model of an electronic spectrum of a metal whose isoenergy surfaces $\varepsilon(p)=\varepsilon$ are described by an equation of fourth degree:

$$\varepsilon(p_0)=\varepsilon_c+\left(\frac{p_{0x}^2+p_{0y}^2+p_{0z}^2}{2m}\right)^2\frac{1}{\varepsilon_c}-2\left(\frac{p_{0z}^2-p_{0x}^2-p_{0y}^2}{2m}\right), \tag{1}$$

where p_{0i} are the components of the electron momentum, m is the free-electron mass, and ε_c is the critical energy. The form of the isoenergy surfaces, specifically, the topological properties, depends on the relation between the energies ε and ε_c. Aside from the differences in the topological character, the family of isoenergy surfaces $\varepsilon(p)=\varepsilon$ of this model electronic spectrum of a metal also includes surfaces with substantially different differential-geometric characteristics.

We introduce the dimensionless coordinates $p_{0i}^2/2m\varepsilon_c=p_i^2$ and write Eq. (1) in a cylindrical coordinate system:

$$\varepsilon(p)=\varepsilon_c(1+(\rho_\perp^2+p_z^2)^2-2(p_z^2-\rho_\perp^2)), \tag{2}$$

where $\rho_\perp^2=p_x^2+p_y^2$. The surfaces $\varepsilon(p)=\varepsilon$, which we are studying, are surfaces of revolution and can be represented by rotating meridian curves.

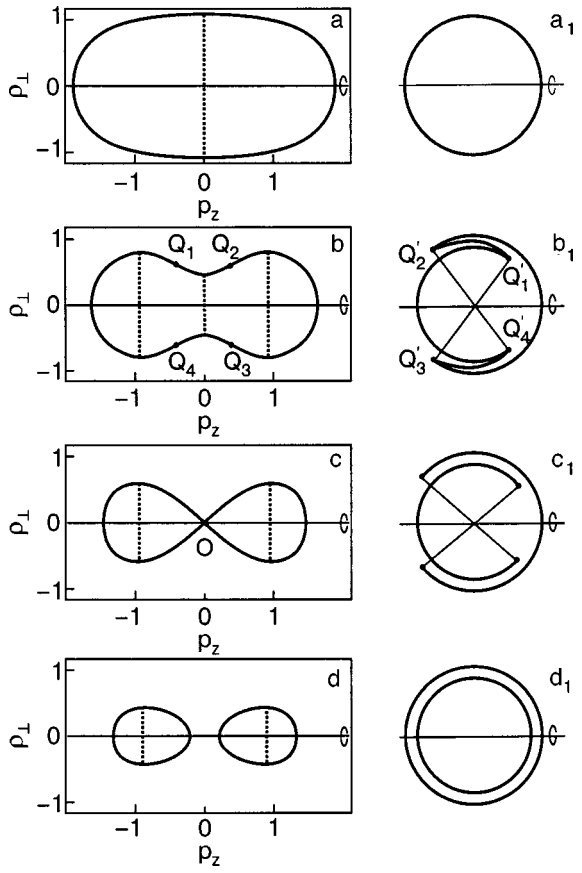

FIG. 1. Characteristic Fermi surfaces for the model spectrum (1), which are represented in cylindrical coordinates by rotatable meridian curves, and their spherical images: ''ovaloid,'' regular closed convex surface with positive Gaussian curvature (a); ''dumbbell,'' regular closed nonconvex surface with sign-alternating Gaussian curvature (b); closed nonconvex surface with positive Gaussian curvature, containing a singular point (c); two mutually symmetric regular closed convex surfaces with positive Gaussian curvature (d); a_1, b_1, c_1, and d_1—spherical images of the Fermi surfaces a, b, c, and d, respectively.

Figure 1 (left-hand column) shows the surfaces $\varepsilon(p)=\varepsilon_F$, characteristic for this model electronic spectrum, with fixed $\varepsilon_c=1$ eV and different values of the energies ε_F, eV: 5.0 (a), 1.5 (b), 1 (c), and 0.7 (d).

The two-dimensional surface (2) is a Cassini ovaloid. This surface of revolution is symmetric with respect to the coordinate origin and with respect to a plane passing through the coordinate origin orthogonally with respect to the rotation axis.

For $\varepsilon_F>4\varepsilon_c$ the Cassini ovaloid is a closed, strictly convex surface with positive Gaussian curvature (Fig. 1a).

For $\varepsilon=4\varepsilon_c$ the Cassini ovaloid is a closed convex surface whose Gaussian curvature is positive everywhere with the exception of the equatorial circle where the Gaussian curvature is zero.

For $\varepsilon_c<\varepsilon_F<4\varepsilon_c$ the Cassini ovaloid is a closed surface, reminiscent of a dumbbell, with sign-alternating Gaussian curvature. The surface contains two cap regions where the Gaussian curvature is positive (elliptical points), a belt region with points of negative Gaussian curvature (hyperbolic points), and two circles formed by parabolic points with zero Gaussian curvature (Fig. 1b). The points of inflection of the rotated curve Q_1, Q_2, Q_3, and Q_4 are marked in the figure. The elliptic caps are obtained by rotating the arcs Q_1Q_4 and Q_2Q_3, the hyperbolic belt is obtained by rotating the arcs Q_1Q_2 and Q_3Q_4, and the parabolic circles are obtained by rotating points Q_1, Q_2, Q_3, and Q_4.

In all of these cases the Cassini ovaloid has no singular points and is topologically equivalent to a sphere, though the differential-geometric characteristics change substantially from case *a* to case *b*.

For $\varepsilon_F=\varepsilon_c$ the Cassini ovaloid will contain a singular point of the conical type at the origin ($\rho_\perp=0$ and $\rho_z=0$), and at all other points of the ovaloid the Gaussian curvature will be positive (Fig. 1c).

For $\varepsilon_F<\varepsilon_c$ the Cassini ovaloid possesses two components each of which is a closed convex surface with positive Gaussian curvature (Fig. 1d).

The topological type of the Cassini ovaloid changes as one passes from case *b* through case *c* to case *d*.

Finally, as $\varepsilon_F\to 0$ the Cassini ovaloid contracts into two singular points with the coordinates $\rho_\perp=0$ and $p_z=p_c=\pm\sqrt{2m\varepsilon_c}$ on the axis of rotation.

In summary, as the parameters ε_F and ε_c vary the topological and differential-geometric characteristics change in the family of Cassini ovaloids.

2. NEW TYPE OF TOPOLOGICAL ELECTRONIC TRANSITION AND THE SPHERICAL IMAGE OF THE FERMI SURFACE

We shall now analyze how the changes in the differential-geometric characteristics of the model Fermi surfaces $\varepsilon(p)=\varepsilon_F$ will be reflected in the electronic properties of a metal, for example, in the de Haas-van Alphen oscillations (see Fig. 1).

It is well known that the spectrum of de Haas-van Alphen oscillations is determined by the number of extremal sections of the Fermi surface by a plane perpendicular to the direction of the magnetic field.[5] Let the field H be oriented along the p_z axis. Then the spectrum in the de Haas-van Alphen oscillations will be as follows.

For Fermi surfaces of the ''ovaloid'' type, where $\varepsilon_F\geqslant 4\varepsilon_c$, de Haas-van Alphen oscillations with one period corresponding to one extremal section $S(\varepsilon_F, p_{0z}=0)$ of the Fermi surface will be observed.

For a dumbbell-type Fermi surface, where $\varepsilon_c<\varepsilon_F<4\varepsilon_c$, the de Haas-van Alphen oscillations will contain oscillations with two periods, corresponding to three extremal sections $S(\varepsilon_F, p_{0z}=0)$ and $S(\varepsilon_F, p_{0z}=\pm\sqrt{m(4\varepsilon_c-\varepsilon_F)/2})$ of the Fermi surface. As $\varepsilon_F\to\varepsilon_c$ the section $S(\varepsilon_F, p_{0z}=0)$ of the Fermi surface contracts into a point.

For Fermi surfaces of the type ''two ovaloids,'' where $0<\varepsilon_F<\varepsilon_c$, the de Haas-van Alphen oscillations with one period corresponding to two identical extremal sections $S(\varepsilon_F, p_{0z}=\pm\sqrt{m(4\varepsilon_c-\varepsilon_F)/2})$ of the Fermi surface will be observed. As $\varepsilon_F\to 0$ these extremal sections of the Fermi surface contract into a point with the coordinates $p_z=p_c=\pm\sqrt{2m\varepsilon_c}$.

In summary, the spectrum of de Haas-van Alphen oscillations changes abruptly as the topology of the Fermi surface changes and with a transition from a Fermi surface with a sign-constant Gaussian curvature to a Fermi surface with a sign-alternating Gaussian curvature (''ovaloid-dumbbell'' transitions). Up to now it has been assumed that an abrupt change in the spectrum of de Haas-van Alphen oscillations is

a reliable indicator of a change in the topology of the Fermi surface.[1,5] We shall prove that a feature common to both of these two types of electronic topological transitions is a qualitative change in the spherical image of the Fermi surface. The right-hand column in Fig. 1 (a_1, b_1, c_1, and d_1) shows schematically the spherical images of Cassini ovaloids with the corresponding characteristic values of the Fermi energy ε_F.

We recall how a spherical image of an arbitrary, oriented, regular surface F^2 is constructed in a three-dimensional Euclidean space.[5,6] At each point P of the surface F^2 there is a single normal corresponding to the orientation chosen. Let us parallel transport this normal so that the origin of the normal coincides with the coordinate origin in E^3. Then the tip of the normal will mark a certain point Q on the unit sphere S^2. The mapping $F^2 \rightarrow S^2$ associating the point P to the point Q according to the scheme indicated is called a spherical mapping (Gaussian mapping). The set of points on the sphere S^2 which form the image of the surface F^2 under a spherical mapping is called a spherical image (Gaussian image) of the surface. The spherical image can have a quite complicated structure. Specifically, a spherical mapping degenerates at the parabolic points of the surface F^2, i.e. at points where the Gaussian curvature is zero. Specifically, if a curve of parabolic points separates regions on F^2 with negative and positive curvature, then this curve will correspond to a fold in the spherical image.

Returning to Fig. 1, we shall now examine the spherical images of Cassini ovaloids. Since a Cassini ovaloid is a surface of revolution, its spherical image is also a surface of revolution.

The spherical image of a Cassini ovaloid for $\varepsilon_F > 4\varepsilon_c$ will be a singly covered sphere—it is obtained by rotating the circle shown in Fig. $1a_1$.

For $\varepsilon_F = 4\varepsilon_c$ the spherical image will once again be a singly covered sphere described by rotating a circle, but now a distinguished equatorial circle, which is the image of a circle of parabolic points on a Cassini ovaloid, which can be regarded as a removable singularity of the spherical mapping, will appear on the sphere.

For $\varepsilon_c < \varepsilon_F < 4\varepsilon_c$ an idea of the qualitative form of the spherical image can be obtained by rotating the curve shown in Fig. 1b (irregularly covered circle). Therefore two circles of singular points forming folds will appear in the spherical image. These circles are images of the parabolic circles on a Cassini ovaloid; the points Q_i', which correspond to the points Q_i and form circles-folds when rotated, are marked in the figure. The belt on the sphere bounded by these circles-folds is covered three times; each of the remaining caps on the sphere is covered once.

For $\varepsilon_F = \varepsilon_c$ there is one singular conical point on the Cassini ovaloid. This is the coordinate origin O where the normal is not defined. The remaining regular part of the ovaloid separates into two connected open components. For each of these components the spherical image will be a part of a sphere with no cap, whose size is determined by the size of the opening of the tangent cone of the Cassini ovaloid at the singular point O. As a result the spherical image of the regular part of the Cassini ovaloid in this case will consist of a doubly covered belt on a sphere and two singly covered spherical caps—an idea of such a spherical image can be obtained by rotating the curve shown in Fig. $1c_1$ (two open partially overlapping arcs of a circle).

Finally, for $\varepsilon_F < \varepsilon_c$ the spherical image of each of two connected convex components forming a Cassini ovaloid will be a singly and regularly covered sphere so that the spherical image of the entire Cassini ovaloid will be a doubly and regularly covered sphere—it is obtained by rotating the doubly covered sphere shown in Fig. $1d_1$.

We note that as $\varepsilon_F \rightarrow 0$ the spherical image of a Cassini ovaloid will once again be a doubly and regularly covered sphere, irrespective of any decrease in the size of the ovaloid itself.

Therefore the changes of the topological and differential-geometric properties of a Cassini ovaloid are reflected in qualitative changes in the properties of its spherical image which are associated with a change in the number of pre-images of a point under a spherical mapping. This is manifested in a breakdown of continuity (appearance of breaks) and the appearance of singular points which form folds.

In summary, it can be concluded that a feature common to topological electronic transitions in metals with a change in the Fermi energy is a qualitative change in the spherical image of the Fermi surface due a change in the number of pre-images of a point under a spherical mapping. These two types of electronic topological transitions differ by the following:

—electronic topological transitions of the first type with a change in topology of the spherical image of the Fermi surface are due to a change in the topology of the Fermi surface at some critical energy ε_c; the isoenergy surface $\varepsilon(p) = \varepsilon_c$ contains singular points;[7,8]

—electronic topological transitions of the second type with a change in the topology of the spherical image of a Fermi surface are associated with an abrupt change in the local differential-geometric characteristics of the Fermi surface at some critical energy ε_d with no change in the topology of the surface; the isoenergy surface $\varepsilon(p) = \varepsilon_d$ has no singular points.

The electronic topological transitions of the first type were predicted by Lifshitz[1] and first observed experimentally in Refs. 2–4. The electronic topological transitions of the second type, which are due to a change in the differential topology of the spherical image of the Fermi surface, is studied for the first time. It can be asserted on the basis of the model considered for the electronic spectrum that an abrupt change in the thermodynamic and kinetic characteristics of metals which is due to a topological transition of the second type will be observed in all phenomena and effects where the extremal geometric dimensions of the Fermi surface and the effective masses of the conduction electrons are determined. If only these phenomena are studied, then the type of topological transition observed experimentally cannot be distinguished. Consequently, for example, an abrupt change in the spectrum of de Haas-van Alphen oscillations cannot be regarded as a reliable indicator of a change in the topology of the Fermi surface.

However, if the thermodynamic and kinetic characteristics of metals which are sensitive to the appearance or vanishing of singularities in the electronic density of states are

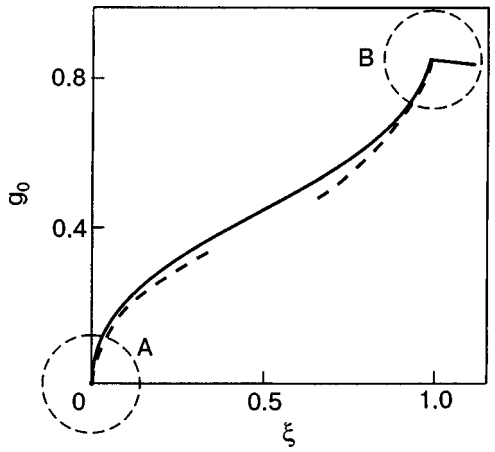

FIG. 2. $g_0(\xi)$ for the model spectrum (1) in a wide energy range. The distinguished regions are a region where new sections of the isoenergy surfaces arise (A) and a region where "bridges" between sections of isoenergy surfaces arise (B).

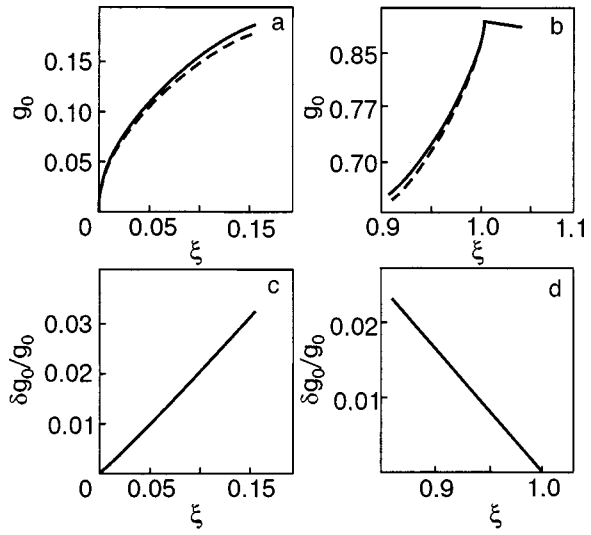

FIG. 3. $g_0(\xi)$ near topological transitions: regions where new sections of the isoenergy surfaces arise (a); region where "bridges" arise between sections of isoenergy surfaces (b), solid curves—the functions $g_0(\xi)$ (5), broken curves—approximating functions Eqs. (6) and (7). The relative error of the approximate expressions (6) and (7) with respect to the exact expression (5) (c, d).

also studied, then the type of electronic topological transition being observed can be easily determined experimentally. It is shown in Refs. 7 and 8 that singularities arise in the electron density of states only if the topology of the isoenergy surfaces of quasiparticles changes. For electronic topological transitions of the second type no singularities arise in the electron density of states.

It is well known that the electron density of states is given by the expression

$$\nu(\varepsilon)=\frac{V}{(2\pi\hbar)^3}\int dp\,\delta(\varepsilon(p)-\varepsilon). \tag{3}$$

It is easy to calculate the dependence of the electron density of states on the energy for the electronic spectrum given by Eq. (1):

$$\nu(\varepsilon)=\frac{V(2m)^{3/2}}{(2\pi\hbar)^3}\sqrt{\varepsilon_c}g_0(\xi), \tag{4}$$

$$\xi=\varepsilon/\varepsilon_c,$$

where the function $g_0(\xi)$ is given by the formula

$$g_0(\xi)=\begin{cases}\ln((1+\sqrt{1+\sqrt{\xi}})/(1+\sqrt{1-\sqrt{\xi}})), & 0\leqslant\xi\leqslant 1,\\ \ln((1+\sqrt{1+\sqrt{\xi}})/\sqrt[4]{\xi}), & \xi\geqslant 1.\end{cases} \tag{5}$$

It follows from Eq. (5) that there are two types of singularities in the electron density of states in the energy range $0<\varepsilon\leqslant\varepsilon_c$ which are due to topological transitions (Fig. 2). In a small neighborhood near the critical energies—the regions A and B in Fig. 2—the function $g_0(\xi)$ can be approximated by the function $g_a(\xi)$. We shall determine the function $g_a(\xi)$. As the Fermi energy increases by a small amount from $\varepsilon_F=0$, two ovaloids are "created." These ovaloids increase in size as ε_F increases, and the density of states (5) has a square-root singularity at $\varepsilon=\varepsilon_F=0$ (i.e., as $\xi\to 0$). The approximating function $g_a(\xi)$ has the form

$$g_a(\xi)=\frac{1}{2}\sqrt{\xi}=\frac{1}{2}\sqrt{\frac{\varepsilon_F}{\varepsilon_c}}. \tag{6}$$

As the Fermi energy increases further, $\varepsilon=\varepsilon_F\to\varepsilon_c$, a connected closed surface with one conical singular point is formed from two ovaloids. At the energies $\varepsilon=\varepsilon_F=\varepsilon_c$ (i.e. as $\xi\to 1$) the square-root singularity in the density of states vanishes and the function $g_a(\xi)$ can be written in the form

$$g_a(\xi)=\ln(1+\sqrt{2})-\frac{\sqrt{2}}{2}\sqrt{1-\xi}$$

$$=\ln(1+\sqrt{2})-\frac{\sqrt{2}}{2}\sqrt{\frac{\varepsilon_c-\varepsilon_F}{\varepsilon_c}}. \tag{7}$$

On the other hand it follows from the expression (5) that for $4\varepsilon_c-\varepsilon_F=\pm\delta\varepsilon$ there are no singularities in the density of states, and the function $g_a(\xi)$ approximating $g_0(\xi)$ as $\varepsilon_F\to 4\varepsilon_c$ has the form

$$g_a(\xi)=\ln\left(\frac{\sqrt{3}+1}{\sqrt{2}}\right)+\frac{\sqrt{3}}{48}(4-\xi)$$

$$=\ln\left(\frac{\sqrt{3}+1}{\sqrt{2}}\right)+\frac{\sqrt{3}}{48}\left(\frac{4\varepsilon_c-\varepsilon_F}{\varepsilon_c}\right). \tag{8}$$

This model makes it possible to determine numerically the energy range where the singularities of the density of states can be approximated, to a good degree of accuracy, by a square-root dependence on the quantity $\varepsilon_F/\varepsilon_c$ or $\delta\varepsilon/\varepsilon_c=|\varepsilon_F-\varepsilon_c|/\varepsilon_c$, respectively (see Fig. 3). Calculations show that near an electronic topological transition the anomalies occurring in the macroscopic characteristics of conducting crystals as a result of a special part of the density of states can be approximated by two terms: a linear term proportional to the external action and a nonlinear term due to the square-root singularity in the density of states. The relative accuracy of such an approximation $\delta g(\xi)/g_0(\xi)=|g_0(\xi)-g_a(\xi)|/g_0(\xi)$ is 1–2% up to the values $\varepsilon/\varepsilon_c=0.1$ or $\delta\varepsilon/\varepsilon_c=0.1$ (Figs. 3c, d, respectively). This result makes it possible to justify a methodology for analyzing experimental

data where macroscopic anomalies are observed in the thermodynamic characteristics of superconductors and the thermo-emf under the influence of pressure and impurity concentration.[9–11] If a topological transition is observed under a change in external pressure, then the scale of quantity $\delta\varepsilon/\varepsilon_c$ is

$$\delta\varepsilon/\varepsilon_c \approx \delta V/V = \gamma P,$$

where $\delta V/V$ is the relative change in the volume of the body under pressure P and γ is the compressibility of the metal. Since for metals the compressibility $\gamma \approx 10^{-6}$ cm^2/kg, up to pressures $P \approx 10^5$ kg/cm^2 the experimental data can be described using Eqs. (6) and (7).

In summary, the proposed model electronic spectrum (1), which has a large set of different differential-geometric and topological characteristics of the Fermi surface, made it possible to predict a new type of electronic topological transition in metals with a change in Fermi energy and to introduce a new concept which generalizes different types of electronic topological transitions occurring in metals with a change in Fermi energy—a change in the topology of the spherical image of the Fermi surface.

A number of metals possess ''dubbell-type'' sections of the Fermi surface. For example, for thallium such sections of the Fermi surface lie in the fifth Brillouin zone.[12] It can be inferred that if the Fermi energy is changed in an appropriate manner, then a dumbbell-ovaloid transition associated with a change in the topology of the spherical image of the Fermi surface is possible for these metals.

*E-mail: vimakarov@ic.kharkov.ua

[1] I. M. Lifshitz, Zh. Éksp. Teor. Fiz. **38**, 1569 (1960) [JETP **11**, 1130 (1960)].
[2] V. I. Makarov and V. G. Bar'yakhtar, Zh. Éksp. Teor. Fiz. **48**, 1717 (1965) [JETP **21**, 1151 (1965)].
[3] N. B. Brandt, N. I. Ginzburg, T. A. Ignat'eva, B. G. Lazarev, L. S. Lazareva, and V. I. Makarov, Zh. Éksp. Teor. Fiz. **49**, 85 (1965) [JETP **22**, 61 (1965)].
[4] C. W. Chu, T. F. Smith, and W. E. Gardner, Phys. Rev. Lett. **20**, 198 (1968).
[5] D. Hilbert and S. Cohn-Vóssen, *Geometry and the Imagination*, Chelsea Pub. Co., New York (1990) [Russian translation, Nauka, Moscow (1981)].
[6] Yu. A. Aminov, *Geometry of Submanifolds*, Naukova-dumka, Kiev (2002).
[7] L. Van Hove, Phys. Rev. B **89**, 1189 (1953).
[8] J. C. Phillips, Phys. Rev. **104**, 1263 (1956).
[9] N. V. Zavaritskiĭ, V. I. Makarov, and A. A. Yurgens, JETP Lett. **42**, 182 (1985).
[10] V. G. Bar'yakhtar, V. V. Gann, V. I. Makarov, and T. A. Ignat'eva, Zh. Éksp. Teor. Fiz. **62**, 1118 (1972) [JETP **35**, 591 (1972)].
[11] T. A. Ignat'eva and A. N. Velikodnyĭ, Fiz. Nizk. Temp. **30**, 523 (2004) [Low Temp. Phys. **30**, 388 (2004)].
[12] P. M. Holtham, J. Phys. F: Met. Phys. **3**, 1361 (1973).

Translated by M. E. Alferieff

Spin-orbit interaction in thin bismuth films

Yu. F. Komnik, I. B. Berkutov, and V. V. Andrievskiĭ*

B. N. Verkin Institute for Low-Temperature Physics and Engineering, Ukrainian National Academy of Sciences, 47 pr. Lenina, Khar'kov 61103, Ukraine

(Submitted November 1, 2004)
Fiz. Nizk. Temp. **31**, 429–435 (March–April 2005)

The magnetic-field dependences of the resistance of thin (100–700 Å thick) bismuth films at low temperatures are analyzed using quantum corrections to the conductivity with weak electron localization. It is shown that the spin-orbit scattering time τ_{so} is much shorter than the phase relaxation time τ_φ of the electrons (the case of a strong spin-orbit interaction). It is found that τ_{so} tends to increase with the film thickness. This shows that the surface scattering of the electrons plays a dominant role in spin-orbit processes. Apparently, strong spin relaxation in the presence of surface scattering is due to the gradient of the internal crystal-field potential near the surface of the metal, resulting in lifting of the spin degeneracy and in the appearance of a spin gap (Rashba mechanism). © *2005 American Institute of Physics.*
[DOI: 10.1063/1.1884436]

1. INTRODUCTION

The behavior of the conductivity of a metal in a magnetic field yields information about the structure and parameters of the electronic energy spectrum.[1] For example, the asymptotic behavior of the conductivity in strong magnetic fields reflects the topological properties of the electronic spectrum, and the magnetoquantum effects (Shubnikov-de Haas oscillations) yield information about the characteristic parameters of the spectrum.[2] An understanding of quantum effects of an interference nature, weak electron localization,[3–5] and the electron-electron interaction[5–8] has opened up the possibility of obtaining information about the relaxation times and interaction parameters of electrons from the behavior of the magnetoresistance.

Thin bismuth films were the first object where the effects of weak localization and the interaction of electrons were observed.[9–12] Subsequently, these effects were observed in many weakly disordered conductors of different dimensions.[13,14] According to theory,[5] the contribution of weak localization to the conductivity of a two-dimensional system as a function of a magnetic field B oriented perpendicular to the film plane has the form

$$\Delta\sigma_B=\sigma(B)-\sigma_0(B)=\frac{e^2}{2\pi^2\hbar}\times\left[\frac{3}{2}f_2\left(\frac{4eBD}{\hbar}\tau_\varphi^*\right)-\frac{1}{2}f_2\left(\frac{4eBD}{\hbar}\tau_\varphi\right)\right], \quad (1)$$

where $f_2(x)=\ln x+\Psi(1/x+1/2)$; Ψ is the logarithmic derivative of the Γ function; D is the electron diffusion coefficient; τ_φ is the phase relaxation time; τ_φ^* is the modified time taking account of the spin-orbit interaction: $(\tau_\varphi^*)^{-1}=\tau_\varphi^{-1}+4/3\tau_{so}^{-1}$; and, τ_{so} is the spin relaxation time due to the spin-orbit interaction.

For a weak spin-orbit interaction ($\tau_{so}\gg\tau_\varphi$) Eq. (1) describes a positive magnetoconductivity (negative magnetoresistance), which is typical for the manifestation of weak localization. For a strong spin-orbit interaction ($\tau_{so}<\tau_\varphi$) the second term in Eq. (1) determines $\Delta\sigma_B$; this corresponds to the manifestation of an anomalous positive magnetoresistance. Then Eq. (1) becomes

$$\Delta\sigma_B=-\frac{1}{2}\frac{e^2}{2\pi^2\hbar}f_2\left(\frac{4eBD}{\hbar}\tau_\varphi\right). \quad (2)$$

The case of a positive anomalous magnetoresistance in the weak localization effect has been termed ''antilocalization.''

It is a positive magnetoresistance that has been found to be characteristic for thin bismuth films manifesting weak localization, whence it was concluded that a strong spin-orbit interaction is characteristic for this object. The reason for this remained unclear. After all, in a bulk bismuth crystal whose crystal lattice is described by a weakly distorted cube with a center of inversion there is no reason for a strong spin-orbit interaction to appear in the absence of a magnetic field.

In works concerning the effects due to weak localization in bismuth films the expression (2) was used to describe the behavior of the magnetoconductivity, so that information was obtained only about the phase relaxation time τ_φ. In Ref. 12 it is noted that the spin-orbit interaction time τ_{so} in bismuth films is much shorter than τ_φ and apparently varies with the film thickness. Modern computers make it possible to analyze the change in magnetoconductivity using Eq. (1) and to determine the behavior of τ_{so} as a function of the thickness and other parameters. This could be helpful for determining why the spin-orbit interaction in bismuth films is strong.

2. EXPERIMENTAL AND COMPUTATIONAL PROCEDURES

The experimental magnetic-field dependences of the resistance measured at liquid-helium and higher temperatures for four series of thin-film bismuth samples, in each of which three or four thicknesses were represented, were analyzed. The samples were obtained by condensing a molecular bismuth beam in a high vacuum (5×10^{-6} mm Hg) on a substrate (glass, mica) at room temperature. The films possessed texture: the C_3 axis was oriented in a direction normal to the film plane. The film thickness range was 100–700 Å; the

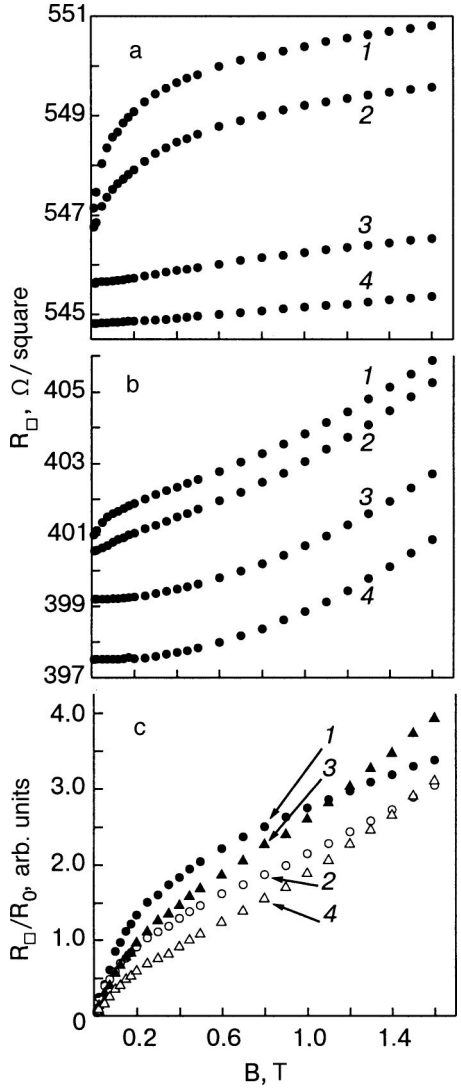

FIG. 1. Magnetic field variation of the resistance of samples in series 3 with thicknesses 380 Å (a) and 570 Å (b) at temperatures T, K: 2 (*1*), 4.2 (*2*), 14 (*3*), and 20 (*4*). Magnetic field variation of the resistance of samples in series 2 with thicknesses (in Å): 180 (*1*), 280 (*2*), 400 (*3*), and 450 (*4*) at temperature 4.2 K (c).

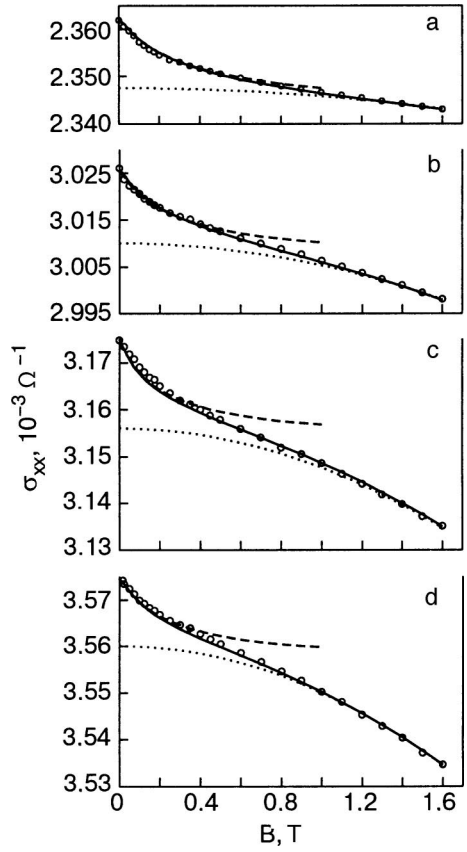

FIG. 2. Description of the experimental dependences (○) of the conductivity of bismuth films on the magnetic field by Eq. (1) for weak localization taking account of the Drude contribution to the magnetoconductivity (—); separation of the Drude contribution (···) from the magnetic field variation of the conductivity; magnetic field variation of the quantum correction due to weak localization (with respect to the conductivity at $B=0$) (– –). Examples are demonstrated for samples in series 2 at temperature $T=4.2$ K with different thicknesses (in Å): 180 (a), 280 (b), 400 (c), and 450 (d).

effects due to weak electron localization are not manifested clearly for larger thicknesses. The sample series differed somewhat by the conditions under which the films were condensed (substrate temperature and condensation rate) and, correspondingly, by their transport characteristics. The traces of the magnetoresistance curves were obtained in magnetic fields up to 1.6 T at temperatures 1.5–4.5 K and also at 14–20 and 77 K (examples of magnetoresistance traces are displayed in Fig. 1).

For comparing with theory the magnetoresistance traces were converted into the magnetic-field variation of the conductivity of a two-dimensional system using the relation $\Delta\sigma=-(\Delta R/R)\cdot(1/R_\square)$, where $R_\square$ is the resistance of a square section of film, which is an analog of the resistivity in the two-dimensional case. This transformation is valid because the ratio $\Delta R/R$ is small and because measurements have shown that for a perpendicular orientation of the magnetic field the Hall component of the magnetoresistance $R_{\square xy}\sim 10^{-2}R_{\square xx}$.

To determine the quantum correction introduced into the conductivity by weak electron localization it is important to take account of the contribution of the classical (Drude) magnetic-field variation of the resistance of the form μ^2B^2 (μ is the mobility) to the magnetoresistance, which was not done in previous works on weak localization in bismuth films. We used a technique proposed in Ref. 15, specifically, in the range of logarithmic saturation of the function (1) the mobility values for which the function $\sigma_B=\sigma_0^D/1+\mu^2B^2$ is identical to the experimental dependence $\sigma(B)$ were determined.[1)] In Fig. 2 the dotted line demonstrates the procedure for finding the Drude magnetoresistance of one series of samples.

Next, the value of the ''two-dimensional'' concentration n_2 follows from the expression $\sigma_0=(R_\square^0)^{-1}=ne\mu$. The relation $n_3=n_2L^{-1}$, where L is the film thickness, should be used for comparing with the data on the ''three-dimensional'' concentration obtained in Refs. 16–18. It should be noted that bismuth films exhibit a quantum-size effect,[19–21] resulting in resistance oscillations as a function of the film thickness. These oscillations are clearly seen for thicknesses $L>1000$ Å. Resistance oscillations can be neglected in the thickness range studied in the present work.

After the Drude contribution was removed from the magnetic-field dependences obtained for the conductivity (see dashed curves in Fig. 2), the dependence calculated us-

ing Eq. (1) and the desired values of the parameters τ_φ and τ_{so} were matched with the experimentally determined dependence reflecting the contribution of quantum corrections. The diffusion coefficient D was determined using Einstein's formula $D=G/2e\nu$, where G is the specific volume conductivity and ν is the electron density of states at the Fermi surface (for bismuth films $\nu\approx 10^{20}$ eV^{-1} cm^{-3} taking account of the change in the charge carrier concentration and the Fermi energy with decreasing film thickness[17]). The cyclotron mass of the electrons and holes in bismuth with the magnetic field oriented along the C_3 axis is $m^*=0.063m_0$, where m_0 is the free-electron mass. It is this value of the effective mass of electrons and holes that was used to determine the elastic time τ from the conductivity. The time τ was found to be of the order 10^{-15} s.

The matching procedure was quite successful in all cases. This is demonstrated in Fig. 2 (solid curves). Aside from weak electron localization, the contribution of other corrections due to the electron-electron interaction is negligible. Our estimates show that for reasonable values of the interaction constant λ_B^D and known values of the Landé factor g (for $B\|$. C_3 $g=1.06$ for electrons and $g=4.26$ for holes) for bismuth the quantum corrections to the magnetic-field dependence of the conductivity in the diffusion channel are much smaller than for weak localization (in contrast to their temperature dependence where the interaction corrections are greater than the correction due to weak localization).[22] Similarly, including in the matching procedure the quantum correction due to interaction in the Cooper channel simply degrades appreciably the agreement between the experimental curves and Eq. (1) describing weak electron localization.

3. COMPUTATIONAL RESULTS

Our calculations of the contribution of weak localization to the magnetic-field variation of the conductivity of bismuth films differ from previous calculations[9,10] by the following important features: in the first place the expression (1) was used in the calculations, making it possible to determine τ_{so}, and in the second place the contribution of the Drude variation of the magnetoconductivity was singled out and taken into account.

The computational results agree with the basic behavior of characteristics such as the concentration and mobility, determined in Refs. 16–18, where the galvanomagnetic properties of bismuth films were studied.

All calculations were performed in the SI system. The values found for the mobility lie in the range 0.01–0.07 m^{2}V^{-1}s^{-1}, which agrees with calculations of the average mobility using the system of equations for galvanomagnetic properties of bismuth films.[18] The values of μ increase smoothly with film thickness in each series, but they are different for different series because of differences in the structural characteristics of the films. This is also observed for the thickness dependences of the diffusion coefficient D and the average mean-free path length l. In the more perfect series 1 and 2 the path lengths l are somewhat greater than the thickness L; in the series 3 and 4 l is slightless less than the film thickness.

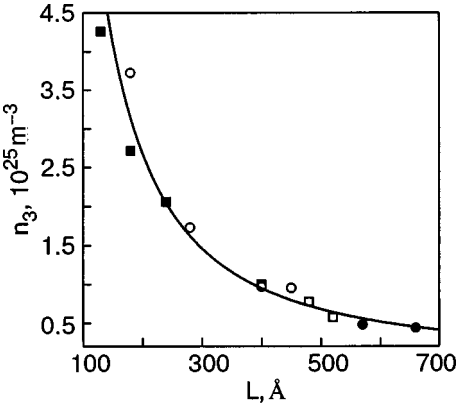

FIG. 3. Charge carrier concentration versus bismuth film thickness for different series: 1 (●), 2 (○), 3 (■), and 4 (□). Dependence of the form $n_3=7.6\times10^{28}\cdot L^{-1.5}$(—).

In contrast to the transport characteristics the values of the ''three-dimensional'' charge carrier concentration fall on a single curve versus the film thickness (see Fig. 3). This dependence is essentially the same as that obtained in calculations using the system of equations for galvanomagnetic properties of films.[16–18] The increase in carrier concentration with decreasing bismuth film thickness, first established in Ref. 16, was explained in Refs. 17 and 23 as being due to the nonuniform distribution of the potential, which has a bend near the surfaces, in the film. The nonuniform static potential in a semimetal results in an effective increase of band overlapping and increases the average carrier density.

The film-thickness and temperature dependences of the times τ_φ and τ_{so} are qualitatively different. The phase relaxation time τ_φ does not exhibit a clear dependence on L (Fig. 4a), and the spin-orbit relaxation time τ_{so} tends to increase somewhat with increasing thickness (Fig. 4b). As temperature increases, τ_{so} remains unchanged and τ_φ decreases (Fig. 5). This time is determined by inelastic scattering

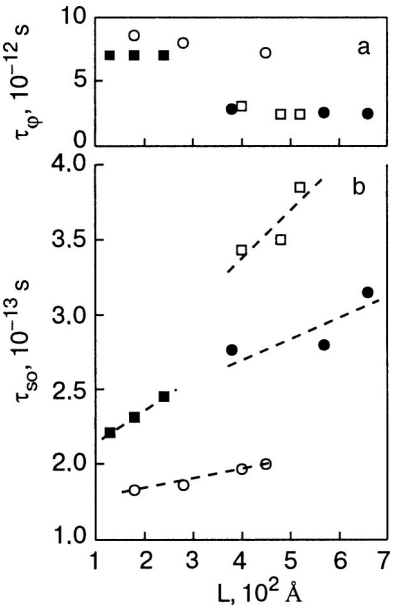

FIG. 4. Variation of the phase time τ_φ (a) and spin-orbit relaxation time τ_{so} (b) with increasing bismuth film thickness. The labeling of the series of samples is the same as in Fig. 3. The broken lines are drawn for clarity.

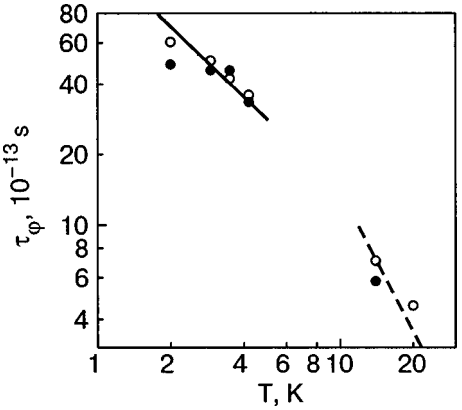

FIG. 5. Temperature variation of the phase relaxation time τ_φ of samples in series 3 with thickness, (in Å): 380 (○) and 570 (●); $\tau_\varphi = 3.9\times10^{-13}\cdot T^{-1}$ (—), $\tau_\varphi = 4\times10^{-12}\cdot T^{-2}$ (— — —).

processes—electron-electron and electron-phonon. At temperatures below 4 K electron-electron scattering predominates; for these processes the theory of the electron-electron interaction in disordered two-dimensional conductors predicts $\tau_{ee}^{-1}\propto T$.[7,8] This dependence is satisfactorily realized for the groups of points in Fig. 5 below 4 K. As temperature increases, the electron-phonon scattering processes play an increasingly larger role. The dependence $\tau_\varphi^{-1}\propto T^2$ is observed in bismuth films at temperatures above 4 K.[24] The reasons for the appearance of such a temperature dependence of τ_φ for bismuth films at $T>4$ K and for beryllium,[25] niobium, and aluminum[26] films at $T>10$ K are discussed in Ref. 24.

4. DISCUSSION

In this work the values of the time τ_{so} in bismuth films indicating a strong spin-orbit interaction were obtained. It was also found that τ_{so} tends to increase with film thickness.

The high spin-orbit scattering rate in thin bismuth films is due, in our opinion, to carrier interaction with the surface. We shall try to substantiate this below.

The idea that spin-orbit interaction plays a substantial role for electrons in small samples was first advanced in Refs. 27 and 28 in connection with the observation of a nonzero nuclear magnetic resonance frequency shift in superconducting films as $T\to0$ (Knight shift). It was inferred that the direction of the spin of an electron scattered by the boundary can change, as a result of which the total spin of the system is no longer zero. In connection with this idea, Abrikosov and Gor'kov constructed a theory of spin-orbit interaction in the scattering of electrons by impurities.[29] The experimental data for the spin-orbit relaxation time determined from the Knight shift, the critical magnetic field of ultrathin films, experiments on tunneling of spin-polarized electrons into a superconductor, and spin resonance of conduction electrons in normal metals were analyzed in Ref. 30. In this work a check was made of whether or not the dependence of τ_{so}^{-1} on the atomic number Z of a metal satisfies the relation from Ref. 29:

$$\frac{\tau_{so}^{-1}}{\tau^{-1}}\approx(aZ)^4, \tag{3}$$

where τ is the elastic scattering time and $a=e^2/\hbar c=1/137$ is the fine structure constant. The ratio $\tau_{so}^{-1}/\tau-1=\varepsilon$ characterizes the probability of a spin-orbit process in elastic scattering. In Ref. 30 it was assumed that since all data for τ_{so} refer to thin films, the main momentum scattering mechanism is surface scattering, so that the transit time $\tau^{sf}=L/v_F$ of an electron between two surfaces, where v_F is the Fermi velocity, was used as the time τ. It was found that the Z dependences of $\tau_{so}^{-1}/(\tau^{sf})^{-1}$ functionally agree with Eq. (3), but the experimental values are severalfold greater than the values calculated from this expression, ranging from small values ($\sim10^{-5}$–10^{-7}) for light metals (such as Li) up to very large values for heavy metals (for Sn ~0.1, Pb~0.5). Thus, for heavy metals a collision of an electron with the surface is very likely to be accompanied by a change in spin orientation. The strong spin-orbit interaction observed in bismuth films (the time τ_{so} turned out to be close in order of magnitude to the elastic scattering time τ) corresponds to the results of an analysis of the experimental data for τ_{so} in Ref. 30.

The ratio of the probabilities of spin-orbit scattering processes at the surface ε^{sf} and in the bulk ε^b of a film was estimated in Refs. 31 and 32. In Ref. 31 it was found for Mg films that ε^{sf} is one to two orders of magnitude greater than ε^b, depending on the type of substrate. In Ref. 32 it was also established for Au films that $\varepsilon^{sf}\gg\varepsilon^b$ (the values obtained were $\varepsilon^{sf}\approx2\times10^{-2}$ and $\varepsilon^b\approx4\times10^{-4}$).

It is completely obvious that the tendency for τ_{so} to increase with film thickness (Fig. 4b) shows that the computed values of τ_{so} reflect primarily spin-orbit processes at a surface, since a decrease of the influence of the surface with increasing thickness where $\varepsilon^{sf}\gg\varepsilon^b$ should result in a weaker spin-orbit interaction in the film, i.e. an increase of τ_{so}. We shall illustrate this using the following qualitative relations. Let the conduction electrons in the film undergo elastic scattering in the bulk and at the surface of the film. Let the time τ_{so} found be represented by two components for spin-orbit processes in the bulk and at the surface:

$$\frac{1}{\tau_{so}}=\frac{1}{\tau_{so}^b}+\frac{1}{\tau_{so}^{sf}}=\frac{\varepsilon^b}{\tau^b}+\frac{\varepsilon^{sf}}{\tau^{sf}}, \tag{4}$$

where τ^b and τ^{sf} are the corresponding times of the elastic processes. Let $\tau^b\approx l/v_F$ and τ^{sf} equal to approximately L/v_F in the "pure" limit ($l>L$), and in the "dirty" limit ($l<L$) let τ^{sf} be determined by the electron diffusion time from one surface to the other $\tau^{sf}\approx L^2/D$, where the diffusion coefficient $D\approx v_F l$. Then it follows from the expression (4) that

for the "pure" limit

$$\frac{1}{\tau_{so}}=\frac{\varepsilon^b v_F}{l}+\frac{\varepsilon^{sf}v_F}{L}, \tag{5}$$

for the "dirty" limit

$$\frac{1}{\tau_{so}}=\frac{\varepsilon^b v_F}{l}+\frac{\varepsilon^{sf}v_F l}{L^2}. \tag{6}$$

It is obvious that for $\varepsilon^b\ll\varepsilon^{sf}$ the integral time τ_{so} found in both cases should increase with film thickness. An intermediate case ($l\approx L$) is realized in the objects studied. This makes it impossible to use the formulas presented above for the analysis.

We believe that the reason for the strong spin-orbit process accompanying surface reflection of electrons could be a mechanism associated with the bending of the potential near the surface of a conductor, which follows from the requirement that the wave function of charge carriers vanish at the boundary. The spin state of an electron changes in a region where a gradient $\nabla V(r)$ of the potential exists. The spin-orbit interaction Hamiltonian has the form[33]

$$H_{so}=\frac{\hbar}{(2m_0c)^2}[\nabla V(r)\times\mathbf{p}]\hat{\sigma}, \tag{7}$$

where $\mathbf{p}$ is the quasimomentum of an electron and $\hat{\sigma}$ is a Pauli matrix. The electron spin is oriented perpendicular to its momentum and to the gradient of the potential. For $k\neq 0$ (k is the wave number) the spin degeneracy is lifted and the states are split (the Rashba mechanism). The corresponding theory[34,35] developed for a two-dimensional electron gas in heterojunctions in semiconductors predicts the appearance of two branches in the electron energy spectrum:

$$E^{\pm}(k)=\frac{\hbar^2k^2}{2m}\pm\alpha k, \tag{8}$$

(α is the spin-splitting parameter) and the existence of a spin gap

$$\Delta_s=E^{+}+E^{-}=2\alpha k_F. \tag{9}$$

These ideas have been extended to inversion layers in semiconductors, i.e. regions of bending of the potential near a surface.

The existence of two branches in the spectrum of mear-surface electrons with different spin polarization creates an additional channel for the spin-orbit process accompanying surface reflection of electrons. As a result the probability of a spin-orbit process accompanying scattering by the surface of a crystal is much higher than for elastic scattering of electrons by impurity atoms.

5. CONCLUSIONS

In summary, according to the ideas presented above, the answer to the question of why the manifestation of weak localization in thin bismuth films has the character of ''antilocalization'' is that the strong spin-orbit relaxation in thin bismuth films is associated primarily with surface scattering of electrons. It is supposed that electron scattering from a surface occurs under conditions where a gradient of the crystal potential exists near the surface, lifting the spin degeneracy in the electron spectrum near the surface and giving rise to intense spin relaxation accompanying surface scattering. As the film thickness increases and the contribution of surface scattering to the conductivity decreases, the spin-orbit interaction should become much weaker, as is qualitatively confirmed by the fact that the values found for the spin-orbit relaxation time τ_{so} tend to increase.

This work was supported in part by a stipend awarded to young scientists by the Ukrainian National Academy of Sciences.

*E-Mail: Andrievskii@ilt.kharkov.ua

[1)]We have in mind the average mobility of two types of carriers, since calculations have shown[16–18] that the electron and hole mobilities found for bismuth films from the system of equations for the conductivity, the magnetoresistance, and the Hall coefficient are close. The electron and hole concentrations remain equal to one another.

[1] E. S. Borovik, *Doctoral Dissertation in Physical and Mathematical Sciences*, Kharkov State University, Khar'kov (1954).
[2] I. M. Lifshitz, M. Ya. Azbel', and M. I. Kaganov, *Electron Theory of Metals*, Consultants Bureau, New York (1973) [Russian original, Nauka, Moscow (1971)].
[3] P. W. Anderson, E. Abrahams, and T. V. Ramakrishnan, Phys. Rev. Lett. **43**, 718 (1979).
[4] B. L. Altshuler, D. E. Khmel'nitskii, A. I. Larkin, and P. A. Lee, Phys. Rev. B **22**, 5142 (1980).
[5] B. L. Al'tshuler, A. G. Aronov, A. I. Larkin, and D. E. Khmel'nitskiĭ, Zh. Éksp. Teor. Fiz. **81**, 768 (1981) [JETP **54**, 411 (1981)].
[6] B. L. Altshuler, A. G. Aronov, and P. A. Lee, Phys. Rev. Lett. **44**, 1288 (1980).
[7] B. L. Altshuler, A. G. Aronov, and D. E. Khmelnitskii, J. Phys. C **15**, 7367 (1982).
[8] B. L. Altshuler and A. G. Aronov, in *Electron-Electron Interaction in Disordered Systems. Modern Problems in Condensed Matter Science*, edited by A. L. Efros and M. P. Pollak, North-Holland, Amsterdam (1985), Vol. 10, p. 1.
[9] Yu. F. Komnik, E. I. Bukhshtab, V. V. Andrievskii, and A. V. Butenko, J. Low Temp. Phys. **52**, 315 (1983).
[10] F. Komori, S. Kobayashi, and W. Sasaki, J. Phys. Soc. Jpn. **52**, 368 (1983).
[11] A. K. Savchenko, A. S. Rylik, and V. N. Lutskiĭ, Zh. Eksp. Teor. Fiz. **85**, 2210 (1983) [JETP **58**, 1279 (1983)].
[12] A. V. Butenko, Yu. F. Komnik, and E. I. Bukhshtab, Fiz. Nizk. Temp. **9**, 1171 (1983) [Low Temp. Phys. **9**, 604 (1983)].
[13] P. A. Lee and T. V. Ramakhrishnan, Rev. Mod. Phys. **53**, 287 (1985).
[14] B. L. Altshuler, A. G. Aronov, M. E. Gershenson, and Yu. V. Sharvin in Sov. Sci. Rev. A **9**, Harwood Academic Publishers Gmbh, Schur, Switzerland (1987), p. 223.
[15] Y. Y. Proskuryakov, A. K. Savchenko, S. S. Safonov, M. Pepper, M. Y. Simmons, and D. A. Ritchie, Phys. Rev. Lett. **86**, 21, 4895 (2001).
[16] Yu. F. Komnik, E. I. Bukhshtab, Yu. V. Nikitin, and V. V. Andrievskiĭ, Zh. Éksp. Teor. Fiz. **60**, 669 (1971) [JETP **33**, 364 (1971)].
[17] Yu. F. Komnik and V. V. Andrievskiĭ, Fiz. Nizk. Temp. **1**, 104 (1975) [Sov. J. Low Temp. Phys. **1**, 51 (1975)].
[18] A. S. Anopchenko, V. Yu. Kashirin, and Yu. F. Komnik, Fiz. Nizk. Temp. **21**, 451 (1995) [Low Temp. Phys. **21**, 353 (1995)].
[19] Yu. F. Ogrin, V. N. Lutskiĭ, and M. I. Elinson, JETP Lett. **3**, 71 (1966).
[20] Yu. F. Komnik and E. I. Bukhshtab, Zh. Éksp. Teor. Fiz. **54**, 63 (1968) [JETP **27**, 34 (1968)].
[21] Yu. F. Komnik, *Physics of Metallic Films. Size and Structural Effects*, Atomizdat, Moscow (1979).
[22] Yu. F. Komnik, E. I. Bukhshtab, A. V. Butenko, and V. V. Andrievskii, Solid State Commun. **44**, 865 (1982).
[23] A. Ya. Shik, Fiz. Tver. Tela (Leningrad) **16**, 2801 (1974) [Sov. Phys. Solid State **16**, 1822 (1974)].
[24] V. Yu. Kashirin and Yu. F. Komnik, Fiz. Nizk. Temp. **18**, 1246 (1992) [Low Temp. Phys. **18**, 872 (1992)].
[25] A. V. Butenko, E. I. Bukhshtab, V. Yu. Kashirin, and Yu. F. Komnik, Fiz. Nizk. Temp. **14**, 421 (1988) [Low Temp. Phys. **14**, 233 (1988)].
[26] M. E. Gershenzon, V. N. Gubankov, and Yu. E. Zhuravlev, Zh. Eksp. Teor. Fiz. **85**, 287 (1983) [JETP **58**, 167 (1983)].
[27] R. A. Farrell, Phys. Rev. Lett. **3**, 262 (1959).
[28] P. W. Anderson, Phys. Rev. Lett. **3**, 325 (1959).
[29] A. A. Abrikosov and L. P. Gor'kov, Zh. Éksp. Teor. Fiz. **42**, 1088 (1962) [JETP **15**, 752 (1962)].
[30] R. Meservey and P. M. Tedrow, Phys. Rev. Lett. **41**, 805 (1978).
[31] P. E. Lindelof and Shiguang Wang, Phys. Rev. B **33**, 1478 (1986).
[32] B. I. Belevtsev, Yu. F. Komnik, and E. Yu. Beliayev, Phys. Rev. B **58**, 8079 (1998).
[33] L. D. Landau and E. M. Lifshitz, *Quantum Mechanics: Nonrelativistic Theory*, Pergamon Press, New York [Russian original, Nauka, Moscow (1989)].
[34] Yu. A. Bychkov and É. Rashba, JETP Lett. **39**, 78 (1984).
[35] É. I. Rashba and V. I. Sheka, Fiz. Tver. Tela **1**, collection of articles II, 162 (1959).

Translated by M. E. Alferieff

LOW-DIMENSIONAL AND DISORDERED SYSTEMS

Noninteracting electrons in one-dimensional systems

V. F. Gantmakher*

Institute of Solid State Physics, Russian Academy of Sciences, Chernogolovka, Russia
(Submitted September 7, 2004)
Fiz. Nizk. Temp. **31**, 436–444 (March–April 2005)

The theoretical fundamentals for describing the behavior of noninteracting electrons in one-dimensional systems are presented: the transport characteristics of an ideal wire connecting two thermostats; a description of elastic scattering by a chaotic sequence of barriers using Landauer's formula; gigantic chaotic oscillations of the resistance; localization; and, the influence of correlations in a random potential on the localization. [DOI: 10.1063/1.1884437]

The purpose of the present brief review is to present the theoretical fundamentals for describing one-dimensional systems of noninteracting electrons and illustrating their behavior on the basis of known experiments. The number of one-dimensional objects which are available to experimentalists has increased substantially in the last few years. Examples are organic metals,[1] semiconductor nanowires,[2] carbon nanotubes,[3] and even real, short chains of metal atoms.[4] This has drawn more people into working with such objects and has made it necessary to provide them with a quite rigorous introduction to this problem.

The criterion for one-dimensionality is associated with the structure of the electron spectrum of free electrons with wave functions $\exp(i\mathbf{k}\cdot\mathbf{r})$ and the appropriate geometry of the region of their existence

$$\varepsilon=\hbar^2k_\parallel^2/2m+\varepsilon_\perp(i), \quad i=1,2,\ldots. \tag{1}$$

Here $k_\parallel$ is the wave number in the direction in which the electron motion is unbounded; $\varepsilon_\perp$ is the size-quantized part of the energy associated with motion in bounded directions; i enumerates the size-quantized subbands. A system is one-dimensional ($1D$) if all electrons fit into the bottom subband. For a degenerate electronic system the criterion is

$$\varepsilon_F<\Delta_s, \quad \Delta_s\equiv\varepsilon_\perp(i=2)-\varepsilon_\perp(i=1). \tag{2}$$

If several size-quantized subbands lie below the Fermi level, then the system is quasi-one-dimensional.

Generally speaking, interelectronic interactions have a large effect on the behavior of electrons in $1D$ systems. Concepts such as the Luttinger liquid and a wave of charge or spin density arose precisely from studying $1D$ systems. Taking account of interactions greatly complicates the analysis of the experimental data and often makes the analysis ambiguous. Consequently, it is helpful to have as a starting basis a clear picture of the behavior of noninteracting electrons in $1D$ systems. This picture is presented in the present review. First, it is postulated that the wave function of an electron is a plane wave $\exp(i\mathbf{k}\cdot\mathbf{r})$ and interference processes in the wave field formed as a result of the propagation and scattering of this wave in a one-dimensional potential are examined.

According to the Peierls theorem a $1D$ system with an ideal periodic potential is unstable with respect to the appearance of a new period and a wave of charge density,[5] and arbitrarily weak disorder in a one-dimensional medium results in localization.[6] Nonetheless, conduction in a $1D$ system of noninteracting electrons is possible because of temperature, the finite length of the $1D$ system, and correlations in a random potential.

1. IDEAL WIRE

We consider first an ideal wire with no scattering, even elastic scattering. Let an ideal wire of length Λ connect two reservoirs to which a potential difference V is applied. Then any electron entering the wire on one side leaves the wire on the other side with probability one. In addition, let the diameter of the wire be so small that the spectrum (1) of the wire below the Fermi level ε_F contains a finite number $\nu=2N_s$ of size-quantized subbands (they are also called channels; in the absence of a magnetic field, for every $i\leqslant N_s$ there exist two channels with different spin directions):

$$\varepsilon_\perp(i)<\varepsilon_F \quad \text{for} \quad i=1,2,\ldots,N_s. \tag{3}$$

If $N_s=1$, then the $1D$ system is said to be a single-channel system (taking the spin of the system into account it could also be called a two-channel system), and for $N_s>1$ it is called a multichannel system. Since the wire is ideal, the channels inside the wire are independent of one another and do not exchange electrons. The electron density n_i in channel i, the longitudinal velocity of the electrons v_i, and the density of states g_i at the Fermi level are related by the relations

$$v_i=\hbar^{-1}(\partial\varepsilon/\partial k)_{\varepsilon=\varepsilon_i}, \quad g_i=(\partial n_i/\partial\varepsilon)_{\varepsilon=\varepsilon_i}=1/2\pi\hbar v_i,$$

$$\varepsilon_i=\varepsilon_F-\varepsilon_\perp(i), \quad 2\sum_{i=1}^{N_s} n_i=n. \tag{4}$$

The presence of a potential difference V between the reservoirs means that because of the difference in the electron

density $\delta n_i = g_i eV$ there is a difference between the electron fluxes entering the channel i from the right- and left-hand sides. In the expression for the current the concrete parameters of the channel appearing in the relations (4) cancel, so that the current J_i in the channel is independent of the index i and equals

$$J_i = ev_i \delta n_i = (e^2/2\pi\hbar)V. \tag{5}$$

The conductance $y_{\rm id} = J/V$ and the resistance $\rho_{\rm id} = 1/y_{\rm id}$ of such a wire are determined by the total current $J = \Sigma_1^{\nu} J_i$ and equal

$$y_{\rm id} = (e^2/2\pi\hbar)\nu, \quad \rho_{\rm id} = (2\pi\hbar/e^2)(1/\nu). \tag{6}$$

The index here underscores the fact that Eq. (6) refers to an ideal wire.

The result (6) is remarkable in several respects. In the first place it has been found that in a $1D$ system, even a multichannel system, dissipation occurs even in the absence of scattering. In the second place, however surprisingly, the resistivity $\rho_{\rm id}$ of the wire is independent of its length and is determined only by the quantization of the electronic spectrum. Both of these circumstances are a manifestation of the principle of nonlocality. The electrons acquire energy in locations where a field is present, i.e. in or at the edges of the wire, and give up energy when they are thermalized in a reservoir, i.e. far from the wire.

It is no accident that we do not specify more accurately where the electric field is concentrated. The arguments which have led to Eq. (6) do not predetermine the distribution of the electric field along the wire. Additional considerations are required to determine this distribution. Ordinarily, it is found that the field is distributed nonuniformly along a channel and concentrated predominantly near its ends. In this respect an interesting example are edge channels which are formed along the edge of a sample between the contacts in the presence of a quantum Hall effect. In a strong magnetic field perpendicular to the plane of a two-dimensional electron gas all electrons colliding with and reflected from the surface necessarily collide with the surface again in the next turn of their cyclotron motion. The direction of their displacement along the surface in the time between two collisions with the surface is determined by the sign of the vector product of the field and the normal to the region of the two-dimensional gas and is independent of the angle of incidence and the angle of reflection of the electron. The current along the surface is described using the concept of a one-dimensional channel, which is ideal because of the absence of backscattering. The tangential electric field along the edge of a sample, i.e., along a $1D$ channel, is everywhere zero in the presence of a quantum effect of the field, and the entire voltage drop is concentrated at the boundary with one of the contacts.[7]

It would appear that the assertion that the resistance of a wire is independent of its length contradicts a simple argument. Imagine an ideal wire to be divided into two parts which are connected in series. If the resistance is $\rho_{\rm id}$ in each part, then the total resistance should be $2\rho_{\rm id}$. But it is not enough to simply divide the wire into two parts. In order for both parts to be independent resistances an additional reservoir-thermostat must be inserted between them, and this reservoir-thermostat would make the electronic waves passing through it incoherent. If the temperature of the wire is different from absolute zero, $T \neq 0$, so that there exists a finite length $L_\varphi < \infty$ over which an inelastic collision and phase interference of the electronic wave occur, then such thermostats appear automatically at distances L_φ from one another.

Thus there is an upper bound on the length of an ideal wire, $\Lambda < L_\varphi$. The lower bound is actually the diameter of the wire. This is evident from an analysis of a Sharvin contact,[8] where an insulating flat diaphragm with an opening with area S divides two three-dimensional metal half-spaces, one of which is an ''ideal'' crystal in the sense that the mean-free path length there is $l \gg \sqrt{S}$. The resistence of such a contact is

$$R \approx \frac{\hbar k_F}{ne^2 S} \approx \frac{\hbar}{e^2}\left(\frac{\hbar^2/mS}{\varepsilon_F}\right), \tag{7}$$

where n, m, $k_F = (3\pi^2 n)^{1/3}$ and $\varepsilon_F = \hbar^2 k_F^2/2m$ are the concentration, mass, Fermi momentum, and Fermi energy, respectively, of the electron gas in an ideal half-space, and the $\approx$ sign appearing instead of an $=$ sign signifies that numerical coefficients are dropped in the expression. It is easy to verify that the expression (7) is identical in structure to the expression (6) for $\rho_{\rm id}$, and the numerator in the fraction in parentheses in Eq. (7) is the characteristic splitting $\varepsilon_\perp$ between the size-quantized subbands. It is easy to verify for a square opening that this distance is indeed proportional to S^{-1}.

Since an experimental channel can be very short, Eq. (6) can be checked experimentally. Figure 1 shows the results of measurements of the conductivity of a narrow channel under a split gap connecting two regions of a $2D$ electron gas in a GaAs–$Al_xGa_{1-x}As$ heterostructure.[9] As the blocking voltage V_g on the gate increases, the depleted region expands somewhat because it extends slightly beyond the edge of the gate. As one can see in the inset in Fig. 1, the conducting channel narrows, which means that the number of channels N_s decreases. The short length of the channel makes it possible to obtain a ballistic regime, i.e. a no-scattering regime, in it. In

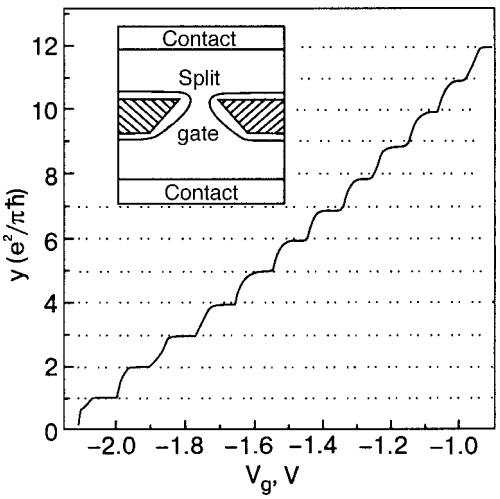

FIG. 1. Conductance y of a ballistic contact between $2D$ regions of a GaAs-$Al_xGa_{1-x}As$ heterostructure as a function of the gate voltage regulating the width of the contact.[9] Inset: layout of the measuring cell.

the structure shown in Fig. 1 the electron density is 3.56×10^{11} cm^{-2}, the mean-free path length at 0.6 K is about 8.5 μm, and the characteristic dimensions of the channel are of the order of 0.25 μm.

It is evident in the inset in Fig. 1 that the measurement is performed by a two-contact scheme, so that the measured resistance $R_{\rm meas}$ contains the resistance $R_{\rm cont}$ of the contacts and the resistance of the adjoining wide sections of the $2D$ layer. The conductance, which is of interest to us, is $y \equiv \rho^{-1} = (R_{\rm meas} - R_{\rm cont})^{-1}$. The resistance $R_{\rm cont}$ was assumed to be 4.35 kΩ, so that it corresponds approximately to the results of independent measurements. After this quantity is subtracted the function $y(V_g)$ becomes a sequence of steps of the same height

$$\Delta y_{\rm id} = (e^2/2\pi\hbar)\Delta\nu = e^2/\pi\hbar, \tag{8}$$

in complete agreement with Eq. (6).

2. ELASTIC SCATTERERS

We now assume the wire to be nonideal and, for simplicity, a one-channel system. Let elastic scatterers be present in the hatched section of the wire (Fig. 2). There is no need to specify their relative arrangement more accurately—we shall consider the entire hatched region to be a single scattering object. In quantum mechanics, it is characterized in the one-dimensional case by complex reflection r and transmission t coefficients, which couple the amplitudes of the reflected and transmitted waves with the amplitude of the incident wave. Electronic fluxes $j_{\rm in}/e$ and $j'_{\rm in}/e$ are incident from the left and right on the hatched region. Each electron is reflected with probability $\mathcal{R} = |r|^2$ and is transmitted with probability $\mathcal{T} = |t|^2$.

$$\mathcal{R} = j_r/j_{\rm in} = j'_r/j'_{\rm in}, \quad \mathcal{T} = j_t/j_{\rm in} = j'_t/j'_{\rm in}, \tag{9}$$
$$\mathcal{R} + \mathcal{T} = 1.$$

If the voltage drop on the hatched region is zero, then the total electron flux in the wire is also zero. In the presence of a potential difference δV, a density difference $\delta n = ge\,\delta V$ appears at the boundaries of the region. In one-dimensional systems all electrons move along the wire and therefore belong to one of the fluxes appearing in Eqs. (9). This makes it possible to relate δn with the electron densities in the fluxes and express δV in terms of the current:

$$\delta V = \frac{\delta n}{ge} = \frac{j_{\rm in} + j_r + j'_t}{e^2 g v} - \frac{j'_{\rm in} + j'_r + j_t}{e^2 g v} = \frac{2\mathcal{R}(j_{\rm in} - j'_{\rm in})}{e^2 g v}. \tag{10}$$

Here g and v are the density of states and the modulus of the velocity of the electrons at the Fermi level. Since the total current J is

$$J = j_{\rm in} - j_r - j'_t = j'_{\rm in} - j'_r - j_t = \mathcal{T}(j_{\rm in} - j'_{\rm in}), \tag{11}$$

the ratio $J/\delta V$ makes it possible to represent the conductance $y_{\rm imp} = J/\delta V$ and the resistance $\rho_{\rm imp} = y_{\rm imp}^{-1}$ of the hatched region in the form

$$y_{\rm imp} = \frac{e^2}{2\pi\hbar}\frac{\mathcal{T}}{\mathcal{R}} = \frac{e^2}{2\pi\hbar}\frac{\mathcal{T}}{1-\mathcal{T}},$$

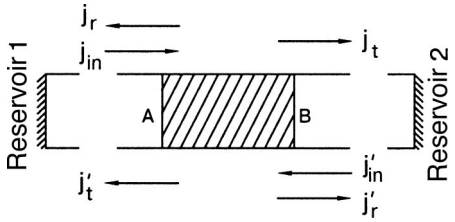

FIG. 2. One-dimensional conductor connecting two reservoirs and consisting of two ideal sections along the edges and the scattering section AB at the center.

$$\rho_{\rm imp} = \frac{2\pi\hbar}{e^2}\frac{\mathcal{R}}{\mathcal{T}} = \frac{2\pi\hbar}{e^2}\frac{\mathcal{R}}{1-\mathcal{R}}. \tag{12}$$

The idea of representing elastic scattering centers as potential barriers in the path of propagating waves and expressing the transport characteristics of the system in terms of the reflection and transmission coefficients of the wave for these barriers was first advanced by Landauer.[10] Consequently, the corresponding formulas, specifically, the expression for the conductance (12), are named after Landauer. In principle Landauer's technique is applicable to systems of any dimension, but it is especially convenient and often used for $1D$ systems.

Landauer's formula in the form (12) was derived under the assumption that the potential difference is applied directly to the scattering region between the points A and B in Fig. 2. This is why the conductance (12) with weak scattering, $\mathcal{T} \sim 1$, $\mathcal{R} \ll 1$, can be greater than the conductance (6) of a system with no scatterers. If the potential difference in the system in Fig. 2 is applied to the reservoirs, then the resistances of the ideal wire and the scattering region are connected in series and the conductance of the entire system is

$$y^{-1} = y_{\rm id}^{-1} + y_{\rm imp}^{-1} \equiv \rho_{\rm id} + \rho_{\rm imp} = \frac{2\pi\hbar}{e^2}\left(1 + \frac{\mathcal{R}}{\mathcal{T}}\right),$$

$$y = \frac{e^2}{2\pi\hbar}\mathcal{T}. \tag{13}$$

Now, the conductance $y \to y_{\rm id}$ as $\mathcal{T} \to 1$, as should be. The expression (13) for y can also be obtained directly by applying a potential difference to the reservoirs, writing the electron flux from one reservoir into another, and taking account of single scattering (compare with the derivation of Eq. (6)). This means that adding the resistances in accordance with Ohm's law in the arguments for Eq. (13) was justified. How-

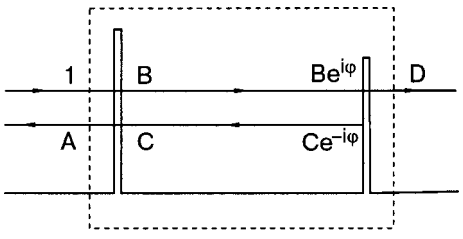

FIG. 3. Scattering section in a $1D$ conductor consisting of two barriers. The complex amplitudes $A, \ldots, D$ of the waves arriving at and leaving both barriers are normalized to the initial arriving wave, indicated by the number 1.

ever, this is by no means always the case for one-dimensional systems because the incident and reflected waves interfere with one another.

We shall now consider two successive barriers in a single-channel one-dimensional conductor (Fig. 3) and we shall express in terms of the parameters $\mathcal{T}_1$, $\mathcal{R}_1$, $\mathcal{T}_2$, and $\mathcal{R}_2$ of the initial barriers the parameters $\mathcal{T}$ and $\mathcal{R}=1-\mathcal{T}$ of the compound scattering object formed. If a wave with amplitude 1 is incident on the barrier from the left, then the stationary wave field formed will contain four additional waves: the reflected wave A, the transmitted wave D, and two oppositely propagating waves B and C between the barriers ($A,\ldots,D$ are the complex amplitudes of the waves). Expressing the amplitudes of the waves moving to the right and left of each of the barriers in terms of the amplitudes of the incident waves, we obtain four equations:

$$A=r_1+Ct_1, \quad B=t_1+Cr_1, \quad C\mathrm{e}^{-i\varphi}=B\mathrm{e}^{i\varphi}r_2,$$

$$D=B\mathrm{e}^{i\varphi}t_2. \tag{14}$$

Here the fact that the reflection coefficient of the barrier is independent of the side from which the wave is incident is taken into account, $r_1=r_1'$; the factors $\exp(\pm i\varphi)$ take account of the phase shift of the wave over the distance from one barrier to the other. From Eqs. (14) follows

$$D=\frac{\mathrm{e}^{i\varphi}t_1t_2}{1-\mathrm{e}^{2i\varphi}r_1r_2},$$

$$\mathcal{T}=|D|^2=\frac{\mathcal{T}_1\mathcal{T}_2}{1+\mathcal{R}_1\mathcal{R}_2-2\sqrt{\mathcal{R}_1\mathcal{R}_2}\cos\theta}, \tag{15}$$

where $\theta=2\varphi+\arg(r_1r_2)$. The conductance Y_2 of the a compound "two-barrier" scatterer, marked in Fig. 3 by the dotted line, is

$$Y_2=\frac{e^2}{2\pi\hbar}\frac{\mathcal{T}}{1-\mathcal{T}}=\frac{e^2}{2\pi\hbar}\frac{\mathcal{T}_1\mathcal{T}_2}{\mathcal{R}_1+\mathcal{R}_2-2\sqrt{\mathcal{R}_1\mathcal{R}_2}\cos\theta}. \tag{16}$$

If a compound "double-barrier" scatterer consists of two identical barriers, $r_1=r_2=r'$, $t_1=t_2=t'$, $\mathcal{R}_1=\mathcal{R}_2=\mathcal{R}'$, and so on, then

$$Y_2=\frac{e^2}{2\pi\hbar}\frac{(\mathcal{T}')^2}{4\mathcal{R}'\sin^2\theta/2},$$

$$\theta/2=\varphi+\arg(r')=kl+\arg(r'), \tag{17}$$

where k is the wave number and l is the distance between the barriers.

The conductance (16) depends not only on the parameters of the two initial barriers. Through the angle θ it also depends on the distance between the barriers. Ultimately, we are interested in a $1D$ conductor with a large number of randomly positioned barriers. Therefore we can average over all possible distances between them, making the assumption that the angle θ assumes any value from 0 to 2π with equal probability. Such averaging is not entirely correct, but it makes it possible to follow the trends arising as the length of the chain of one-dimensional barriers increases (see Ref. 11 and also the original work[12] for a more detailed discussion). The average conductance $\overline{Y_2}$ of a system of two barriers follows from the average value $\overline{\cos\theta}=0$:

$$\overline{Y_2}=\frac{e^2}{2\pi\hbar}\frac{\mathcal{T}_1\mathcal{T}_2}{\mathcal{R}_1+\mathcal{R}_2}=\frac{e^2}{2\pi\hbar}\frac{(1-\mathcal{R}_1)(1-\mathcal{R}_2)}{\mathcal{R}_1+\mathcal{R}_2}. \tag{18}$$

For comparison we shall give the classical expression for a sum of two successive resistances $\rho_1=y_1^{-1}$ and $\rho_2=y_2^{-1}$:

$$Y_2^{(\mathrm{cl})}=(y_1^{-1}+y_2^{-1})^{-1}\equiv(\rho_1+\rho_2)^{-1}$$
$$=\frac{e^2}{2\pi\hbar}\left(\frac{\mathcal{R}_1}{1-\mathcal{R}_1}+\frac{\mathcal{R}_2}{1-\mathcal{R}_2}\right)^{-1}$$
$$=\frac{e^2}{2\pi\hbar}\frac{(1-\mathcal{R}_1)(1-\mathcal{R}_2)}{\mathcal{R}_1+\mathcal{R}_2-2\mathcal{R}_1\mathcal{R}_2} \tag{19}$$

In Eq. (19) there is an extra, compared with Eq. (18), term in the denominator, proportional to the product of the transmission coefficients $\mathcal{R}_1\mathcal{R}_2$ for two barriers.

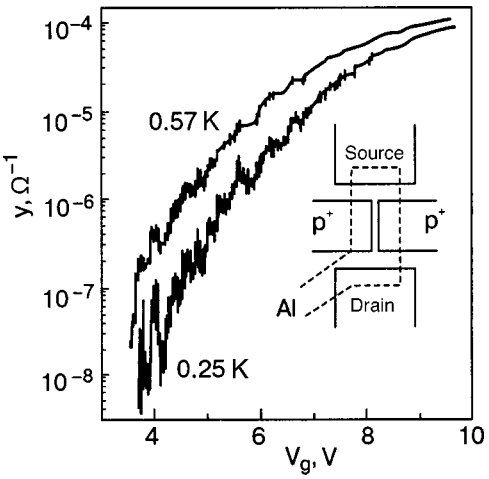

FIG. 4. Conductance y of a long quasi-one-dimensional channel in a field-effect transistor, fabricated on the surface of n-Si, in the accumulating layer regime as a function of the gate voltage V_g.[13] The width of the channel can vary from 0 up to the maximum value ~ 1 μm, set by the construction (see the scheme shown in the inset), using voltages on the control electrodes p^+ and on the gate.

3. GIGANTIC OSCILLATIONS OF THE RESISTANCE

We shall discuss one other feature of transport in $1D$ systems. Figure 4 shows the transport characteristics of a quasi-one-dimensional system fabricated on the basis of an accumulating layer in a field-effect transistor on a n-Si surface.[13] At low temperatures a noise-like component with very large amplitude appears in the dependence of the conductance y on the gate voltage V_g. This is not real noise. The signal does not depend on the time, and if the sample is not heated to room temperature, then in a repeated experiment the curve $y(V_g)$ will be reproduced right down to the smallest details. It is evident that at low temperatures and gate voltages V_g allowing for a narrow channel and low carrier concentration, the conductance undergoes as a function of V_g chaotic narrow oscillations whose total range increases with decreasing temperature. For a different sample, and even for the same sample, with repeated cooling from room temperature the detailed structure of the oscillations is differ-

ent with the same overall pattern of evolution of oscillations with a change in the temperature and voltage V_g.

The fundamental reason for the chaotic oscillations is one-dimensionality. All defects in a wire are connected in series, and the current lines cannot circumvent any of them. Consequently, switching off one strongly scattering defect can strongly influence the total resistance. The question is how a change in V_g that changes the concentration and Fermi energy ε_F of the carriers can switch on, switch off, or change the effectiveness of individual defects.

Let us return to the expression (17) for the conductance Y_2 of a symmetric ''double-barrier'' scatterer. In the discussion above we averaged the expression (16) over $\cos\theta$ on the basis that there is a spread in the values of the distances l_i between the barriers. But the angle $\varphi = kl_i$ appearing in θ depends not only on l_i but also on the wave number k, i.e., on the energy ε_F of the scattering electron. For one specific scattering pair of barriers with a fixed value of l_i it follows from Eq. (17) that R_2 assumes values from 0 to 4ρ,

$$0 \leqslant R_2 \leqslant 4\rho, \tag{20}$$

depending on the energy of the incident electron. Here it should be recalled that the transport properties of a $1D$ system are determined precisely by the electrons from a neighborhood of ε_F because the opposite electron fluxes with lower energies compensate one another. We mentioned above that there are problems with averaging the expression for the resistance (16). They are due precisely to the wide range (20) of variation of R_2.

The space between two barriers is a potential well. In this well, generally speaking, there is a collection of levels ε_i whose widths are due to the transmittances t_1 and t_2 of the barriers. As the electron energy ε_F shifts relative to the system of levels in this well the tunneling probability oscillates, reaching a maximum at resonance $\varepsilon_F = \varepsilon_i$. Consequently, the gigantic chaotic oscillations of the resistance can be described theoretically precisely in terms of resonance tunneling.[14]

The model of localized states in $1D$ systems employs the idea of electronic levels inside composite scatterers. At sufficiently low temperatures reflections from distant barriers

$$1 \ll N \ll L_\varphi / l \tag{21}$$

remain coherent. Consequently, according to the relation (25) presented below, these reflections for sufficiently large L_φ compensate the barrier transmittances of t_1 and t_2 and make the state between them localized. Hopping conductivity should be expected under these conditions. Indeed, Fig. 5 displays measurements of the temperature dependence of the conductance which were performed at several minima of the curve presented in Fig. 4. It is evident that for measurements on the left-hand side of the plot in Fig. 4, for lower values of V_g when the conductance is small, the oscillations are large and there is every reason to regard the channel to be one-dimensional, the points follow well the functional dependence

$$y = y_0 \exp[-(T_M/T)^{1/2}] \tag{22}$$

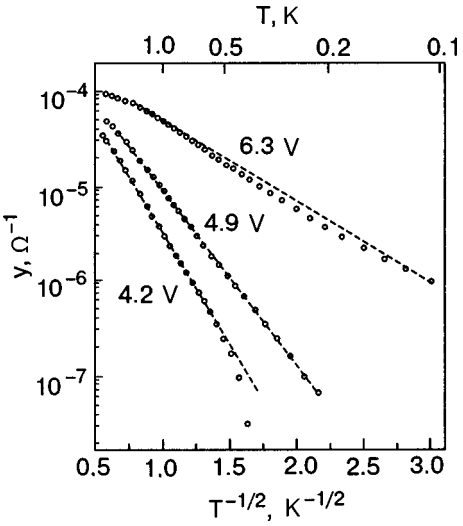

FIG. 5. Temperature dependences at the minima of the conductance of a channel of a field-effect transistor for three different values of the gate voltage V_g.[13]

in complete agreement with Mott's formula for the temperature dependence of hopping conductivity with variable hopping distance:

$$\rho = \rho_0 \exp\left(\frac{T_M}{T}\right)^{1/(d+1)}, \quad T_M \approx (g_\mu \xi^d)^{-1}, \tag{23}$$

where d is the dimension of the space and ξ is the decay length of localized states.

For large values of V_g the channel expands and gradually converts into a two-dimensional channel. The conductance increases, and the amplitude of the chaotic oscillations decreases. The experimental points of the function $\log y(T^{-1/2})$ obtained with gate voltage $V_g = 6.3$ V deviate in Fig. 5 from a straight line, but they rectify in the $(\log y, T^{-1/3})$ plane, once again in complete agreement with Eq. (23).

4. LOCALIZATION

Let us consider a long chain of identical, weakly scattering barriers, $\mathcal{R}' \ll 1$ and $\mathcal{T}' \sim 1$, located at random distances l_i from one another and each having a small resistance $\rho' = (2\pi\hbar/e^2)(\mathcal{R}'/\mathcal{T}') \ll 2\pi\hbar/e^2$ (the average distance between the barriers $l = \overline{l_i}$ is the elastic mean-free path length). We shall calculate the resistance $R_N = Y_N^{-1} = (2\pi\hbar/e^2) \times (\mathcal{R}_N/\mathcal{T}_N)$ of a compound scattering object consisting of N barriers using a recurrence relation following from Eq. (18):

$$\frac{\mathcal{R}_N}{\mathcal{T}_N} = \frac{\mathcal{R}_{N-1} + \mathcal{R}'}{\mathcal{T}_{N-1}\mathcal{T}'}. \tag{24}$$

As long as the number of barriers N is small, so that $N\rho' \ll 2\pi\hbar/e^2$, the resistance R_N increases linearly: $R_N \approx N\rho \propto N$. The reflection probability $\mathcal{R}_N$ also increases almost linearly. But $\mathcal{R}_N$ cannot exceed 1. Consequently, at some value of N we can set $\mathcal{R}_N \approx \mathcal{R}_{N-1} \approx 1$ in Eq. (24), whence it immediately follows that

$$\mathcal{T}_N \approx \mathcal{T}_{N-1}\mathcal{T}', \quad \mathcal{T}_N \to s(\mathcal{T}')^N = se^{\alpha N} \text{ as } N \to \infty,$$
$$(s = \text{const}, \quad \alpha = \ln \mathcal{T}' < 0). \tag{25}$$

The exponential decrease of the transmitted-wave intensity $\mathcal{T}_N$ with increasing N is a demonstration of $1D$ localization for a specific example.

5. ROLE OF CORRELATIONS IN A RANDOM POTENTIAL

The general assertion of Ref. 16 that $1D$ localization occurs in a random potential and the illustration (25) of this assertion for a specific model assumed that there are no correlations. However, localization may not occur if the chaotic one-dimensional potential is not completely random but contains correlators. To show this we return to Eq. (17) for the conductance Y_2 of the symmetric ''double-barrier'' scatterer shown in Fig. 3. It follows form this formula that there exists a wave number $k_0 = -\arg(r')/l$ for which the barrier is completely transparent to the incident wave and there is no reflected wave $\mathcal{R}_2' = 0$. If in our model (24)–(25) the isolated barriers are replaced with double barriers (17), then an electron with energy $\varepsilon_0 = \hbar^2 k_0^2/2m$ will be delocalized.

This idea was elaborated in the so-called dimer model.[15] This model uses not one-dimensional barriers but rather a one-dimensional chain of periodically arranged potential wells. The chain consists of two types of wells with energy levels E_a and E_b. The wells are distributed along the odd lattice sites completely randomly, without any correlations, and each even site contains a well of the same type as the odd site to the left of it. This means that identical wells occur in pairs, whence the name of the model (Fig. 6a). If the distance between the wells is a, then the lattice obtained can be represented as a sum of two random but identical *sublattices*, shifted by a with respect to one another, both with period $2a$ and an entirely random distribution of wells over the sites.

We shall assume that pairs with energy E_a belong to the main lattice and pairs with energy E_b are defects. As we have already seen, in this model localized states can exist for certain specified values of the energy. Now, it is necessary to formulate the condition under which electrons with this energy can propagate in the main lattice.

Consider one dimer defect consisting of two wells with energy E_b in an ideal lattice consisting of E_a wells (Fig. 6b). Let the overlap integral between neighboring wells be J. Then bands with a quasicontinuous distribution of levels $\varepsilon = E_a - 2J\cos ka$ are formed to the right and left of a defect. If

$$|E_a - E_b| < 2J, \tag{26}$$

then the unperturbed energy level E_b of a defect falls within the band and a distinguished value $k = k_0$, $\cos k_0 = -2J/(E_a - E_b)$, for which the reflection probability of a defect $\mathcal{R} = 0$, appears in the band.

In the dimer model correlations exist only between nearest neighbors. For such correlations delocalized states arise only for discrete values of the energy. To obtain a band of delocalized states distant correlations must be used, retaining in so doing an element of randomness. An algorithm for constructing such a potential was proposed in Refs. 16 and 17. Here we present only a specific example of such an algorithm, constructed to perform an experimental check by means of microwave simulation.

Microwave simulation of localization processes is possible because the time-dependent Schrödinger equation

$$i\hbar \frac{\partial \Psi}{\partial t} = -\frac{\hbar^2}{2m}\Delta\Psi + U\Psi \tag{27}$$

and the classical wave equation

$$\frac{1}{c^2}\frac{\partial^2 \Psi}{\partial t^2} = \Delta\Psi - U\Psi \tag{28}$$

(c is the speed of light) have much in common.[8] The substitution $\Psi = e^{-i\theta t}\psi$ reduces both equations to

$$(\Delta - U + k^2)\Psi = 0 \tag{29}$$

the only difference being that for the Schrödinger equation

$$\omega = (\hbar/2m)k^2, \tag{30}$$

and for the wave equation

$$\omega = ck. \tag{31}$$

As an example of microwave simulation we present the experiment of Ref. 19 where the transmission cofficient of a long waveguide was measured as a function of frequency for an electromagnetic wave in the microwave range. The waveguide scheme is shown in Fig. 7. The working frequency range was chosen to lie inside the frequency range where the waveguide is in a single-mode regime: $7.5\ \text{GHz} = c/2a < \omega/2\pi < c/a = 15\ \text{GHz}$, where a is the large dimension of the transverse cross section of the waveguide.

To simulate the random potential $N = 100$ scatterering pins are inserted at equal distances along the waveguide. Using micrometric screws the pins can be inserted to different depths u_n, where $1 \leqslant n \leqslant N$. The depth is set using the formula

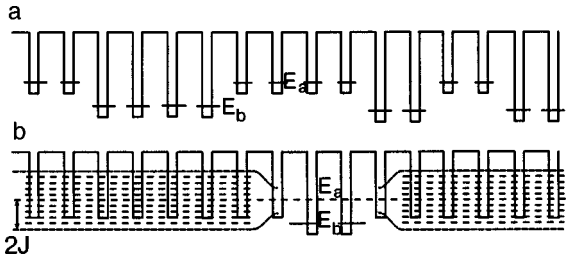

FIG. 6. Dimer model of a one-dimensional random potential. The changes occurring in the positions of the levels as a result of the overlapping of the wells are not shown (a). The electron levels in a one-dimensional lattice with one dimer defect (b).

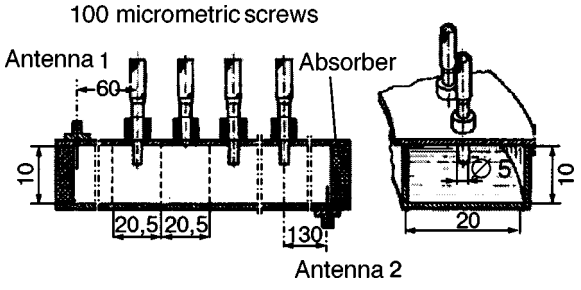

FIG. 7. Schematic diagram of a single-mode waveguide with 100 scatterers, in which the transmission coefficient t for an electromagnetic wave was measured as a function of the frequency.[19] All dimensions are given in mm.

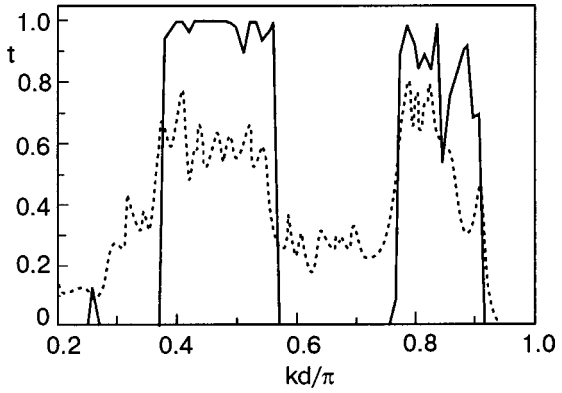

FIG. 8. Transmission coefficient t of a wave in a one-dimensional channel in the presence of periodically arranged random scatterers which are correlated by means of a specially chosen correlation function.[19] Solid line—numerical experiment with $N=10^4$ scatterers; dashed line—microwave experiment with $N=100$ scatterers, averaged over five different realizations. The correlation function is the same.

$$u_n = \sqrt{\overline{u_n^2}} \sum_{m=-\infty}^{\infty} \beta_m Z_{n+m},$$

$$\beta_m = \frac{2}{\pi} \int_0^{\pi/2} \sqrt{\varphi(\mu)} \cos(2m\mu)\, d\mu. \tag{32}$$

Here Z_{n+m} are random numbers from -1 to $+1$. They introduce an element of randomness into the potential. The correlations between all u_n are provided by the factors β_m, determined in terms of the function $\varphi(\mu)$. The latter function is chosen using a special mathematical algorithm depending on the type of transmission spectrum required for the one-dimensional system. An example of the implementation of such a program is shown in Fig. 8. This was used to choose a function $\varphi(\mu)$ for which two transmission bands should arise inside the working range. The solid line in the figure shows the transmission coefficient, determined in a numerical experiment, of a waveguide with a one-dimensional sequence of $N=10^4$ scatterers chosen in accordance with Eq. (32) using the prescribed function $\varphi(\mu)$. The dashed line shows the result of a real microwave experiment with a sequence of $N=100$ scatterers averaged over five different realizations.

6. CONCLUSIONS

These are the basic fundamentals of the behavior of noninteracting electrons in one-dimensional systems with a random potential. They should be kept in mind when discussing any experiments in such systems, even if the interelectronic interactions play the main role in the observed phenomena.

This work was supported by grant NSH-2170.2003.2 and grants from the Ministry of Science of the Russian Federation.

*E-Mail: gant@issp.ac.ru

[1] D. Jérome and H. J. Schulz, Adv. Phys. **31**, 299 (1982); *ibid.* **51**, 293 (2002).
[2] F. P. Millkén, C. P. Umbach, and R. A. Webb, Solid State Commun. **7**, 309 (1996).
[3] M. Bockrath, D. H. Cobden, J. Lu, A. G. Rinzler, R. E. Smally, L. Balents, and P. L. McEuen, Nature (London) **397**, 598 (1999).
[4] J. L. Costa-Krämer, N. Garsia, P. Garsia-Mochales, and P. A. Serena, Surf. Sci. **342**, L1144 (1995).
[5] R. E. Peierls, *Quantum Theory of Solids*, Clarendon Press, Oxford (1955) [Russian translation, Izd. Inostr. Lit., Moscow (1956)].
[6] V. L. Berezinskiĭ, Zh. Éksp. Teor. Fiz. **65**, 1251 (1973) [JETP **38**, 620 (1973)].
[7] M. Büttiker, Adv. Solid State Phys. **30**, 40 (1990).
[8] Yu. V. Sharvin, Zh. Éksp. Teor. Fiz. **48**, 984 (1965) [JETP **21**, 655 (1965)].
[9] B. J. van Wees, L. P. Kouwenhoven, H. van Houten, C. W. J. Beenakker, J. E. Mooij, C. T. Foxon, and J. J. Harris, Phys. Rev. B **36**, 3625 (1988).
[10] R. Landauer, Philos. Mag. **21**, 863 (1970).
[11] Y. Imry, *Introduction to Mesoscopic Physics*, Oxford University Press (2002).
[12] P. W. Anderson, D. J. Thouless, E. Abrahams, and D. S. Fisher, Phys. Rev. B **22**, 3519 (1980).
[13] A. B. Fowler, A. Harstein, and R. A. Webb, Phys. Rev. Lett. **48**, 196 (1982).
[14] M. Ya. Azbel, Solid State Commun. **45**, 527 (1983).
[15] D. H. Dunlap, H.-L. Wu, and P. W. Phillips, Phys. Rev. Lett. **65**, 88 (1990).
[16] H.-J. Stöckmann, *Quantum Chaos (An Introduction)*, Cambridge University Press (1999) [Russian translation, Fizmatgiz, Moscow (2004)].
[17] F. M. Izrailev and A. A. Krokhin, Phys. Rev. Lett. **82**, 4062 (1999).
[18] F. M. Izrailev and N. M. Makarov, Opt. Lett. **26**, 1604 (2001).
[19] U. Kuhl, F. M. Izrailev, A. A. Krokhin, and H.-J. Stöckmann, Appl. Phys. Lett. **77**, 633 (2000).

Translated by M. E. Alferieff

Transmission of electrons through a linear molecule: role of delocalized and localized electronic states in current formation

É. G. Petrov*

N. N. Bogolyubov Institute of Theoretical Physics, Ukrainian National Academy of Sciences, 14-b ul. Metrologicheskaya, Kiev 03143, Ukraine

(Submitted September 1, 2004; revised September 13, 2004)
Fiz. Nizk. Temp. **31**, 445–462 (March–April 2005)

Exact formulas are obtained for the electronic current in the presence of quasielastic and elastic transmission of an electron through a molecule. The elastic transmission mechanism is analyzed in detail. It is shown that ''metallization'' of a molecule occurs in the presence of electron delocalization, so that all energy levels of the molecule undergo the same shift when a potential difference is established between the electrodes. This explains the appearance of resonance peaks in the conductivity of the molecule. When an electron in the molecule is strongly localized the appearance of conductivity peaks is due to resonance hopping of the electron between the Fermi levels of the electrodes and localized levels of the molecule, with which the appearance of negative conductivity of the molecule is also associated. © *2005 American Institute of Physics.* [DOI: 10.1063/1.1884438]

1. INTRODUCTION

The possibility of measuring a current through an individual molecule in contact with microelectrodes[1–6] has made it possible for molecular electronics to reach a fundamentally new level of development where different types of physical models of electron-transport processes can now be checked by directly measuring the conductivity of molecules and molecular chains. Thus the idea, advanced in the 1970–1980s,[7–9] of creating molecular computers with an enormous memory is no longer as fantastic as first thought. The modern problems of molecular electronics are tied to clarifying the physical foundations of the operation of the basic elements of molecular devices, such as, the molecular wires, rectifiers, filters, transistors, and so on. Here progress has been made mainly in understanding the mechanism of elastic tunneling of electrons through individual molecules and molecular layers (see, for example, the reviews in Refs. 3, 10–12). The important role of contacts between a molecule and electrodes in the formation of a single multinuclear complex and in treating electrodes as a macroscopic system with a continuous (quasicontinuous) energy spectrum has been clarified.[13–20] The latter circumstance results in the appearance of an imaginary correction to the energy spectrum of the molecule,[10,21,22] giving rise thereby to broadening of the elastic resonance tunneling peak of electrons tunneling through a molecule. The Coulomb interaction between electrons transported through a molecule start to play an important role at high currents.[1,23–27] This interaction is also important for the inelastic mechanism of the formation of a current through a molecular wire.[28–31]

Even though substantial progress has been made in describing electron transport through individual molecules and molecular wires a number of important factors remain unclear. This concerns, first and foremost, the role of delocalized and localized electronic states of a molecule in the transmission of an electron through a molecule and thereby in the formation of an interelectrode current. Modern powerful quantum-mechanical computational methods make it possible to find the energy spectrum of and the electron density distribution in a molecule.[5,32–35] But, as a rule, the spectrum is quite complicated and it is by no means clear whether a given value of the energy of a molecule should be assigned to a localized or delocalized molecular orbital (MO). In addition, the position and form of the spectrum and electron density depend on the magnitude and direction of the potential difference V applied to the electrodes.

The objective of the present work is to obtain a strictly valid expression for the quasielastic current formed by a molecule inserted between electrodes and then use this expression to determine the exact formula for the elastic current. The current–voltage ($I-V$) characteristics are presented for molecules where either purely delocalized or localized MO contribute to the formation of the *elastic* current. Examples are organic molecules containing saturated (covalent) σ bonds and triple/double bonds formed by σ and π electrons (see examples in Refs. 3, 5, 6, and 36). In the present work attention is focused mainly on obtaining and analyzing analytical expressions for the current I and the conductance $g=\partial I/\partial V$ as functions of the applied voltage V.

2. MODEL AND BASIC EQUATIONS

The characteristic vibrational relaxation time τ_{rel} in molecular systems is of the order of $10^{-11}-10^{-13}$ s.[37,38] Since vibrational relaxation is the most rapid of the possible relaxation processes in molecules, quasielastic and elastic electron transport through a molecule becomes possible if the characteristic time τ_{tr} of this transport is much less than τ_{rel}. The time τ_{tr} can be roughly estimated from the relation $I=|e|/\tau_{\mathrm{tr}}$, where $|e|\approx 1.6\cdot 10^{-19}$ C is the electron charge expressed in Coulombs. This relation shows that the electron-transport process can be elastic if a current I of the order of 1 nA or higher passes through the molecule. Experiment shows (see, for example, Refs. 5, 6, 16, and 39–44) that such currents are attainable for short molecules. For

$$\tau_{\rm tr} \ll \tau_{\rm rel} \tag{1}$$

aside from elastic process, a quasielastic process, where the state of the molecule changes during electronic transmission, is also possible. In this case, in the transmission process the molecule gives/takes up (at nonzero temperature) or only takes up (at low temperature) part of the energy of the transported electron. Just as for elastic transmission, there is not enough time for relaxation processes in a molecule to occur during the transport of an electron from one electrode to the other.

A. Quasielastic current through a molecule

In the present work only the elastic transmission of an electron is studied in detail. The more complicated quasielastic transmission process will be analyzed separately. However, since both processes reflect the dynamical character of electronic transport (when relaxation in a molecule does not play an appreciable role during transmission), we shall obtain the basic expressions for the current using the same approach. Then the expression for the elastic current follows from the more general expression for the quasielastic current. The Hamiltonian of the system ''electrode L—molecule—electrode R'' (LMR system) is

$$H = H_0 + H_{\rm int}, \tag{2}$$

where the interaction $H_{\rm int}$ leads to transitions between the states $|a\rangle$ of the main Hamiltonian H_0. In the absence of relaxation and an external variable field a transition under the action of $H_{\rm int}$ occurs only when in the absence of such an interaction the energy of the initial state E_a is equal to the energy of the final state E_b. We note that these energies are eigenvalues of the Hamiltonian H_0 but not of the complete Hamiltonian H. Quantum mechanics shows[45] that irrespective of the type of dynamical system the probability P_{ba} of a transition from the state $|a\rangle$ into the state $|b\rangle$ per unit time is given by the expression

$$P_{ba} = \frac{2\pi}{\hbar} |T_{ba}|^2 \delta(E_a - E_b), \tag{3}$$

where the matrix element $T_{ba} = \langle b|\hat{T}|a\rangle$ is calculated using the operator for a transition on the energy shell

$$\hat{T} = H_{\rm int} + H_{\rm int}\hat{G}(E_a)H_{\rm int}. \tag{4}$$

Here we have introduced the Green's function

$$\hat{G}(E) = \frac{1}{E - H + i0^+}, \tag{5}$$

where H is the Hamiltonian of the entire system. The expression (3) refers to the transition channel between the specific states a and b of the dynamical system. If there are sets $A = \{a\}$ and $B = \{b\}$ of such states, then the total probability P_{AB} is no longer a sum of transitions along all possible channels. Such a situation is valid for a closed dynamical system. However, if the dynamical system is open, i.e., it is in a thermal contact with the environment (this is the situation of interest to us), then the contribution of each channel to the total transport process becomes dependent on the statistical probability $W_{a(b)}$ that this channel is open. Thus the total probability of the transition with the participation of all possible channels will be

$$P_{AB} = \sum_{ab} W_{a(b)} P_{ab}. \tag{6}$$

This is an exact formula obtained outside the framework of perturbation theory. The only condition used is that there is not enough time for relaxation (dissipative) processes in the system to occur over the time of an isoenergy transition in the system itself. The Born approximation is obtained if the total Hamiltonian H is replaced in the Green's function (5) by H_0.

In our problem the LMR system (electrodes + molecule) is a dynamical system. We shall analyze the transition of an electron from the left- to the right-hand electrode. In this case the initial state $|a\rangle$ is characterized by the fact that in this state the transported electron is located at the electrode L in the conduction band with a definite wave vector $\mathbf{k}$ and the molecule is in a quantum state M (in general determined by the electronic, vibrational, and spin states of the molecule), so that for $H_{\rm int} = 0$ we have $|a\rangle = |L\mathbf{k}, M\rangle = |L\mathbf{k}\rangle|M\rangle$, $E_a = E_{L\mathbf{k}} + E_M$. Similarly, the final state and energy of the system are given by $|b\rangle = |R\mathbf{q}, M'\rangle = |R\mathbf{q}\rangle|M'\rangle$, $E_b = E_{R\mathbf{q}} + E_{M'}$, where $\mathbf{q}$ is the wave vector of an electron in the conduction band on the right-hand electrode and the symbol M' denotes the state of the molecule formed after an electron passes through the molecule. Therefore $E_a - E_b = (E_{L\mathbf{k}} + E_M) - (E_{R\mathbf{q}} + E_{M'})$. We recall that for purely elastic transmission of an electron the internal state of the molecule does not change, and therefore $M = M'$. Correspondingly, $E_a - E_b = E_{L\mathbf{k}} - E_{R\mathbf{q}}$.

In what follows, to obtain specific formulas we shall assume for definiteness that the left-hand electrode is maintained at zero voltage and a constant electric field acts on the right-hand electrode. As a result the potential difference between the electrodes is V. For this choice of the direction of the electric field the Fermi distribution functions $f_s(E) = [\exp(E - E_F)/k_B T] + 1^{-1}$ (k_B and T are, respectively, Boltzmann's constant and temperature) for the left- ($s = L$) and right-hand ($s = R$) electrodes will be $f_L(E_{L\mathbf{k}})$ and $f_R(E_{R\mathbf{q}} - eV)$. The fact that the electron charge e is negative has been taken into account. The probability $W_{a(b)}$ of realization of a state a in an isoenergetic transition $a \to b$ assumes that there is no electron with wave vector $\mathbf{q}$ on the right-hand electrode. The corresponding statistical probability of a transition of an electron from left to right will be $W_{a(b)} = f_L(E_{L\mathbf{k}})(1 - f_R(E_{R\mathbf{q}} - eV))W(E_M)$, where the last factor is the statistical weight of the state $|M\rangle$ of the molecule before the arrival of the transported electron. The electron current from left to right is determined by summing over all single-electron channels (i.e. over all $\mathbf{k}$, M and $\mathbf{q}$, M'). Since $I_{L\to R} = -2eP_{LR}$ (the appearance of the factor of 2 reflects the additional summation over the projections of the electron spin), we obtain

$$I_{L\to R}=-\frac{4\pi e}{\hbar}\sum_{\mathbf{kq}}\sum_{MM'}[f_L(E_{L\mathbf{k}})(1-f_R(E_{R\mathbf{q}}-eV))]\times W(E_M)|T_{R\mathbf{q}M'L\mathbf{k}M}|^2\delta(E_{L\mathbf{k}}+E_M-E_{R\mathbf{q}}-E_{M'}). \quad (7)$$

The current $I_{R\to L}$ due to the motion of electrons from the right- to the left-hand electrode is found similarly. The observed interelectrode current I is the difference of the currents $I_{L\to R}$ and $I_{R\to L}$.

We introduce the matrix (operator) for the spectral density of the sth electrode using the collection of quantities

$$[\Gamma_M^{(s)}(E)]_{\mu\mu'}=2\pi\sum\mathbf{k}\,\langle\mu|H_{\rm int}|s\mathbf{k},M\rangle\langle s\mathbf{k},M|H_{\rm int}|\mu'\rangle\times\delta(E-E_{s\mathbf{k}}), \quad (8)$$

where $\langle\mu|H_{\rm int}|s\mathbf{k},M\rangle$ is the matrix element of a transition from the state $|s\mathbf{k},M\rangle$, characterizing the LMR system in the absence of an interaction of electrodes with the molecule (i.e. an eigenstate for the Hamiltonian H_0), into an arbitrary state of the system $|\mu\rangle$. Since

$$\delta(E_1-E_2)=\int_{-\infty}^{\infty}dE\,\delta(E-E_1)\,\delta(E-E_2),$$

we obtain the following basic expression for the quasielastic interelectrode current:

$$I=-\frac{2\pi e}{h}\int_{-\infty}^{\infty}dE\sum_{MM'}\{W(E_M)f_L(E-E_M)\times[1-f_R(E-E_{M'}-eV)]-W(E_{M'})\times[1-f_L(E-E_M)]f_R(E-E_{M'}-eV)\}T_{M'M}(E,V), \quad (9)$$

where we have introduced the partial transmission function of the system LMR:

$$T_{M'M}(E,V)=\mathrm{Tr}(\hat\Gamma_{M'}^{(R)}(E-E_{M'})\hat G(E)\times\hat\Gamma_M^{(L)}(E-E_M)\hat G^+(E)). \quad (10)$$

If the molecular currents are measured at and below room temperature, then in the calculations the Fermi function $f_s(E)$ can be replaced by the step function $\Theta(E_F-E)$.[1] Then the integration limits in Eq. (9) become finite: $E_F+E_{M'}\leqslant E\leqslant E_F+E_M+eV$ (if $E_M+eV\geqslant E_{M'}$) and $E_F+E_M+eV\leqslant E\leqslant E_F+E_{M'}$ (if $E_M+eV\leqslant E_{M'}$).

B. Elastic current through a molecule

Elastic transmission is a particular case of quasielastic transmission. The form of the current follows from the exact expressions (9) and (10). For $M'=M$ this gives

$$I=\sum_M W(E_M)I_M. \quad (11)$$

The partial current through the molecule

$$I_M=\frac{2e}{h}\int_{E_F}^{E_F+eV}dE\times\mathrm{Tr}(\hat\Gamma_M^{(R)}(E-E_M)\hat G(E)\hat\Gamma_M^{(L)}(E-E_M)\hat G^+(E)), \quad (12)$$

reflects the contribution of the Mth state of a molecule to the total interelectrode current. At low temperatures only the ground state of the molecule $M=M_0$, whose energy $E_M=E_0$ we shall set equal to zero, is responsible for current formation. In addition we introduce the notation $\hat\Gamma^{(R)}\equiv\hat\Gamma_{M_0}^{(R)}$. Finally, the formula for the elastic interelectrode current becomes

$$I=\frac{2e}{h}\int_{E_F}^{E_F+eV}dE\,T(E,V),$$

$$T(E,V)=\mathrm{Tr}(\hat\Gamma^{(R)}(E)\hat G(E)\hat\Gamma^{(L)}\hat G^+(E)). \quad (13)$$

The expression (13) has the same form as the expression used by different authors to calculate the $I-V$ and $g-V$ characteristics of molecules (see, for example, the reviews in Refs. 3, 10, 12). However, these is also a difference. In Eq. (13) the transmission function (10) contains the Green's function $\hat G(E)$ of the entire LMR system (see Eq. (5)). Therefore the expression (13) is mathematically exact (as is the preceding expression for the quasielastic current). The calculations performed thus far employed the approach developed by Landé and Bütteker[46,47] which were specially modified to describe a current through a molecule (see, for example, Refs. 48 and 49). The transmission function was determined not in terms of the Green's function of the entire LMR system, as a strict theory requires, but rather in terms of the Green's function either of the molecule or a complex of the molecule with part of the surface atoms of the electrodes. The difference from the exact formula will be negligible if the coupling between the molecule and the electrodes is weak. But if this coupling is strong, then the difference can have an appreciable effect on the $I-V$ and $g-V$ characteristics of the elastic current.

3. LOW-TEMPERATURE ELASTIC CURRENT THROUGH A MOLECULE

In what follows we shall study the formation of a low-temperature interelectrode current associated with the conductivity of the molecule which before the arrival of an excess electron is in its ground state $M=M_0$ with a fixed potential difference V. It should be noted that the ground state can be not only charge-neutral but also ionized. Ionization is possible, for example, because under the action of a potential difference one of the electrons of the molecule has already crossed onto the electrode (or arrived from the electrode) even before a stationary current is established in the LMR system. In any case an electron transported from one electrode to another will be considered to be an excess electron for the molecule.

For specific calculations it is important to choose a basis $\{|\mu\rangle\}$ in which the quantities (8) are determined and the matrix elements $G_{\mu'\mu}(E)\equiv\langle\mu'|\hat G(E)|\mu\rangle$ of the Green's function are calculated. We note that in an exact description of the transmission this basis is tied to the states of the entire

LMR system. Consequently, if a basis in which the Hamiltonian H of the LMR system is diagonal is chosen for $\{|\mu\rangle\}$, then according to the definition (5) we obtain

$$G_{\mu'\mu}(E)=\frac{\delta_{\mu\mu'}}{E-\varepsilon_\mu+i0^+}, \tag{14}$$

where ε_μ is an eigenvalue (in general complex) of the complete Hamiltonian H, containing the interaction of the molecule with the electrodes. Using Eq. (14) the exact transmission function (13) becomes

$$T(E,V)=\sum_{\mu\mu'}\Gamma^{(R)}_{\mu\mu'}\frac{1}{E-\varepsilon_{\mu'}+i0^+}\Gamma^{(L)}_{\mu'\mu}\frac{1}{E-\varepsilon^*_\mu-i0^+}. \tag{15}$$

The dependence of $T(E,V)$ on the potential V is contained in the quantities $\Gamma^{(R,L)}_{\mu\mu'}=|\Gamma^{(R,L)}_{M_0}(E,V)|_{\mu\mu'}$ and $\varepsilon_\mu=\varepsilon_\mu(V)$. The specific form of these quantities is determined by choosing a model for the LMR system.

A. Single-electron Hamiltonian of the LMR system

To study the single-electron transmission we shall use the widely applied model where the LMR Hamiltonian has the form

$$H=H_L+H_R+H_M+H_{LM}+H_{RM}. \tag{16}$$

Here the first two terms refer to the Hamiltonians of the left- and right-hand electrodes. In experiments studying the conductivity of molecules, ordinarily, gold electrodes are used. For gold, one wide conduction band participates in electron transport. Consequently, it is assumed that

$$H_s=\sum_{\mathbf{k}}E_{s\mathbf{k}}|s\mathbf{k}\rangle\langle s\mathbf{k}|,\quad s=L,R. \tag{17}$$

Here $E_{s\mathbf{k}}$ is the energy of an electron with wave vector $\mathbf{k}$ in the conduction band of the sth electrode. The spin index is dropped in the energy $E_{s\mathbf{k}}$ and the state $|s\mathbf{k}\rangle$, since single-electron transport in the absence of a magnetic field and magnetic ions is studied. The third term in Eq. (16) refers to the Hamiltonian of a molecule with $N-2$ internal ($n=2,3,\ldots,N-1$) and two terminal ($n=1$ and $n=N$) binding centers for the excess electron (such a molecule plays the role of a molecular wire). When the excess (transported) electron is localized on the nth center it is in one of the λ_n orbital states (these could be, for example, p_x, p_y, or p_z states of individual atoms). When several orbital states are present, we shall represent the Hamiltonian of the molecule, written in the basis of localized states (expanded Hückel model), as

$$\begin{aligned}H_M=&\sum_{n=1}^{N}\sum_{\lambda_n}E_{n\lambda_n}|n\lambda_n\rangle\langle n\lambda_n|\\&+\sum_{n=1}^{N-1}\sum_{\lambda_n\lambda_{n+1}}[V_{n\lambda_n n+1\lambda_{n+1}}|n\lambda_n\rangle\\&\times\langle n+1\lambda_{n+1}|+\text{h.c.}],\end{aligned} \tag{18}$$

where $E_{n\lambda_n}$ is the energy of the excess electron on the nth center of the molecule in the λ_n orbital state, $V_{n\lambda_n n+1\lambda_n}$ is the transition matrix element for an electron making a transition between nearest centers. The last two terms in Eq. (16) characterize the coupling of the terminal centers of the wire with the adjoining electrodes:

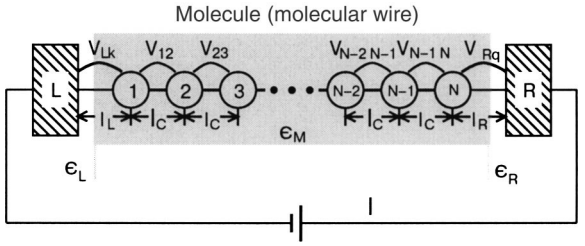

FIG. 1. Linear molecule (molecular wire) with N centers of localization of the transported electron. The current is formed by quantum hops of an electron between the terminal centers of the molecule and the adjoining electrodes and between neighboring internal centers of the molecule. $V_{L\mathbf{k}}(V_{R\mathbf{q}})$ and V_{nn+1} ($n=1,2,\ldots,N-1$) are transition matrix elements: $\delta_L=l_L/\epsilon_L$, $\delta_R=l_R/\epsilon_R$, $\delta_c=l_c/\epsilon_M$ are the effective distances between the electron localization sites, where l_L and l_R are the distances from the terminal centers to the surfaces of the corresponding elecrodes, and l_c is the distance between neighboring regularly spaced centers; $\epsilon_L(\epsilon_R)$ and ϵ_M are the permittivities near the electrode $L(R)$ and near the molecule.

$$H_{sM}=\sum_{\mathbf{k}n\lambda_n}[V_{s\mathbf{k}n\lambda_n}(\delta_{sL}\delta_{n1}+\delta_{sR}\delta_{nN})|s\mathbf{k}\rangle\langle n\lambda_n|+\text{h.c.}]. \tag{19}$$

This coupling is due to the transition matrix elements $V_{L\mathbf{k}\lambda_0}$ between the state $|1\lambda_1\rangle$ of the system (excess electron on the left-hand terminal center of the molecule) and the initial state of the system $|L\mathbf{k},M_0\rangle$. The transition matrix elements $V_{R\mathbf{k}\lambda_N}$ have a similar meaning. The quantities $V_{L\mathbf{k}\lambda_1}$, $V_{R\mathbf{k}\lambda_N}$, and $V_{n\lambda_n n+1\lambda_{n+1}}$ play a key role in electron transport through a molecule and a molecular wire. (Figure 1 shows a situation where only one orbital state in each of the centers participates in electron transport. In this very simple case the symbols λ_n do not carry any additional information and are therefore dropped.) Depending on the structure of the specific molecule these matrix elements can characterize electron hopping between neighboring atoms (for example, along σ or π bonds) and long-range superexchange electron hopping with the participation of the virtual states of intermediate (bridge) atoms.[50]

Modern quantum-mechanical methods make it possible in some cases (by no means always) to obtain satisfactory qualitative agreement between theory and experiment in studying the $I-V$ characteristics of molecules (see, for example, Ref. 40), but to obtain agreement with experiment the authors had to use adjustable parameters (specifically, they introduced scaling for the gap between the highest occupied MO (HOMO) and the lowest unoccupied MO (LUMO)). One of the main reasons for the lack of agreement between calculations and experiments is that to find single-electron wave functions the exact Coulomb interaction of individual electron with the nuclei and other electrons is replaced by an average self-consistent field and therefore the transition to the real situation is achieved using the Aufbau principle (see discussion in Ref. 51). As a result, among other things, the LUMO-HOMO gap is larger than the experimental value.[35,52,53] The other reason is that a limited basis is used to calculate the states containing an excess electron (in the calculations the position of the LUMO levels is ordinarily

sought for a molecule which does not contain an excess electron or for a molcule with an excess electron but using the same basis as the basis used to find the HOMO levels). Another important circumstance is that it is quite difficult to find a substantiated physical criterion for the number of surface atoms of a metal that should be included in calculations of a cluster consisting of the conducting molecule and a portion of an electrode. Finally, the computed position of the Fermi levels of the electrodes can differ from the experimental position by an amount of the order of 1 eV or more, which in many cases makes it impossible to establish whether an electron or hole mechanism is responsible for the conductivity of the molecule. Datta *et al.* propose that the position of the Fermi level (a very important quantity) be regarded as an adjustable parameter.[1,11] All this shows that the development of physical models of the conductivity of a molecule (using the minimum number of fundamentally important parameters) remains a very important problem of the theory and a great deal of attention is being devoted to this problem (Refs. 10, 21, 24, 25, 27–31, 40; see also Refs. 50, 51, 54–57).

In the present paper physical models which make it possible to switch from the general (exact) expression (13) for the elastic current to specific formulas for the current in the case of delocalized and localized MO molecules are proposed. This makes it possible to attain a deeper understanding of the physics of the formation of the interelectrode microcurrent and to analyze the $I-V$ and $g-V$ characteristics of the molecule.

B. Effective Hamiltonian of the LMR system

The existing calculations of the current are based on a calculation of a transmission function of the type (13) where the Green's function of the molecule (cluster) $\hat{G}(E)=[E-H_M-\hat{\Sigma}^{(L)}(E)-\hat{\Sigma}^{(R)}(E)+i0^+]^{-1}$ appears instead of the Green's function of the entire LMR system, and $\hat{\Gamma}^{(s)}(E)=i[\hat{\Sigma}^{(s)}(E+i0^+)-\hat{\Sigma}^{(s)}(E-i0^+)]^{-1}$.[1,10,11,21,49] Here H_M is the Hamiltonian of the molecule neglecting the interaction with the electrodes. The influence of electrodes on the molecule is taken into account in the renormalization of the energy of the molecule (the self-energy), $\hat{\Sigma}^{(s)}(E)$. The practical implementation of this approach lies in numerical estimation of the matrix elements of the Green's function (by solving the Dyson equation). Consequently, the current itself is found only numerically.

The approach proposed below makes it possible to obtain analytical expressions for the current in many important cases. Instead of solving the Dyson equation the Hamilton H of the LMR system is diagonalized. Theoretically if the eigenenergies ε_μ and eigenstates $|\mu\rangle$ of the Hamiltonian H of the entire LMR transport system can be found, then in accordance with the exact expressions (8) and (15) the current can be calculated by summing over all values of μ. There would be no need to renormalize the energy of the molecule. However, in practice it is impossible to diagonalize the Hamiltonian H exactly. Consequently, we shall examine an approximate diagonalization based on the fact that the formation of a single-electron current through a molecule in contact with two macroscopic objects (electrodes) is studied. In the usual situation, even when there is a chemical bond between the terminal groups of molecules and the adjoining electrodes, the coupling of these groups with the electrode atoms is weaker than the coupling of the electrode atoms with one another. Nonetheless, for more accurate calculations the contacting electrode atoms can be included in a ''combined'' molecule (supercluster). Here the following remark needs to be made. Often, several surface layers are included in the ''combined'' molecule. This inclusion of additional electrode atoms (aside from the atoms chemically bound with the molecule) in a supercluster is undesirable from the physical standpoint, since the supercluster formed will contain terminal atoms which are identical to the atoms of the bulk electrode. Therefore renormalization of the energies of the ''combined'' molecule becomes meaningless, and the results of the current calculations may be too high by an order of magnitude. In what follows we shall assume that only surface atoms which are chemically bound with the molecule can be included in the ''combined'' molecule. The remaining electrode atoms will be referred to the bulk part of the electrodes. The Hamiltonians presented in Eq. (17) refer precisely to such an unperturbed part of the electrodes. We shall use the term ''molecule'' in the wide sense of the word, including also a ''combined'' molecule.

Before diagonalizing the Hamiltonian (1) we shall determine its components H_0 and $H_{\rm int}$. We shall use the single-electron Hamiltonian (16) as the Hamiltonian H. The physical meaning of the eigenstates $|\mu\rangle$ is tied to the MO belonging to the entire LMR system. We shall diagonalize H in two steps. First, using the transformation

$$|a\rangle=\sum_{n\lambda_n} u_a(n,\lambda_n)|n,\lambda_n\rangle \tag{20}$$

we shall diagonalize the Hamiltonian of the molecule (18) and find its eigenenergies ξ_a and eigenstates $|a\rangle$ (i.e. the MO). The coefficients $u_a(n,\lambda_n)$ will determine the contribution of each localized state $|n,\lambda_n\rangle$ to the MO $|a\rangle$ of the molecule. It is important that the static influence of the electrodes on the molecule can be taken into account directly in the energies $E_{n\lambda_n}$ of the localized states of the molecule (in the simplest form—in terms of the image force). The influence of the electric field applied to the electrodes is also included in $E_{n\lambda_n}$. The dynamical coupling of electrodes with the molecule is contained in the interactions H_{LM} and H_{RM} (see the expression (19)), and it is this coupling that is responsible for the transition of the electron between the electrode and the molecule. Since the Hamiltonian (18) of the molecule is diagonal,

$$H_M=\sum_a \xi_a|a\rangle\langle a|, \tag{21}$$

the Hamiltonian (22) of the entire LMR system can now be divided into parts so that $H_0=H_L+H_R+H_M$ and $H_{\rm int}=H_{LM}+H_{RM}$. Using Eqs. (19) and (20) we rewrite the latter expression in the form

$$H_{\rm int}=\sum_{s=L,R}\sum_a [V_{as\mathbf{k}}|a\rangle\langle s\mathbf{k}|+V^*_{as\mathbf{k}}|s\mathbf{k}|\rangle\langle a|]. \tag{22}$$

Here the quantities

$$V_{as\mathbf{k}}=\sum_{n\lambda_n} u_a^*(n,\lambda_n)[\delta_{sL}\delta_{u0}+\delta_{sR}\delta_{aN+1}]V_{n\lambda_n s\mathbf{k}} \qquad (23)$$

characterize the coupling of the ath MO of the molecule with the electrodes. Correspondingly, the quantities (8) acquire the form

$$\Gamma^{(s)}_{\mu\mu'}(E)=\sum_{aa'} \Theta_\mu(a)\Theta^*_{\mu'}(a')\Gamma^{(s)}_{aa'}(E), \qquad (24)$$

where $\Theta_\mu(a)$ are the coefficients coupling the MO $|a\rangle$ of the molecule with the MO $|\mu\rangle$ of the entire LMR system, and

$$\Gamma^{(s)}_{aa'}(E)=2\pi\sum_{\mathbf{k}} V_{as\mathbf{k}}V^*_{a's\mathbf{k}}\delta(E-E_{s\mathbf{k}}) \qquad (25)$$

are the electrode densities of states with respect to the MO of the molecule. The latter, in turn, are related with the local electrode densities

$$\Gamma^{(s)}_{\lambda_n\lambda_n'},(E)=2\pi\sum_{\mathbf{k}} V_{n\lambda_n s\mathbf{k}}V^*_{n\lambda_n' s\mathbf{k}}\delta(E-E_{s\mathbf{k}}) \qquad (26)$$

by the relation

$$\Gamma^{(s)}_{aa'}(E)=2\pi\sum_{\lambda_n\lambda_n'} u_a(n,\lambda_n)u^*_{a'}(n,\lambda_n')\Gamma^{(s)}_{\lambda_n\lambda_n'}(E). \qquad (27)$$

In the formulas (26) and (27) $n=1$ if $s=L$ and $n=N$ if $s=R$.

As follows from the formulas (15) and (24) the exact expression for the transmission function requires knowing the transformation coefficients $\Theta_\mu(a)$ and the energies ε_μ. Both quantities are found by diagonalizing the Hamiltonian H using the transformation

$$|\mu\rangle=\sum_a \Theta_\mu(a)|a\rangle+\sum_{s=L,R}\sum_{\mathbf{k}} \Theta_\mu(s\mathbf{k})|s\mathbf{k}\rangle, \qquad (28)$$

which leads to the system of equations ($s=L,R$)

$$(E_{s\mathbf{k}}-\varepsilon_\mu)\Theta_\mu(s\mathbf{k})+\sum_a V_{as\mathbf{k}}\Theta_\mu(a)=0,$$

$$(\xi_a-\varepsilon_\mu)\Theta_\mu(a)+\sum_{s=L,R}\sum_{\mathbf{k}} V^*_{as\mathbf{k}}\Theta_\mu(s\mathbf{k})=0. \qquad (29)$$

It follows from the first equation that

$$\Theta_\mu(s\mathbf{k})=\frac{1}{\varepsilon_\mu-E_{s\mathbf{k}}}\sum_a V_{as\mathbf{k}}\Theta_\mu(a). \qquad (30)$$

Substituting the results obtained into the second equation of the system gives the reduced system of equations

$$\sum_{a'} [(\xi_a-E)\delta_{aa'}+\Sigma^{(L)}_{aa'}(E)+\Sigma^{(R)}_{aa'}(E)]\Theta_\mu(a')=0, \qquad (31)$$

where the quantities

$$\Sigma^{(s)}_{aa'}(E)=\sum_{\mathbf{k}} \frac{V_{as\mathbf{k}}V^*_{a's\mathbf{k}}}{E-E_{s\mathbf{k}}+i0^+} \qquad (32)$$

determine the matrix of energy renormalizations due to the interaction of the molecule with the sth electrode. We note that the electrode density of states is related with the renormalization of the energy (self-energy) by the exact relation $\Gamma^{(s)}_{aa'}(E)=2\,\mathrm{Im}\,\Sigma^{(s)}_{aa'}(E+i0')$.

Since the reduced system (31) is exact and the quantities (32) depend on E, the equations (31) can be used to find the eigenenergies $E=\varepsilon_\mu$ of the LMR system and the coefficients $\Theta_\mu(a)$. The macroscopic nature of the electrodes makes this impossible to to exactly. However, it is precisely the macroscopic nature of the electrodes that makes it possible to obtain the approximate values of the energies $E=\varepsilon_\mu$. For example, in the zeroth approximation the influence of the molecule on the electrodes can be neglected, retaining only the action of the electrodes on the molecule through the quantity (32). The MO of the entire LMR system are divided into two types. Type-I MO are identical to the electrode states. We denote these MO by $|\mu(s\mathbf{k})\rangle\approx|s\mathbf{k}\rangle$ ($s=L,R$). These MO correspond to the energies $\varepsilon_{\mu(s\mathbf{k})}\approx E_{s\mathbf{k}}$. Because the influence of the molecule on the state of the electrode is neglected the quantum weight of the MO $|a\rangle$ of the molecule in the MO $|\mu(s\mathbf{k})\rangle$ of the electrode can be taken as zero, and therefore

$$\Theta_{\mu(s\mathbf{k})}(a)\simeq 0. \qquad (33)$$

Typie-II MO are identical to the MO of the molecule $\mu=\mu(a)$. However, these MO, because of the presence of energy renormalizations (32), are different from the initial states $|a\rangle$ of the molecule found in the absence of the dynamical interaction of the molecule with the electrodes.

In the expression (15), to calculate the transmission function summation must be performed over all states μ of the LMR system. However, when the condition (33) holds the summation only over the MO of the molecule (in general—over the MO of a cluster) contributes to the transmission function. This is because in accordance with the relation (30) the quantities $\Theta_{\mu(s'\mathbf{k}')}$ are zero. But, even with a small nonzero value of $\Theta_{\mu(s\mathbf{k})}(a)$ the presence of a small denominator $\varepsilon_\mu-E_{s\mathbf{k}}$ can cause the coefficients $\Theta_{\mu(s\mathbf{k})}(a)$ to differ appreciably from zero, having including thereby additional MO (modified electrode states) in current formation. This subtle question will be analyzed separately. Here we shall assume that the condition (33) holds exactly. It corresponds to complete absence of any influence of the molecule (cluster) on the state of the electrodes.

In the approximation (33) the eigenenergies of the effective Hamiltonian

$$H^{(\mathrm{eff})}=H_M+\hat{\Sigma}^{(L)}+\hat{\Sigma}^{(R)}, \qquad (34)$$

where H_M is the diagonal single-electron Hamiltonian of the molecule (21), found in the absence of any dynamical coupling between the molecule and the electrodes. The relations (32) determine the energy renormalization matrices $\hat{\Sigma}^{(s)}$. The form of the Hamiltonian (34) is reminiscent of the form that appears in the Green's function of the molecule (see beginning of this section). However it should be underscored that we have obtained the Hamiltonian (34) in the basis of eigenstates of the molecule, which makes it possible to investigate correctly the role of delocalized and localized electronic states in current formation. Since $\langle a|H^{(\mathrm{eff})}|a'\rangle=\xi_a\delta_{aa'}+\Sigma^{(L)}_{aa'}+\Sigma^{(L)}_{aa'}$, the eignenergies $\varepsilon=\varepsilon(a)$ and the eigenstates $|\mu\rangle=|\mu(a)\rangle$ of the Hamiltonian (34) are found by solving the

reduced system of equations (31) with the condition (33). The solution is greatly simplified by the fact that the quantities $\Gamma^{(s)}_{aa'}(E)$ are essentially independent of E (see Refs. 1, 10, 11, 21, 49), and therefore this dependence can be neglected.

The expressions (23)–(27) make it possible to represent the transmission function (15) in the form

$$T(E,V)=\sum_{\lambda_1\lambda_1'}\sum_{\lambda_N\lambda_N'}\Gamma^{(R)}_{\lambda_N\lambda_N'}(E)G_{N\lambda_N'1\lambda_1'}(E)\Gamma^{(L)}_{\lambda_1'\lambda_1}(E)\times(G^{+})_{1\lambda_1 N\lambda_N}(E), \tag{35}$$

where the matrix element of the Green's function

$$G_{N\lambda_N 1\lambda_1}(E)=\sum_{\mu}\frac{U^{*}_{\mu}(N\lambda_N)U_{\mu}(1\lambda_1)}{E-\varepsilon_{\mu}+i0^{+}}, \tag{36}$$

obtained using the localized states of the molecule, contains the elements

$$U_{\mu}(n\lambda_n)=\sum_{a}\Theta_{\mu}(a)u_a(n\lambda_n),\quad (n=1,N), \tag{37}$$

which establish a relation between the localized states $|n\lambda_n\rangle$ and the eigenstates $|\mu\rangle$ of the molecule. If only one localized orbital state forms the MO $|\mu\rangle$, the index λ_n is dropped in the notation for the states. Consequently,

$$|n\lambda_n\rangle\to|n\rangle,\quad V_{n\lambda_n n\pm1\lambda_{n\pm1}}\to V_{nn\pm1},$$

$$U_{\mu}(n\lambda_n)\to U_{\mu}(n),\quad \Gamma^{(s)}_{\lambda_n\lambda_n'}(E)\to\Gamma^{(s)}(E).$$

Therefore the expression (35) becomes

$$T(E,V)=\Gamma^{(L)}(E)\Gamma^{(R)}(E)\left|\sum_{\mu=1}^{N}\frac{U_{\mu}(1)U^{*}_{\mu}(N)}{E-\varepsilon_{\mu}+i0^{+}}\right|^{2}. \tag{38}$$

4. CURRENT FORMATION BY STRICTLY DELOCALIZED STATES OF THE MOLECULE

The formation of a current through a molecule is closely related with the distribution of the electric potential in the interelectrode space, since this distribution reflects the energy characteristics of the molecule. Recently there have appeared a large number of works where the profile of the electric potential in the region of the molecule and the charge distribution in the molecule were found by a self-consistent solution of the Poisson and Schrödinger equations (see, for example, the discussion in Refs. 58–60). It was shown that for certain molecules the electric potential along the molecule remains unchanged, and the voltage drop occurs only near the contacts.[1,60] But, for other molecules and chains of atoms the voltage drop is nearly linear.[61,62] Calculations have shown[58] that the stronger the screening of the charges in the molecular wire the more strongly the profile of the potential approaches a linear profile characteristic for a potential acting on a test charge in a uniform dielectric medium. At the same time the weaker the screening, the more strongly the molecular wire "metallizes." Since "metallization" is due to delocalization of an electron over a quantum object, it can be concluded that, neglecting the matrix elements for electron hopping between the centers of electron localization in the molecule, the molecule can be represented as a dielectric medium with fixed centers of electron localization. Correspondingly, the linear voltage drop between the indicated centers will also form the distribution of the electric potential along the molecule or molecular wire. This conclusion is confirmed by direct experiments with single- and multiwell carbon nanotubes.[63] For nanotubes of the first type (where an electron is delocalized along the entire well) the potential profile is constant along the entire length of a nanotube. At the same time, in multiwell nanotubes an almost linear voltage drop is observed along the entire nanotube.

In what follows it will be shown analytically that it is precisely the delocalization of an electron along a molecule that "metallizes" the molecule. In consequence the linear distribution of the potential along the molecule becomes a constant, signifying the absence of a voltage drop along the molecule. To obtain analytical results we shall examine the formation of a current through a linear molecule with regularly arranged centers (molecular wire), each of which is characterized by only one free MO. In this case the initial Hamiltonian of the molecule (18) acquires the simple form

$$H_M=\sum_{n=1}^{N}E_n|n\rangle\langle n|+V_B\sum_{n=1}^{N}(|n\rangle\langle n+1|+|n+1\rangle\langle n|). \tag{39}$$

where $V_B\equiv V_{12}=V_{23}=\ldots=V_{N-1N}$ denote the matrix elements for electron hopping between neighboring centers (see Fig. 1). In contrast to delocalization ($V_B=0$) the molecule is a collection of equidistant localization centers, i.e., the position of the excess electron on a center is similar to the position of a test charge. Consequently, the expression for the energy of an excess electron on the nth center can be written in the form $E_n=E_B+\Delta E_B$, where E_B is the electron energy on the center with $V=0$, and

$$\Delta E_n=eV[\delta_L+(n-1)\delta_c]/\delta \tag{40}$$

is the correction due to the potential difference V. In Eq. (40) $\delta=\delta_L+(N-1)\delta_c+\delta_R$ is the effective interelectrode distance, which is the sum of the effective lengths (see Fig. 1). (Each effective length $\delta_j=l_j/\varepsilon_j$ $(j=L,c,R)$ is determined by dividing the geometric length l_j by the corresponding permittivity ϵ_j of the medium.) We note that because of the applied potential difference V the energy gap $eV\delta_c/\delta$ between the nearest centers linearly increases with V, forming a linear potential drop along the entire molecule. This drop is $E_N-E_1=eV(N-1)\delta_c/\delta$. When the interaction V_B is switched on, resulting in electron hopping between centers, the electron strives to delocalize along the molecule, in the process forming the collectivized states and collectivized energy levels of the molecule. In this section we shall examine the case of strong delocalization of an electron, when

$$|\overline{\xi}_a-\overline{\xi}_{a'}|\gg|t_{aa'}|,\quad |\Sigma^{(s)}_{aa'}|, \tag{41}$$

where $\overline{\xi}_a=\xi_a+\Delta\xi_a+\Sigma^{(L)}_{aa}+\Sigma^{(R)}_{aa}$ is the renormalized electron energy,

$$\Delta\xi_a=\sum_{n}|u_a(n)|^2\Delta E_n \tag{42}$$

is the energy shift, caused by the application of a voltage, of the delocalized state, and $t_{aa'}=\Sigma_n u^{*}_a(n)u_{a'}(n)\Delta E_n$ is the

transition matrix element between delocalized states. When the condition (41) is satisfied the ''mixing'' of delocalized states can be neglected in the zeroth approximation and $\Theta_\mu(a)\approx\delta_{\mu a}$ can be used. As a result the exact MO $|\mu\rangle$ are actually identical to the initial MO $|a\rangle$. However the energies change, acquiring a shift and an imaginary correction so that $\varepsilon_\mu\approx\delta_{\mu a}\overline{\xi_a}$. Since $\mathrm{Im}\,\Sigma_{aa}^{(s)}=(1/2)\Gamma^{(s)}$, we obtain

$$\varepsilon_\mu=\xi_\mu+\eta eV-i\gamma_\mu. \tag{43}$$

Here

$$\xi_\mu=E_B-2|V_B|\cos\frac{\pi\mu}{N+1}\,(\mu=1,2,...,N) \tag{44}$$

is the energy obtained for the μth delocalized state of an electron by diagonalizing the Hamiltonian (39) (with $V=0$),

$$\gamma_\mu=[|u_\mu(1)|^2\Gamma^{(L)}+|u_\mu(N)|^2\Gamma^{(R)}]/2 \tag{45}$$

is the imaginary correction to the energy, due to the influence of the electrodes on the molecule, and the factor

$$\eta=[1+(\delta_L-\delta_R)/\delta]/2 \tag{46}$$

controls the shift of the delocalized levels of the molecule under the action of the applied potential difference. This factor appears because any delocalized energy level ε_μ undergoes the same linear shift (42). For a molecule with regularly spaced centers this fact can be proved by direct calculation of the quantity (42) using the expression (40) and the explicit form of the coefficients

$$u_\mu(n)=\sqrt{\frac{2}{N+1}}\sin\frac{\pi\mu n}{N+1}, \tag{47}$$

characterizing the transition matrix between localized and delocalized bases. The appearance of the identical shift ηeV for all delocalized levels of the molecule means that there is no voltage drop near the position of the molecule, i.e., ''metallization'' of the molecule occurs. This can be seen more directly by initially placing the molecule symmetrically relative to the electrodes ($\delta_L=\delta_R$), and applying the potentials $-V/2$ and $+V/2$ to the electrodes symmetrically. Then the shift of the delocalized energy levels (42) becomes zero, and for this reason the levels of the molecule are not shifted at all by the field (only the Fermi levels of the electrodes shift symmetrically but in opposite directions). However if one electrode is grounded and a potential V is applied to the other electrode, then all delocalized levels and the Fermi level of one of the electrodes (in our case the right-hand electrode) shift by the *same* amount.

The formulas (43)–(47) completely determine the transmission function (38). Using Eq. (43) it is evident that for constant $\Gamma^{(s)}$ the following important property holds:

$$T(E,V)=T(E-\eta eV). \tag{48}$$

Consequently, the entire dependence of the current on the potential difference V can be put into the integration limits. Indeed, introducing the variable

$$x=E-E_F-\eta eV, \tag{49}$$

and the quantities $\Delta E_B\equiv E_B-E_F$ and

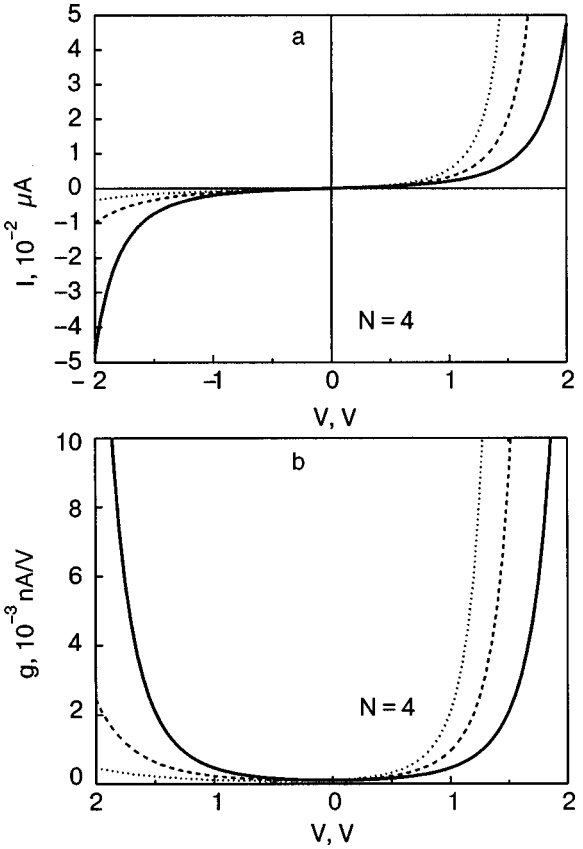

FIG. 2. $I-V$ (a) and $g-V$ (b) characteristics of a molecule calculated using Eqs. (51) and (54) with the parameters $\Delta E_B=2.8$ eV, $V_B=1$ eV, $\Gamma^{(L)}=0.2$, $\Gamma^{(R)}=0.1$ eV with η: 0.5 (——), 0.6 (— — —), and 0.7 (· · ·).

$$x_\mu=\Delta E_B-2|V_B|\cos\frac{\pi\mu}{N+1}, \tag{50}$$

we obtain the following final expression for the elastic low-temperature current through strictly delocalized states of the molecule:

$$I=I_0\int_{-(1-\eta)|e|V}^{\eta|e|V}dxT(x), \tag{51}$$

where the dependence of the transmission function

$$T(x)=\Gamma^{(L)}\Gamma^{(R)}[A^2(x)+B^2(x)] \tag{52}$$

on the integration variable x is determined by the quantities

$$A(x)=\sum_{\mu=1}^{N}\frac{u_\mu(1)u_\mu(N)(x-x_\mu)}{(x-x_\mu)^2+\gamma_\mu^2},$$
$$B(x)=\sum_{\mu=1}^{N}\frac{u_\mu(1)u_\mu(N)\gamma_\mu}{(x-x_\mu)^2+\gamma_\mu^2}. \tag{53}$$

The following formula for the conductivity of the molecule follows from the expression (51):

$$g=g_0[\eta T(\eta|e|V)+(1-\eta)T(-(1-\eta)|e|V)]. \tag{54}$$

In Eqs. (51) and (54) the current and conductivity are expressed in the standard units of current $I_0\equiv 2|e|/h\approx 80$ μA and conductance $g_0=2e^2/h\approx 7.75\cdot 10^4$ nA/V.[10–12] All energy quantities, including Γ^s and the limits of integration, must be expressed in electron-volts.

Figures 2–4 show the $I-V$ and $g-V$ characteristics of a

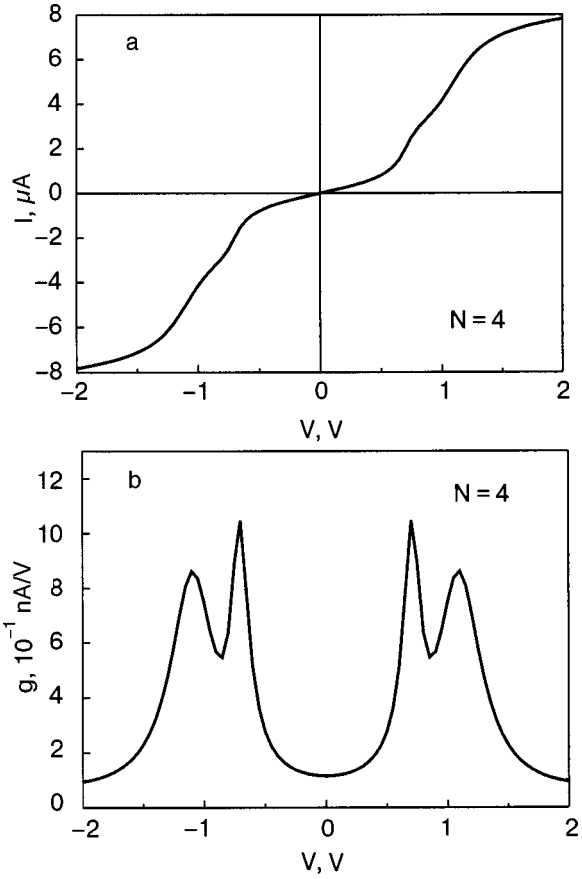

FIG. 3. $I-V$ (a) and $g-V$ (b) characteristics of a molecule calculated with the parameters $\Delta E_B=1.1$ eV, $V_B=0.9$ eV, $\Gamma^{(L)}=0.2$, $\Gamma^{(R)}=0.1$ eV with $\eta=0.5$.

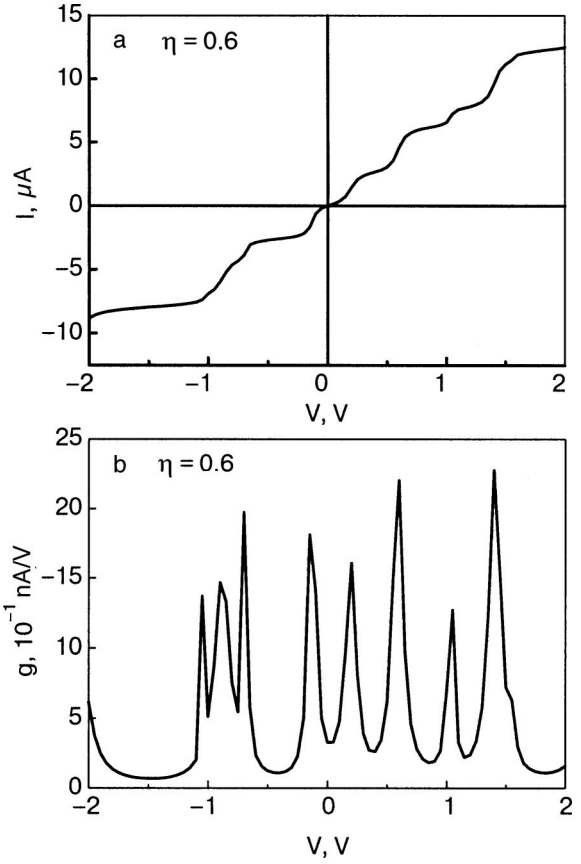

FIG. 4. $I-V$ (a) and $g-V$ (b) characteristics of a molecule calculated with the same parameters as in Fig. 3 but with $N=10$.

molecule when only one orbital state from each of the identical centers of the molecule participates in the formation of MO. The calculations were performed using the formulas (51)–(54), which are inconvenient for interpreting results. This is because the integration limits were shifted artificially on account of the relation (48). Consequently, it seems that not only the right-hand but also the left-hand Fermi levels are shifted. In reality, according to the conditions of the problem, the left-hand electrode is maintained at zero potential and a potential V is applied to the right-hand electrode.

Consequently, the position of the Fermi level of the left-hand electrode remains unchanged, and the position of the Fermi level of the right-hand electrode shifts by the amount eV. Since all N levels of the molecule undergo the same shift (by the amount ηeV), this explains the physics of the formation of a current through delocalized states of a molecule. Resonance transmission occurs if the energy of the μth level of the molecule (43) (neglecting the broadening γ_μ) is the same as the energy E_F for the left-hand electrode and the energy E_F+eV for the right-hand electrode. This situation occurs if

$$x_\mu=-\eta eV \tag{55}$$

for the left-hand electrode and

$$x_\mu=(1-\eta)eV \tag{56}$$

for the right-hand electrode. For $\mu=1$ the left-hand sides of the expressions (55) and (56) determine the energy gap $\Delta E_L(0)=\Delta E_R(0)$ existing between LUMO and the Fermi level in the absence of a potential difference between the electrodes. If $V\neq 0$, then the energy gaps become dependent on V:

$$\Delta E_L(V)=x_1+\eta eV, \quad \Delta E_R(V)=x_1-(1-\eta)eV. \tag{57}$$

Figure 5 illustrates the mechanism of current formation. For $V\approx 0$ elastic transmission prevents an electron from occupying the free levels of the molecule, since these levels are separated from the Fermi levels of both electrodes by the initial energy gaps

$$\Delta E_L(0)=\Delta E_R(0)=\Delta E_B-2|V_B|\cos\frac{\pi}{N+1}>0. \tag{58}$$

For $V>0$ the levels of the molecule shift downward by the amount $\eta|e|V$ and at the same time the Fermi energy of the right-hand electrode drops by an amount $|e|V$. Ultimately, the gap $\Delta E_R(V)$ increases. At the same time the left-hand electrode is constantly maintained at zero potential and for this reason its Fermi level does not shift. In consequence the gap $\Delta E_L(V)$ decreases. For $\Delta E_L(V)=0$ the first resonance transmission occurs and the first peak appears in the conductivity of the molecule. A subsequent increase of V results in resonance transmission through higher energy levels of the molecule. The condition (55) determines the corresponding resonance values of V. We note that for $V>0$ all resonance peaks are associated with the left-hand potential and appear for a negative value of the gap $\Delta E_L(V)$ (see Fig. 5b). Physically, the same situation occurs for $V<0$, the difference be-

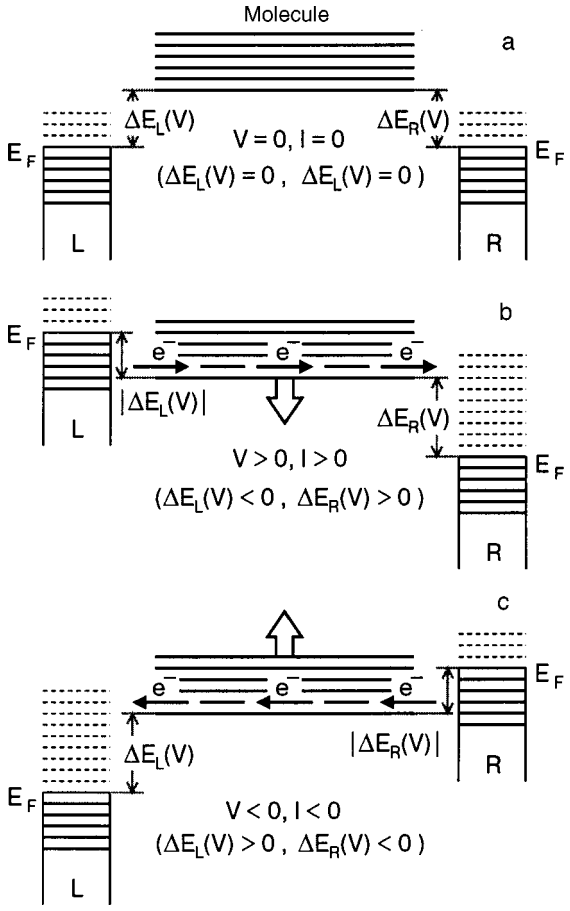

FIG. 5. Scheme of the formation of a purely elastic current through delocalized MO. For $V\approx 0$ purely elastice interelectrode electron transport is impossible because of the presence of gaps $\Delta E_L(0)=\Delta E_R(0)>0$ (a). For $V>0$ the energies of all MO are shifted down by the same amount $\eta|e|V$. The position of the Fermi level of the right-hand electrode shifts by $|e|V$; the Fermi level of the left-hand electrode remains unshifted. The gap $\Delta E_R(V)$ increases, and the gap $\Delta E_L(V)$ decreases to zero and then becomes negative. For $\Delta E_L(V)\leqslant 0$ electron transmission is possible from the left- to the right-hand electrode (b). If a negative voltage is applied to the right-hand electrode, then for $\Delta E_R(V)\leqslant 0$ a negative elastic current through the molecule arises (c).

ing that the left-hand gap $\Delta E_L(V)$ increases and the right-hand gap $\Delta E_R(V)$ decreases. The first resonance transmission from the right- to the left-hand electrode occurs for $x_1=(1-\eta)eV$. Subsequent resonance transmissions arise for $\Delta E_L(V)<0$ and are determined by the condition (56).

The $I-V$ and $g-V$ characteristics of the molecule are symmetric if $\eta=0.5$ and asymmetric if $\eta\neq 0.5$. In Fig. 2 asymmetry is manifested in the rectifying properties of the molecule, which are all the stronger the more the factor η differs from 0.5. For example, for $V=1.5$ eV and $\eta=0.7$ the positive current is more than an order of magnitude greater than the negative current, while for $\eta=0.5$ the currents are identical. If the initial gaps (58) decrease, then it becomes possible to observe resonance transmission in the same voltage drop range $[-2,+2]$ eV. The dependence $I=I(V)$ becomes nonmonotonic and peaks appear in the conductivity. In Fig. 3 there are two peaks in the interval $[-2,+2]$ eV.[1] If the molecule contains more centers, then in this interval $[-2,+2]$ eV the current starts to exhibit a stepped character, and the conductivity will be characterized by a larger number of peaks (Fig. 4).[2] In concluding this section we note the following important indicator of transmission through delocalized states: as V changes, the conductivity can increase (as a resonance peak is approached) or decrease (after passing through a peak), but in principle it cannot become negative.

5. ROLE OF LOCALIZATION IN ELECTRON TRANSMISSION THROUGH A MOLECULE

Negative conductivity was first observed experimentally by Reed *et al.*[2,64] We shall show that its appearance could be due to the participation of localized states in the transmission of a molecule. For definiteness we shall consider a model where the molecule has only two centers of electron localization ($n=1$ and $n=N=2$, see Fig. 1), and each center is characterized by only one orbital state that participates in transmission. Such a model makes it possible to obtain analytical results with an arbitrary (small and large) magnitude of the transition matrix element V_{12} and also with an arbitrary magnitude of the potential difference V. The elastic current is determined by the general expression (13), where the transmission function has the form

$$T(E,V)=\frac{\Gamma^{(L)}\Gamma^{(R)}|V_{12}|^2}{[(E-\varepsilon_{\rm I})^2+\gamma_{\rm I}^2][(E-\varepsilon_{\rm II})^2+\gamma_{\rm II}^2]}. \tag{59}$$

Just as in the case of transmission through a purely delocalized state, we shall neglect the unessential dependence of the quantities $\Gamma^{(s)}$ on the energy E. However, the quantities $\Gamma^{(s)}$ can depend on V if both electron localization centers are sufficiently far-removed from the electrode surfaces. A separate aanalysis is needed to determine the reasons for the dependence of $\Gamma^{(s)}$ on the applied potential difference. Here we assume that both centers are close to the electrode surfaces and are treated as terminal groups of the molecule. In this case the V dependence is concentrated in the quantity V_{12} and in the characteristic energies of the electron

$$\varepsilon_{\rm I,II}=(E_1+E_2\mp\rho\cos\psi)/2 \tag{60}$$

and the broadenings of these energies

$$\gamma_{\rm I,II}=(\Gamma^{(L)}+\Gamma^{(R)}\mp\rho\sin\psi)/2. \tag{61}$$

In Eqs. (60) and (61)

$$E_1=E_1^{(0)}+eV(\delta_L/\delta),\quad E_2=E_2^{(0)}+eV(1-\delta_R/\delta) \tag{62}$$

are the energies of the localized states of electrons transported along the molecule ($E_1^{(0)}$ and $E_2^{(0)}$ are the same energies in the absence of an applied field),

$$\rho\cos\psi=\frac{1}{\sqrt{2}}\frac{2|\Delta E_{21}\Delta_{21}|}{\sqrt{\rho^2-[D^2+\Delta_{21}^2\zeta]}}, \tag{63}$$

$$\rho\sin\psi=\frac{1}{\sqrt{2}}\sqrt{\rho^2-[D^2+\Delta_{21}^2\zeta]}\,\frac{\Delta E_{21}\Delta_{21}}{|\Delta E_{21}\Delta_{21}|}, \tag{64}$$

$$\rho=\{4\Delta E_{21}^2\Delta_{21}^2+[D^2+\Delta_{21}^2\zeta]^2\}^{1/4}, \tag{65}$$

$$D=\sqrt{\Delta E_{21}^2+4|V_{12}|^2},\quad \Delta E_{21}=E_2-E_1, \tag{66}$$

$$\Delta_{21}=(\Gamma^{(R)}-\Gamma^{(L)})/2,\quad \zeta=1-2\Delta E_{21}^2/D^2. \tag{67}$$

As a result of the complicated dependence of the transmission function (59) on V the property (48) now no longer holds and consequently the general expressions (52) and (54), which are valid for transmission through strictly delocalized MO, also no longer hold. However if the strict inequality

$$4|V_{12}|^2 \gg \Delta E_{21}^2, \Delta_{21}^2 \tag{68}$$

holds, then delocalization occurs independently of the applied potential difference V, and we arrive at the situation studied in the preceding section. Indeed, when the inequalities (68) are satisfied we have $\rho\cos\psi \approx 2|V_{12}|$ and $\rho\sin\psi \approx 0$. Therefore

$$\varepsilon_{\mathrm{I,II}} = (E_2^{(0)} - E_1^{(0)})/2 \mp 2|V_{12}| + \eta eV, \tag{69}$$

$$\gamma_{\mathrm{I,II}} = (\Gamma^{(L)} + \Gamma^{(R)})/2. \tag{70}$$

Once again it is evident that strong delocalization of an electron in a molecule results in ''metallization'' of the molecule, which manifests as the absence of a voltage drop along the molecule (the difference of the energy levels $\varepsilon_I - \varepsilon_{II}$ does not depend on V). At the same time the delocalized levels themselves shift by the same amount ηeV. In consequence the relation (48) is now satisfied. This is a universal relation for the transmission function in the case of current formation by the delocalized states of a molecule. Therefore the same factor η controlling the voltage shift (see Eq. (46)) arises, and the current and conductivity can be calculated using Eqs. (51) and (54).

The situation is completely different for weak delocalization

$$\Delta E_{21}^2 \gg 4|V_{12}|^2, \Delta_{21}^2. \tag{71}$$

In this case

$$\varepsilon_{\mathrm{I}} \approx E_1, \quad \varepsilon_{\mathrm{II}} \approx E_2, \quad \gamma_{\mathrm{I}} \approx \Gamma^{(L)}/2, \quad \gamma_{\mathrm{II}} \approx \Gamma^{(R)}/2. \tag{72}$$

Now, even though the broadening of the levels is once again independent of V, and the electron energies in the molecule undergo a different shift with a change in V (see Eq. (62)). There can be no talk about any ''metallization'' of the molecule, and consequently the property (48) is not satisfied. The transmission function remains V-dependent for any change of variable in the integral (13). This means that the current and the conductivity are found by integrating.

We shall now obtain an analytical expression for the interelectrode current. Substituting into Eq. (13) the expression for the transmission function (59) and introducing the V-independent average energy gap

$$\Delta E = (\Delta E_2 + \Delta E_1)/2, \quad \Delta E_j^{(0)} \equiv E_j - E_F, \tag{73}$$

and the quantities

$$x_{\mathrm{I,II}} = \Delta E \mp (1/2)\rho\cos\psi, \tag{74}$$

we obtain after integrating

$$I = I_0 \frac{|V_{12}|^2 (\Gamma^{(L)}\Gamma^{(R)}/\gamma_{\mathrm{I}}\gamma_{\mathrm{II}})}{[(x_{\mathrm{II}} - x_{\mathrm{I}})^4] + (\gamma_{\mathrm{II}}^2 - \gamma_{\mathrm{I}}^2)^2 + 2(x_{\mathrm{II}} - x_{\mathrm{I}})^2(\gamma_{\mathrm{II}}^2 + \gamma_{\mathrm{I}}^2)}$$
$$\times \Bigg\{ \gamma_{\mathrm{I}}\gamma_{\mathrm{II}}(x_{\mathrm{II}} - x_{\mathrm{I}})$$
$$\times \ln\left[\frac{[(x_{\mathrm{II}} - \eta|e|V)^2 + \gamma_{\mathrm{II}}^2][(x_{\mathrm{I}} + (1-\eta)|e|V)^2 + \gamma_{\mathrm{I}}^2]}{[(x_{\mathrm{II}} + (1-\eta)|e|V)^2 + \gamma_{\mathrm{II}}^2][(x_{\mathrm{I}} - \eta|e|V)^2 + \gamma_{\mathrm{I}}^2]}\right]$$
$$+ [(\gamma_{\mathrm{II}}^2 - \gamma_{\mathrm{I}}^2) - (x_{\mathrm{II}} - x_{\mathrm{I}})^2]$$
$$\times \gamma_{\mathrm{I}}\left(\arctan\frac{x_{\mathrm{II}} + (1-\eta)|e|V}{\gamma_{\mathrm{II}}} - \arctan\frac{x_{\mathrm{II}} - \eta|e|V}{\gamma_{\mathrm{II}}}\right)$$
$$- [(\gamma_{\mathrm{II}}^2 - \gamma_{\mathrm{I}}^2) + (x_{\mathrm{II}} - x_{\mathrm{I}})^2]\gamma_{\mathrm{II}}\left(\arctan\frac{x_{\mathrm{I}} + (1-\eta)|e|V}{\gamma_{\mathrm{I}}}\right.$$
$$\left. - \arctan\frac{x_{\mathrm{I}} - \eta|e|V}{\gamma_{\mathrm{I}}}\right)\Bigg\}. \tag{75}$$

The exact expression (75) for the current opens up the possibility of analyzing various regimes of current formation, including the limiting cases of electron transmission through purely delocalized and localized MO. Here we shall consider only the role of two physically important parameters of a molecule in the formation of a current through a two-center molecule. We are talking about the energy difference between localized states

$$\Delta E_{21} = \Delta E_{21}^{(0)} + (1 - \eta_L - \eta_R)eV \tag{76}$$
$$(\Delta E_{21}^{(0)} \equiv \Delta E_2 - \Delta E_1, \quad \eta_L \equiv \delta_L/\delta, \quad \eta_R \equiv \delta_R/\delta),$$

(see Eq. (62)) and the hopping matrix element V_{12}. As shown in the preceding section, for electron transmission through delocalized MO, current asymmetry and therefore the rectifying properties of the molecule arise if the parameter η becomes different from 0.5. In accordance with the expression (46) this occurs if the effective distances δ_L and δ_R of the terminal groups of the molecules from the electrode surfaces are not equal to one another, i.e., for an asymmetric arrangement of the molecule relative to the electrodes. However the splitting between local energy levels in the molecule in the absence of a potential difference also plays an important role in the formation of current asymmetry. In our case of a molecule with two centers this splitting is $\Delta E_{21}^{(0)}$. Physically, the smaller the energy difference (76) and the larger V_{12} the sharper the delocalization in the molecule is. Nonetheless, delocalization is possible even for small V_{12} if the applied electric field can make the energy difference (76) a vanishingly small quantity. For definiteness, let $\Delta E_{21}^{(0)} > 0$. Then if $V > 0$, we obtain $\Delta E_{21} = 0$ provided that $(1 - \eta_L - \eta_R)|e|V = \Delta E_{21}^{(0)}$. However, as the potential difference increases further, the quantity $(1 - \eta_L - \eta_R)|e|V$ becomes greater than $\Delta E_{21}^{(0)}$ so that ΔE_{21} starts to increase in absolute magnitude, which degrades the localization. For $V < 0$ the splitting between the localized levels increases with $|V|$, and delocalization in the molecule only weakens. The applied potential difference strongly regulates the transmission mechanism.

Figure 6a illustrates current intensification with increasing $|V_{12}|$ in the presence of strong electron localization in the

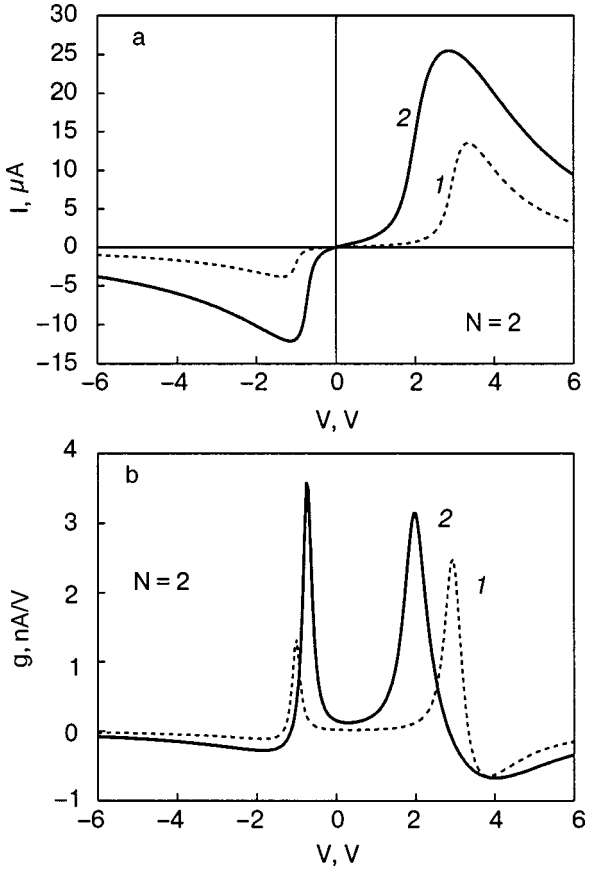

FIG. 6. $I-V$ (a) and $g-V$ (b) characteristics of a two-center molecule with different values of the electron transmission matrix element $|V_{12}|$, eV: 0.5 (1) and 1 (2). The calculations were performed using Eq. (75) and the parameters $\Delta E_1=1$ eV, $\Delta E_2=3$ eV, $\Gamma^{(L)}=0.2$ eV, $\Gamma^{(R)}=0.4$ eV, $\eta_L=\eta_R=0.1$.

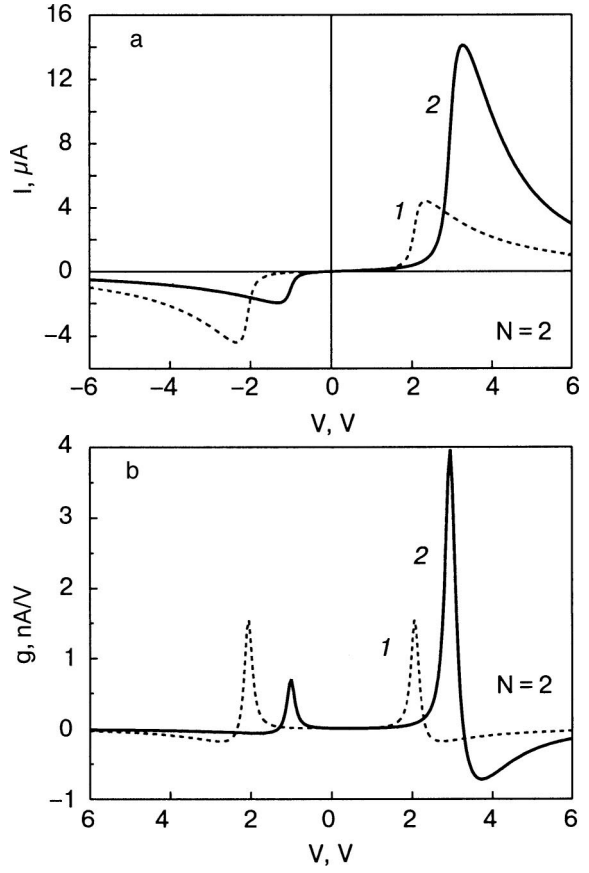

FIG. 7. $I-V$ (a) and $g-V$ (b) characteristics of a two-center molecule with different values of the local energy gaps: $\Delta E_1=\Delta E_2=2$ eV (1) and $\Delta E_1=1$ eV, $\Delta E_2=3$ eV (2). The calculations were performed using Eq. (75) and the parameters $|V_{12}|=0.5$ eV, $\Gamma^{(L)}=0.2$ eV, $\Gamma^{(R)}=0.4$ eV, $\eta_L=\eta_R=0.1$.

molecule ($\Delta E_{21}^{(0)}=2$ eV). The current asymmetry is due mainly to the different splitting of localized energy levels ($\Delta E_1=1$ eV, $\Delta E_2=3$ eV) from the Fermi level (see definition (73)). This same factor is responsible for the nonmonotonic behavior of the current and the decrease of the magnitude of the current after the maximum resonance value is reached. The conductivity even becomes negative (Fig. 6b). Figure 7 shows that the presence of an initial energy asymmetry in the molecule increases the magnitude of the resonance current and the rectifying properties of the molecule. We shall analyze the completely symmetric case first. Then for $\Delta E_1=\Delta E_2$ and $\Gamma_1=\Gamma_2$ completely symmetric $I-V$ characteristics of the molecule are observed. In the region $[-2, +2]$ eV the initially delocalized states of the molecule remain delocalized, and consequently it is these states that are responsible for electron transmission. Outside the region $[-2,+2]$ eV the electric field becomes sufficiently strong to transform the delocalized states into localized states. Thus even in the completely symmetric case resonance transmission is found to be associated with localized states. The conductivity can become negative. If energy asymmetry ($\Delta E_1=1$ eV, $\Delta E_2=3$ eV) exists initially, then the $I-V$ and $g-V$ characterisitics remain asymmetric relative to a change in sign of V for any value of V. The ratio of the peak values of the current and the conductivity change substantially. The physics of current formation is illustrated in Fig. 8. The general case with an asymmetric initial position ($\Delta E_2>\Delta E_1$) of localized energy levels of the excess electron in the molecule is considered. The local energy gaps

$$\Delta E_1(V)=\Delta E_1+\eta_L eV,$$
$$\Delta E_2(V)=\Delta E_2-(1-\eta_R)eV \tag{77}$$

depend on the magnitude and direction of V. Under conditions of elastic tunneling a current appears when the energy of at least one localized level becomes equal to the Fermi energy. In our case the position of the Fermi level of the left-hand electrode remains unchanged with $V\neq 0$, and both electron localization centers are assumed to lie close to their own electrodes. Since in this case η_L, $\eta_R \ll 1$, in accordance with Eq. (77) only the gap $\Delta E_2(V)$ undergoes large changes. For $V>0$ the energy E_2 and the Fermi level of the right-hand electrode shift downwards. Although the gap $\Delta E_2(V)$ increases, this only helps the level 2 come into resonance with the Fermi level of the right-hand electrode. The first conductivity peak appears. However, a second peak appears only for very large values of V, and it will be associated with level 1 coming into resonance. If $\Delta E_1=1$ eV and $\eta_L=0.1$, then a potential diffference of 10 eV is needed for the second resonance peak to appear. For this reason the second peak is absent in Fig 8. When $V<0$ both energy levels and the Fermi level of the right-hand electrode shift upward. The gap $\Delta E_1(V)$ increases and the gap $\Delta E_2(V)$ slowly decreases.

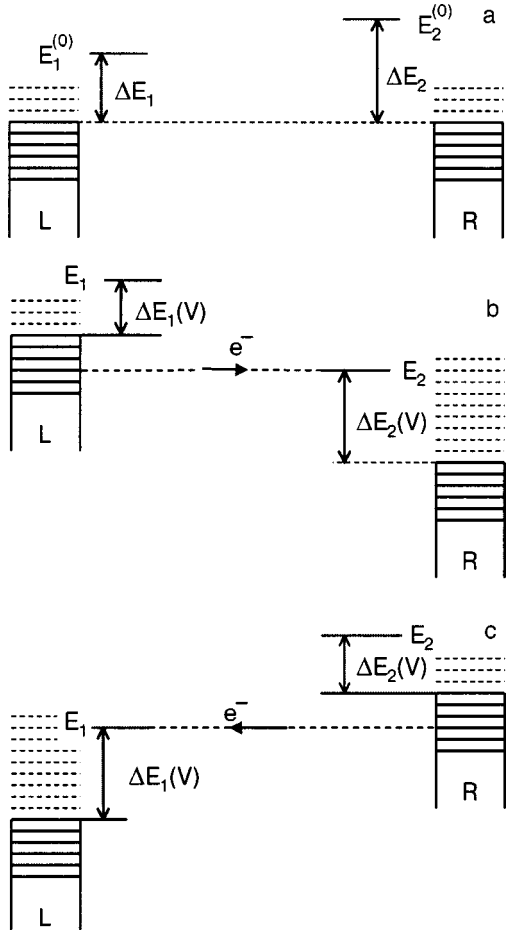

FIG. 8. Formation of an interelectrode current through localized electronic energy levels of a two-center molecule. The magnitudes of the left-hand (ΔE_1) and right-hand (ΔE_2) gaps existing for $V=0$ eV change when $V \neq 0$ (a). For centers located close to the electrodes these gaps vanish only for large values of $|V|$. For much smaller $|V|$ the right-hand level comes into resonance with the Fermi level of the left-hand electrode (b) and the left-hand level comes into resonance with the Fermi level of the right-hand electrode (c).

However the main point is that now the level 1 comes into resonance with the Fermi level of the right-hand electrode. This explains the current peak for $V<0$. The second peak appears only for large values of V, just as in the case $V>0$.

6. CONCLUSIONS

Exact expressions were obtained for the elastic and quasielastic current. These expressions were used to study the physics of the formation of an elastic current through a molecule with several centers of localization of the transported electron. It was shown that for transmission through strictly delocalized MO the influence of the potential difference applied to the electrode is manifested in the fact that the shift of the energy levels of the molecule, determined by the single factor η (46), is the same for all MO. Only in this case does the transmission function of the molecule possess the property (48), making it possible to express the conductivity of the molecule in the simple analytical form (54). However if the MO is of a localized type, then the property (48) no longer holds and the expression (54) becomes meaningless—this is an important result of the theory. When transmission occurs through localized states of a molecule the transmission function $T(E,V)$ depends separately on the energy E and on the potential difference V. This means that the elastic current must be calculated using the general formula (13), and the conductivity must be found by differentiating the expression obtained for the current. In connection with the different shift of the localized levels in an electric field (this shift is related with the factors η_L and η_R) resonance transmission will occur for each level separately, matched with its specific resonance value of V. Thus elastic transmission through localized states differs substantially from transmission through delocalized states, and consequently it cannot be described by the simplified expressions (51) and (54)—this is the second fundamental result obtained in this work.

Here only some of the problems of electron transmission through a molecule were examined: the derivation and the conditions of applicability of the theoretical formulas. A detailed analysis of the $I-V$ and $g-V$ characteristics of a molecule taking account of specific experimental data will be presented in separate works.

This work was performed under contract No. M/230-2004.

*E-Mail: epetrov@bitp.kiev.ua

[1)]The arrangement of the peaks is symmetric with respect to $V=0$, which is characteristic for the case $\eta=0.5$, irrespective of the fact that $\Gamma^{(L)} \neq \Gamma^{(R)}$.

[2)]Asymmetry due to the fact that the factor η controlling the shift of the delocalized levels of the molecule is greater than 0.5 is observed.

[1] W. Tian, S. Datta, S. Hong, R. Reifenberger, J. I. Henderson, and C. P. Kubiak, J. Chem. Phys. **109**, 2874 (1998).
[2] J. Chen, M. A. Reed, A. M. Rawlett, and J. M. Tour, Science **286**, 1550 (1999).
[3] R. M. Metzger, Acc. Chem. Res. **32**, 950 (1999).
[4] F. Moresco, G. Meyer, and K.-H. Rieder, Phys. Rev. Lett. **86**, 672 (2001).
[5] H. B. Weber, J. Reichert, F. Weigend, R. Ochs, D. Beckmann, M. Mayor, R. Ahlrichs, and H. von Löhneyson, Chem. Phys. **281**, 113 (2002).
[6] J. Chen and M. A. Reed, Chem. Phys. **281**, 127 (2002).
[7] A. Avirom and M. Ratner, Chem. Phys. Lett. **29**, 277 (1974).
[8] *Molecular Electronic Devices*, edited by F. L. Carter, Marcel Dekker, New York (1982).
[9] F. L. Carter, World Biotech. Rep. **2**, 127 (1984).
[10] A. Nitzan, Annu. Rev. Phys. Chem. **52**, 681 (2001).
[11] F. Zahid, M. Paulsson, and S. Datta, in *Advanced Semiconductors and Organic Nano-Techniques*, edited by H. Morkos, Academic Press, New York (2003), Chap. 2, p. 41.
[12] A. Nitzan and M. A. Ratner, Science **300**, 1384 (2003).
[13] S. N. Yaliraki and M. A. Ratner, J. Chem. Phys. **109**, 5036 (1998).
[14] S. N. Yaliraki, A. E. Roitberg, C. Gonzales, M. Mujica, and M. A. Ratner, J. Chem. Phys. **111**, 6997 (1999).
[15] S. N. Yaliraki, M. Kemp, and M. A. Ratner, J. Am. Chem. Soc. **121**, 3428 (1999).
[16] C. Kergueris, J.-P. Bourgoin, S. Palacin, D. Esteve, C. Urbana, M. Magoga, and C. Joachim, Phys. Rev. B **59**, 12505 (1999).
[17] E. G. Emberly and G. Kirczenow, Phys. Rev. B **64**, 235412 (2001).
[18] J. Taylor, H. Guo, and J. Wang, Phys. Rev. B **63**, 245407 (2001).
[19] J. T. Taylor, M. Brandybyge, and K. Stokbro, Phys. Rev. Lett. **89**, 138301 (2002).
[20] H. Bash and M. A. Ratner, J. Chem. Phys. **120**, 5771 (2004).
[21] V. Mujica, M. Kemp, and M. Ratner, J. Chem. Phys. **101**, 6849 (1994); *ibid.* p. 6856 (1994).
[22] L. E. Hall, J. R. Reimers, N. S. Hush, and K. Silverbrook, J. Chem. Phys. **112**, 1510 (2000).
[23] A. L. Yeyati, A. Martin-Rodero, and F. Flores, Phys. Rev. Lett. **71**, 2991 (1993).
[24] M. H. Hettler and H. Schoeller, Europhys. Lett. **57**, 571 (2002).
[25] P. Orellana and F. Claro, Phys. Rev. Lett. **90**, 178302 (2003).

[26] M. H. Hettler, W. Wentzel, M. R. Wegewijs, and H. Schoeller, Phys. Rev. Lett. **90**, 076805 (2003).
[27] V. Mujica, A. Nitzan, S. Datta, M. A. Ratner, and C. P. Kubiak, J. Phys. Chem. B **107**, 91 (2003).
[28] E. G. Petrov and P. Hänggi, Phys. Rev. Lett. **86**, 2862 (2001).
[29] E. G. Petrov, V. V. Marchenko, and Ya. R. Zelinsky, Mol. Cryst. Liq. Cryst. **385**, 121/1 (2002).
[30] É. G. Petrov, V. May, and P. Hänggi, Chem. Phys. **281**, 211 (2002).
[31] É. G. Petrov, Fiz. Nizk. Temp. **28**, 872 (2002) [Low Temp. Phys. **28**, 630 (2002)].
[32] P. Damle, A. W. Ghosh, and S. Datta, Chem. Phys. **281**, 171 (2002).
[33] M. Di Ventra, N. D. Lang, and S. T. Pantelidis, Chem. Phys. **281**, 189 (2002).
[34] A. W. Ghosh, F. Zahid, S. Datta, and R. R. Birge, Chem. Phys. **281**, 225 (2002).
[35] H. Chen, J. Q. Lu, J. Wu, R. Note, H. Mizuseki, and Y. Kawazoe, Phys. Rev. B **67**, 113408 (2003).
[36] A. Marchenko, N. Katsonis, D. Fichou, C. Aubert, and M. Malacria, J. Am. Chem. Soc. **124**, 9998 (2002).
[37] F. K. Fong, *Theory of Molecular Relaxation*, Wiley-Interscience, New York (1975).
[38] A. K. Felts, W. T. Pollard, and R. A. Friesner, J. Phys. C **99**, 2929 (1995).
[39] X. D. Cui, A. Primak, X. Zarate, J. Tomfohr, O. F. Sankey, A. L. Moore, T. A. Moore, D. Gust, G. Harris, and S. M. Lindsay, Science **294**, 571 (2001).
[40] M. Toerker, T. Fritz, and H. Proehl, Phys. Rev. B **65**, 245422 (2002).
[41] D. J. Wold, R. Haag, M. A. Rampi, and C. D. Frisbie, J. Phys. Chem. **106**, 2813 (2002).
[42] B. Xu and N. J. Tao, Science **301**, 1221 (2003).
[43] J. Stokbro, J. Taylor, and M. Brandbyge, J. Am. Chem. Soc. **125**, 3674 (2003).
[44] F. Jäckel, Z. Wang, M. D. Watson, K. Müllen, and J. P. Rabe, Chem. Phys. Lett. **387**, 372 (2004).
[45] A. S. Davydov, *Quantum Mechanics*, Pergamon Press, New York (1976) [Russian original, Nauka, Moscow (1973)].
[46] R. Landauer, Phys. Lett. A **8**, 91 (1981).
[47] M. Bütteker, Phys. Rev. B **33**, 3020 (1986).
[48] Y. Meir and N. S. Wingreen, Phys. Rev. Lett. **68**, 2512 (1992).
[49] S. Datta, *Electronic Transport in Mesoscopic Systems*, University Press, Cambridge (1995).
[50] E. G. Petrov, V. May, and P. Hänggi, Chem. Phys. **296**, 251 (2004).
[51] I. R. Peterson, D. Vuillaume, and R. M. Metzger, J. Phys. Chem. A **105**, 4702 (2001).
[52] M. Rohlfing, R. Kruger, and J. Pollmann, Phys. Rev. B **52**, 1905 (1995).
[53] J. Q. Lu, H. Chen, J. Wu, H. Mizuseki, and Y. Kawazoe, Mater. Trans., JIM **42**, 2270 (2001).
[54] V. Mujica, A. E. Roitberg, and M. A. Ratner, J. Chem. Phys. **112**, 6834 (2000).
[55] E. G. Petrov, I. S. Tolokh, A. A. Demidenko, and V. V. Gorbach, Chem. Phys. **193**, 237 (1995).
[56] A. M. Kuznetsov and J. Ulstrup, J. Chem. Phys. **116**, 2149 (2002).
[57] W. Schmickler, Chem. Phys. **289**, 349 (2003).
[58] A. Nitzan, M. Galperin, G.-L. Ingold, and H. Grabert, J. Chem. Phys. **117**, 10837 (2002).
[59] S. Pleutin, H. Grabert, G.-L. Ingold, and A. Nitzan, J. Chem. Phys. **118**, 3756 (2003).
[60] V. Mujica, A. E. Roitberg, and V. Ratner, J. Chem. Phys. **112**, 6834 (2000).
[61] N. D. Lang and A. P. Avouris, Phys. Rev. Lett. **84**, 358 (2000).
[62] P. S. Damle, A. W. Ghosh, and S. Datta, Phys. Rev. B **64**, 201403 (2001).
[63] A. Bachtold, M. S. Fuhrer, S. Plyasunov, F. Forero, E. H. Anderson, A. Zettl, and P. L. McEuen, Phys. Rev. Lett. **84**, 6082 (2000).
[64] J. Chen and M. A. Reed, Chem. Phys. **281**, 127 (2002).

Translated by M. E. Alferieff

Novel laser based on magnetic tunneling

A. Kadigrobov*

Department of Microelectronics and Nanoscience, Chalmers University of Technology, S-412 96 Göteborg, Sweden; Department of Applied Physics, Chalmers University of Technology and Göteborg University, SE-412 96 Göteborg, Sweden; Theoretische Physik III, Ruhr-Universität Bochum, D-44780 Bochum, Germany

R. I. Shekhter and M. Jonson

Department of Applied Physics, Chalmers University of Technology and Göteborg University, SE-412 96 Göteborg, Sweden

(Submitted September 28, 2004)
Fiz. Nizk. Temp. **31**, 463–470 (March–April 2005)

A new principle for a compact spin-based solid-state laser is proposed. It operates in the 1–100 THz regime, which is difficult to reach with small size lasers. Spin-flip processes in ferromagnetic conductors form a basis—the mechanism is due to a coupling of light to the exchange interaction in magnetically ordered conductors via the dependence of the exchange constant on the conduction electron momenta. The interaction strength is proportional to the large exchange energy and exceeds the Zeeman interaction by orders of magnitude. A giant lasing effect is predicted in a system where a population inversion has been created by injection of spin-polarized electrons from one ferromagnetic conductor into another through an intermediate tunnel region or weak link; the magnetizations of the two ferromagnets have different orientations. We show that the laser frequency will be in the range 1–100 THz if the experimental data for ferromagnetic manganese perovskites with nearly 100% spin polarization are used. The optical gain is estimated to be $g_{\mathrm{opt}} \sim 10^7$ cm^{-1}. This exceeds the gain of conventional semiconductor lasers by 3 or 4 orders of magnitude. An experimental configuration is proposed in order to solve heating problems at a relatively high threshold current density. © *2005 American Institute of Physics.* [DOI: 10.1063/1.1884439]

1. INTRODUCTION

Conventional electronics, which is based on the manipulation of electronic charge, has been studied intensively for years and has enjoyed wide applications. It will suffice to mention such devices as semiconductor diodes and semiconductor lasers. An appealing alternative is pursued in a new field of solid state physics, the field of ''spintronics,'' [1,2] where one explores the possibility of controlling the spins of conduction electrons and hence to further extend both the area of scientific investigation and the field of applications. Spin-dependent tunneling of electrons has already found commercial applications based on the ''giant'' magnetoresistance of certain layered structures.[1,2] Other applications are bound to follow. In this area magnetically ordered, layered conductors with nearly 100% spin polarization of the conduction electrons[3] show considerable promise.

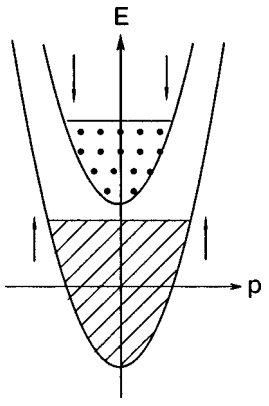

FIG. 1. Schematic representation of the band structure of a magnetically ordered conductor. The hatched region corresponds to an equilibrium distribution of spin-up electrons in the lower band, while the dotted region indicates a nonequilibrium distribution of ''hot'' spin-down electrons in the upper band. The arrows show the electron spin directions in the bands.

A bias voltage applied to a magnetically ordered conductor allows control not only of the energy but also of the spin distribution of electrons that are injected into the magnetic conductor. An example of such a system is presented in Fig. 1, where the hatched region corresponds to an equilibrium distribution of (spin-up) electrons in a spin-polarized conductor. The dotted area marks a nonequilibrium distribution of ''hot'' (spin-down) electrons. Relaxation of the spin-down electrons to an equilibrium configuration requires spin-flip processes and is therefore completely blocked if such processes are not allowed. In the presence of such a ''spin lock'' against relaxation, highly excited states in the material may have a long lifetime, which, in turn, may make for novel ''spintronics'' effects in spin-polarized conductors.

The objective of this paper is to demonstrate how electromagnetic radiation may remove the spin lock, resulting in a giant lasing effect. A short description of this effect has been published as a Letter.[4] It is based on a new mechanism for creating spin-flip processes due to a coupling of the radiation to the exchange interaction in magnetically ordered conductors. This comes about via the dependence of the electron spin-magnetic moment exchange interaction on the mo-

menta of the conduction electrons. As a result, the lasing effect is shown to occur in systems where an inverted electron population has been created by the tunneling injection of spin-polarized electrons from one ferromagnetic conductor to another (the orientation of the magnetization being different in the two ferromagnets). An example of such a system is presented in Fig. 2.

Our estimates show that a laser with an optical gain that exceeds the gain of conventional semiconductor lasers by three or four orders of magnitude can be built, and we argue that laser action can be achieved provided care is taken to design the system so that the active region is not overheated. This is enabled by the high efficiency of the electron spin-flip mechanism described below and the possibility of creating a very high inverted population of electrons in the system under consideration. The frequency of such a laser can be in a wide range that includes the interval 1–100 THz, in which attempts to fabricate small-size lasers up till now have met severe technical problems.[5–10]

In Sec. 2 we present the above-mentioned spin flip exchange mechanism and find the wave functions of injected electrons in the absence of the electromagnetic field. In Sec. 3 we calculate the rate of the stimulated photon emission and present estimates of the laser optical gain and the threshold current. In the Conclusion we summarize the main results and estimates of the paper, while a cursory description of the laser action is presented in an Appendix for the convenience of the reader.

2. POPULATION INVERSION IN FERROMAGNETIC CONDUCTORS AND A NEW MECHANISM FOR CREATING SPIN-FLIP PROCESSES

The Hamiltonian for the electrons in a magnetically ordered conductor can be written as

$$\hat{H}_0 = \hat{\sigma}_0 \frac{\hat{p}^2}{2m^*} - \hat{\boldsymbol{\sigma}}\mathbf{I}, \tag{1}$$

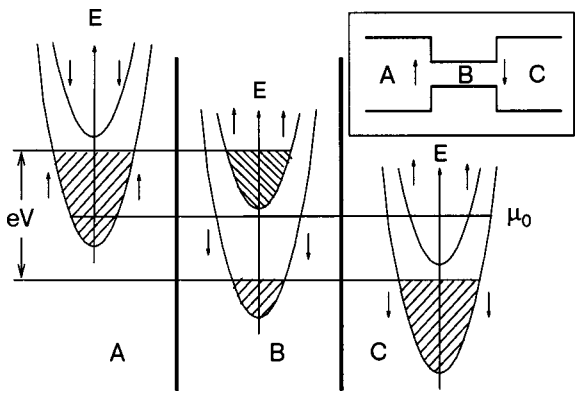

FIG. 2. Schematic illustration of population inversion in a magnetic conductor (region B). A bias voltage V is applied between magnetic conductors (A and C) which have opposite directions of their magnetizations (the thick vertical lines represent potential barriers). Arrows show the electron spin directions in the electron energy bands; μ_0 is the equilibrium chemical potential (in the absence of bias). The inset shows a possible realization of the structure in which two magnetic conductors with opposite magnetization directions are coupled through a microbridge (B).

where m^* is the effective mass, $\hat{p}$ is the momentum operator, $\hat{\sigma}$ are Pauli matrices, σ_0 is the 2×2 unity matrix, and I is the exchange energy. According to Eq. (1) the dispersion law for electrons with spins up/down is

$$E_{\uparrow\downarrow}(p) = \frac{p^2}{2m^*} \mp I. \tag{2}$$

We will deal with a system, schematically presented in Fig. 2, in which two potential barriers divide the magnetic conductor into three parts; the magnetization of two adjacent magnetic conductors (regions A and B) are pointing in opposite directions. A bias voltage V is applied between regions A and C. We assume that the spin relaxation time ν_s^{-1} (Ref. 11), the time t_E of electron energy relaxation without changing spin direction, and the electron tunneling time t_{tun} obey the double inequality $t_E \ll t_{\text{tun}} \ll \nu_s^{-1}$. In the absence of spin-flip processes, the energy relaxation of injected spin-polarized electrons creates a nonequilibrium state in which equilibrium is established only inside each group of electrons with a fixed spin polarization. Therefore, in region B electrons inside the spin-up and spin-down energy bands are in local equilibria described by the different chemical potentials $\mu_\uparrow$ and $\mu_\downarrow$, while the system as a whole is far from equilibrium.

According to Eq. (2) the energy conservation law for vertical transition of electrons with emission of photons of frequency ω does not depend on the electron momentum:

$$\hbar\omega = E_\downarrow(p) - E_\uparrow(p) = 2I. \tag{3}$$

It follows that for $\omega = 2I/\hbar$ all "hot" electrons are in resonance with the electromagnetic field, and hence stimulated emission of light due to transitions of electrons from filled states in the upper band to empty states in the lower band is possible for all electrons in an energy range $\mu_\uparrow - \mu_\downarrow$. As is seen from Fig. 2, the population inversion needed for lasing requires a bias voltage $V > 2I/e$ (e is the electron charge).

The conventional Zeeman term $\hat{H}_Z = (g\mu_B/2)\mathbf{H}\cdot\hat{\boldsymbol{\sigma}}$ describing interaction between the (hot) electrons and an electromagnetic field does provide a mechanism for stimulated radiative transitions between the energy bands containing electrons with opposite spin directions. However, it is relatively small in magnitude and it is not the most important mechanism. For ferromagnets, we would like to suggest a much more effective mechanism of interaction between light and conduction electron spins. This mechanism is based on the dependence of the exchange energy $\mathbf{I}$ on the momentum $\mathbf{p}$ of the conduction electron. The momentum dependence has to do with the overlap of the wave functions of the conduction electron and the magnetic subsystem (see, e.g., Ref. 12). It is determined by the value of $pa/\hbar$, where a is the characteristic size of the orbital (that is, one may estimate $\partial I/\partial p \sim (a/\hbar)I$, where a is an atomic-scale length). That is why it varies with the momentum of the conduction electron. In the absence of an electromagnetic field the Hamiltonian that describes this situation can be written as

$$\varepsilon(\hat{\mathbf{p}}) = \hat{\sigma}_0 \frac{\hat{\mathbf{p}}^2}{2m^*} - \hat{\boldsymbol{\sigma}}\cdot\mathbf{I}(\hat{\mathbf{p}}). \tag{4}$$

In the presence of an electromagnetic field described by a vector potential $\mathbf{A}$, the momentum operator $\hat{\mathbf{p}}$ in Eq. (4)

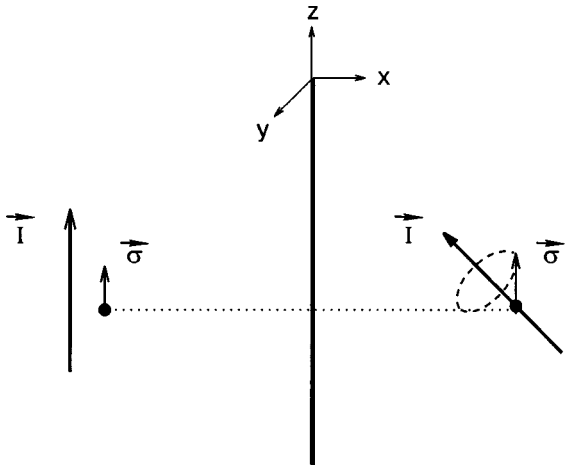

FIG. 3. Schematic illustration of how electrons are injected into the active region for the case that the adjacent ferromagnets have different magnetization directions (shown with long arrows; the electron spins, σ, are shown with short arrows with black dots at the end). An electron from the left-side ferromagnet with its spin parallel to the magnetization direction passes through a sharp boundary (shown as a vertical thick line) between the ferromagnets without changing spin direction. In the right-side ferromagnet it emerges with its spin in a superposition of the spin-up and spin-down states. The classical precession of the spin is indicated by a dashed-line ellipse.

must be changed to $\hat{\mathbf{p}}-(e/c)\mathbf{A}$ (c is the light velocity), and one obtains an effective Hamiltonian $\hat{H}_{\text{eff}}=\varepsilon(\hbar\mathbf{p}-(e/c)\mathbf{A}) -\hat{\sigma}\cdot\mathbf{I}(\hat{\mathbf{p}}-(e/c)\mathbf{A})$. Expanding in powers of $(e/c)\mathbf{A}$, one gets an effective Hamiltonian of the form

$$\hat{H}_{\text{eff}}=\varepsilon(\hat{\mathbf{p}})+\hat{H}^{(1)}_{\text{eff}}, \tag{5}$$

where the perturbation Hamiltonian[13] is

$$\hat{H}^{(1)}_{\text{eff}}=-\frac{e}{2c}\,\hat{\boldsymbol{\sigma}}\cdot\left(A_i\frac{\partial\mathbf{I}}{\partial p_i}+\frac{\partial\mathbf{I}}{\partial p_i}A_i\right)_{\mathbf{p}=\hat{\mathbf{p}}}. \tag{6}$$

In Eq. (6) we have omitted the term

$$\hat{H}^{(1)}_{\text{eff}}=\hat{\sigma}_0\frac{e}{m^*c}\mathbf{A}\cdot\hat{\mathbf{p}}, \tag{7}$$

which does not flip spins; summation over repeated indices is implied: $a_ib_i\equiv\mathbf{a}\cdot\mathbf{b}$.

If the injected electrons are prepared in such a way that their spins are not parallel to the magnetization in the active region B (see Fig. 2), the Hamiltonian (6) produces spin flips and hence stimulates the needed radiative transitions of hot electrons in the upper band to the lower energy band. This process is illustrated in Fig. 3, where an electron (with its spin parallel to the magnetization) impinges on the boundary from the left, passes through the boundary, and is scattered into a quantum superposition of spin-up and spin-down states in the active region B to the right of the boundary.

In order to find the probability amplitude for a radiative transition of an electron caused by perturbation Eq. (6) we obtain the zero-approximation wave function of the electron as a solution of the Schrödinger equation $\varepsilon(\hat{\mathbf{p}})|\Psi\rangle=E|\Psi\rangle$, neglecting the dependence of the exchange interaction $\mathbf{I}$ on $\hat{\mathbf{p}}$. Taking into account the fact that the electron wave function is a two-component spinor,

$$\Psi(\mathbf{r})=\begin{pmatrix}\Psi_1\\ \Psi_2\end{pmatrix}, \tag{8}$$

and using Eq. (4), one can write the Schrödinger equation as

$$\left(\frac{\hat{\mathbf{p}}^2}{2m^*}-E-I_z(x)\right)\Psi_1-I^*_+(x)\Psi_2=0$$

$$\left(\frac{\hat{\mathbf{p}}^2}{2m^*}-E+I_z(x)\right)\Psi_2-I_+(x)\Psi_1=0. \tag{9}$$

Here the x axis is perpendicular and the y and z axes parallel to the boundary (see Fig. 3), and we assume that in the left-side ferromagnet ($x<0$) the direction of $\mathbf{I}$ is along the z axis (i.e., $\mathbf{I}=(0,0,I)$) while in the right-side ferromagnet ($x>0$) its direction is different and all three components of $\mathbf{I}$ are present: $\mathbf{I}=(I_x,I_y,I_z)$, $I_x^2+I_y^2+I_z^2=I^2$, and $I_+=I_x+iI_y$. We also assume that the width d of the intermediate layer between the left and right ferromagnets (the width of the ''domain wall'') satisfies the inequality $d\ll\hbar v_F/I$ (v_F is the electron Fermi velocity). In this case an electron passes this region without changing spin direction and hence one may solve Eq. (9) considering $\mathbf{I}$ to be constant in the injecting region (left-hand side of Fig. 3) and in the active region (the right-hand side of Fig. 3) and matching the wave functions at the boundary $x=0$.

Considering the case of an electron incident from the injection region with its spin parallel to the magnetization direction, one readily finds the wave function of the electron in the injection region ($x<0$) to be

$$\Psi^{(l)}(\mathbf{r})=\exp(i\mathbf{p}_\perp\mathbf{r}_\perp)\left\{\begin{pmatrix}1\\0\end{pmatrix}\exp(ip_1x)+a_1^{(l)}\begin{pmatrix}1\\0\end{pmatrix}\times\exp(-ip_1x)+a_2^{(l)}\begin{pmatrix}0\\1\end{pmatrix}\exp(-ip_2x)\right\}, \tag{10}$$

while in the active region ($x>0$) the wave function is

$$\Psi^{(r)}(\mathbf{r})=\exp(i\mathbf{p}_\perp\mathbf{r}_\perp)\left\{a_1^{(r)}\begin{pmatrix}1\\ I_+/(I_z+I)\end{pmatrix}\exp(ip_1x)+a_2^{(r)}\times\begin{pmatrix}1\\ I_+/(I_z-I)\end{pmatrix}\exp(ip_2x)\right\}. \tag{11}$$

Here the projections of the electron momentum and the coordinate on the boundary are denoted by $\mathbf{p}_\perp=(0,p_y,p_z)$ and $\mathbf{r}_\perp=(0,y,z)$, while $p_{1,2}=\sqrt{2m^*(E\pm I)-p_\perp^2}$. Matching the wave functions (10) and (11), one finds the coefficients $a^{(l,r)}_{(1,2)}$ to be

$$a_1^{(l)}=\frac{p_1(p_2-p_1)}{(p_1+p_2)^2-(p_1-p_2)^2\cos^2\varphi/2}\left(\frac{I_+}{|I_+|}\sin\varphi\right),$$

$$a_2^{(l)}=\frac{p_2^2-p_1^2}{(p_1+p_2)^2-(p_1-p_2)^2\cos^2\varphi/2}\left(\frac{I_+}{|I_+|}\sin^2\varphi/2\right) \tag{12}$$

and

$$a_1^{(r)}=\frac{4p_1p_2}{(p_1+p_2)^2-(p_1-p_2)^2\cos^2\varphi/2}\cos^2\varphi/2,$$

$$a_2^{(r)}=\frac{2p_1(p_1+p_2)}{(p_1+p_2)^2-(p_1-p_2)^2\cos^2\varphi/2}\sin^2\varphi/2. \tag{13}$$

3. STIMULATED EMISSION RATE AND GIANT LASER EFFECT IN FERROMAGNETIC CONDUCTORS

The characteristics of lasers can be described by rate equations which are obtained by considering the time evolution of the number of photons and the number of nonequilibrium electrons in the active region (see, e.g., Refs. 16, 17). The simplest form of the set of rate equations for the density of photons N_p and the density of electrons $N_\uparrow$ in the upper band can be written as

$$\begin{cases} \dot{N}_p = G(N_\uparrow)N_p - \nu_p N_p \\ \dot{N}_\uparrow = \eta J/eV_0 - \nu_s N_\uparrow - G(N_\uparrow)N_p \end{cases} \tag{14}$$

(see Sec. 3.3.6 in Ref. 17). Here $G(N_\uparrow)$ and the stimulated emission rate $R_{\rm st}$ are related, $R_{\rm st}=G(N_\uparrow)N_p$; ν_p is the photon relaxation rate; J is the injection current; η is the internal efficiency: the fraction of the injection current that generates electrons in the upper band of the active region; V_0 is the volume of the active region.

With the electron wave functions defined we can find the rate $R_{\rm st}$ of radiative electronic transitions by assuming the vector potential $\mathbf{A}(\mathbf{r},t)$ in Eq. (6) to be a plane wave of the form $A_0 \exp i(-\mathbf{k}\cdot\mathbf{r}+\omega t)$ and using Fermi's Golden Rule:

$$R_{\rm st}=\frac{2\pi}{\hbar}\int |H_{21}|^2[f_2(1-f_1)-f_1(1-f_2)] \times \delta(E_2(\mathbf{p})-E_1(\mathbf{p})-\hbar\omega)\frac{d\mathbf{p}}{(2\pi\hbar)^3}. \tag{15}$$

Here

$$H_{21}\equiv\langle\Psi_f|\hat{H}^{(1)}_{\rm eff}|\Psi_i\rangle=\int \Psi^*_f(\mathbf{r})\hat{H}^{(1)}_{\rm eff}\Psi_i(\mathbf{r})d^3\mathbf{r} \tag{16}$$

is the matrix element corresponding to the transition from the initial state $\Psi_i(\mathbf{r})$ (which belongs to the initial energy E_i in the upper band) to the final state $\Psi_f(\mathbf{r})$ (which belongs to the final energy E_f in the lower band); the functions $f_{1,2}$ are the Fermi functions of electrons in the upper and lower bands:

$$f_{1,2}=\frac{1}{\exp(E-\mu_{\uparrow,\downarrow})/kT+1}. \tag{17}$$

Using Eq. (6) and Eq. (11), one sees that the matrix element $\langle\Psi_f|\hat{H}^{(1)}_{\rm eff}|\Psi_i\rangle$ (the probability amplitude for a radiative electron transition between the unperturbed energy bands) is nonzero if $p_1(E_i)=p_2(E_f)$. From here it follows that the difference between the initial and the final energies should be

$$E_i(\mathbf{p})-E_f(\mathbf{p})=2I(\mathbf{p}).$$

As the dependence of $I(\mathbf{p})$ on the electron momentum $\mathbf{p}$ is relatively weak, the dependence of the argument of the δ function in Eq. (15) on $\mathbf{p}$ is also weak. This can result in a divergent integral under the resonance condition $\hbar\omega=p_1(E_i)-p_2(E_f)=2I(\mathbf{p})$. As is often the case, the amplitude of the resonance is cut off by the finite electron lifetime in a given state. We assume the energy δ function to be broadened due to the spin-flip processes and rewrite Eq. (15) as

$$R_{\rm st}=\frac{2\pi}{\hbar}\int |H_{21}|^2(f_2-f_1) \times\frac{\pi^{-1}\hbar\nu_s}{(2I(\mathbf{p})-\hbar\omega)^2+(\hbar\nu_s)^2}\frac{d\mathbf{p}}{(2\pi\hbar)^3}. \tag{18}$$

Taking the wave functions of Eq. (11) as the initial and final states and performing standard calculations using Eqs. (6), (16), and (18), one readily finds the stimulated transition rate.

i) Under the assumption that $|I'|p_{F\uparrow}<\hbar\nu_s$ ($p_{F\uparrow}$ is the Fermi momentum of electrons in the upper band), that is, the additional dispersion caused by the dependence of I on the electron momentum (see Eq. (4)) is smaller than the broadening of the electron energy due to spin-flip processes, the stimulated transition rate per unit volume of active material is

$$R_{\rm st}=\frac{32\pi e^2\mu}{n^2}\frac{|\mathbf{I}'|^2}{\omega}\frac{\hbar\nu_s(b_1N_\uparrow-b_2N_\downarrow)}{(\hbar\omega-2I)^2+(\hbar\nu_s)^2}N_p \times\{([\boldsymbol{\epsilon}_a[\boldsymbol{\epsilon}_{\rm dr}\cdot\boldsymbol{\epsilon}_a]]\cdot\boldsymbol{\epsilon}_i)^2+([\boldsymbol{\epsilon}_{\rm dr}\cdot\boldsymbol{\epsilon}_a]\cdot\boldsymbol{\epsilon}_i)^2\}. \tag{19}$$

Here μ and n are the magnetic permeability and the refractive index of the medium, respectively, $N_\uparrow$ and $N_\downarrow$ are the densities of electrons with spin up and down, N_p is the photon density, ω is the photon frequency, the constants b_1 and b_2 are of order unity, the unit vectors $\boldsymbol{\epsilon}_a$ and $\boldsymbol{\epsilon}_i$ are directed along the magnetizations in the active (right-hand side of Fig. 3) and injection (left-hand side of Fig. 3) regions, respectively, while $\boldsymbol{\epsilon}_{\rm dr}$ is parallel to the vector $\mathbf{I}\equiv e_i\partial\mathbf{I}/\partial p_i$, where $\mathbf{e}$ is the unit polarization vector in the direction of the vector potential $\mathbf{A}$.

ii) In the opposite limit, $|I'|p_{F\uparrow}\gg\hbar\nu_s$, one has

$$R_{\rm st}=\frac{32\pi}{\hbar\omega}\frac{e^2\mu}{n^2}|\mathbf{I}'|^2(b_3N_\uparrow^{2/3}-b_4N_\downarrow^{2/3})N_p \times\{([\boldsymbol{\epsilon}_a[\boldsymbol{\epsilon}_{\rm dr}\cdot\boldsymbol{\epsilon}_a]]\cdot\boldsymbol{\epsilon}_i)^2+([\boldsymbol{\epsilon}_{\rm dr}\cdot\boldsymbol{\epsilon}_a]\cdot\boldsymbol{\epsilon}_i)^2\}, \tag{20}$$

where the constants $b_{3,4}\sim 1$.

As is seen from the set of rate equations (14) (see also the Appendix), one of the necessary conditions for the lasing effect to be realized is

$$R_{\rm st}=\nu_p N_p. \tag{21}$$

We consider the case when damping of electromagnetic waves is mainly due to absorption by free charge carriers, the frequency of the photon relaxation being $\nu_p=2k\omega/n$.[18] For estimating the parameters of the problem we use standard formulas for the refractive index n and the absorption coefficient k for metals subject to electromagnetic fields,[19]

$$\nu_p=\frac{\mu}{n^2}\frac{4\pi\sigma(0)}{1+(\omega t_0)^2}, \tag{22}$$

where $\sigma(0)$ is the static conductivity of the conductor and t_0 is the transport electron relaxation time.

Using Eqs. (19) and (22) and the estimate $|I'|\sim I/p_0$, one can rewrite Eq. (21) as

$$\frac{(N_\uparrow-N_\downarrow)}{N_\uparrow+N_\downarrow}\approx\frac{\hbar\nu_s}{2I}\frac{p_0^2/m^*}{\hbar t_0^{-1}}\frac{1}{1+(\omega t_0)^2}, \tag{23}$$

where $p_0=\hbar/a\sim 10^{-19}$ erg·s/cm.

It seems that to achieve the lasing effect the most favorable materials are ferromagnetic manganese perovskites with nearly 100% spin polarization of the conduction electrons.[3,20,21] The high degree of polarization of the carriers permits the creation of a population inversion of the energy bands in the active region B (see Fig. 2). Here and below we use experimental values of the needed parameters: the mean free path $l_0 = 1.4\times 10^{-7}$ cm, the Fermi velocity $v_F \approx 10^8$ cm/s, $t_0 \approx 10^{-15}$ s, and $m^* = 0.3m_e$, where m_e is the free electron mass, the number of carriers $\approx 3.4\times 10^{21}$, and the resistivity $\rho \sim 10^{-4}-10^{-3}\ \Omega\cdot$cm.[22] Inserting these values into Eq. (23), one finds this lasing condition to be

$$\frac{N_\uparrow - N_\downarrow}{N_\uparrow + N_\downarrow} \approx 5\,\frac{\hbar \nu_s}{I}.$$

For the case $|I'|p_{F\uparrow} \gg \hbar\nu_s$ (see Eq. (20)), the lasing condition Eq. (21) is

$$\frac{N_\uparrow^{2/3} - N_\downarrow^{2/3}}{N_\uparrow + N_\downarrow} \approx 0.5\times 10^7\ \ \mathrm{cm}^{-1}.$$

It follows from these equations that the lasing condition $R_{\mathrm{st}} = \nu_s N_p$ is easily satisfied, since one needs $\hbar\nu_s/I$ to be less than 10^{-1}, while theoretical estimate of the spin relaxation rate ν_s gives the value 10^{-2} for this ratio. Estimations based on the above experimental values of the parameters show the optical gain to be $g_{\mathrm{opt}} = (n/c)R_{\mathrm{opt}} \sim 10^7$ cm^{-1} and the threshold current density $j_{\mathrm{th}} = el\nu_s N_\uparrow \sim 10^7 - 10^8$ A/cm^2 for an active region of length $l = 10^{-5}$ cm. Estimations for $N_e \sim 10^{18}$ cm^{-3} show the optical gain and the threshold current to be $g_{\mathrm{opt}} \sim 10^3 - 10^4$ cm^{-1} and $j_{\mathrm{th}} \sim 10^5$ A/cm^2.

We predict an extremely large optical gain in systems with a high density of charge carriers. The price to be paid for the gain exceeding what can be achieved in semiconductors by 3 or 4 orders of magnitude is the high currents needed for an effective tunneling pumping of the system. The current value $j = 10^6 - 10^8$ A/cm^2 seems to be very large for homogeneous bulk metals because of the accompanying Joule heating. Special measures are needed to avoid heating the active, lasing region. One solution to that problem is to arrange for the current injection to be inhomogeneous in space. This can be achieved if the magnetic conductors are electrically connected through an electric point contact. In such systems the spreading of the current far from the narrow point contact provides for an efficient dissipation of heat.[24] A current density $j \sim 10^8$ A/cm^2 can be reached without significant heating of the contact region.[24,25] On the other hand, the extremely large optical gain $g_{\mathrm{opt}} \sim 10^7$ cm^{-1} means that it is enough to have a small volume of active lasing region. Such a structure can be prepared on the basis of the technique suggested in Ref. 26 for fabrication of biepitaxial films of $La_{0.7}Sr_{0.3}MnO_3$ with 45° in-plane rotated domains. In this case the proposed laser is a series of point contacts in a thin film of the ferromagnetic metal with the resonator cavity above it.

4. CONCLUSION

We have proposed a new principle for a compact solid-state laser working in the 1–100 THz regime. The proposed laser is based on a new mechanism for creating spin-flip processes in ferromagnetic conductors. The mechanism is due to the interaction of light with conduction electrons; the interaction strength, being proportional to the large exchange energy, exceeds the Zeeman interaction by orders of magnitude. On the basis of this interaction, a giant lasing effect was predicted for systems where a population inversion can be created by tunneling injection of spin-polarized electrons from one ferromagnetic conductor to another—the magnetization of the two ferromagnets having different orientations. Using experimental data for ferromagnetic manganese perovskites with nearly 100% spin polarization we showed the laser frequency to be in the range 1–100 THz. The optical gain was estimated to be of order 10^7 cm^{-1}, which exceeds the gain of conventional semiconductor lasers by 3 or 4 orders of magnitude. An experimental study based on a point contact geometry to avoid heating by the necessarily large injection currents was proposed and discussed.

We thank L. Y. Gorelik, V. Kozub, G. D. Mahan, and R. Gunnarsson for helpful discussions. We are also grateful to T. Claeson for fruitful discussions and critical reading of the manuscript. A.K. acknowledges the hospitality of the Theoretische Physik III Institut at the Ruhr-Universität, Bochum, Germany.

A.K. gratefully acknowledges financial support from the Royal Swedish Academy of Sciences (KVA) and SFB 491. M.J. and R.S. acknowledge financial support from the NANODEV SSF center and from the SSF program on Magnetoelectronic Nanodevice Physics.

APPENDIX

The set of differential nonlinear equations (14) allows two types of steady-state solutions (see, e.g., Refs. 16, 17):

$$N_P = 0; \quad N_\uparrow^{(0)} = \frac{\eta J}{eV_0\nu_s} \tag{24}$$

and

$$G(N_\uparrow^{(\mathrm{las})}) = \nu_p; \quad N_p^{(\mathrm{las})} = \frac{\eta J/eV_0 - \nu_s N_\uparrow^{(\mathrm{las})}}{\nu_p} \tag{25}$$

[for the case under consideration, the explicit forms of $G(N_\uparrow) = R_{\mathrm{st}}/N_p$ are easily found from Eqs. (19) and (20)].

The steady-state solution Eq. (24) exists for any value of the injection current, while the steady-state solution Eq. (25) is nonphysical ($N_p^{(\mathrm{las})} < 0$) until the value of the injection current exceeds the threshold $J^{(\mathrm{th})}$ at which the right-hand side of the second equation in Eq. (25) becomes positive. As follows from Eq. (25) the value of the threshold current is

$$J^{(\mathrm{th})} = \frac{e\nu_s V_0 N_\uparrow^{(\mathrm{las})}}{\eta}. \tag{26}$$

The steady-state solution (24) describes a state of the system in which the lasing effect is absent: photons are not emitted and the number of electrons in the upper band is controlled exclusively by the injection current and the nonradiative relaxation ν_s. One can see from Eq. (14) that this state is stable in the range of injection currents $J < J^{(\mathrm{th})}$.

When the strength of the injection current exceeds the threshold ($J > J^{(\mathrm{th})}$) this nonradiative state becomes unstable, and the system spontaneously switches to a new stable state

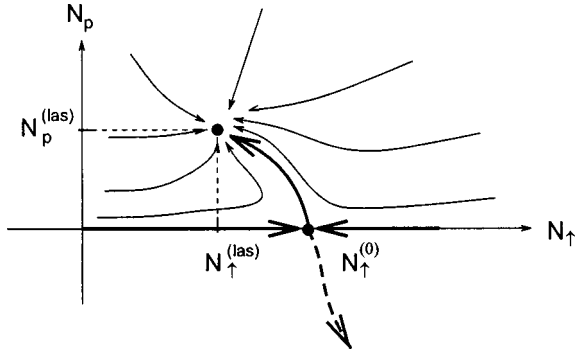

FIG. 4. Schematic presentation of the phase plane of Eq. (14); thick dots show the stable fixed point $(N_p^{(las)},N_\uparrow^{(las)})$ and the saddle point $(N_p^{(0)},N_\uparrow^{(0)})$; the thick arrows are separaterices and the thin arrows show trajectories starting from various initial points; all of them end up at the stable point $(N_p^{(las)},N_\uparrow^{(las)})$, which corresponds to the stationary state of the laser.

which is described by Eq. (25): the population of electrons in the upper band is clamped to the threshold value $N_\uparrow^{(las)}$ while the number of photons in the system increases with an increase of the injection current. Figure 4 shows schematically the phase plane $(N_p(t),N_\uparrow(t))$ of Eq. (14) for the case $J>J^{(th)}$. The thick dots are the stable fixed point $(N_p^{(las)},N_\uparrow^{(las)})$ and the saddle point $(N_p^{(0)},N_\uparrow^{(0)})$, whose separatrices are shown by thick lines (the separatrix lying in the nonphysical part of the plane is shown by a thick dashed line); thin lines in the figure represent trajectories of the system which start from various initial states and finish in the stable fixed point $(N_p^{(las)},N_\uparrow^{(las)})$; arrows show the direction of motion along the trajectories.

*E-mail: kadig@tp3.ruhr-uni-bochum.de

[1] G. A. Prinz, Science **282**, 1660 (1998).
[2] S. A. Wolf, D. D. Awschalom, R. A. Buhrman, J. M. Daughton, S. von Molnar, M. L. Roukes, A. Y. Chtchelkanova, and D. M. Treger, Science **294**, 1488 (2001).
[3] Yoshinori Tokura (ed.), *Colossal Magnetoresistive Oxides*, Gordon and Breach Science Publishers, Amsterdam (2000).
[4] A. Kadigrobov, Z. Ivanov, T. Claeson, R. I. Shekhter, and M. Jonson, Europhys. Lett. **67**, 948 (2004).
[5] R. Kohler, A. Tredicucci, F. Beltram, H. Beere, E. Linfeld, A. Giles Devies, D. A. Ritchle, R. C. Lotti, and F. Rossi, Nature (London) **417**, 156 (2002).
[6] S. G. Pavlov, R. Kh. Zhukavin, E. E. Orlova, V. N. Shastin, A. V. Kirsavin, H.-W. Hübers, K. Auen, and H. Riemann, Phys. Rev. Lett. **84**, 5220 (2000).
[7] E. Bründermann, D. R. Chamberlin, and E. E. Haller, Appl. Phys. Lett. **76**, 2991 (2000).
[8] D. M. Matsuura, M. Tani, and K. Sakai, Appl. Phys. Lett. **70**, 559 (1997).
[9] R. Kersting, K. Unterreiner, G. Strasser, H. F. Kauffmann, and E. Gornik, Phys. Rev. Lett. **79**, 3038 (1997).
[10] B. B. Hu, X.-C. Zhang, and D. H. Auston, Phys. Rev. Lett. **67**, 2709 (1991).
[11] The main mechanism for relaxation of hot electrons is the spin-flip process caused by emission of spin waves.
[12] H. J. Zeiger and G. W. Pratt, *Magnetic Interactions in Solids*, Clarendon Press, Oxford (1973); S. V. Vonsovskii, *Magnetism*, Vol. 2, Wiley, New York (1974).
[13] The Hamiltonian Eq. (6) gives an effective spin-orbit interaction in magnetic films, which are usually under a strong strain caused by the substrate and grain boundaries (see, e.g., Refs. 14 and 15 and references therein). If $pa/\hbar \ll 1$, for bulk materials $\partial \mathbf{I}/\partial_i = 0$, one should take the next term in the expansion, that is, change $\partial \mathbf{I}/\partial p_i$ to $p_k \partial^2 \mathbf{I}/\partial p_k \partial p_i$ in Eq. (6).
[14] Yan Wu, Y. Suzuki, U. Rudiger, J Yu, and A. D. Kent, Appl. Phys. Lett. **74**, 2295 (1999).
[15] Yeong-Ah Soh, P. G. Evans, Z. Cai, B. Lai, C.-Y. Kim, G. Aeppli, N. D. Mathur, M. G. Blamire, and E. D. Isacs, J. Appl. Phys. **91**, 7742 (2002).
[16] G. P. Agrawal and N. K. Dutta, *Long-Wavelength Semiconductor Lasers*, Van Nostrand Reinhold, New York (1986).
[17] G. P. Agrawal, *Fiber Optic Communication Systems*, Wiley New York (1997).
[18] F. J. Blatt, *Physics of Electronic Conduction in Solids*, McGraw-Hill, New York (1968).
[19] J. M. Ziman, *Principles of the Theory of Solids*, Cambrige (1964).
[20] J.-H. Park, E. Vescovo, H.-J. Kim, C. Kwon, R. Ramesh, and T. Venkatesan, Nature (London) **392**, 794 (1998).
[21] Y.-D. Chuang, A. D. Gromko, D. S. Dessau, T. Kimura, and Y. Tokura, Science **292**, 1509 (2001).
[22] The values are taken for a compound similiar to the perovskite manganites found to be nearly 100% spin polarized; see Ref. 21.
[23] S. J. Lloid, N. D. Mathur, J. C. Loudon, and P. A. Midgley, Phys. Rev. B **64**, 172407 (2001).
[24] A. V. Khotkevich and I. K. Yanson, *Atlas of Point Contact Spectra of Electron-Phonon Interactions in Metals*, Kluwer Academic Publishers, Boston-Dordrecht-London (1995).
[25] J. J. Versluijs, M. A. Bari, and M. D. Coey, Phys. Rev. Lett. **87**, 026601 (2001).
[26] R. Mathieu, P. Svedlindh, R. A. Chakalov, and Z. G. Ivanov, Phys. Rev. B **62**, 3333 (2000).

This article was published in English in the original Russian jounral. Reproduced here with stylistic changes by AIP.

Magnetic resonance and magnetic anisotropy oscillations in Co/Cu (111) superlattices

A. I. Kaplienko, É. P. Nikolova, and K. V. Kut'ko

B. I. Verkin Institute for Low-Temperature Physics and Engineering, Ukrainian National Academy of Sciences, 47 pr. Lenina, Kharkov 61103, Ukraine

A. G. Anders*

V. N. Karazin Kharkov National University, 4 pl. Svobody, Khar'kov 61077, Ukraine; B. I. Verkin Institute for Low-Temperature Physics and Engineering, Ukrainian National Academy of Sciences, 47 pr. Lenina, Kharkov 61103, Ukraine

V. V. Zorchenko** and A. N. Stetsenko

National Engineering University "Kharkov Polytechnical Institute," 21 ul. Frunze, Khar'kov 61002, Ukraine

(Submitted July 29, 2004; revised September 28, 2004)
Fiz. Nizk. Temp. **31**, 471–478 (March–April 2005)

Magnetic resonance was studied in magnetic fields parallel or perpendicular to the film plane in magnetron-sputtered $[\mathrm{Co}(8\ \text{Å})/\mathrm{Cu}(d_{\mathrm{Cu}})(111)]_{20}$ multilayers. Oscillations of the magnetic anisotropy K_A and the width ΔH_{res} of the resonance line as a function of the thickness of the copper interlayers were found in the interval $d_{\mathrm{Cu}}=7-19$ Å. Extrema of K_A and ΔH_{res} were observed at $d_{\mathrm{Cu}}=nd_{(111)}$, where n is an integer or half-integer, and $d_{(111)}=2.087$ Å—the distance between the (111) planes in Cu. In addition, the distances between the neighboring maxima or minima were 1, 1.5, and $2d_{(111)}$. The K_A and ΔH_{res} oscillations occurred synchronously with oscillations of the resistivity at saturation (in the field $H=15$ kOe) and oscillations of the magnetoresistance. An interlayer antiferromagnetic exhange interaction was found in the ranges $d_{\mathrm{Cu}}=8-11$ Å and $d_{\mathrm{Cu}}\geqslant 18$ Å. The effects observed were due to nonmonotonic variation of the interlayer interface roughness with increasing d_{Cu}. © *2005 American Institute of Physics.* [DOI: 10.1063/1.1886925]

1. INTRODUCTION

The gigantic magnetoresistance effect and the prospects for wide applicationss of this effect have stimulated great interest in studying metallic multilayer nanostructures consisting of alternating magnetic and nonmagnetic layers.[1] These systems show a great diversity of properties as a function of the composition, the technical conditions of fabrication, the thickness of the magnetic layers and nonmagnetic interlayers, and so on. All these factors largely determine the basic energy parameters of the system and, first and foremost, the magnetic anisotropy energy. In layered systems anisotropy often is complicated because it can be due to a combination of volume and surface contributions, taking account of magnetocrystalline and magnetoelastic effects. Consequently, an effective method for studying multilayered structures is the magnetic resonance method, since magnetic anisotropy directly determines the frequency-field dependences of the resonance spectrum.

In turn, surface effects at an interface between the layers, primarily, the roughness of the interface, largely determine the galvanomagnetic properties of multilayered structures. The same effects should also be reflected in the width of the magnetic resonance line, determined mainly by the nonuniformities of the magnetic and crystal structures of the films.

The purpose of this work was to study the influence of interface structure on the resonance and galvanomagnetic characteristics of Co/Cu multilayer structures. In the course of the investigation a quantitative determination was made of the anisotropy parameters for a number of multilayer films with the composition $[\mathrm{Co/Cu}]_{20}$ and fixed thickness of the ferromagnetic cobalt layers $d_{\mathrm{Co}}=8$ Å, while the thickness d_{Cu} of the nonmagnetic copper interlayers varied from 7 to 19 Å with step $\sim 1-2$ Å. The results of the investigation of the magnetoresistance properties of these multilayers are presented in Ref. 2.

2. SAMPLES AND EXPERIMENTAL PROCEDURE

The samples were obtained on mica (fluorophlogopite) by magnetron sputtering of Co and Cu targets in a vacuum apparatus with residual atmosphere $\sim 10^{-6}$ torr at argon pressure $1.3\cdot 10^{-3}$ torr. The layer thicknesses were determined to within no more tha 2% using multibeam optical interferometry. First, a copper sublayer (50 Å) was condensed on mica. Twenty pairs of Co/Cu layers were formed on this sublayer, and the top copper layer was 12.5 Å thick in all samples. The Co and Cu condensation rates were 0.45 and 0.58 Å/s, respectively.

The samples possessed a polycrystalline structure, where the Cu (111) planes were parallel to the substrate surface without any distinguished orientations of the other crystallographic surfaces of the grains relative to the mica. The copper and cobalt layers grew epitaxially on one another. Only one grain fit within the thickness of a sample, and the grain boundaries passed through the entire thickness of a sample

virtually perpendicular to the surface of the mica. The grains have an equiaxial shape in the plane of the sample. The grain size was ~80–100 Å irrespective of d_{Cu}. X-Ray studies showed good periodicity and thickness uniformity of the layers in these multilayers.

The basic measurements of the resonance spectra were performed at room temperature with a JEOL-XK spectrometer in the 3-cm wavelength range and magnetic fields up to 1.5 T. Additional verifying measurements were performed at $\lambda \approx 1$ cm. The largest error in determining the values of the resonance fields was ± 60 Oe for fields oriented close to a direction normal to the film plane; this was due to the large width of the resonance line for this orientation.

The samples were cut out in the form of 3-mm in diameter disks and placed on a rotating apparatus at the center of a cylindrical resonator operating on the H_{011} wave. The measurements were performed for field directions normal and tangent to the film plane. For all samples no anisotropy was observed in the resonance field or the linewidth in the film plane. This agrees with previously obtained data on the crystal structure of the films.

3. THEORY AND EXPERIMENTAL RESULTS

All experimental samples contain the same number of cobalt layers with nominally identical thickness. Consequently, the free energy of a system of identical ferromagnetic layers with moments M, neglecting interlayer exchange, should be written in the form

$$E = -HM\cos(\theta - \theta_H) + 2\pi M^2 \cos^2\theta - K_1 \cos^2\theta - K_2 \cos^4\theta. \quad (1)$$

Here the first term takes account of the Zeeman interaction of the magnetic moments with an external field, the second term is the magnetostatic energy, and the last two terms are first- and second-order terms describing the anisotropy energy; θ and θ_H are the angles between the normal to the plane of the layers and the direction of the moments and external field, respectively.

In thin (of the order of 1 nm thick) single-crystal layers of a magnetically ordered metal, including cobalt, uniaxial easy-axis crystal anisotropy with K_1, $K_2 > 0$ occurs because of growth deformations and surface breaking of the symmetry of the atomic environment. Nonetheless, in the absence of a field the layer magnetic moments lie in the plane of the layer because of the substantial magnetostatic energy, i.e. the resulting anisotropy parameter $K_{\text{eff}} = K_A - 2\pi M^2$ and the effective internal field $H_{\text{eff}} = 2K_{\text{eff}}/M$ due to it are negative.

The expressions for the ferromagnetic resonance frequencies are quite simple for field directions $\theta_H = 0$ and $\theta_H = \pi/2$, when $\theta = \theta_H$. For the acoustic mode of oscillations, for which the moments of all layers precess in phase, these frequencies are

$$\omega/\gamma = H_\perp + H_{\text{eff}}, \quad (2)$$

when the field is directed along the normal to the plane, $\theta = \theta_H$, and

$$(\omega/\gamma)^2 = H_\parallel (H_\parallel - H'_{\text{eff}}) \quad (3)$$

when the field lies in the plane of the film. Here $H'_{\text{eff}} = 2K_1/M - 4\pi M$ and γ is the gyromagnetic ratio. In the case (2) the system should be in a saturated ferromagnetic state, i.e., $H_\perp > |H_{\text{eff}}|$.

Since resonance experiments are performed, as a rule, at a fixed frequency, the values of the resonance fields $H_\perp$ and $H_\parallel$ can be used to determine directly the uniaxial anisotropy parameter $K_A = K_1 + K_2$. Its value is determined by the bulk and surface components of the anisotropy

$$K_A = K_v + 2K_{\text{surf}}/d_{\text{Co}}, \quad (4)$$

where the latter is customarily determined per unit thickness of the film. The coefficient 2 takes account of the presence of two interfaces. In turn, the bulk part of the anisotropy is a sum of the magnetocrystalline (K_c) and magnetoelastic (K_e) contributions. Thus all anisotropy components, including the components due to the interfaces of the magnetic and nonmagnetic layers, can be studied separately.

When the interlayer exchange interaction is taken into account the free energy (1) must be supplemented by the terms $J_{i,i+1}(\mathbf{M}_i \cdot \mathbf{M}_{i+1})/M_i M_{i+1}$ (i enumerates the layer), where $J < 0$ and $J > 0$ correspond to ferromagnetic and antiferromagnetic interlayer coupling, respectively. For $J < 0$ the exchange term does not appear in the expressions (2) and (3) for the frequencies of the acoustic mode of ferromagnetic resonance.[3] For $J > 0$ the expression (2) for the orientation of the external field $\theta_H = 0$ remains the same. For the orientation $\theta_H = \pi/2$ in weak fields $H < 2H_{\text{exc}} = 2J_{i,i+1}/Md_{\text{Cu}}$ the frequency-field relation for the acoustic mode is linear

$$\omega/\gamma = H_\parallel (1 + H_{\text{eff}}/2H_{\text{exc}})^{1/2} \quad (5)$$

and transforms into the relation (3) for $H > 2H_{\text{exc}}$.

The values of the resonance fields $H_\perp$ and $H_\parallel$ obtained for our series of samples at room temperature are presented in Table I. The working frequency $\nu = 9.685$ GHz corresponds to the ratio $\omega/\gamma = 3.101$ kOe used in calculations; $\gamma = g|e|/2mc$ is the gyromagnetic ratio and the effective g-factor of cobalt is 2.16. These values are used in calculations of the effective internal fields and anisotropy parameters for each sample. The required saturation magnetization of an 8 Å thick cobalt layer ($M = 1350$ G) is taken to be the average value obtained in a number of works[4–7] for several series of Co/Cu multilayer samples with layer thicknesses close to 8 Å.

The computed values of the parameters K_1 and K_2, satisfying the expressions (2) and (3), are also presented in Table I. The behavior of the second anisotropy constant K_2 with $d_{\text{Cu}} = 8-11$ Å is interesting. Here this parameter changes sign, and its modulus can reach values appreciably greater than the average value for the experimental series of samples. Such an anomaly is most likely due to the presence of antiferromagnetic (AF) interlayer exchange coupling in this range of d_{Cu}, as a result of which the dependence of the resonance frequency on the external field in a parallel orientation should be described by the expression (5). The values obtained for the exchange field when analyzing resonance spectra in the AF exchange model for samples with $d_{\text{Cu}} = 8-11$ Å are also presented in Table I. Unfortunately, the limited tuning range of the microwave generator in the 3-cm

TABLE I. Magnetic parameters of Co/Cu (111) multilayers.

d_{Cu}, Å	$H_\perp$, kOe	$H_\parallel$, kOe	$-H_{eff}$, kOe	$-K_{eff}$, 10^6 erg/cm^3	K_A, 10^6 erg/cm^3	K_1 10^6 erg/cm^3	K_2 10^6 erg/cm^3	$2H_{exc}$, kOe
7	8.054	1.245	4.953	3.34	8.11	7.07	1.04	
8	10.4	1.5	7.299	4.93	6.52	8.12	−1.6	2.23
9	10.414	1.582	7.313	4.94	6.51	8.41	−1.9	2.58
10	9.636	1.35	6.535	4.11	7.04	7.54	−0.5	1.52
11	9.782	1.25	6.681	4.51	6.94	7.09	−0.15	1.3
12	8.533	1.246	5.432	3.67	7.78	7.07	0.71	
13.5	10.0	1.123	6.899	4.66	6.79	6.42	0.37	
15	8.836	1.309	5.735	3.87	7.58	7.36	0.22	
17	9.0	1.245	5.899	3.98	7.47	7.07	0.4	
19	8.81	1.28	5.709	3.85	7.6	7.23	0.37	

Note: The volume anisotropy $K_v = K_A - 2.5 \cdot 10^6 \text{erg/cm}^3$.

range and the substantial width of the resonance line made it impossible to perform a detailed investigation of this linear section of the frequency-field relations.

The anisotropic contributions can be separated, in accordance with the expression (4), by taking account of the surface anisotropy. The value of this parameter has been obtained in a number of experiments for various cobalt-based multilayer structures.[4,5,8,9] It has been established that this value is determined mainly by the interface materials, and its dependence on the crystalline structure, orientation, thickness, and mechanism of growth of the layers introduces a substantial variance in the experimental results. For our Co/Cu system the average value $K_{surf} = 0.1$ erg/cm^2, obtained in Refs. 4, 5, 8, and 9 for samples with close parameters of the layers, was used to obtain estimates. It is much lower than in Co/Mn or Co/Pd systems, where $K_{surf} \approx 0.5$ erg/cm^2.[10,11]

The volume anisotropy K_v depends strongly on the crystalline perfection of the magnetic layers and their interfaces. Many experiments where K_v was determined give a substantial variance in the values,[4,5,8–14] explained either by the presence of an uncontrollable hcp impurity phase, where the value of K_v is much larger,[15,16] in the main fcc phase or by the influence of magnetoelastic stresses. Figure 1a shows the values of K_A which correspond to our values of the parameters M and K_{surf} and depend nonmonotonically on the thickness of the nonmagnetic copper layer with minima near 8.5, 11.5, 13.5, and 17.5 Å. Figures 1b and 1c also show the dependences of the resonance linewidth, the magnetoresistance $\Delta\rho_\parallel^-$, and the resistance $\rho_s^\parallel$ in the saturation state (in a field $H = 15$ kOe parallel to the current) of the experimental samples on the thickness of the copper interlayers.[2] All dependences show an oscillatory character with clearly coinciding extrema, which shows that they are all formed by the same mechanism.

4. DISCUSSION

It is well known that multilayer systems can manifest property periodicity as a function of the thickness of a nonmagnetic interlayer.[1] Ordinarily, this is attributed to a change in the character of the interlayer exchange coupling in the multilayer system. This dependence is oscillatory with amplitude decreasing and the sign of the interaction alternating as the thickness of the interlayer increases. Such dependences can be investigated using three-layer structures, where optical and acoustic magnetic resonance modes are observed, and the relative arrangement of the modes determines the magnitude and sign of the interlayer exchange.[17] In a number of other experiments the nonmagnetic interlayer was made in the form of a wedge, which made it possible to track smoothly, using magnetooptic methods, the change in the interlayer exchange over the thickness of the wedge.

It can be regarded as established that for a Co/Cu (111) system the first region of antiferromagnetic exchange lies in the copper layer thickness range $d_{Cu} = 5–12.5$ Å,[18,21–23] where the exchange parameter at the maximum reaches $J \sim 0.5$ erg/cm^2.[21,22] When the samples are obtained under not very good vacuum conditions (as in our case) this value can be $J \sim 0.15$ erg/cm^2. Here the exchange field $2H_{exc} = 2J_{i,i+1}/Md_{Cu}$, appearing in the expression (5), can be 2.8 kOe, which agrees well with our experimentally obtained values in samples with $d_{Cu} = 8–11$ Å for the AF coupling model adopted. The next AF maximum of much smaller magnitude lies in the range $d_{Cu} = 18–32.5$ Å, which falls outside the thickness range of our series of samples. We note that the maximum negative value of K_2 from Table I occurs at $d_{Cu} = 9$ Å, which is the most often encountered value for the position of the first AF maximum (for the Co/Cu (111) samples prepared by magnetron sputtering[23] the maximum was observed at $d_{Cu} = 7$ Å). Analysis of the magnetoresistance curves of our samples[2] also shows that within the lim-

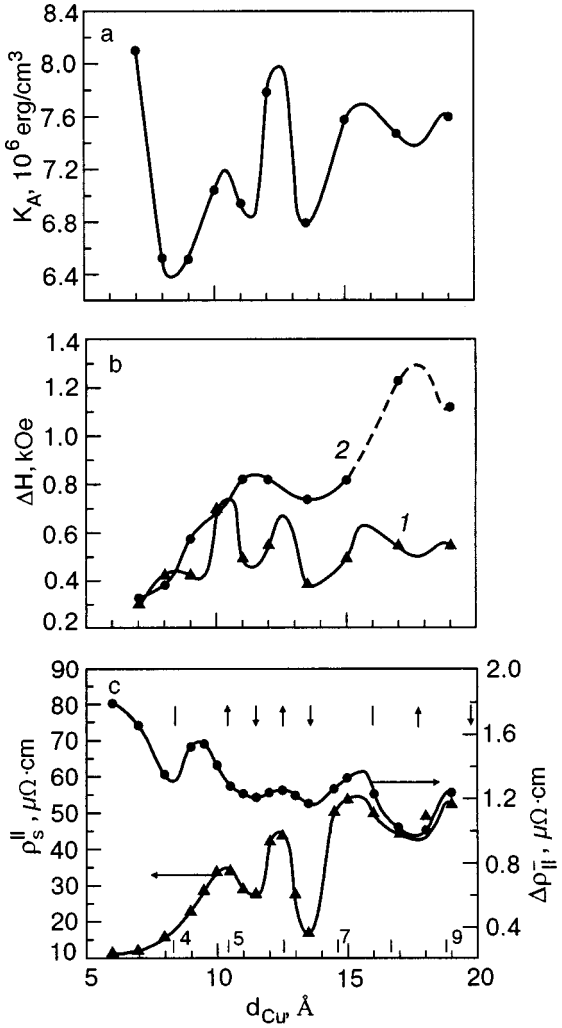

FIG. 1. Magnetic anisotropy K_A (a), width of the resonance line in a magnetic field directed parallel (1) and perpendicular (2) to the plane of the samples (b), resistivity $\rho_s^{\parallel}$ of Co/Cu multilayers in a saturation state in a magnetic field $H=15$ kOe parallel to the current, and $\Delta\rho_{\parallel}^{-}=\rho_{\parallel}(H=0)-\rho_s^{\parallel}$ as functions of the thickness d_{Cu} of the copper interlayers (c). The solid lines show the supposed behavior of K_A and $\Delta H_{\perp,\parallel}$ as functions of d_{Cu}. The behavior of $\Delta H_{\perp}$ for $d_{\mathrm{Cu}}>15$ Å could be different from the expected behavior (dashed line). The vertical tics mark the values of $d_{\mathrm{Cu}}=nd_{(111)}$, where n is an integer and $d_{(111)}=2.087$ Å is the distance between the Cu (111) planes. The upward and downward pointing arrows and the vertical tics indicate the positions of the maxima, minima, and inflection points of the relative magnetoresistance $(\Delta R/R_s)_{\parallel}(d_{\mathrm{Cu}})$ (see Ref. 2).

its noted above there are two regions of AF interaction.

Another reason for the oscillatory behavior of the properties of the samples in our experimental series could be nonmonotonic variations in the structure and geometry of the interfaces between the layers. In general the boundaries should be step-like. The boundary roughness contribution to the anisotropy is ordinarily expressed as the ratio of the standard deviation σ of the experimental surface from an ideal flat plane to the average size ξ of the flat areas. In the literature a number of models have been proposed in the literature for analyzing the dependence of the properties of layered and multilayered systems on the value of the ratio σ/ξ.[24–26] It has been shown that a large contribution should be expected for the magnetoelastic part because of the quite high magnetostriction constants of cobalt.[24] Roughness makes an appreciable contribution to the magnetization of ferromagnetic layers and to the magnetocrystalline and surface components of the anisotropy (the experimental results from a study of the effect of steps on the anisotropy of Co/Cu (001) films and the corresponding literature can be found in Ref. 32 r32).[24–31]

Analysis of the oscillations of the resistance and magnetoresistance of our samples showed that the oscillations of the exchange interaction of the layers and interface roughness occur in our structures and result in the observed behavior of the magnetoresistance properties.[2] Evidently, these same factors give rise to oscillations of the magnetic anisotropy and resonance linewidth $\Delta H_{\parallel}$ which are synchronized with the resistance and magnetoresistance oscillations. The maxima and minima of K_A correspond to the maxima and minima of $\rho_s^{\parallel}$, which occur with the largest and smallest roughness of the interfaces between the layers.

The results of investigations of the effect of boundary roughness on the magnetic parameters of layered systems, resulting in short-period (in one monolayer) oscillations of the parameters, are described in the literature. For example, in Ref. 33 oscillations of step-induced magnetic anisotropy with a period of 1 Co monolayer, which, undoubtedly, is due to the layerwise growth of the Co film and the periodic change in its surface roughness which depends on it, were observed for Co films on a Cu (100) single crystal with a system of oriented steps. Oscillations of the coercive force with a period of 1 Pd monolayer were observed for Fe/Pd (100) multilayers.[34] These oscillations are probably due to the corresponding oscillations of the magnetic anisotropy. Our results qualitatively agree with these data.

In summary, interface roughness has a large effect on the formation of the integral parameters of magnetic layers, determining the internal effective field H_{eff}. Consequently, roughness should also be expected to be manifested in the average value of the nonuniformities of these parameters, to which the width of the magnetic resonance line is very sensitive. The width $\Delta H(\omega)$ of the resonance line is usually represented in the form

$$\Delta H(\omega)=\Delta H(0)+1.16\frac{\omega}{\gamma}\frac{G_{\mathrm{eff}}}{\gamma M}. \tag{6}$$

Here the first term is due to magnetic nonuniformities, and consequently, by its very nature, it is associated with the defect structure of the samples. The second term in this expression depends on the frequency and describes the so-called ''magnetic viscosity'' of a system with an effective Gilbert parameter G_{eff}.

It is well known[35] that the contribution of nonuniformities to the broadening of the resonance line in multilayer films can be represented in the form

$$\Delta H_{\mathrm{inhom}}=|\partial H_{\mathrm{res}}/\partial\theta_H|\Delta\theta_H+|\partial H_{\mathrm{res}}/\partial H_{\mathrm{eff}}|\Delta H_{\mathrm{eff}}, \tag{7}$$

where H_{res} is the resonance field at a fixed frequency, which depends on the orientation of the field; $\Delta\theta_H$ is the spread of the orientations of the crystallographic axes on different sections of the film; and, ΔH_{eff} is the nonuniformity of the effective field in the sample. The second term in Eq. (7) should make the largest contribution to the linewidth when the field is oriented in a direction normal to the plane. Ac-

cording to Fig. 1b, for our series of samples the substantial oscillations of the linewidth are observed precisely to this orientation of the magnetic field.

The second term in the expression (6) can also be sensitive to interface roughness. The Gilbert parameter G_{eff} in general includes a ''intrinsic'' part and a part due to the defect structure of the films. Recent theoretical studies (see the review of these works in Refs. 36 and 37) have shown that for thin ferromagnetic layers surrounded on both sides by films of a nonmagnetic metal the mechanism of electron transport of the moment from the ferromagnet into the nonmagnetic layers followed by dissipation of the moment as a result of spin-flip scattering makes a very large contribution to the value of G_{eff}.[37] The following circumstance can attest to the importance of this mechanism of the formation of the resonance linewidth for our system. According to Fig. 1, for a magnetic field parallel to the film the maxima and minima of the roughness and $\rho_s^{\parallel}$ correspond to the maxima and minima of $\Delta H_{\parallel}$. The oscillations of the function $\Delta H_{\parallel}(d_{\text{Cu}})$ gradually decay with increasing d_{Cu}, and this function, apparently, becomes constant for $d_{\text{Cu}} > 20$ Å or slowly increases, while the function $\Delta H_{\perp}(d_{\text{Cu}})$ increases nonmonotonically with increasing d_{Cu}. In the theory of Ref. 36 the increase of the Gilbert constant ΔG_{eff} because of the electronic mechanism of dissipation of the moment in films of a nonmagnetic metal surrounding a ferromagnet is proportional to $\ln(D/a)$, where D is the thickness of the nonmagnetic films and a is the interlayer separation in a direction the normal to the film (in our case $d_{(111)} = 2.087$ Å). Then for $d_{\text{Cu}} = 19$ Å and $d_{\text{Cu}} = 7$ Å the ratio of the corresponding logarithms is 1.825. If the contribution of the defect structure to G_{eff} can be neglected and it can be assumed that $\Delta H(0) = 0$, then the ratio of $\Delta H_{\parallel}(\omega, d_{\text{Cu}})$ for $d_{\text{Cu}} = 19$ Å and $d_{\text{Cu}} = 7$ Å will be 1.817, which is virtually equal to the ratio of the logarithms $(d_{\text{Cu}}/d_{(111)})$. Consequently, for this orientation of the field it is very likely that the electronic mechanism of dissipation of the moment in the nonmagnetic interlayers is the main mechanism. For field orientation perpendicular to the film the ratio of the values of $\Delta H_{\perp}(\omega, d_{\text{Cu}})$ is 3.42, which is almost two times greater than the ratio of the corresponding logarithms $(d_{\text{Cu}}/d_{(111)})$. Consequently, for this field orientation $\Delta H_{\perp}(\omega, d_{\text{Cu}})$ clearly increases more rapidly with increasing d_{Cu} and structural defects, especially grain boundaries, passing along the normal to the layers through the entire thickness of the multilayers (see Ref. 2 for details), probably play the main role here in broadening of the resonance line.

In conclusion, it should be noted that the contributions described by the expression (6) to the width of the resonance line can be separated by investigating the frequency dependence of the linewidth. In combination with an analysis of the angular dependences of the resonance field and linewidth this will make it possible to make a quantitative determination of all parameters determining homogeneous and inhomogeneous broadening processes in our system. Such investigations are now in progress.

5. CONCLUSIONS

The results of these investigations of the magnetoresonance and magnetoresistance properties of a series of samples from the system $[\text{Co}(8\text{ Å})/\text{Cu}(d_{\text{Cu}})]_{20}$ demonstrate oscillatory dependences, which have much in common with one another, on the thickness of the copper layers d_{Cu} with a characteristic step of 1–2 copper monolayers. This shows that the same mechanism is responsible for the formation of these dependences. Such structures with nominally identical (over the thickness) crystal structure and conditions of growth of epitaxial layers of the ferromagnetic metal exhibit an appreciable difference in the magnetic anisotropy parameters, the width of the resonance line, and the magnetoresistance as functions of the thickness of the nonmagnetic interlayer. Since interlayer diffusion is minimal in this system (as is indicated by the fact that the properties of the samples, including the resistance, remain unchanged for several years), the observed behavior of the system must be attributed to the roughness of the interfaces separating the layers of magnetic and nonmagnetic metals.

This work was supported by the Ukrainian National Academy of Sciences as part of the program ''Nanostructure systems, nanomaterials, and nanotechnologies'' under grant No. 3-026/2004.

*E-mail: aanders@ilt.kharkov.ua
**E-mail: zorch@kpi.kharkov.ua

[1] R. E. Camley and R. L. Stamps, J. Phys.: Condens. Matter **5**, 3727 (1993).
[2] V. V. Zorchenko, A. N. Stetsenko, A. G. Anders, and K. V. Kut'ko, Fiz. Nizk. Temp. [Low Temp. Phys.] (in press).
[3] P. E. Wigen and Z. Zhang, Braz. J. Phys. **22**, 267 (1992).
[4] F. J. A. Broeder, W. Hoving, and P. J. H. Bloemen, J. Magn. Magn. Mater. **93**, 562 (1991).
[5] L. Albini, G. Carlotti, G. Gubbiotti, L. Pareti, and G. Turilli, J. Magn. Magn. Mater. **198–199**, 363 (1999).
[6] T. R. McGuire, J. M. Harper, C. Cabral, Jr., and T. S. Plaskett, J. Appl. Phys. **76**, 6601 (1994).
[7] H. Holloway and D. J. Kubinski, *ibid.* **83**, 2705 (1998).
[8] Z. S. Shan, S. Nafis, J. Woollam, S. H. Liou, and D. J. Sellmyer, J. Appl. Phys. **73**, 6347 (1993).
[9] C. Gao and M. J. O'Shea, *ibid.* **69**, 5304 (1991).
[10] K. Ounadjela, Y. Henry, M. Farle, and P. Vennegues, J. Appl. Phys. **75**, 5601 (1994).
[11] B. N. Engel, C. D. England, R. A. Van Leeuwen, M. H. Wiedmann, and C. M. Falco, Phys. Rev. Lett. **67**, 1910 (1991).
[12] C. D. England, W. R. Bennett, and C. M. Falco, J. Appl. Phys. **64**, 5757 (1988).
[13] H. He, C. H. Lee, F. J. Lamelas, W. Vavra, D. Barlett, and R. Clarke, J. Appl. Phys. **67**, 5412 (1990).
[14] H. Awano, O. Taniguchi, T. Katayama, F. Inoue, A. Itoh, and K. Kawanishi, J. Appl. Phys. **64**, 6107 (1988).
[15] W. Sucksmith and J. E. Thompson, Proc. R. Soc. London, Ser. A **225**, 362 (1954).
[16] J. A. Wolf, I. I. Krebs, and G. A. Prinz, Appl. Phys. Lett. **65**, 1057 (1994).
[17] B. Heinrich, J. F. Cochran, M. Kowalewski, J. Kirschner, Z. Celinski, A. S. Arrott, and K. Myrtle, Phys. Rev. B **44**, 9348 (1991).
[18] A. J. R. Ives, R. J. Hicken, J. A. C. Bland, C. Daboo, M. Gester, and S. J. Gray, J. Appl. Phys. **75**, 6458 (1994).
[19] Z. Q. Qiu, J. Pearson, and S. D. Bader, Phys. Rev. B **46**, 8659 (1992); J. Appl. Phys. **73**, 5765 (1993).
[20] M. T. Johnson, S. T. Purcell, N. W. E. McGee, R. Coehoorn, J. aan de Stegge, and W. Hoving, Phys. Rev. Lett. **68**, 2688 (1992); P. J. H. Bloemen, R. van Dalen, W. J. M. de Jonge, M. T. Johnson, and J. aan de Stegge, J. Appl. Phys. **73**, 5972 (1993); P. J. H. Bloemen, M. T. Johnson, M. T. H. van de Vorst, R. Coehoorn, J. J. de Vries, R. Jungblut, J. aan de Stegge, A. Reinders, and W. J. M. De Jonge, Phys. Rev. Lett. **72**, 764 (1994).
[21] M. T. Johnson, R. Coehoorn, J. J. de Vries, N. W. E. McGee, J. aan de Stegge, and P. J. H. Bloeman, Phys. Rev. Lett. **69**, 969 (1992).

[22] A. Schreyer, K. Brohl, J. F. Ankner, C. F. Majkrzak, Th. Zeidler, P. Bodeker, N. Metoki, and H. Zabel, Phys. Rev. B **47**, 15334 (1993).
[23] M. J. Hall, B. J. Hickey, M. A. Howson, M. J. Walker, J. Xu, D. Greig, and N. Wiser, Phys. Rev. B **47**, 12785 (1993); M. A. Howson, B. J. Hickey, J. Xu, D. Greig, and N. Wiser, *ibid.* **48**, 1322 (1993).
[24] P. Bruno and J.-P. Renard, Appl. Phys. A: Solids Surf. **49**, 499 (1989).
[25] P. Bruno, J. Appl. Phys. **64**, 3153 (1988).
[26] Ching-Ray Chang, J. Appl. Phys. **72**, 596 (1992).
[27] H. P. Oepen, C. M. Schneider, D. S. Chuang, C. A. Ballentine, and R. C. O'Handley, J. Appl. Phys. **73**, 6186 (1993); P. Krams, B. Hillebrands, G. Güntherodt, and H. P. Oepen, Phys. Rev. B **49**, R3633 (1994).
[28] D. S. Chuang, C. A. Ballentine, and R. C. O'Handley, Phys. Rev. B **49**, 15084 (1994).
[29] B. Schulz and K. Baberschke, Phys. Rev. B **50**, 13467 (1994).
[30] W. Weber, R. Allenspach, and A. Bischof, Appl. Phys. Lett. **70**, 520 (1997).
[31] R. E. Kawakami, E. J. Escorcia-Aparicio, and Z. Q. Qiu, Phys. Rev. Lett. **77**, 2570 (1996).
[32] R. E. Kawakami, M. O. Bowen, H. J. Choi, E. J. Escorcia-Aparicio, and Z. Q. Qiu, Phys. Rev. B **58**, R5924 (1998).
[33] W. Weber, C. H. Back, A. A. Bischof, Ch. Wursch, and R. Allenspach, Phys. Rev. Lett. **76**, 1940 (1996).
[34] J. R. Childress *et al.*, J. Magn. Magn. Mater. **130**, 13 (1994).
[35] C. Chappert, K. Le Dang, P. Beauvillain, H. Hurdequint, and D. Benard, Phys. Rev. B **34**, 3192 (1986).
[36] E. Simanek and B. Heinreich, Phys. Rev. B **67**, 144418 (2003).
[37] D. L. Mills, Phys. Rev. B **68**, 014419 (2003).

Translated by M. E. Alferieff